THE STRUCTURAL AND METAMORPHIC EVOLUTION OF THE HIGH HIMALAYAN SLAB IN SE ZANSKAR AND NW LAHAUL

Thesis submitted for the degree of Doctor of Philosophy
to the University of Oxford

by

James David Walker B.Sc. (Hons.) Leicester

Michaelmas Term 1998

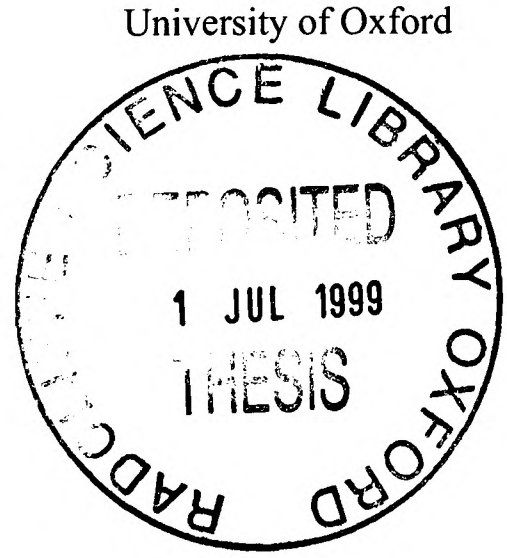


University College

and

Department of Earth Sciences

University of Oxford





Photograph of an Indian road sign (taken during fieldwork in NW Lahaul, near the village of Udaipur). Little did I know at the time how apt this photograph would prove to be...

ACKNOWLEDGEMENTS

There are many people to whom I must extend an enormous amount of gratitude for their assistance in helping me complete this D. Phil. Initial thanks should go to Drs. Mike Searle and Dave Waters, who, in conceiving this project and putting their faith in my abilities, provided me with a once in a lifetime opportunity to spend eight months of my life living and working in a remote part of the Indian Himalaya. Thanks to them, I have experienced the privileges of an Oxford education, as well as the perils of Indian bus driving and the discomfort of 'Delhi belly'.

Accepting this project was a somewhat selfish gesture and special thanks must go to Antoinette, whose love, encouragement and unerring support has kept me going through good times and bad. The same gratitude is extended to my parents, sister, close family and friends, without whom this thesis may never have been finished. Peter Hildebrand deserves a special mention in this respect for his patience and words of wisdom which have kept me going during the final stages of this work. Rest assured that successful completion of this thesis marks the end of my student career and that I now intend to start life in what many of you have constantly referred to as a 'proper job'.

There are many people who will unfortunately never have the opportunity to read these acknowledgements, but deserve a special mention nonetheless. They are of course the locals, porters, cooks, guides and pony-men who provided gracious hospitality and skilfully guided me through the Himalaya, tending to my every need. Ashok Chandra and family, Vineet Khana, Baldip, Pieray Lal, Tik-Ram, Manoo, Amin Zanskari, Fida Hussein and Ali Hussein are singled out for their friendship and loyalty. In addition, I would also like to thank those people who dared to spend extended periods of time with me in the field, braving the confines of a two-man tent and a diet of dhal, curried cabbage and boiled eggs. I am pleased to say that Louise Purton, Alasdair MacDonald, Ben Stephenson and Steve Frankland were marvellous field companions and remain good friends with whom I share many fond memories.

Thanks must also go to the countless technical and administrative staff who have helped contribute to this thesis. This includes: Norman Charnley (for persuading the electron microprobe to work every other Thursday), Richard McAvoy (for looking after the films I gave him three years ago), Roy Goodwin, Steve Wyatt, Keith Parish, Steve Usher, Steve Baker, Jeremy Hyde, Phil Jackson, Sally Thompson, Diana Relton and John O'Sullivan. In addition to those people here at Oxford, special thanks is extended to Sam Bowring and Kip Hodges for providing me with the opportunity to use the U-Pb and $^{40}Ar/^{39}Ar$ facilities at the Massachusetts Institute of Technology (M.I.T.), Boston, USA. Mark Martin, Kathy Davideck, Mike Krol and Bill Oszewski are also thanked for their invaluable assistance in preparing and running my samples. Audrey Huerta is thanked for providing me with a place to live during my two month stay in Boston.

NERC grant GT4/94/235/G is gratefully acknowledged, as are the many other sources of funding which have helped make this thesis possible. These include additional monies provided by NERC, the Burdett-Coutts fund and University College.

THE STRUCTURAL AND METAMORPHIC EVOLUTION OF THE HIGH HIMALAYAN SLAB IN SE ZANSKAR AND NW LAHAUL

Thesis submitted for the degree of Doctor of Philosophy to the University of Oxford

by
James David Walker BSc Hons. (Leicester)
Department of Earth Sciences
&
University College

Michaelmas Term 1998

ABSTRACT

This thesis attempts to unravel the complex thermal and structural history of part of the High Himalayan Slab in NW India and combines reconnaissance-style field structural mapping of an area covering ~10,000 km^2 with petrography, microstructural analysis, thermobarometry and geochronology techniques.

The results of this work show that the oldest protoliths of the High Himalayan Slab are at least Cambrian in age and that they may have experienced a major pre-Himalayan metamorphism at *c.*500 Ma. The youngest protoliths are Mesozoic in age (the Tandi Group) and demonstrate that the High Himalayan Slab represents the metamorphosed equivalents of the Tibetan Sedimentary Series. Metamorphism was achieved via substantial crustal shortening and thickening following the India-Asia collision at 50-54 Ma ago. Phase relationships demonstrate that metamorphism was a regional Barrovian-type event associated with the growth of biotite-, garnet-, staurolite-, kyanite- and sillimanite-bearing assemblages in metapelites. Quantitative thermobarometry demonstrates that near-peak conditions of *c.*6-8 kbar and 550-650°C were attained in the deepest exposed levels. Growth of metamorphic assemblages was underway by at least 30 Ma, as indicated by U-Pb ages of metamorphic monazites.

Exhumation of the High Himalayan Slab was achieved through a combination of extensional unroofing along major detachments (namely the Zanskar Shear Zone), thermal doming, thrusting along the Main Central Thrust and surface erosion. Exhumation is closely associated with the growth of sillimanite- and cordierite-bearing assemblages in pelites and the generation and emplacement of crustal melt leucogranites in the upper parts of the slab. U-Pb dating of accessory phases from one of the crustal melt leucogranites (the Gumburanjon leucogranite) constrains its crystallisation and emplacement age at *c.*21-22 Ma. This is only slightly older than its $^{40}Ar/^{39}Ar$ muscovite and biotite cooling ages of *c.*20-21 Ma, which is attributed to the emplacement of the Gumburanjon leucogranite into the immediate footwall of the ZSZ. Field and geochronological data therefore support a strong temporal and spatial relationship between upper crustal melting and extension in a convergent orogen.

THE STRUCTURAL AND METAMORPHIC EVOLUTION OF THE HIGH HIMALAYAN SLAB IN SE ZANSKAR AND NW LAHAUL

Thesis submitted for the degree of Doctor of Philosophy to the University of Oxford

by
James David Walker BSc Hons. (Leicester)
Department of Earth Sciences
&
University College

Michaelmas Term 1998

EXTENDED ABSTRACT

The High Himalayan Slab (also commonly known as the Tibetan Slab or the Greater Himalayan sequence), refers to the zone of Indian plate metasediments, orthogneisses, paragneisses and crustal melt leucogranites which are bounded between the South Tibetan Detachment (STD) system of normal faults and the Main Central Thrust (MCT). It extends for ~2500 km along the entire length of the Himalayan orogen and was formed by the burial and subsequent exhumation of the Indian plate margin following the India-Asia collision some 50-54 Ma. This thesis presents new lithological, structural and metamorphic maps of the High Himalayan Slab in SE Zanskar and NW Lahaul, together with new microstructural, thermobarometric, geochemical and geochronological data which are used to elucidate the pre-, syn- and post-collisional history of this part of the Himalaya. Unlike many other parts of the High Himalayan Slab, over 25 km of crustal section is exposed between the MCT and STD in SE Zanskar and NW Lahaul. This permits a detailed examination of the structural and metamorphic processes which operated at progressively deeper structural levels during continent-continent collision.

The thesis is divided into eight chapters, the first two of which provide an introduction to the tectonic framework of the Himalaya and a synthesis of previous geological studies in the High Himalayan Slab respectively. Chapters 3 gives a regional geological overview of the structure, lithology and metamorphism in the High Himalayan Slab of SE Zanskar and NW Lahaul, paying particular attention to lithological descriptions of the metamorphic protoliths. Chapters 4-6 describe the structural and metamorphic evolution in different parts of the slab, whilst Chapter 7 presents new U-Pb and $^{40}Ar/^{39}Ar$ data from metamorphic and magmatic samples collected from different structural positions within the slab. Chapter 8 summarises this work and presents a model for the structural and metamorphic evolution in this part of the Himalaya.

The results of this work demonstrate that the metasedimentary protoliths of the High Himalayan Slab in SE Zanskar and NW Lahaul consist of a 3-5km-thick succession of unfossiliferous sands, silts and shales which were deposited in an extensive sedimentary basin during the Precambrian/Cambrian. These sediments are collectively referred to as the Haimantas and are tentatively correlated with similar sediments in the Tibetan Sedimentary Series of SE Zanskar. They are discordantly intruded

by a number of large, megacrystic granites of purported Precambrian-Ordovician age, suggesting that the protoliths of the slab may have experienced a major pre-Himalayan tectonic event. The possibility that some of these granites represent the crystalline basement upon which the Haimantas were deposited cannot be unequivocally ruled out from the available field evidence, but seems unlikely given the occurrence of hornfelsed and discordant contacts along some of the granite margins.

Field and microstructural observations failed to establish whether all of the deformation in the High Himalayan Slab is Himalayan in age. Given the Precambrian/Cambrian age of the Haimantas and the fact that they are discordantly intruded by large granites suggests that these sediments probably experienced some sort of pre-Himalayan deformation and metamorphism. This is supported by geochronological data presented in Chapter 7, which demonstrate that metamorphic monazite growth occurred at *c.*500 Ma in the Haimantas in different parts of the slab. Whilst this could be related to a regional Barrovian-type metamorphism, it could equally be interpreted to reflect localised monazite growth in contact aureoles. The available data cannot distinguish between these two possibilities.

Following the India-Asia collision some 50-54 Ma ago, the protoliths of the High Himalayan Slab in SE Zanskar and NW Lahaul experienced a polyphase deformation history associated with the progressive burial and subsequent exhumation of this metamorphic terrane. The net result of this was to create a ~70-100-km-wide zone of chlorite- to sillimanite-grade lithologies which are structurally bounded along the base by the Main Central Thrust (MCT) and along the top by the Zanskar Shear Zone (ZSZ), a local equivalent of the South Tibetan Detachment system. Deformation was extremely heterogeneous across the slab and it is virtually impossible to correlate structural fabrics and stages of metamorphic mineral growth from one region to another from field and microstructural observations alone.

Burial of the High Himalayan Slab was associated with intense crustal shortening and thickening, which was largely achieved by multiple generations of tight to isoclinal folding. The kinematics associated with crustal shortening and thickening in the upper part of the slab are poorly constrained. Metamorphic grade is observed to increase towards the north, suggesting the possibility that burial was achieved by overthrusting of the Tibetan Sedimentary Series towards the SW along a major thrust, which may have been a precursor to the ZSZ. At the base of the slab, the earliest stage of deformation (D_1) is characterised by a major phase of NE-directed isoclinal folding, which led to the development of the NE-facing Tandi Syncline. Similar NE-facing folds can be traced along strike into the western part of the study area (the Chamba Syncline), suggesting that NE-directed deformation was developed on a regional scale in this part of the Himalaya. The unusual facing direction of these folds cannot be reconciled with classic Himalayan models which show that deformation in the High Himalayan Slab propagated down structural section towards the SW through time. The development of the Tandi Syncline is therefore attributed to a major phase of backfolding, which may have been controlled by the distribution of rigid crustal blocks within the High Himalayan Slab (i.e. the large, megacrystic Precambrian/Ordovician granites). In the Chamba Syncline, NE-

facing folds become progressively more upright towards the south and eventually give way to SW-facing folds, suggesting that this part of the slab may be located within a major pop-up zone. This interpretation also explains why sediments within the Chamba Syncline have not been metamorphosed beyond chlorite-grade conditions.

Beneath the Tandi Syncline, fold structures are consistently overturned towards the SW, suggesting that the NE-facing D_1 deformation was overprinted by a subsequent phase of top-to-the-south-west directed folding (D_2). The change in polarity of deformation is attributed to the increasing ductility of rocks at higher metamorphic grades. D_2 deformation is associated with the development of a large nappe-like structure (the Phojal-Kallath megafold), which is located immediately above the projected level of the MCT at the base of the slab. This is a syn-metamorphic structure which is interpreted to have developed immediately prior to the main phase of thrusting along the MCT.

Growth of typical Barrovian-type metamorphic assemblages is related to the prograde thermal history (M_1) of the slab, which reached conditions of 6-8 kbar and 550-650°C in the deepest exposed levels. $^{40}Ar/^{39}Ar$ cooling ages of metamorphic muscovite from these regions demonstrates that peak-metamorphic conditions were attained prior to *c.*22 Ma. Metamorphic monazite from the upper and lower parts of the slab record $^{207}Pb/^{235}U$ ages of *c.*29 Ma and *c.*32 Ma respectively. Given the fact that monazite is not especially prone to Pb-loss, these ages are interpreted to reflect new monazite growth at temperatures in excess of *c.*500°C. However, whether this growth occurred during the prograde P-T pathway, or whether it reflects near-peak conditions remains uncertain. The possibility that these results reflect an age-averaging of growth zoned monazite cannot be ruled out.

In deeper structural levels, temperatures were sufficiently high to promote *in situ* migmatisation of sillimanite-grade pelitic schists, leading to the generation of crustal melt leucogranites. Crustal melting is closely associated with the growth of sillimanite- and cordierite-bearing assemblages and is attributed to an M_2 metamorphic stage, which post-dated the growth of garnet-, staurolite- and kyanite-bearing assemblages during the M_1 metamorphic stage. It should be stressed, however, that both M_1 and M_2 form part of a continuously evolving metamorphic event, with no evidence to support a period of cooling between them. U-Pb dating of accessory phases from one of the crustal melt leucogranites (the Gumburanjon leucogranite) constrains its crystallisation and emplacement age at *c.*21-22 Ma. This is considerably younger than the *c.*30 Ma ages recorded by the metamorphic monazite data and suggests that peak-metamorphism in the High Himalayan Slab may have spanned several million years. M_2 metamorphism is related to decompression of the High Himalayan Slab under high temperature conditions and is associated with the development of large-scale metamorphic domes which are flanked by extensional detachments, namely the Zanskar Shear Zone (ZSZ) and Miyar Fault Zone (MFZ).

Exhumation of the High Himalayan Slab was achieved through a combination of extensional unroofing along major detachments (namely the ZSZ and possibly the MFZ), thermal doming, thrusting along the Main Central Thrust and surface erosion. Comparisons of metamorphic grade either side of the ZSZ suggest that the throw across this fault is in the order of *c.*20 km. Simple

angular relationships imply that rocks exposed in the footwall were once located ~35-55km to the north of their current position. Extension is believed to have been an extremely rapid process which occurred between *c.*23-20 Ma. This is based on field and geochemical data which highlight a strong temporal and spatial link between extensional deformation and granite generation/emplacement, and geochronological data which are indicative of rapid chilling in the footwall of the ZSZ at this time. Indeed, the U-Pb crystallisation age of the Gumburanjon leucogranite (21-22 Ma) is only slightly older than its $^{40}Ar/^{39}Ar$ muscovite and biotite cooling ages of *c.*20-21 Ma, a feature which is attributed to the emplacement of the Gumburanjon leucogranite into the immediate footwall of the ZSZ.

Movement along the ZSZ between *c.*23-20 is broadly synchronous with movement along the MCT, thus implying that the entire High Himalayan Slab was extruded as a metamorphic wedge during the early Miocene. The Himalaya may have reached their maximum elevation at this time. For the past 20 million years, unroofing in the High Himalayan Slab is believed to have been accommodated by limited brittle normal faulting and erosional exhumation.

Table of contents

Chapter 1: Introduction

1.1 Project aims 1
1.2 Thesis outline 2
1.3 Tectonic evolution of southern Asia 2
1.4 Tectonic framework of the Himalaya 3
1.4.1 The Indus-Tsangpo Suture Zone (ITSZ) 4
1.4.2 The Tibetan Sedimentary Series 4
1.4.3 The High Himalayan Slab 4
1.4.4 The Lesser Himalaya 5
1.4.5 The Sub-Himalaya (Siwaliks) 5
1.5 The timing of collision 5
1.6 Crustal shortening mechanisms 6

Chapter 2: The High Himalayan Slab

2.1 Definition of the High Himalayan Slab 8
2.1.1 The Main Central Thrust (MCT) 8
2.1.2 The South Tibetan Detachment system (STD) 9
2.1.3 Metamorphic protoliths 9
2.2 Previous quantitative P-T-t studies 10
2.2.1 Bhutan 11
2.2.2 Eastern Nepal (Everest and Makalu) 11
2.2.3 Eastern central Nepal (Langtang) 12
2.2.4 Western-central Nepal (Manaslu) 13
2.2.5 Western-central Nepal (Annapurna) 14
2.2.6 Eastern Garhwal 15
2.2.7 Western Garhwal 16
2.2.8 Western and central Zanskar 16
2.3 Tectonic synthesis: the current state of knowledge 17
2.3.1 Burial and metamorphism in the High Himalayan Slab 18
2.3.2 Origins of inverted metamorphism in the MCT zone 19
2.3.3 Melting in the High Himalayan Slab 20
2.3.4 Exhumation history of the slab 21
2.3.5 Development of normal faults in collisional orogens 22

Chapter 3: The High Himalayan Slab of SE Zanskar and NW Lahaul: a regional geological overview

3.1 Field location and geographical setting 25
3.2 Definition of the High Himalayan Slab in SE Zanskar and NW Lahaul 26
3.3 Previous works 26
3.4 Structural overview 27
3.5 Lithological overview 28
3.5.1 The Precambrian-Cambrian Haimantas and Middle Cambrian Karsha Formation 28
3.5.2 Sediments and stratigraphy of the Chamba Syncline 31
3.5.3 Precambrian-Ordovician granites 34
3.5.4 The Mesozoic Tandi Group 38
3.5.5 Metabasites 41
3.5.6 The High Himalayan Crystallines (HHC) and High Himalayan leucogranites (HHL) 42
3.5.7 Lithological summary 43
3.6 Metamorphic overview 44
3.7 Introduction to Chapters 4-6 45

Chapter 4: Geology of the lower-central slab (the Crystalline Nappe)

4.1 Introduction 46
4.2 Structure of the Crystalline Nappe 46
4.2.1 D_1 deformation (the Tandi Syncline) 47
4.2.2 D_2 deformation (the Phojal-Kallath megafold) 51
4.2.3 D_3 deformation (regional warping of D_1 and D_2 fabrics) 52
4.2.4 D_3/D_4 deformation (dextral transpression?) 53
4.2.5 The MCT zone 54
4.3 Metamorphism in the Crystalline Nappe 55
4.3.1 Metamorphic mineral growth in relation to deformation in metapelites 55
4.3.2 Garnet zoning profiles 57
4.3.3 Mineral chemistry and thermobarometry 59
4.3.4 P-T evolution 61
4.4 Melting/pegmatite formation in the Crystalline Nappe 61
4.5 Summary and discussion 62
4.5.1 Burial of the Crystalline Nappe 63
4.5.2 Exhumation of the Crystalline Nappe 63
4.5.3 Tectonic significance of the NE facing Tandi Syncline 63

Chapter 5: Geology of the western-central slab (the Chamba Syncline and Miyar nala)

5.1 Introduction 65
5.2 Structure of the Chamba Syncline and Miyar nala 65
5.2.1 Deformation to the south of the Kade granite 65
5.2.2 Deformation in the Kade granite 68
5.2.3 Deformation in the Miyar Fault Zone and Kang La Dome 68
5.3 Metamorphism in the Chamba Syncline and Miyar nala 70
5.3.1 Metamorphic mineral growth in the Miyar Fault Zone and Kang La Dome 72
5.3.2 Garnet zoning profiles 75
5.3.3 Mineral chemistry and thermobarometry 76
5.3.4 Melting in the Miyar Fault Zone and Kang La Dome 77
5.3.5 P-T-t evolution in the MFZ and Kang La Dome 78
5.4 Summary 79

Chapter 6: Geology of the upper slab (Darcha-Kargyak)

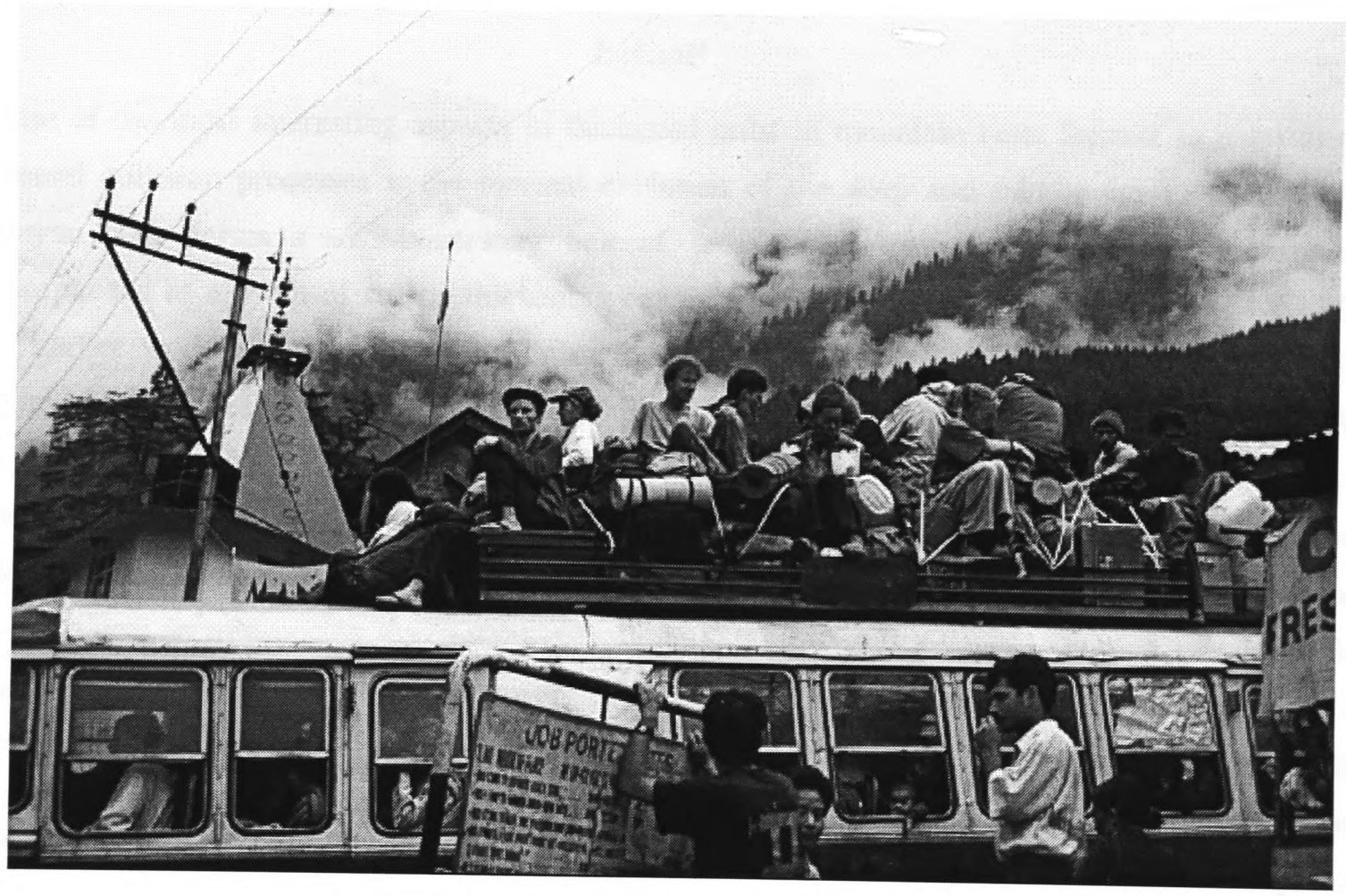
6.1 Introduction 81
6.2 Structural observationsU 81
6.2.1 Contact of the Haimantas with the Kade granite 81
6.2.2 Structure to the south of the Shingo La 82
6.2.3 Structure to the north of the Shingo La 83
6.2.4 The Zanskar Shear Zone 84
6.3 Metamorphism in the ZSZ 87
6.3.1 Metamorphic mineral growth in relation to deformation in metapelites 87
6.3.2 Garnet zoning profiles 89
6.3.3 Mineral chemistry and thermobarometry 90
6.3.4 P-T evolution 92
6.3.5 Estimated throw across the ZSZ 92
6.4 Crustal melting: the Gumburanjon leucogranite 93
6.4.1 Field relationships 93
6.4.2 Phase relationships and geochemistry 94
6.4.3 Generation of the Gumburanjon leucogranite 97
6.4.4 Emplacement of the Gumburanjon leucogranite 100
6.5 Summary and discussion 101

Chapter 7: U-Pb and $^{40}Ar/^{39}Ar$ geochronology
7.1 Introduction 103
7.2 Previous geochronological studies in SE Zanskar and NW Lahaul 103
7.3 Sample choice and location 104
7.4 U-Pb geochronology 105
7.4.1 U-Pb systematics of monazite, xenotime and uraninite 105
7.4.2 Metamorphic age constraints (results and interpretation) 106
7.4.3 Magmatic age constraints (results and interpretation) 109
7.4.4 Summary of the U-Pb data 113
7.5 $^{40}Ar/^{39}Ar$ geochronology 116
7.5.1 Metamorphic $^{40}Ar/^{39}Ar$ results and interpretation (Wak 3, Wak 6, Wak 9) 117
7.5.2 Magmatic $^{40}Ar/^{39}Ar$ results and interpretation (Wak 21, Wak 23, Wak 26 and Wak 27) 118
7.5.3 Summary of the $^{40}Ar/^{39}Ar$ data 119
7.6 Thermal modelling 120
7.6.1 Description of the model 120
7.7 Discussion: crustal melting and extension 123

Chapter 8: Summary and conclusions
8.1 Introduction 125
8.2 Pre-collision history 125
8.3 Syn/post-collisional history 126
8.3.1 Burial history 126
8.3.2 Exhumation history 128
8.4 Regional tectonic implications 129
8.5 Future work 130

REFERENCES 131

APPENDIX A: Mineral chemistry and thermobarometry: methods and techniques 147
APPENDIX B: Averaged mineral analyses used in thermobarometric calculations 151
APPENDIX C: Whole-rock geochemistry: XRF analysis 155
APPENDIX D: Whole-rock Rb-Sr analysis 157
APPENDIX E: U-Pb analytical techniques 159
APPENDIX F: $^{40}Ar/^{39}Ar$ analytical techniques 160



First Class public transport - Himalayan style.

Chapter 1

Introduction

1.1 Project aims

'The structural and metamorphic evolution of the High Himalayan Slab in SE Zanskar and NW Lahaul'

One of the most interesting aspects in thickened crust in mountain belts formed as a result of continental collision processes is the thermal evolution of the deep and middle crust. The High Himalayan Slab forms a ~2500-km-long belt of Indian plate metamorphic rocks which were metamorphosed as a result of crustal thickening caused by the India-Asia collision some ~54-50 Ma ago. Earlier workers in the High Himalayan Slab relied purely on field mapping combined with petrological techniques to elucidate the tectonic history of this metamorphic terrane (e.g. Wadia, 1931; Heim & Gansser, 1939; Gansser, 1964). With the development of experimental petrology and thermobarometry, it became possible to estimate pressures and temperatures associated with different structural levels and thus, quantify the burial and exhumation history of the slab. However, one of the major problems in unravelling the metamorphic and structural evolution of exhumed metamorphic terrains has been our inability to accurately constrain the timing of peak-metamorphism. Whereas U-Pb techniques have been successfully applied to magmatic rocks, the majority of age constraints from metamorphic rocks have tended to be cooling, rather than crystallisation ages, and have relied on $^{40}Ar/^{39}Ar$ and K-Ar techniques, rather than U-Pb or Sm-Nd. Only recently have crystallisation ages of metamorphic rocks been recorded and even then, with limited success (e.g. Smith & Barreiro, 1990; Hodges *et al.*, 1996; Vance & Harris, 1996).

This thesis attempts to unravel the complex thermal and structural history of part of the High Himalayan Slab in NW India and combines reconnaissance-style field structural mapping of an area covering ~10,000 km^2 with petrography, microstructural analysis and thermobarometry. In addition, U-Pb and $^{40}Ar/^{39}Ar$ geochronological techniques have been used on metamorphic and magmatic samples to quantitatively constrain the timing of important thermal events. Thermal models which utilise structural, thermobarometric and geochronological data help to constrain the rates and duration of various structural and metamorphic episodes associated with the burial and exhumation history of the slab.

1.2 Thesis outline

The remainder of this chapter summarises the tectonic evolution of southern Asia and introduces the tectonic framework of the Himalaya - the world's youngest example of a classic continent-continent collision (Dewey & Bird, 1970).

Chapter 2 discusses the geology of the High Himalayan Slab, paying particular attention to previous quantitative P-T-t works along strike.

Chapter 3 introduces the field area in SE Zanskar and NW Lahaul and presents a regional geological overview of the structure, lithology and metamorphism in this part of the High Himalayan Slab.

Chapters 4-6 present more detailed descriptions of the structure and metamorphism in different parts of the study area, paying particular attention to the relationship between sequential fabric development during different phases of deformation and metamorphic mineral growth. New quantitative P-T estimates from different structural levels within the slab are presented in each of these chapters.

Chapter 7 presents new U-Pb and $^{40}Ar/^{39}Ar$ data from different parts of the slab and attempts to interpret these data in terms of crystallisation and cooling ages of major thermal episodes. This chapter also presents simple thermal models which attempt to constrain the timing and duration of important tectono-thermal events.

Chapter 8 is a discussion/summary chapter which synthesises the work presented in Chapters 3-7.

1.3 Tectonic evolution of southern Asia

The Himalaya are the end result of a complex series of collision processes which have recorded the accretion of several allochthonous terranes to the southern margin of Eurasia during the Mesozoic and early Tertiary (Figure 1.1). Major suture zones, which young from north to south, separate each of these terranes (Dewey *et al.*, 1988). This accretion process is attributed to the northward migration of fragmented crustal blocks which were separated from Gondwana during a phase of rifting and continental break-up in the Permian (Sengör, 1985). Palaeogeographic reconstruction of these crustal blocks has been attempted by numerous workers on the basis of palaeontological and lithological comparisons (e.g. Wang & Sun, 1985; Chang *et al.*, 1986; Smith, 1988) and relative plate motions as determined from marine magnetic anomalies (e.g. Molnar & Tapponnier, 1975; Patriat & Achache, 1984; Besse & Courtillot, 1988). Terrestrial palaeomagnetic data form the African, Indian and Eurasian plates place further constraints on the palaeogeographic positioning of individual crustal blocks (e.g. Allègre *et al.*, 1984; Besse *et al.*, 1984; Klootwijk, 1984; Klootwijk *et al.*, 1985, 1992; Besse & Courtillot, 1988; Lin & Watts, 1988; Enkin *et al.*, 1992; Chen *et al.*, 1993). Particular attention has been given to palaeogeographic reconstructions of India relative to Eurasia, largely because of the interest which surrounds the exact timing of collision between these two plates.

Summarised accretion history of southern Asia prior to the India-Asia collision

The Tibetan Plateau - covering an area of approximately 1500,000 km^2 at an average altitude of 5000m - is comprised of at least three tectonic blocks which were successively sutured to the Eurasian margin by the latest Jurassic (Allègre *et al.*, 1984; Chen *et al.*, 1993). At the western end of the plateau, the Karakoram Terrane is believed to be the western extension of the Lhasa block (Figure 1.1), (Searle, 1991). Following accretion of the Karakoram-Lhasa blocks, northward subduction of Neo-Tethys beneath the Eurasian margin developed at *c.*120 Ma (Allègre *et al.*, 1984, Besse & Courtillot, 1988), marking the beginning of ocean closure which culminated in the India-Asia collision ~50-54 Ma ago (see section 1.5).

In the western part of the southern Eurasian margin, the Kohistan-Dras island-arc complex was sutured against the Karakoram-Lhasa block between 102-85 Ma (Schärer *et al.*, 1984a, b; Coward *et al.*, 1986; Pudsey, 1986; Searle *et al.*, 1987; Reuber, 1989; Khan *et al.*, 1993) and is intruded by the ~2500 km long Transhimalayan batholith (Ladakh-Gangdese and Kohistan granites): a suite of sub-alkaline and calc-alkaline Andean-type granites intruded along the southern destructive plate margin of Eurasia (Schärer *et al.*, 1984a, b; Petterson & Windley, 1985; Coward *et al.*, 1986; Debon *et al.*, 1986). U-Pb dates from the Transhimalayan batholith constrains the onset of Andean-type plutonism in Ladakh at a minimum of 103 ± 3 Ma (Honegger *et al.*, 1982) and 101 ± 2 Ma (Schärer *et al.*, 1984a). Termination of magmatism along the Transhimalaya is thought to be related to the initiation of continent-continent collision (Debon *et al.*, 1986), the upper age limits of which are constrained by the youngest ages recorded from the batholith: 60.7 ± 0.4 Ma in Ladakh (Schärer *et al.*, 1984a) and 48-41 Ma in southern Tibet (Schärer *et al.*, 1984b). In Pakistan, forearc magmatism has been recorded between 60-55 Ma (Sullivan *et al.*, 1993), indicating that marine conditions still prevailed at this time.

1.4 Tectonic framework of the Himalaya

The Himalaya extend in an arcuate belt for over 2500 km, from Pakistan in the west to Bhutan in the east. They are divided into a series of strike-parallel tectonic zones (Figure 1.2), which are almost perpendicular to the main transport direction of the Indian plate (Figure 1.3). Zones of sinistral and dextral transpression along the western and eastern flanks of the Himalayan chain help delineate the shape of the Indian indentor (Figure 1.3). Geophysical evidence (e.g. Hirn *et al.*, 1984a, b; Lyon-Caen & Molnar, 1985; Hirn, 1988), suggests that the continental crust beneath both southern Tibet and the Himalaya is ~70km-thick, double that of average continental crust (Figure 1.4). This has been attributed to shortening and thickening following the India-Asia collision (Molnar, 1988).

From north to south, five tectonic zones are recognised in the Himalaya (Figures 1.2 & 1.5): (1) the Indus-Tsangpo Suture Zone (ITSZ); (2) the Tibetan Sedimentary Series; (3) the High Himalayan Slab (also referred to as the Tibetan Slab in Nepal); (4) the Lesser Himalaya and (5) the Sub-Himalaya (also referred to as the Siwaliks). The simple arcuate nature of the Himalayan belt breaks down somewhat in Pakistan, where accretion of the Kohistan-Dras island-arc complex to the Eurasian plate

complicates the structure. In addition, the Kohistan arc is spilt in two by the N-S trending Nanga Parbat-Harmosh Massif (Butler *et al.*, 1989; Zeitler *et al.*, 1989).

1.4.1 The Indus-Tsangpo Suture Zone (ITSZ)

This suture zone marks the site of final closure of the Neo-Tethyan ocean (Gansser, 1964, 1977; Allègre *et al.*, 1984; Garzanti & van-Haver, 1988; Searle *et al.*, 1987) and separates the Indian plate from the Karakoram Terrane in the west, and from the Lhasa block in the east (Figure 1.2). Rocks within the ITSZ include Permian and Mesozoic deep-water sediments (the Lamayuru complex of Ladakh (see Searle *et al.*, 1988, 1997b and references therein), ophiolite klippen (for example, the Spontang ophiolite in NW Ladakh, Searle, 1986; Searle *et al.*, 1997b) and ophiolitic mélanges and olistoliths (see Reuber, 1986; Searle *et al.*, 1988). The latter include fragments of glaucophane-bearing blueschists, MORB-tholeiitic basalts, alkali basalts, pillow lavas, gabbros, harzburgites, dunites, radiolarian cherts and deep-sea sediments. Terrestrial sediments (e.g. the Indus Group molasse of Searle *et al.*, 1987, 1988), rest unconformably above this oceanic sequence and mark the end of oceanic sedimentation in Neo-Tethys.

1.4.2 The Tibetan Sedimentary Series

The Tibetan Sedimentary Series is bounded to the north by the ITSZ and to the south by the South Tibetan Detachment (STD) system of normal faults (Figure 1.2), (Burg *et al.*, 1984; Searle, 1986; Herren, 1987; Burchfiel *et al.*, 1992). It represents an almost continuous sequence of fossiliferous marine shelf sediments deposited on the passive northern-margin of the Indian plate during the Precambrian to mid-Eocene (Figure 1.6), (Gansser, 1964; Fuchs, 1979; Thakur, 1981; Tapponnier *et al.*, 1981a; Baud *et al.*, 1984; Gaetani *et al.*, 1986; Searle, 1986; Garzanti *et al.*, 1987; Gaetani & Garzanti, 1991; Garzanti, 1993). The Carboniferous-Permian Panjal trap volcanics are associated with rifting along this margin, which eventually led to the opening of the Neo-Tethys ocean, in which a sequence of middle-Permian to mid-Eocene shelf carbonates, sands and shales were deposited. The original sedimentary thickness of the Tibetan Sedimentary Series is difficult to estimate due to lateral variations in facies and post-deposition shortening and thickening, but is believed to be in the order of 2.5-5km in NW India (McElroy *et al.*, 1990; Gaetani & Garzanti, 1991).

1.4.3 The High Himalayan Slab

The High Himalayan Slab is bounded between the South Tibetan Detachment system and the Main Central Thrust (Figure 1.2). It represents a zone of Indian plate metasediments and orthogneisses which experienced a poly-metamorphic evolution during the Tertiary, involving at least two phases of metamorphic mineral growth and a period of leucogranite emplacement during the early Miocene. A more detailed account of the geology of the High Himalayan Slab is given in Chapter 2.

1.4.4 The Lesser Himalaya

The Lesser Himalaya form the footwall of the Main Central Thrust (MCT) and are bounded along their base by another intracontinental shear zone, the Main Boundary Thrust (MBT). Displacement along this thrust is reported to be in the order of tens (Heim & Gansser, 1939; Valdiya, 1980b), if not hundreds of kilometres (Molnar, 1984). Rocks in the Lesser Himalaya comprise weakly metamorphosed Proterozoic gneisses, Ordovician granite intrusions and thick Palaeozoic and thin Mesozoic sediments. Metamorphic grade in the Lesser Himalaya is generally low, although amphibolite-facies units have been mapped immediately below the MCT zone (Le Fort, 1975; Valdiya, 1980b; Pêcher, 1989). Whether these units actually belong to the Lesser Himalaya *sensu stricto* largely depends on how the MCT is defined (see Chapter 2).

1.4.5 The Sub-Himalaya (Siwaliks)

The Siwalik basin is located in the footwall of the MBT and presently contains over 10 km of terrestrially derived sediment which has been eroded from the uplifted Himalaya since the late Eocene (e.g. Copeland *et al.*, 1987; Najman *et al.*, 1997). It is estimated that ~35 km of vertical section must have been eroded from the Himalaya to account for the volume of sediment contained within the Siwalik basin, together with that in deltas and fans to the south of the Himalayan topographic front (Johnson, 1994). The Siwalik basin developed by lithospheric flexure as a direct result of crustal loading in the north brought about by continued stacking of foreland propagating thrust sheets (Lyon Caen & Molnar, 1983). At the base of the basin, the youngest of all the Himalayan thrusts, the Main Frontal Thrust (MFT) terminates at tip-lines beneath the Indo-Gangetic plains.

1.5 The timing of collision

For the purpose of clarity, the India-Asia collision is defined here as the time at which the Neo-Tethyan ocean finally closed (ie. the time at which the Indian and Eurasian plates were finally sutured), and not the time at which the Indian plate first made contact with southern Eurasia. Age constraints of: (1) blueschist facies metamorphism in the ophiolitic mélanges of the ITSZ (80 ± 5 Ma in Pakistan, (Maluski & Matte, 1984), and ~100 Ma in Ladakh (Honegger *et al.*, 1989)); and (2) Maastrichtian ophiolite emplacement ages for the Spontang ophiolite (Searle, 1986; Searle *et al.*, 1987, 1988, 1997b) cannot, therefore, be used to establish the time of this closure.

Palaeomagnetic data provide a reasonable database from which to estimate the timing of continent-continent collision. However, similar looking data has been interpreted in different ways by various workers, giving rise to a number of postulated collision ages. Molnar and Tapponnier (1975) use the slowing of the northward-drifting Indian plate at ~38 Ma as evidence for collision, whilst Patriat & Achache (1984) argue that the change in direction of the Indian plate from a north-easterly to a more northerly direction at 50 Ma is a better estimate of the age of collision. Using the same marine anomaly dataset as Patriat & Achache (1984), Dewey *et al.* (1988, 1989) proposed a collision age of

45 Ma. By incorporating terrestrial magnetic data into their kinematic models, Besse *et al.* (1984) proposed a 50 Ma age, in good agreement with Patriat & Achache (1984).

Given the problems associated with the use of palaeomagnetic data, the most accurate way of constraining the age of suturing is to establish the time at which terrestrial sedimentation is first encountered in the ITSZ. Searle *et al.* (1997) demonstrate that in Ladakh, Lower Eocene Nummulitic limestones are overlain by continental molasse red beds and fluviatile conglomerates. These stratigraphic relationships date the age of collision between *c.*50-54 Ma. Beck *et al.* (1995) agree that suturing was complete by ~49 Ma, although they suggest that collision in western Pakistan occurred between 66-55.5 Ma. Indeed, several authors maintain that the India-Asia collision was diachronous along strike. Dewey *et al.* (1988, 1989) use palaeomagnetic data to suggest that peninsular north-west India was sutured to the southern Eurasian margin before suturing occurred in more easterly regions (Figure 1.7a). The extended dataset of Besse & Courtillot (1988) appears to show the north-west prong of India colliding with Eurasia at 53 Ma and before collision occurred in central Tibet (Figure 1.7b). These interpretations are at odds with that of Searle *et al.* (1997), who argue that similar Nummulitic limestones have been observed in locations as far apart as southern Tibet and the Salt Ranges of Pakistan (Searle & Khan, 1996: map), leading them to conclude that "there is no concrete stratigraphic evidence that the India-Asia collision was diachronous along strike".

In conclusion, it would appear that palaeomagnetic data, isotopic ages from the Transhimalayan batholith and Kohistan island-arc (see section 1.5) and sedimentary and palaeontological data from the ITSZ and Tethyan shelf are suggestive of final suturing along the Neo-Tethyan margin between 50-54Ma.

1.6 Crustal shortening mechanisms

Current estimates suggest that the Indian plate has been moving northwards at an average rate of ~50 mma^{-1} since it collided with Eurasia c.50-54 Ma ago (Patriat & Achache, 1984; Dewey et al., 1989). Of this, an estimated ~18 mma^{-1} is thought to be accommodated across the Himalaya, (Figure 1.3), (Avouac & Tapponier, 1993). These figures suggest that since collision, an estimated 2500 km of shortening has occurred across central Asia (e.g. Besse & Courtillot, 1988; Chen *et al.* 1993) and that less than half of this (~1000km) has been accommodated by folding and thrusting within the Himalaya (Dewey *et al.*, 1989, Chen *et al.*, 1993), (Figure 1.8). This implies that the remaining ~1500km of shortening must be taken up by deformation north of the ITSZ. The relative importance of the mechanisms by which this shortening has been accommodated remains conjectural and includes three end-member models:

1. Wholesale underthrusting of the Indian plate beneath Eurasia (Argand, 1924; Bird, 1978; Powell, 1986).
2. Shortening and thickening of the Asian lithosphere (Dewey & Burke, 1973; England & Houseman, 1988).
3. Lateral extrusion of Tibet (Molnar & Tapponier, 1975; Tapponnier *et al.*, 1986).

Seismic profiling by the project INDEPTH team suggest that at least 200 km of crustal shortening has been accommodated by underthrusting of the Indian plate beneath Tibet (Zhao *et al.*, 1993). However, there is strong evidence to suggest that this cannot account for more than ~300-400 km of the total shortening (Dewey et al, 1989; Harrison *et al.* 1992). Tapponnier *et al.* (1986) suggest that ~500-750 km of deformation could be accommodated by lateral extrusion of Tibet along major strike-slip faults (Figure 1.3). More recent data has shown that despite the overall length of these faults, the total displacement along them is unlikely to exceed 250 km (Dewey et al., 1989; Searle, 1996a). In any case, lateral extrusion of Tibet cannot account for the doubling of the continental crust beneath southern Tibet. Together, underthrusting and strike-slip faulting seem incapable of accounting for more than ~500 km of the total shortening north of the ITSZ. The remaining 1000 km must, therefore, be attributed to shortening and thickening of the crustal lithosphere, as suggested by England and Houseman (1988) and Dewey *et al.* (1989). This is supported by analogue models which show that a 60 km thick continental crust can be produced by 50% shortening of a buckled layer of normal continental thickness (Burg *et al.*, 1994). However, the extent to which this thickening is accommodated in the continental crust rather than the entire lithosphere remains a matter of debate. Steps in the Moho revealed by seismic profiling show that at least some thickening must have occurred in the lower crust (Hirn *et al.*, 1984a, b; Hirn, 1988). It has also been suggested that the excessive elevation of the Tibetan plateau is related to catastrophic delamination of the Tibetan lithosphere as a result of overthickening (England and Houseman, 1988; Dewey, 1988).

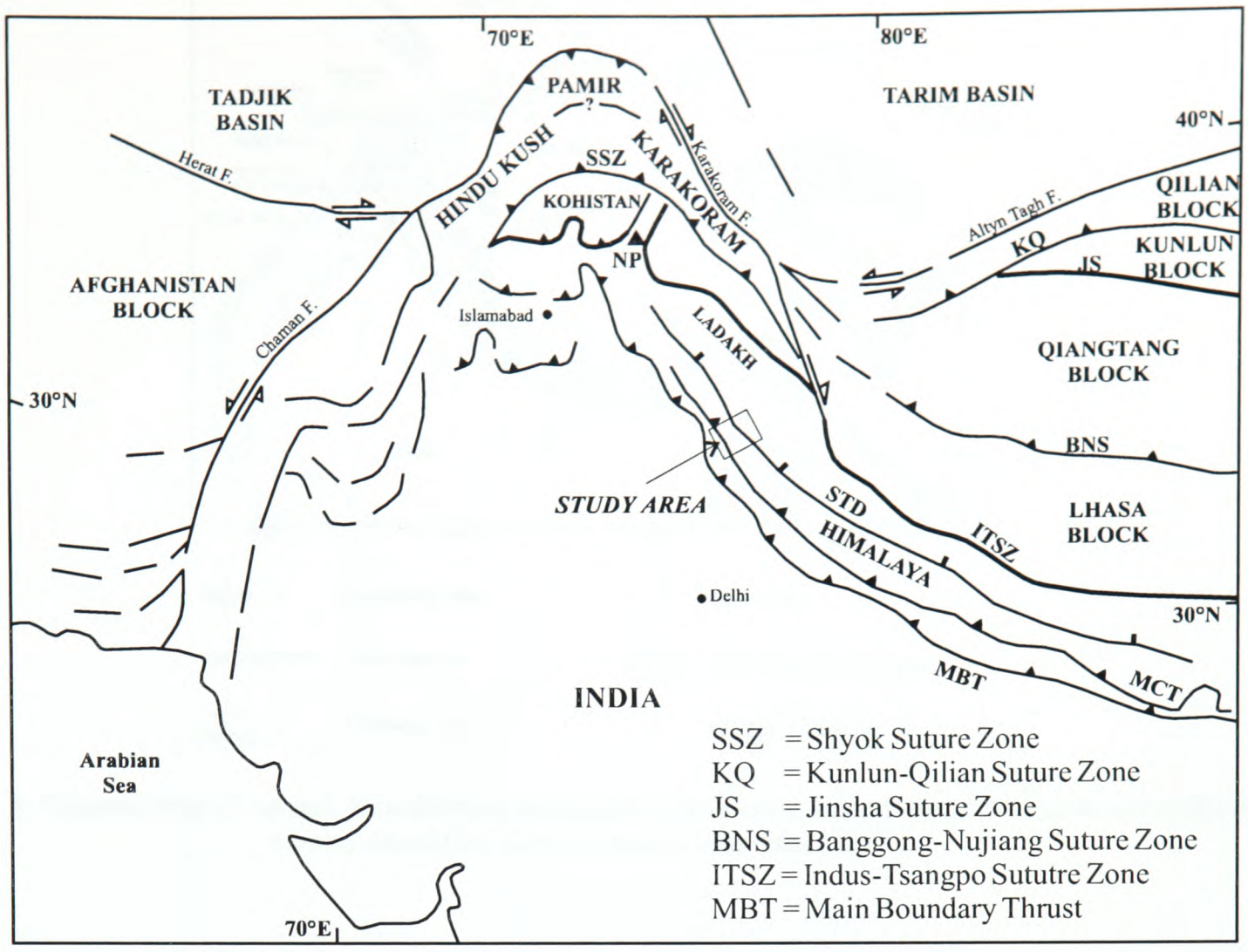


Figure 1.1: Tectonic framework of southern Asia illustrating the location of major crustal blocks, which are separated by suture zones (modified after Searle, 1991).

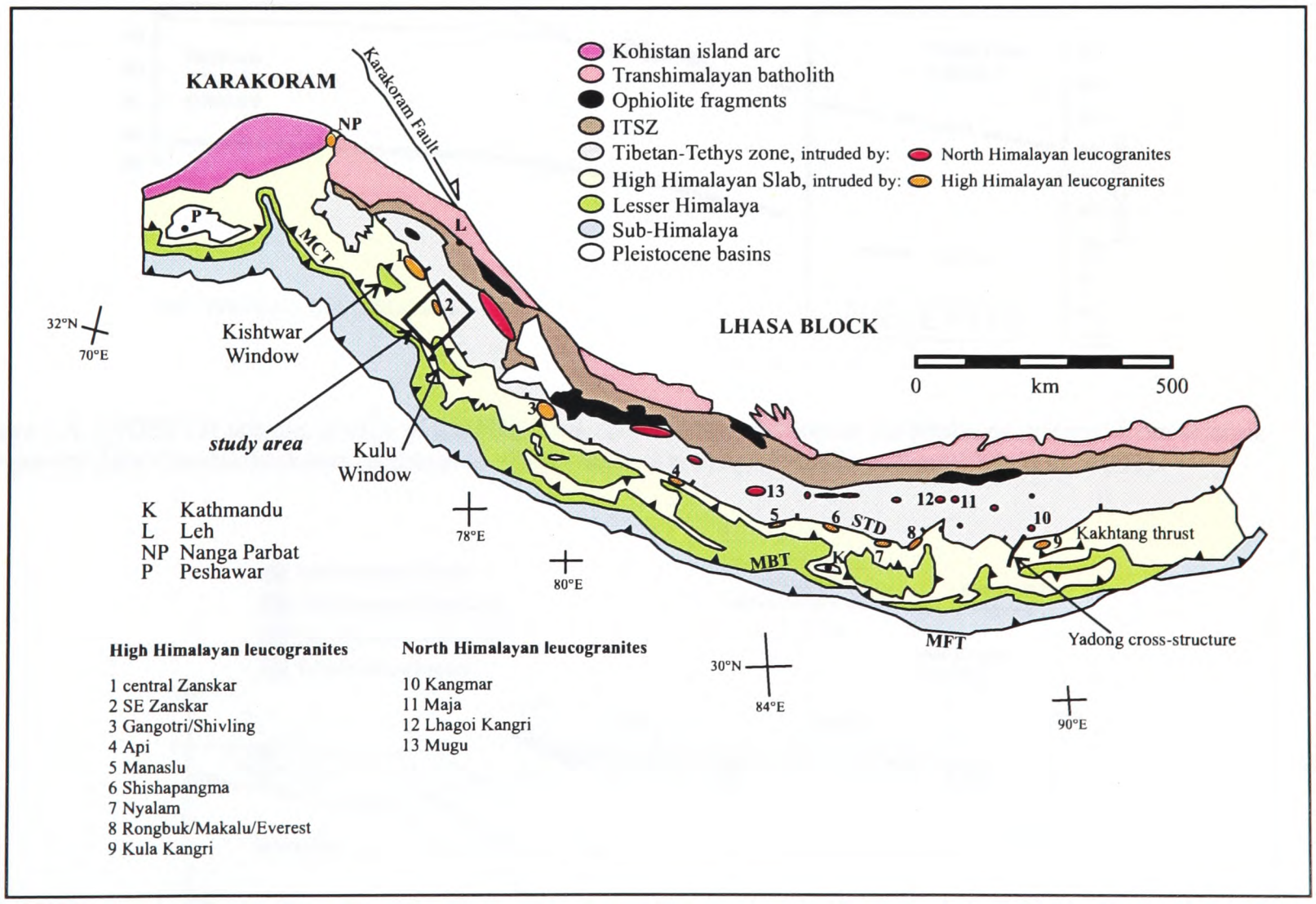


Figure 1.2: Tectonic framework of the Himalaya showing the location of the study area in relation to the main structural and magmatic features of the orogen. MFT = Main Frontal Thrust, MBT = Main Boundary Thrust, MCT = Main Central Thrust, STD = South Tibetan Detachment (based on Gansser, 1964; and incorporating data from Le Fort, 1986; Stephenson, 1997; Harrison et al, 1997b).

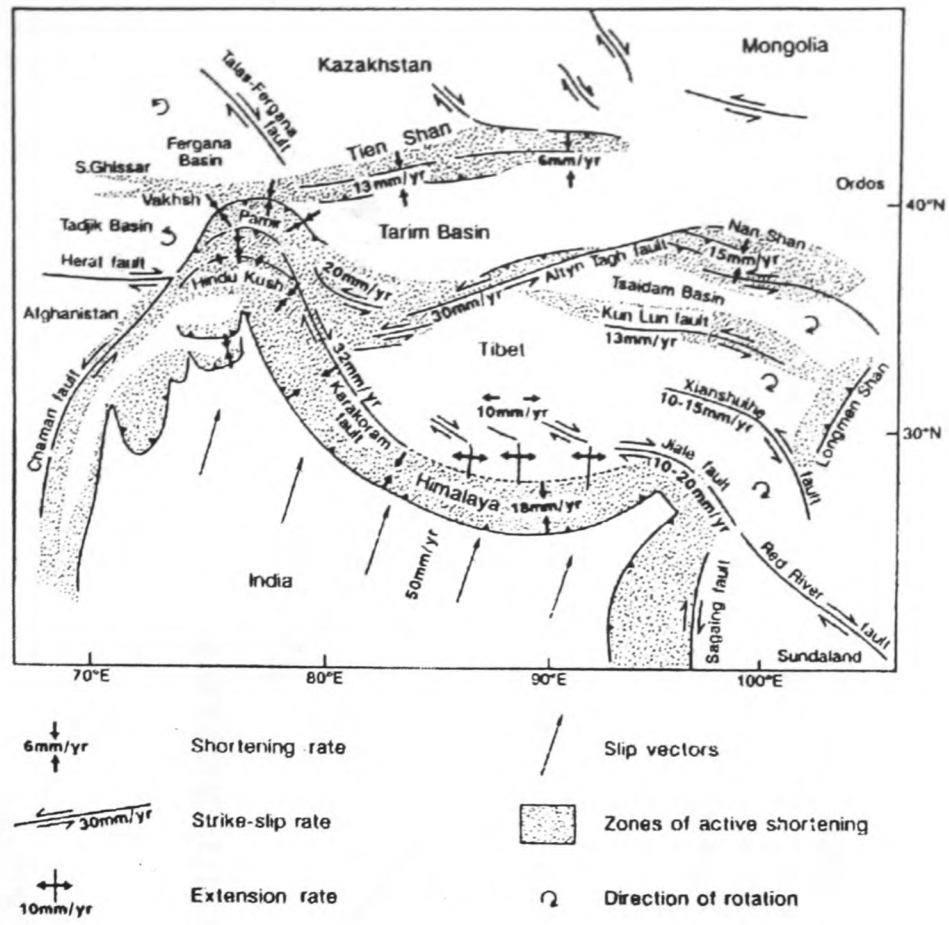


Figure 1.3: Tectonic map of central Asia showing estimated rates of crustal shortening, extension and strike-slip motion (modified after Avouac & Tapponier, 1993).

[redacted]

Figure 1.4: INDEPTH seismic profile of the Himalaya showing the position of the Moho as inferred from seismic and gravity data. Crustal thickness increases to ~70km north of the High Himalaya (from Zhao et al., 1993).

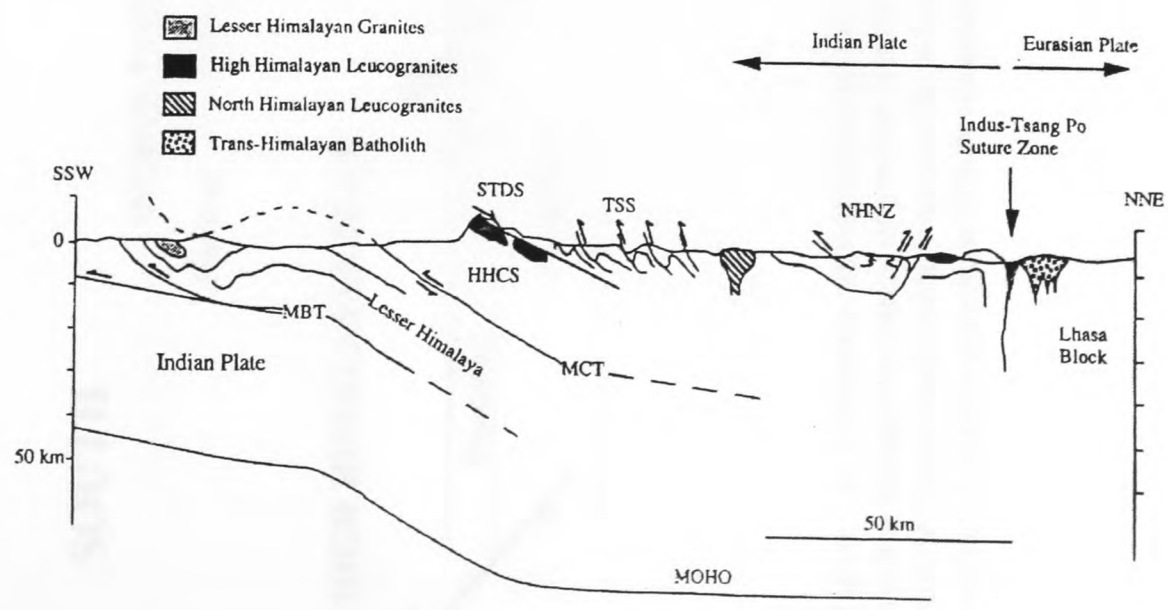


Figure 1.5: Schematic cross-section across the central Himalaya (based on Gansser, 1964; and incorporating data from Molnar et al., 1983).

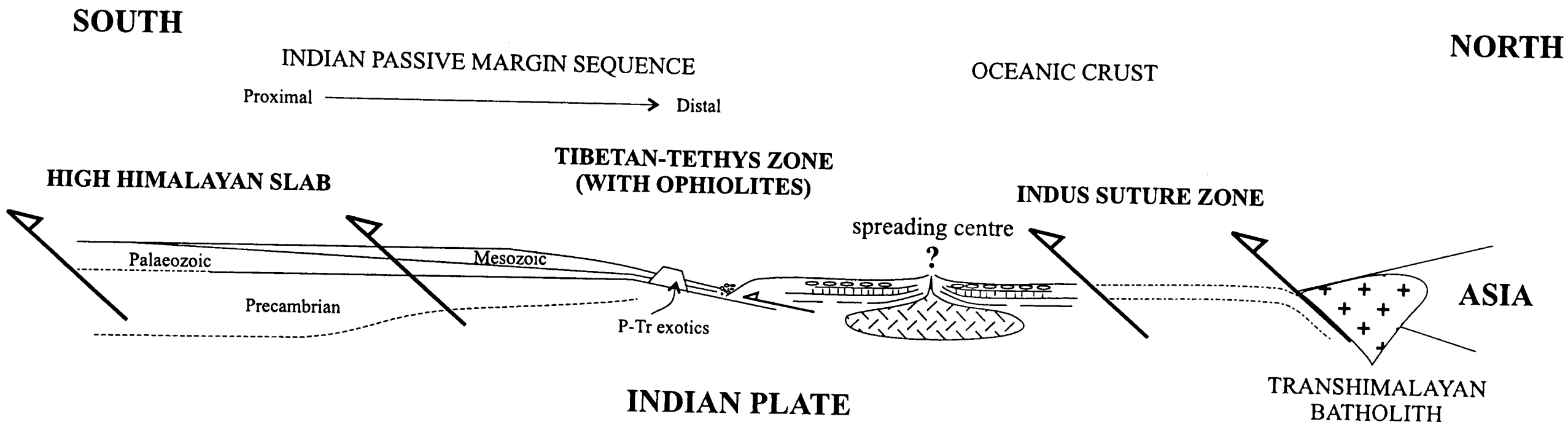


Figure 1.6: Schematic representation of the Indian plate margin prior to ophiolite obduction in the late Cretaceous (based on Searle et al, 1997). The High Himalayan Slab to the south is thought to consist of predominantly Palaeozoic rocks overlying Precambrian basement. The Tibetan Sedimentary Series consists of an almost continuous Precambrian-middle Eocene sedimentary succession, which has been overthrust in places by ophiolites. The Transhimalayan batholith represents an Andean-type destructive plate margin on the southern Eurasian margin, which developed as a result of north-directed subduction of the leading edge of the Indian oceanic margin. (Modified after Searle et al, 1997b).

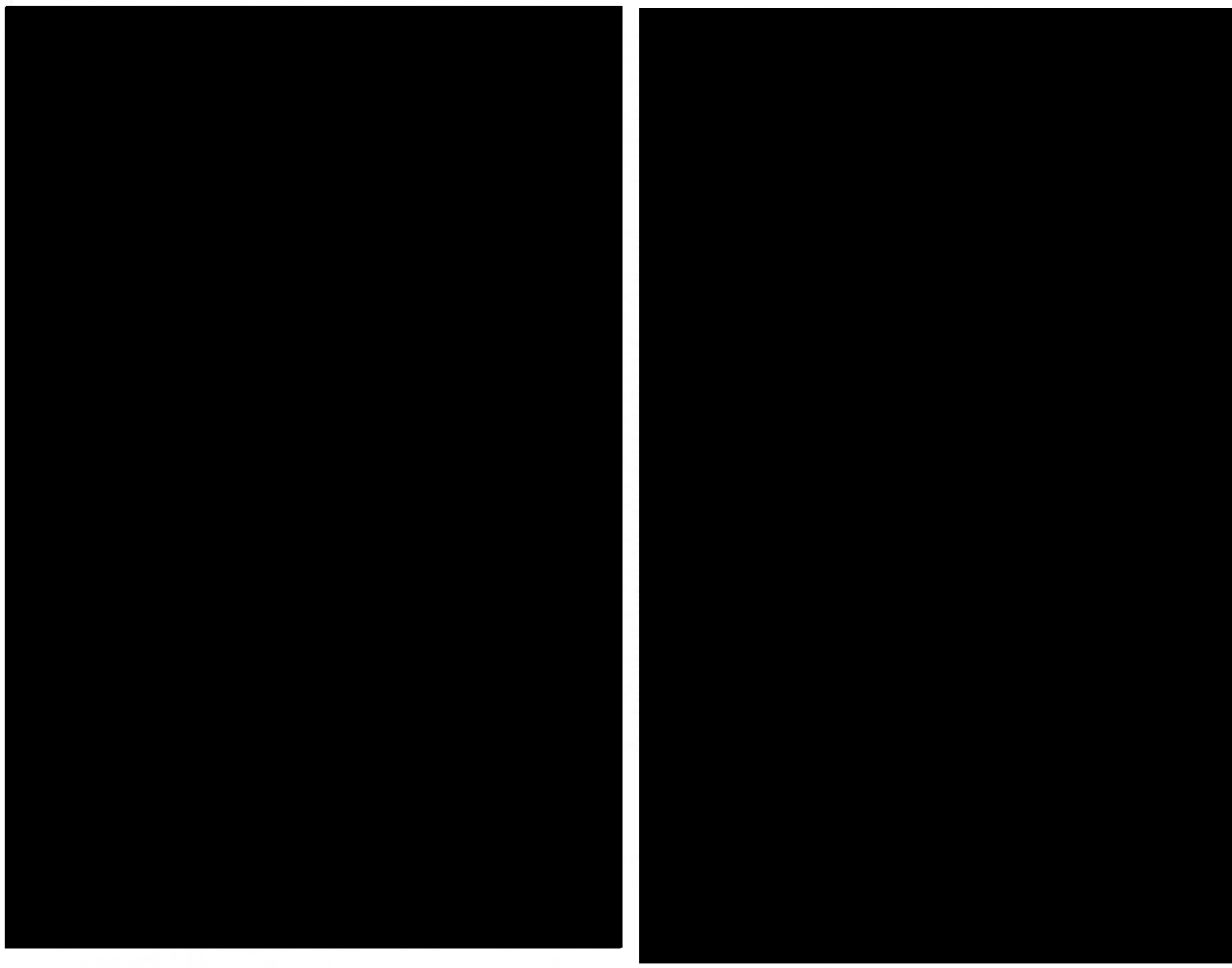
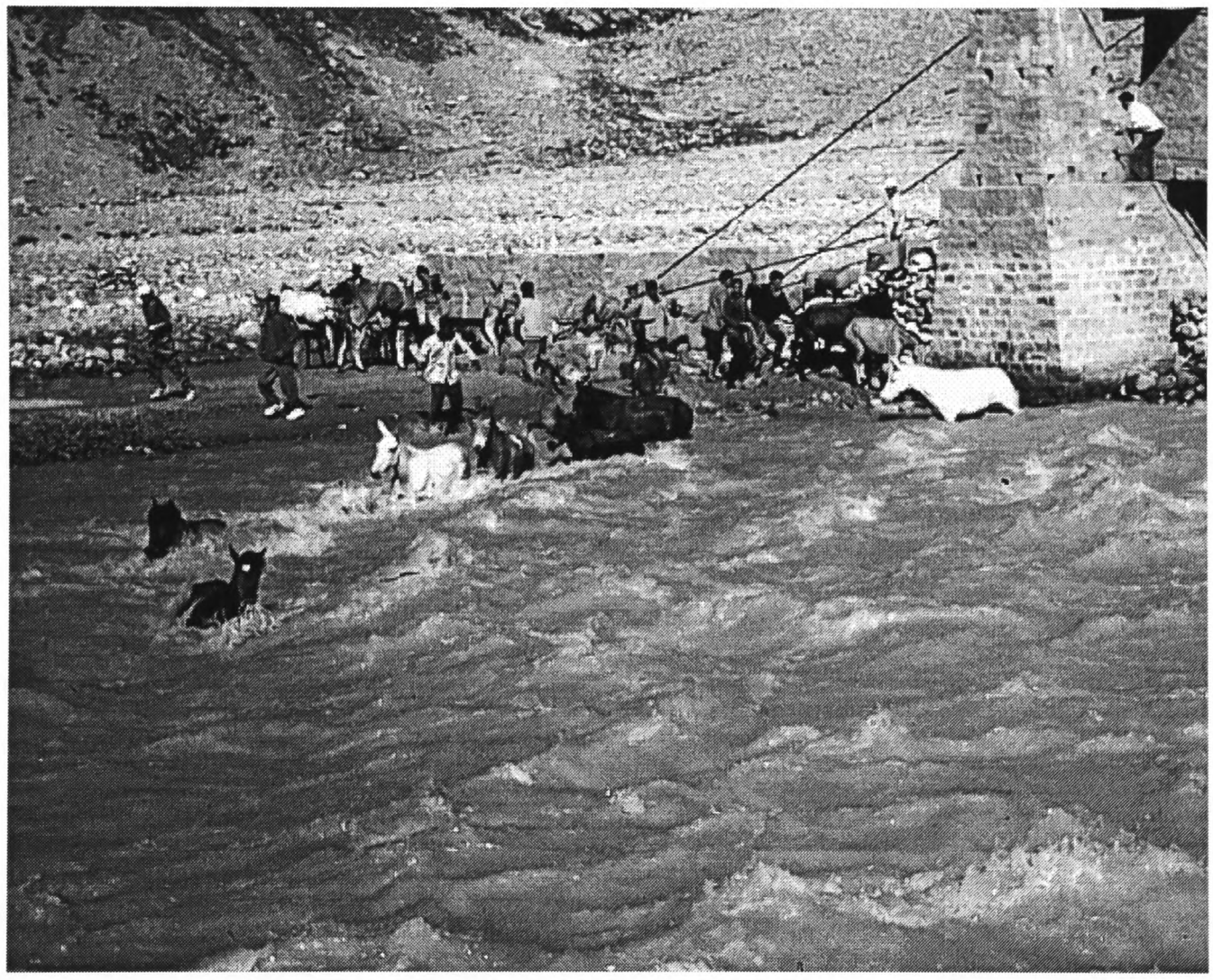


Figure 1.7: Palaeogeographic reconstructions illustrating the NW promontary of India colliding with the southern Eurasian margin prior to suturing in the east: (a) Dewey et al. (1989); and (b) Besse & Courtillot (1988).



Figure 1.8: Schematic Cretaceous paeogeographic reconstruction of Asia with estimates of crustal shortening between blocks (from Chen et al., 1993).



Horses being forced to swim across a flooded river
(Barai nala, south of the Shingo La).

Chapter 2

The High Himalayan Slab

2.1 Definition of the High Himalayan Slab

The High Himalayan Slab (also commonly known as the Tibetan Slab or the Greater Himalayan sequence), refers to the zone of Indian plate metasediments, orthogneisses, paragneisses and crustal melt leucogranites which are bounded between the South Tibetan Detachment (STD) system of normal faults and the Main Central Thrust (MCT), (Figure 2.1). In certain parts of the Himalaya, the MCT and STD are poorly defined, resulting in disagreement concerning the precise location of the upper and lower structural limits of the High Himalayan Slab *sensu stricto* (Figure 2.2).

The High Himalayan Slab is generally between 10-15 km thick in most parts of the Himalaya, although variations do exist along strike (Figure 2.1). It is thickest in Bhutan and Zanskar where over 25km of crustal thickness is exposed, and thinnest in the Annapurna region of western-central Nepal where it is only 5km thick (Pêcher, 1989). Few structural discontinuities have been recognised within the High Himalayan Slab, with the possible exception of Bhutan and the Annapurna range in central Nepal, where thrusts have been recognised in the internal parts of the slab (Gansser, 1983; Swapp & Hollister, 1991; Grujic *et al.*, 1996; Vannay and Hodges, 1996).

2.1.1 The Main Central Thrust (MCT)

The Main Central Thrust (MCT) is a major NE-dipping intracontinental shear zone which separates the High Himalayan Slab from the underlying Lesser Himalaya (Heim and Gansser, 1939; Gansser, 1964), (Figures 2.1 & 2.2). No single structural, metamorphic or lithological criteria have been adopted to define the precise location of the MCT, hence, different authors have placed it at different structural levels in the same section of study (Figure 2.2). The MCT is therefore best thought of in most parts of the Himalaya as a several-kilometre-wide zone of intense deformation which displays lithological affinities both to the High Himalayan Slab and underlying Lesser Himalaya (Figure 2.2). In all regions of the Himalaya, the base of the High Himalayan Slab and the uppermost part of the Lesser Himalaya preserve an inverted metamorphic gradient which increases up structural section from the chlorite zone through to kyanite-grade assemblages (Figures 2.2 & 2.4).

To date, no seismic profiles have been shot to the south of the South Tibetan Detachment system, hence the structure of the MCT at depth remains largely speculative. Current interpretations suggest that it has a ramp-flat structure which bottoms out into a basal décollement at a depth of *c.*50 km (Figure 2.3). The MCT is believed to be responsible for the translation of the High Himalayan Slab some ~100-200 km towards the SW (Brunel & Kienast, 1986; Schelling & Arita, 1991; Epard *et al.*, 1995; Parrish & Hodges, 1996).

2.1.2 The South Tibetan Detachment system (STD)

The structural top of the High Himalayan Slab is defined by the South Tibetan Detachment system (STD) of normal faults, which can be traced almost undisrupted along the length of the Himalaya from Bhutan in the east, to Zanskar in the west (Figures 2.1 & 2.2). Early mapping suggested that the sediments of the Tibetan Sedimentary Series passed unconformably downwards into the High Himalayan Slab (Gansser, 1964). In the past, the STD has also been incorrectly interpreted as a thrust (e.g. Jain & Manickavasagam, 1993). However, most authors now accept that the STD represents a major intracontinental shear zone which separates the amphibolite-facies rocks of the High Himalayan Slab from the weakly metamorphosed Tibetan Sedimentary Series (Figures 2.2).

Below depths of *c.*20 km, the STD appears to merge into a low-velocity-zone and does not form a prominent seismic reflector (Zhao *et al.*, 1993; Nelson *et al.*, 1996). Current data suggest that it may bottom-out into the same basal décollement as the MCT (Figure 2.3). Where it is exposed at the surface, the STD is recognised as a northwards-dipping zone of distributed deformation displaying top-to-the-north-east shear-sense indicators (Burg *et al.*, 1994; Burchfiel & Royden, 1985; Searle, 1986; Herren, 1987; Burchfiel *et al.*, 1992). Extension along the STD is believed to have been predominantly down-dip (ie. to the north/north-east), with very little evidence for strike-slip movement. Current estimates from eastern Nepal suggest that 10-15 km of stratigraphic section has been faulted out along the STD and that it has accommodated up to 35 km of northward displacement (Burchfiel *et al.*, 1992).

2.1.3 Metamorphic protoliths

For the most part, the metasediments in the High Himalayan Slab are unfossiliferous, hence their exact age and provenance is uncertain. Recent isotopic and geochronological data from the Langtang MCT section in eastern-central Nepal suggest that the High Himalayan Slab has a different sedimentary provenance to the underlying Lesser Himalaya, and that the protoliths of the High Himalayan Slab are no older than Late Proterozoic and no younger than the early Cambrian (Parrish and Hodges, 1996), thus implying that the Precambrian crystalline basement of the Indian plate does not form part of the exposed metamorphic sequence in eastern-central Nepal. Similar observations and interpretations have been made in the Bhutan section of the High Himalayan Slab (Parrish *et al.*, 1997). It is generally thought that the protoliths of the High Himalayan Slab represent the metamorphosed equivalents of the Tibetan Sedimentary Series and are believed to have been were deposited on the thinned continental margin of the Indian plate from the Precambrian(?) through to the Mesozoic (Figure 1.6). Metapelitic and metapsammitic assemblages are the dominant lithologies, with subordinate calc-silicates, marbles, quartzites and amphibolites. Large Cambro-Ordovician granites discordantly intrude the metasedimentary sequence (see review by Le Fort *et al.*, 1986), suggesting that the protoliths are at least Cambrian in age and raising the possibility that they experienced a major pre-Himalayan thermal event.

2.2 Previous quantitative P-T-t studies

Figure 2.1 divides the High Himalayan Slab longitudinally into a series of geographical zones, in which a number of quantitative P-T and geochronological studies have been performed. The following sub-sections review some of this work. Table 2.1 summarises previously published thermobarometric data pertaining to metamorphic conditions experienced in different parts of the High Himalayan Slab, whilst Table 2.2 summarises the known range of ages for various High Himalayan leucogranites exposed at the top of the slab. The location of these granites is shown on Figure 2.1.

Table 2.1: Peak metamorphic conditions across the High Himalayan Slab

Area	M_1 (regional Barrovian) Pressure (kbar)	M_1 (regional Barrovian) Temperature (°C)	M_2 (sillimanite overprint) Pressure (kbar)	M_2 (sillimanite overprint) Temperature (°C)	Reference
Bhutan	~7	480-500	4-6	650-700	Swapp & Hollister (1991)
Eastern Nepal	8-10	550-680	4-7	650-750	Pognante & Benna (1993)
Eastern-central Nepal	9-12	425-525	4-12	490-660	MacFarlane (1995)
	9 ± 1	710 ± 30	5.8 ± 0.4	760 ± 30	Harris & Inger (1992)
Western-central Nepal	7-8.5	600-690	7	650-710	Pêcher (1978)
Western Garhwal	6-12	550-640	6-8	550-700	Metcalfe (1993)
Eastern Garhwal	8.6-9.1	580-650	3-5	500-700	Hodges & Silverberg (1988)
Central/western Zanskar	9.5-10.5	550-680	4.5-7	650-770	Searle et al (1998)
SE Zanskar & NW Lahaul	6-8	550-650	4-7	650-700	This study (Chapters 4-6)

Table 2.2: Crystallisation ages of the Himalayan leucogranites shown in Figure 2.1.

	High Himalayan belt	Age (Ma)	Authors
1	Central Zanskar	20.0 ± 0.5	Noble & Searle (1995)
2	SE Zanskar	21-22	This study (Chapter 7)
3	Gangotri/Shivling	22.4 ± 0.5	Harrison *et al.* (1997b)
4	Api	no published ages	
5	Manaslu	22.4 ± 0.5	Harrison *et al.* (1995)
		18-25	Deniel *et al.* (1987), Copeland *et al.* (1990) Guillot et al (1994b)
		19.0 ± 1.0	Coleman & Parrish (1995)
	Annapurna	22.5-18.5	Nazarchuk (1993), Hodges *et al.* (1996)
		22 ± 1.0	Parrish & Hodges (1992)
6	Shisha Pangma	20-17	Searle *et al.* (1997a)
	Langtang	21	Parrish & Hodges (1992)
7	Nyalam	16.8 ± 0.6	Schärer *et al.* (1986)
8	Rongbuk/Makalu/Everest	23.0 ± 1.0	Schärer (1984), Harrison *et al.* (1995)
		21.6-19.5	Hodges *et al.* (1992)
		14.3 ± 0.6	Schärer *et al.* (1986)
9	Khula Kangri	12.5 ± 0.5	Edwards *et al.* (1997)
	North Himalayan belt		
10	Kangmar	~13-11	(reference unknown, taken from Searle, 1996b)
11	Maja	9.5 ± 1.0	Schärer *et al.* (1986)
12	Lhagoi Kangri	15.1 ± 0.5	Schärer *et al.* (1986)
13	Mugu	17.6 ± 0.3	Harrison *et al.* (1997b)

2.2.1 Bhutan

The MCT in Bhutan is reported to form a major ductile shear zone up to 10km thick in places (Grujic *et al.*, 1996). The base of this zone defines a sharp metamorphic discontinuity between the greenschist-facies rocks of the Lesser Himalaya and the amphibolite-facies rocks of the overlying High Himalayan slab (MCT I in Figure 2.2), thus implying that the MCT represents a major post-metamorphic discontinuity (Gansser, 1983; Grujic *et al.*, 1996).

Swapp and Hollister (1991) divide the High Himalayan Slab of Bhutan into two structural domains. The upper part is dominated by high-temperature, low-pressure sillimanite-bearing assemblages and zones of *in situ* migmatisation formed at ~700 °C and 4 kbar. The lower unit contains earlier mineral assemblages formed at 480-500C and ~7 kbar (Table 2.1). Swapp and Hollister (1991) suggest that the uppermost unit was thrust above the lower structural domain prior to movement on the MCT and that *in situ* migmatisation and generation of the High Himalayan leucogranites was the result, rather than the cause of high-temperature metamorphism at the top of the slab (*cf. Eastern Garhwal*: Hodges & Silverberg 1988).

Approximately twelve tourmaline-bearing leucogranites concordantly intrude the metamorphic gneisses in the footwall of the STD in Bhutan (Gansser, 1983; Ferrara *et al.*, 1991). Many of the granites contain ductile deformation fabrics consistent with a top-to-the-north-east sense-of-shear, suggestive of emplacement contemporaneous with extension along the STD. The Khula Kangri granite has an extremely young age of 12.5 ± 0.5 Ma (Edwards *et al.*, 1997), which may suggest that extension along the STD in Bhutan was considerably younger than that to the east (compare emplacement ages of the various High Himalayan leucogranites in Table 2.2).

West of Bhutan, the STD is cross-cut by the Yadong Cross Structure (Figure 2.1), a north-striking extensional graben which offsets the crest of the Himalaya and the STD by ~70 km relative to that in Nepal (Burchfiel *et al.*, 1992). This structure is clearly younger than the STD, although it does not extend as far south as the MCT, resulting in a greater outcrop width of the High Himalayan Slab in Bhutan compared to that in Nepal. Similar north-south striking faults are observed throughout southern Tibet and have been related to a phase of east-west extension across the Tibetan Plateau (Molnar & Tapponnier, 1978; Tapponnier *et al.*, 1981a, 1981b). The relationship between northwards extension at the top of the High Himalayan Slab and east-west extension in Tibet remains uncertain, although it is clear that the latter are the younger structures.

2.2.2 Eastern Nepal (Everest and Makalu)

In eastern Nepal (*Everest section*), the MCT is reported to form a 3-5 km-thick ductile shear zone within rocks of garnet- to kyanite-grade which share affinity to both the High Himalayan Slab and underlying Lesser Himalaya (Hubbard, 1989, 1996), (Figure 2.4a). Hubbard reports no distinct structural or metamorphic discontinuity across the MCT zone in the Everest region. Conversely, Pognante and Benna (1993) describe the Everest MCT section as a several-hundred-metre-wide zone of mylonites which clearly separate the High Himalayan Slab from the underlying Lesser Himalaya. Slightly to the east of Everest (Makalu section), Brunel and Kienast (1986) describe the MCT section as an imbricate thrust

system which marks a distinct metamorphic break between the High Himalayan Slab and the underlying Lesser Himalaya at the structural level of the kyanite isograd (Figure 2.2).

Hubbard (1989) presented a P-T traverse across the Dudh Kosi and Hinku-Honku drainages to the south of Mt. Everest region (Figure 2.4a). Pressures in the hangingwall of the MCT appear to decrease uniformly across the slab at a rate which is consistent with a normal lithostatic gradient of ~3.5 km/kbar. Temperatures in the hangingwall increase markedly directly above the MCT zone from ~500°C to ~720°C and then decrease slightly to ~540°C in the central part of the slab. These data were originally interpreted by Hubbard (1989) as being consistent with syn-metamorphic thrusting along the MCT and compatible with the hot-over-cold model of Le Fort (1975). Subsequent work by Hubbard (1996) on the same transect has since revealed that the main phase of metamorphism pre-dated movement on the MCT and that the inverted temperature gradient is the result of late-stage thermal re-equilibration of the hangingwall. In this respect, it is possible that the MCT has exhumed a well-preserved right-way-up section of the mid-lower crust which has experienced higher temperatures in the immediate vicinity of the MCT owing to the effects of thrust-related shear heating (cf. England *et al.*, 1992; England & Molnar, 1993a; Harrison *et al.*, 1997a).

Geochronological data from eastern Nepal suggest that movement along the MCT at temperatures in excess of ~500°C occurred at ~21 Ma (hornblende cooling age, Hubbard &Harrison, 1989). A 20.2 ± 0.2 Ma biotite cooling age from a leucogranite located in the middle part of the slab is interpreted to suggest that leucogranite emplacement was contemporaneous with thrusting along the MCT (Hubbard & Harrison, 1989). Muscovite (12.0 ± 0.2 Ma) and K-feldspar (8.0 ± 0.2 Ma) cooling ages from the MCT zone may be suggestive of a younger phase of MCT thrusting (Hubbard & Harrison, 1989). A number of muscovite, biotite and K-feldspar cooling ages from the lower part of the slab are consistent with post-MCT deformation at ~8 Ma (Hubbard & Harrison, 1989).

The top of the High Himalayan Slab in the Everest region is bounded by the Everest Normal Fault (also known as the Qomolangma Detachment). Hodges *et al.* (1992) report the Rongbuk pluton cross-cutting the STD, which implies that the latest phase of slip along the STD at this locality cannot be younger than the age of the granite itself (21.6-19.5 Ma; Table 2.2).

2.2.3 Eastern central Nepal (Langtang)

In eastern-central Nepal (*Langtang section*), the MCT is described as a 2-3-km-thick brittle-ductile duplex showing lithological affinities to both the Lesser Himalaya and the High Himalayan Slab (MacFarlane *et al.*, 1992; Inger & Harris, 1992), (Figure 2.4b). Inger and Harris (1992) and Reddy *et al.* (1993) suggest that the MCT in Langtang is located immediately below the kyanite isograd and that the entire hangingwall was passively carried over the Lesser Himalaya during a phase of post-metamorphic thrusting along the MCT. MacFarlane (1995) suggests that the MCT was a syn-metamorphic structure and that no distinct metamorphic break is discernible between the High Himalayan Slab and underlying Lesser Himalaya. The slab becomes increasingly migmatitic towards the top, where it is believed that a higher-temperature sillimanite-grade metamorphism (M_2) has overprinted the earlier-formed kyanite-grade M_1 assemblages (Inger & Harris, 1992; MacFarlane *et al.*, 1992; Reddy *et al.*, 1993). Reddy *et al.* (1993) suggest that the juxtaposition of sillimanite-grade assemblages above kyanite has occurred along late-stage

thrusts. This is not supported by the P-T profile presented by MacFarlane (1995), (Figure 2.4b). MacFarlane (1995) suggests that the M_2 stage of metamorphic mineral growth was pervasive across the entire slab and occurred at lower temperatures in the MCT zone.

P-T profiles across Langtang have been performed by Inger and Harris (1992) and MacFarlane (1995), (Figure 2.4b). It is interesting to note that the temperatures recorded by Inger and Harris (1992) are consistently 100-200°C higher than those recorded by MacFarlane (1995), (see Table 2.1). This has been attributed to the choice of geothermometer used and suggests that temperature estimates may only be of use for comparative purposes, rather than reliable indicators of absolute values. The data presented by both Inger and Harris (1992) and MacFarlane (1995) is suggestive of a linear decrease in pressure above the MCT, which closely matches that of a normal lithostatic gradient (~3.7 km/kbar). MacFarlane (1995) presents a more comprehensive temperature profile across the slab, which is suggestive of near isothermal conditions of ~600°C. MacFarlane (1995) interprets this to be the result of "diachronous attainment of equilibrium temperature conditions in a lithostatic palaeopressure profile after ductile faulting of the sequence".

Geochronological studies in Langtang suggest that M_1 developed prior to ~34 Ma and M_2 between 20-17 Ma (Inger & Harris, 1992). Parrish and Hodges (1996) presented metamorphic monazite ages of 15.4 to 20.7 Ma, which they interpret to be related to the timing of peak metamorphism. Whether this relates to M_1 or M_2 remains uncertain. The Shisha Pangma leucogranite intrudes into the immediate footwall of the STD at the top of the Langtang section (Figure 2.4b) and is believed to be genetically related to the high-temperature M_2 metamorphism (Searle *et al.*, 1997a). U-Pb and $^{40}Ar/^{39}Ar$ age constraints from this pluton suggest that M_2 occurred between 20-17 Ma (Table 2.2) and that rapid cooling and unroofing at the top of the slab occurred between 17-14 Ma at rates of ~4 mm/yr (Searle *et al.*, 1997a). An estimated 12 km of overburden is believed to have been removed during this period by normal faulting along the STD and erosion (Searle *et al.*, 1997a). MacFarlane *et al.* (1992) suggest that the latest phase of brittle faulting along the MCT zone occurred at ~8 Ma and that ductile movement was initiated between ~15-20 Ma. This is consistent with geochronological data from other parts of the slab which show that thrusting along the MCT was broadly synchronous with M_2 metamorphism and emplacement of leucogranites at higher structural levels.

2.2.4 Western-central Nepal (Manaslu)

In the Manaslu section of western-central Nepal, Arita *et al.* (1982) proposed the existence of two MCT sections which are located at the same structural levels as the chlorite and kyanite isograds respectively (Figure 2.2). Le Fort (1986) and Pêcher (1989) refute this suggestion and believe that only one MCT exists in the Manaslu region, corresponding to the MCT-II of Arita *et al.* (1982), at the approximate structural level of the kyanite isograd (Figure 2.4c). Current geochronological data from the footwall of the MCT zone suggest that garnet-bearing assemblages are as young as 6-8 Ma and that the MCT must, therefore, be located above the level of the garnet-in isograd (Harrison *et al.*, 1997a).

The High Himalayan Slab in the Manaslu district records a poly-metamorphic history. M_1 assemblages formed at high-pressures and medium-temperatures (7-8.5 kbar and 600-690°C) are

overprinted in the upper parts of the slab by a later lower-pressure, higher-temperature M_2 stage of growth (<7 kbar and 650-710±C), (Table 2.1). Hodges *et al.* (1988a) presented a P-T profile across the High Himalayan Slab in the Manaslu region (Figure 2.4c), which demonstrates that pressures decrease linearly at a rate which is compatible with a normal lithostatic gradient of ~3.71 kbar/km. Isothermal conditions at ~600°C are recorded across the slab and are thought to be related to thermal buffering during anatexis (M_2). However, this implies that the entire High Himalayan Slab was cooled rapidly and uniformly during exhumation, before lower-temperature assemblages could be frozen-in. Vannay & Grasseman (1997) suggest that the closure temperature of the garnet-biotite thermometer at ~600°C could account for the observed isothermal temperatures in both the Langtang and Manaslu sections.

The Manaslu leucogranite pluton at the structural top of the slab Manaslu is one of the few granites which is reported to cut across the STD (Guillot *et al.*, 1994a). However, the structural location of the STD is poorly defined in this part of the Himalaya owing to the progressive northwards decrease in metamorphic grade from amphibolite facies in the High Himalayan Slab to the anchizone sediments of the Tibetan Sedimentary Series (Guillot *et al.*, 1995). In addition, the isotope systematics of the Manaslu pluton are particularly complex, making it difficult to date accurately (cf. Le Fort, 1981; Copeland *et al.*, 1990; Guillot *et al.*, 1994b). The most geologically reasonable age for intrusion appears to be 22.4 ± 0.5 Ma (Harrison *et al.*, 1995). Guillot *et al.* (1995) suggest that movement along the STD occurred prior to the intrusion of the Manaslu pluton, which is inconsistent with observations and interpretations from other parts of the slab (with the possible exception of Rongbuk in eastern Nepal).

2.2.5 Western-central Nepal (Annapurna)

In the Annapurna region of western-central Nepal (approximately 40 km to the west of Manaslu), the MCT is mapped as a ~1-3-km-thick mylonitic zone with no observable metamorphic or tectonic discontinuity within this unit (Vannay & Hodges, 1996). The structural position of the MCT in the Annapurna region is coincident with the location of the kyanite isograd, thus placing garnet- and sub-garnet-grade rocks in the Lesser Himalaya (Figure 2.4d).

Vannay and Hodges (1996) presented a P-T profile across this very narrow part of the High Himalayan Slab (Figure 2.4d) and observed that no sillimanite-bearing assemblages are found anywhere in the slab. This is reflected by the low temperatures recorded in central part of the slab (~500°C) and implies that either M_2 metamorphism is absent in the Annapurna region, or occurred at lower temperature conditions (cf. *Langtang*: MacFarlane, 1995). Pressures and temperatures show several fluctuations in the Annapurna region, which Vannay and Hodges (1996) interpret as the result of a protracted M_1 metamorphism. Monazite ages of ~34-36 Ma have been recorded from the Formation III augen gneiss in the Annapurna region, which may be related to mineral growth associated with the M_1 metamorphic stage (Hodges *et al.*, 1996). The highest P-T estimates are preserved in the MCT zone and in the Kalopani Shear Zone, both of which are interpreted to have been exhumed soon after peak-M_1 conditions were attained. Those parts of the slab which record lower P-T estimates are interpreted to have been exhumed more slowly and have therefore had longer to re-equilibrate at shallower crustal levels. A closer look at the P-T profile shows that pressures decrease rapidly immediately above the MCT at a rate far greater than that of a

normal lithostatic gradient and flatten-out at ~7 kbar in the central part of the slab. Pressures increase rapidly within the Kalopani Shear Zone and decrease again slightly in the immediate footwall of the Annapurna Detachment. Temperatures within the MCT zone are observed to increase slightly before decreasing sharply in the lowermost part of the slab. This initial increase in temperature may be due to the shear-heating effects felt by the immediate hangingwall (cf. *Everest*: Hubbard, 1996). Temperatures are almost isothermal at ~500°C across the central part of the slab and are observed to rapidly increase within the Kalopani Shear Zone. Temperatures decrease sharply again in the immediate footwall of the Annapurna Detachment.

In the Annapurna region, the boundary between the High Himalayan Slab and Tibetan Sedimentary Series is marked by a relatively complex system of ductile (Deorali detachment) and brittle (Machhapuchhare detachment) normal faults belonging to the STD (Figure 2.4d), (Brown & Nazarchuk, 1993; Hodges *et al.*, 1996; Coleman, 1996; Vannay & Hodges, 1996). Ductile extension along the Deorali detachment is constrained between 22.5 Ma and 18.5 Ma and brittle normal faulting on the Machhapuchhare detachment between 19-14 Ma (Hodges *et al.*, 1996). Geochronological data suggest that the earliest phase of thrusting in the MCT zone occurred at ~22.5 Ma and that the latest phase of motion may be as young as the Pliocene (Hodges *et al.*, 1996). Thrusting along the base of the slab therefore appears to be contemporaneous with ductile extension at the top during the Miocene. In addition, Coleman and Hodges (1995) constrained the timing of east-west extension at ~14-18 Ma in the Annapurna region, thus confirming that east-west extension post-dates northwards extension on the STD.

2.2.6 Eastern Garhwal

In eastern Garhwal, growth of metamorphic mineral assemblages is associated with two distinct stages of crystallisation (Valdiya, 1988; Hodges & Silverberg, 1988). The first of these (M_1) is related to the crystallisation of a typical Barrovian metamorphic mineral succession (biotite ± garnet ± staurolite ± kyanite), which records peak pressures of 600-650°C and 9-10kbar (Hodges & Silverberg, 1988). These are overprinted in the upper part of the slab by M_2 metamorphic assemblages which are associated with the growth of sillimanite- and cordierite-bearing assemblages at lower pressures and higher temperatures (3-5kbar and 650-700°C), (Hodges & Silverberg, 1988). Hodges and Silverberg (1988) believe that the M_2 metamorphism was generated as a direct result of the heating effects felt during the emplacement of higher level leucogranite at the top of the slab. This contrast sharply with the interpretation of Swapp and Hollister (1991) in Bhutan, who believe that the leucogranites are the result and not the cause of this high-temperature metamorphism. Hodges and Silverberg (1988), cite late Eocene (*c.*38Ma) $^{40}Ar/^{39}Ar$ ages for M_1 hornblendes collected near the base of the slab, which places a minimum constraint on the timing of this prograde metamorphism. No accurate age constraints have been published for the leucogranites or migmatites associated with the M_2 event in eastern Garhwal.

2.2.7 Western Garhwal

In western Garhwal (NW Indian Himalaya), the MCT forms a 10-12 km-thick zone of distributed deformation which is floored by a relatively discrete brittle-duplex system (the Munsiari Thrust) and is delineated along its top by the high-temperature Vaikrita Thrust (Metcalfe, 1993), (Figure 2.4e). Geochronological data from the MCT zone suggests that it experienced both ductile and brittle phases of motion along the Vaikrita and Munsiari thrusts at 19.8 ± 2.6 Ma and ~6 Ma respectively (Metcalfe, 1993). Biotite cooling ages of ~20 Ma are recorded from the Jhala Normal Fault (STD) at the top of the slab, suggesting that both the MCT and STD may have been moving at roughly the same time (Metcalfe, 1993). Younger cooling ages from the MCT zone are consistent with the overall decrease in cooling ages towards the south-west (Figure 2.4e), which Metcalfe attributes to a piggy-back style of thrusting towards the south-west through time.

Four stages of metamorphic mineral growth are recognised in western Garhwal (Metcalfe, 1993). M_1 and M_3 in western Garhwal are correlatable to the Barrovian-M_1 and sillimanite-grade-M_2 stages of mineral growth observed in other part of the High Himalayan Slab. M_2 metamorphic mineral growth in western Garhwal is related to the development of inclusion-free garnet overgrowths in the MCT zone. Metcalfe (1993) interprets this to be the result of syn-kinematic growth during thrusting on the MCT. M_4 mineral growth in western Garhwal relates to late-stage retrogression of earlier formed assemblages (Metcalfe, 1993).

Metcalfe's (1993) P-T profile across the High Himalayan Slab shows both pressure and temperature increasing slightly in the immediate hangingwall of the Vaikrita Thrust and that the majority of the High Himalayan Slab is isobaric and isothermal at ~7 kbar and ~600°C respectively (Figure 2.4e).

2.2.8 Western and central Zanskar

The High Himalayan Slab in central and western Zanskar is one of the best studied parts of the High Himalaya anywhere along its ~2500 km length (e.g. Herren, 1987; Kundig, 1989; Stäubli, 1989; Searle *et al.*, 1992; Dransfield, 1994; Noble & Searle, 1995; Stephenson, 1997), largely because of its accessibility and excellent exposure. The protoliths of the slab in western Zanskar comprise a thick succession of clastic and carbonate lithologies which are believed to be lateral equivalents of the Mesozoic successions exposed in the Tibetan Sedimentary Series to the north of the Zanskar Shear Zone (a lateral equivalent of the STD), (Searle *et al.*, 1992). U-Pb ages also suggest that some of the granites which intrude these sediments are Permian in age (the Sankoo granite, Noble & Searle, 1998). The majority of these lithologies have experienced amphibolite-facies metamorphism. However, fossiliferous Palaeozoic and Mesozoic sedimentary successions are exposed in areas of low metamorphic grade (the Chamba Syncline), which has led various authors to postulate whether these sediments are an integral part of the slab, or whether they are a tectonic cover-sequence (e.g. Thakur & Pande, 1971; Rattan, 1973), (Figure 2.5a).

The structure of the High Himalayan Slab in central and western Zanskar is dominated by sillimanite-grade migmatitic domes which are flanked by extensional detachments (Kundig, 1989; Stäubli, 1989). Large-scale SW-verging nappes are observed above these domal structures in western Zanskar (Searle *et al.*, 1992), (Figure 2.5a). The slab is bounded along its top by the Zanskar Shear Zone (ZSZ), a local equivalent of the STD (Searle, 1986; Herren, 1987; Dransfield, 1994). It is bounded along its base by the

MCT, although this has been removed in western Zanskar by late-stage NE-directed backthrusting along a major structure referred to as the Suru-Warwan cross fault, or Warwan Backthrust (Searle *et al.*, 1992; Stephenson, 1997), (Figure 2.5a). In central Zanskar the MCT represents a 1-3-km-thick zone of distributed ductile deformation which displays lithological affinities to both the High Himalayan Slab and underlying Lesser Himalaya (Stephenson, 1997). $^{40}Ar/^{39}Ar$ cooling ages from MCT in central Zanskar constrain the latest phase of ductile motion along this thrust between 15-17 Ma (Stephenson, 1997). Late-stage doming of the MCT exposes the Lesser Himalaya through the Kishtwar Window (Figure 2.5a). Exposure of sillimanite-grade lithologies to the south of the Kishtwar Window provides strong evidence that thrusting along the MCT was post-metamorphic (Figure 2.5b). Inversion of the metamorphic isograds in the MCT zone in central Zanskar is attributed to a combination of syn/post-metamorphic folding and post-metamorphic ductile thrusting of the High Himalayan Slab above the Lesser Himalaya following the attainment of peak-metamorphic conditions (Searle *et al.*, 1992; Stephenson, 1997).

The metamorphic history of the High Himalayan Slab in western and central Zanskar is similar to that observed in other parts of the Himalaya. Both M_1 and M_2 stages of metamorphic mineral growth are recognised (Searle *et al.*, 1992), with sillimanite-grade assemblages located towards the middle/upper parts of the slab. In western Zanskar (Suru Valley traverse), kyanite is the stable aluminosilicate across the ~35-km width of the slab, where peak-M_1 conditions of 8-10 kbar and ~700C are recorded (Figure 2.5c). In central Zanskar (Umasi La traverse), pressures and temperatures increase sharply above a narrow high-strain zone, which is thought to represent the upper part of the MCT zone (Stephenson, 1997), (Figure 2.5d). Temperatures increase towards the central part of the slab, where lithologies are dominated by sillimanite-grade migmatites and zones of localised *in situ* partial melting related to the M_2 metamorphic stage (Figure 2.5d). A corresponding decrease in pressure towards the centre of the slab accompanies this temperature increase. In both western and central Zanskar, pressures and temperatures are observed to rapidly decrease towards the top of the slab where isograds have been strongly sheared and condensed by extensional normal faulting along the ZSZ (Searle, 1986; Herren, 1987; Dransfield, 1994). Migmatitic leucosomes believed to have formed during the M_2 metamorphic stage have been dated at 20.6-19.5 Ma across central Zanskar (Noble & Searle, 1995). Using Sm-Nd techniques, Vance and Harris (1996) suggested that garnet growth during the M_1 metamorphic stage occurred at *c.*35-25 Ma.

2.3 Tectonic synthesis: the current state of knowledge

The above synthesis of previous works in the High Himalayan Slab demonstrate that a number of structural, metamorphic and magmatic features show remarkable spatial and temporal consistency along the entire length of this metamorphic terrane. Local variations do exist, but in general, the following features are common to all parts of the slab:

i) It consists of a metamorphosed sequence of Precambrian(?) to Mesozoic sediments, Permo-Carboniferous volcanics and Lower Palaeozoic granites.

ii) It is structurally bounded by the MCT to the south and the STD to the north.

iii) Metamorphic isograds are inverted in the MCT zone and are parallel to the thrust-related mylonitic fabrics.

iv) It contains textural evidence for two phases of Tertiary metamorphic mineral growth: a medium/high-pressure and medium-temperature stage (M_1) and a lower-pressure, higher-temperature stage (M_2).

v) M_1 is constrained between 15-38 Ma at conditions of *c.* 10-12 kbar and 450-650°C.

vi) M_2 is constrained between 12.5-25 Ma at conditions of *c.* 3-12 kbar and 650-750°C.

vii) Sillimanite-grade migmatites (M_2) are located structurally above kyanite-grade bearing assemblages (M_1) towards the top of the slab.

viii) Emplacement of High Himalayan leucogranites (syn/post-M_2) occurred at *c.* 12.5-25 Ma, and was broadly contemporaneous with extension along the STD and thrusting along the MCT at ~17-25 Ma..

ix) Rejuvenation of thrusting along the MCT occurred at <10 Ma.

2.3.1 Burial and metamorphism in the High Himalayan Slab

Metamorphism in the High Himalayan Slab is dominantly Tertiary in age, although this does not necessarily preclude the possibility that some of the protoliths preserve pre-Himalayan metamorphic assemblages. Two texturally distinct phases of metamorphic mineral growth are recognised in all parts of the High Himalayan Slab (M_1 and M_2). The Eo-Himalayan or M_1 metamorphism (Le Fort, 1975; Hodges & Silverberg, 1988; Pêcher, 1978, 1989; Kündig, 1989) is characterised by the growth of regional Barrovian-type metamorphic assemblages and is generally attributed to crustal shortening and thickening of the High Himalayan Slab following the India-Asia collision (Figure 2.6a). Thermobarometric constraints from across the slab suggest peak-metamorphic conditions during M_1 were in the order of *c.* 6-12 kbar and 450-750°C (Table 2.2), suggestive of a total overburden of *c.* 30-45 km (assuming a lithostatic gradient of 3.71 km/kbar). Few published ages pertain to the timing of this metamorphism. Inger and Harris (1992) speculated that M_1 metamorphic assemblages in the Langtang section were developing prior to ~34 Ma, but presented no accurate geochronological constraints to support this interpretation. Hodges and Silverberg (1988) cite late Eocene (*c.* 38 Ma) $^{40}Ar/^{39}Ar$ ages for M_1 hornblendes collected near the base of the Vaikrita Group in eastern Garhwal, which seems to preclude the possibility of M_1 being any younger than this in this part of the Himalaya. In the Langtang section of Nepal, Parrish and Hodges (1992) presented metamorphic monazite ages of 15.4-20.7 Ma (metapelite samples), which they interpret to represent the time of peak-metamorphic conditions. Whether this age corresponds to the timing of Eo-Himalayan metamorphism (M_1), or the later M_2 stage remains unclear. Monazite ages of ~34-36 Ma have been recorded from the Formation III augen gneiss in the Annapurna region of Nepal, which may be related to mineral growth associated with the M_1 metamorphic stage (Hodges *et al.*, 1996). Vance and Harris (1996) report ages of 35-25 Ma for M_1 porphyroblastic garnets in the Zanskar Himalaya.

A higher-temperature (*c.* 650-750°C) and lower-pressure (*c.* 4-7 kbar) phase of metamorphic mineral growth is recorded in the middle and upper sections of the High Himalayan Slab (Figure 2.1). This is generally referred to as the M_2 metamorphism (Hodges & Silverberg, 1988; Kündig, 1989) and is recognised texturally by a number of characteristic reactions involving the breakdown of pre-existing M_1 mineral assemblages and the growth of sillimanite. M_2 assemblages are absent in the MCT zone, giving

rise to an apparent inversion of sillimanite above kyanite in the central and upper parts of the slab (Figure 2.2). M_2 is interpreted to be related to decompression and/or heating of the slab during exhumation (Figure 2.6a), although in certain parts of the Himalaya it has been suggested that M_2 is the result of out-of-sequence thrusting in Tibet (Figure 2.6b). M_2 metamorphism is closely associated with *in situ* migmatisation and the generation and emplacement of the High Himalayan leucogranites (HHL) in the uppermost part of the slab (Le Fort, 1981; Searle & Fryer, 1986; Searle *et al.*, 1997a), (Figures 2.1 & 2.2). Crystallisation ages of migmatitic leucosomes and higher-level leucogranite plutons, which are believed to be temporally linked to the M_2 stage of metamorphic development, provide accurate constraints pertaining to the timing of M_2 and also provide a minimum estimate of the age of M_1 metamorphism. These ages vary between 12.5-25 Ma across the High Himalayan Slab (Table 2.2).

2.3.2 Origins of inverted metamorphism in the MCT zone

An inverted metamorphic sequence is preserved in the MCT zone along almost the entire ~2500km length of the High Himalayan Slab (Figures 2.2 & 2.4). The origins of this have been the focus of several intensive studies over the years, with various thermal and structural models proposed to explain its development. Simple thermal models predicting the development of an inverted metamorphic sequence by hot-over-cold thrusting (e.g. Le Fort, 1975: Figure 2.7a) have been largely discounted owing to the fact that the inverted geotherm in such models is extremely transient and is unlikely to be preserved during uplift (e.g. Oxburgh & Turcotte, 1974; Shi & Wang, 1987; England and Molnar, 1993a). Shear heating along the MCT provides an additional source of heat which allows an inverted thermal structure to be preserved (Arita, 1983; England *et al.*, 1992; England and Molnar, 1993a). However, structural and thermobarometric work in the Everest (Hubbard, 1996), Langtang (Inger & Harris, 1992; Reddy *et al.*, 1993; MacFarlane, 1995), western Garhwal (Metcalfe, 1993) and Zanskar (Stephenson, 1997) regions have shown that the MCT is predominantly a post-metamorphic structure, which questions the validity of such models. Structural models suggest that inverted metamorphism in the MCT could be generated through a combination of syn/post-metamorphic recumbent folding of a previously formed right-way-up sequence of metamorphic isograds (Figure 2.7b), and flexural slip in the MCT zone (Figure 2.7c).

Given the structural complexity of the MCT zone along strike, it seems likely that no single mechanism can satisfactorily account for the origins of inverted metamorphism in all parts of the Himalaya. Part of the problem lies in the definition of the MCT, with different authors using various structural, lithological and metamorphic criteria to distinguish it. Consequently, the MCT is described in different ways in the same part of the Himalaya. An additional problem is that deformation and metamorphism in the MCT zone was likely to have been diachronous. For example, Harrison *et al.* (1997a) recently discovered ~6-8 Ma garnets in the Lesser Himalaya in western-central Nepal, which they suggest provides strong evidence that the MCT was active as recently as the Upper Miocene/Pliocene (Figure 2.4e). These ages demonstrate that textural relationships alone cannot be used to correlate the growth of metamorphic assemblages which, at first glance, appear to form a contemporaneous metamorphic succession.

2.3.3 Melting in the High Himalayan Slab

Related to the problem of inverted metamorphism in the MCT is the location of sillimanite-grade migmatites and crustal melt leucogranites in the upper part of the slab (Figure 2.2). The High Himalayan leucogranites (HHL) form a series of s-parallel sheets surrounded by a larger area of anastomosing dykes and sills in the footwall of the STD (Le Fort, 1981; Searle & Fryer, 1986; Searle *et al.*, 1997a). They are believed to have formed by partial melting of a metasedimentary source equivalent to the underlying High Himalayan Slab (Dietrich & Gansser, 1981; Vidal *et al.*, 1982; Le Fort *et al.*, 1987; Scaillet *et al.*, 1990; Harris *et al.*, 1993). The majority of granites record early Miocene crystallisation ages of *c.*20 Ma (Table 2.2), although the spread of ages is quite large and suggests that melting was a diachronous and protracted event across the High Himalayan Slab. Since the majority of granites are cut by the STD, the latest phase of extension along this fault must be younger than the crystallisation age of the granite.

The HHL are clearly the product of high temperature metamorphism and are generally associated with the M_2 metamorphic stage. Various models have been proposed to account for the generation of the these leucogranites and their preferred distribution in the footwall of the STD (no leucogranites have ever been observed in the MCT zone). Le Fort *et al.* (1987) proposed a model whereby overthrusting of the High Himalayan Slab caused devolatilisation reactions to occur in the underlying Lesser Himalaya. These fluids were released up structural section, causing partial melt reactions to occur in the High Himalayan Slab. Generation of the High Himalayan leucogranites in this way seems unlikely, given the fact that temperatures in the immediate footwall of the MCT will never approach those in the immediate hanging-wall (England & Molnar, 1993a), thus questioning the magnitude of devolatilisation in the Lesser Himalaya. This model also implies that melting should develop first in more northerly regions, since these would be the first to be overthrust if foreland propagating thrust geometries were adhered to. Geochronological data show that the age of magmatism decreases northwards, with the North Himalayan leucogranites (NHL) consistently recording younger ages than the HHL (Table 2.2).

England *et al.* (1992) and more recently Harrison *et al.* (1997b) believe that the High Himalayan leucogranites could have been generated by dissipative shear heating along the MCT during thrusting. Shear heating would increase temperatures in the MCT zone, which could facilitate incongruent melting of muscovite. Geochronological evidence suggests that thrusting along the MCT at temperatures above 500°C occurred at ~20 Ma (Hubbard & Harrison, 1989; MacFarlane *et al.*, 1992; Metcalfe, 1993) and is therefore similar in age to the crystallisation age of the High Himalayan leucogranites (Table 2.2). However, the main criticism of any model that relates the generation of the HHL to the MCT is that it fails to explain why no leucogranites are ever observed in the MCT zone anywhere in the Himalaya and why the ~16 or so major High Himalayan leucogranite plutons are located in the immediate footwall of the STD (Figure 2.1).

Jaupart and Provost (1985) suggested that the location of the HHL along the STD could be attributed to conductivity differences between the overlying Tibetan Sedimentary Series (low conductivity) and the underlying High Himalayan Slab (high conductivity and enriched in radiogenic elements). Melting would occur at the top of the slab as a direct result of heat focusing along the STD. This model is particularly appealing since it also predicts that the increased temperature effects would be felt later in more northerly

regions and would, therefore, account for the age disparity between the NHL and HHL (Table 2.2). Furthermore, since this model is based on the distribution of heat-producing radiogenic elements in the crust, it is also capable of explaining the wide spread of ages recorded by the High Himalayan leucogranites along strike (Pinet & Jaupart, 1987). One of the main criticisms of this model, however, is that it assumes that the contact between the High Himalayan Slab and Tibetan Sedimentary Series is a thrust. Whilst the most recent phase of motion along this structure is extensional, it does not preclude the possibility that earlier movements were compressional.

The close temporal and spatial association of the High Himalayan leucogranites to the STD has led to the suggestion that melting was related to decompression of the slab during M_2 metamorphism (Harris and Massey, 1994). Their conclusions are partly based on modelled P-T-t paths which show that isothermal decompression of rocks can occur in the early exhumation history of a thrust-thickened metamorphic terrane (e.g. England & Richardson, 1977; England & Thompson, 1984a; Thompson & England, 1984).

2.3.4 Exhumation history of the slab

Constraints pertaining to the exhumation and erosional history of the High Himalayan Slab come from three sources: (1) foreland sedimentary basins which contain the eroded detritus of the High Himalayan Slab; (2) marine geochemical anomalies; and (3) cooling ages from the High Himalayan Slab itself. Detrital micas in the Siwalik basin and Bengal Fan, which are believed to be sourced from the High Himalayan Slab record $^{40}Ar/^{39}Ar$ cooling ages of 28-21 Ma, which in some cases, are identical to the stratigraphic age of the sediment and suggest that erosion of the High Himalaya was underway by the early Miocene (Copeland & Harrison, 1990; Harrison *et al.*, 1993; Najman *et al.*, 1997). Abrupt changes in the $^{87}Sr/^{86}Sr$ ratios recorded by marine carbonates at 18 Ma (Edmond, 1992) and a prominent increase in the common Pb isotopic signature of Indian Ocean manganese nodules at *c.*20-14 Ma (Frank & O'Nions, 1998) are also interpreted to be related to erosion of the High Himalayan Slab. This implies that the High Himalayan leucogranites were being eroded shortly after their emplacement between 12.5-25 Ma (Table 2.2).

A compilation of the temperature-time data from the High Himalayan Slab in Nepal confirms that exhumation was initiated at about 20-25 Ma (Figure 2.8). In western Garhwal, cooling ages are also largely bracketed between 20-25 Ma and show an apparent younging towards the south-west (Figure 2.4e). This is consistent with the interpretation that structures in the Himalayan orogen propagate down structural section towards the south-west with time. Similar relationships were observed in western Zanskar by Searle *et al.* (1992), who obtained K-Ar and $^{40}Ar/^{39}Ar$ muscovite and biotite ages of *c.*20-15 Ma in different parts of the slab. Cooling ages of *c.*25-15 Ma from the High Himalayan Slab are similar to the age constraints pertaining to the timing of movement along both the MCT and STD, suggesting that exhumation was accomplished via movement along these two structures. These ages are also similar to the crystallisation ages of many of the High Himalayan leucogranites (Table 2.2), suggestive of a temporal and spatial link between thrusting along the MCT, extension along the STD and granite generation and emplacement.

2.3.5 Development of normal faults in collisional orogens

Many orogenic belts exhibit features associated with normal faulting (e.g. *Tibetan plateau*: Molnar & Tapponnier, 1978; *central Andes*: Dalmayrac & Molnar, 1981; *Basin and Range*: Wernicke *et al.*, 1987; *European Hercynides*: Ménard & Molnar, 1988), which suggests extension to be an important aspect of mountain building (Dewey, 1988). The Himalaya have been under constant compression for the last ~50 Ma (Patriat & Achache, 1984) and are currently shortening at a rate of ~18mma^{-1} (Avouac & Tapponnier, 1993). They have never experienced any net crustal extension during this time.

Recent models tend to liken collisional orogens to steady-state deforming orogenic wedges (Davis *et al.*, 1983), which according to Platt's (1986) two-dimensional analysis will not deform internally unless some change occurs to disturb the balance between tractional forces at its base and gravitational forces related to wedge thickening. Providing these forces are balanced, the wedge remains in dynamic equilibrium and extension will not occur. When these forces become unbalanced, the wedge will deform internally by thrusting and/or extensional normal faulting in an attempt to return to a state of dynamic equilibrium. This observation only holds, however, if the rheology of the wedge remains unchanged. Processes such as crustal melting are capable of significantly altering the rheological strength of the wedge which, in turn, could create internal instabilities which result in the development of normal faulting. Extension in collisional orogens will, therefore, tend to develop when the system destabilises and the wedge is no longer able to support itself. This process is generally referred to as 'orogenic collapse' and results from the build up and eventual release of gravitational potential energy in the orogen (e.g. England & Molnar, 1993b).

The geometry of the Himalaya roughly conforms to that of a tapered orogenic wedge, bounded at the base by the Main frontal Thrust (MFT). Within this tapered orogenic wedge, the High Himalayan Slab forms a smaller internal wedge bounded along the top by the STD and at the base by the MCT (Figure 2.3). It has been suggested that any of the following mechanisms could force the High Himalayan Slab out of dynamic equilibrium, leading to extension along the STD:

A change in relative plate motions (resulting in a decrease in the horizontal compressive stress across the Himalaya).

It is generally accepted that since collision at 50-54Ma, India has continued to drift northwards with respect to Asia at an average rate of *c.*50mma^{-1} (Patriat & Achache, 1984; Dewey *et al.*, 1989) placing the High Himalaya under a state of constant horizontal shortening since this time. No change in the relative plate motion of India with respect to Eurasia is evident in the ocean magnetic anomaly data since collision, suggesting this to be an unlikely cause of extension. Furthermore, any change in plate motion is unlikely to be of sufficiently large magnitude for changes in horizontal stresses to lead to the development of normal faulting at the top of the slab (England & Molnar, 1993b).

Uplift of the High Himalayan Slab relative to the surrounding area (resulting in vertical stress > horizontal stress).

Rapid uplift of the High Himalayan Slab relative to sea level would result in the orogenic wedge becoming gravitationally unstable. Normal faulting would develop at the top of the slab to compensate for this instability and would continue until dynamic equilibrium was maintained. Rapid uplift could be triggered by two mechanisms:

i) Delamination of the Indian plate mantle lithosphere (Dewey, 1988; England & Houseman, 1988)
ii) Dynamic compensation (Hodges *et al.*, 1996)

The first of these mechanisms would result in the isostatic uplift of the High Himalayan Slab over a relatively large area and would be capable of generating the observed simultaneous and widespread extension at the top of the slab during the Miocene. Removal of this lithospheric 'root', however, remains somewhat speculative and must be considered a one-off, non-reversible event which cannot explain the repeated phases of extension and contraction observed in the Annapurna region (Coleman, 1996; Hodges *et al.*, 1996). The second of these mechanisms allows the High Himalayan Slab to continually adjust to changes in the regional stress field on time-scales of a few million years. Alternating periods of out-of-sequence thrusting and extension allows the wedge to maintain a stable topographic profile in response to the changing styles of deformation and surface erosion (Figure 2.9).

Reduction of the shear stress along the base of the wedge (shear heating along the MCT).

Shear heating along the MCT could generate crustal melting and significantly lower the shear stress on the fault. If this were to happen, the High Himalayan Slab would no longer be able to support itself and normal faulting would develop at the top of the slab (Burchfiel *et al.*, 1992). England and Molnar (1993b) point out that this model is governed by sluggish thermal processes and that the synchronicity of slip on the STD along the entire length of the Himalaya would require a remarkable coincidence if this was the cause of normal faulting.

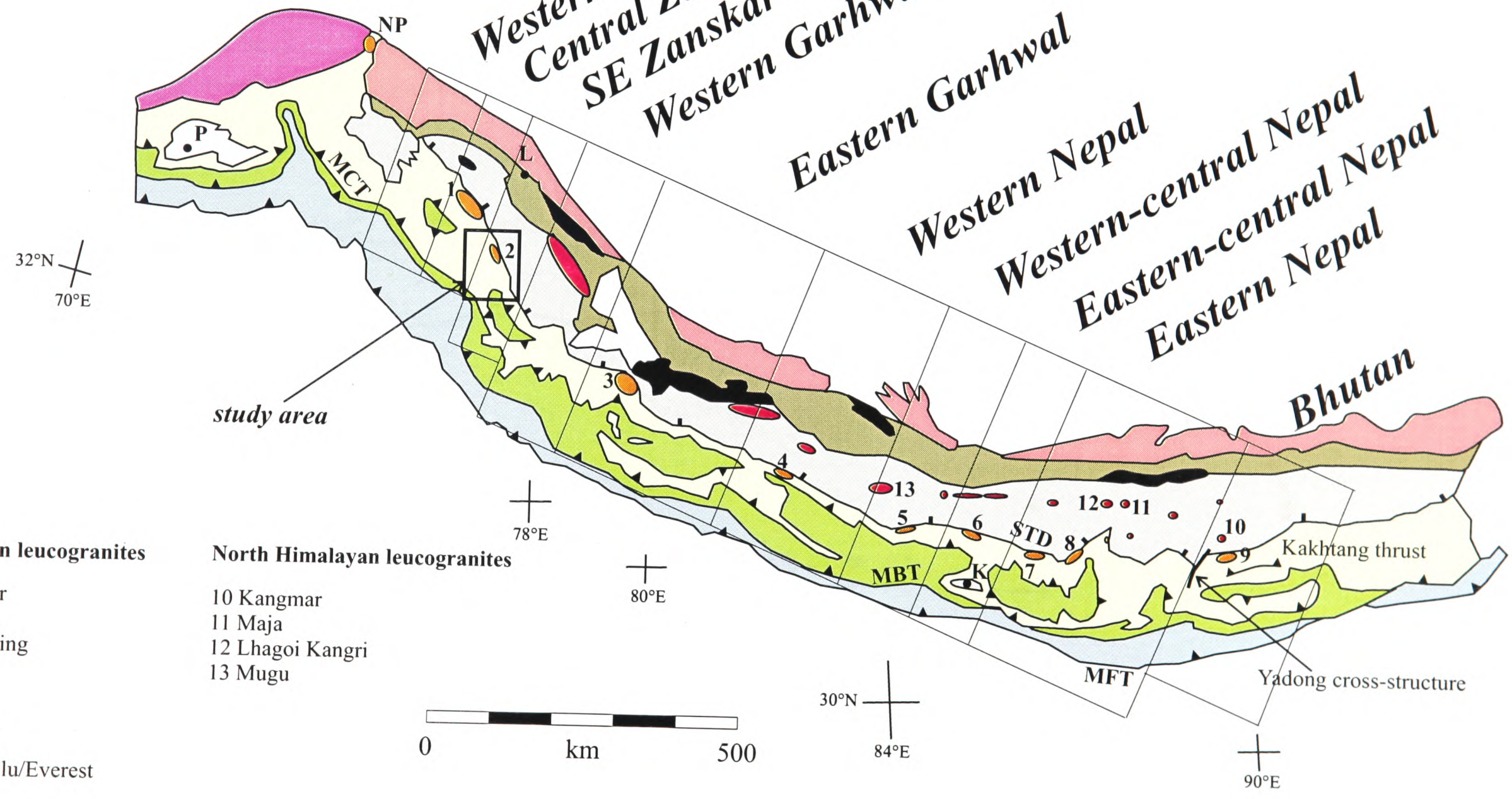
Development of a new thrust beneath the MCT.

If a new fault developed to the south of the MCT, the dynamic stability of the orogenic wedge would be dramatically altered. It is possible that such a change could bring about normal faulting at the top of the slab (England and Molnar, 1993b). This new fault could presumably, though not necessarily be the MBT.

Rheological changes within the High Himalayan Slab

The mechanisms discussed thus far have assumed that dynamic instability of the High Himalayan Slab occurred as a direct result of changing the boundary forces applied to the base of the wedge, or increasing is gravitational potential through isostatic uplift. It is equally possible, however, that rheological changes brought about by metamorphic reactions and crustal melting could weaken the wedge and precipitate normal faulting. Dehydration reactions during prograde metamorphism, for example, would increase pore

pressure and reduce the strength of the wedge (e.g. Etheridge *et al.*, 1984). Migmatisation and generation of the High Himalayan leucogranites may also have played a significant part in the initiation of normal faulting, although it has been suggested that these themselves are related to shear heating along the MCT (Le Fort *et al.*, 1987; Harrison *et al.*, 1997b), in which case, a combination of external and internal changes to the slab could have contributed to the development of the STD.



High Himalayan leucogranites

1 central Zanskar
2 SE Zanskar
3 Gangotri/Shivling
4 Api
5 Manaslu
6 Shishapangma
7 Nyalam
8 Rongbuk/Makalu/Everest
9 Kula Kangri

North Himalayan leucogranites

10 Kangmar
11 Maja
12 Lhagoi Kangri
13 Mugu

Figure 2.1: Geographical subdivision of the Himalaya. Annotation same as Figure 1.1.

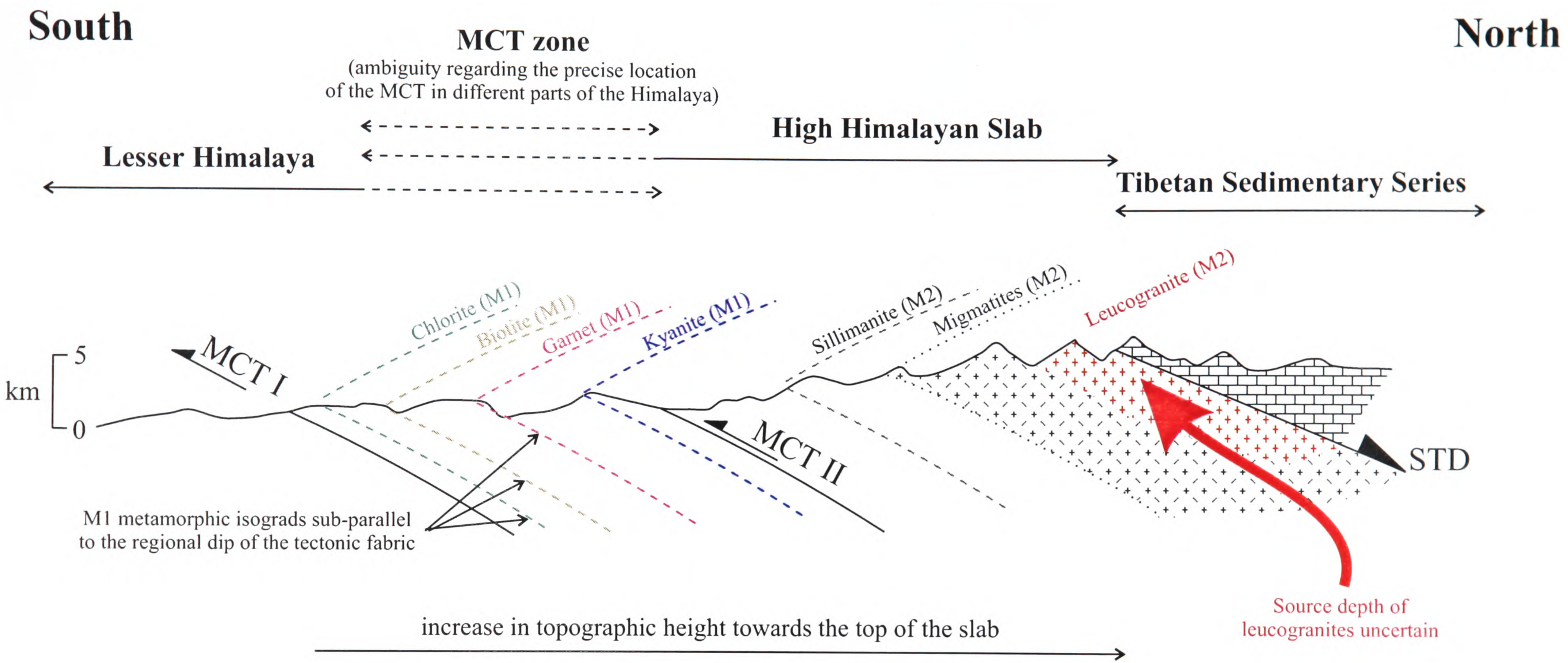


Figure 2.2: Archetypal cross-section through the High Himalayan Slab illustrating features common to all areas of this metamorphic terrane along strike. Note the inversion of metamorphic isograds towards the base of the slab and the location of sillimanite-grade migmatites and leucogranite sheets towards the top of the slab. Location of the MCT is often ambiguous and has been mapped at various structural levels within the slab between the positions of MCT I and MCT II shown above (location of these two MCTs taken from Arita et al., 1982). M1 and M2 refer to stages of metamorphic mineral growth (see text for details).

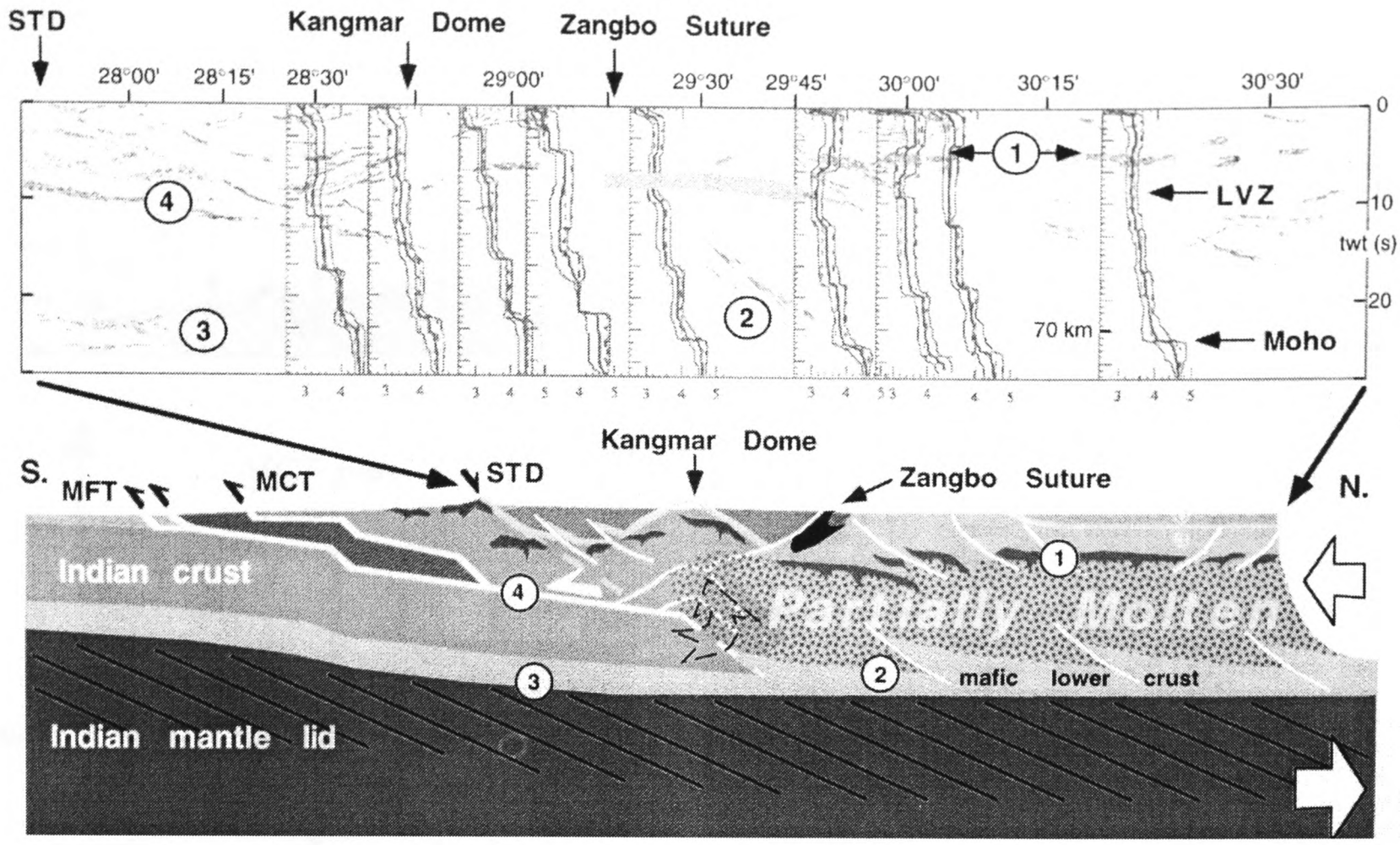


Figure 2.3: Interpretative cross-section across the Himalaya showing the position of the major intracontinental shear zones (after Nelson et al, 1996). MFT = Main Frontal Thrust; MCT = Main Central Thrust; STD = South Tibetan Detachment. The MFT represents a basal décollement along which the Himalaya are currently thrusting. It is interpreted that both the MCT and STD bottom into this décollement at depth, although reflection profiles to support this are lacking (note that the INDEPTH profile was shot to the north of the STD). Numbers refer to: (1) low-amplitude reflector (possible partial melt zone; (2) prominent reflectors beneath the Gangdese batholith (interpreted to be mafic lower crust); (3) Moho; and (4) MFT basal décollement.

P-T-t data from Eastern Nepal

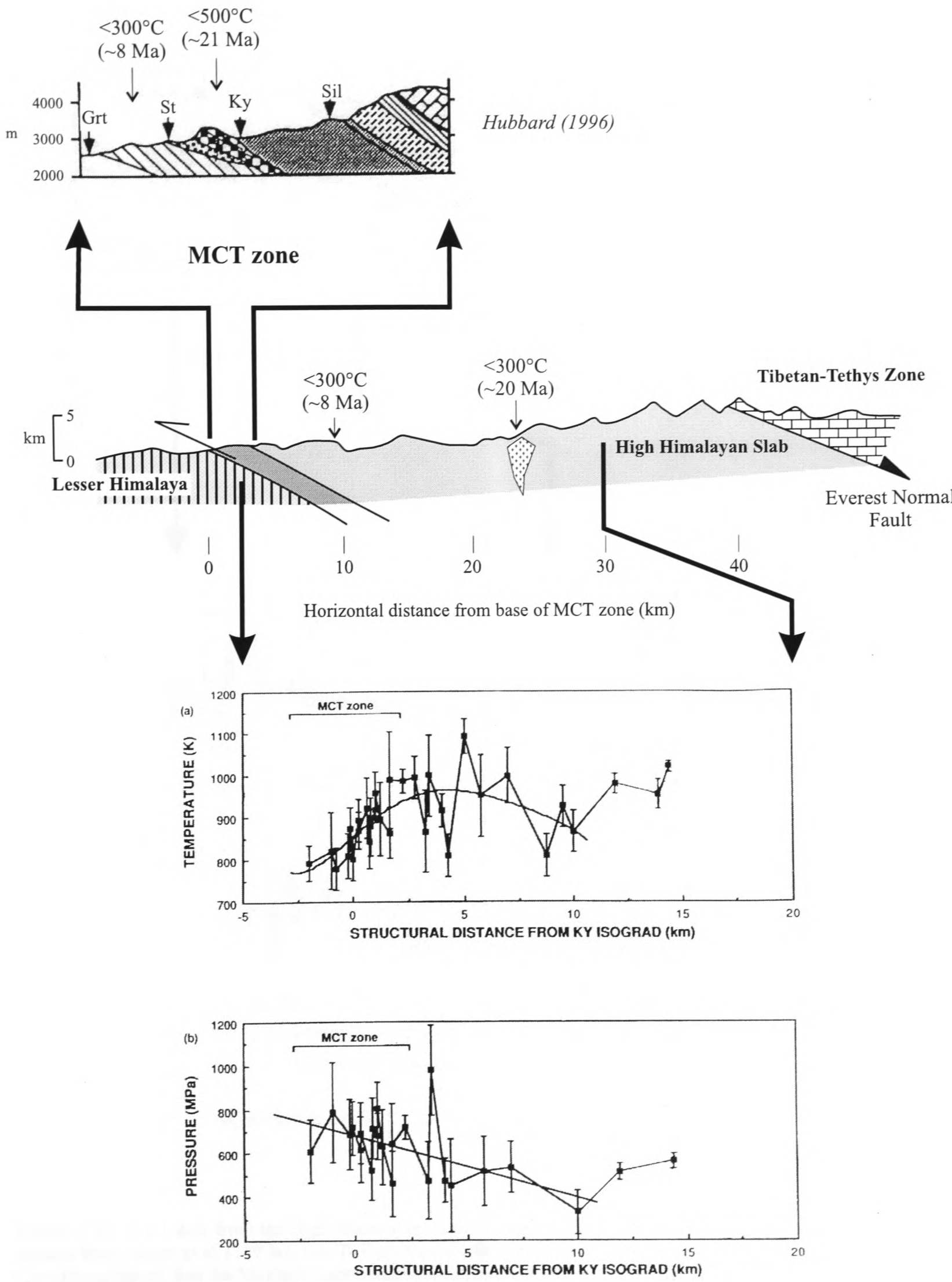
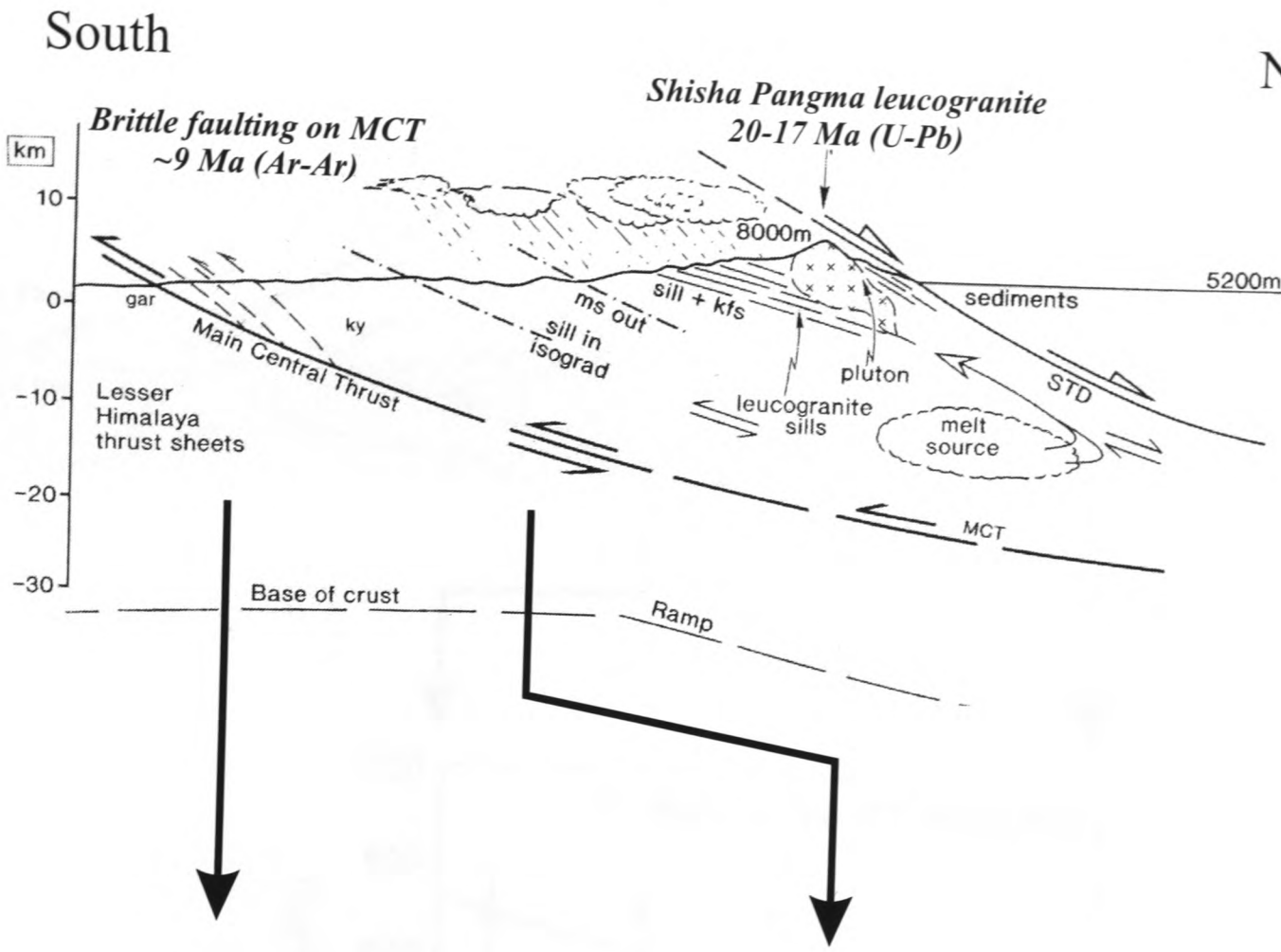
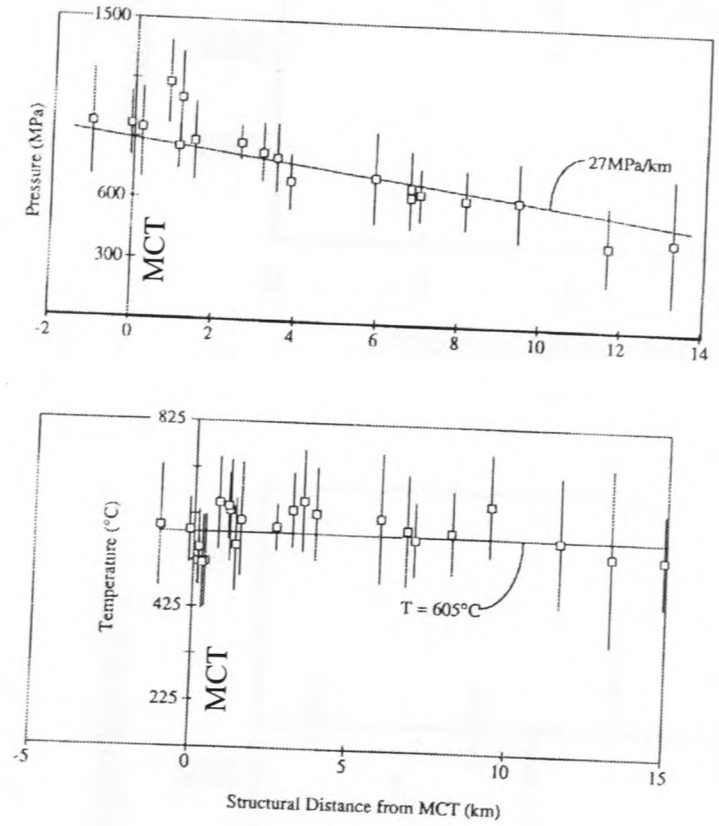


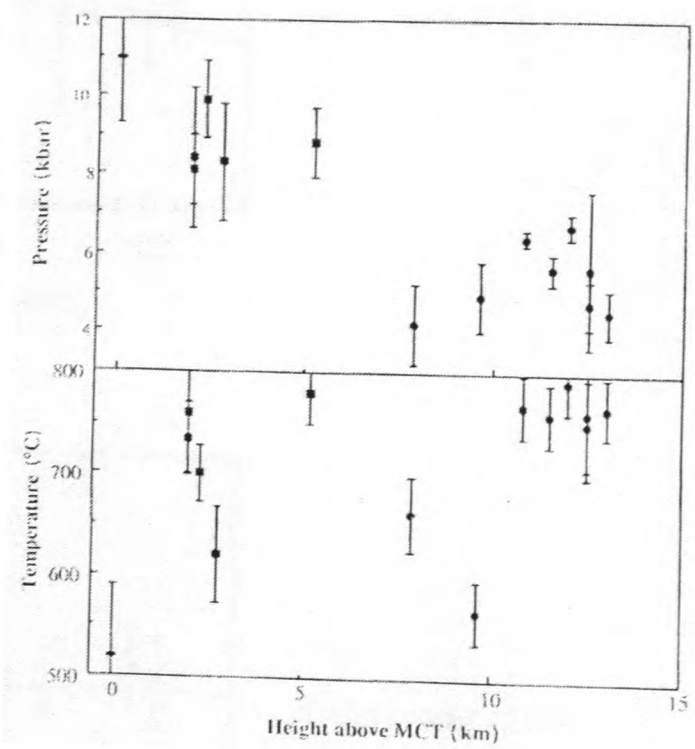
Figure 2.4a: P-T-t data from the High Himalayan Slab in eastern Nepal (Everest transect). P-T data from Hubbard (1989); geochronological data from Hubbard and Harrison (1989).

P-T-t data from Langtang





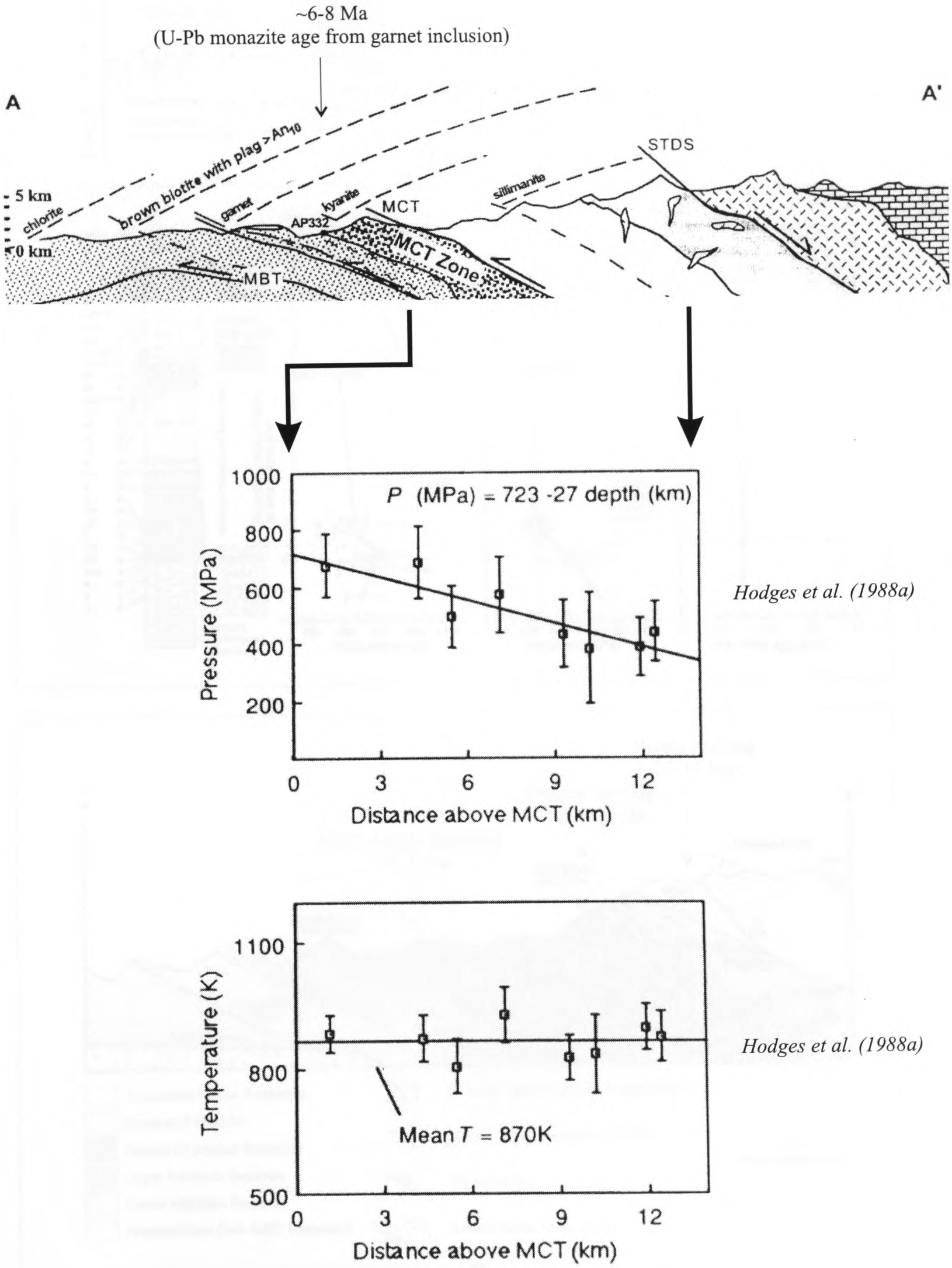
MacFarlane (1995)



Inger & Harris (1992)

Figure 2.4b: P-T-t data from the High Himalayan Slab in eastern-central Nepal (Langtang section). Schematic cross-section from Searle et al. (1997a). Two P-T profiles across approximately the same transect are shown for comparison. Geochronological data for Shisha Pangma leucogranite from Searle et al. (1997a). Geochronological data in the MCT zone from Macfarlane et al. (1992).

P-T-t data from Manaslu

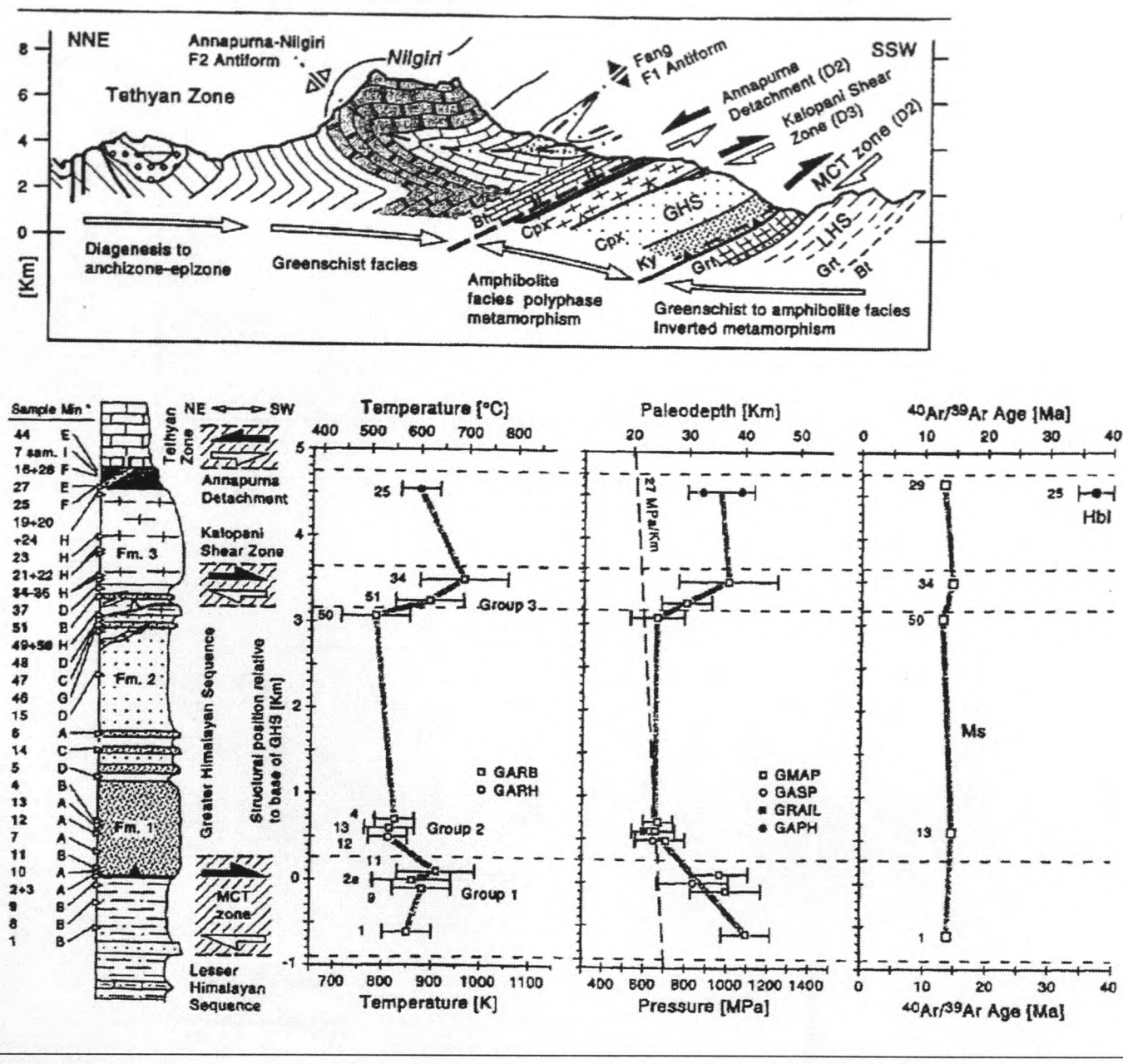


Hodges et al. (1988a)

Hodges et al. (1988a)

Figure 2.4c: P-T-t data from the High Himalayan Slab in western-central Nepal (Manaslu section). Schematic cross-section from Le Fort et al. (1987); P-T data from Hodges et al (1988); geochronological data from Harrison et al. (1997a). See Figure 2.7e for a more detailed explanation of the inverted metamorphism in this part of the slab.

P-T-t data from Annapurna



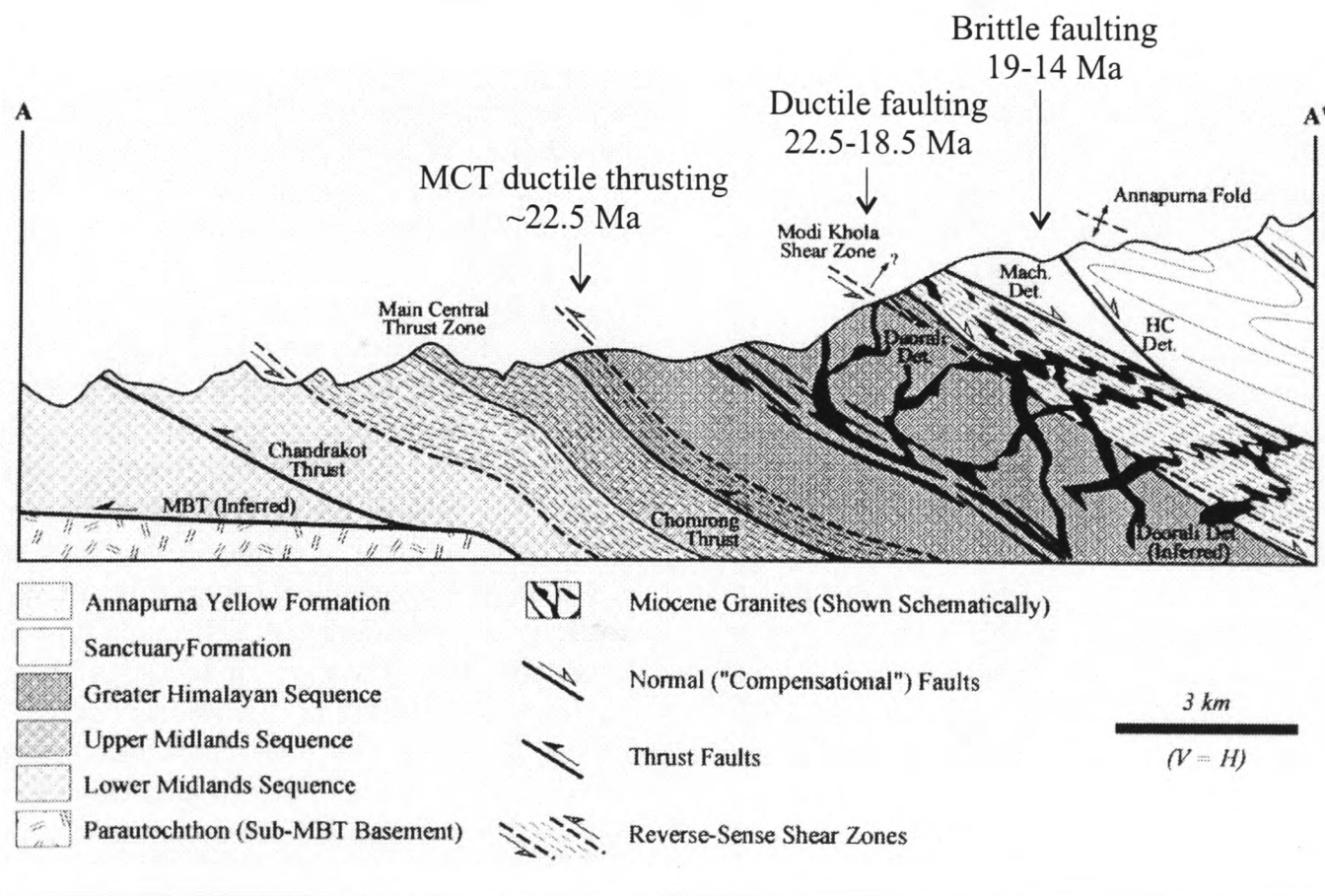
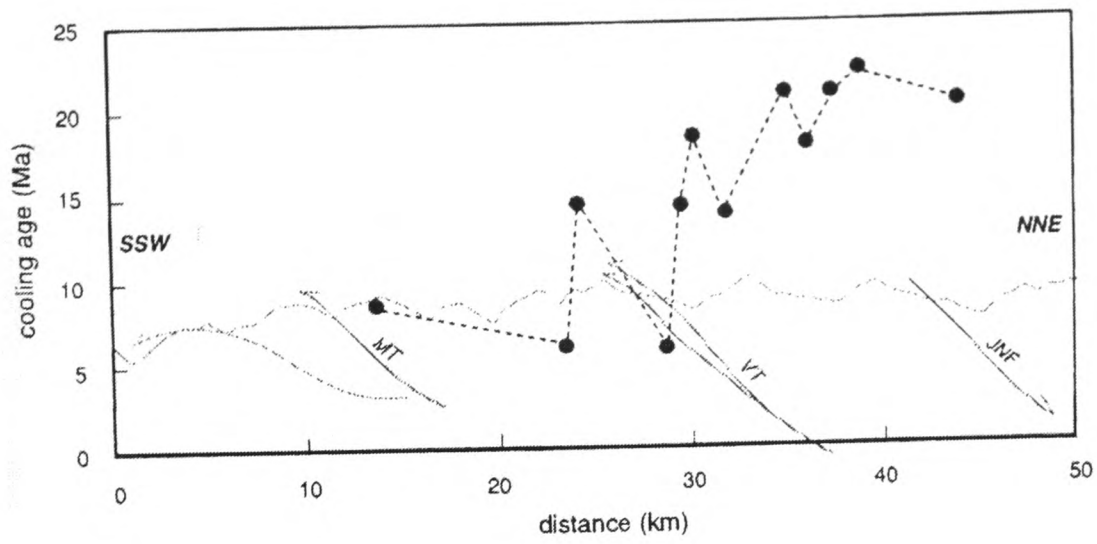
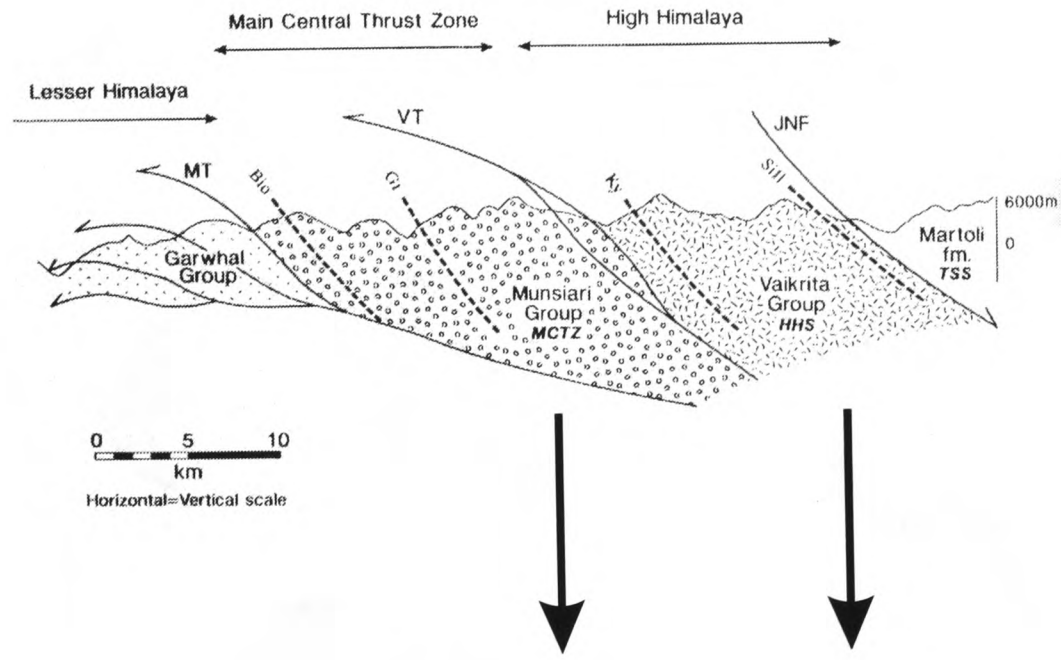
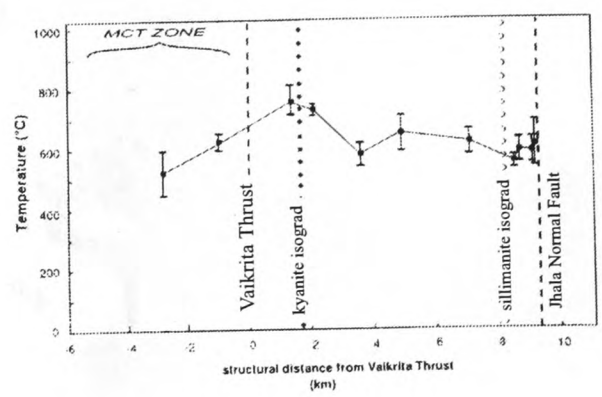


Figure 2.4d: Top: P-T-t data from the High Himalayan Slab in western-central Nepal (Annapurna section), after Vannay and Hodges (1996). Bottom: Schematic cross-section across the Annapurna region showing the location of the Deorali and Machappuchare detachments, both of which form part of the STD at the top of the slab (from Hodges et al., 1996).

P-T-t data from western Garhwal







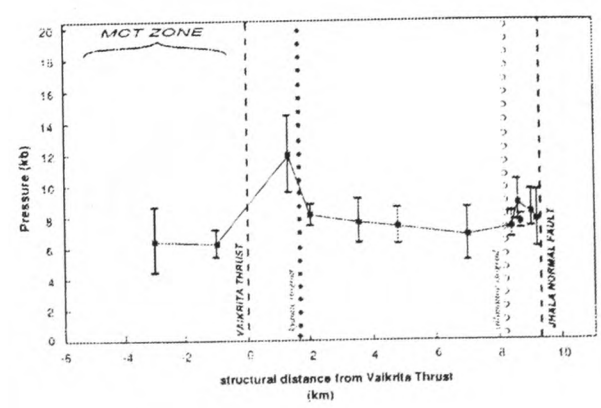


Figure 2.4e: P-T-t data from the High Himalayan Slab in western Garhwal (after Metcalfe, 1993). Top: South-westwards propagation of cooling ages. Middle: Schematic cross-section through the slab showing the location of the Vaikrita and Munsiari Thrusts, which together constitute the ~8-km-thick MCT zone. Bottom: P-T data from upper part of the slab.

Geology of the Kishtwar-Zanskar Himalaya

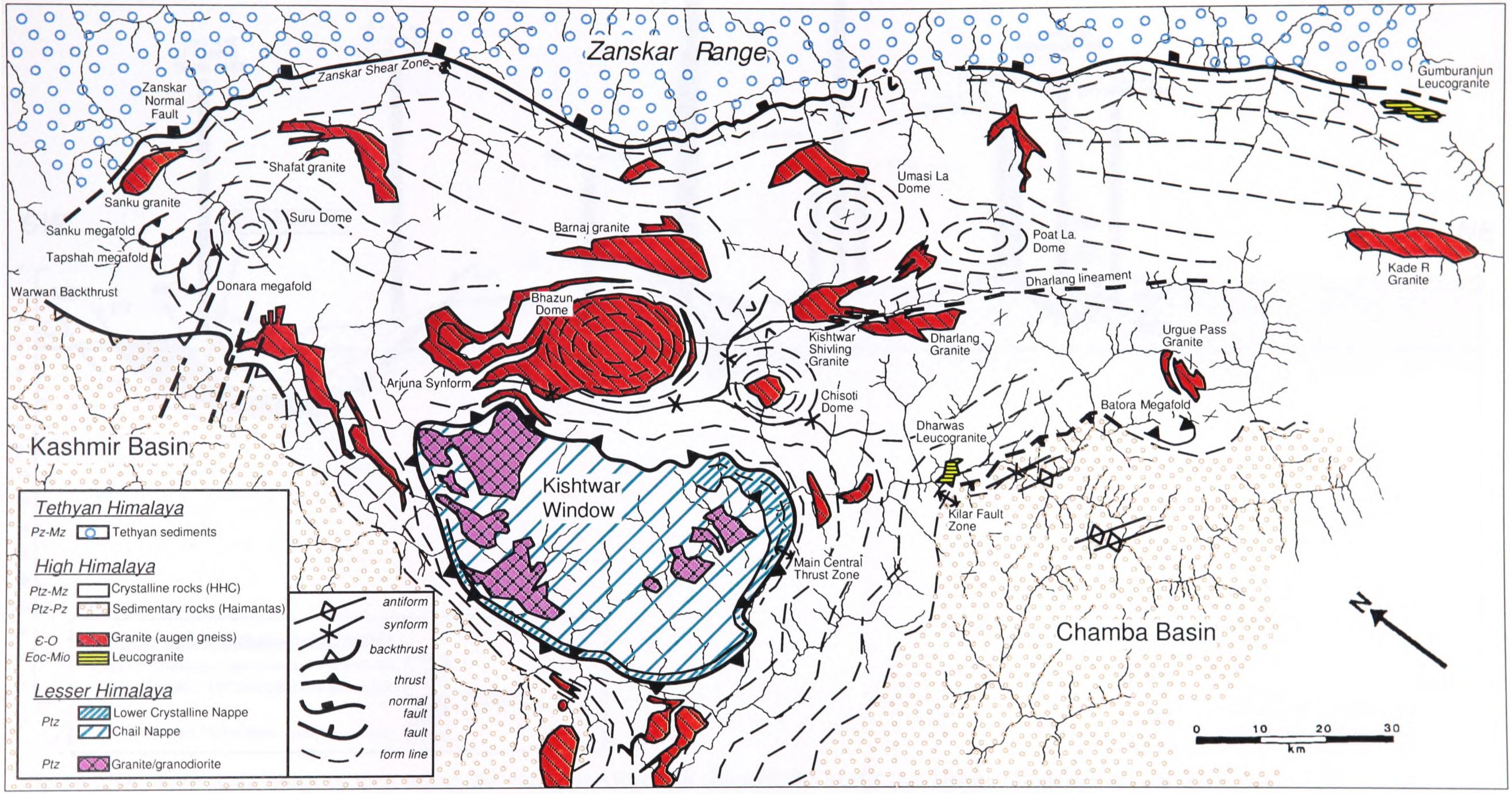


Figure 2.5a: Summarised geological structure of the High Himalayan Slab in central and western Zanskar (after Stephenson, 1997).

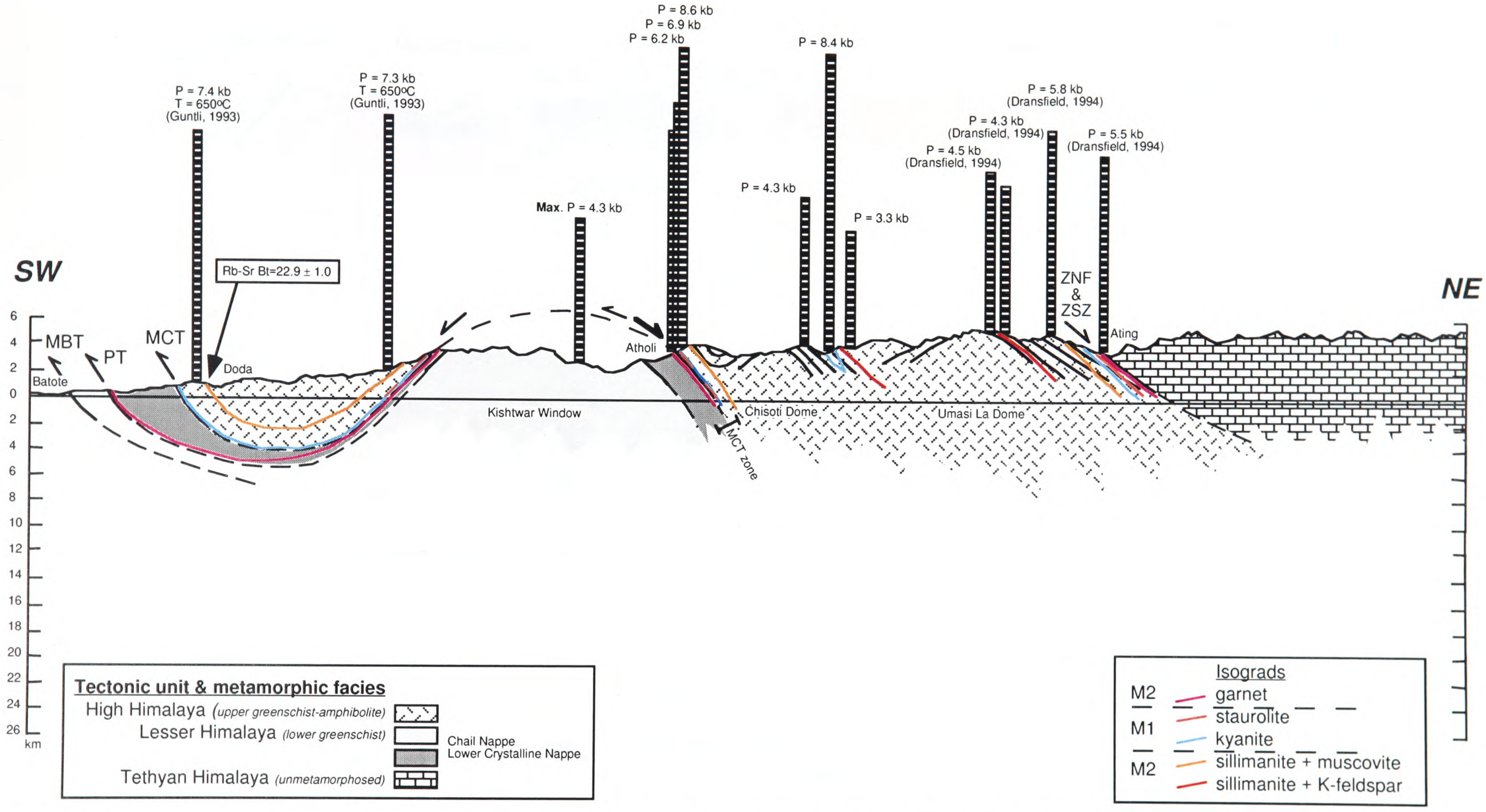


Figure 2.5b: True-scale cross section along the transport direction through the northwest Indian Himalaya showing the position of metamorphic isograds. Columns above the surface indicate the minimum overburden to account for the calculated pressures, assuming a lithostatic gradient of 2.7 kb/km (after Stephenson, 1997). MCT = Main Central Thrust, MBT = Main Boundary Thrust, PT = Panjal Thrust, ZNF = Zanskar Normal Fault, ZSZ = Zanskar Shear Zone.

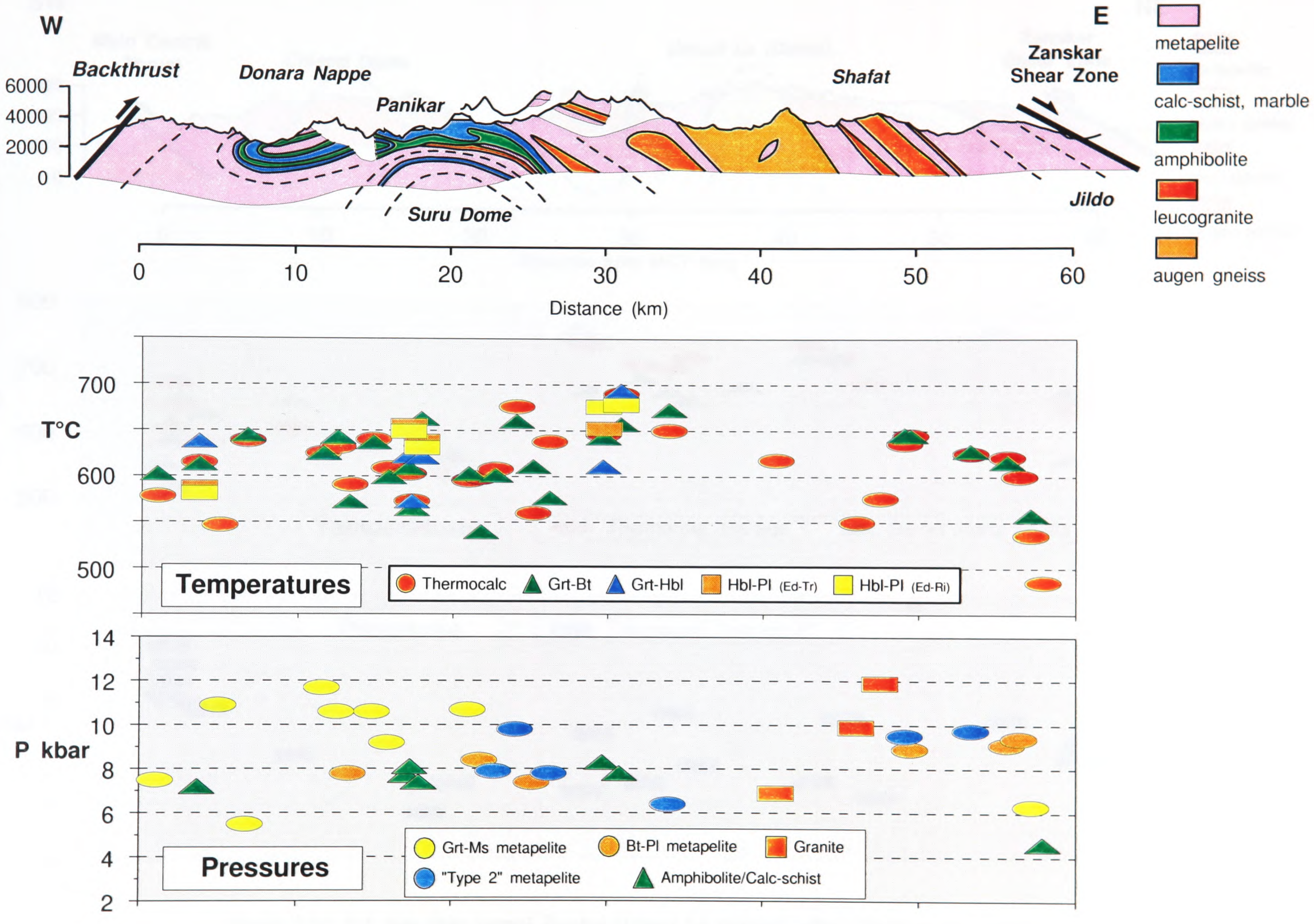


Figure 2.5c: P-T data from western Zanskar (Suru valley traverse), after Waters et al. (1996).

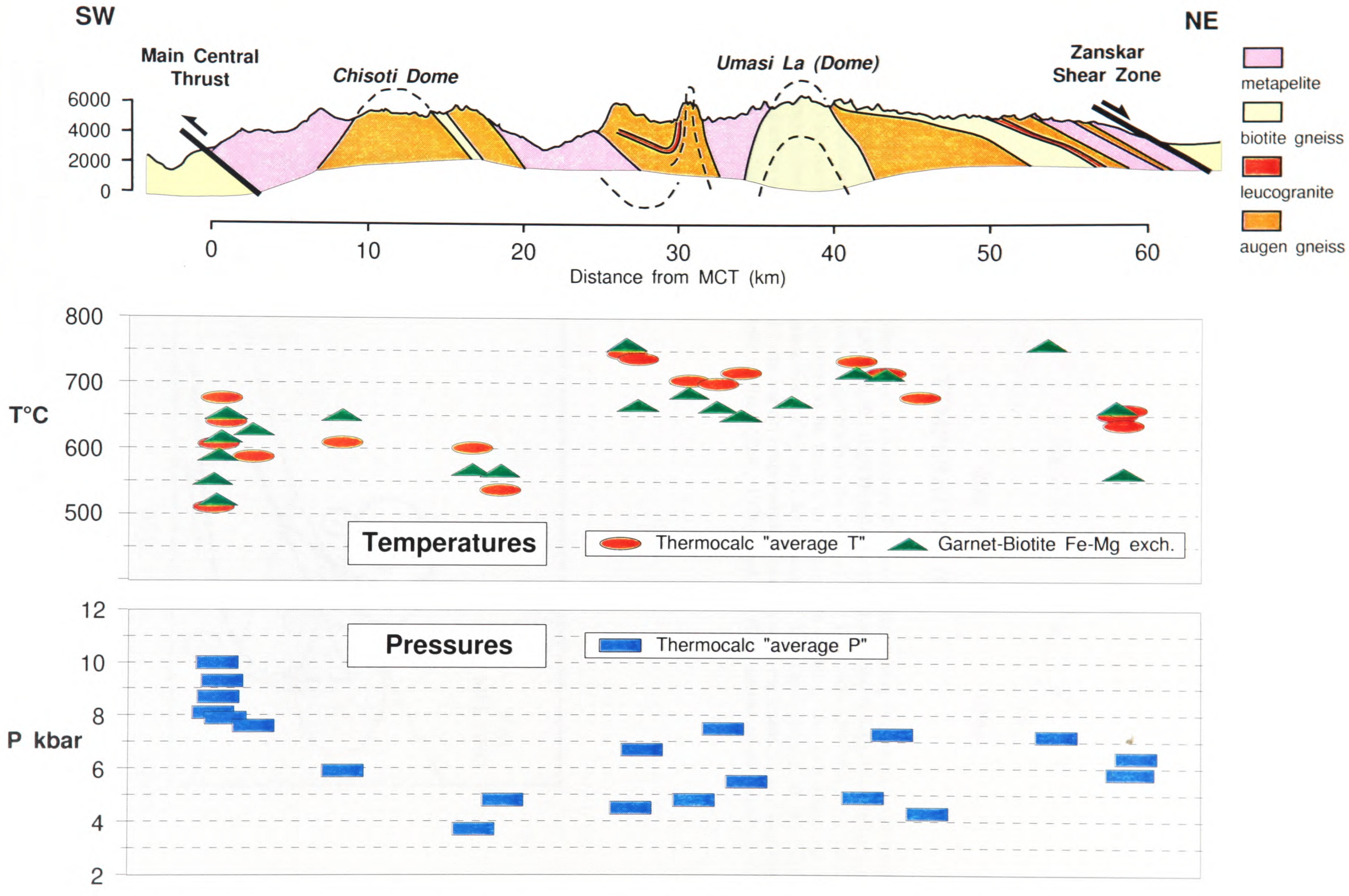


Figure 2.5d: P-T data from central Zanskar (Umasi La traverse), after Waters et al. (1996).

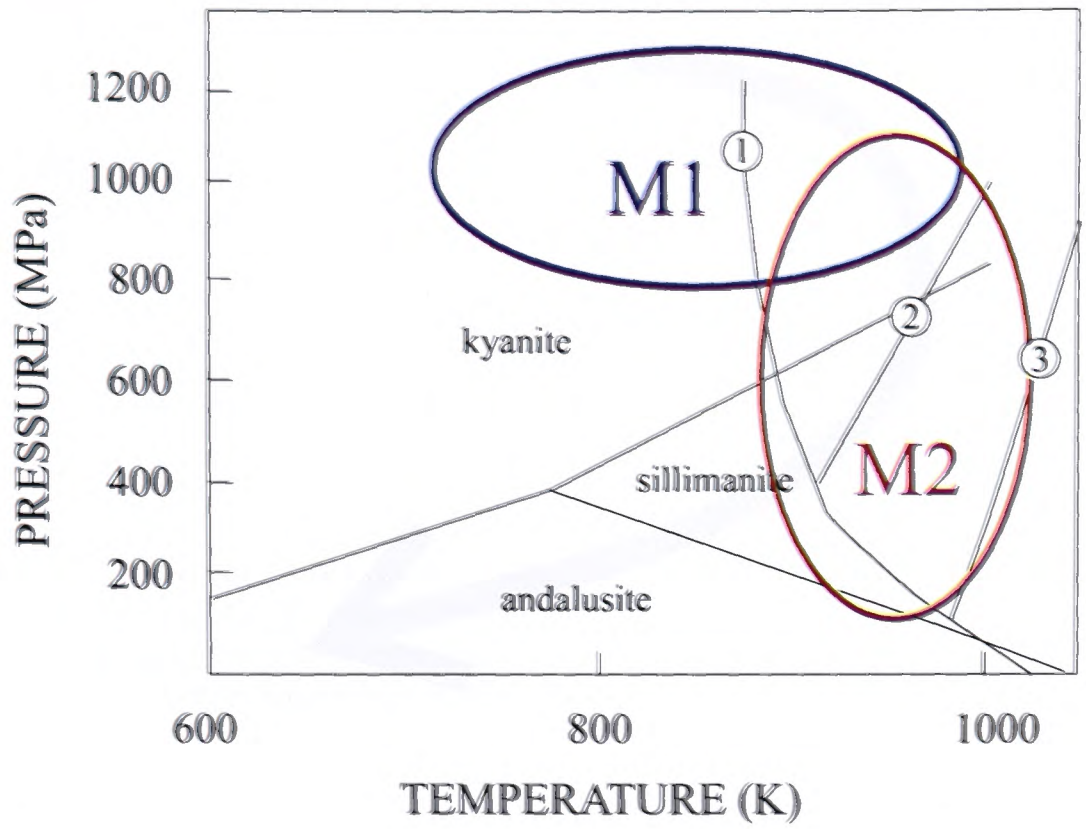


Figure 2.6a: Schematic representation of a clockwise P-T loop representing the single, continuously evolving metamorphic event (grey arrow) affecting the High Himalayan Slab during the Tertiary Himalayan metamorphism. Peak-metamorphic (M1) conditions are generally in the order of 8-12 kbar (800-1200MPa) and 450-700°C (~700-950K) across the slab and are thought to be related to progressive burial of the slab following collision. M2 metamorphism represents the transition of kyanite to sillimanite and emplacement of the High Himalayan leucogranites at the top of the slab during decompression.. Curves shown represent (1) wet melting (Thompson, 1982); (2) fluid absent muscovite melting (Peto, 1976); and (3) fluid absent biotite melting (Le Bretton & Thompson, 1988).

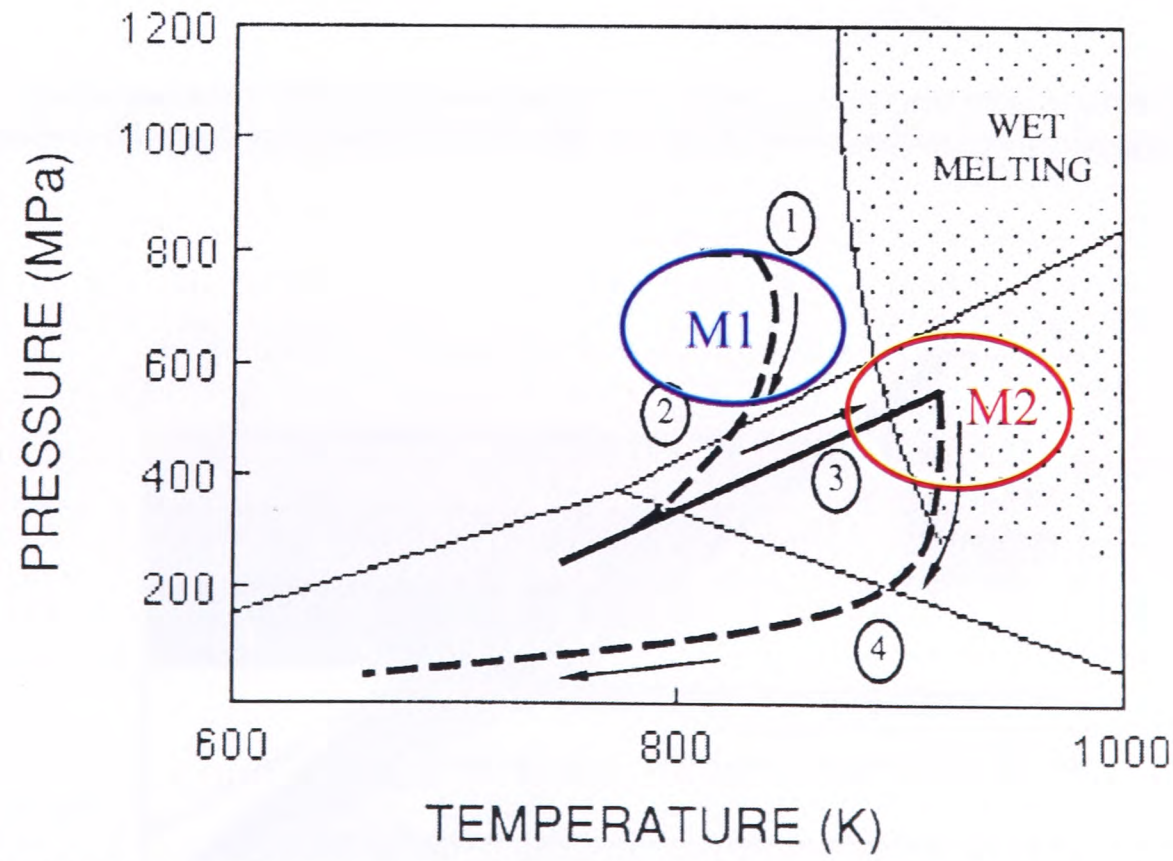


Figure 2.6b: Model showing the interpreted P-T evolution of the upper part of the High Himalayan Slab in eastern Garhwal (after Hodges & Silverberg, 1988). Note that the conventional clockwise P-T loop records peak-metamorphic (M1) conditions at (1), with erosion controlled uplift during (2). Sillimanite-grade M2 metamorphism is attributed to burial of the slab during a period of thrusting in southern Tibet, which is contemporaneous with emplacement of leucogranites into the top of the slab (3). Miocene-Recent uplift of the slab is represented by (4). Solid line refers to portion of P-T path constrained by petrological data, and dashed lines indicate hypothetical path segments.

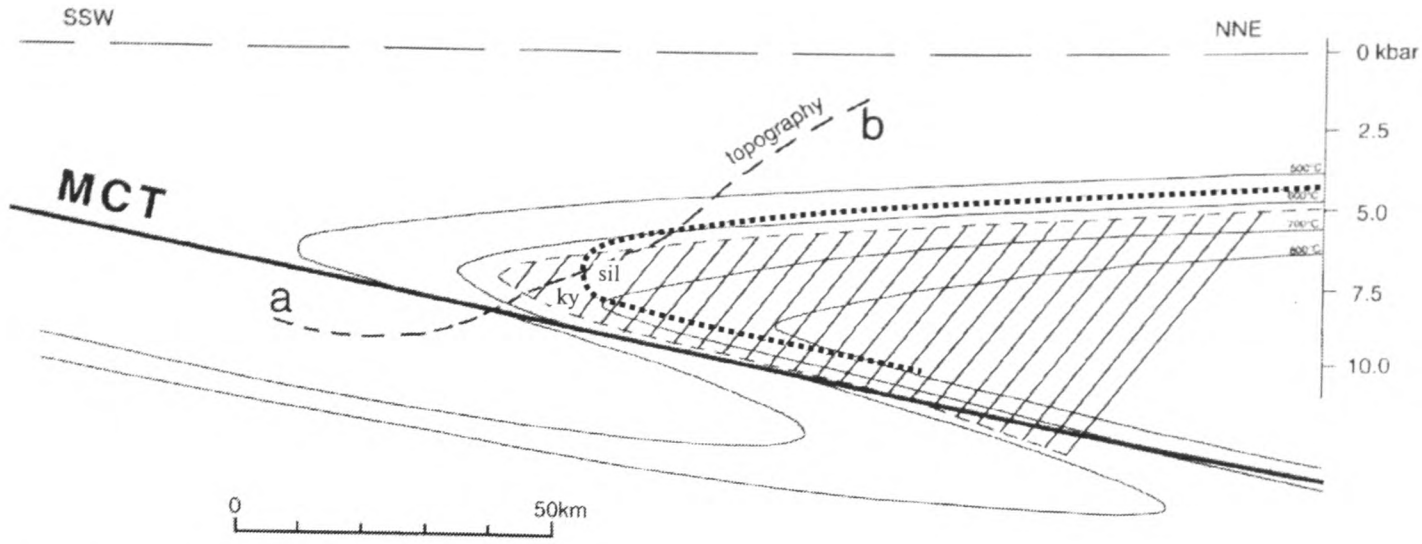


Figure 2.7a: Le Fort (1975) thermal model for inverted metamorphic isograds along the MCT. Thrusting a slab of hot rock over a cold footwall has the effect of temporarily inverting the temperature gradient in the hanging-wall, thus creating an inverted metamorphic sequence. The dotted line represents the kyanite = sillimanite transition, whilst the hatched area corresponds to the zone of partial melting.

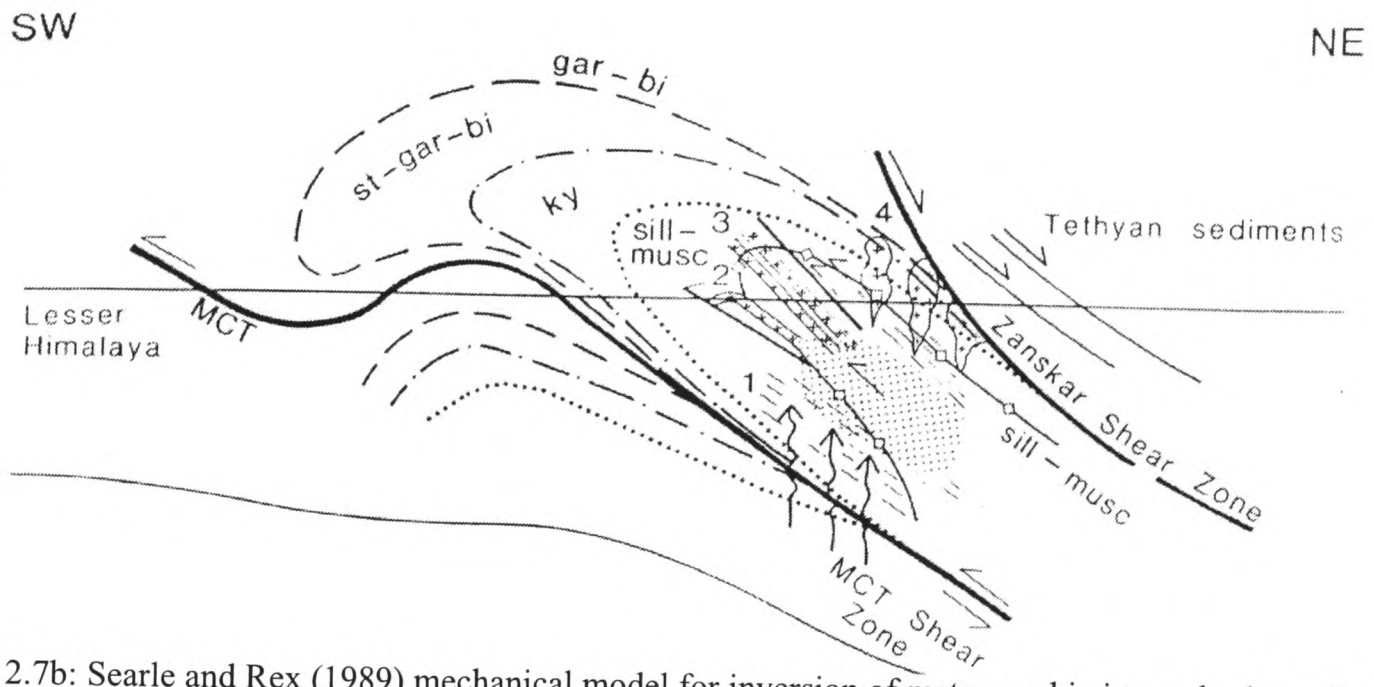


Figure 2.7b: Searle and Rex (1989) mechanical model for inversion of metamorphic isograds above the MCT by post-metamorphic folding of a previously formed right way-up Barrovian metamorphic sequence.

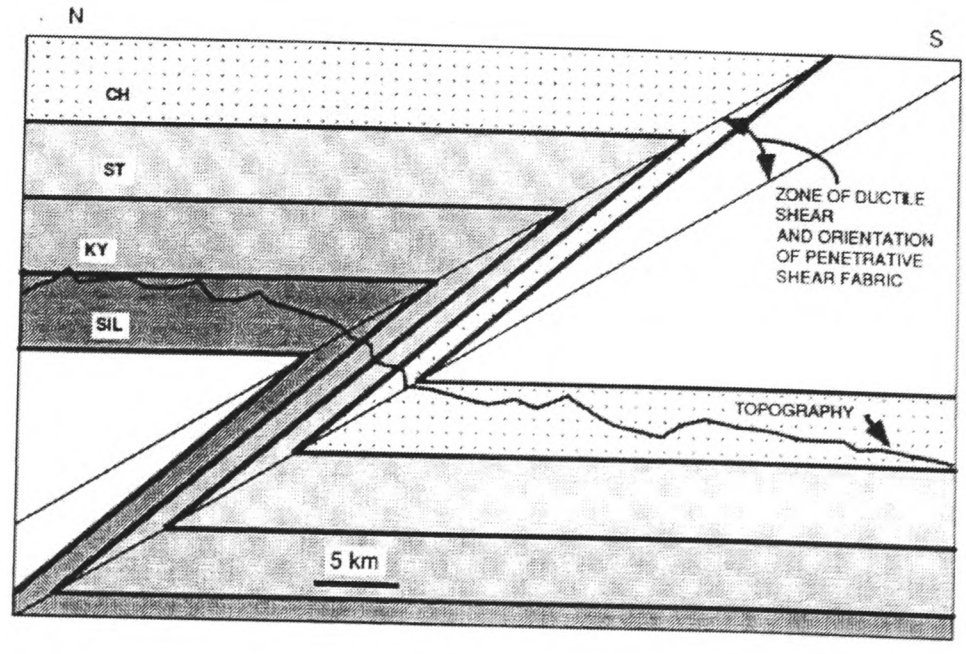


Figure 2.7c: Hubbard (1996) mechanical model for inversion of metamorphic isograds by progressive simple shear along the MCT. Shaded areas represent regions of different metamorphic grade which have been sheared into sub-parallelism with the zone of ductile shear (MCT). This model is similar to that proposed by Jain & Manickavasagam (1993) and Grujic et al. (1996).

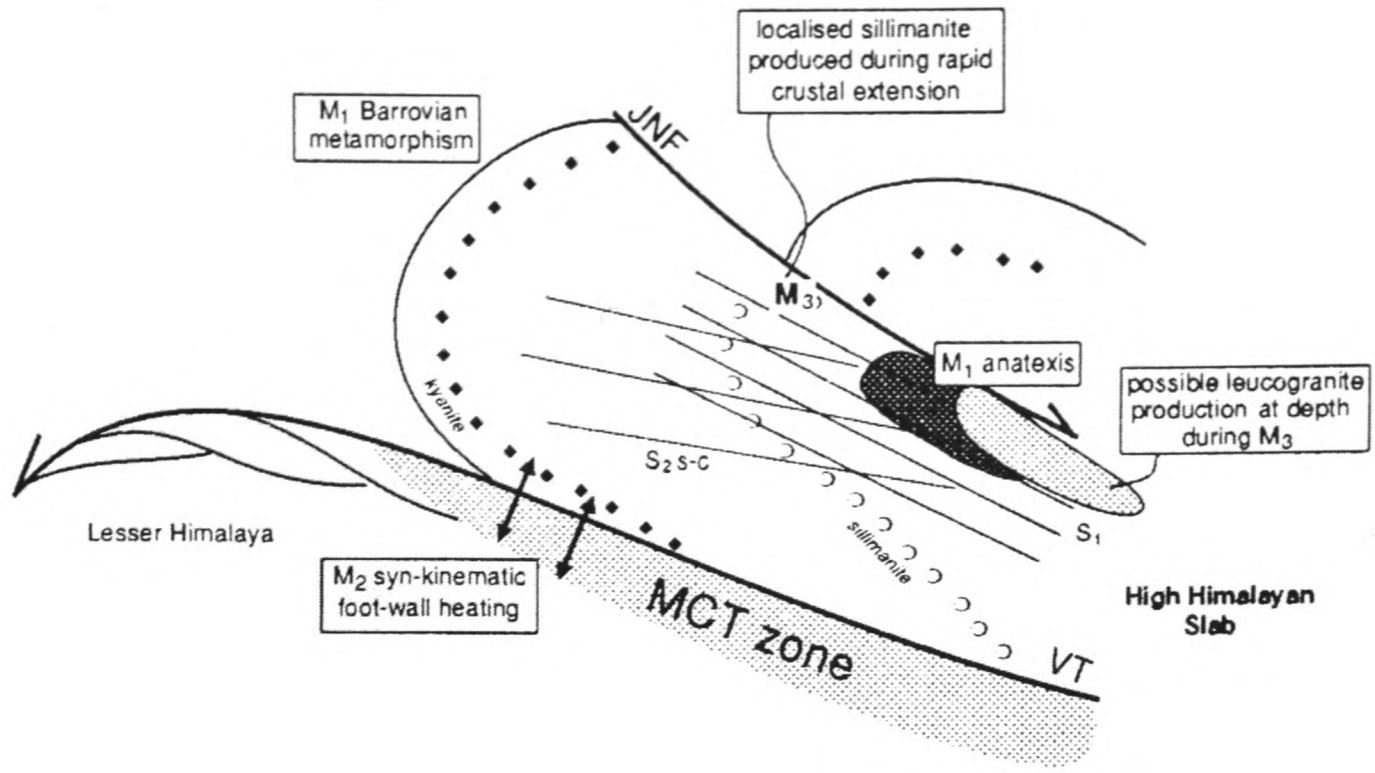


Figure 2.7d: Metcalfe's (1993) model for inversion of metamorphic isograds in the MCT zone of western Garhwal. M1 metamorphic isograds are recumbently folded during subduction of the Lesser Himalaya along the MCT. At the same time, thermal re-equilibration across the MCT results in the growth of garnet-bearing assemblages in the footwall (M2). Late-stage brittle thrusting in the lowermost MCT zone may also act to imbricate rocks of different metamorphic grade.

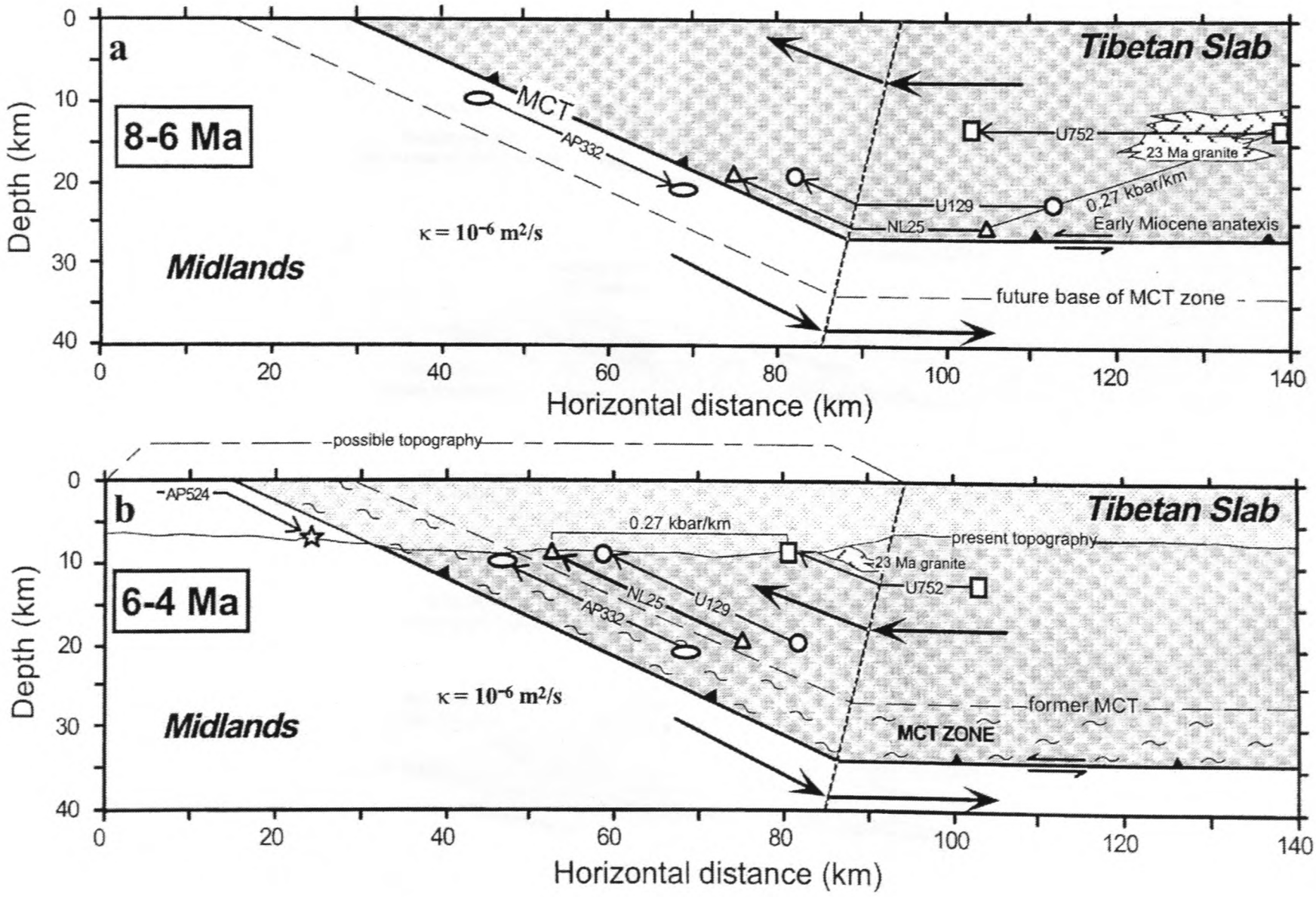


Figure 2.7e: Harrison et al. (1997a) model for inverted metamorphism along the MCT. (a) slip along the MCT begins at 8 Ma, following a period of ~12 Ma inactivity. Between 8-6 Ma sample AP332 experiences burial metamorphism due to overthrusting of the already metamorphosed High Himalayan Slab. (b) the MCT zone is re-activated at 6 Ma at a lower structural level, thus, accreting lower-grade footwall assemblages into the MCT zone. Sample AP332 now forms part of the MCT, which contains metamorphic assemblages which grew at different times (pre-20 Ma in the High Himalayan Slab and 6 Ma for sample AP332).

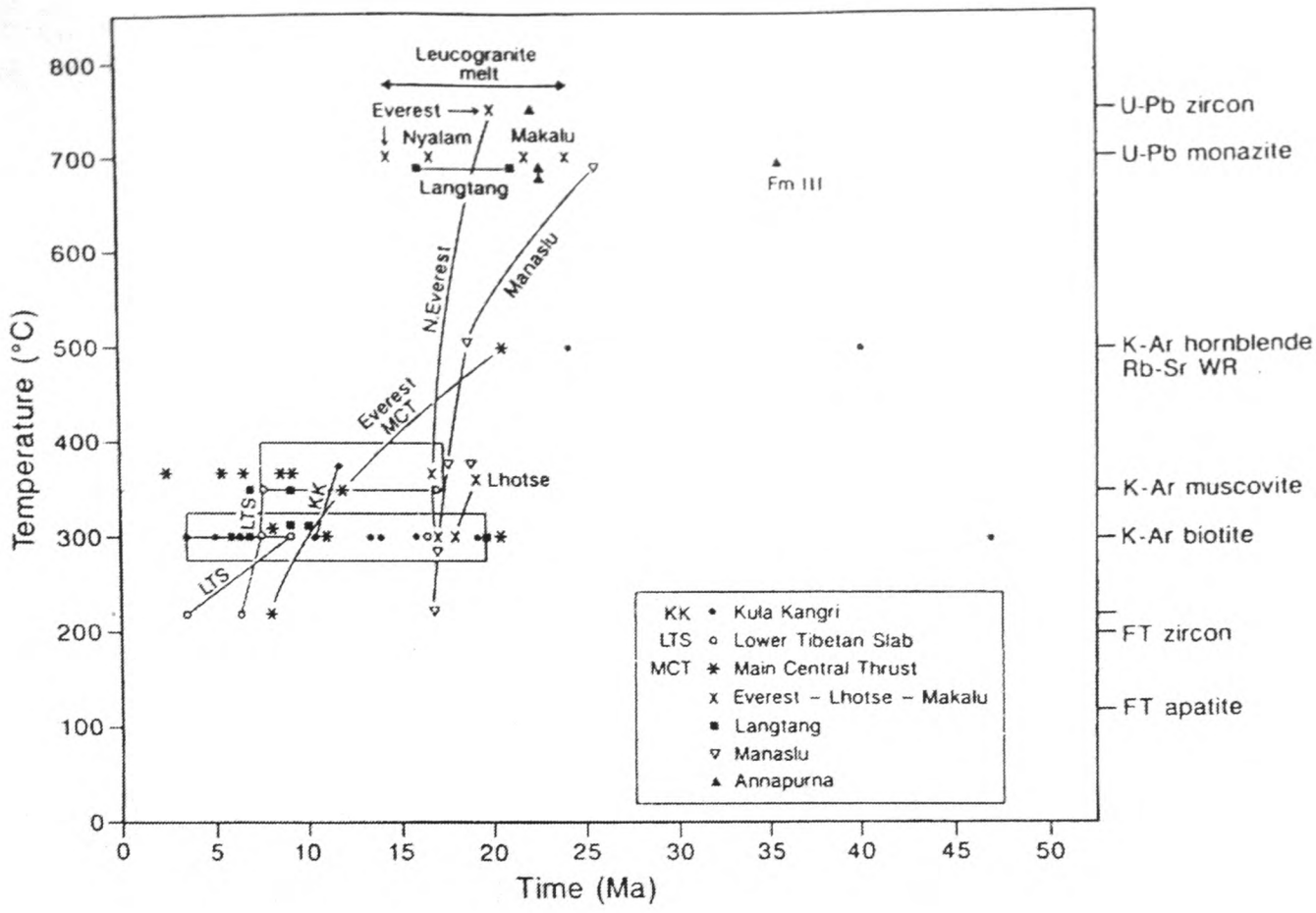


Figure 2.8: Temperature-time cooling data from the High Himalayan Slab in Nepal (from Searle, 1996b). The data are indicative of rapid cooling during the early Miocene, following emplacement of the High Himlayan leucogranites at the top of the slab.

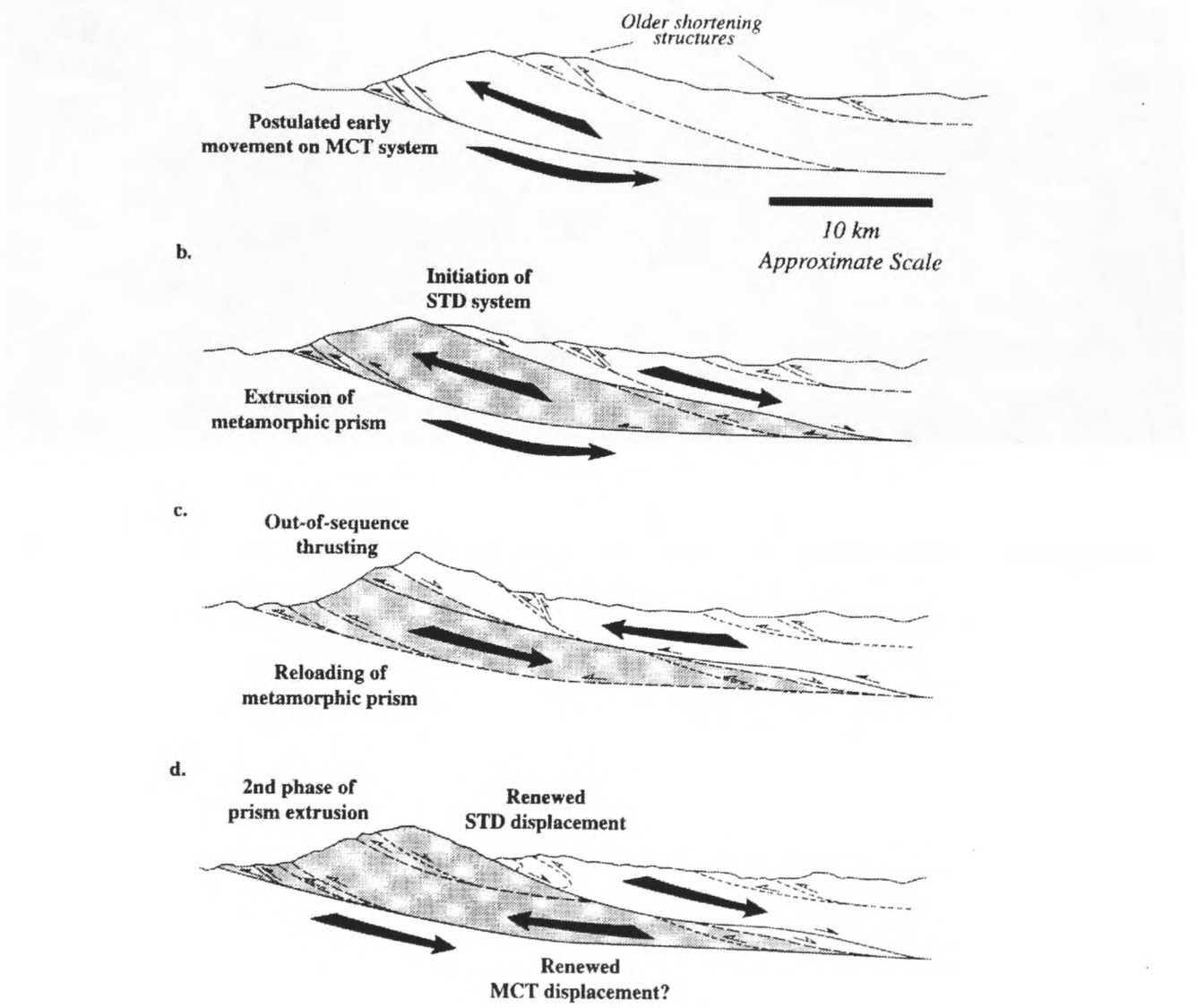
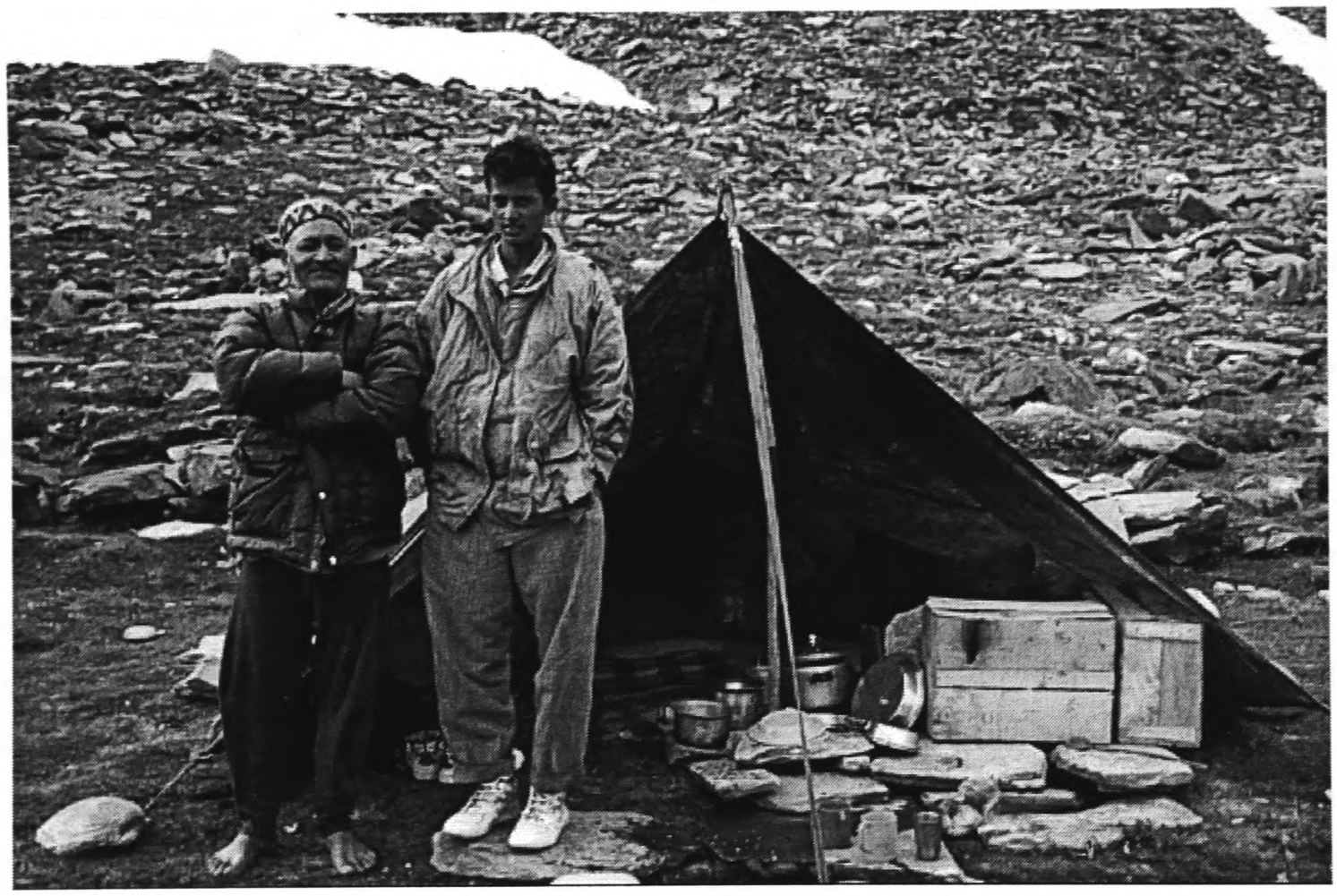


Figure 2.9: Empirical model of Miocene dynamic compensation in the Himalaya (after Hodges et al, 1996). Movement on the MCT (a) forces the High Himalayan Slab out of dynamic equilibrium, resulting in the initiation of faulting at the top of the slab (b). Out-of-sequence thrusting at the top of the slab re-loads the prism, resulting in a second phase of extension along the STD, which may have been contemporaneous with a renewed phase of thrusting along the MCT.



Tik-Ram the cook (left) and Pieray Lal the horse-man (right) posing for a photograph outside their tent.

Chapter 3

The High Himalayan Slab of SE Zanskar and NW Lahaul: a regional geological overview

3.1 Field location and geographical setting

Fieldwork for this thesis was performed in SE Zanskar and NW Lahaul, which form part of the districts of Jammu and Kashmir and Himachal Pradesh respectively. Both districts are located in the north-west Indian Himalaya between latitudes 32°-34°N and longitudes 76°-78°E (Figures 2.1 & 3.1). In the northern part of the study area, the Greater Himalaya form an impressive NW-SE trending range of mountains, many of which are at elevations in excess of 6000m. The central and southern part of the study area encompasses the region between the Greater Himalaya Range to the north and the Pir Panjal Range to the south (Figure 3.1).

Fieldwork took place between August 1994 and September 1996, during which time, a total of eight months was spent in the field making both reconnaissance and detailed structural and metamorphic maps. Geological maps were compiled utilising base maps constructed from: (1) Landsat photographs; (2) 1:350 000 Ladakh-Zanskar Artou trekking map (1989); and (3) 1:250 000 American army Series U502 topographic maps (sheets NI43-12 and 43-16). Owing to the scale of these maps and their general inaccuracy at higher resolutions, a reconnaissance style of mapping was adopted over an area encompassing ~10,000 km^2. Where possible, base camps were established in areas of particular structural and metamorphic interest in order to make more detailed observations.

Continuous reference is made throughout this thesis to a number of enclosures which can be found on the inside back-cover of this volume. Enclosure 1 shows a geological map of the High Himalayan Slab in SE Zanskar and NW Lahaul which has been compiled through extensive personal field observations and includes data from several other published sources. A simplified version of this map is shown in Figure 3.2a. Also shown on Enclosure 1 are a number of interpretative cross-sections through different parts of the study area. Enclosure 2 shows a metamorphic map of the High Himalayan Slab in SE Zanskar and NW Lahaul which presents new and previously published quantitative P-T results from across the study area. A simplified version of this map is shown in Figure 3.2b. Enclosure 3 is a structural map showing the orientation of major fabric elements relating to different phases of deformation in different parts of the study area.

Numerous samples were collected for petrographic, thermobarometric, geochemical and geochronological analysis, the locations of which are shown on Enclosure 4. More precise locations

are given in figures and figure captions throughout the thesis. An attempt was made to sample through all the exposed structural levels from the chlorite zone through to the sillimanite zone. Where possible, metapelitic samples were preferentially collected for the purpose of microstructural and thermobarometric analysis.

3.2 Definition of the High Himalayan Slab in SE Zanskar and NW Lahaul

The High Himalayan Slab in SE Zanskar and NW Lahaul is defined here as the area bounded to the north by the Zanskar Shear Zone (Searle, 1986; Herren, 1987; Dransfield, 1994) and Sarchu Normal Fault (Spring & Crespo-Blanc, 1992; Steck *et al.*, 1993), and to the south by the Main Central Thrust (Thöni, 1977; Frank *et al.*, 1977; Stephenson, 1997), (Figure 3.2). Both the Zanskar Shear Zone (ZSZ) and Sarchu Normal Fault (SNF) represent local equivalents of the South Tibetan Detachment system which separate the upper amphibolite-facies metasediments and orthogneisses of the High Himalayan Slab from the weakly metamorphosed sediments of the Tibetan Sedimentary Series (Figure3.2b). The MCT is exposed in the eastern part of the mapping area, where it is domed around the Larji-Kulu-Rampur Window (Figure 3.2). The MCT is not exposed in the western part of the study area since it is located >50km to the south of the investigated area (see map by Frank *et al.*, 1995). The outcrop width of the High Himalayan Slab between the ZSZ and MCT in SE Zanskar and NW Lahaul varies between 70-100 km, which together with the regional dip of structures and extensive surface erosion, provides a geological window through *c.*25-30 km of crustal section. This compares to an average width of *c.*30-40 km and an average thickness of *c.*10-20 km in the Garhwal and Nepal Himalaya (Figure 2.1).

3.3 Previous works

Several previous workers have compiled lithological, structural and metamorphic maps of the High Himalayan Slab in SE Zanskar and NW Lahaul (e.g. Stoliczka, 1865; Lydekker, 1883; Powell & Conaghan, 1973; Thöni, 1977; Frank *et al.*, 1977; Srikantia & Bhargava, 1982; Searle, 1986; Searle & Fryer, 1986; Rawat & Thakur, 1988; Pognante & Lombardo, 1989; Pognante *et al.*, 1987, 1990; Spring & Crespo-Blanc, 1992; Steck *et al.*, 1993; Vannay, 1993; Frank *et al.*, 1995; Fuchs & Linner, 1995; Vannay & Steck, 1995; Epard *et al.*, 1995; Stephenson, 1997), together with a limited amount of quantitative P-T work (e.g. Pognante & Lombardo, 1989; Pognante *et al.*, 1990; Epard *et al.*, 1995), geochronological constraints (e.g. Frank *et al.*, 1977; Mehta, 1977; Pognante *et al.*, 1990; Ferrara *et al.*, 1987, 1991; Noble & Searle, 1995) and geochemical studies (Thöni, 1977; Ferrara *et al.*, 1991; Ayres, 1997). This thesis utilises data from these works and presents additional lithological and structural observations, together with new quantitative P-T estimates and geochronological constraints from different parts of the slab in an attempt to synthesise the structural and metamorphic evolution in this part of the Himalaya.

3.4 Structural overview

The structure of the High Himalayan Slab in SE Zanskar and NW Lahaul was investigated at all structural levels along a number of NE-SW trending transects. The location of these transects is shown as lines of section A-A' to E-E' on Enclosure 1. From these sections it can be seen that the geometry of the High Himalayan Slab in SE Zanskar and NW Lahaul does not conform to the archetypal north-easterly dipping wedge of kyanite- and sillimanite-grade lithologies seen along the majority of the Himalaya (see Figure 2.2). Indeed, the orientation of major planar fabrics varies considerably in different parts of the slab. At low metamorphic grades, bedding (S_0) forms the dominant planar fabric and is frequently parallel to a strong tectonic fabric (S_1) which is axial planar to isoclinal folds. With increasing metamorphic grade, bedding becomes increasingly difficult to recognise and the dominant planar fabrics are defined by well-developed tectonic foliations. Based on cross-cutting relationships observed in the field and in thin section, these foliations are referred to as S_1, S_2 etc. and are assigned to specific stages of deformation (D_1, D_2 and D_3 etc.). The orientation of these foliations (and associated fold axes and mineral stretching lineations) are shown on Enclosure 3 as a number of equal-area, lower-hemisphere stereographic projections. It is important to stress that these fabrics and associated deformation phases are outcrop specific and cannot, therefore, be correlated across the entire slab. The structural significance of these fabrics is discussed with reference to specific parts of the study area in Chapters 4-6.

The large-scale thermal structure of the High Himalayan Slab in SE Zanskar and NW Lahaul is revealed through the field mapping of metamorphic isograds. The isograds reveal a pattern which is best described as a sequence of high-grade metamorphic domes and low-grade metamorphic depressions Figure 3.2b and Enclosure 2. Field mapping of structural fabrics demonstrate that this thermal structure is partly mirrored by the dip of the regional tectonic foliation in most parts of the slab, thus implying that these domes are major structural, aswell as thermal features. Sillimanite-grade migmatites and crustal melt leucogranites are exposed in the cores of these metamorphic domes, whilst chlorite- and biotite-grade metasediments are exposed in the intervening depressions. This structure is analogous to that seen in central and western Zanskar (see section 2.2.8), where sillimanite-grade metamorphic domes are interpreted to have formed during extensional unroofing of deeper structural levels following the attainment of peak-metamorphic conditions (Stäubli, 1989; Kundig, 1989; Searle *et al.*, 1992). The preservation of chlorite- and biotite-grade depressions is unique to the High Himalayan Slab of SE Zanskar and NW Lahaul. Some authors suggest that these low-grade regions form a sedimentary cover-sequence above the underlying sillimanite-grade crystallines (e.g. Nanda & Singh, 1976; Rawat & Thakur; 1988), whilst other authors suggest that these low-grade regions have been tectonically emplaced above the underlying crystalline units (e.g. Pognante *et al.*, 1990; Thakur, 1994).

3.5 Lithological overview

The High Himalayan Slab in SE Zanskar and NW Lahaul is comprised of a thick succession of flyschoid metasediments, megacrystic K-feldspar granites, metabasites, paragneisses, orthogneisses, migmatitic gneisses and crustal melt leucogranites (Enclosure 1). The protoliths of these are generally believed to be the metamorphosed equivalents of the Tibetan Sedimentary Series exposed in the hangingwall of the ZSZ and SNF. This is confirmed in the upper part of the slab where Spring and Crespo-Blanc (1992) and Vannay (1993) demonstrated that Lower and Upper Palaeozoic lithological units can be correlated across the SNF (Figures 3.2a & 3.3). Those exposed in the footwall of the SNF have experienced kyanite-grade metamorphic conditions, whilst those in the hangingwall are only weakly metamorphosed (Figure 3.2b), thus implying that metamorphism in the upper part of the slab is dominantly Himalayan in age.

In the central and lower parts of the slab, correlation of lithologies in the High Himalayan Slab with those in the Tibetan Sedimentary Series is more tenuous. Four major lithological units were distinguished in the field during personal field mapping: (1) the Precambrian-Cambrian Haimantas and Middle Cambrian Karsha Formation (see section 3.5.1); (2) Intrusive Precambrian-Ordovician(?) granites (see section 3.5.3); (3) the Mesozoic Tandi Group (see section 3.5.4); and (4) the High Himalayan Crystallines (HHC), (see section 3.5.6). These lithological units are sporadically intruded by a number of metabasites of uncertain age and provenance (see section 3.5.5).

3.5.1 The Precambrian-Cambrian Haimantas and Middle Cambrian Karsha Formation

The 'Haimantas System' was first used by Griesbach (1891) to describe a sequence of low-grade slates and schists exposed in NW India. This term has since been used by a number of different authors to describe a thick sequence of unfossiliferous sandstones, silts, shales, pebble beds and thin limestones exposed in the High Himalayan Slab of SE Zanskar and NW Lahaul (e.g. Thakur & Tandon, 1976; Frank *et al.*, 1995; Stephenson, 1997). These sediments have also been referred to by different authors as the Phe Formation (Steck *et al.*, 1993; Vannay & Steck, 1995) and the Kade Unit (Pognante *et al.*, 1987, 1990). Previous authors have suggested them to be at least Lower Palaeozoic in age based on the fact that they are unfossiliferous and are discordantly intruded at a number of localities by granites of purported Precambrian-Ordovician age (see section 3.5.3). Steck *et al.* (1993) correlate these sediments with the Lower Cambrian Phe Formation in the Tibetan Sedimentary Series (Figure 3.3).

The Haimantas are the dominant clastic lithology within the mapping area and account for ~50% of the exposed surface area (Figure 3.2a). They have been metamorphosed to varying degrees and are best described as psammites, semi-pelites, slates, phyllites, schists and paragneisses in different parts of the slab (Figure 3.2b). The similarity of these sediments throughout the study area suggests that they form part of the same stratigraphic unit. Owing to the intensity of deformation within the slab and the similarity of these sediments across the entire mapping area, no attempt was made to subdivide the Haimantas into smaller stratigraphic units.

Sands, silts and shales

The majority of the Haimantas comprise a thick, interbedded sequence of brown-, grey- and green-coloured sandstones (greywackes) and grey/green-coloured silts and shales (pelites). They are extremely graphitic and are locally rich in carbonates (calcite and ankerite at low metamorphic grades, sphene and hornblende at higher metamorphic grades). Quartz-rich sands and silts form the dominant lithology in much of the Haimantas, with individual beds ranging from 1cm- to 4m-thick. The majority of sandstones are thickly bedded and medium to fine grained. Coarser-grained sands are sometimes observed and occasionally preserve evidence of fining-up. With the exception of several occurrences of cross- and convolute-bedding, sedimentary structures were rarely observed in any of the sandstones, which is somewhat surprising given the lateral extent of the Haimantas across SE Zanskar and NW Lahaul. Detrital sedimentary textures are preserved in sandstones up to biotite-grade conditions. Petrographic observations of several sandstones collected from different parts of the study area show that they are texturally immature and contain a high concentration of angular to sub-rounded clasts of quartz (40-80%) and feldspar (5-30%), with some instances of large detrital muscovite (Figures 3.4a & b). Detrital tourmaline, rutile, ilmenite and zircon are common accessory phases in many of these sandstones (Figure 3.4c). Feldspars are frequently twinned and occasionally preserve poikilitic and perthitic textures, suggestive of a magmatic source rock provenance. They are generally albitic in composition, but are occasionally observed to have slightly higher X_{An} compositions (30-40 mole fraction). Clasts are enclosed in a chloritic matrix which can contain a significant amount of graphite in some samples. With increasing metamorphic grade, the chloritic matrix is replaced by the growth of metamorphic muscovite and biotite.

True pelites are a relatively subordinate lithology within the Haimantas and are rarely more than 2m thick. Thicker units are observed in fold hinges and regions of high strain (e.g. within the ZSZ). The majority of pelites are extremely magnesium-rich and aluminium-poor, which inhibits the growth of Fe-rich metamorphic phases such as chloritoid and staurolite. Indeed, chloritoid was not observed in any of the studied samples and staurolite shows an extremely limited distribution across the study area. Chlorite and green-coloured phengitic muscovite are the dominant phyllosilicate minerals in pelites at low metamorphic grades and are progressively replaced by metamorphic muscovite and biotite with increasing metamorphic grade.

Discontinuous beds of pyritiferous black shales form prominent marker horizons within the Haimantas, but cannot be traced laterally for any significant distance. Whether these black shales form part of the same stratigraphic horizon remains uncertain. They are most conspicuous beneath the Mesozoic Tandi Group, where they can be traced discontinuously along both sides of the Chandra valley (Enclosure 1). Similar-looking black shales were observed to the east of the Jispa granite and above the Kade granite in the northern part of the mapping area (Enclosure 1). Pyritiferous black shales were also observed within the Chamba Syncline in the western part of the mapping area (Enclosure 1). However, whether the sediments in the Chamba Syncline form part of the

Precambrian-Cambrian Haimantas has been the focus of several publications (e.g. Rawat & Thakur, 1988; Frank *et al.*, 1995) and is discussed in more detail in section 3.5.2.

The Manjir Conglomerate

Loose boulders of a matrix supported conglomerate were observed within the Haimantas on the northern side of the Chandra valley, ~5 km east of Sissu village (Enclosure 1; cross-section D-D' on Enclosure 1). Although not observed *in situ*, the boulders were extremely fresh-looking and appear to have been locally derived. This lithology is extremely similar to the Manjir Conglomerate described in different parts of the NW Indian Himalaya by several previous authors (e.g. Rattan, 1973; Fuchs, 1975; Rawat & Thakur, 1988; Frank *et al.*, 1995). It consists of a poorly sorted array of white vein quartz and lithic rock fragments enclosed in a fine grained grey/green matrix. The age of this deposit has been the focus of a number of contentious studies over the years. Some authors suggest it to be Upper Precambrian in age (e.g. Frank *et al.*, 1995), whilst others suggest it to be a lateral correlative of the Carboniferous Agglomeratic Slates in the Kashmir Basin (e.g. Rattan, 1973; Rawat & Thakur, 1988). The inferred Cambrian age of the Haimantas supports Lower Palaeozoic, rather than Upper Palaeozoic age for this lithology in the Chandra valley.

Carbonate-rich sediments and the Karsha Formation

The Haimantas are locally enriched in carbonates, as indicated by the presence of calcite, ankerite, sphene and hornblende in some samples. In addition, discontinuous pods/lenses of calcite + garnet + actinolite + zoisite-bearing material are occasionally observed within the Haimantas and are interpreted to be the metamorphosed and deformed remains of carbonate concretions (Figures 3.4d & e). In the northern part of the study area (Darcha-Shingo La region), the Haimantas are especially carbonate-rich, as indicated by a marked increase in the concentration of ankerite in the sediments. South of the Shingo La, tufa is occasionally observed building up on rock surfaces, which reflects the dissolution and re-precipitation of carbonate from the surrounding rocks. The distribution of carbonate-rich lithologies either side of the Shingo La suggests that this 5100m pass might be coincident with a major NW-SE trending synformal axis (cross-section B-B' on Enclosure 1).

North of Darcha, the carbonate-rich sands, silts and shales of the Haimantas are overlain by an interbedded sequence of sands, silts and brown dolomites (Figure 3.5) which have been correlated with the dolomitic Karsha Formation in the Tibetan Sedimentary Series (Figure 3.3). Owing to the inaccessibility of these exposures, the exact nature of the contact between the Haimantas and the Karsha Formation shown in Figure 3.5 could not be ascertained. Whilst the possibility remains that this is a thrust contact, previous work to the north of Darcha demonstrated that the Karsha Formation conformably overlies the Haimantas (Spring *et al..,* 1992; Vannay and Steck, 1995). This suggests that the contact shown in Figure 3.5 is also likely to be sedimentary in origin. Although the precise age of the Karsha Formation is poorly constrained, it is generally quoted as being a Middle to Late Cambrian deposit (e.g. Nanda & Singh, 1976; Srikantia *et al.*, 1980). This implies that the underlying

Haimantas are at least Middle Cambrian in age and supports their correlation with the Lower Cambrian Phe Formation in the Tibetan Sedimentary Series (Figure 3.3).

Carbonate-rich sands, silts and shales similar to those observed beneath the Karsha Formation are also exposed directly beneath the Mesozoic Tandi Group in the Chandra valley (Enclosure 1; cross-sections C-C' & D-D' on Enclosure 1). Whether these form part of the Upper Haimantas, or whether they form part of the basal Tandi Group remains somewhat uncertain. The fact that they are unfossiliferous suggests that they are probably lateral equivalents of the carbonate-rich sediments exposed beneath the Karsha Formation further north.

3.5.2 Sediments and stratigraphy of the Chamba Syncline

The Chamba Syncline (sometimes referred to as the Chamba Basin) is a somewhat enigmatic feature of the High Himalayan Slab in NW India. It forms a strike-parallel elongate structure which extends in a NW-SE direction for ~70 km between the MCT and ZSZ (see Figure 2.5a) and is composed of various chlorite- to biotite-grade metasediments whose age and tectonostratigraphic relationship with the High Himalayan Slab has been the focus of a number of contentious studies over the years (e.g. Thakur & Pande, 1971; Rattan, 1973; Thakur & Tandon, 1976; Rawat & Thakur, 1988; Thakur, 1994; Fuchs & Linner, 1995; Frank *et al.*, 1995). The easternmost extension of the Chamba Syncline is exposed in the western part of the mapping area, directly along strike of the Tandi Syncline (Enclosure 1; Figures 3.2 & 3.6). The bounding limits of this structure are poorly defined and do not correspond to any obvious stratigraphic or metamorphic discontinuity. The lateral extent of the Chamba Syncline within the study area is therefore interpreted to be more or less coincident with the location of the biotite-in isograd (Figure 3.2).

Thakur (1994) suggested that the sediments in the Chamba Syncline are Upper Palaeozoic in age and are in tectonic contact with the underlying Lower Palaeozoic Haimantas. No palaeontological evidence has yet been found in this part of the Himalaya to support this Upper Palaeozoic age. Indeed, lithological, structural and metamorphic observations demonstrate that the sediments in the Chamba Syncline probably represent the low-grade equivalents of the Lower Palaeozoic Haimantas exposed in adjacent parts of the slab. This interpretation is based on: (1) lithological similarities between the magnesium-rich sands, silts and shales of the Haimantas and the sands, silts and shales exposed in the Chamba Syncline; (2) the fact that sediments within the Chamba Syncline can be traced along strike towards the south-east, where they are observed to be in stratigraphic and structural continuity with the Lower Palaeozoic Haimantas exposed in the Chandra valley (Enclosure 1); (3) the observation that metamorphic grade progressively increases towards the north in the Chamba Syncline, with no evidence to support the existence of any major post-metamorphic discontinuity between the Kalicha Pass and the Kade granite (Figure 3.6); and (4) the fact that sediments within the Chamba Syncline are discordantly intruded by the Kade granite to the north of Karpat (Figure 3.6), which has a Rb-Sr whole-rock age of *c.*500-600 Ma (Ferrara *et al.*, 1987; Pognante *et al.*, 1990; Table 3.1).

South of Udaipur the sands, silts and shales in the Chamba Syncline continue without apparent stratigraphic or structural discontinuity and eventually give way to a 100-150m-thick sequence of unfossiliferous blue limestones, which in turn give way to a thick sequence of matrix supported conglomerates which form the core of a major antiform (Figures 3.6). These conglomerates have been correlated with the Manjir Conglomerate by several previous workers (e.g. Rawat & Thakur, 1988; Frank *et al.*, 1995; Fuchs & Linner, 1995) and are identical in appearance to the conglomerate boulders observed in the Chandra valley (see section 3.5.1). Detailed mapping by Frank *et al.* (1995) and Fuchs and Linner (1995) in more westerly parts of the Chamba Syncline demonstrated that these conglomerates are located stratigraphically beneath the Haimantas and must, therefore, be at least Lower Palaeozoic in age. This is consistent with the work of this thesis, but refutes the work of several previous authors, who suggested that these conglomerates represent lateral equivalents of the Middle Carboniferous Agglomeratic Slates (e.g. Rawat and Thakur, 1988). Shanker *et al.* (1989) and Frank *et al.* (1995) both suggest a possible correlation between the Manjir Conglomerate and the Neo-Proterozoic Blaini Boulder Bed of the Lesser Himalaya.

Although there is no evidence to support the existence of any major post-metamorphic discontinuity between the Kalicha Pass and the Kade granite, structural observations presented in Chapter 5 suggest that the northern limit of the Chamba Syncline in the Miyar nala may be coincident with a zone of extensional deformation, hereafter referred to as the Karpat Shear Zone (Figure 3.2). This is consistent with the work of Stephenson (1997), who demonstrated that the Chamba Syncline immediately the west of the study area is bounded to the north by the Kilar Shear Zone (Figure 3.2).

Estimated thickness of the Haimantas

It is virtually impossible to accurately constrain the original sedimentary thickness of the Haimantas for a number of reasons: (1) the base of this sedimentary succession is not exposed in SE Zanskar and NW Lahaul, thus any estimate of their thickness represents a minimum value; (2) they lack good quality marker horizons and have been intensely deformed (and thickened) by multiple phases of deformation associated with the Himalayan orogeny; and (3) the stratigraphic succession is disrupted by the intrusion of Lower Palaeozoic granites. Despite these difficulties, structural sections through different parts of the study area (see Enclosure 1) suggest that the Haimantas must be at least 2-3km thick throughout the majority of the slab and are probably between 3-5km thick in the Chamba Syncline. However, it is important to stress that these estimates are subject to large errors owing to the fact that intense folding and thrusting may be responsible for the repetition of units within the Haimantas. Nevertheless, these estimates are consistent with the thickness of the Phe Formation in the Tibetan Sedimentary Series, which has a minimum thickness of 800-1000m (Figure 3.3).

Interpreted depositional environment of the Haimantas

The huge lateral extent and thickness of the Haimantas in the High Himalayan Slab of SE Zanskar and NW Lahaul suggests that they were deposited in a large sedimentary basin during the Upper Precambrian-Lower Cambrian. Sedimentary structures and textures are indicative of deposition in a flyschoid environment, suggesting that the Haimantas may represent a thick turbidite sequence deposited on the continental shelf/slope. This fits well with the depositional environment of the Phe Formation in the Tibetan Sedimentary Series, which McElroy *et al.* (1990) interpret to represent "a shallow marine shelf or coastal sequence consisting of a clastic wedge which prograded towards the NW". Owing to the intensity of deformation within the High Himalayan Slab, no significance was placed on the present day orientation of palaeo-current indicators within the Haimantas.

Textural immaturity and the clastic composition observed in the sandstones within the Haimantas suggests that they were derived from a relatively local magmatic source. The location of this source remains poorly constrained. Were it not for the observation that many of the granites exposed in SE Zanskar and NW Lahaul discordantly intrude the Haimantas (see section 3.5.3), it would be tempting to assume that these granites were themselves the actual source of the sediments. Frank *et al.* (1995) and Draganits *et al.* (1998) suggest that the Haimantas may have been derived from the South China Block, based on the observation that many of the palaeocurrent directions they measured show a dominant sediment transport direction towards the SE-SW. This is not consistent with the palaeocurrent data recorded in the Phe Formation of the Tibetan Sedimentary Series by McElroy *et al.* (1990). One possible, but extremely unlikely interpretation of this apparent disparity is that the Phe Formation of the Tibetan Sedimentary Series is not a direct correlative of the Haimantas in the High Himalayan Slab. A second interpretation is that intense deformation in the High Himalayan Slab and Tibetan Sedimentary Series has rotated the palaeocurrent data, such that the original sediment transport direction is difficult to accurately constrain. A third interpretation of this apparent disparity is that the palaeogeography of the sedimentary basin in which the Haimantas/Phe Formation were deposited was extremely complex, with sediment being derived from a number of different directions. Given the intensity of deformation within the High Himalayan Slab and the fact that several allochthonous terranes have been sutured against the southern Eurasian margin throughout the Mesozoic and Cenozoic, it seems likely that accurate reconstructions of Upper Precambrian and Lower Palaeozoic basin configurations will remain speculative for the foreseeable future.

The increasing carbonate content in the Haimantas towards the top of the succession and the fact that they are overlain by the dolomitic limestones of the Middle Cambrian(?) Karsha Formation suggests that they record an overall shallowing-up sequence. This is consistent with the observation that the end of the Cambrian is marked by a major unconformity in the Tibetan Sedimentary Series (Figure 3.3) and a period of granite emplacement in the High Himalayan Slab (see section 3.5.3). .

3.5.3 Precambrian-Ordovician granites

Granites, augen gneisses and banded orthogneisses are a dominant lithology in the High Himalayan Slab of SE Zanskar and NW Lahaul and account for ~20-30% of the exposed surface area (Enclosure 1; Figure 3.2a). They generally form large granite massifs extending for distances in excess of 25 km, the bases of which are rarely exposed. This suggests the possibility that some of these granites represent the crystalline basement upon which the Haimantas were deposited. However, no erosion surfaces were observed in the field along any of the granite margins which appears to preclude this possibility. Furthermore, discordant contacts and hornfelsed margins are observed along some of the granite margins (see Figures 3.8-3.10), which implies that these granites are younger than the surrounding Haimantas. Scant geochronological data suggests that the majority of these granites are Upper Precambrian-Lower Palaeozoic in age (Table 3.1). Although the reliability of these ages is questionable owing to the extreme mobility of Rb and Sr during metamorphism, they confirm that the granites are unrelated to Himalayan tectonics. The spread of ages is quite large which suggests the possibility that these granites are not necessarily co-genetic. More detailed geochronological data is needed to verify this.

In regions of low metamorphic grade the granites are only weakly deformed and possess a coarse grained equigranular texture (Figure 3.7a). They are frequently porphyritic, with many of the granites containing large poikiloblastic K-feldspar phenocrysts (Figure 3.7b). At higher metamorphic grades and in regions of high strain, the granites become more intensely deformed and have the appearance of augen gneisses (Figure 3.7c), ultimately becoming banded orthogneisses in regions of very high strain (Figure 3.7d). Owing to the scale of mapping (usually 1:250,000), no distinction was made in the field between orthogneiss, augen gneiss and undeformed granites.

Table 3.1: Geochronological data from the megacrystic K-feldspar granites, augen gneisses and banded orthogneisses of the High Himalayan Slab in SE Zanskar and NW Lahaul.

Granite shown on Figure 3.2a	Age	Technique	Author
Kade granite	621 ± 41 Ma	Rb-Sr whole-rock	Ferrara *et al.* (1987)
Kade granite	549 ± 70 Ma*	Rb-Sr whole-rock	Pognante *et al.* (1990)
Rhotang Gneissic Complex and granites within the Crystalline Nappe	601 ± 9 Ma**	Rb-Sr whole-rock	Mehta, 1977
Hanuman Tibba & Jispa granites	505 ± 16 Ma**	Rb-Sr whole-rock	Frank *et al.*, 1977
Kulu granite (south of Katrain)	517 ± 8 Ma**	Rb-Sr whole-rock	Mehta, 1977
Granitic orthogneiss (collected within the HHC)	472 +9/-6 Ma	U-Pb (zircon)	Pognante *et al.* (1990)
Inherited zircons in Miocene leucogranites	~460 Ma	U-Pb	Noble & Searle (1995)
Inherited monazites in Miocene leucogranites	~500Ma	U-Pb	This study (Chapter 7)

**MSWD = 36.7 (statistically insignificant)*
**recalculated using $\lambda = 1.42 \times 10^{-11} yrs^{-1}$

The granites are mostly leucocratic and have a mineralogical composition of Qtz + Kfs + Pl + Ms ± Bt ± Tur ± Grt. Many of the granites are wholly leucocratic and contain no biotite at all. Others have a fine grained, dark coloured (mesocratic) matrix which encloses numerous K-feldspar

phenocrysts (Figure 3.7e) and are more granodioritic in composition. Geochemical studies of a number of these large, megacrystic K-feldspar granites (e.g. Frank *et al.*, 1977; Mehta, 1977; Ferrara *et al.*, 1987; Pognante *et al.*, 1990) show that they have peraluminous affinities with slightly elevated $^{87}Sr/^{86}Sr$ ratios (0.709-0.726) and low εNd values, suggesting that they were probably derived from a crustal melt source. The majority of these Precambrian-Ordovician granites have remarkably similar mineralogical compositions to the Tertiary High Himalayan leucogranites (HHL) exposed in the upper part of the slab (Enclosure 1). However, a number of lithological, structural and geochemical criteria allows distinctions to be made between these two granite suites in the field: (1) the Precambrian-Ordovician granites are generally much larger than the HHL; (2) the HHL have a restricted distribution and are preferentially located in the upper parts of the High Himalayan Slab in the footwall of the ZSZ, whereas the Precambrian-Ordovician granites have a wide distribution and are exposed at all structural levels; (3) the HHL are generally surrounded by migmatitic leucosomes or zones of anastomosing sills and dykes, whereas the Precambrian-Ordovician granites display none of these characteristics; and (4) the Precambrian-Ordovician granites have a lower concentration of garnet and tourmaline than the HHL. Geochemical and geochronological data also allow distinctions to be made between these two granite suites: (1) the HHL have higher $^{87}Sr/^{86}Sr$ ratios (*c.*0.750-0.780) than the Precambrian-Ordovician granites (*c.*0.709-0.726); and (2) the HHL consistently yield Miocene crystallisation ages (see Chapter 7), which are significantly younger than the Rb-Sr whole-rock ages recorded by the Precambrian-Ordovician granites. However, none of the so-called Precambrian-Ordovician granites have been subjected to a rigorous U-Pb geochronological study.

The Kade granite

The Kade granite is the biggest of all the Precambrian-Ordovician(?) granites in the mapping area and extends in a strike-parallel NW-SE orientation for over 50 km in the central part of the slab (Figure 3.2a; Enclosure 1). It thins towards the SE and eventually pinches out on the southern side of the Barai nala to the west of Darcha, where it is observed discordantly intruding the Haimantas (Figure 3.8). A ~10m-thick zone of heavily weathered, brown-coloured sandstones and silts are observed along the margins of the granite near Darcha (Figure 3.8), which is interpreted to be a narrow baked margin. Internally, the granite has a distinct green hue (Figure 3.8), which reflects the chloritisation of biotite and the growth of epidote associated with deformation and metamorphism of the High Himalayan Slab during the Tertiary. Further west, the Kade granite is observed discordantly intruding the Haimantas in the Chamba Syncline to the north of Karpat (Enclosure 1; Figure 3.6).

The Jispa granite

The Jispa granite forms a relatively small boss in the Bhaga valley to the south of Darcha and is centred on a domal structure, hereafter referred to as the Jispa Dome (Enclosure 1; Figure 3.2a). The base of the granite cannot be seen and is probably connected at depth to the much larger Kade granite which is located immediately along strike and to the west of the Jispa granite. Both bedding-parallel

and discordant contacts are observed along the margins of the Jispa granite (Figure 3.9a). Close examination of the Haimantas immediately adjacent to the granite reveals hornfels textures which pre-date the development of the regional tectonic foliation (Figure 3.9b). This foliation is almost certainly related to Tertiary deformation of the High Himalayan Slab and is weakly developed within the Jispa granite itself, thus suggesting that the Jispa granite is pre-Himalayan in age and supporting the 505 ± 16 Ma Rb-Sr age obtained by Frank *et al.* (1977), (Table 3.1).

The Rhotang Gneissic Complex

The Rhotang Gneissic Complex is exposed in a NW-SE trending swathe along the Chandra valley near the village of Khoksar (Enclosure 1; Figure 3.2a). It extends southwards near the village of Chattru into the much more extensive Deo Tibba granite massif (Thöni, 1977) and has a similar orientation and Rb-Sr whole-rock age to the Kade granite further west, suggesting that these granites are lateral equivalents and are probably connected at depth beneath the Haimantas (cross-section C-C' on Enclosure 1). The Rhotang Gneissic Complex is characterised by an interlayered sequence of megacrystic K-feldspar granites, granitic gneisses, biotite gneisses, leucocratic pegmatites, and kyanite-grade metapelites. Pods of kyanite-grade metapelitic schists within the Rhotang Gneissic Complex are frequently surrounded on all sides by granitic gneisses and are interpreted to be xenoliths/roof pendants of the surrounding Haimantas, thus providing tentative evidence that the Rhotang Gneissic Complex was originally a discordant granite body (any original magmatic contact between the Rhotang Gneissic Complex and the surrounding Haimantas has long since been destroyed by intense deformation in this part of the slab). Some authors have suggested that the pods of kyanite schist are the remains of an old metamorphism (e.g. Powell & Conaghan, 1973; Rawat & Thakur, 1988) and that the Rhotang Gneissic Complex may, therefore, represent the crystalline basement upon which the Haimantas were deposited. Whilst this remains a possibility, textural observations presented in Chapter 4 show that the kyanite porphyroblasts in these schists are weakly deformed and overgrow the regional tectonic foliation, thus suggesting them to be Himalayan in age. Geochronological data presented in Chapter 7, however, shows that these schists contain a *c.*500 Ma inherited monazite component which could be related to a pre-Himalayan metamorphic event.

The Kulti nala granite

The Kulti nala granite is located to the north of the Rhotang Gneissic Complex and forms a relatively small, steep sided boss which discordantly intrudes the surrounding Haimantas (Enclosure 1; Figure 3.2a). The Kulti nala granite has not been intensely deformed and preserves an equigranular, coarse grained magmatic texture. Sediments adjacent to the granite have a distinct baked appearance, although no hornfels textures are evident in thin section. The Kulti nala granite is interpreted to be a higher-level equivalent of the Rhotang Gneissic Complex and is therefore of presumed Lower Palaeozoic age.

The Hanuman Tibba granite

The Hanuman Tibba granite forms an isolated south-westerly dipping pod which is located within the core of a major NW-plunging antiformal closure to the south of the Tandi Syncline (Figure 3.10). Discordant contacts with the surrounding Haimantas are observed along the margins of the Hanuman Tibba granite (Figure 3.10), thus implying that the sediments immediately adjacent to the granite are older than 505 ± 16 Ma, the whole-rock Rb-Sr age of this granite (Table 3.1).

Other megacrystic K-feldspar granites

In addition to the named granites discussed above, other unnamed K-feldspar granites are frequently observed throughout the High Himalayan Slab. In the lower part of the slab, intensely deformed granite sheets are frequently observed inter-fingering within the garnet- and kyanite-grade schists near Manali (Enclosure 1; Figure 3.2a). These granites are parallel to the regional tectonic foliation (cross-section E-E' on Enclosure 1) and probably represent the deformed equivalents of the Precambrian-Ordovician granite massifs discussed above.

In the Chamba Syncline, two granite sheets were observed above the Haimantas to the south of the Kade granite (Figure 3.11). Whether these are in tectonic contact with the Haimantas, or whether they are intrusive could not be ascertained in the field owing to the inaccessibility of the exposures. The flat-lying nature of the contact suggests a probable tectonic origin. The age of these granites remains uncertain.

In the highest-grade parts of the slab (the HHC), numerous megacrystic K-feldspar granites are observed intercalated between sillimanite-grade migmatites, paragneisses and crustal melt leucogranites (see section 3.5.6). The similarity of these granites to the Precambrian-Ordovician granites exposed in the lower-grade parts of the slab suggests they may form part of the same granite suite. Geochronological data supports this interpretation. Pognante *et al.* (1990) obtained a 472 +9/-6 Ma age for one such granite collected from the Temasa nala in the uppermost part of the slab (Enclosure 1). Noble and Searle (1995) demonstrated that the Miocene crustal melt leucogranites and migmatites in the HHC contained a *c.*500 Ma zircon component, which they interpret to be inherited grains sourced from the underlying schists and granites from which the granite was generated. Similar *c.*500 Ma inherited ages are reported from the Gumburanjon leucogranite in Chapter 7 of this thesis.

Interpreted tectonic setting of granite emplacement

Most authors currently agree that the megacrystic K-feldspar granites exposed throughout SE Zanskar and NW Lahaul granites form part of a major Precambrian-Ordovician granite suite (e.g. Mehta, 1977; Frank *et al.*, 1977; Frank *et al.*, 1995; Vannay & Steck, 1995). However, the wide spread of Rb-Sr whole rock ages shown in Table 3.1 suggests the possibility that these granites are not necessarily co-genetic. Nevertheless, the size and areal extent of these granites suggests that they were emplaced in a major magmatic province. The tectonic setting of this province remains

somewhat conjectural. Megacrystic granites of purported Lower Palaeozoic age are exposed along the entire length of the High Himalayan Slab (e.g. the Formation III augen gneiss in central Nepal: Le Fort, 1975). Le Fort *et al.* (1986) suggested that these granites were emplaced in a zone of crustal extension during the Lower Palaeozoic. However, rift-type settings are commonly associated with extensive basaltic magmatism (e.g. Wilson, 1989), which is not observed anywhere along the entire length of the High Himalayan Slab. Mehta (1977) suggested that the Lower Palaeozoic granites in SE Zanskar and NW Lahaul were emplaced in a collisional tectonic setting and represent the end result of a major pre-Himalayan deformation and metamorphism event. Frank *et al.* (1995) reached a similar conclusion based on the fact that: (1) the granites have an S-type geochemistry (elevated $^{87}Sr/^{86}Sr$ and low εNd values) which is indicative of a crustal melt source with little or no mantle input; (2) the Haimantas show evidence of an overall shallowing-up sequence, which is inconsistent with a rift-type setting (see section 3.5.1); and (3) a major unconformity marks the base of the Devonian in the Tibetan Sedimentary Series of SE Zanskar (Figure 3.3), thus suggesting that the end of the Cambro-Ordovician was associated with a major uplift and erosion event. Baud *et al.* (1984) suggested that this may be related to the latest stages of the Pan African Orogeny. Owing to the intensity of Tertiary deformation within the High Himalayan Slab, it is virtually impossible to say with any certainty whether the Haimantas were subjected to a major pre-Himalayan deformation and metamorphic event (see structural and metamorphic data presented in Chapters 4-6). However, geochronological data presented in Chapter 7 do support the existence of a major thermal event in the Haimantas at *c.*500 Ma, which could reflect a major metamorphism at this time, or could merely reflect the thermal effects felt by the country rocks during granite emplacement.

3.5.4 The Mesozoic Tandi Group

The Tandi Group represent the youngest sedimentary rocks exposed within the High Himalayan Slab anywhere along its ~2500km length. They comprise an interbedded sequence of marine limestones, dolomites, graphite-rich marls, sandstones, quartzites and calcarenites exposed in a ~50 km long, NW-SE-trending strike-parallel belt on the southern side of the Chandra and Chenab rivers in NW Lahaul (Enclosure 1; Figure 3.12). They were recognised as early as the nineteenth century by Stoliczka (1865) and Lydekker (1883) and were identified as Permo-Jurassic in age in the late twentieth century following the discovery of various faunal assemblages by a number of different workers (e.g. Powell & Conaghan, 1973; Pickett *et al.*, 1975; Vannay, 1993). Fossils include solitary and colonial corals, bivalve and cephalopod molluscs, crinoid ossicles and foraminifera. The only fossils identified during personal field observations were the deformed remains of coral fragments and several biogenic plates of calcite believed to be part of an echinoid(?) test (Figure 3.16b). Although these fossil remains were too intensely deformed to allow for formal identification, they confirm that the Tandi Group represent a fossiliferous marine succession. The style of preservation of these fragments suggests that the fossils have been extensively reworked and should be used with great caution when attempting to reconstruct palaeo-depositional environments.

The Tandi Group is preserved in the core of an isoclinal SW-dipping synform referred to in the literature as the Tandi Syncline (Figure 3.13). Lithological units are repeated on both sides of this structure (Figures 3.13 & 3.14), which has a rather anomalous NE facing direction as determined from way-up criteria in the overturned limb of this fold (Figure 3.15). The NE facing direction of the Tandi Syncline has important implications for Himalayan tectonics and is discussed in more detail in Chapter 4. The Tandi Syncline reaches a maximum width of *c.*800-1000m in the mountainside behind the village of Goshal, at the confluence of the Chandra, Chenab and Bhaga valleys (Figure 3.14). Allowing for simple doubling of the sediments during folding, this implies that the Tandi Group had a minimum original sedimentary thickness of *c.*400-500m. This should be considered an absolute minimum estimate since only the core of the Tandi Syncline is preserved, hence, it is difficult to be certain how much of the Tandi Group has been removed by pre- and post-tectonic erosion. The Tandi Group is observed to pinch out towards the NW and SE (Figure 3.12), which is largely a result of post-tectonic erosion. The possibility that some of this lateral thickness variation is depositional in origin cannot be ruled out, however, and is tentatively supported by lithological observations which suggest that some units within the Tandi Group thin rapidly over very short distances.

Basal contact of the Tandi Group with the underlying Haimantas

The base of the Tandi Group is difficult to identify since it forms a seemingly conformable sedimentary succession above the carbonate-bearing sands, silts and shales of the underlying Haimantas (Figures 3.16). The base of the Tandi Group is therefore taken to be coincident with the disappearance of clastic sediments and the first appearance of true limestones (hereafter referred to as Unit A). Unit A forms an s-parallel contact with the underlying calcareous sediments of the Haimantas. Any original sedimentary structures along this contact have been totally obliterated by intense deformation associated with the formation of the Tandi Syncline. Structural data presented in Chapter 4 strongly suggest that the Tandi Group was in structural continuity with the underlying Haimantas prior to the earliest recognisable phase of Himalayan deformation in this part of the slab (D_1), thus suggesting that the Tandi Group represent an integral part of the slab and has not been tectonically emplaced above the Haimantas by thrusting of units from the NE towards the SW. This is supported by the work of Vannay (1993), who claims to have observed basal conglomerates in the lowermost units of the Tandi Group.

Lower Tandi Group (unit A)

The lowermost part of the Tandi Group (unit A) consists of a ~50-150m-thick succession of thinly bedded blue-, grey- and white-coloured limestones and dolomites, calcareous black marls and pale grey calcarenites (Figure 3.16). Many of the limestones have a very dark appearance owing to the high concentration of graphite in these sediments (Figures 3.16b & c). Thin section analysis shows that these limestones are a mixture of crystalline calcite and dolomite which contain variable amounts of silica and phyllosilicates (Figure 3.16b). They are best described as micritic muds, or

wackestones and are indicative of deposition in a quiet marine environment. Numerous units of calcareous black marls are observed within unit A, several of which form prominent marker horizons when viewed from a distance (Figures 3.13 & 3.16). The high organic content of these marls suggests that deposition occurred below the oxygen minimum zone in a low energy environment. Discontinuous lenses of pale grey calcarenites are frequently observed interbedded within the limestones of unit A and are interpreted to represent periods of higher energy deposition in an otherwise quiescent basin.

Unit A can be traced along the entire length of the Tandi Syncline where it is exposed both in the overturned and lower limbs of the fold (Figure 3.12). At the north-western closure of the syncline, behind the village of Rape, unit A is observed to thin extremely rapidly over a relatively short horizontal distance: the Tandi Syncline is ~300m-wide to the south-west of Rape village and thins to practically zero to the north-west of the village over a horizontal distance of less than 500m. Such a rapid thickness variation is unlikely to be related to tectonic thinning or to post-tectonic erosion of the core of the Tandi Syncline and must, therefore, be related either to variations in the original sedimentary thickness of unit A, and/or pre-tectonic erosion of the Tandi Group.

Middle Tandi Group (unit B)

Unit B is characterised by the appearance of yellow- and brown-coloured limestones and calcarenites which form distinctive horizons between a thicker succession of blue-coloured micritic limestones (Figures 3.14 & 3.16). Cross-bedding is evident in some calcarenites and demonstrates that the Tandi Group young towards the core of the Tandi Syncline (Figure 3.15). Unit B shows remarkable variation in thickness along the length of the syncline: it is best developed In the mountainside behind Goshal village, where it is ~50-100m-thick (Figure 3.14). It appears to thin towards the NW and SE where it becomes increasingly difficult to distinguish from unit A. This variation is a primary sedimentary feature and suggests that thinning of the Tandi Group is partly related to variations in the original size and shape of the sedimentary basin in which the Tandi Group were deposited.

Upper Tandi Group (unit C)

Unit B passes gradationally upwards into unit C, which consists of a 250-300m-thick sequence of interbedded grey-, blue-, white-, and brown-coloured limestones and dolomites, intermittent black marls and discontinuous yellow-coloured calcarenites (Figures 3.16a & 3.14). These sediments are remarkably similar to those of unit A and are indicative of a return to a lower energy, oxygen-poor environment. Unit C forms the core of the Tandi Syncline and is thickest in the mountainside behind Goshal village. It is absent in the north-western and south-eastern closures of the Tandi Syncline, which is largely attributed to post-tectonic erosion.

Interpreted depositional environment of the Tandi Group

The sediments within the Tandi Group are remarkably similar to lithologies belonging to the Kuling Formation and Lilang Group of the Tibetan Sedimentary Series in the hangingwall of the ZSZ (Figure 3.3). These are described in detail by Baud *et al.* (1984) and are interpreted to represent a sequence of Permian to Jurassic limestones and sandstones deposited on the thinned continental margin of the Indian plate following a phase of Upper Permian rifting (Trommsdorff *et al.*, 1983). Whether the Tandi Group were deposited in the same sedimentary basin as the Kuling Formation and Lilang Group remains largely conjectural since the northern continuation of the Tandi Group has been eroded (Figure 3.17). Even if these basins were connected, the Tandi Group must have been deposited well to the south of the Kuling Formation and Lilang Group given the present day >50km separation of these lithologies (Figure 3.17).

Lithological observations presented above suggest that the Tandi Group thins laterally over a very short distance and that these limestones and marls were deposited in a relatively quiet marine environment which experienced periodic anoxic bottom water conditions. It is not unreasonable, therefore, to infer that the Tandi Group were deposited in a restricted marine environment, possibly an isolated rift basin located well to the south of the main Neo-Tethyan basin (Figure 3.17). This is supported by the observation that the Kuling Formation and Lilang Group are underlain by a thick succession of Lower and Upper Palaeozoic sediments (Figure 3.3), which are conspicuously absent beneath the Tandi Group (Figures 3.16 & 3.17). The absence of these sediments implies that either they were never deposited in the first place, or that they were deposited and subsequently eroded prior to the deposition of the Tandi Group. Previous authors (e.g. Fuchs, 1967) have speculated that a major ridge may have separated the northern part of the slab (i.e. Darcha and Baralacha La regions) from more southerly parts of the slab (i.e. Chandra valley and Rhotang Pass regions), which could account for a period of non-deposition throughout the majority of the Palaeozoic.

3.5.5 Metabasites

Basic igneous intrusives were observed at a number of localities in the High Himalayan Slab of SE Zanskar and NW Lahaul (Enclosure 1). They have been metamorphosed to varying degrees, from lower greenschist-facies through to upper amphibolite-facies conditions, and are hereafter referred to as metabasites. Metabasites were rarely observed *in situ* in the field, but were more frequently encountered as freshly-weathered loose boulders in talus slopes, implying that they are been locally derived. They frequently contain a prominent planar grain shape fabric, suggesting that they were intruded prior to deformation of the High Himalayan Slab. In the absence of geochemical and geochronological data, the age and tectonic significance of these metabasites cannot be accurately constrained. Honegger *et al.* (1983) suggested that many of the amphibolites in western and central Zanskar are directly related to the Panjal Traps volcanics. Conversely, Vannay and Spring (1993) suggested that the metabasites exposed in the footwall of the Sarchu normal Fault (SNF) in upper Lahaul are chemically distinct from the Panjal Traps and were probably emplaced during an earlier

phase of rifting in the Carboniferous. In addition to these Upper Palaeozoic metabasites, Pognante and Lombardo (1989) observed a number of metabasites which are discordantly intruded by the Precambrian-Ordovician orthogneisses in the HHC, thus implying that some metabasites in SE Zanskar and NW Lahaul are at least Lower Palaeozoic in age.

3.5.6 The High Himalayan Crystallines (HHC) and High Himalayan leucogranites (HHL)

The HHC are a poorly defined lithological/tectonic unit in the High Himalayan Slab of SE Zanskar and NW Lahaul. Some authors use the term to describe regions of sillimanite-grade migmatites and crustal melt leucogranites located in the footwall of the ZSZ at the top of the slab (e.g. Pognante *et al.*, 1990), whilst others use the term to describe all of the biotite- to sillimanite-grade metasediments, paragneisses and orthogneisses which constitute the entire High Himalayan Slab (e.g. Stephenson, 1997; Vannay & Steck, 1995). Use of the term HHC in this thesis is restricted to descriptions of regions dominated by sillimanite-grade migmatites and crustal melt leucogranites where the metamorphic protolith cannot be readily identified. In this respect it is similar to the definition used by Pognante *et al.* (1990). Lithologically the HHC comprise an intensely deformed and metamorphosed sequence of banded orthogneisses, augen gneisses, biotite paragneisses, metapelitic schists, migmatites, leucocratic pegmatites, crustal melt leucogranites and discontinuous amphibolite pods (Figure 3.18a). They probably represent the higher-grade equivalents of the Haimantas and Precambrian-Ordovician granites exposed in the lower grade parts of the slab. Pognante and Lombardo (1989) suggested that parts of the HHC preserve evidence for a pre-Himalayan metamorphism which suggests the possibility that parts of the HHC represent crystalline basement upon which the Haimantas were deposited.

The HHC are exposed in the upper part of the slab in the immediate footwall of the ZSZ, where they appear to form the core of a large metamorphic dome, hereafter referred to as the Kang La Dome (Enclosure 2; Figure 3.2b; cross-section A-A' on Enclosure 1). Metamorphic grade decreases away from the core of the Kang La Dome in all directions (Enclosure 2). The decrease in the metamorphic field gradient towards the south-east suggests that the regional plunge of structures in the Kang La Dome is also towards the SE. However, it must be noted that this interpretation is somewhat speculative since the area to the west of the Shingo La is extremely inaccessible and inhospitable and was not investigated during the work of this thesis. Along strike and to the south-east of the Kang La Dome, Thöni (1977) observed an extensive region of sillimanite-bearing orthogneisses and paragneisses within the Deo Tibba granite massif, structurally above and to the north-east of the MCT (Enclosure 2). This part of the slab was not investigated during the work of this thesis and it remains uncertain whether these lithologies are regional correlatives of the HHC exposed in the Kang La Dome.

The High Himalayan leucogranites (HHL)

The High Himalayan leucogranites (HHL) represent a suite of post-collisional Qtz + Kfs + Pl + Ms ± Bt ± Grt ± Tur granites which intrude the HHC as a series of weakly deformed layer-parallel sheets in the uppermost part of the slab (Enclosure 1). They are generally located above zones of sillimanite-grade migmatites (Figure 3.18a), although they are also observed intruding into higher structural levels in the immediate footwall of the ZSZ. The Gumburanjon leucogranite (Figure 3.18b), is a classic example of one such granite and is discussed in more detail in Chapter 6. Several migmatitic leucosomes and HHL have been dated in SE Zanskar, all of which consistently yield Miocene crystallisation and cooling ages (e.g. Noble & Searle, 1995; Ferrara *et al.*, 1987, 1991). Chapter 7 presents new U-Pb and $^{40}Ar/^{39}Ar$ data from the Gumburanjon leucogranite which are consistent with these ages.

3.5.7 Lithological summary

The High Himalayan Slab in SE Zanskar and NW Lahaul is predominantly composed of a 3-5km-thick, unfossiliferous sequence of sands, silts and shales collectively referred to in this thesis as the Haimantas. The age of these sediments remains poorly constrained, but is believed to be at least Lower/Middle Cambrian based on the observation that they are overlain in the upper part of the study area by the dolomitic limestones of the Middle Cambrian Karsha Formation and that they are discordantly intruded at several localities by a number of large, megacrystic K-feldspar granites which yield Cambro-Ordovician Rb-Sr whole rock ages (Table 3.1). Some of these granites yield Upper Precambrian Rb-Sr ages, which if correct, suggests that either the Haimantas are significantly older than the Cambrian, or that these granites represent the basement upon which the Haimantas were deposited. The Haimantas are tentatively correlated with the Lower Cambrian Phe Formation in the Tibetan Sedimentary Series of SE Zanskar. Sediments within the Chamba Syncline in the western part of the study area are remarkably similar to the Haimantas exposed in adjacent parts of the slab and are also considered to be at least Lower Palaeozoic in age.

An almost continuous sequence of Lower and Upper Palaeozoic sediments are preserved above the Haimantas in the uppermost part of the High Himalayan Slab in NW Lahaul (Spring & Crespo-Blanc, 1992; Vannay, 1993). These sediments are absent in the central and southern part of the slab, which reflects either non-deposition or extensive erosion prior to the deposition of the Permo-Jurassic Tandi Group. The Tandi Group represents a fossiliferous sequence of Permo-Jurassic marine limestones and are interpreted to form an integral part of the High Himalayan Slab. They appear to be correlatives of the Kuling Formation and Lilang Group exposed in the Tibetan Sedimentary Series of SE Zanskar, and are interpreted to have been deposited in a small rift basin to the south of the main Neo-Tethyan ocean. The post-Jurassic history of the High Himalayan Slab is unknown since no sediments younger than the Tandi Group are preserved in the study area.

Many parts of the High Himalayan Slab in SE Zanskar and NW Lahaul have experienced amphibolite facies metamorphic conditions. The highest grade lithologies are collectively referred to

as the High Himalayan Crystallines (HHC). The protoliths of these cannot readily be identified, but appear to be the high-grade equivalents of lithologies exposed in the lower grade parts of the slab. However, the possibility that parts of the HHC represent a crystalline basement upon which the Lower Palaeozoic Haimantas were deposited could not be ruled out from field observations alone.

Owing to the intensity of deformation within the High Himalayan Slab and the similarity of sediments within the Haimantas, it is extremely difficult to correlate lithologies over large areas. An attempt to correlate lithologies across the slab is shown in Figure 3.19. These correlations are tentatively based on comparisons of similar-looking units of pyritiferous black shales and carbonate-rich horizons within the Haimantas.

3.6 Metamorphic overview

Field mapping of metamorphic index minerals in metapelites, calc-silicates and metabasites across SE Zanskar and NW Lahaul revealed a regular pattern of metamorphic mineral zones which are defined by characteristic metamorphic assemblages (Table 3.2; Figure 3.2b & Enclosure 2). These mineral assemblages are characteristic of a Barrovian-type metamorphism associated with crustal shortening and thickening, rather than a Buchan-type metamorphism associated with high geothermal gradients. It is important to emphasise that no major metamorphic discontinuities were observed between these metamorphic zones, suggesting that the High Himalayan Slab in SE Zanskar and NW Lahaul represents a more-or-less coherent tectonic unit. The regularity of this isograd pattern suggests that metamorphism in the High Himalayan Slab is dominantly Himalayan in age since it would require a remarkable coincidence for such a pattern to be produced by the superposition of two or more metamorphic terranes. However, the possibility that some metamorphic assemblages in the higher-grade parts of the High Himalayan Slab in SE Zanskar are pre-Himalayan has been suggested by Pognante and Lombardo (1989).

Table 3.2: Typical metamorphic assemblages observed in different lithologies in different metamorphic zones in the High Himalayan Slab of SE Zanskar and NW Lahaul. Abbreviations after Kretz (1983).

Metamorphic Zone	Pelitic/semi-pelitic schists*	Psammitic schist/ biotite gneiss	Calc-silicates**	Metabasites
Chlorite	Qtz + Ab + Ms + Chl (± Cal ± Ank)	Qtz + Pl ± Chl ± Bt ± Ms	None observed in the field	Qtz + Ab + Act + Ep ± Chl ± Cal
Biotite	Qtz + Ab + Ms + Bt ± Chl (± Cal ± Ank ± Sph)	Qtz + Pl + Bt ± Ms	Qtz + Ab + Grt + Hbl + Zo/Czo ± Cal ± Ep ± Sph	Qtz + Ab + Act + Ep ± Chl ± Cal
Garnet	Qtz + Ab/Olg + Ms + Bt + Grt ± Chl (± Hbl ± Zo/Czo)	Qtz + Pl + Bt ± Ms ± Grt	Qtz + Ab + Grt + Hbl + Zo/Czo ± Cal ± Ep ± Sph	Qtz + Ab/Olg + Hbl + Grt + Bt ± Ep ± Cal ± Chl
Staurolite/ kyanite	Qtz + Ab/Olg + Ms + Bt ± Grt ± St ± Ky (± Hbl)	Qtz + Pl + Bt ± Ms ± Grt	Qtz + Ab + Grt + Hbl + Czo ± Cal ± Ep ± Sph	Qtz + Ab/Olg + Hbl + Grt + Bt ± Ep ± Cal ± Chl
Sillimanite	Qtz + Pl + Bt + Sil ± Ms ± Grt ± St ± Ky ± Kfs	Qtz + Pl + Bt ± Ms ± Grt ± Sil	None observed in the field	None observed in the field

* Brackets denote additional phases seen in carbonate-bearing pelites.

** Observed as discontinuous pods within the pelitic and psammitic schists of the Haimantas (interpreted to represent the deformed remains of carbonate concretions).

3.7 Introduction to Chapters 4-6

This chapter has presented a regional geological overview of the High Himalayan Slab in SE Zanskar and NW Lahaul using information gleaned from previous works and personal field observations. The following three chapters discuss in more detail the structure and metamorphism of different parts of the study area. In the absence of any major structural or metamorphic discontinuities within the study area it was not possible to sub-divide the study area on the basis of structural or metamorphic criteria. Consequently, the sub-divisions shown in Figure 3.20 are geographical. Chapter 4 discusses the structure and metamorphism of the lower part of the slab, which is generally referred to in the literature as the Crystalline Nappe. Chapter 5 discusses the geology of the Chamba Syncline which is located immediately along strike and to the west of the Crystalline Nappe (Figure 3.20). Chapter 6 discusses the geology of the upper part of the slab in the region between Darcha and Kargyak, paying particular attention to the Gumburanjon leucogranite and Zanskar Shear Zone (ZSZ).

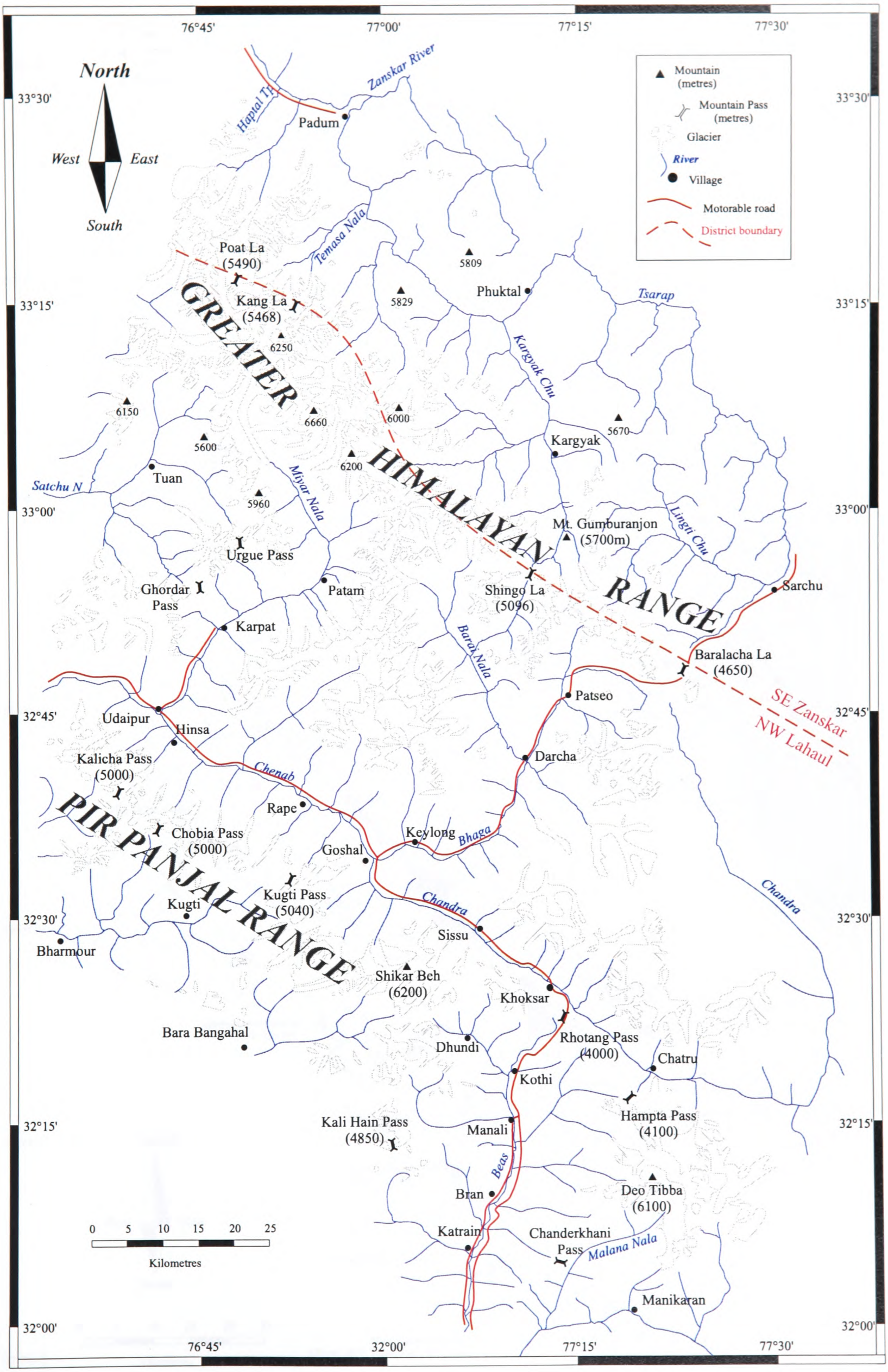


Figure 3.1: Geographical map of SE Zanskar and NW Lahaul showing the location of major rivers, villages and mountain passes referred to in this thesis.

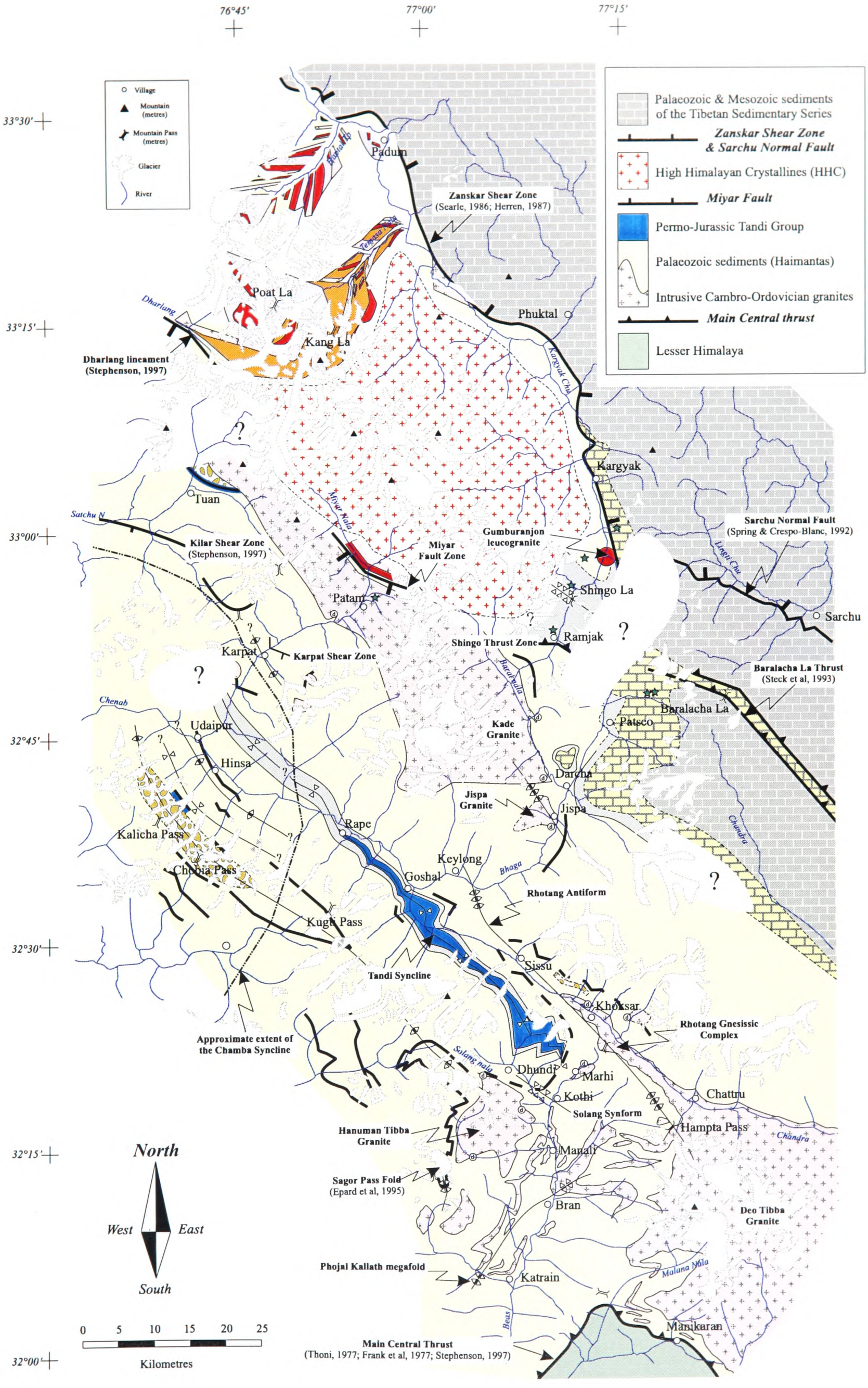


Figure 3.2a: Simplified geological map of the High Himalayan Slab in SE Zanskar and NW Lahaul. See Enclosure 1 for more detailed version.

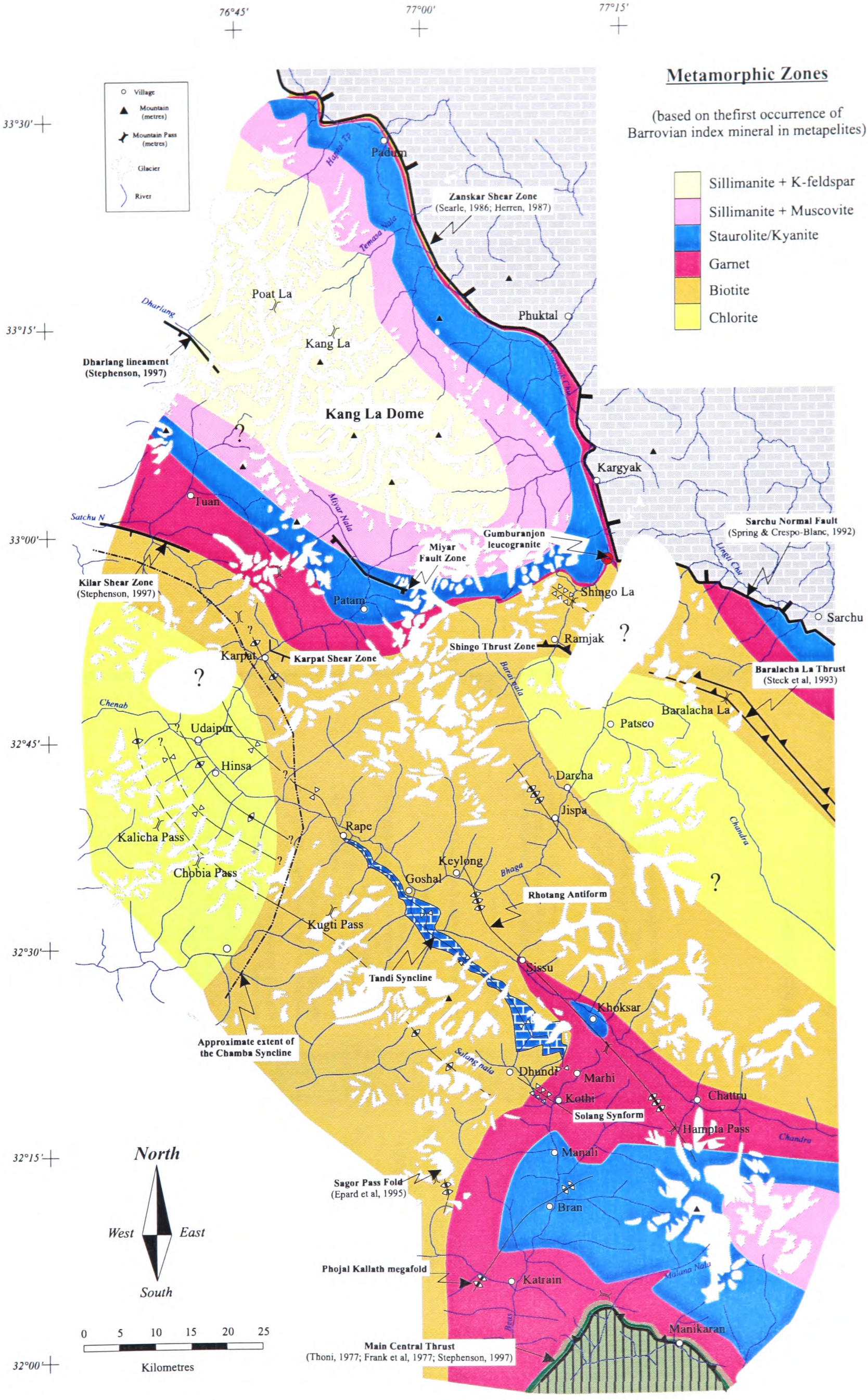


Figure 3.2b: Simplified metamorphic map of the High Himalayan Slab in SE Zanskar and NW Lahaul. See Enclosure 2 for more detailed version with quantitative P-T data.

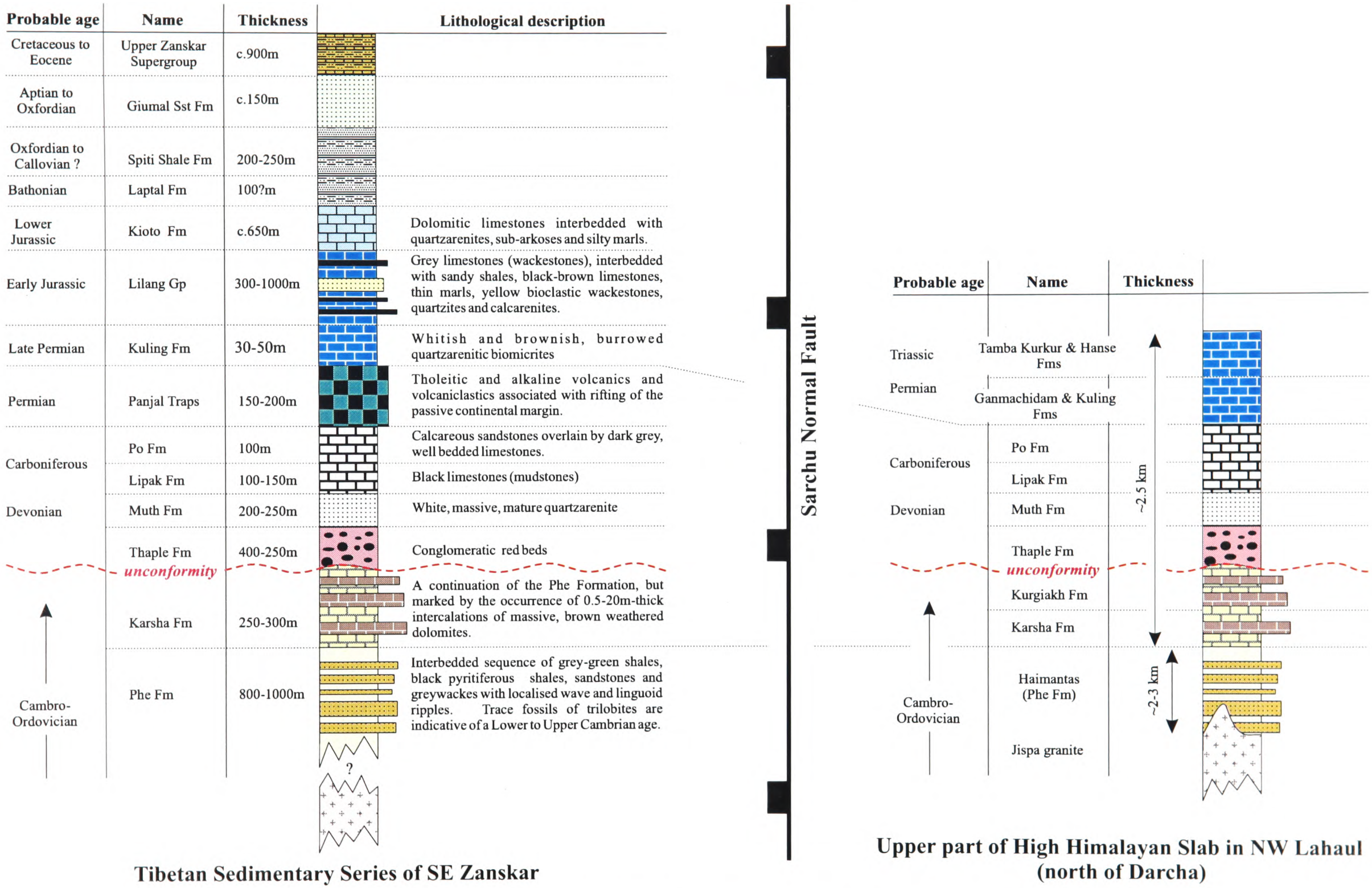
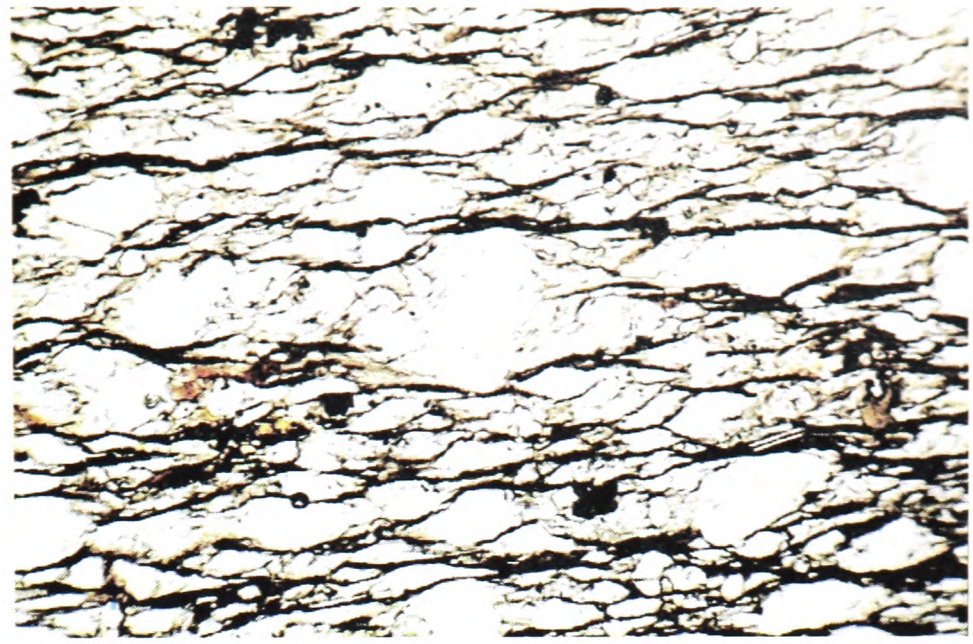
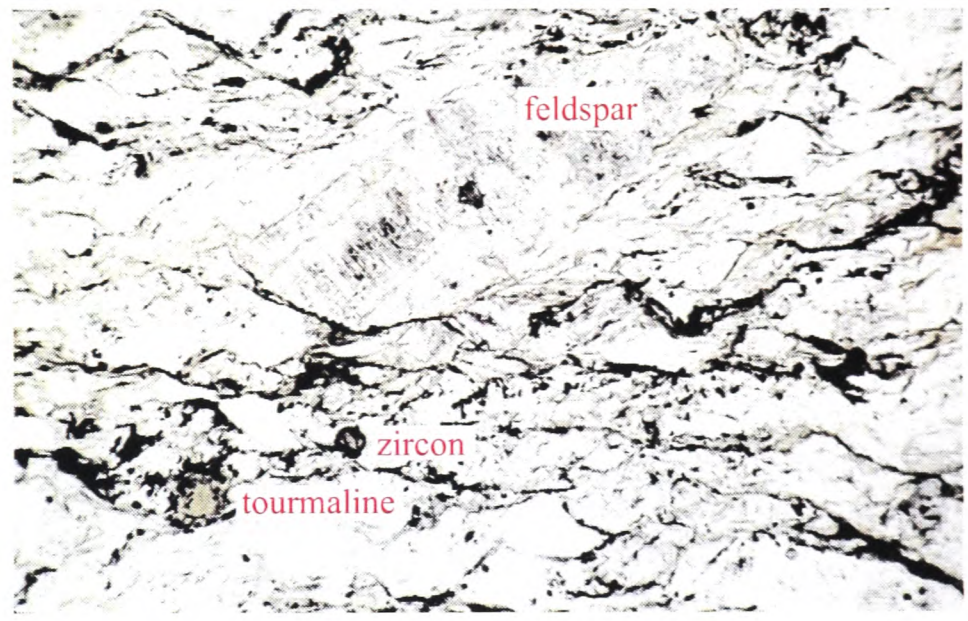


Figure 3.3: Comparison of stratigraphic units across the Sarchu Normal Fault (SNF) in the upper part of the High Himalayan slab in NW Lahaul. Stratigraphy of the Tibetan Sedimentary Series is summarised from data published by Baud et al (1984), Garzanti et al (1987), McElroy et al (1990) and Hughes and Droser (1992). Stratigraphy of the High Himalayan Slab is summarised from Spring and Crespo-Blanc (1992) and Vannay and Steck (1995).

Figure 3.4: Detrital textures in sandstones collected from the Precambrian-Cambrian Haimantas. Field of view is approximately 3mm in all of the photomicrographs.



(a) Detrital grains of quartz and feldspar wrapped by a well-developed axial planar fabric (S1) defined by metamorphic muscovite and biotite. (Sample JDW 61, collected within the biotite zone, ~500m north of Hanuman Tibba granite in the overturned limb of the Tandi Syncline).



(b) Poorly sorted array of detrital quartz, sodic feldspar, tourmaline, rutile and zircon grains enclosed within a graphite-rich chloritic matrix. The large clast in the central part of the photograph is a perthitic feldspar. (Sample JDW 130, collected within the chlorite zone, ~500m south of the police checkpoint at the Darcha).



(c) A heavy mineral band defined by detrital grains of rounded zircon, tourmaline and ilmenite. The mineral band is overgrown by large grains of metamorphic biotite. (Sample JDW 147, collected within the biotite zone, ~1km north of the Shingo La).



Figure 3.4d: Irregularly shaped zoisite + calcite + actinolite + garnet bearing metacarbonate pod within a biotite-grade greywacke (~1km north of Shingo La).



Figure 3.4e: Isoclinally folded actinolite-and garnet-bearing metacarbonate pods within an interlayered sequence of garnet-grade psammites and metapelites of the Haimantas (upper limb of the Phojal-Kallath megafold, ~ 5km south of Bran village on western bank of Beas vallley)

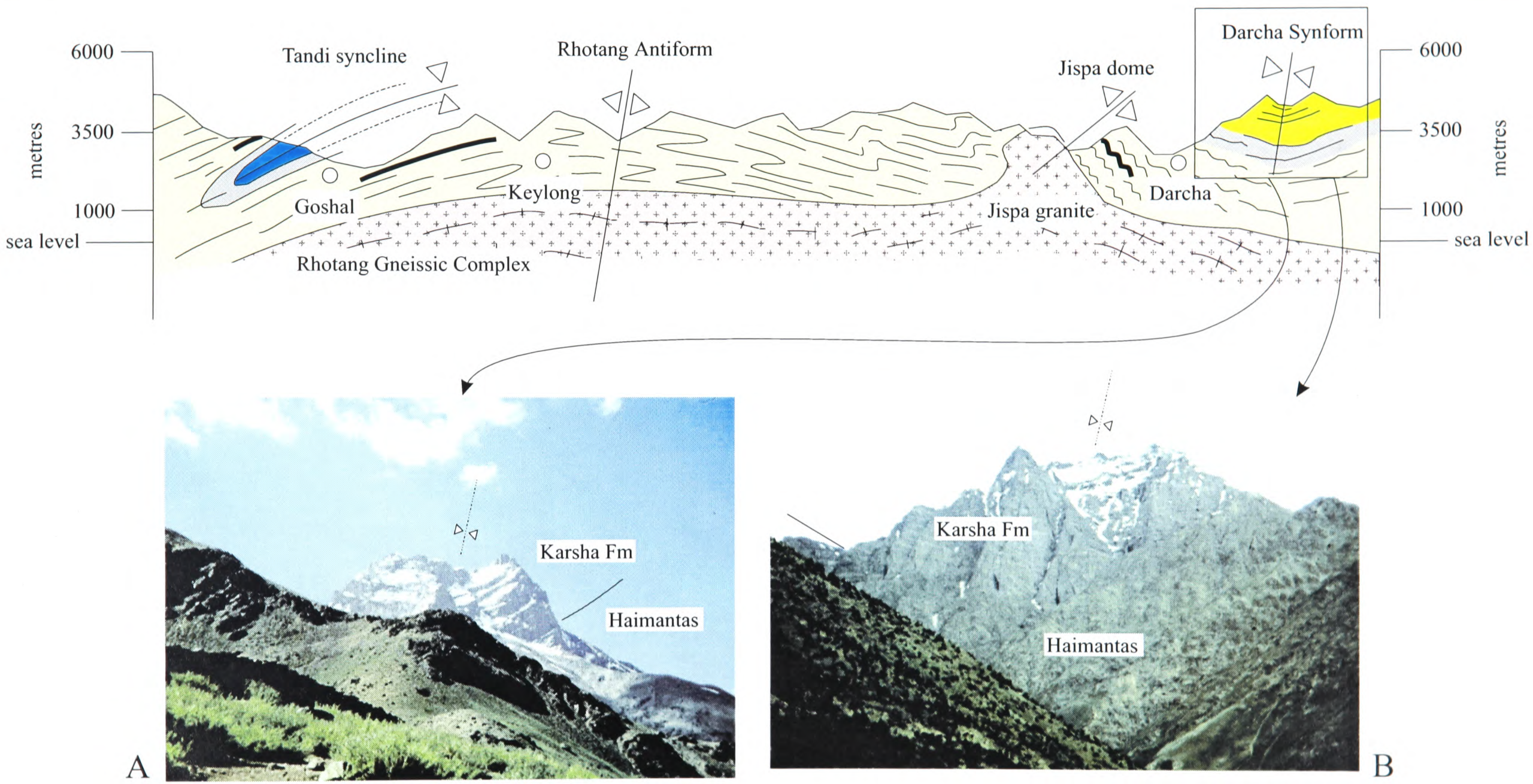
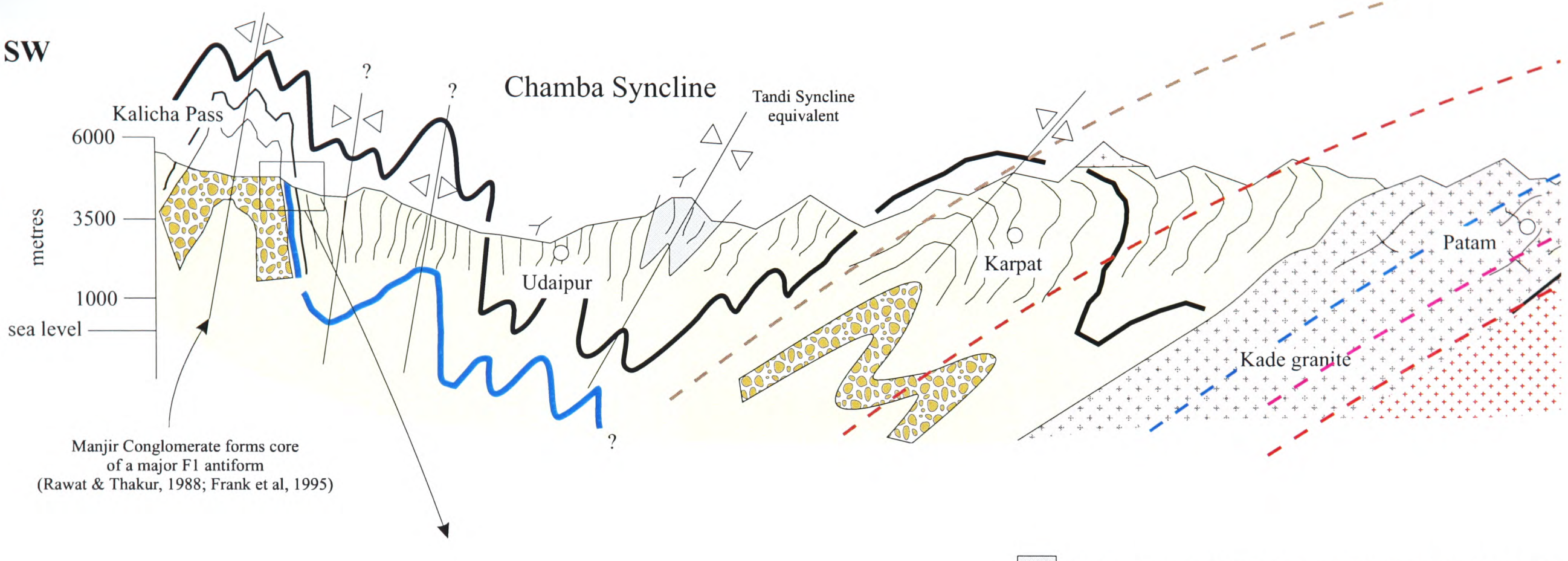
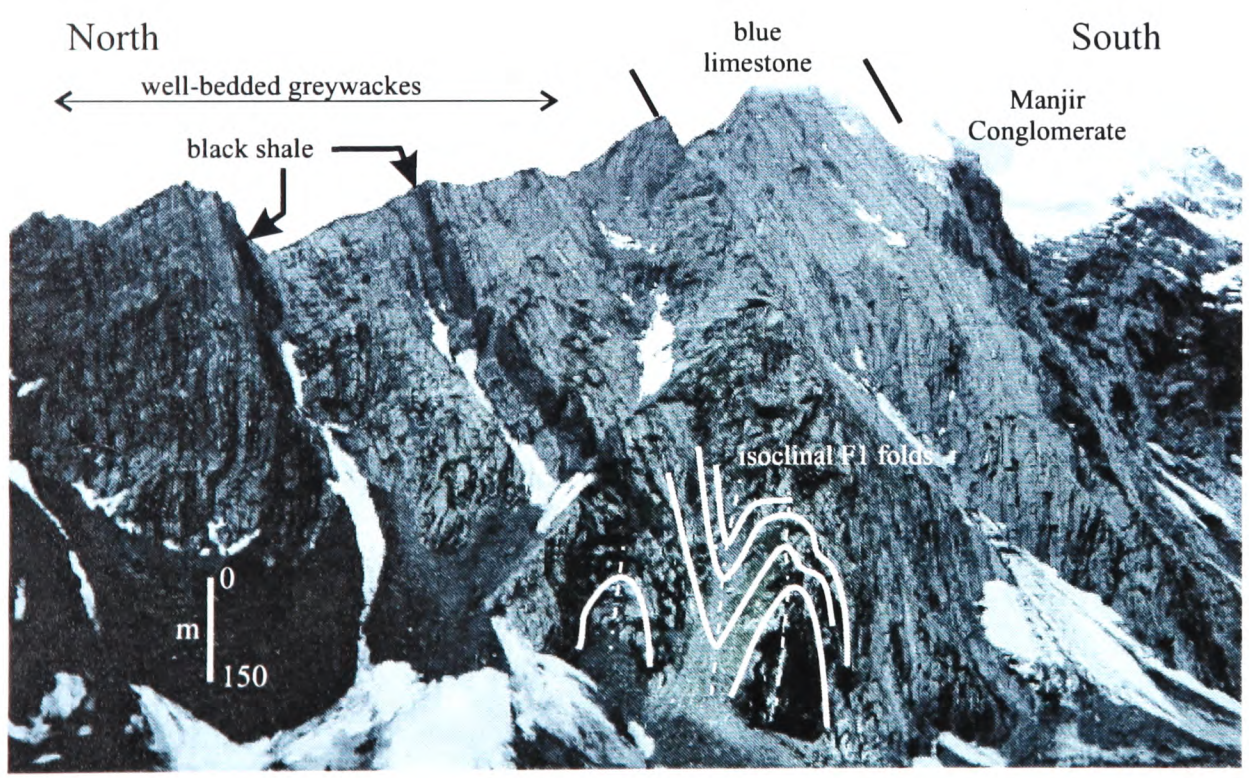


Figure 3.5: The dolomitic Middle Cambrian(?) Karsha Formation above the carbonate-rich sands, silts and shales of the Haimantas in the northern part of the mapping area. Photo (A) was taken looking NW into the western bank of the Bhaga valley, north of Darcha. Photo (B) was taken looking NE into the eastern bank of the Bhaga valley from the Darcha police checkpoint. The exact nature of the contact was not determined, but is thought to be of sedimentary origin. See Enclosure 1 for lithological legend.





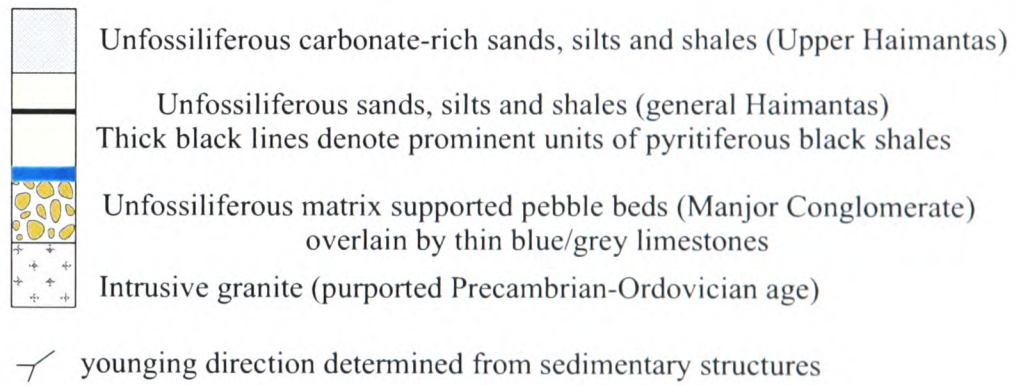
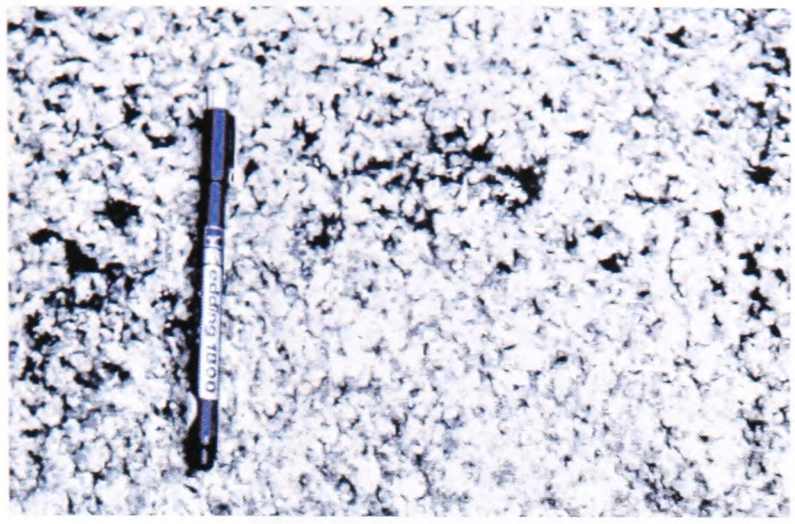
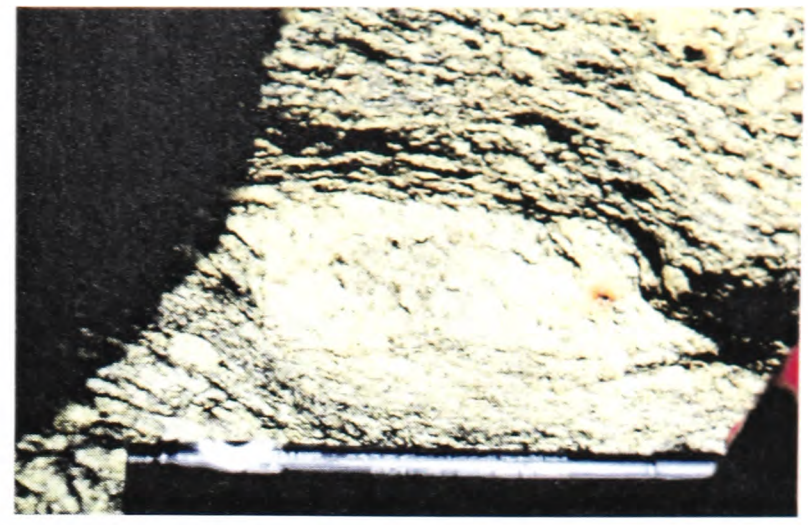


Figure 3.6: Cross-section through the easternmost extension of the Chamba Syncline (cross-section A-A' shown on Enclosure 1). Photograph shows the contact between the sands, silts and shales of the Haimantas and the underlying blue limestones and Manjir Conglomerate immediately north of the Kalicha Pass. Bedding (S0) is parallel to a strong axial planar cleavage (S1), which can be traced throughout the Haimantas towards the north.

Figure 3.7: Textures and mineralogy of Precambrian-Ordovician granites in the High Himalayan Slab of SE Zanskar and NW Lahaul



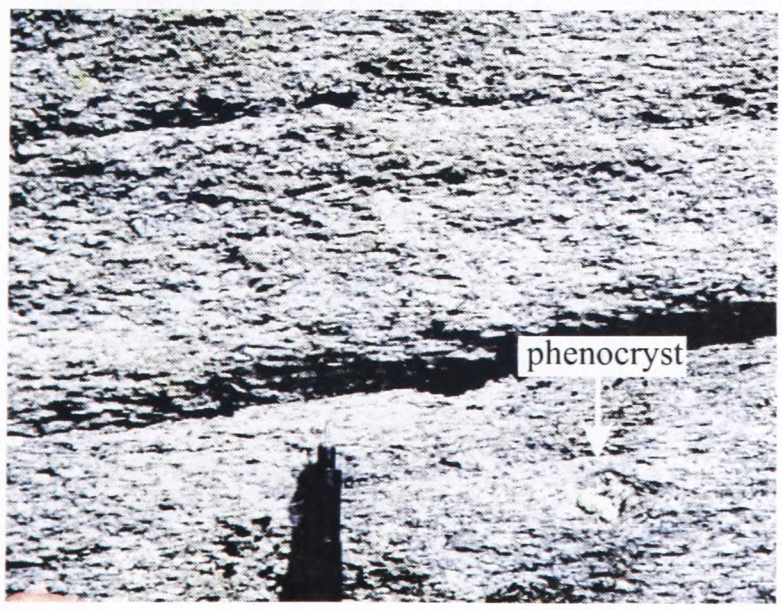
(a) weakly deformed coarse grained equigranular leucocratic granite (Hanuman Tibba granite)



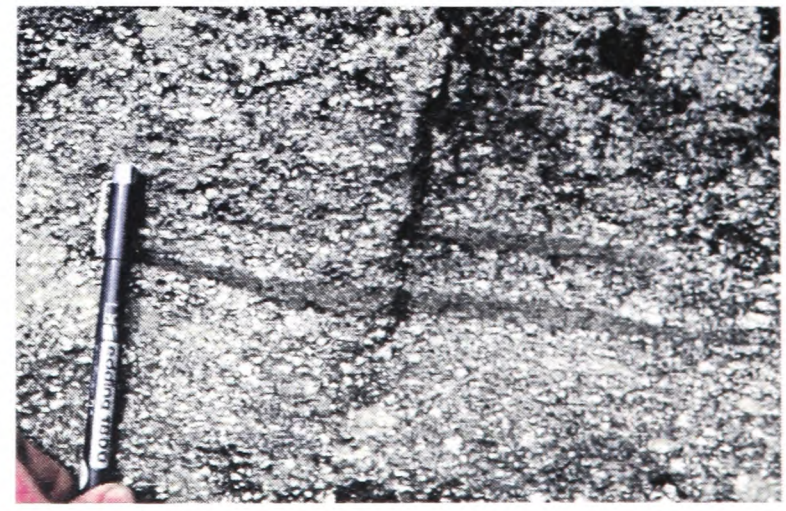
(b) large K-feldspar phenocrysts in a porphyritic leucocratic granite exposed in the immediate footwall of the ZSZ at the top of the slab (beneath the Gumburanjon leucogranite).



(c) intensely deformed leucocratic augen gneiss within the Rhotang Gneissic Complex showing a top-to-the-north-east extensional shear band fabric



(d) mylonitised leucocratic granite (orthogneiss) in the Crystalline Nappe (Manaslu nala, west of Manali). A large K-feldspar phenocryst is wrapped by the gneissic foliation. Pressure shadows around this phenocryst are symmetrical.



(e) mesocratic granodiorite containing abundant K-feldspar phenocrysts and lentiular enclaves of mafic paragneiss (Crystalline Nappe, Manaslu nala, near Manali)

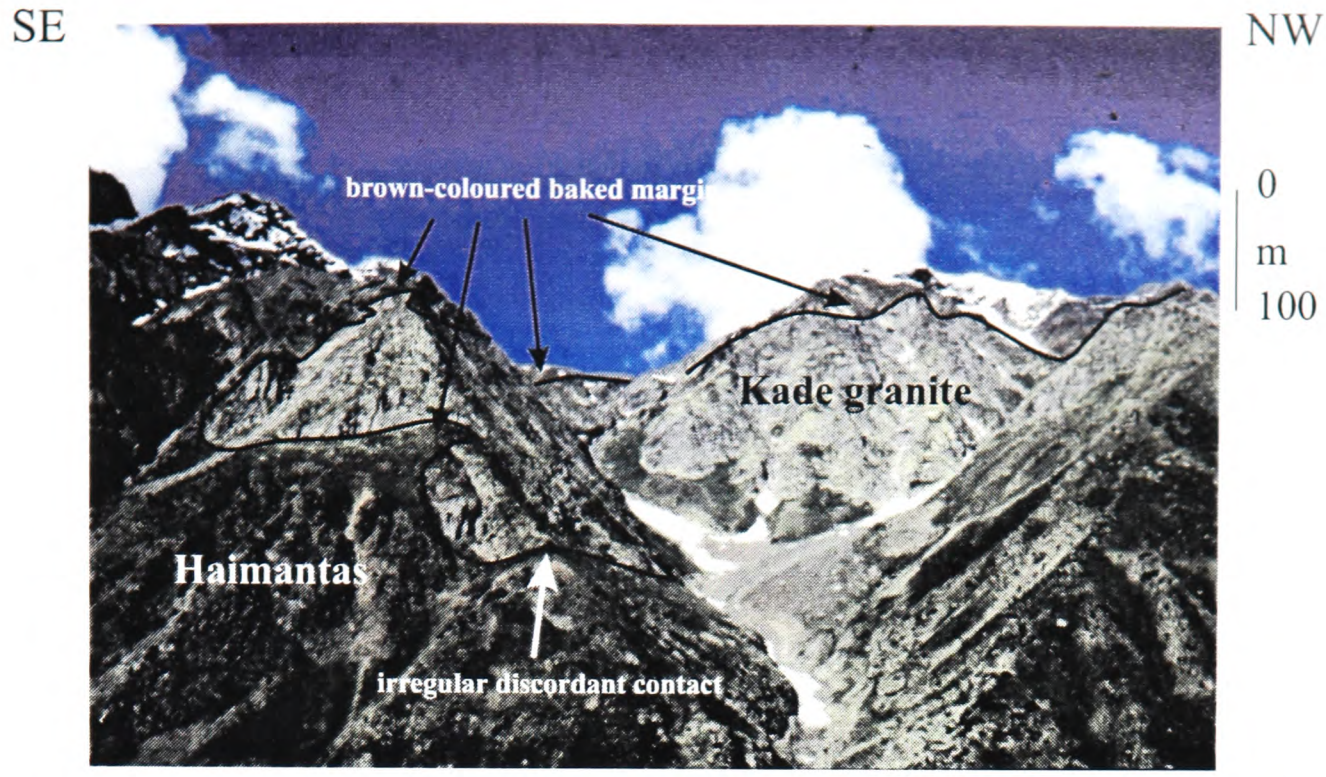
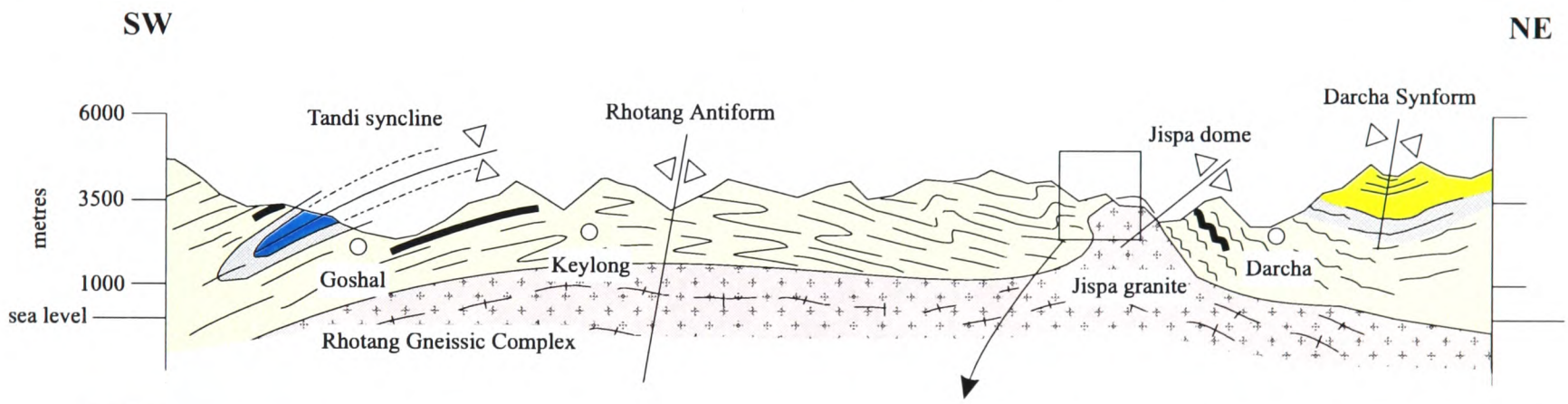
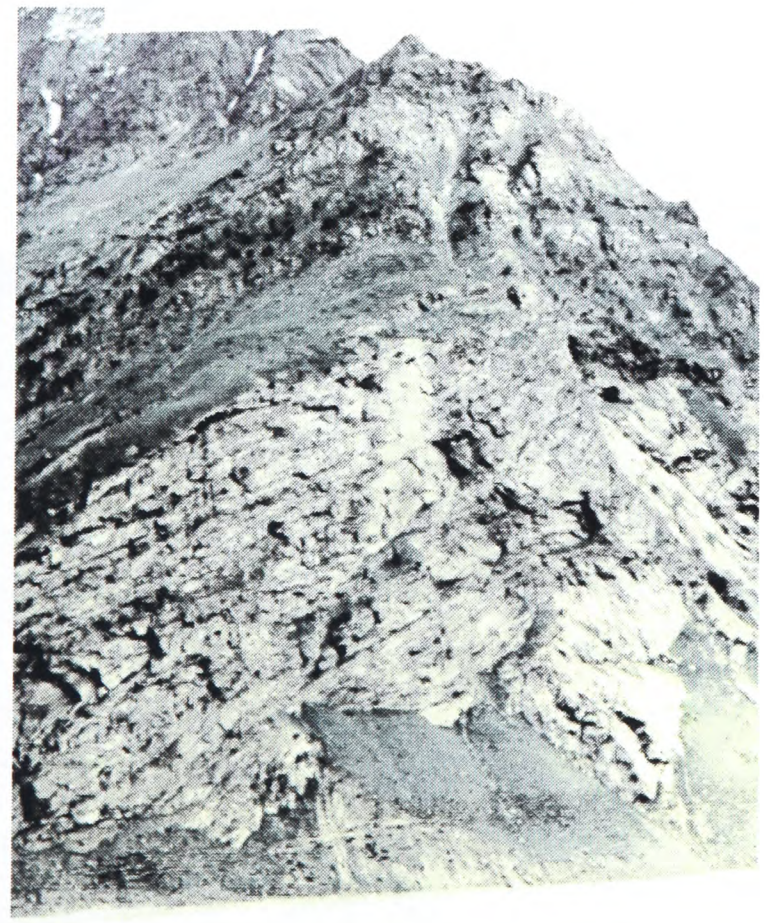


Figure 3.8: Discordant contact of the Kade granite with the surrounding sediments of the Haimanatas. A prominent zone of heavily weathered brown-coloured sandstones and siltstones is evident is evident along the margins of the granite and is interpreted to be a baked margin. The granite has a distinct green appearance which is related to the chloritisation of biotite and growth of epidote during deformation and metamorphism of the High Himalayan Slab. (photo taken on the northern side of the Kade granite, ~ 1km west of Darcha)







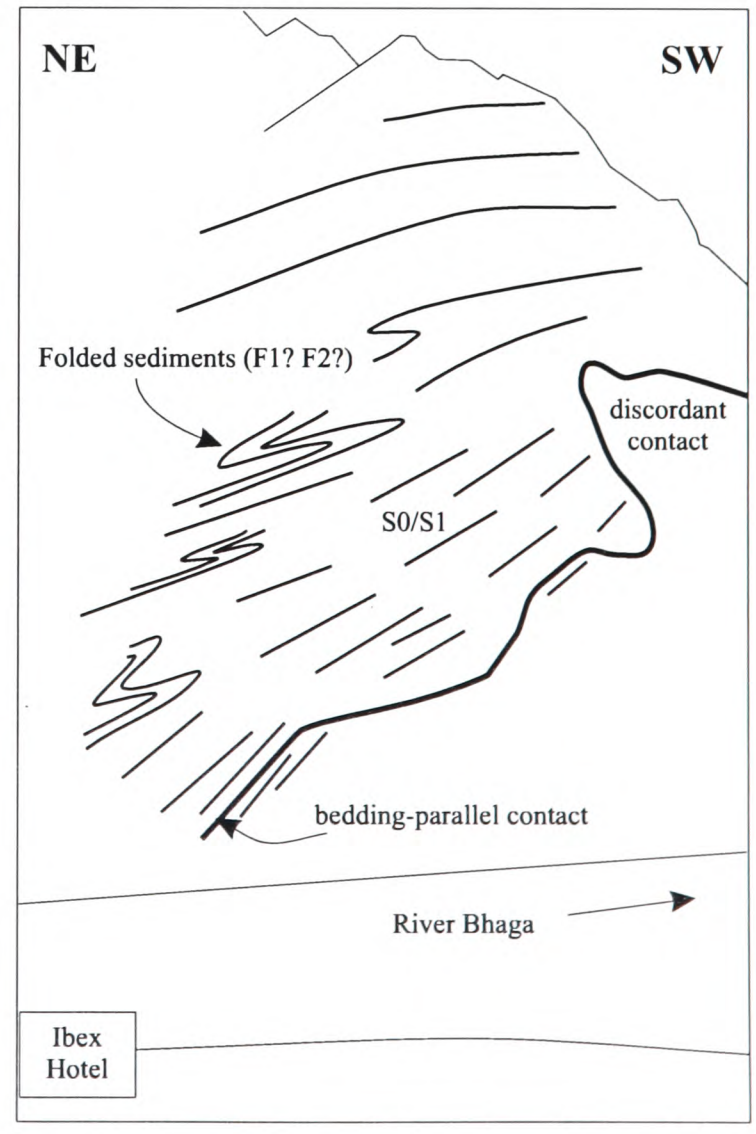
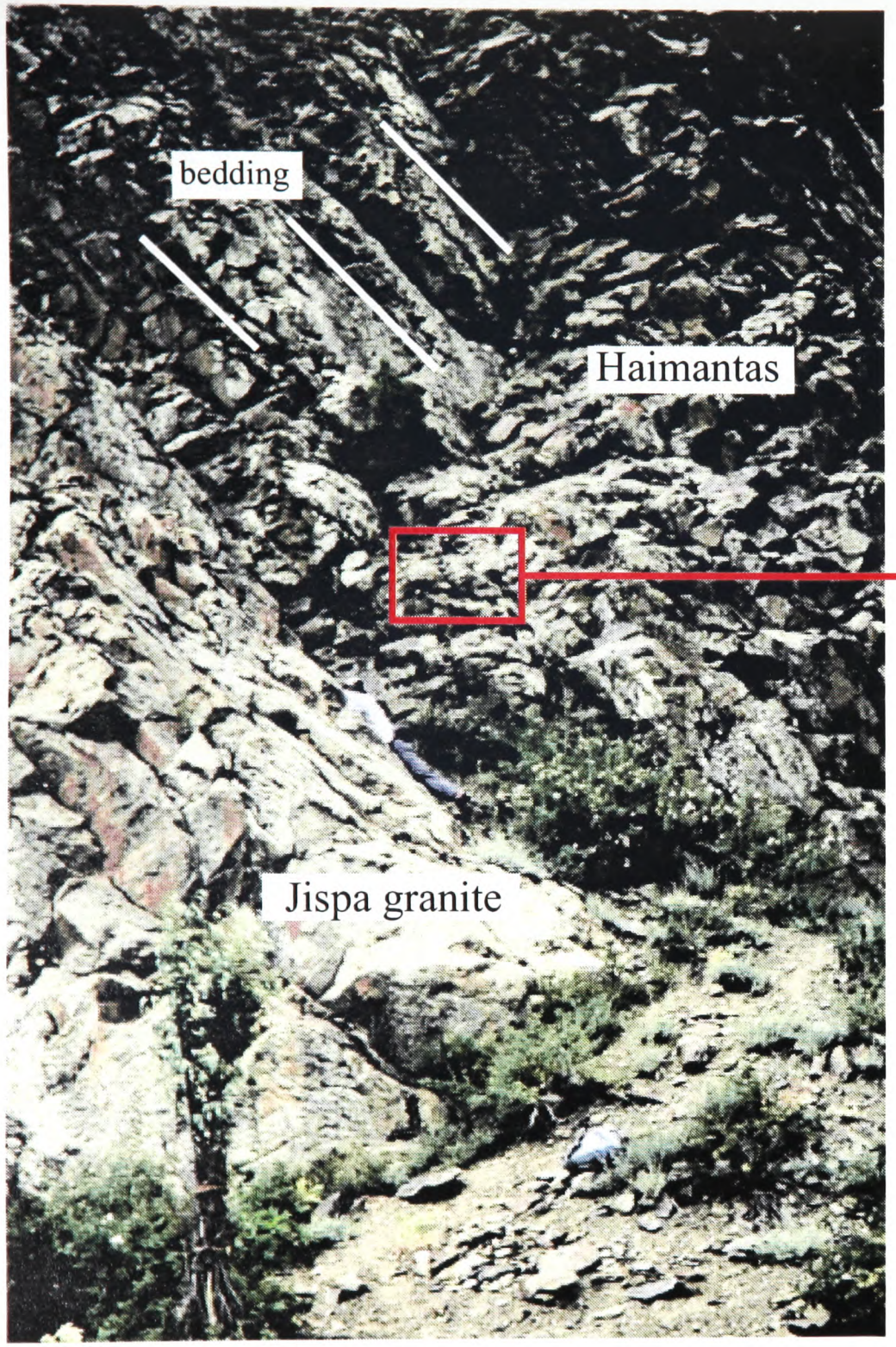


Figure 3.9a: Bedding-parallel and discordant contact of the Jispa granite with the surrounding sediments of the Haimantas. A weak tectonic fabric (S1) is developed along the margins of the granite. Hotel in bottom left of picture gives an idea of scale. (photograph taken looking into the east bank of the Bhaga valley to the south of Jispa campsite).



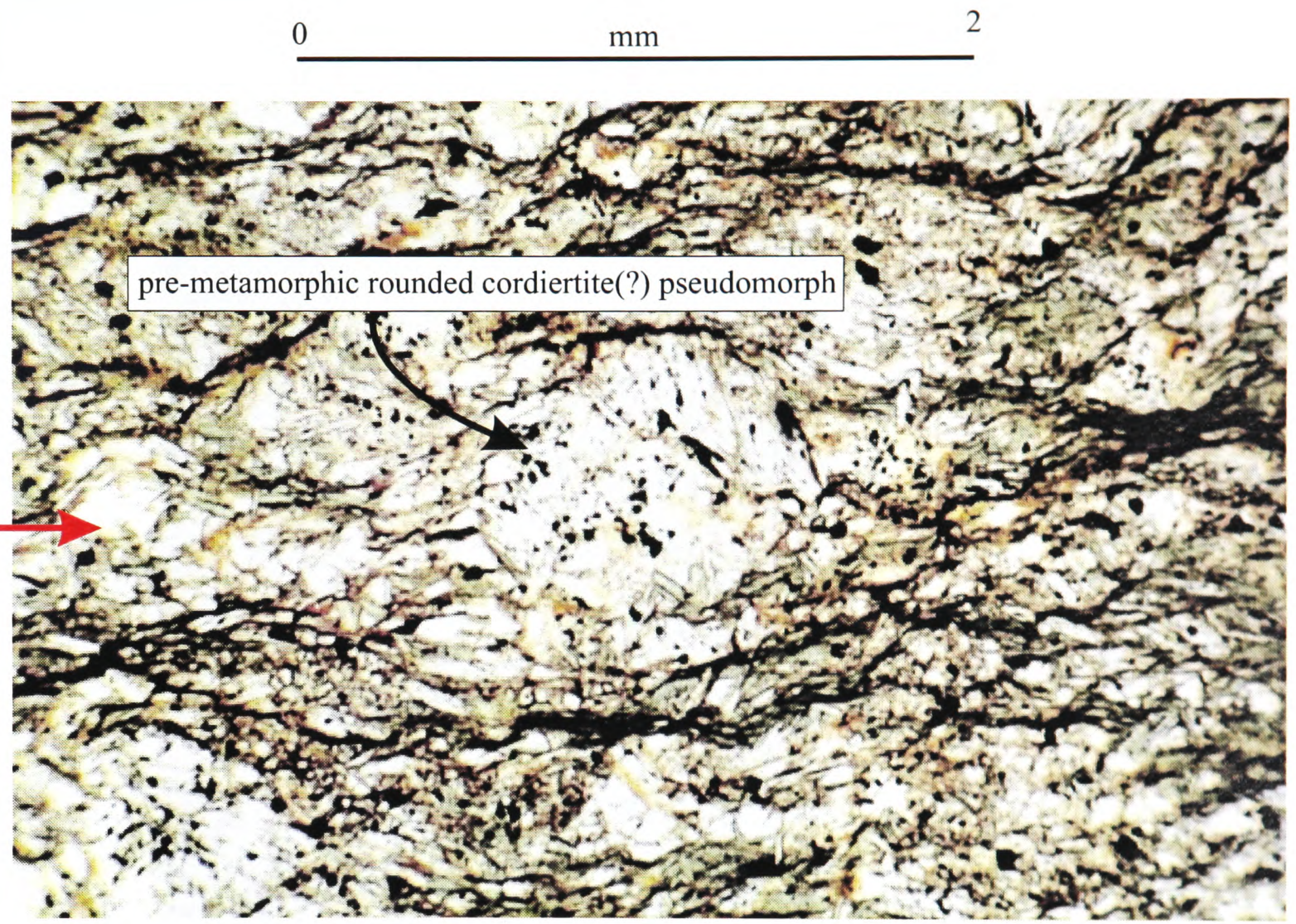
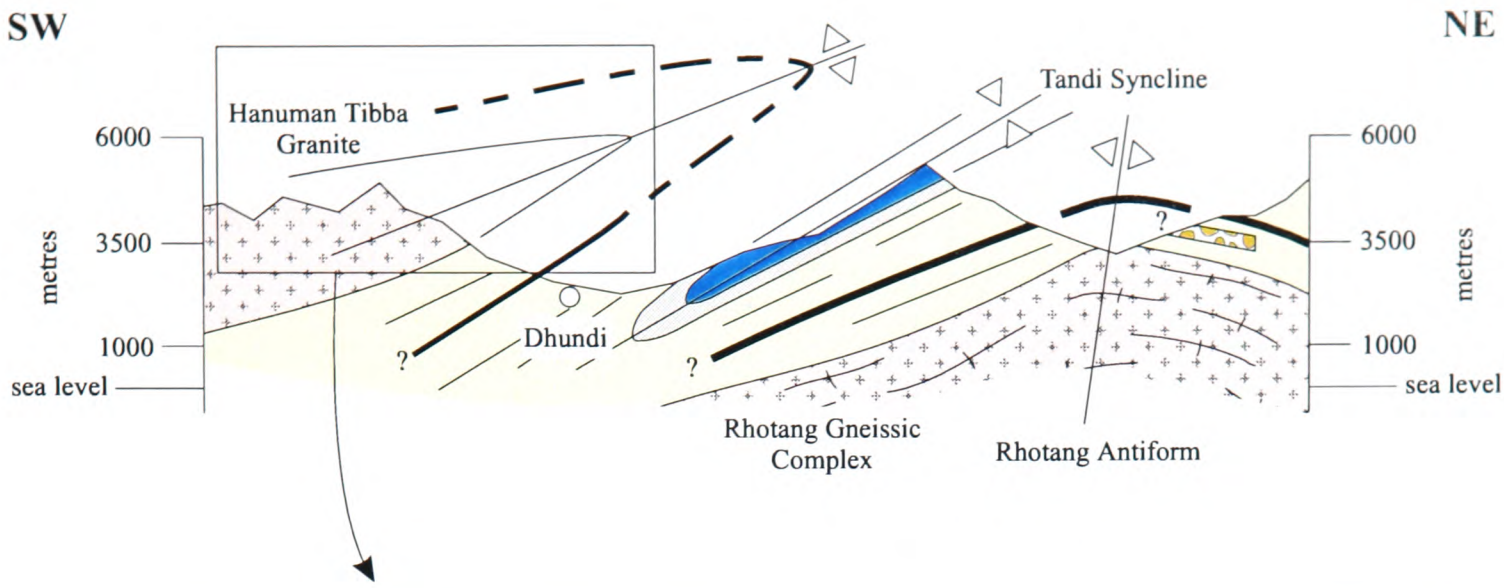


Figure 3.9b: (Left) Planar (s-parallel) contact of the Jispa granite with sandstones and silts of the Haimantas (western bank of the River Bhaga, opposite Jispa campsite). The human figure in the middle of photograph is lying on the actual contact, which dips ~40° NNE. The Haimantas immediately adjacent to the granite are hornfelsed. (Right) The hornfels texture is recognised by numerous rounded pseudomorphs of cordierite(?) which have been replaced by muscovite and ilmenite during Tertiary metamorphism of the High Himalayan Slab. The pseudomorphs are clearly pre-metamorphic and also pre-date the development of the sub-horizontal tectonic foliation, which is defined by aligned flakes of metamorphic muscovite and biotite.





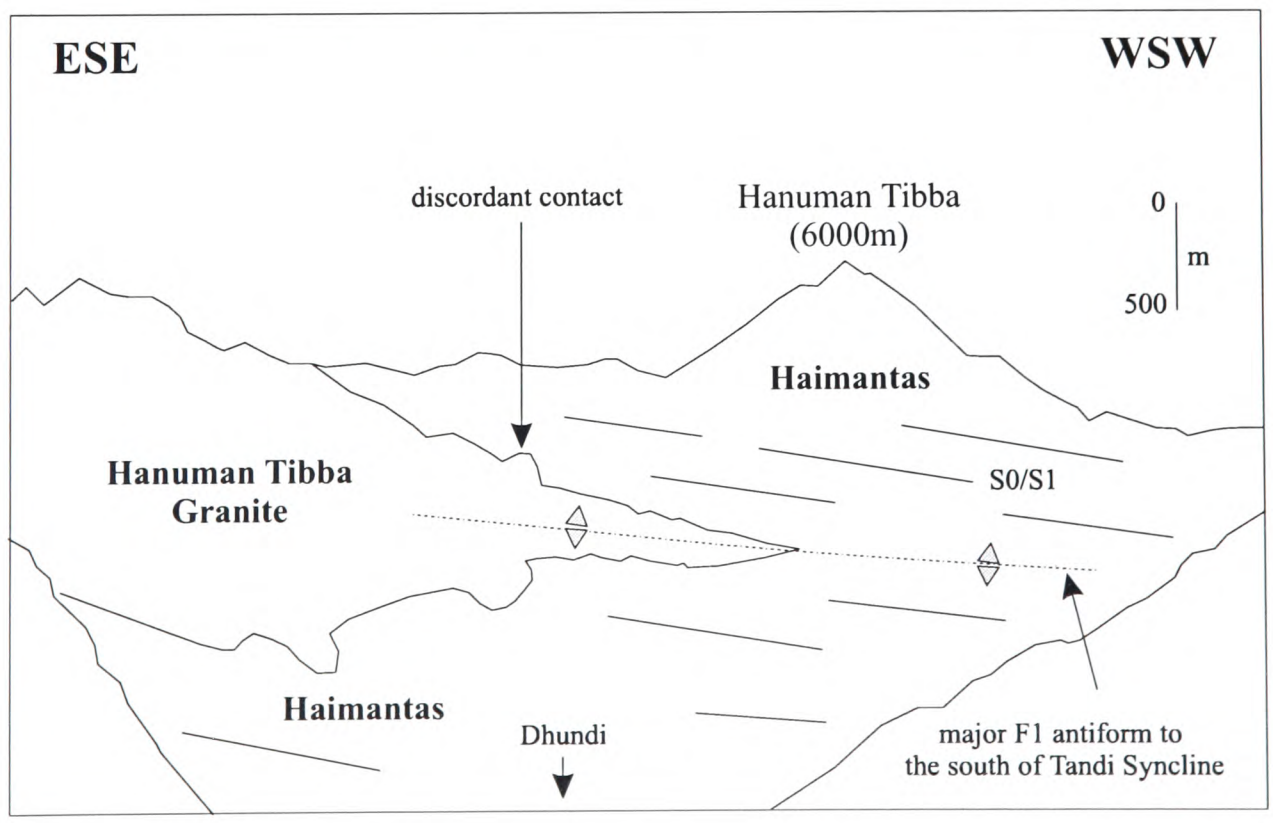
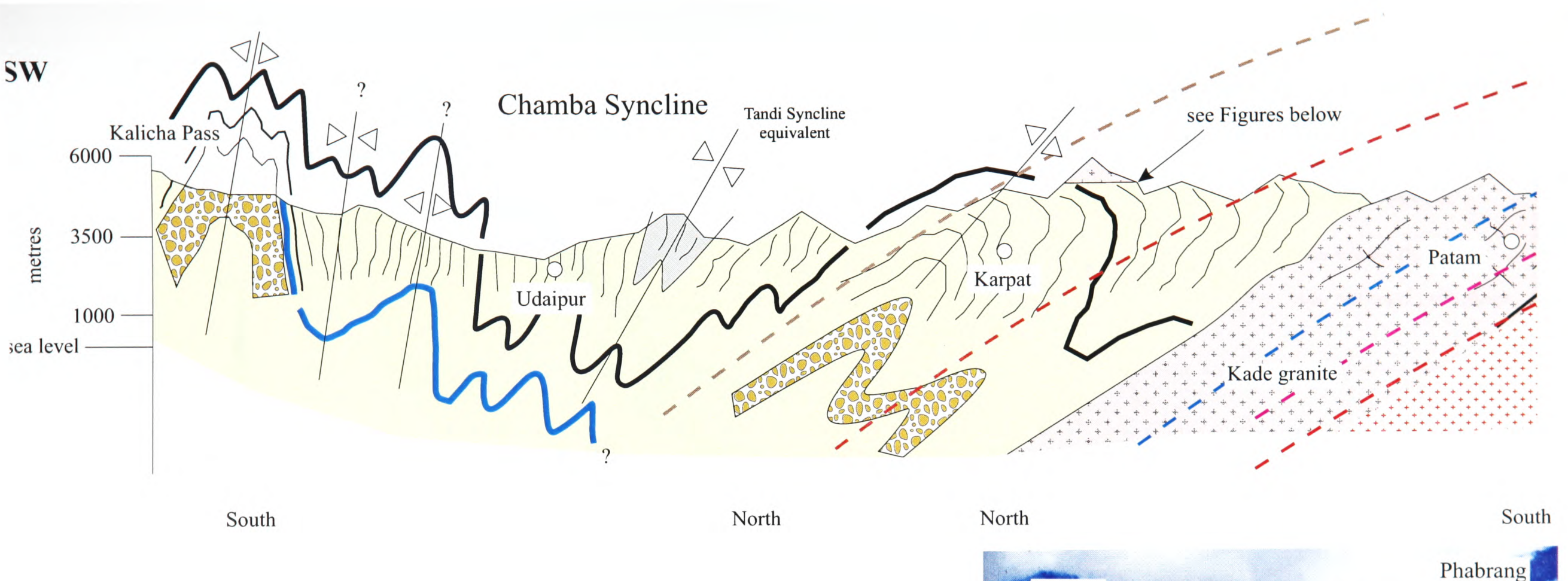
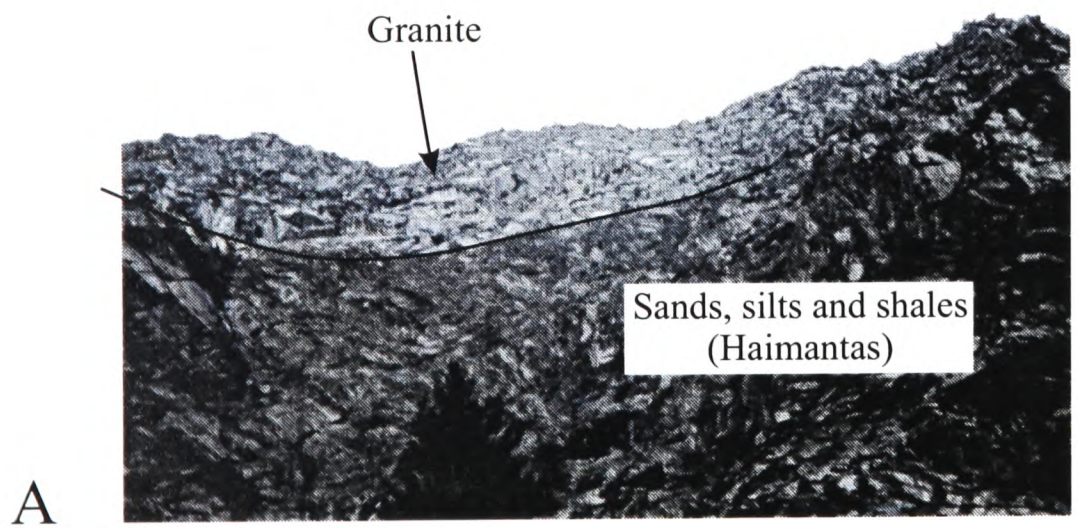
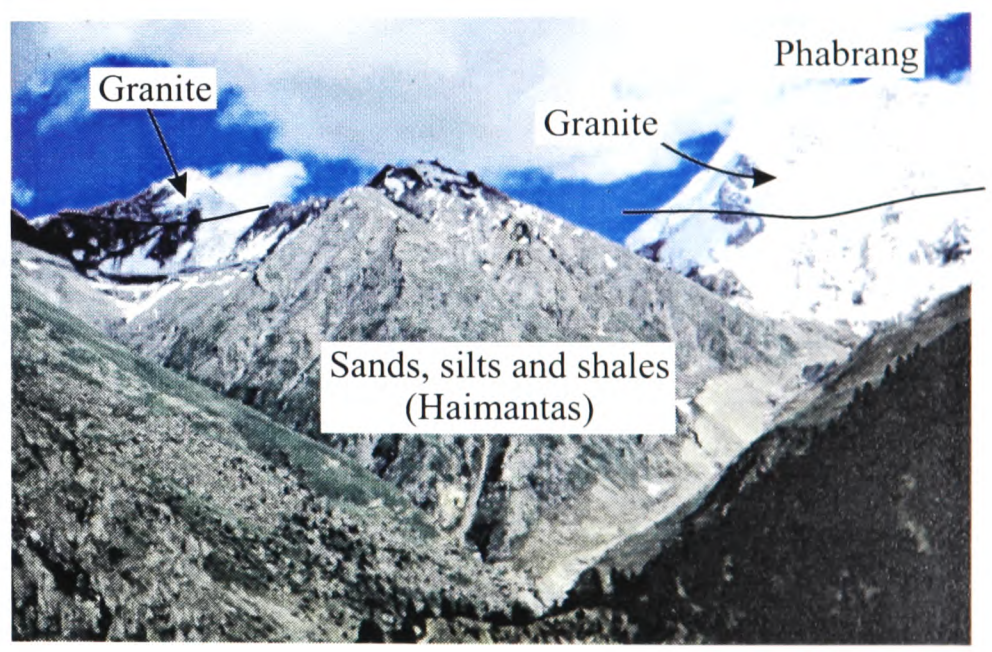


Figure 3.10: Discordant contact of the Hanuman Tibba granite against the Lower Palaeozoic Haimantas. The granite closes in a major NE verging, NW plunging F1 antiform to the south of the Tandi Syncline. The granite is largely undeformed (Figure 3.8a), although is locally mylonitised along some of its margins. (photograph taken looking south from a ridge high above Dhundi campsite).





A



B

Figure 3.11: Granite sheets located above the sub-vertically dipping sediments of the Haimantas in the Chamba Syncline. Photograph A was taken looking west into the hillside on the western bank of the Miyar nala, ~2km south of Karpat. Photograph B was taken looking east at the summit of Phabrang from Karpat village. The nature of these contacts could not be established owing to the inaccessibility of the exposures. The contacts are almost perpendicular to bedding, suggesting that they may be tectonic in origin.

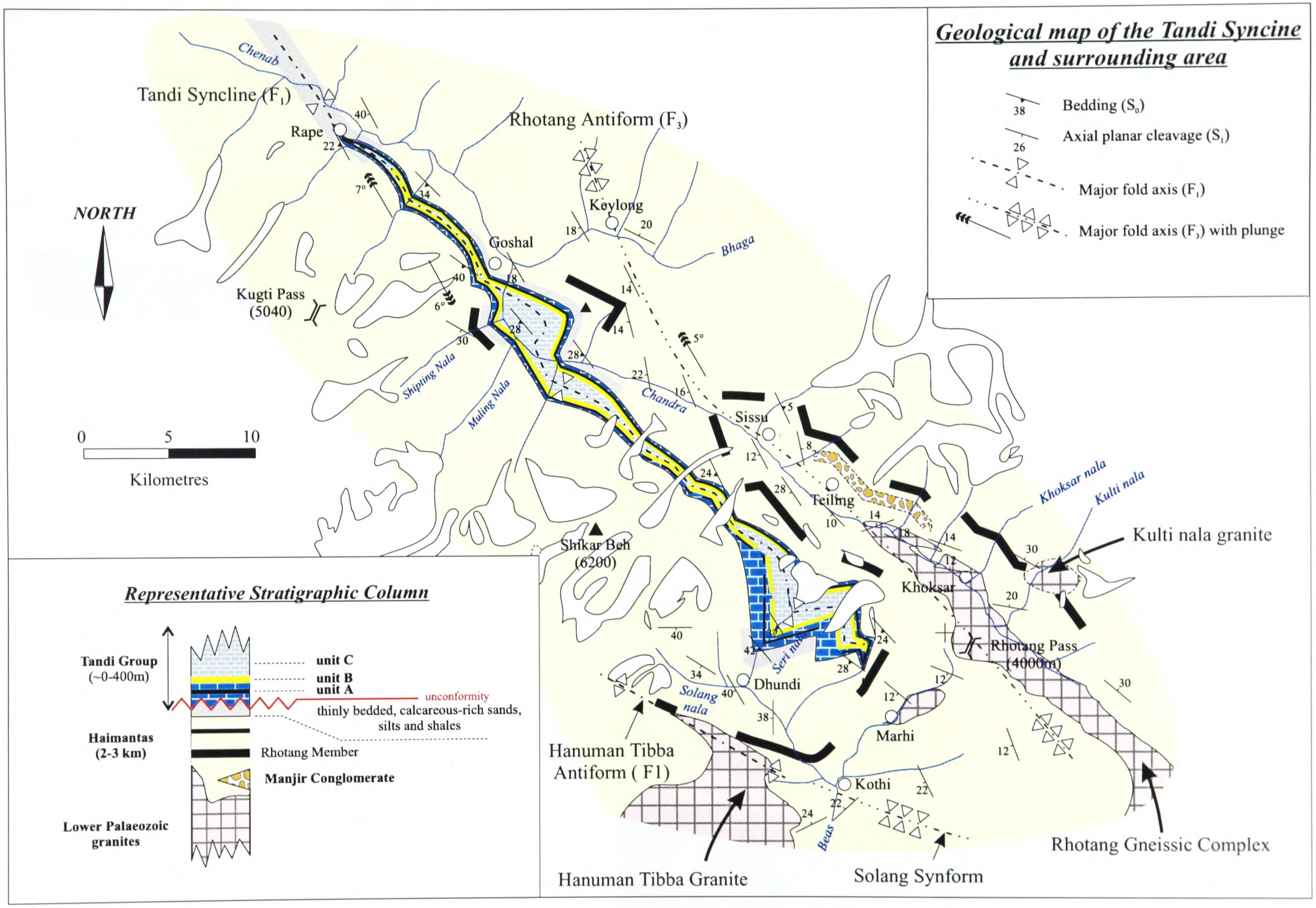
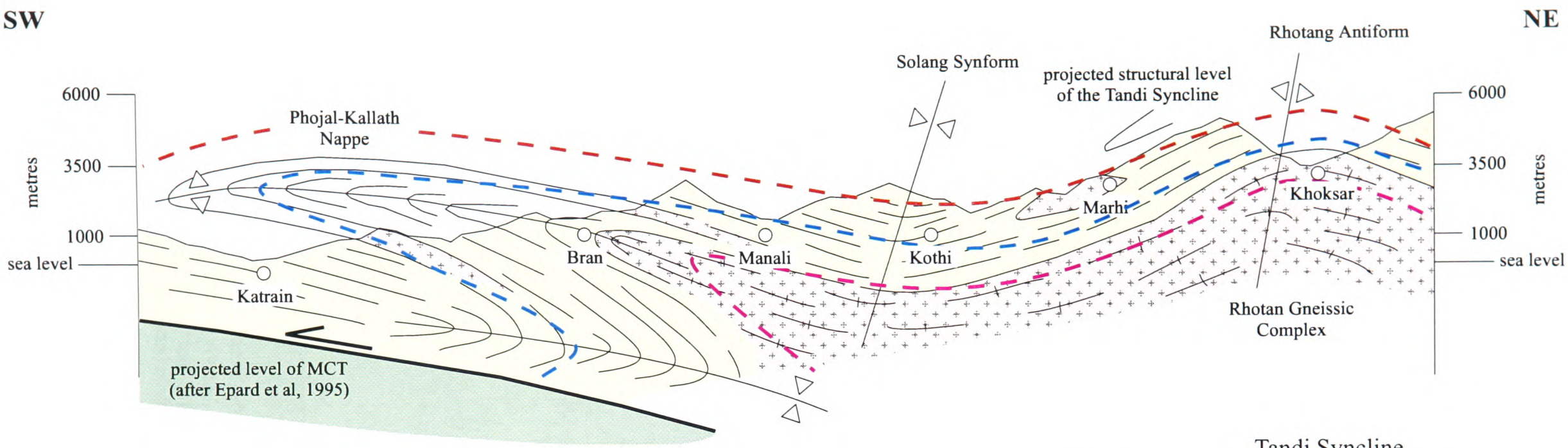


Figure 3.12: Geological map of the Tandi Syncline and surrounding area



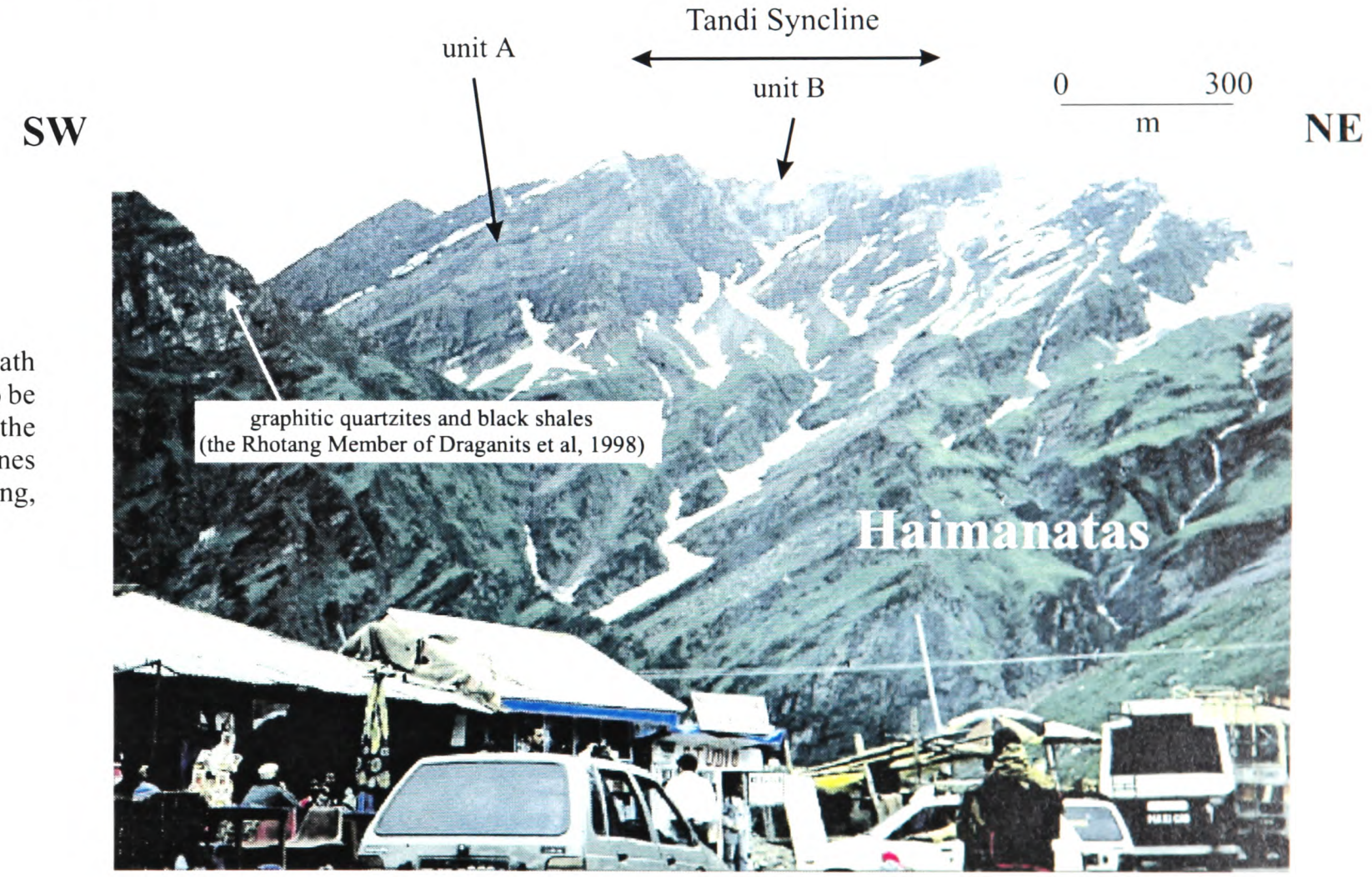


Figure 3.13: The south-eastern closure of the Tandi Syncline as viewed from beneath the Rhotang Pass at the village of Marhi. The base of the Tandi Group is taken to be concomitant with the first appearance of true limestones and the disappearance of the brown-coloured clastic sediments of the Haimantas. Interbedded blue limestones and yellow quartzites of unit B form the core of the syncline. Unit C is missing, which is attributed to post-tectonic erosion of the core of the syncline.



Figure 3.14: Closure of the Tandi Syncline in the mountainside behind Goshal village, at the confluence of the Chandra, Bhaga and Chenab rivers. Units A, B and C can be readily distinguished above the brown-coloured sediments of the underlying Haimantas. Note that bedding (S0) is parallel to the axial planar cleavage (S1) and that both S0 and S1 are re-folded by flat-lying SW-vergening F2 folds.

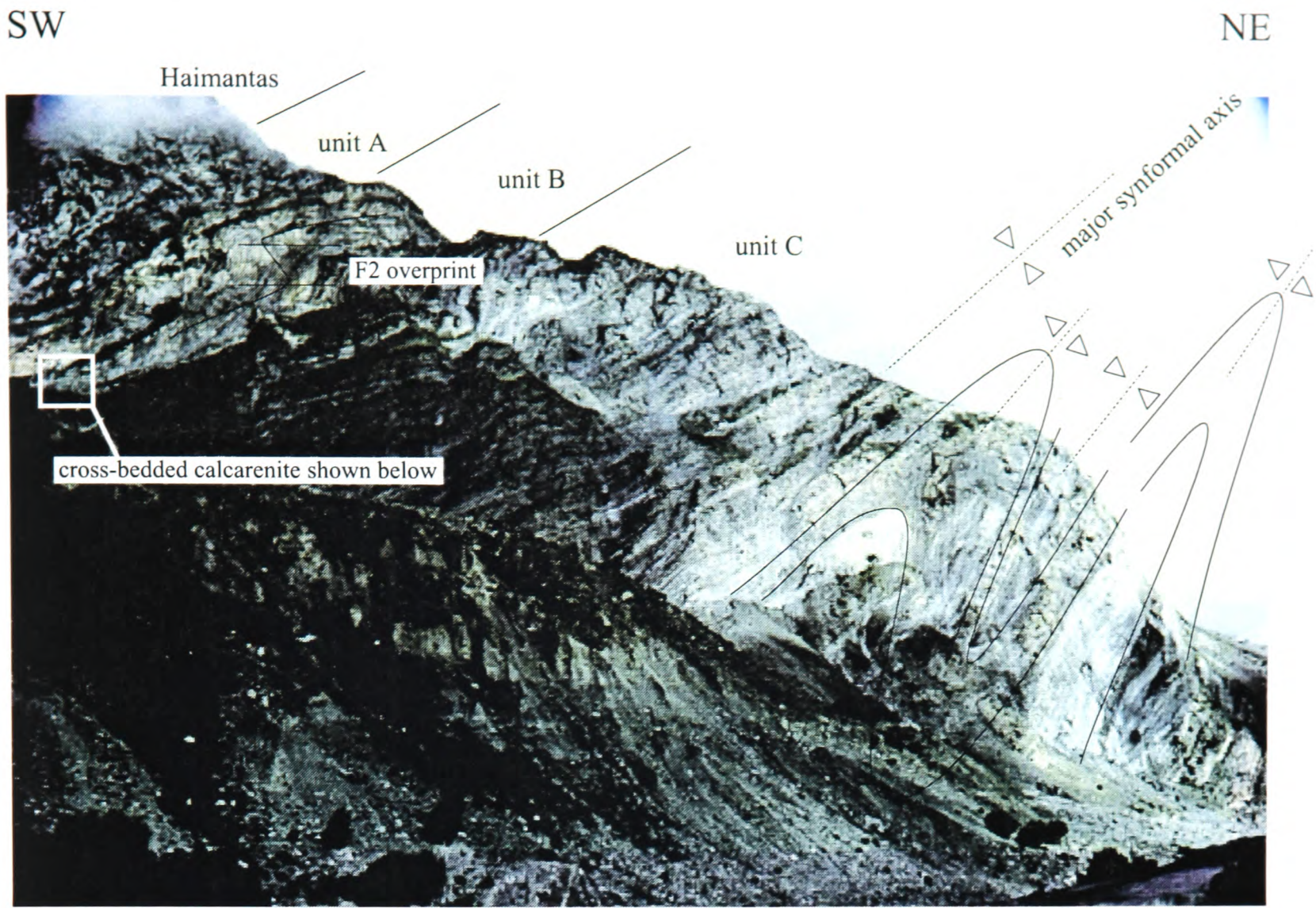


Figure 3.15: Inverted cross-bedding in the overturned limb of the Tandi Syncline. The younging direction gives this structure a rather anomalous NE facing direction. (photograph taken looking approximately west through a slightly oblique section through the Tandi Syncline near Goshal village).

Unit C (250-300m)

Interbedded sequence of siliceous blue limestones, white limestones, yellow calcarenites and dolomites, grey grits and thin black marls. Very similar in appearance to unit A. Forms the core of the Tandi Syncline and is the youngest stratigraphic unit preserved in the Tandi Group. Younger sediments have either been eroded prior to the India-Asia collision, and/or were never deposited.

Unit B (50-100m)

Prominent unit of interbedded siliceous blue and yellow limestones and dolomites containing a significant proportion of 10cm-3m-thick beds of grey sandstones, cross-bedded yellow quartzites and calcarenites.

Unit A (50-150m)

Basal unit of the Tandi Group. Characterised by a repetitive sequence of thinly bedded, blue-coloured graphitic wackestones and micrites, thin grey grits and black marls.

unconformity

Haimantas (Lower Cambrian?)

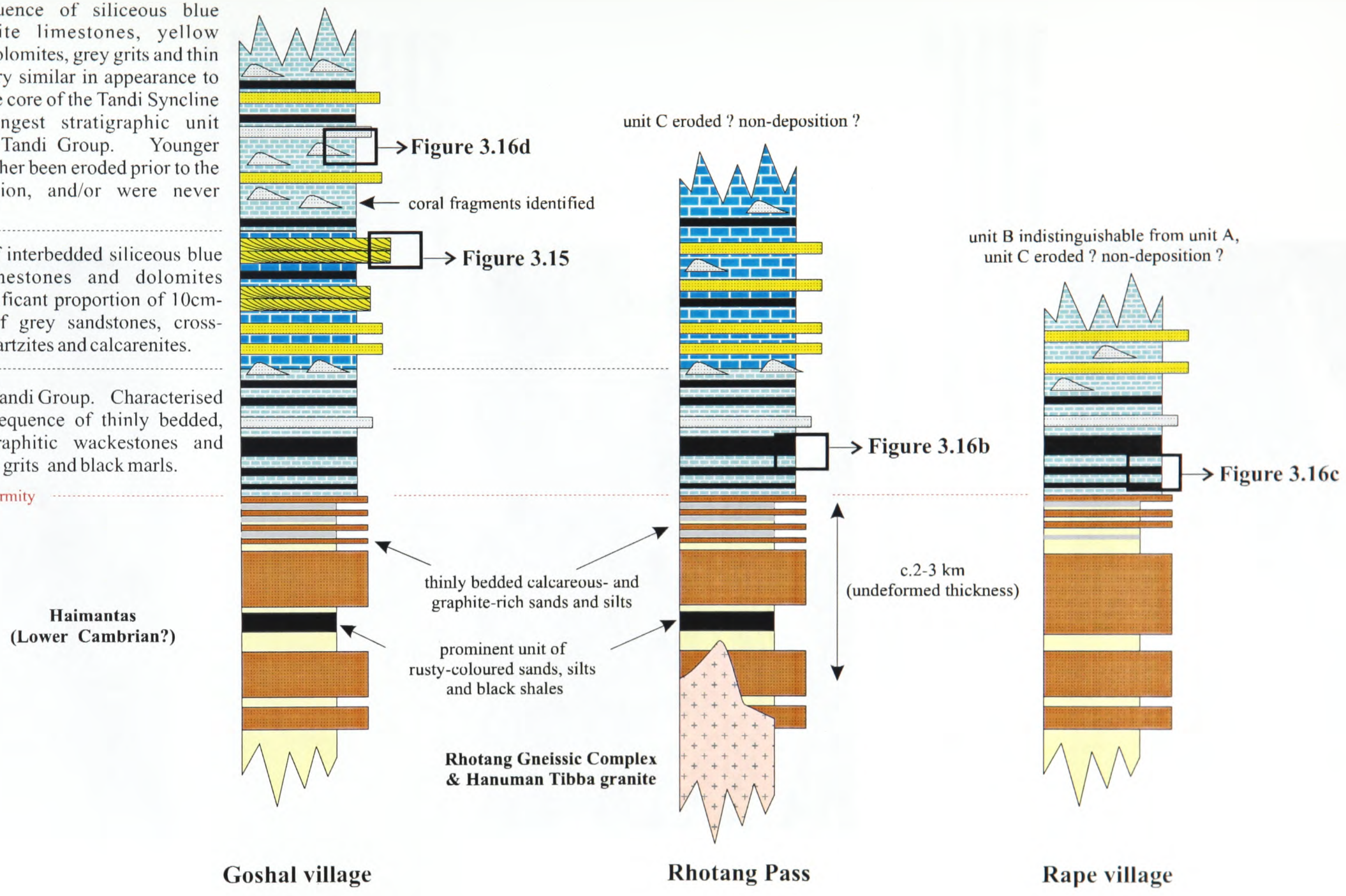


Figure 3.16a: Summarised stratigraphic sections through the Permian to Jurassic Tandi Group in the High Himalayan Slab of SE Zanskar and NW Lahaul. Location of stratigraphic section is shown at the base of each column. The most complete section is preserved at Goshal village where least erosion of the Tandi Syncline has occurred.. The Tandi Group thin towards the SE (Rhotang Pass) and NW (Rape), which is largely an artefact of post-tectonicerosion, but is also partly attributed to original sedimentary thinning. Boxed areas show location of subsequent figures.

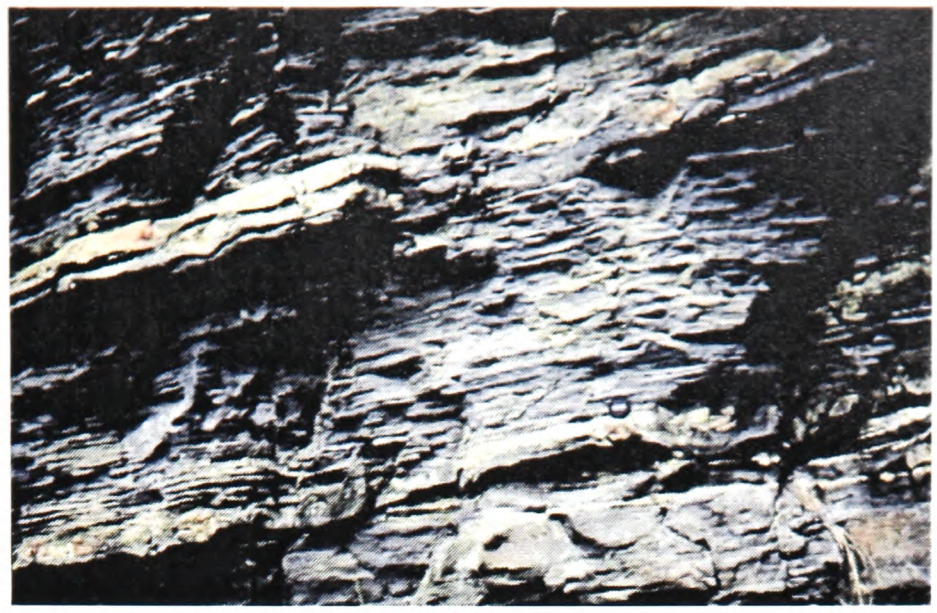


Figure 3.16b: Graphite-rich micritic limestones and black marls within unit A of the Lower Tandi Group (photograph taken in the overturned limb of the Tandi Syncline, in the Seri nala, south of the Rhotang Pass). The white horizons are calcite veins which have developed as a result of fluid fluxing during deformation and metamorphism. Some veins are discordant with respect to both bedding (S0) and the main axial planar cleavage (S1).

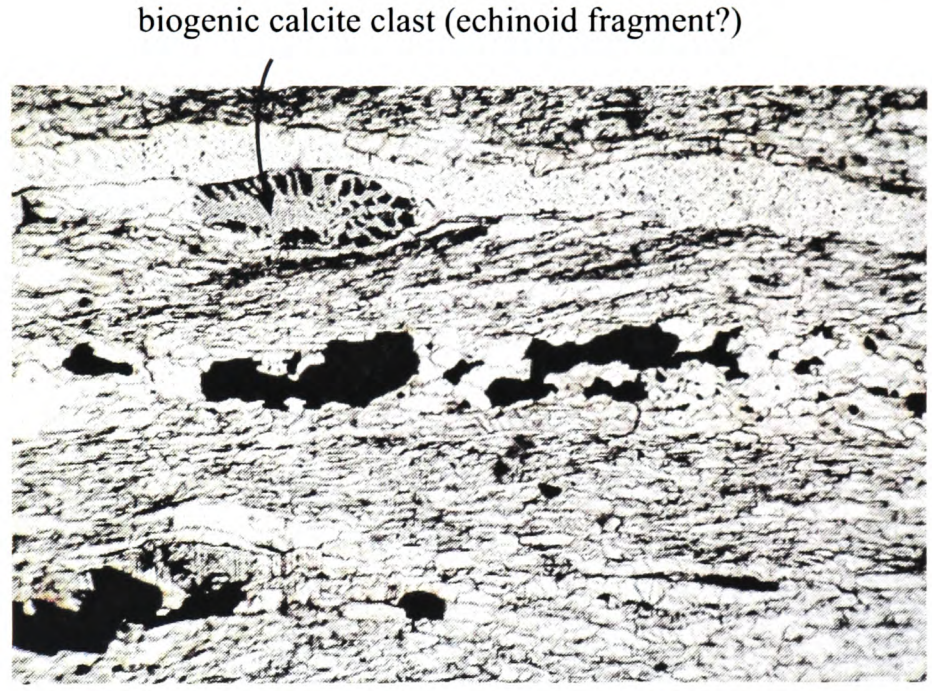


Figure 3.16c: Photomicrograph of a limestone collected from the basal part of the Tandi Group (unit A). The limestone is finely crystalline and defines a strong bedding-parallel fabric (S1) which is axial planar to the Tandi Syncline (F1). The dark colour of the limestone is due to the high concentration of graphite in these carbonates. Ilmenite, rutile and pyrite are parallel to the S0/S1 layering and are observed to overgrow this tectonic foliation in places, thus implying that they are partly diagenetic/metamorphic in origin. One of the most intriguing aspects of this slide is the presence of a biogenic calcite clast in the top left of the photograph. This is interpreted to be the reworked remains of an echinoid test (M. Brasier, pers. com.). Similar clasts were observed in other samples and confirm that the Tandi Group represent a marine succession. Note that this clast forms a rigid body, around which the tectonic foliation is wrapped. (Sample JDW 203, collected immediately behind Rape village. Field of view is approximately 3mm).



Figure 3.16d: Stringers of carbonate-rich sandstone standing proud of the surrounding crystalline micritic wackestone in unit C of the Tandi Group. The sandstones form discontinuous bodies and are interpreted to have been deposited during higher-energy episodes. (photograph taken in overturned limb of the Tandi Syncline, ~5km north of Dhundi).

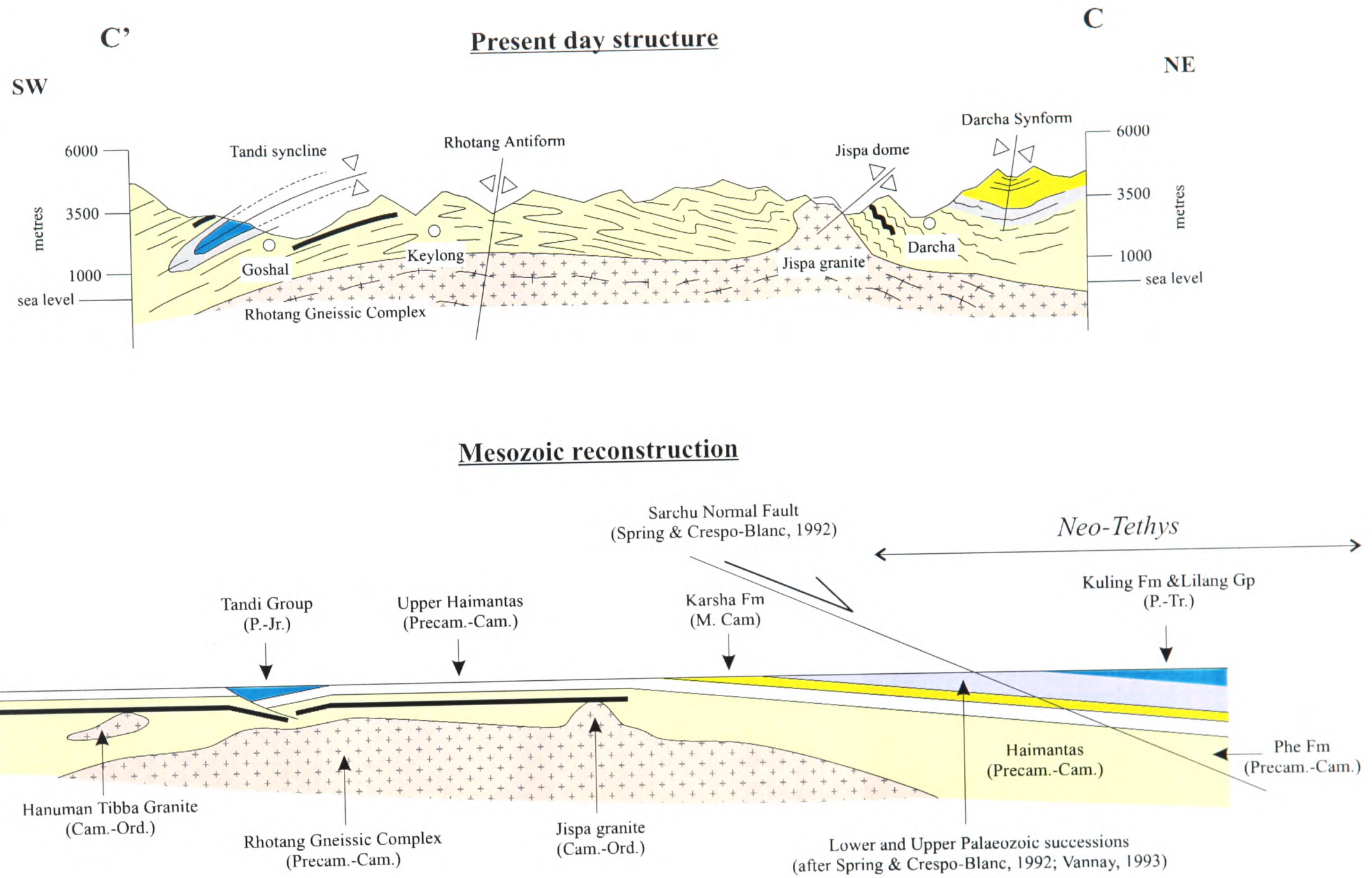


Figure 3.17: Restored schematic section across the north Indian continental margin showing the palaeogeographic position of various lithological units in the High Himalayan Slab and Tibetan Sedimentary Series of SE Zanskar and NW Lahaul during the Mesozoic. Lithological units have been correlated across the Sarchu Normal Fault (Spring & Crespo-Blanc, 1993; Vannay, 1993), suggesting that the Tibetan Sedimentary Series and High Himalayan Slab shared a common Palaeozoic and Mesozoic depositional history. The Tandi Group do not appear to be in tectonic contact with the underlying Haimantas, suggesting that they form an integral part of the High Himalayan Slab. They were probably deposited in a minor rift basin located to the south of the main Neo-Tethyan ocean.



Figure 3.18a: Layered sequence of banded orthogneisses, augengneisses, paragneises, metapelitic schists, sillimanite-grade migmatites and weakly deformed crustal melt leucogranites forming part of the High Himalayan Crystallines (HHC) in the immediate footwall of the Zanskar Shear Zone (photograph taken looking into the eastern bank of the Temasa nala; see Enlcosure 1 for location).



Figure 3.18b: The Gumburanjon leucogranite intruding into the kyanite-grade metapelitic schists and gneisses in the immediate footwall of the Zanskar Shear Zone at the eastern end of the Kargyak Chu in SE Zanskar (see Chapter 6 for a more detailed discussion about this granite).

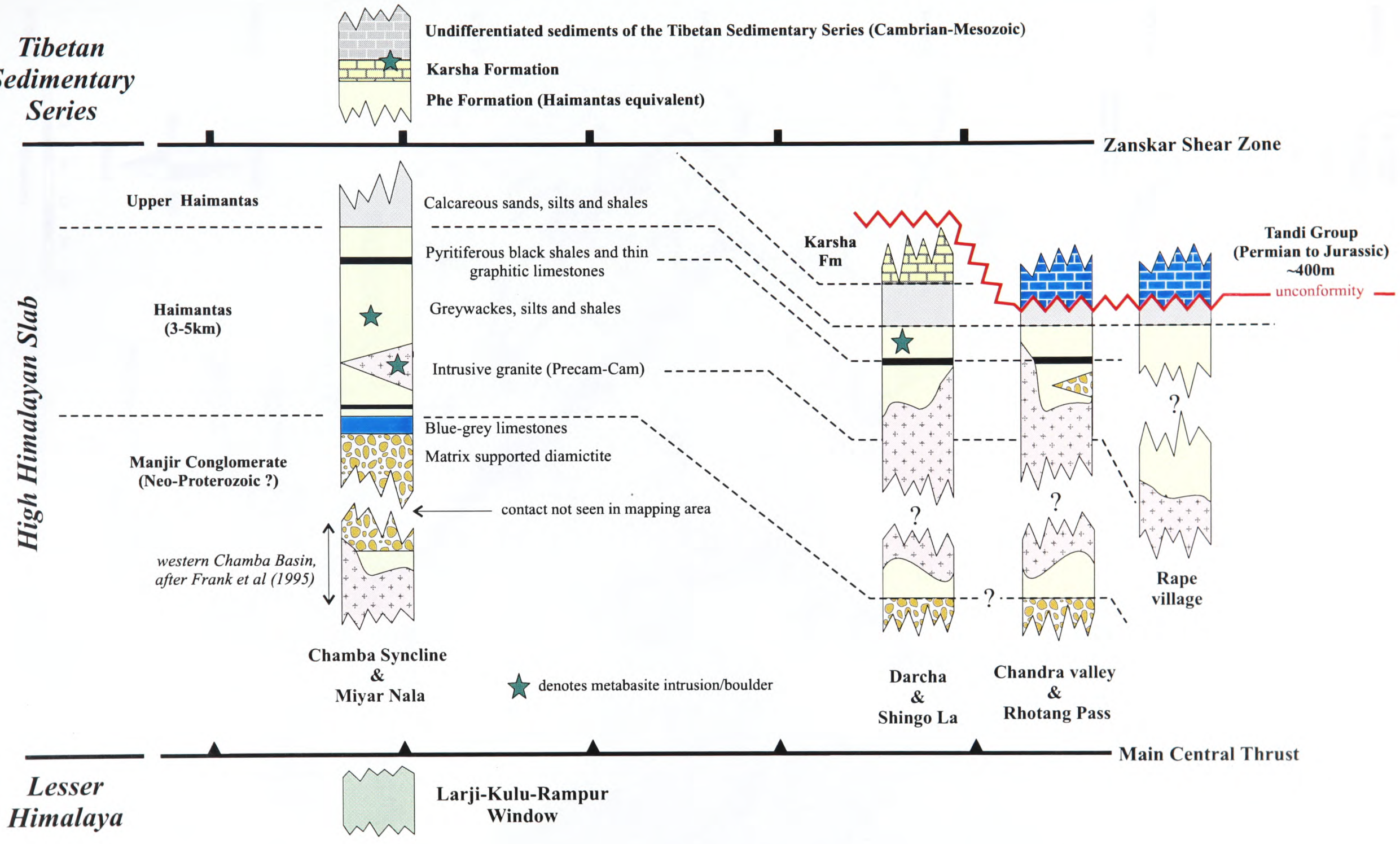


Figure 3.19: Summarised stratigraphy and correlation of lithologies within the High Himalayan Slab of SE Zanskar and NW Lahaul (excluding the HHC).

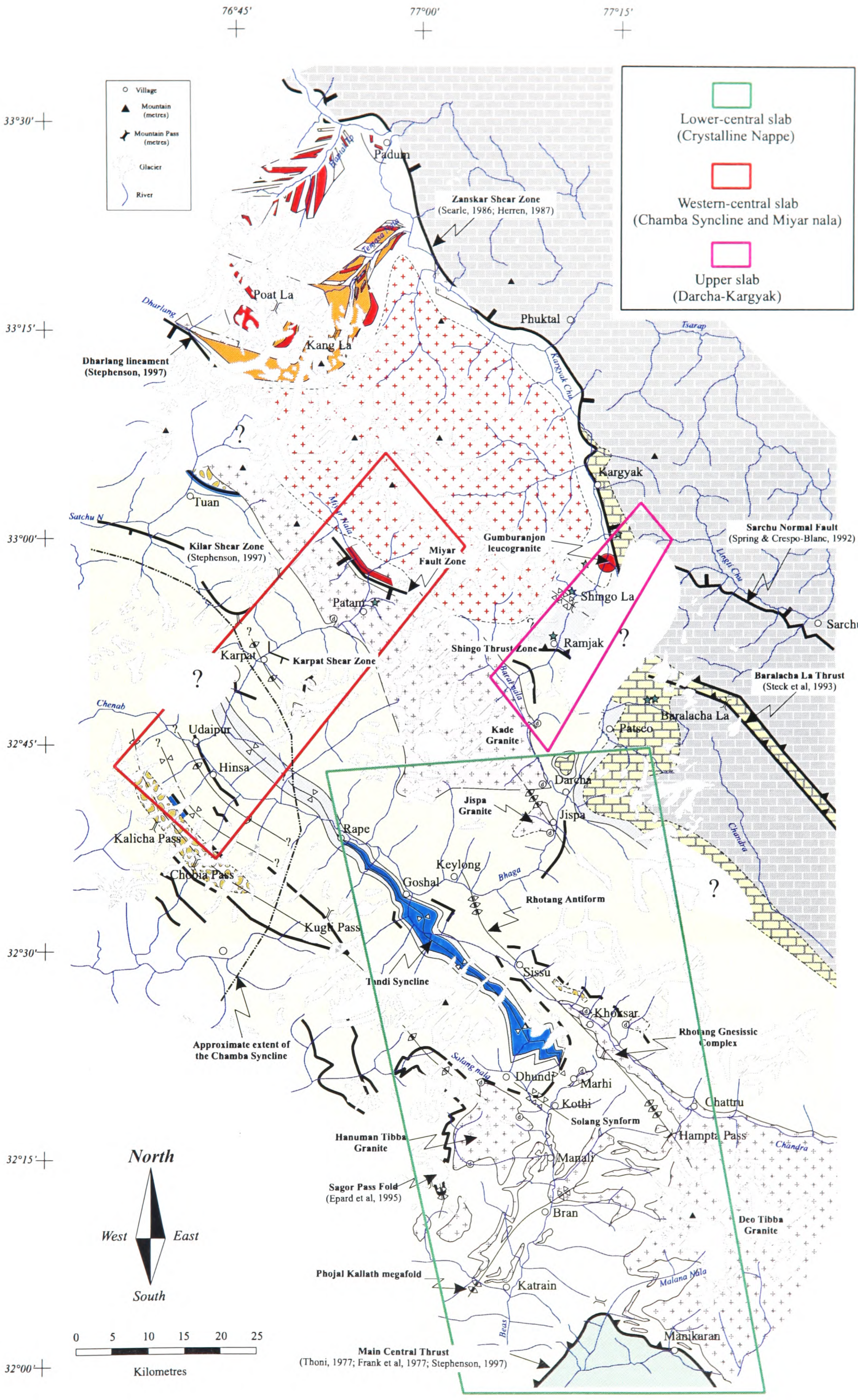
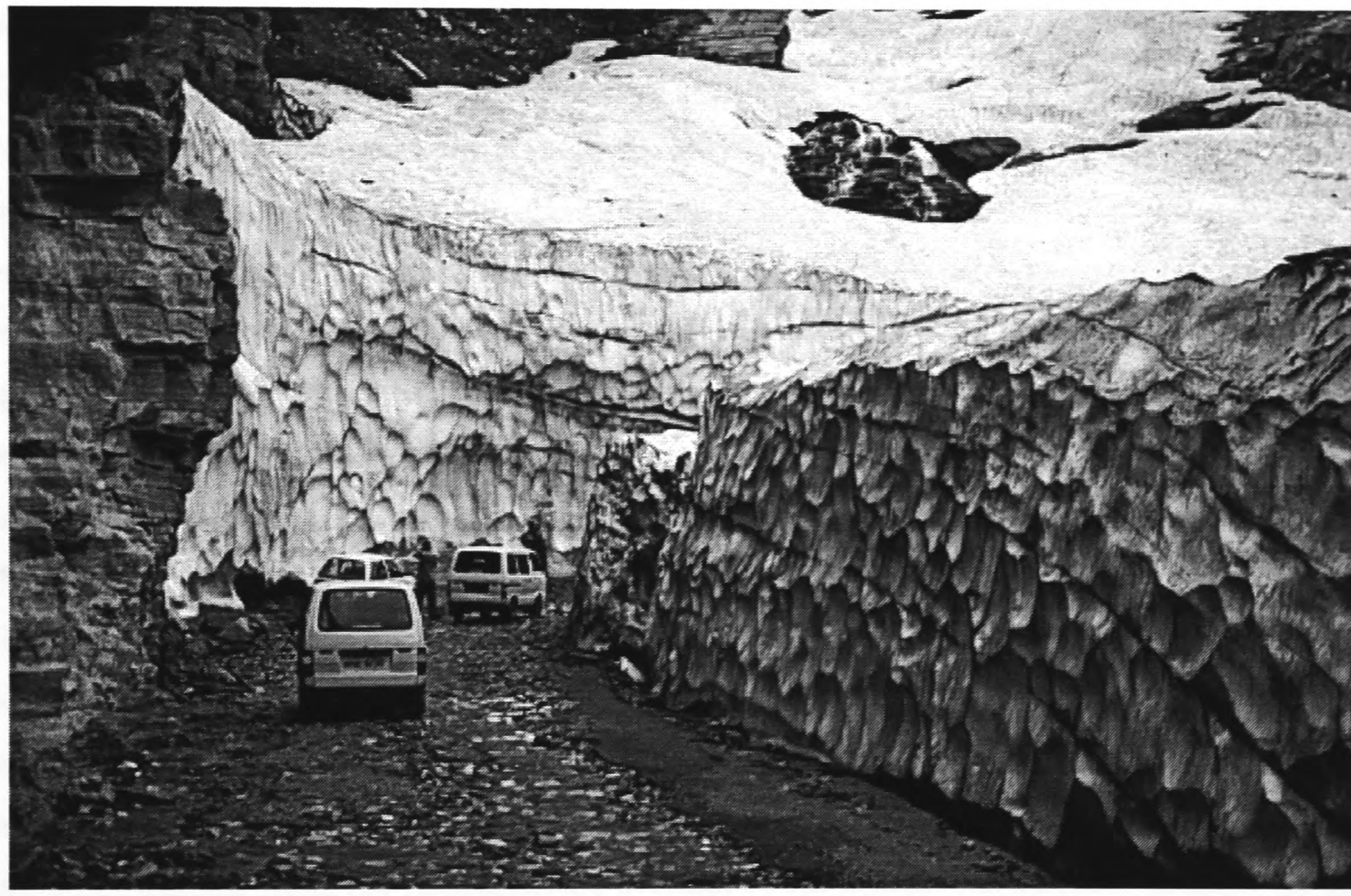


Figure 3.20: Geographical subdivision of the High Himalayan Slab. Boxed areas refer to regions discussed in Chapters 4-6.



Roadway blasted through the remains of the winter snows near the summit of the 4000m-high Rhotang Pass in NW Lahaul.

Chapter 4

Geology of the lower-central slab (the Crystalline Nappe)

4.1 Introduction

This chapter discusses the structure and metamorphism of the lower-central part of the High Himalayan Slab in NW Lahaul (Figures 3.20 & 4.1), which is generally referred to in the literature as the Crystalline Nappe (e.g. Thöni, 1977; Epard *et al.*, 1995). The base of the Crystalline Nappe is defined by the MCT, which thrusts the high-grade rocks of the High Himalayan Slab above the weakly metamorphosed rocks of the Lesser Himalaya (Thöni, 1977; Stephenson, 1997). The northern extent of the Crystalline Nappe is more difficult to define since it does not correspond to any obvious structural or metamorphic discontinuity. For the purpose of this work, the village of Darcha is taken to represent the northern limit of the Crystalline Nappe since this marks the northern extent of the studied area (Figure 4.1b). The structure of the area to the north of Darcha is described in detail by Spring and Crespo-Blanc (1992), Steck *et al.*. (1993), Vannay and Steck (1995) and Fuchs and Linner (1995).

Lithologically, the Crystalline Nappe consists of a thick sequence of metamorphosed sands silts and shales belonging to the Precambrian-Cambrian Haimantas which are intruded by a number of Precambrian-Ordovician(?) granites. The Permo-Jurassic Tandi Group unconformably overlie the Haimantas in the upper part of the Crystalline Nappe along the southern bank of the Chandra valley (Figure 4.1). Further north, the Haimantas are overlain by the Middle Cambrian(?) Karsha Formation above Darcha (Figure 4.1b). These lithologies have been metamorphosed to varying degrees, ranging from the chlorite zone through to upper amphibolite facies conditions (Enclosure 2). Structural and petrographic observations presented in this chapter demonstrate that this metamorphism is dominantly Himalayan in age.

4.2 Structure of the Crystalline Nappe

The structure of the Crystalline Nappe varies considerably with structural depth and distance from the MCT. Based on cross-cutting relationships of structural fabrics at the outcrop scale, together with petrographic observations in thin section, four discrete phases of deformation are recognisable in the Crystalline Nappe (Table 4.1).

Table 4.1: Fabric elements relating to different deformation phases in the Crystalline Nappe

Deformation phase	Fold generation	Planar Fabric	Mineral lineation	Structural features
Deposition	None	S_0	None	Bedding
D_1	F_1	S_1 (axial planar cleavage)	L_1	NE facing folds (the Tandi Syncline)
D_2	F_2	S_2 (composite axial planar cleavage)	L_2	SW facing folds (the Phojal-Kallath megafold)
D_3	F_3	None	None	Domal structures
D_3/D_4	None	None	None	Dextral strike slip?

D_1 structures are only preserved at shallow structural levels within the Crystalline Nappe and are exemplified by the NE facing Tandi Syncline (see section 4.2.1). D_2 structures totally obliterate D_1 fabrics to the south of the Tandi Syncline and are associated with the development of SW verging folds, the most spectacular example of which is the Phojal-Kallath megafold (see section 4.2.2). D_3 structures are recognised as large-scale domes which are responsible for warping D_1 and D_2 fabrics (see section 4.2.3). D_3/D_4 deformation is associated with a strong E-W trending mineral lineation which cannot be temporally related to either the D_1 or D_2 deformation phases and is probably related to a late-stage phase of dextral transpression (see section 4.2.4). The MCT zone was not studied in detail during the work of this thesis, but is nonetheless an important structure which is discussed in section 4.2.5.

4.2.1 D_1 deformation (the Tandi Syncline)

Macroscopically, the earliest recognisable phase of deformation in the Crystalline Nappe (D_1) is recognised in the field as first-order folds (F_1) of bedding (S_0). F_1 folds are typically isoclinal, as exemplified by the Tandi Syncline (see below) and are associated with the development of a strong axial planar fabric (S_1) which is frequently parallel to bedding (Figure 4.2). The intensity of D_1 deformation is so intense along the Chandra valley that S_1 forms the dominant planar fabric in this part of the slab (Figure 4.1; stereonets 5-7 & 11 on Enclosure 3). In the flyschoid sediments of the Haimantas, F_1 folds are frequently intrafolial, with fold hinges preserved as isolated boudins of competent psammites surrounded by less competent phyllites and schists. The limbs of these folds are intensely sheared and may be coincident with zones of thrusting. However, owing to the lack of prominent marker horizons within the Haimantas, no D_1 thrusts were identified in the field. None of the F_1 folds observed within the Haimantas gave any indication of the shear-sense associated with the D_1 deformation phase.

Microstructurally, the S_1 cleavage in the Haimantas is defined by a strong layering of phyllosilicates (chlorite, muscovite and biotite) and flattened grains of quartz and feldspar (Figures 4.9a & b), which occasionally show pressure solution textures along their margins. No evidence was found in any of the studied samples to suggest that S_1 is a crenulation fabric of a pre-existing foliation. Given the probable Precambrian-Cambrian age of the Haimantas (see Chapter 3), it is possible that D_1 fabrics are pre-Himalayan in age. This possibility is ruled out, however, by the observation that the S_1

cleavage can be traced from the Haimantas into the Mesozoic Tandi Group (Figure 4.2), thus suggesting that D_1 is associated with the earliest stages of Himalayan-related deformation in the High Himalayan Slab.

The Tandi Syncline

The Tandi Group form an excellent marker horizon above the Haimantas and are preserved in the core of a kilometre-scale, SW-dipping, isoclinal synform (Figures 4.1 & 4.2). This structure is referred to in the literature as the Tandi Syncline and has been the focus of several previous studies (e.g. Powell & Conaghan, 1973; Srikantia & Bhargava, 1982; Steck *et al.*, 1993; Vannay & Steck, 1995). The Tandi Syncline appears to be a first-order fold of bedding and is therefore associated with the D_1 deformation phase. This is consistent with the work of Powell and Conaghan (1973) and Steck *et al.* (1993), but refutes the early work of Srikantia and Bhargava (1982), who suggested that the Tandi Syncline was related to late-stage backthrusting along a NE-dipping backthrust (the South Lahaul Thrust), contemporaneous with but antithetic to movement on the MCT.

Folding of sediments within the Tandi Group is extremely intense and is readily identifiable due to strong lithological layering (Figures 4.2; 4.3 & 3.15). Microstructurally, the S_1 cleavage is often well annealed in the limestones of the Tandi Group (Figure 4.3d), but is occasionally observed forming a planar fabric which wraps larger calcite/dolomite porphyroblasts and is statically overgrown by cubes of pyrite/limonite (Figure 4.3e). The S_1 fabric can be traced from the core of the Tandi Syncline into the underlying clastic sediments of the Haimantas (Figure 4.2), thus providing strong evidence that the Tandi Group and Haimantas were in structural continuity prior to the D_1 deformation phase.

The Permo-Jurassic age of the Tandi Group strongly suggests that the Tandi Syncline is a Himalayan structure which developed in response to crustal shortening and thickening of the Indian plate following the India-Asia collision ~54-50 Ma. It is possible, albeit difficult to prove, that the earliest stages of this deformation were temporally related to ophiolite obduction during the Maastrichtian (Searle *et al.*, 1997b). However, given that the Spontang ophiolite and Tandi Syncline are separated by a present day horizontal distance equivalent to *c.*70km, it seems unlikely that any significant thickening of the High Himalayan Slab in NW Lahaul occurred during this obduction phase.

Orientation and lateral extent of the Tandi Syncline

The Tandi Syncline extends in a NW-SE orientation along the Chandra and Chenab valleys and dips ~30-40° towards the south-west (Figure 3.12; Enclosure 1). The north-western continuation of the Tandi Syncline remains largely conjectural owing to the fact that the Tandi Group pinches out near Rape village. However, carbonate-rich sands, silts and shales similar to those observed directly beneath the Tandi Group are exposed ~8 km north of Udaipur in the lower Miyar nala (Enclosure 1). Although correlation of these calcareous sediments along strike is somewhat tenuous, it strongly

suggests that the Tandi Syncline continues towards the NW into the Chamba Syncline (cross-section A-A' on Enclosure 1). The south-eastern continuation of the Tandi Syncline is less well constrained. It cannot be traced to the south-east of the Rhotang Pass, which is attributed to the fact that the Tandi Syncline plunges ~5° towards the NW along the Chandra valley, resulting in erosion of the Tandi Group at altitudes in excess of *c.*4000m (Figure 4.1c).

The location of antiformal closures either side of the Tandi Syncline remains entirely speculative, largely because there are no prominent marker horizons within the Haimantas by which to identify them. The Hanuman Tibba granite appears to be folded into the core of a major F_1 antiform to the south of the Tandi Syncline (Figures 3.10 & 4.1a) and is probably the antiformal pair to the Tandi Syncline. Frank *et al.* (1995) suggest that this fold can be traced along strike towards the north-west where it is responsible for folding the Manjir Conglomerate into a major upright F_1 antiform (Enclosure 1; cross-section A-A' on Enclosure 1).

The regional trend of F_1 fold axes in the Crystalline Nappe is defined by the NW-SE strike of the Tandi Syncline. This trend is parallel to the strike of other major structural features in this part of the Himalaya and is consistent with a chain-parallel style of folding. However, at the outcrop scale, F_1 folds in the Chandra valley and Rhotang Pass region have extremely variable orientations which range from NW-SE to N-S (Figure 4.1; stereonets 5-7 & 11 on Enclosure 3). Vannay and Steck (1995) made similar observations and interpreted this to reflect the re-orientation of F_1 fold axes during subsequent deformation phases. Whilst this is entirely possible, it is equally possible that this reflects deformation partitioning brought about by rheological contrasts and/or localised variations in the orientation and magnitude of the principal stresses during D_1.

Facing direction of the Tandi Syncline

Way-up criteria in the overturned limb of the Tandi Syncline give this structure a rather anomalous NE facing direction (Figure 3.15). This is interpreted to be an artefact of the D_1 deformation phase and is unlikely to represent the effects of re-orientation during subsequent deformation phases. Several lines of evidence support this interpretation: (1) metamorphic isograds are the right way-up beneath the Tandi Syncline (Figure 4.1), which precludes the possibility that subsequent deformation phases have significantly affected the original orientation of this fold (indeed, doming of D_1 structures during the D_3 deformation phase (see section 4.2.3) suggests that the Tandi Syncline may once have occupied a more recumbent position than its present day orientation suggests); (2) NE verging F_1 folds can be traced along strike into the Chamba Syncline and Miyar nala to the NW of the Tandi Syncline (see Chapter 5), thus implying that NE verging structures were regionally developed during the D_1 deformation phase; and (3) the Tandi Syncline is overprinted by SW verging F_2 folds which are temporally related to the D_2 deformation phase in the Crystalline Nappe (see section 4.2.2). The NE facing direction of the Tandi Syncline therefore attests to the fact that D_1 deformation in the Crystalline Nappe was NE directed. This is antithetic to the kinematic transport direction associated with most structures in the Himalaya and proves that the Tandi Group

could not have been tectonically emplaced above the Haimantas by SW directed thrusting from the Tibetan Sedimentary Series. The kinematic significance of the NE facing direction of the Tandi Syncline is discussed in the summary section at the end of this chapter.

D_1 deformation to the north of the Tandi Syncline

The Tandi Syncline is not exposed in the Bhaga valley to the north of Keylong owing to erosion of shallower structural levels (Figure 4.1b). Consequently, the lateral extent of the Tandi Syncline towards the north is difficult to constrain. Observations of structures in the underlying Haimantas suggests that the isoclinal style of D_1 deformation continues towards the north at least as far as the Jispa granite (Figure 4.1b). Isoclinal F_1 folds immediately north of the Tandi Syncline have a recumbent attitude, which is interpreted to reflect their location on the crest of the Rhotang Antiform above the projected level of the Rhotang Gneissic Complex (Figure 4.1b). With increasing distance northwards, the S_0/S_1 fabric is observed to dip progressively more steeply towards the N/NE (Figure 4.1b). On the northern side of the Jispa granite S_0/S_1 dips ~50-70° towards the N/NE and is deformed by MW-style folds (Figures 4.1b & 4.4). A weak tectonic fabric is developed in the Jispa granite which is parallel to the S_0/S_1 fabric in the Haimantas (Figure 4.4). North of the Jispa granite there is no strong evidence to support the existence of a pervasive phase of isoclinal folding in the Haimantas. Despite this, bedding remains parallel to a strong tectonic fabric which is defined by aligned flakes of muscovite, biotite and chlorite. Although this is similar in appearance to the axial planar S_1 fabric seen in the Tandi Syncline, the absence of isoclinal fold closures suggests that it is unlikely to be an axial planar cleavage, and is therefore interpreted to be a compaction fabric related to burial of the upper part of the High Himalayan Slab. This is consistent with the work of Vannay and Steck (1995) who demonstrated that the structure to the north of Darcha is dominated by a relatively simple sequence of Lower and Upper Palaeozoic sediments which have been thrust towards the SW along flat-lying thrusts.

D_1 deformation to the south of the Tandi Syncline

D_1 structures are more difficult to identify in the deeper parts of the Crystalline Nappe owing to strong overprinting by D_2 deformation and higher-grade metamorphism (see section 4.2.2). Isoclinally folded quartz veins are frequently observed within the garnet- and kyanite-grade metapelitic schists in the deeper parts of the Crystalline Nappe and are interpreted to represent the preserved remains of F_1 fold hinges (Figure 4.5e). They cannot be used to infer anything about the kinematics associated with the D_1 deformation phase.

4.2.2 D_2 deformation (the Phojal-Kallath megafold)

Beneath the Tandi Syncline, D_1 structures are overprinted by a second generation of folds which consistently show a top-to-the-south-west shear sense (Figure 4.5). These folds cannot be temporally related to the NE verging D_1 deformation phase and are therefore interpreted to have formed during a subsequent D_2 deformation phase. Although great caution must be exercised when using folds as shear-sense indicators, the consistent SW vergence of F_2 folds in the Crystalline Nappe suggests that D_2 deformation was SW directed. This is antithetic to the kinematic transport direction associated with the D_1 deformation phase and requires a 180° change in the polarity of deformation at some point in time between D_1 and D_2. Despite this change in polarity, structural measurements demonstrate that both F_1 and F_2 fold axes are co-axial in the Crystalline Nappe (Figure 4.1; stereonets 5-7 & 11 on Enclosure 3). This implies that either there was no significant change in the orientation of the principal stresses between D_1 and D_2 deformation phases, or that both D_1 and D_2 structures have been rotated into parallelism by subsequent deformation phases.

F_2 folds are associated with the development of a second axial planar cleavage (S_2) and a second mineral lineation (L_2) on S_2 surfaces. The S_2 cleavage is only weakly developed at shallow structural levels and becomes progressively more intense at higher metamorphic grades where it is recognised as a well-developed crenulation cleavage of S_0/S_1 which is defined by the growth of muscovite and biotite along cleavage domains and the segregation of quartz and feldspar into microlithons (Figures 4.9c-e). The increasing dominance of D_2 fabrics at higher metamorphic grades is interpreted to reflect the increasing ductility of rocks in deeper structural levels. D_2 fabrics become more intense towards the base of the slab and are reported to be most intense in the MCT zone (Thöni, 1977; Stephenson, 1997). This suggests a possible relationship between SW-verging F_2 folds and thrusting along the MCT. The most striking example of an F_2 fold in the Crystalline Nappe is the Phojal-Kallath megafold, which is located on the western bank of the Beas valley between Manali and Katrain (Figure 4.6).

The Phojal-Kallath megafold

The Phojal-Kallath megafold, first described by Thöni (1977), represents an overturned (almost recumbent) fold of bedding (S_0) and the S_1 cleavage and is located immediately above the projected level of the MCT near the base of the slab (Figure 4.6). It is analogous to the large SW-verging nappes observed in western Zanskar (see section 2.2.8). The upper limb of the Phojal-Kallath megafold is exposed in the Beas valley to the south of Manali and in the mountainside to the south-west of Manali (Enclosure 1). S_0/S_1 and S_2 are generally sub-parallel in this region and dip gently towards the WNW (Figure 4.1a). Owing to the intensity of deformation in the Phojal megafold, distinguishing between S_1 and S_2 is extremely difficult in the field. F_2 folds and crenulation lineations plunge ~4-10° towards the NW, which is taken to reflect the regional plunge of the Phojal-Kallath megafold in the same direction. Mineral lineations (defined by streaked out sheaves of muscovite and biotite) in the upper limb of the Phojal-Kallath megafold plunge shallowly towards the WSW (Figure

4.1a), which is slightly oblique to the trend of F_2 fold axes and similar to the orientation of mineral lineations in the Chandra valley. The core and overturned limb of the Phojal megafold are exposed in the Beas valley to the north of Katrain (Figure 4.6; Enclosure 1). S_0/S_1 are sub-parallel to S_2 in the overturned limb of the fold and dip ~30-40° towards the NNE (Figure 4.1a). Mineral lineations plunge towards the NE in a down-dip direction in the overturned limb and are interpreted to be related to SW-directed folding and overthrusting during the development of this kilometre-scale structure. Curiously, the Phojal-Kallath megafold is not evident on the eastern bank of the Beas valley. This has been interpreted by Frank *et al.* (1977) to reflect the dominance of flexural slip over recumbent folding as the dominant deformation mechanism above the MCT.

Thöni (1977) suggested that metamorphic isograds are folded around the Phojal-Kallath megafold. This is partly supported by personal field observations which show that metamorphic grade decreases in all directions away from the core of the fold (Figure 4.6). However, it is not possible to accurately trace metamorphic isograds around this structure. Whether all of the metamorphic assemblages in the Crystalline Nappe are entirely Himalayan in age remains uncertain. Textural observations presented in section 4.3.1 demonstrate that rocks in the Crystalline Nappe experienced kyanite-grade conditions during the Tertiary

D_2 deformation in the Bhaga valley

The intensity of SW verging folding decreases towards the north away from the MCT. SW verging folds are occasionally observed in the Bhaga valley to the north of Keylong village and are tentatively assigned to the D_2 deformation phase (Figure 4.7). North of Darcha, Vannay and Steck (1995) demonstrated that the D_2 deformation phase is associated with gentle folding, backthrusting and minor SW verging thrusts (e.g. the Baralacha La Thrust shown on Enclosure 1).

4.2.3 D_3 deformation (regional warping of D_1 and D_2 fabrics)

D_3 deformation in the Crystalline Nappe is characterised by the development of a number of large antiforms and synforms with NW-SE trending axes (Enclosure 1). These include: (1) the Rhotang Antiform; (2) the Solang Synform; (3) the Jispa dome; and (4) the Larji-Kulu-Rampur Window. Whether all of these developed contemporaneously remains uncertain. Some of these domes are likely to be syn-metamorphic structures (e.g. the Rhotang Antiform), whilst others post-date thrusting on the MCT (the Larji-Kulu-Rampur Window).

The Rhotang Antiform

The Rhotang Antiform was first recognised by Powell and Conaghan (1973) as a major NW-SE trending F_3 fold in the Chandra valley which plunges ~5-7° towards the NW (Enclosure 1). It is recognised in the field by: (1) the increase in metamorphic grade up the Chandra valley towards Khoksar; and (2) the plunge of the Tandi Syncline towards the NW, resulting in the exposure of the Tandi Group at river level near Goshal village (Figure 4.1c). It is also defined by a best-fit great

circle through $S_0/S_1/S_2$ in the Chandra valley (Figure 4.1c). The axis of this fold can be traced along the Chandra valley from just north of Keylong and as far south as the Hampta Pass (Enclosure 1). It appears to be centred on the Rhotang Gneissic Complex, which extends along the Chandra valley in a NW-SE orientation.

The Rhotang Antiform is clearly a relatively late-stage syn/post-metamorphic structure. Whether this fold developed under high temperature conditions, or whether it represents a late-stage low-temperature structure remains uncertain. Extensional shear band fabrics were recognised in a granitic gneiss within the Rhotang Gneissic Complex on the northern flank of the Rhotang Antiform near the village of Khoksar (Figure 3.7c). Similar fabrics were observed in kyanite-bearing metapelites collected from within the Rhotang Gneissic Complex at Khoksar village. Both these fabrics give a top-to-the-north-east sense of shear and could be interpreted to reflect tectonic thinning of deeper structural levels during thermal doming. Tectonic thinning along the flanks of the Rhotang Antiform would account for the observation that metamorphic isograds are extremely condensed on the northern side of the Chandra valley near Khoksar village (Enclosure 2). It is possible that similar extensional fabrics with a top-to-the-south-west sense of shear exist on the southern side of the Chandra valley directly beneath the lower limb of the Tandi Syncline. However, recognising these fabrics would be extremely difficult since the regional dip of structures on the southern limb of the Rhotang Antiform is towards the SW. Furthermore, D_2 deformation in this part of the slab is associated with a top-to-the-south-west sense of shear, hence distinguishing between D_2 and D_3 deformation fabrics is virtually impossible.

The Solang Synform

South of the Rhotang Pass, both D_1 and D_2 structures show a pronounced change in orientation (Figures 4.1a & 4.5a). This is related to folding around a broad synformal structure of inferred D_3 origin, hereafter referred to as the Solang Synform. This fold is co-axial with the Rhotang Antiform and is probably related to the same phase of folding. The north-western and south-eastern continuations of this fold are poorly constrained.

The Jispa dome

The Jispa dome is centred on the Jispa granite in the Bhaga valley (Enclosure 1), and is recognised by a pronounced steepening of bedding on the northern side of this small granite boss (Figure 4.4). Drag folds and a semi-brittle normal fault are evident on the northern margin of the Jispa granite (Figure 4.4), and are interpreted to have formed during this doming event. Small-amplitude, MW-style folds are also observed on the northern margin of the Jispa granite (Figure 4.4). Although these appear to be first-order folds of bedding (F_1), they are unlikely to be related to the D_1 deformation phase associated with the development of the Tandi Syncline further south. They are therefore associated with the development of the Jispa dome and are tentatively correlated with the development of domal structures during the D_3 deformation phase.

The Larji-Kulu-Rampur Window

At the base of the slab, the MCT is domed around the Larji-Kulu-Rampur window (Enclosure 1). Whether this domal structure is temporally related to the development of the Rhotang Antiform, Solang Synform and the Jispa dome remains entirely speculative.. Stephenson (1997) interpreted the L-K-R to be a late-stage structure which post-dated thrusting along the MCT. Since underthrusting of the Lesser Himalaya beneath the High Himalayan Slab would cause a chilling effect in the hangingwall, it is difficult to reconcile how the L-K-R Window could have developed contemporaneously with doming along the Rhotang Antiform if the latter represents a high-temperature syn-metamorphic domal structure. The LKR Window is therefore interpreted to be a late-stage structure which post-dated thermal doming of the Rhotang Antiform.

4.2.4 D_3/D_4 deformation (dextral transpression?)

L_1 and L_2 mineral lineations are frequently observed on S_1 and S_2 surfaces in the Crystalline Nappe and are defined by streaked out sheaves of chlorite, muscovite, biotite and ilmenite. In the absence of fold closures, it is extremely difficult to distinguish between S_1 and S_2 surfaces in the field, hence, all mineral lineation data has been combined as L_1/L_2 indiscriminate on Enclosure 3. Equal-area stereonet plots on Enclosure 3 show all of the mineral lineation data collected in this part of the slab, whilst the black ellipses show the mean orientation of these data. Lineations in the lower Bhaga valley plunge shallowly towards the SW in a down-dip direction (stereonet 4 on Enclosure 3) and are at a high angle to the F_1/F_2 fold axes, suggesting that they are probably related to NE-SW directed deformation during the D_1/D_2 deformation phases. Similarly, lineations in the Beas valley to the south of Manali have a pronounced down-dip NE-SW orientation, which is consistent with SW-directed deformation during development of the Phojal-Kallath megafold and thrusting on the MCT. Mineral lineations in the Chandra valley, however, consistently plunge shallowly towards the WSW and are highly oblique to both F_1 and F_2 fold axes (stereonets 5-7 & 11 on Enclosure 3). The unusual strike of these lineations could be interpreted to suggest that D_1 and D_2 deformation phases in the Chandra valley were transpressional. They could equally be interpreted to post-date D_1 and D_2 deformation phases, thus suggesting that the Chandra valley is located within a *c.*20km-wide dextral shear zone (the Chandra Dextral Shear Zone, or CDSZ), as proposed by Vannay and Steck (1995). These authors claim that the CDSZ is laterally continuous with the Garhwal Dextral Shear Zone (GDSZ), which was mapped in the Garhwal Himalaya ~300km along strike of the Chandra valley by Pêcher and Scaillet (1989). However, the existence of such shear zones remains somewhat conjectural owing to the fact that they have no definite structural boundaries. The CDSZ cannot be traced along strike into the Chamba Syncline, in the western part of the study area.

4.2.5 The MCT zone

The MCT is an extremely important structure which has implications for the evolution of the High Himalayan Slab as a whole. The MCT zone was not studied in detail during fieldwork for this thesis. The following descriptions are therefore based on observations made by Thöni (1977), Frank *et al.* (1977) and Stephenson (1997). The MCT zone is located at the base of the Crystalline Nappe and forms a 1-3km-thick region of high-strain brittle-ductile deformation which displays a characteristic inverted metamorphic gradient (Enclosure 2). Thöni (1977) interpreted this to be the result of rapid thrusting and recumbent folding along the Phojal-Kallath nappe during D_2 deformation, thus suggesting that the MCT is a syn/post-metamorphic structure. Mylonitic fabrics in the MCT zone show a top-to-the-south-west shear sense, which is consistent with kinematic indicators in the MCT zone along the entire length of the Himalaya. These are locally overprinted by top-to-the-north shear sense indicators which are interpreted to reflect late –stage extensional reactivation of the MCT (Stephenson, 1997). Rocks in the MCT zone show lithological affinity both to the Lesser Himalaya and High Himalayan Slab, suggesting that through time, the MCT has propagated down structural section and has incorporated footwall assemblages into the zone of active deformation (Stephenson, 1997). The thrust front of the MCT is located ~60 km south-west of the most north-easterly exposure of Lesser Himalayan rocks in the Larji-Kulu-Rampur Window, which provides a minimum estimate of the total displacement along the MCT (Stephenson, 1997). Epard *et al.* (1995) suggest that this distance is likely to be in excess of 100 km, based on the estimated translation of structures in the Crystalline Nappe.

4.3 Metamorphism in the Crystalline Nappe

Lithologies within the Crystalline Nappe have been metamorphosed to varying degrees, ranging from chlorite- to kyanite-grade conditions (Enclosure 2). No obvious metamorphic discontinuities were observed in the field between these metamorphic zones, suggesting a gradual transition from low- to high-grade conditions with increasing structural depth. This implies that metamorphism is likely to be entirely Himalayan in age, although the possibility that pre-Himalayan assemblages are preserved within the Crystalline Nappe cannot be ruled out entirely.

4.3.1 Metamorphic mineral growth in relation to deformation in metapelites

Three major phases of deformation are recognised in the Crystalline Nappe (D_1-D_3). The structural characteristics of each of these are described in detail in section 4.2. This section focuses on the relationship between the fabrics developed during these deformation phases and the growth of metamorphic assemblages in metapelites, in particular the growth of porphyroblastic phases such as garnet, staurolite and kyanite. These observations are summarised in Figure 4.8. It should be noted that metapelites are not the only lithology within the Crystalline Nappe and that psammites, biotite gneisses and granitic gneisses are the more dominant lithologies. Unfortunately these rarely preserve

good textural relationships between structural fabrics and different generations of metamorphic mineral growth.

Muscovite and biotite

Muscovite and biotite are ubiquitous phases in the metapelites and semi-pelites of the Crystalline Nappe. They define the well developed S_1 axial planar cleavage (Figures 4.9a & b) and the S_2 crenulation cleavage in deeper structural levels beneath the Tandi Syncline (Figures 4.9c-e). Muscovite and biotite therefore appear to have grown continuously throughout the D_1 and D_2 deformation phases in the Crystalline Nappe (Figure 4.8). Porphyroblastic biotite is observed helicitically overgrowing the S_1 fabric in some of the relatively low-grade metapelites within the biotite zone (Figures 4.9a & b), suggesting that D_1 was associated with the earliest stages of crustal shortening and thickening in the Crystalline Nappe and pre-dated peak-metamorphism (Figure 4.8). Biotite shows an overall coarsening trend towards higher-grade regions and is observed forming large, unorientated laths in the kyanite-grade metapelites near Khoksar (Figure 4.9j). Growth of biotite appears to have been by the continuous KFMASH reaction:

phengite + chlorite → biotite + phengite-poor muscovite + quartz + H_2O

based on the observation that chlorite and phengitic green muscovite are stable at low metamorphic grades, but are absent at higher metamorphic grades (compare Figures 4.9a & b with 4.9c & d). In more calcareous lithologies the incoming of biotite may also involve decarbonation of an ankerite by a reaction similar to:

muscovite + quartz + ankerite + H_2O → calcite + chlorite + biotite +CO_2

Garnet

Garnets show a wide range of morphologies and textural relationships with the S_1 and S_2 fabrics in the Crystalline Nappe (Figure 4.9b-i). Some garnets are observed helicitically overgrowing the S_1 cleavage beneath the Tandi Syncline (Figure 4.9b), thus implying that garnet growth was inter/post-kinematic with respect to the D_1 deformation phase. Garnets are also observed helicitically overgrowing the S_2 crenulation cleavage beneath the Tandi Syncline (Figure 4.9d), which implies that garnet growth in these samples was syn/post-kinematic with respect to the D_2 deformation phase. Other garnets are partly resorbed along the S_2 cleavage planes (Figure 4.9e), implying that garnet growth was pre/syn-D_2. Many of the larger garnets preserve straight and curved inclusion trails which trend at a high angle to the external S_2 schistosity (Figure 4.9f-h). These inclusion trails are interpreted to be the preserved remains of the S_1 fabric and are indicative of a relative rotation between the garnet and the matrix foliation during growth (e.g. Bell, 1985). Garnet growth in these samples was therefore pre/syn kinematic with respect to the D_2 deformation phase. Curiously, pressure

shadows around many of these garnets are symmetrical, suggesting that the latest stage of deformation in the Crystalline Nappe may have involved a degree of co-axial flattening. Other garnets appear to statically overgrow the S_2 fabric in the Crystalline Nappe (Figures 4.9h-& i), thus suggesting that garnet growth in these samples was inter/post-kinematic with respect to the D_2 deformation phase.

The above textural observations are consistent with continued garnet growth throughout the D_1 and D_2 deformation phases in the Crystalline Nappe (Figure 4.8). The extreme variability of garnet morphologies and textural relationships with the S_1 and S_2 fabrics undoubtedly reflects the diachroneity of deformation and metamorphic mineral growth within the Crystalline Nappe which results from variations in bulk-rock composition, fluid fluxing and heterogeneous P-T conditions.

Staurolite and kyanite

Staurolite was rarely observed in the metapelites of the Crystalline Nappe, which probably reflects a bulk composition control. Where observed, it generally forms skeletal poikiloblasts within quartz-rich microlithons (Figure 4.9g) and shows no obvious relationship to either the S_1 or S_2 fabrics. Although largely speculative, staurolite is interpreted to have grown during the D_2 deformation phase following the growth of garnet (Figure 4.8).

Kyanite is observed forming large (up to 5cm in length) randomly orientated porphyroblasts in the metapelitic schists near Khoksar. The majority of these porphyroblasts are straight and show no evidence of bending or undulose extinction (Figure 4.9j), suggesting that they are inter/post-kinematic with respect to the D_2 deformation phase (Figure 4.8). Kyanite was rarely observed to the south of the Rhotang Pass, largely because the majority of lithologies examined at outcrop in the field had psammitic or granitic bulk-rock compositions. The lateral extent of the kyanite isograd shown on Enclosure 2 is therefore largely based on observations made by Thöni (1977) and Epard *et al.* (1995). Where observed, kyanite forms skeletal porphyroblasts which show a crude NE-SW alignment on S_2 surfaces (Figure 4.9k), suggesting that kyanite growth was pre/syn-kinematic with respect to D_2 deformation in the Crystalline Nappe.

Amphiboles

Many of the carbonate-rich pelites within the garnet and kyanite zones in the Crystalline Nappe contain small prisms of actinolite and hornblende which are observed growing parallel to the S_2 schistosity (Figure 4.9l). Growth of these amphiboles is interpreted to be pre/syn-kinematic with respect to the D_2 deformation phase.

4.3.2 Garnet zoning profiles

Thirteen garnet-bearing metapelitic/psammitic schists and biotite gneisses collected from the Crystalline Nappe were selected for microprobe analysis to establish whether they displayed any element zoning patterns. Samples were collected along two traverses in a direction perpendicular to

the metamorphic field gradient. The location of these samples is shown on Enclosure 2 and Figures 4.10a & 4.11a..

Chandra valley traverse (Figure 4.10a)

Seven metapelitic/psammitic samples were collected for analysis at progressively deeper structural levels along the Chandra valley (Figure 4.10a; Enclosure 2). Representative garnet zoning profiles from each of these samples, together with a sketch of the analysed garnet and any inclusion patterns are shown in Figure 4.10b. Inclusions within these garnets include quartz, apatite, ilmenite and tourmaline, none of which define any obvious inclusion trail patterns. Despite the absence of evidence for textural zoning, chemical data reveal two types of zoning profiles in these garnets: (1) bell-shaped profiles characterised by a progressive decrease in X_{Sps} and X_{Grs} and an increase in X_{Alm} and X_{Prp} from core to rim (e.g. JDW 26 & JDW 28); and (2) flat zoning profiles characterised by relatively small changes in X_{Sps}, X_{Alm}, X_{Prp} and X_{Grs} from core to rim (e.g. JDW 18, JDW 22). The former are generally referred to as 'normal growth zoning profiles' and are interpreted to be indicative of garnet growth by fractionation during prograde metamorphism (e.g. Tracy *et al.*, 1976). The absence of compositional zoning in garnets has been attributed both to rapid crystal growth (e.g. Hodges *et al.*, 1988a; Hodges & Silverberg, 1988), and/or homogenisation of a previously formed zoning profile by diffusion at temperatures in excess of *c.*600°C (e.g. Vannay & Grasseman, 1998). Given the relatively small size of many of the garnets analysed (<0.5mm diameter), either of these two possibilities could explain the relatively flat zoning profiles observed in samples JDW 18, 22 & 32. Minor retrograde rims are evident in some of the zoning profiles shown in Figure 4.10b, as indicated by a slight increase in X_{Sps} at the garnet edge (e.g. JDW 22 & JDW 29). This is consistent with petrographic observations which show that some garnets in the Crystalline Nappe are partly resorbed along their margins (e.g. Figure 4.9e).

Beas valley traverse (Figure 4.11a)

Epard *et al.* (1995) performed a detailed P-T traverse through the Crystalline Nappe to the south of the Rhotang Pass (Figure 4.11a; Enclosure 2). It was not felt necessary to repeat this work, hence only six samples were selected for microprobe analysis in this part of the study area (Figure 4.11a; Enclosure 2). Representative garnet zoning profiles from each of these samples, together with a sketch of the analysed garnet and any inclusion patterns are shown in Figure 4.11b. The majority of these garnets do not display any textural evidence of zoning. Inclusions are randomly orientated and consist of a mixture of annealed quartz, ilmenite, tourmaline and apatite. Sample JDW 129 preserves a straight inclusion trail which helicitically overgrows the S_0/S_1 fabric, thus displaying similar textural relationships to those shown in Figure 4.9b.

With the exception of JDW 93, all of the analysed garnets preserve prograde growth zoning profiles with limited evidence for retrograde rims (Figure 4.11b). These profiles are extremely similar to those seen in the Chandra valley on the northern side of the Rhotang Pass (Figure 4.10b) and

to those published by Thöni (1977; pp148) from samples collected within the Phojal-Kallath megafold. Sample JDW 93 displays a rather unusual zoning profile (Figure 4.11b). The rims of this garnet preserve a flat zoning profile, whilst the core is depleted in calcium and enriched in iron. The garnet shows no textural evidence of zoning and the reason for this calcium depletion remains uncertain. It may be related to calcium disequilibrium during garnet growth (Chernoff & Carlson, 1997).

4.3.3 Mineral chemistry and thermobarometry

In all of the above samples, mineral analyses of muscovite, biotite and plagioclase were made both adjacent to and away from the garnet of interest in an attempt to determine whether there was any variation in composition at the thin section scale. Using the techniques outlined in Appendix A, minerals believed to be in textural equilibrium were chosen for use in quantitative P-T analysis in an attempt to constrain the conditions of final re-equilibration (compositions of the minerals used are given in Appendix B). Based on the prograde growth zoning profiles shown in Figures 4.10b and 4.11b, these estimates are likely to reflect near-peak conditions. This is consistent with textural observations which demonstrate that retrograde textures are only locally developed within the Crystalline Nappe (see section 4.3.4).

Discussion of P-T results (Chandra valley traverse)

The P-T results of the samples collected along the Chandra valley traverse are shown in Table 4.2, Figures 4.10d & e and Enclosure 2. Several conventional garnet-biotite geothermometers were used for comparative purposes. Although there is considerable variations in the absolute temperature recorded by the different thermometers (as much as ± 100°C in some cases), relatively speaking, each thermometer shows similar trends. The trends shown in Figure 4.10d are consistent with a slight temperature increase up the Chandra valley, which fits well with the field observation that metamorphic grade progressively increases towards kyanite-grade conditions near Khoksar village (Figure 4.10a). However, the temperature difference between samples JDW 18 (collected near the garnet-in isograd) and JDW 29 (collected near the kyanite-in isograd) is not all that great (<50°C). This may imply that the temperatures recorded reflect slightly post-peak estimates and are not indicative of near-peak conditions. Alternatively, if these are near-peak temperature estimates, then it implies that the appearance of kyanite in the metapelites near Khoksar may reflect a bulk composition control, rather than a major difference in P-T conditions.

THERMOCALC consistently gives higher temperature estimates than conventional garnet-biotite (GB) thermometry (Table 4.2). Massey (1994) observed similar trends in samples collected from the Langtang valley in central Nepal: he attributed this to the fact that the GB geothermometer effectively records the closure temperature for Fe-Mg diffusion between garnet and biotite at temperatures of ~600°C. THERMOCALC does not appear to be susceptible to lower-temperature re-setting, owing to

Table 4.2: Chandra valley P-T results

			Conventionall geothermobarometry results												THERMOCALC results											
			Barometry				Garnet-Biotite thermometry																			
Sample	assemblage	comments	P* (kbar)	P** (kbar)	P*** (kbar)	Ave	B 92 (HW)	B 92 (GS)	Das 91	FS 78	HS 82	PL 83	T 76	HL 77	P (kbar)	sd	T (°C)	sd	corr	fit	number of reactions	XH20	end-members excluded	preferred result	estimated overburden (3.71km/kbar)	sd
JDW 18	Grt + Bt + Ms + Pl + Qtz + H2O (metapelite)	average garnet rim and matrix (post-peak)	-	6.8	5.5	6.1	**534**	523	500	521	543	551	554	540	6.7	1.1	605	35	0.672	0.94	7	1.0				
															6.4	1.0	565	31	0.670	0.90	7	0.5				
															6.2	**1.0**	**537**	**29**	**0.668**	**0.91**	**7**	**0.3**	**none**	**X**	23.0	3.7
															5.8	1.0	470	28	0.649	1.10	7	0.1				
JDW 22	Grt + Bt + Ms + Pl + Qtz + H2O (metapelite)	average garnet rim and matrix (post-peak)	-	6.7	5.3	6.0	**494**	449	489	503	534	541	540	527	6.9	1.3	594	41	0.661	1.22	7	1.0				
															6.6	1.2	554	37	0.660	1.22	7	0.5				
															6.4	**1.2**	**527**	**35**	**0.659**	**1.24**	**7**	**0.3**	**none**	**X**	23.7	4.5
															5.9	1.3	460	36	0.642	1.42	7	0.1				
JDW 23	Grt + Bt + Ms + Pl + Qtz + H2O (metapelite)	average garnet rim and matrix (post-peak)	-	7.1	5.7	6.4	**551**	537	533	546	576	565	574	557	6.8	1.1	617	35	0.681	0.91	7	1.0				
															6.5	1.0	576	32	0.678	0.92	7	0.5				
															6.3	**1.0**	**547**	**30**	**0.676**	**0.98**	**7**	**0.3**	**none**	**X**	23.4	3.7
															5.7	1.1	478	33	0.658	1.26	7	0.1				
JDW 26	Grt + Bt + Ms + Pl + Qtz + H2O (metapelite)	average garnet rim and matrix (post-peak)	-	7.5	6.0	6.8	**528**	504	512	515	554	547	549	535	7.3	1.1	600	36	0.693	1.04	7	1.0				
															7.0	1.0	561	32	0.690	1.05	7	0.5				
															6.8	**1.0**	**533**	**32**	**0.687**	**1.10**	**7**	**0.3**	**none**	**X**	25.2	3.7
															6.2	1.2	466	34	0.670	1.34	7	0.1				
JDW 28	Grt + Bt + Ms + Pl + Qtz + H2O (metapelite)	average garnet rim and matrix (post-peak)	-	7.1	5.7	6.4	**578**	583	539	565	587	576	589	570	6.5	1.1	624	36	0.678	0.56	7	1.0				
															6.2	**1.0**	**582**	**32**	**0.676**	**0.55**	**7**	**0.5**	**none**	**X**	23.0	3.7
															6.1	1.0	553	30	0.674	0.61	7	0.3				
															5.6	0.9	485	27	0.653	0.95	7	0.1				
JDW 29	Grt + Bt + Ms + Pl + Qtz + H2O (metapelite)	average garnet rim and matrix (post-peak)	-	7.6	6.3	6.9	**558**	565	508	521	549	551	555	540	7.2	1.1	626	36	0.692	1.00	7	1.0				
															6.9	**1.1**	**584**	**32**	**0.688**	**0.90**	**7**	**0.5**	none	**X**	25.6	4.1
															6.7	1.0	555	30	0.685	0.86	7	0.3				
															6.2	0.9	485	27	0.666	0.96	7	0.1				
JDW 32	Grt + Bt + Ms + Pl + Qtz + H2O (metapelite)	average garnet rim and matrix (post-peak)	-	7.5	6.0	6.8	**566**	565	529	547	576	566	576	558	7.1	1.1	618	35	0.688	0.87	7	1.0				
															6.8	**1.0**	**577**	**32**	**0.685**	**0.83**	**7**	**0.5**	**none**	**X**	25.2	3.7
															6.5	1.0	548	30	0.682	0.85	7	0.3				
															6.0	1.0	479	28	0.664	1.07	7	0.1				

Garnet-Biotite thermometer abbreviations

B 92 (HW): Bhattacharya et al (1992), using garnet mixing model of Hackler & Wood (1989)
B 92 (GS): Bhattacharya et al (1992) using garnet mixing model of Ganguly & Saxena (1984)
Das 91: Dasgupta et al (1991)
FS 78: Ferry & Spear (1978)
HS 82: Hodges & Spear (1982)
PL 83: Perchuk & Lavrent'eva (1983)
T 76: Thompson (1976)
HL 77: Holdaway & Lee (1977)

Barometer reactions

* GASP (Grt + Als = Pl)
** GPMB-Mg (Grs + Prp + Ms = 3An + Phl)
*** GPMB-Fe (Grs + Alm + Ms = 3An + Ann)

Table 4.3: Beas valley P-T results

			Conventionall geothermobarometry results												THERMOCALC results											
			Barometry				Garnet-Biotite thermometry																			
Sample	assemblage	comments	P* (kbar)	P** (kbar)	P*** (kbar)	Ave	B 92 (HW)	B 92 (GS)	Darg 91	FS 78	HS 82	PL 83	T 76	HL 77	P (kbar)	sd	T (°C)	sd	corr	fit	number of reactions	XH20	end-members excluded	preferred result	estimated overburden (3.71km/kbar)	sd
JDW 92	Grt + Bt + Ms + Pl + Ky + Qtz + H2O (metapelite)	average garnet rim and matrix (post-peak)	7.7	8.8	7.2	7.9	**618**	623	586	638	661	617	655	621	8.3	1.4	691	40	0.682	1.12	8	1.0				
															7.9	**1.2**	**635**	**33**	**0.677**	**0.98**	**8**	**0.5**	**none**	**X**	29.3	4.5
															7.6	1.1	598	30	0.670	0.93	8	0.3				
															6.9	1.1	514	28	0.643	1.07	8	0.1				
JDW 93	Grt + Bt + Ms + Pl + Qtz + H2O (mafic paragneiss)	average garnet rim and matrix (post-peak)	-	9.2	7.5	8.3	**578**	560	596	569	636	580	601	575	8.2	1.2	614	41	0.740	1.17	7	1.0				
															7.8	**1.1**	**574**	**36**	**0.733**	**1.13**	**7**	**0.5**	**none**	**X**	28.9	4.1
															7.5	1.1	546	34	0.728	1.15	7	0.3				
															6.8	1.1	478	35	0.713	1.32	7	0.1				
JDW 57	Grt + Bt + Ms + Pl + Qtz + H2O (metapelite)	average garnet rim and matrix (post-peak)	-	7.0	5.5	6.3	**574**	582	508	545	568	565	573	556	6.3	1.1	618	35	0.681	0.79	7	1.0				
															6.1	**1.0**	**576**	**32**	**0.679**	**0.75**	**7**	**0.5**	**none**	**X**	22.6	3.7
															5.9	1.0	547	30	0.677	0.78	7	0.3				
															5.4	0.9	478	27	0.658	1.02	7	0.1				
JDW 129	Grt + Bt + Ms + Pl + Qtz + H2O (metapelite)	average garnet rim and matrix (post-peak)	-	5.4	4.2	4.8	**466**	426	447	449	482	508	495	488	5.7	1.2	566	41	0.679	1.27	7	1.0				
															5.4	1.2	529	38	0.679	1.29	7	0.5				
															5.2	1.2	503	37	0.678	1.33	7	0.3				
															5.0	**1.2**	**480**	**37**	**0.674**	**1.39**	**7**	**0.2**	**none**	**X**	18.6	4.5
JDW 54	Grt + Bt + Ms + Pl + Qtz + H2O (metapelite)	average garnet rim and matrix (post-peak)	-	7.2	5.8	6.5	**538**	536	485	502	531	540	539	526	6.9	1.1	610	35	0.685	0.84	7	1.0				
															6.6	1.0	569	32	0.682	0.77	7	0.5				
															6.4	**1.0**	**541**	**30**	**0.680**	**0.77**	**7**	**0.3**	**none**	**X**	23.7	3.7
															5.8	0.9	472	26	0.661	0.96	7	0.1				
JDW 50	Grt + Bt + Ms + Pl + Qtz + H2O (metapelite)	average garnet rim and matrix (post-peak)	-	8.5	7.0	7.7	**572**	557	587	572	618	580	595	575	7.5	1.0	604	34	0.704	0.55	7	1.0				
															7.2	**1.0**	**565**	**31**	**0.700**	**0.53**	**7**	**0.5**	**none**	**X**	26.7	3.7
															7.0	1.0	538	29	0.697	0.58	7	0.3				
															6.4	0.9	472	26	0.680	0.93	7	0.1				

Garnet-Biotite thermometer abbreviations

B 92 (HW): Bhattacharya et al (1992), using garnet mixing model of Hackler & Wood (1989)
B 92 (GS): Bhattacharya et al (1992) using garnet mixing model of Ganguly & Saxena (1984)
Das 91: Dasgupta et al (1991)
FS 78: Ferry & Spear (1978)
HS 82: Hodges & Spear (1982)
PL 83: Perchuk & Lavrent'eva (1983)
T 76: Thompson (1976)
HL 77: Holdaway & Lee (1977)

Barometer reactions

* GASP (Grt + Als = Pl)
** GPMB-Mg (Grs + Prp + Ms = 3An + Phl)
*** GPMB-Fe (Grs + Alm + Ms = 3An + Ann)

the fact that it places greater emphasis on net transfer reactions, rather than cation exchange reactions to calculate P-T estimates. The activity of H_2O and CO_2 can be changed when running THERMOCALC, which gives a degree of control in determining fluid compositions (assuming a two-component fluid system). Generally speaking, by reducing X_{H2O} temperature estimates become progressively lower and can be made to match those recorded using conventional GB thermometry. Comparing the conventional GB temperatures with those recorded by THERMOCALC therefore provides a potential means of estimating fluid compositions during metamorphism. Given the observation that the Haimantas in general are ubiquitously graphite-rich and locally rich in carbonates (see Chapter 3 for lithological discussion), it seems reasonable to assume that $X_{H2O}<1$ during metamorphism. The preferred P-T results for all of the samples analysed in the Chandra valley suggest that X_{H2O} was probably between 0.3-0.5 (Table 4.2).

In the absence of kyanite in any of the studied samples, pressures were calculated using Grt-Bt-Pl-Ms barometry (Table 4.2). This barometer relies upon the exchange of calcium between garnet and plagioclase. Since plagioclase was rarely observed adjacent to garnet in any of the analysed samples, the average composition of matrix plagioclase was used for P-T work. Plagioclase compositions vary between X_{An}10-20 in all of the analysed samples (Figure 4.10c), with <5% variation in molar An in any one sample. No zoning was observed in any of the analysed plagioclase grains in any of the samples. Using the average plagioclase composition in each sample, the preferred THERMOCALC pressure result is shown on Figures 4.10d & e and is indicative of final re-equilibration at *c.*6-7kbar (22-26km assuming a lithostatic gradient of 3.71km/kbar). Pressures appear to increase slightly towards Khoksar, which is consistent with the observed increase in the metamorphic field gradient up the Chandra valley towards deeper structural levels.

Discussion of P-T results (Beas valley traverse)

The P-T results of the samples collected along the Beas valley traverse are shown in Table 4.3, Figures 4.11d & e and Enclosure 2. As with the Chandra valley data, absolute temperature estimates vary considerably between the different garnet-biotite thermometers, but show similar overall trends. The trends show a pattern of increasing temperature with increasing structural depth beneath the Tandi Syncline and are, therefore, consistent with the pattern of metamorphic isograds mapped in the field and the pattern of isotherms mapped by Epard *et al.* (1995).

As with the samples in the Chandra valley, samples in the Beas valley showed no significant variation in X_{An} in any one sample (Figure 4.11c), hence average matrix feldspar compositions were used during P-T calculations. Those samples which record the highest temperatures also record the highest pressures (Figure 4.11d). Pressures are observed to increase towards the core of the Phojal-Kallath megafold, with samples JDW 92 and JDW 93 both recording comparable estimates of 7.9 ± 1.2 and 7.8 ± 1.1 kbar respectively (corresponding to an overburden maximum of 26-33km assuming a lithostatic gradient of 3.71km/kbar). Sample JDW 92 contains kyanite which appears to be in equilibrium with garnet (Figure 4.9k) and was therefore incorporated into the thermodynamic dataset

(Table 4.3). Samples JDW 54 and JDW 50 were collected structurally beneath the lower limb of the Tandi Syncline and record significantly higher pressures than does sample JDW 129, which was collected from the overturned limb of the Tandi Syncline. These results confirm that the orientation of the Tandi Syncline is likely to be a relic of the D_1 deformation phase and suggest the possibility that it may have occupied a more recumbent attitude than its current position suggests.

4.3.4 P-T evolution

There is limited evidence for a P-T-time path in any of the studied samples in the Crystalline Nappe. Prograde reaction textures are not preserved, hence the exact reaction responsible for the growth of garnet, staurolite and kyanite could not be established. Similarly, the absence of suitable inclusions in any of the garnet porphyroblasts precluded the determination of prograde metamorphic conditions using quantitative thermobarometric techniques (cf. St. Onge, 1987). However, given the present day mineral assemblages observed in metapelites, together with the garnet zoning profiles shown in Figures 4.10b and 4.11b, it is reasonable to assume that lithologies within the Crystalline Nappe experienced a clockwise prograde P-T path during the D_1 and D_2 deformation phases. This corresponds to the M_1 metamorphic stage seen along the entire length of the Himalaya (see Chapter 2). Based on textural observations presented in section 4.3.1 it would appear that peak-metamorphic conditions were attained during the later stages of the D_2 deformation phase and that the D_3 deformation phase marked the onset of exhumation in the Crystalline Nappe (Figure 4.8). This interpretation is slightly at odds with that of Epard *et al.* (1995), who suggested that peak-metamorphic conditions were attained during the D_1 deformation phase and that D_2 was associated with slightly retrograde conditions.

The retrograde P-T pathway of rocks in the Crystalline Nappe is also difficult to constrain. Quantitative P-T data show that *c.*25-30km of overburden must have been eroded from parts of the Crystalline Nappe in order to expose kyanite-grade lithologies in the deepest structural levels. Exhumation of these rocks must have been associated with considerable decreases in both pressure and temperature. However, retrograde textures are only locally developed in the Crystalline Nappe and are generally recognised as the breakdown of garnet to chlorite and the sericitisation of kyanite (Figures 4.9j, m & n). Such reactions could have occurred at any point on the retrograde P-T path. The general absence of retrograde textures therefore suggests that either: (1) lithologies in the Crystalline Nappe were rapidly exhumed following the attainment of peak conditions; and/or (2) the development of retrograde reactions is strongly controlled by fluids, thus implying that exhumation may have occurred in the absence of metamorphic fluids following the attainment of peak conditions.

4.4 Melting/pegmatite formation in the Crystalline Nappe

A large proportion of the Crystalline Nappe is comprised of megacrystic K-feldspar granites of purported Precambrian-Ordovician age (see Chapter 3). These are chemically and isotopically distinct from the High Himalayan leucogranites and are unrelated to Himalayan metamorphism. No

discordant High Himalayan leucogranites were observed in any part of the Crystalline Nappe, which questions the validity of models which seek to explain the origins of crustal melting by shear heating along the MCT (e.g. Harrison *et al.*, 1997b). Despite the absence of leucogranites, leucocratic pegmatites and aplite dykes were observed in the deeper structural levels of the Crystalline Nappe (Figures 4.12 & 4.13).

Leucocratic pegmatites are frequently observed parallel to the S_1/S_2 cleavage surfaces in the kyanite-grade lithologies near Khoksar village (Figures 4.12a-c). They contain a strong internal fabric which is parallel to the regional tectonic foliation (Figures 4.12a-c) and are occasionally folded by SW verging F_2 folds (Figure 4.12b). The pegmatites are entirely leucocratic and have a mineralogical composition of Qtz + Kfs + Pl + Ms ± Grt ± Tur and show a close spatial relationship with biotite gneisses which have a typical mineralogy of Qtz + Pl + Bt ± Ms ± Grt. The pegmatites are clearly related to devolatilisation reactions at high temperatures, although whether this occurred during Himalayan metamorphism remains uncertain. It is possible (albeit unlikely) that these pegmatites are pre-Himalayan in age and that they were associated with the emplacement of the Rhotang Gneissic Complex during the Precambrian/Lower Palaeozoic.

S-parallel and discordant leucocratic pegmatites are also observed in the kyanite-grade parts of the Crystalline Nappe to the south of the Rhotang Pass (Figure 4.13). Earlier generations of pegmatites are intensely folded by SW verging folds related to the D_2 deformation phase (Figure 4.13a & b). These are clearly pre/syn-tectonic and may be unrelated to Himalayan metamorphism. Later generations of pegmatites and aplites intrude along the S_2 schistosity and are only weakly deformed (Figure 4.13b). These are clearly syn/post-tectonic in origin and must be related to Himalayan metamorphism (Figure 4.8). The youngest generation of pegmatites discordantly intrude across the S_2 schistosity in the Crystalline Nappe (Figure 4.13c) and are undoubtedly Himalayan in age.

4.5 Summary and discussion

Field and petrographic observations of structures and metamorphic textures in the rocks of the Crystalline Nappe in the lowermost part of the High Himalayan Slab in NW Lahaul show evidence of polyphase deformation and metamorphism associated with the Himalayan orogeny (Figure 4.8). No evidence was found to support the existence of a major pre-Himalayan deformation and metamorphic event. However, given the intensity of deformation in deeper structural levels, it seems likely that any pre-Himalayan fabrics have been completely obliterated by Himalayan deformation and metamorphism. The possibility that some metamorphic assemblages are pre-Himalayan in age is therefore difficult to rule out from textural observations alone. The presence of numerous large Precambrian-Ordovician granites in this part of the slab suggests that the Haimantas probably experienced some sort of deformation prior to the India-Asia collision.

4.5.1 Burial of the Crystalline Nappe

Four main phases of Himalayan deformation are recognised (Table 4.1), the earliest of which (D_1) was associated with the development of the NE facing Tandi Syncline. D_1 structures are only preserved at shallow structural levels and are overprinted by D_2 structures which are associated with top-to-the-south-west folding and thrusting. Both D_1 and D_2 are interpreted to be syn-metamorphic deformation events which were associated with the burial of the Crystalline Nappe and the development of a regional Barrovian-type metamorphism, which reached kyanite-grade conditions in the deepest exposed crustal levels (*c.*600 ± 50°C and 7.8 ± 1.1 kbar). This corresponds to the M_1 metamorphism seen throughout the entire High Himalayan Slab. The absence of crustal melt leucogranites and sillimanite-grade assemblages suggests that the M_2 metamorphism was not developed in the Crystalline Nappe. However, the intrusion of late-stage leucocratic pegmatites and aplitic dykes attests to localised melting in the deeper structural levels of the Crystalline Nappe.

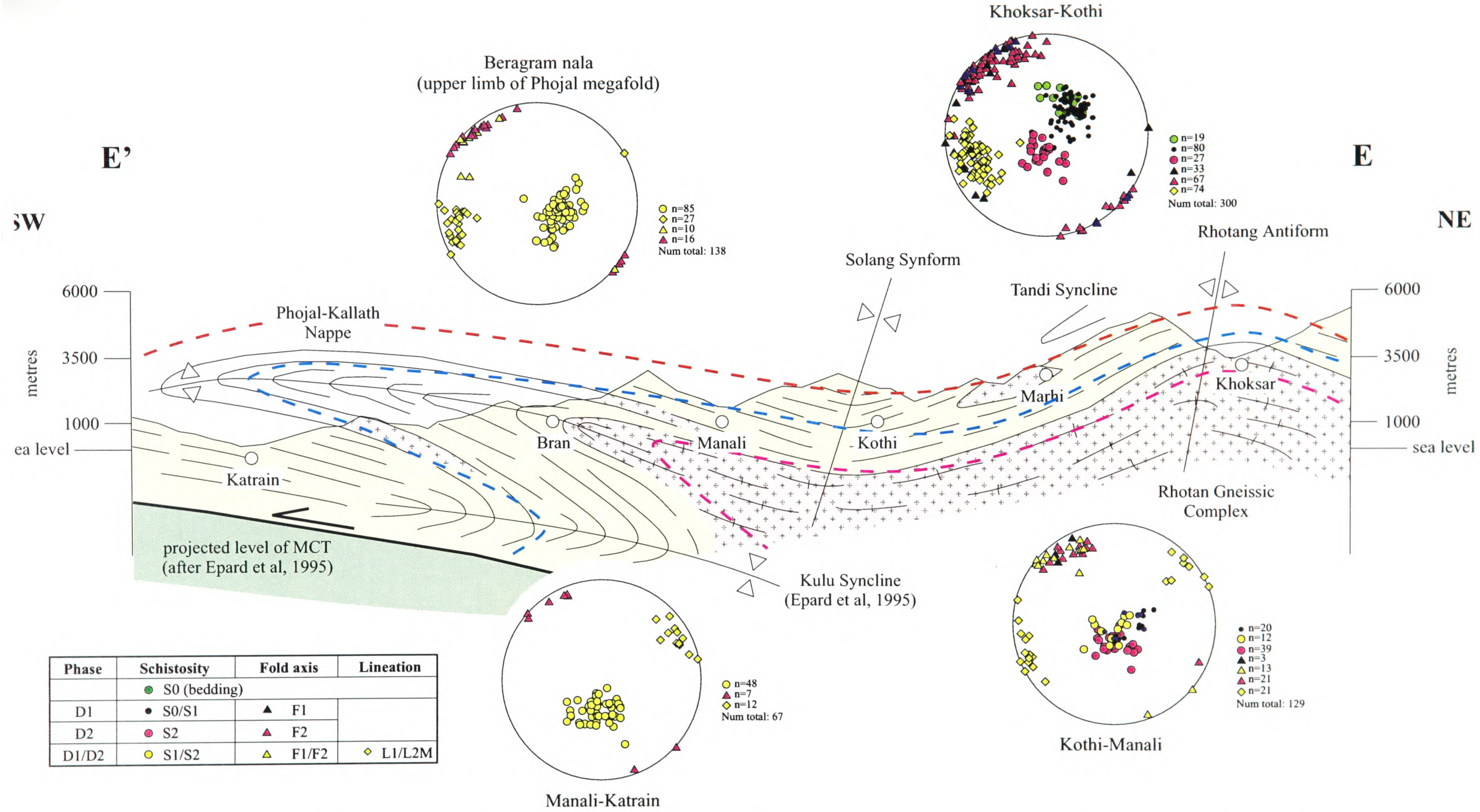
4.5.2 Exhumation of the Crystalline Nappe

Given the absence of any obvious extensional detachments in the Crystalline Nappe, exhumation of garnet- and kyanite-grade lithologies is interpreted to have been accomplished by uplift and erosion. The possibility that an extensional detachment was located at higher structural levels above the Crystalline Nappe cannot be ruled out entirely, but seems unlikely given the observed decrease in metamorphic grade towards the north (Enclosure 2). Whilst uplift may have partly been accommodated through thermal doming during the D_3 deformation phase (e.g. along the Rhotang Antiform), it is extremely unlikely that this doming could account for the removal of *c.*20-25km of overburden. The only obvious means of uplifting the Crystalline Nappe through *c.*20-25km is by thrusting along the MCT at the base of the slab. Movement along the MCT has previously been correlated with the development of the Phojal-Kallath megafold and the folding of metamorphic isograds during the D_2 deformation phase (Thöni, 1977; Epard *et al.*, 1995). However, underthrusting of the Lesser Himalaya would result in the rapid chilling of the hangingwall and the cessation of metamorphic mineral growth in the Crystalline Nappe. Textural relationships demonstrate that that metamorphic mineral growth persisted throughout the D_2 deformation phase in parts of the Crystalline Nappe, thus implying that significant movement on the MCT must have post-dated the D_2 deformation phase and was probably broadly synchronous with high temperature doming during D_3 (Figure 4.8).

4.5.3 Tectonic significance of the NE facing Tandi Syncline

The NE facing direction of the Tandi Syncline has been the focus of a number of studies over the years (e.g. Powell & Conaghan, 1973; Srikantia & Bhargava, 1982; Frank *et al.*, 1987; Steck *et al.*, 1993), each of which have proposed a different tectonic origin for this structure. Some of these can be readily discounted. For example, Powell and Conaghan (1973) suggested that the Tandi Syncline was actually an antiform closing towards the NE, whilst Srikantia and Bhargava (1982) suggested that the Tandi Syncline was the product of late-stage backthrusting. Both these interpretations are ruled

out by personal observations described in section 4.2.1. The NE facing direction of the Tandi Syncline almost certainly attests to a phase of NE directed isoclinal folding during the D_1 deformation stage. Frank *et al.* (1987) account for this by deformation partitioning between rigid crustal blocks and suggest that the distribution of Precambrian-Ordovician granites may have exerted a strong control on deformation. The fact that the Tandi Syncline is bounded to the south by the Hanuman Tibba granite and to the north by the Rhotang Gneissic Complex and Kade granite (Enclosure 1), makes this a distinct possibility. Steck *et al.* (1993) prefer to explain the Tandi Syncline in terms of a major phase of NE directed nappe-stacking (the Shikar Beh Nappe) during the D_1 deformation phase. These authors cite two supporting lines of evidence for this theory: (1) the decreasing intensity of D_1 deformation towards the north; and (2) the decrease in metamorphic grade towards the north. However, the decreasing intensity of D_1 deformation towards the north could be explained by deformation partitioning between rigid crustal blocks, whilst the decrease in metamorphic field gradient could be explained by tectonic thinning and doming during the D_3 deformation phase. The existence of the Shikar Beh Nappe is therefore conjectural. Fuchs and Linner (1995) refute the existence of this nappe on the grounds that large-scale nappes do not terminate over such short distances. These authors therefore liken the Tandi Syncline to a major backfold. This is consistent with the observation that structures beneath the Tandi Syncline show top-to-the-south-west sense of shear, which is more characteristic of Himalayan deformation. However, structural observations presented in the next chapter demonstrate that NE facing D_1 structures continue along strike of the Tandi Syncline into the Chamba Syncline, thus implying that the Tandi Syncline forms part of a regional structure and is therefore unlikely to be a localised backfold.



Phase	Schistosity	Fold axis	Lineation
	S0 (bedding)		
D1	S0/S1	F1	
D2	S2	F2	
D1/D2	S1/S2	F1/F2	L1/L2M

Figure 4.1a: Cross-section through the lower part of the Crystalline Nappe showing the orientation of major structural elements (lower-hemisphere equal-area stereographic projections). See Enclosure 1 for location of section.

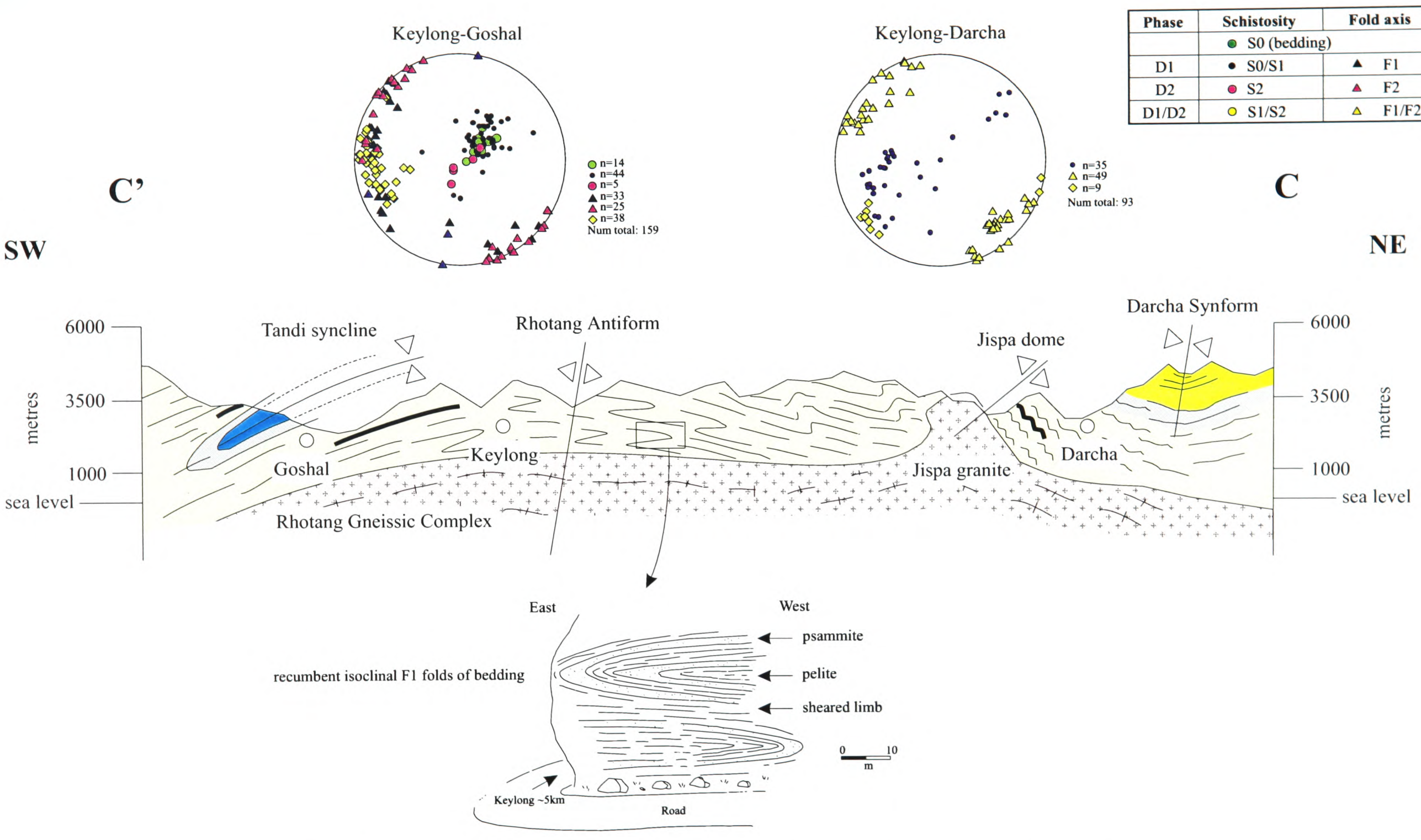
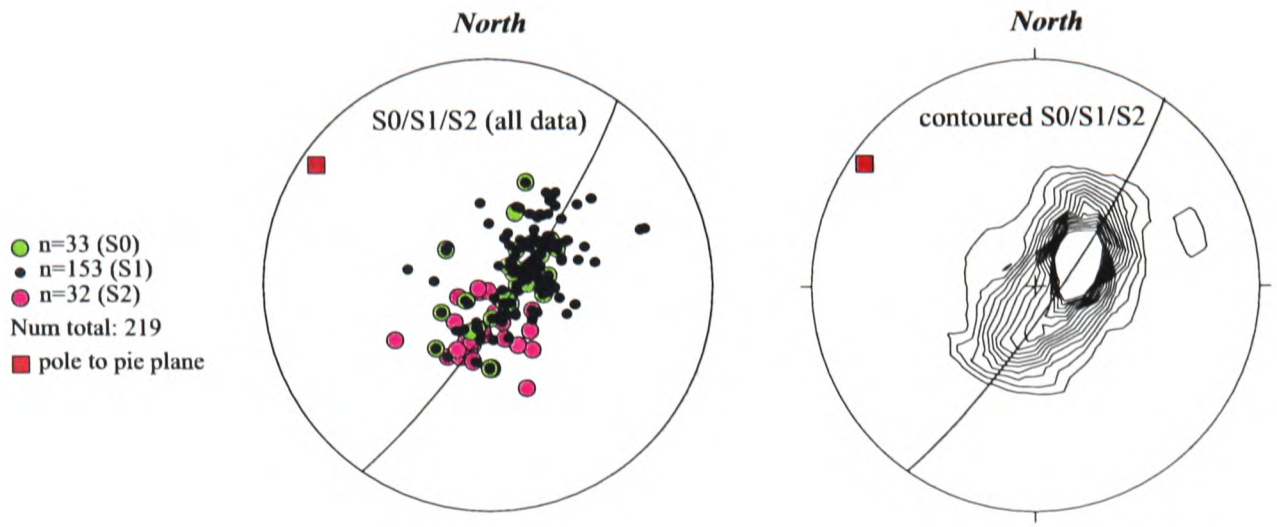


Figure 4.1b: Cross-section through the northern part of the Crystalline Nappe showing the orientation of major structural elements (lower-hemisphere equal-area stereographic projections). See Enclosure 1 for location of section.



n=33 (S0)
n=153 (S1)
n=32 (S2)
Num total: 219
pole to pie plane

Phase	Schistosity	Fold axis	Lineation
	S0 (bedding)		
D1	S0/S1	F1	
D2	S2	F2	
D1/D2	S1/S2	F1/F2	L1/L2M

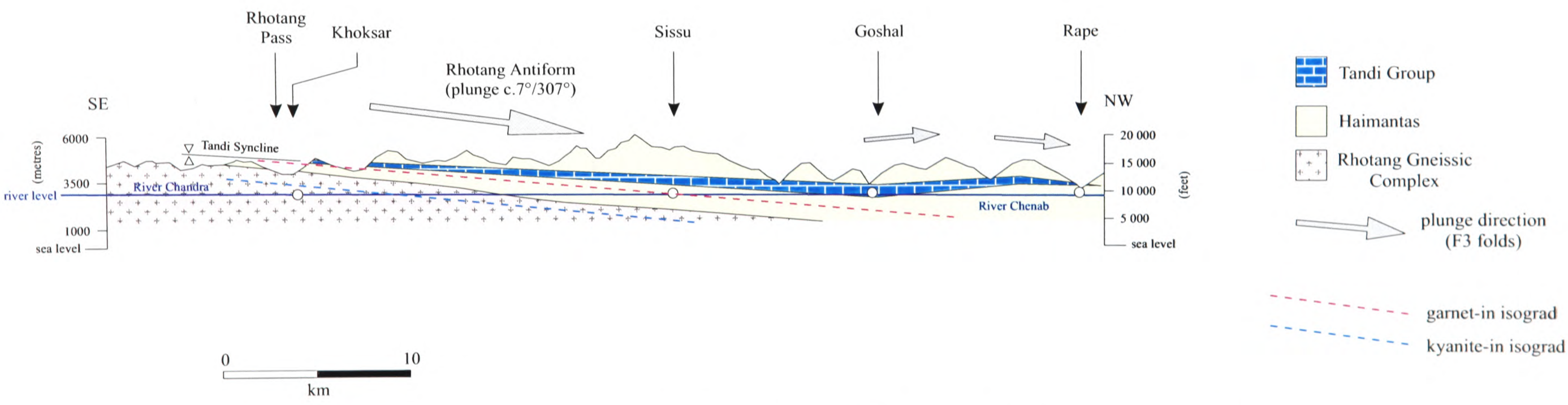
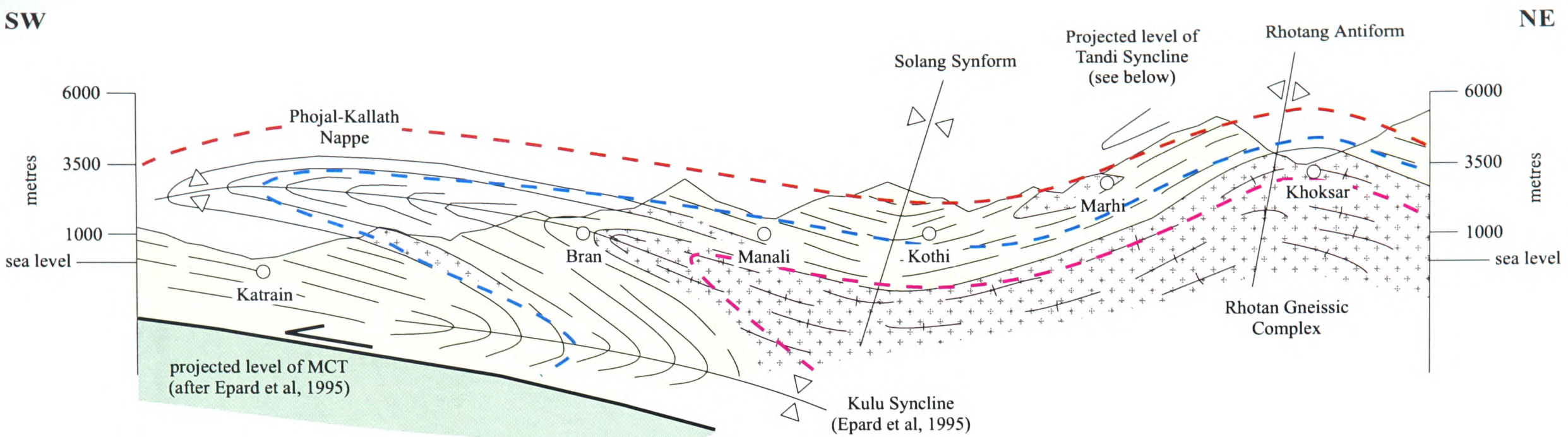


Figure 4.1c: Schematic cross-section looking south along the Chandra valley showing the plunge of the Tandi Syncline from high above the Rhotang Pass at Khoksar village, to river level at Goshal village some ~28 km downstream. Equal-area stereographic projection of S0/S1 and S2 in the Chandra valley defines an F3 fold plunging ~7°/307°. Metamorphic isograds are the right way-up beneath the Tandi Syncline, suggesting that the NE vergence and facing direction of this structure is not the result of post-D1 re-orientation. Petrographic observations show that metamorphic mineral growth in the Chandra valley post-dates the D1 deformation phase, thus suggesting that metamorphism is dominantly Himalayan in age.



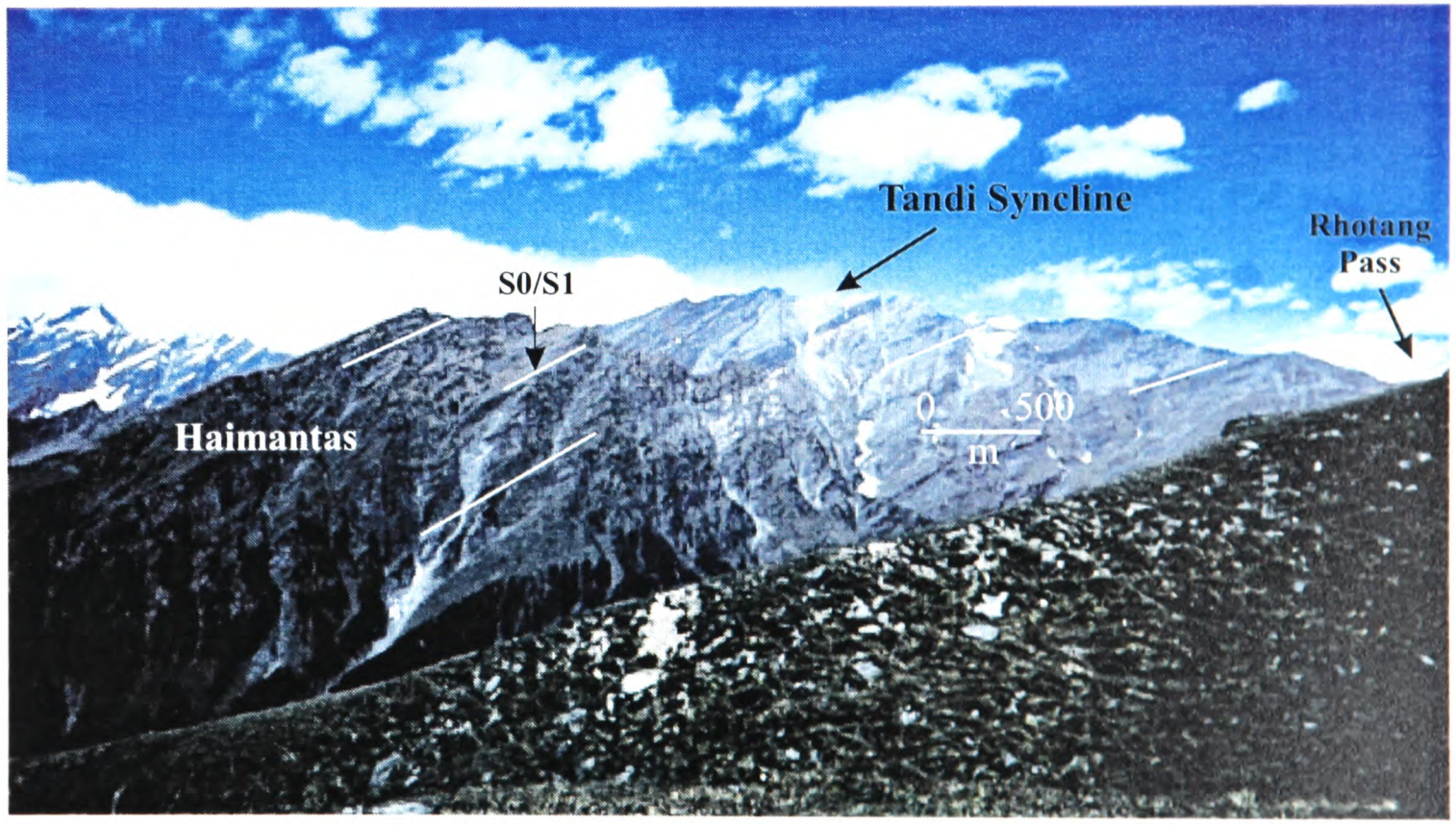
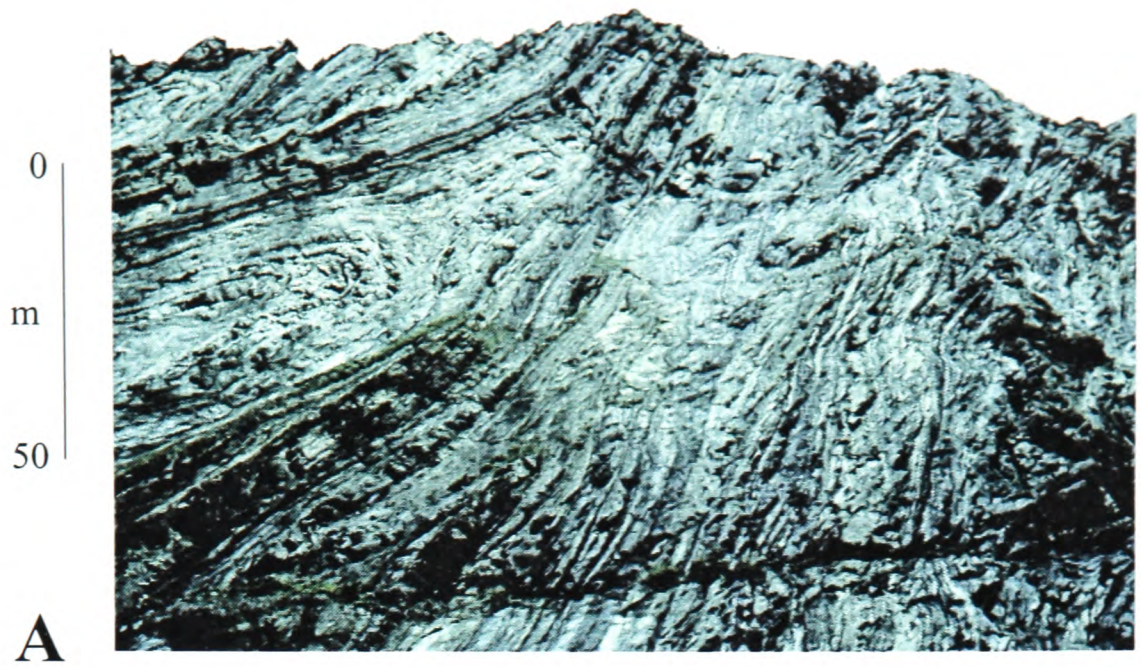


Figure 4.2: The south-eastern closure of the Tandi Syncline viewed from high above the Rhotang Pass to the east of Marhi village. Blue limestones mark the base of the Tandi Group (unit A), and are underlain by the brown-coloured calcareous sands, silts and shales belonging to the Lower Palaeozoic Haimantas. Note the unusual NE vergence of this fold and that bedding (S0) is parallel to the main axial planar cleavage (S1) which forms the prominent SW-dipping slopes. The S1 cleavage can be traced from the core of the syncline into the underlying Haimantas.





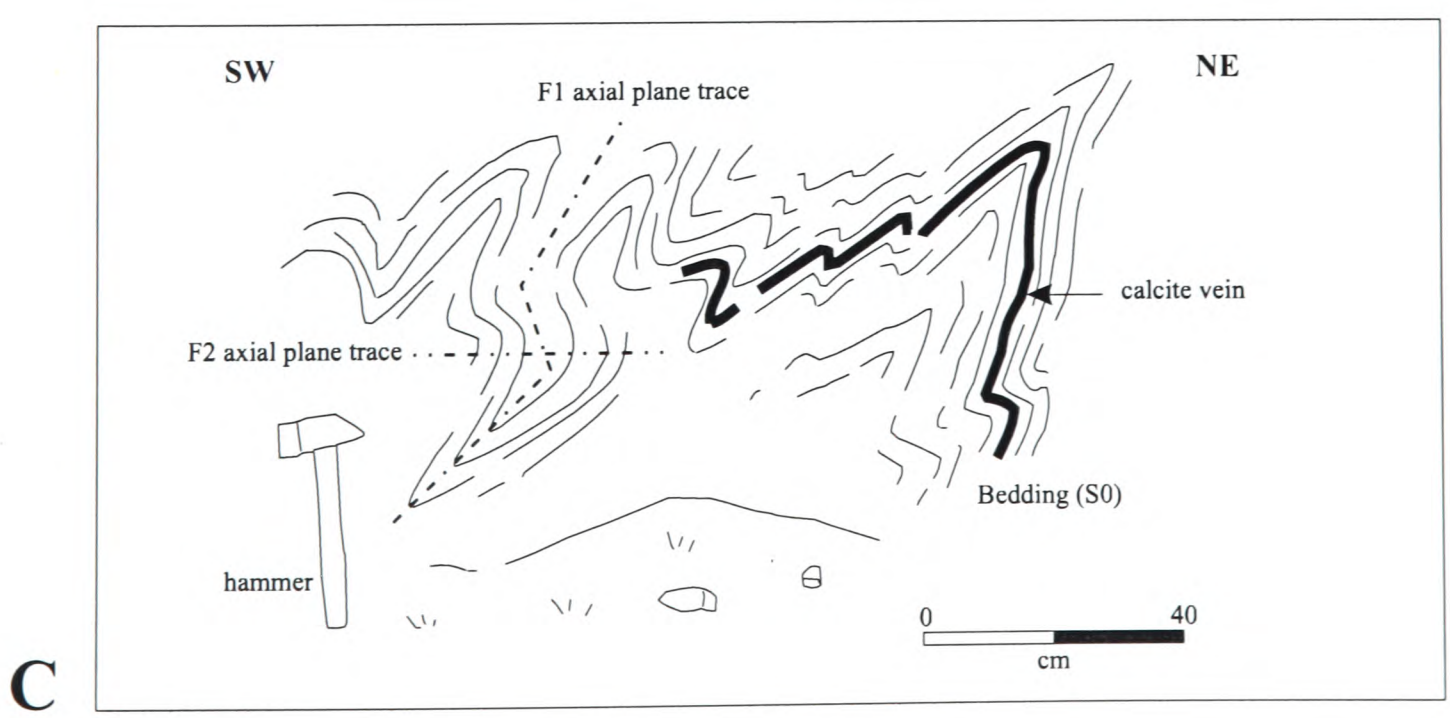


Figure 4.3: F1 fold structures in the Tandi Group
(a) Similar style isoclinal F1 folds in unit C of the Tandi Group (lower limb of Tandi Syncline, Goshal village).
(b) Isoclinal F1 fold hinge preserved in a competent unit of brown limestone beloning to unit B of the Tandi Group (lower limb of Tandi Syncline, Goshal village).
(c) NE verging F1 folds in the lower limb of the Tandi Syncline overprinted by F2 folds (south of Rape village).

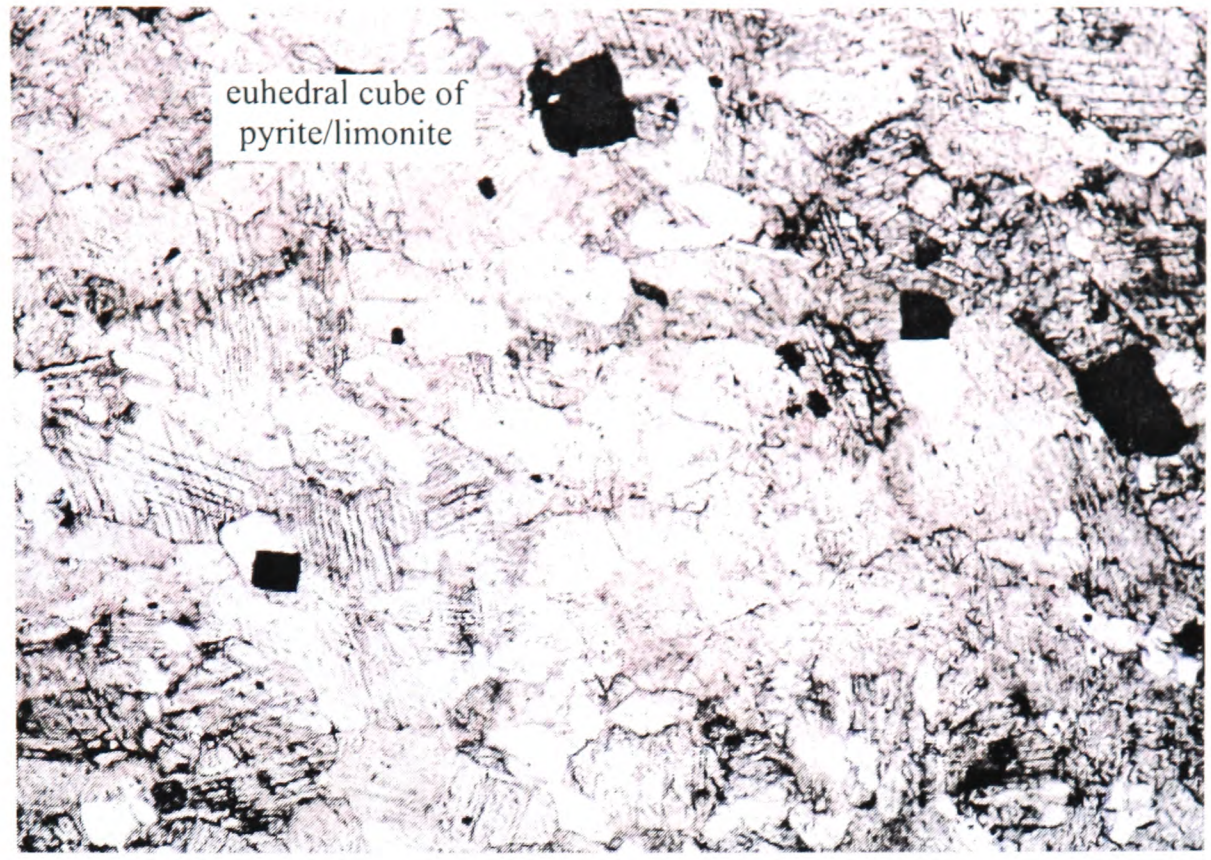


Figure 4.3d: Annealed microstructure in a calcarenite collected from unit A of the Tandi Group. Crystals of dolomite, calcite and quartz (recognised by the absence of cleavage planes) are overgrown by euhedral cubes of pyrite/limonite. (Sample JDW 202, collected south of Rape village).
Field of view c.3mm.

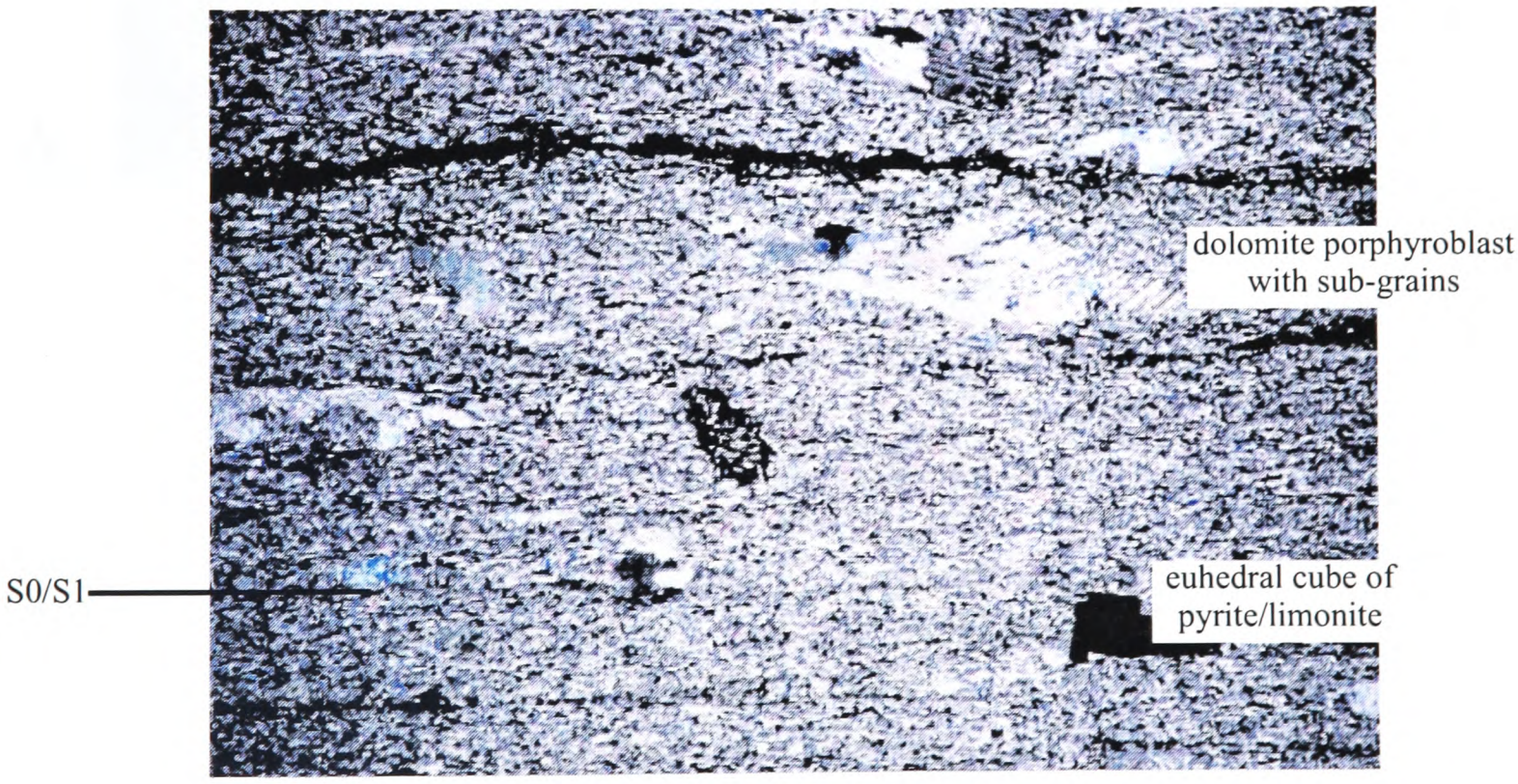


Figure 4.3e: S1 fabric in the Tandi Limestones. Note the large dolomite porphyroblast in the upper right part of the picture which shows evidence of sub-grain development. The S1 fabric is overgrown by cubes of pyrite/limonite which are discernible in the lower-right of the picture (sample JDW 126, collected in the Seri nala, ~7km north of Dhundi). Field of view c.3mm.

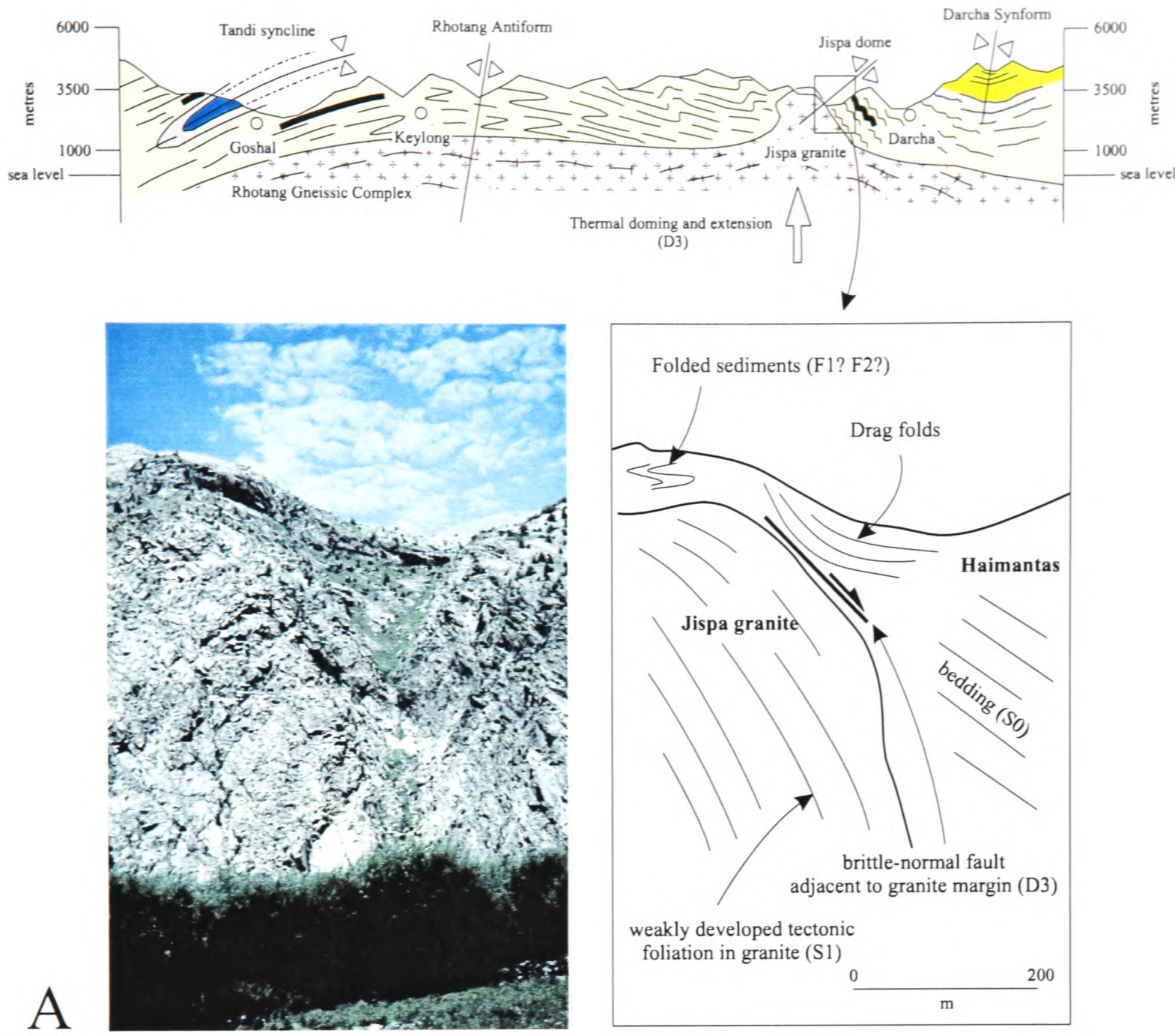




Figure 4.4: (A) The northern contact of the Jispa granite against the Haimantas. Bedding (S0) is parallel to a regionally developed flattening fabric (S1), which is also weakly developed in the granite. The contact between the granite and the Haimantas is bedding parallel. Drag folds are evident along the margin of the granite and are interpreted to be associated with doming and extensional normal faulting during the development of the Jispa dome. (B) MW-style folds of bedding developed in sediments on the northern side of the Jispa dome, south of Darcha. They are interpreted to be related to the development of the Jispa dome.

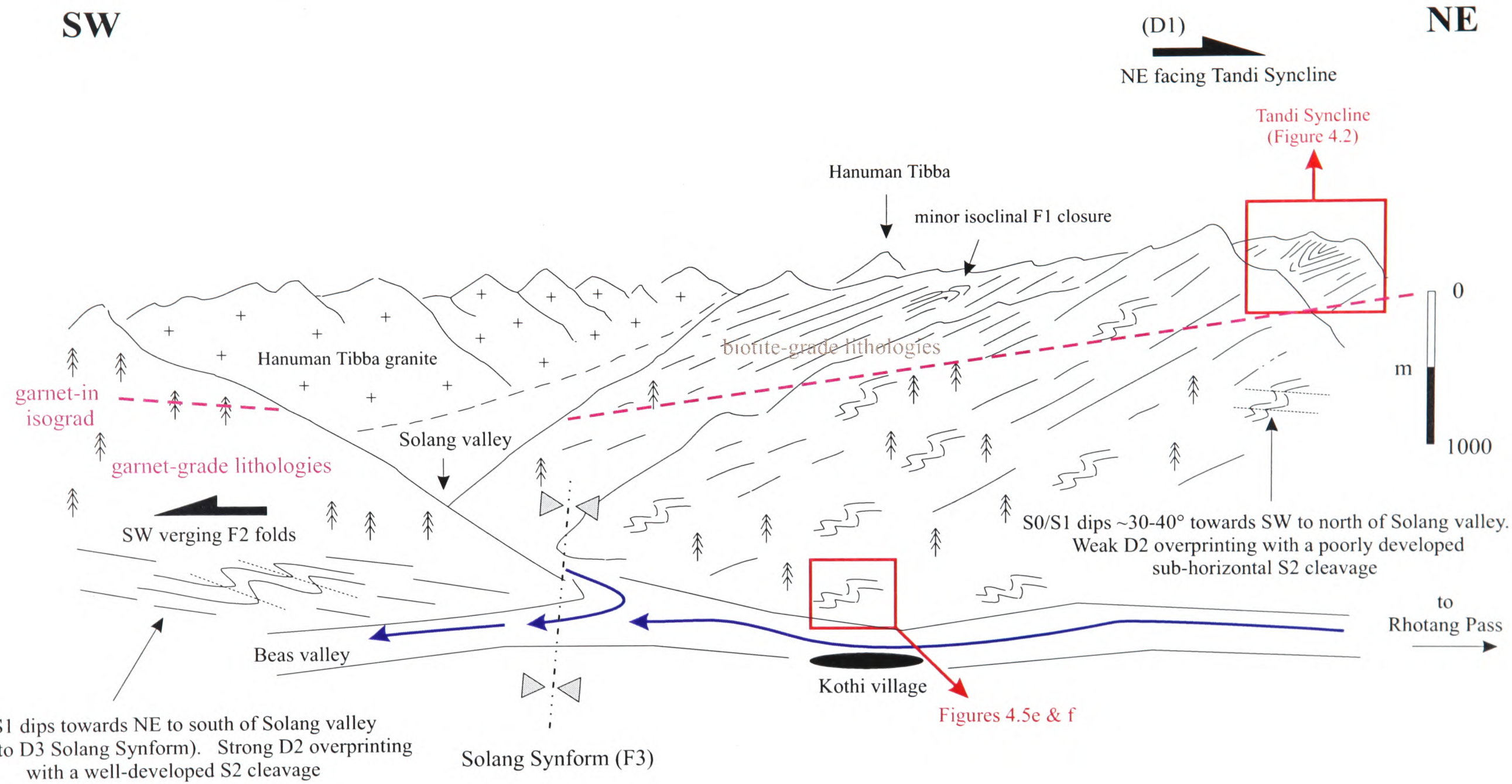
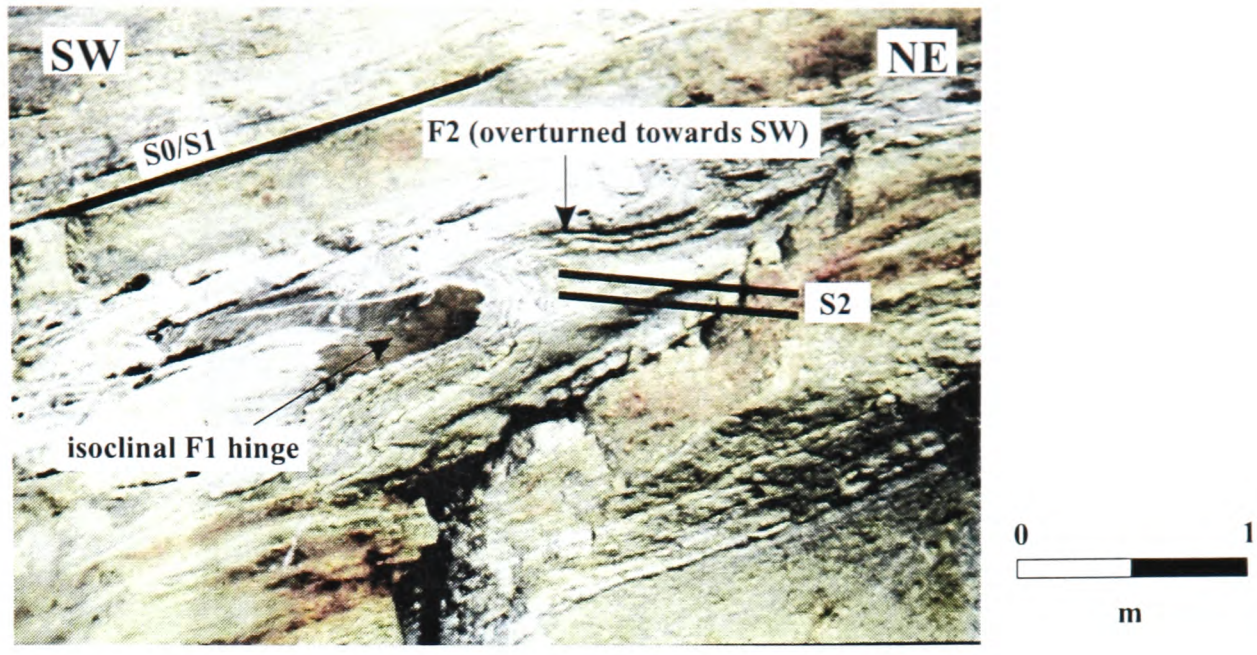
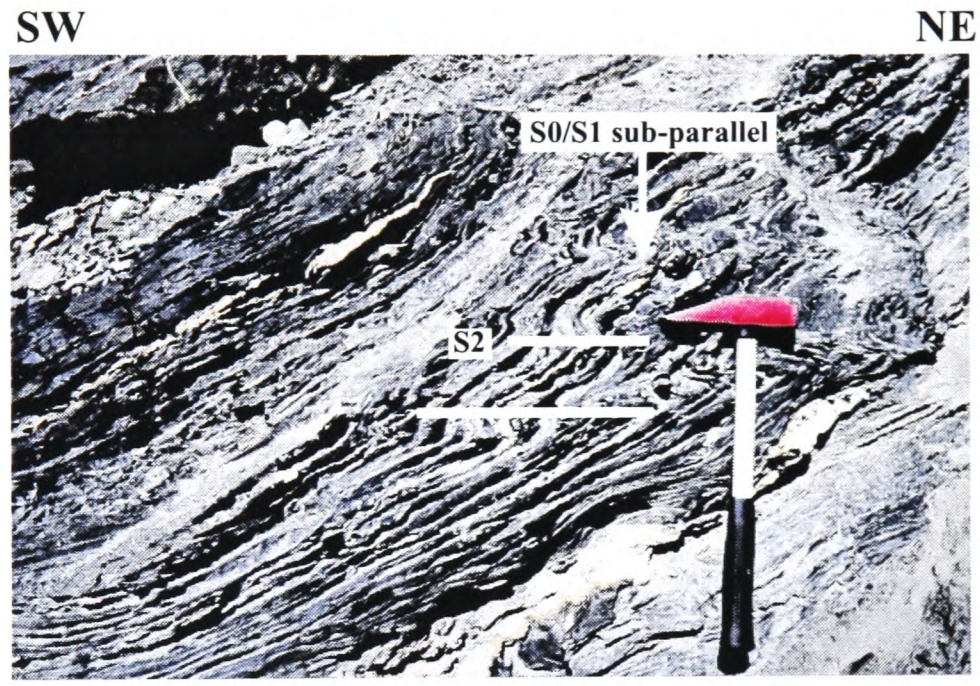


Figure 4.5a: Field sketch of the upper part of the Crystalline Nappe immediately south of the Rhotang Pass. The NE facing Tandi Syncline is preserved at shallow structural levels and is a remnant of the D1 deformation phase. D2 structures become progressively more dominant with increasing structural depth and consistently show a top-to-the-south-west kinematic transport direction. Red boxes show the location of other figures.

B



C



D

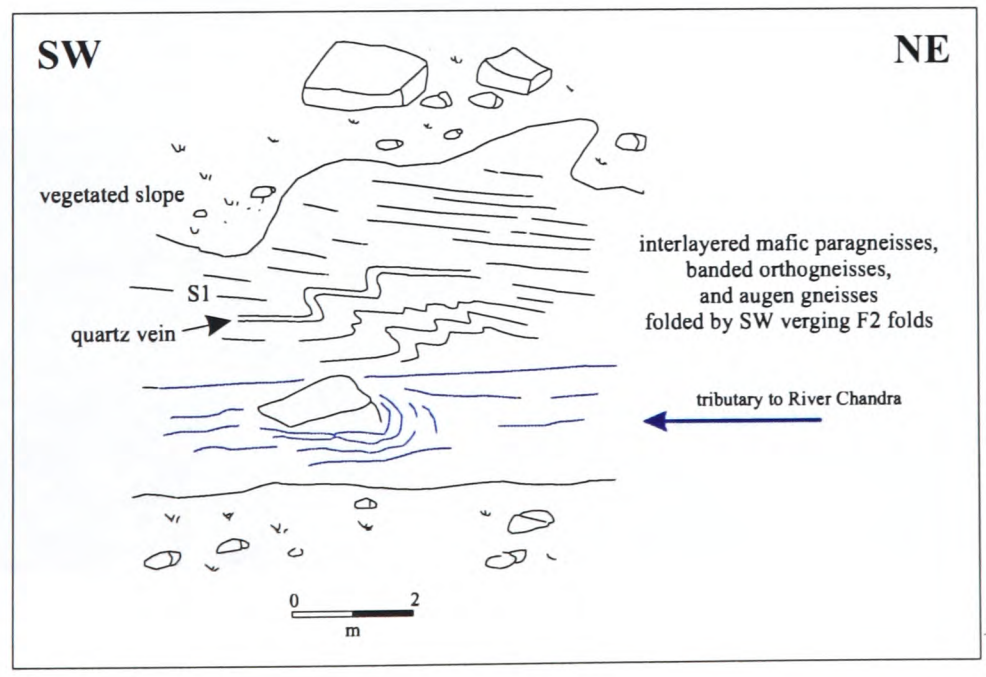
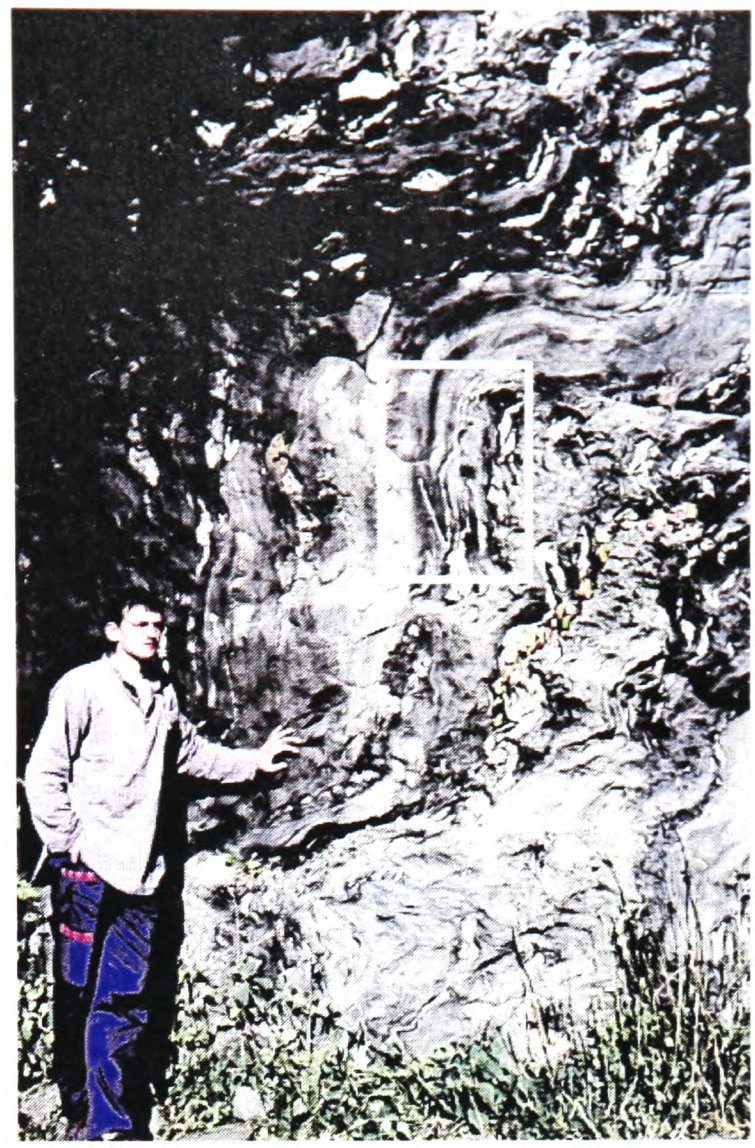


Figure 4.5: (Continued) F2 fold structures in the Crystalline Nappe
(b) SW verging F2 fold overprinting the boudinaged remains of an isoclinal F1 fold hinge in the overturned limb of the Tandi Syncline. S2 is weakly developed and is sub-horizontal. (unit A of the Tandi Group, ~5km into north of Dhundi).
(c) SW verging F2 folds in the lower limb of the Tandi Syncline. Calcite and quartz veins are sub-parallel to the S0/S1 fabric. S2 is weakly developed and is sub-horizontal. (lower limb of Tandi Syncline, Goshal village).
(d) SW verging F2 folds in banded augen gneisses and mafic paragneisses belonging to the Rhotang Gneissic Complex (structurally beneath the Tandi Syncline, Chandra valley, ~3km west of Khoksar).

SW NE



E

SW NE



F

Figure 4.5: Continued
(e) SW verging F2 fold of S0/S1. An isoclinally folded quartz vein shown within the boxed area represents a remnant of the D1 deformation phase. (Kothi village, see 4.5a for location).
(f) SW verging F2 folds of S0/S1. (Kothi village, see 4.5a for location).

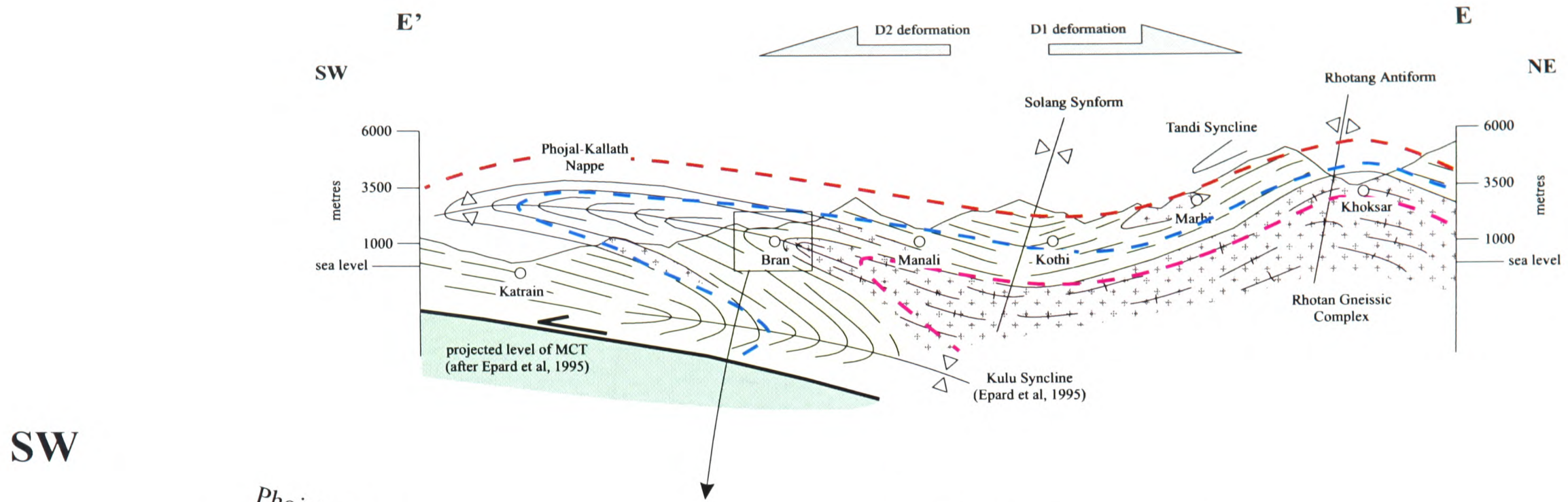
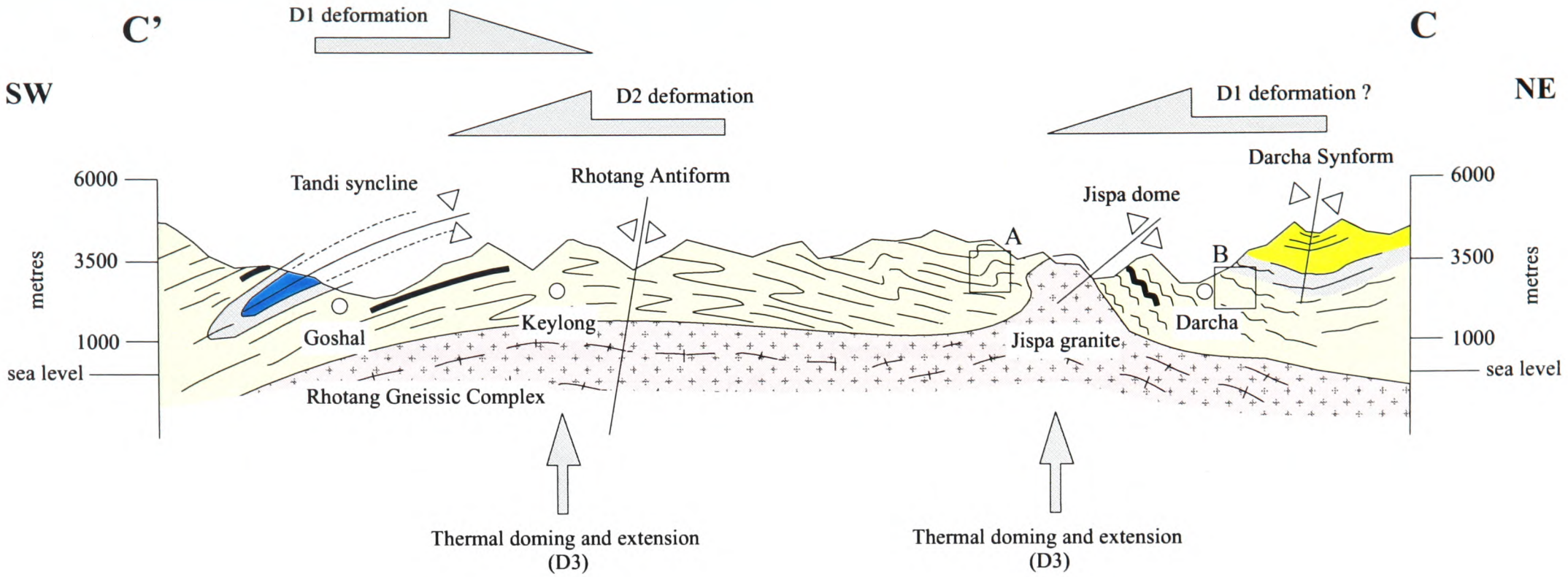
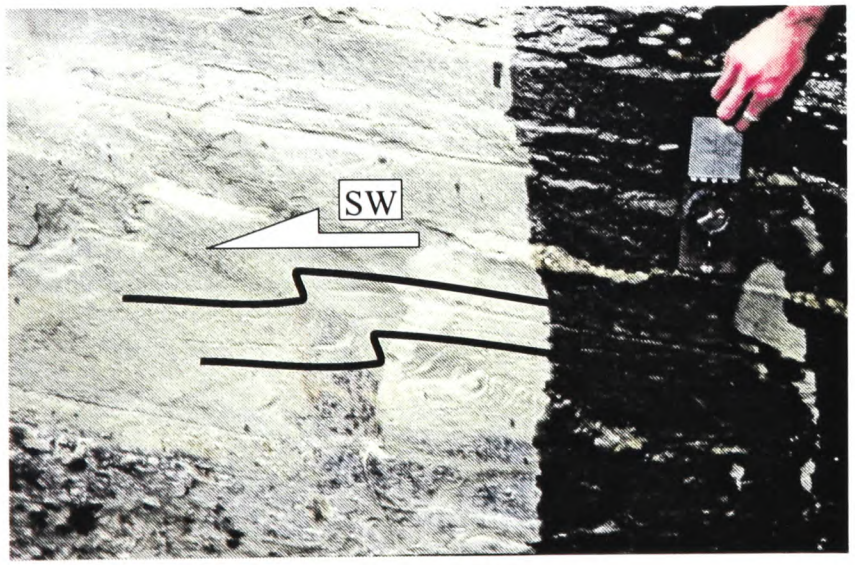


Figure 4.6: Field sketch of the core of the Phojal-Kallath megafold as viewed from the village of Haripur, on the eastern bank of the Beas valley.





A



B

Figure 4.7: SW verging F2 folds in the uppermost part of the Crystalline Nappe. (A) SW verging F1?/F2? fold in a competent psammite (~3km south of Jispa). (B) Steeply dipping, SW verging F1?/F2? fold with a curvilinear fold axes towards the SW (~500m north-west of Darcha).

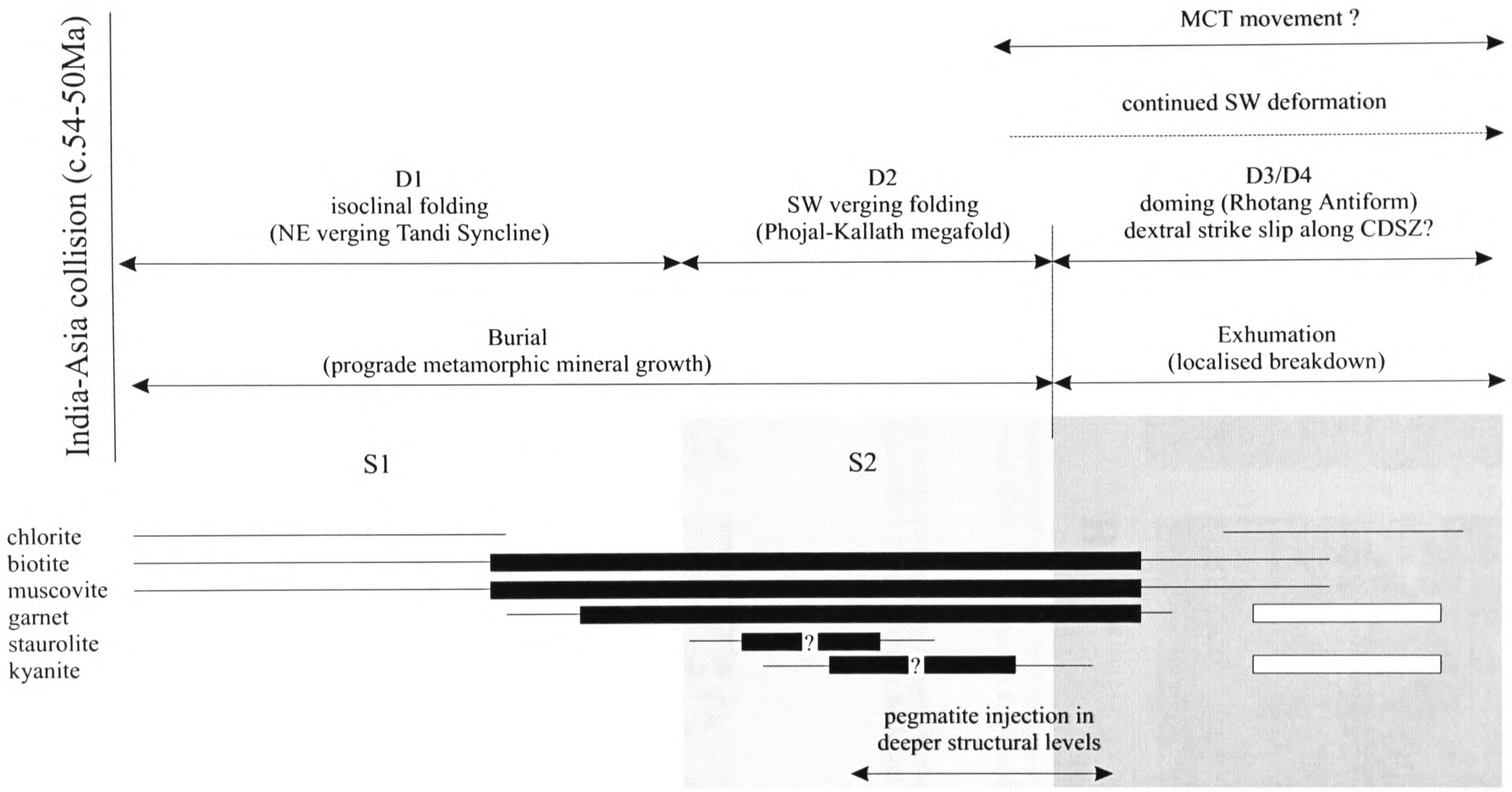


Figure 4.8: Growth of metamorphic mineral assemblages in relation to D1-D3 deformation phases in the Crystalline Nappe. Black boxes denote porphyroblastic growth. White boxes denote breakdown of porphyroblasts.

Figure 4.9: Microstructures and textural relationships observed in pelites and semi-pelites in the Crystalline Nappe. Unless otherwise stated, field of view in all photomicrographs is ~3mm.



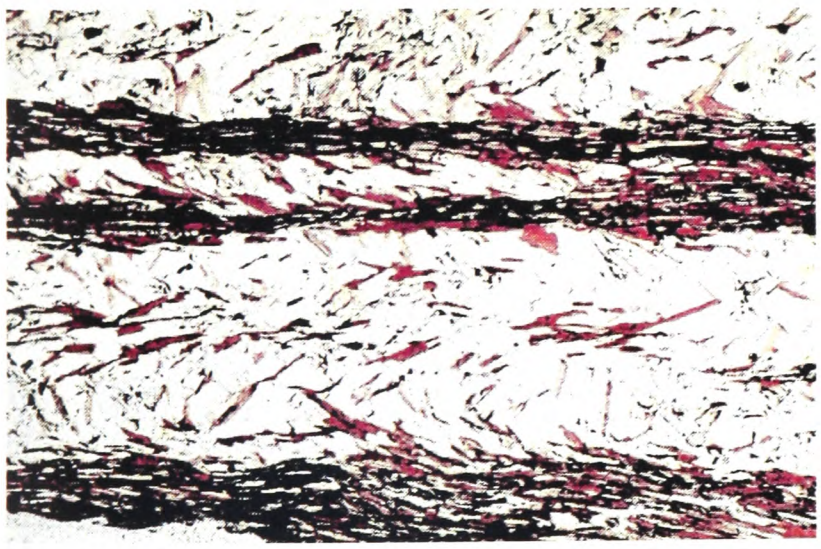
A



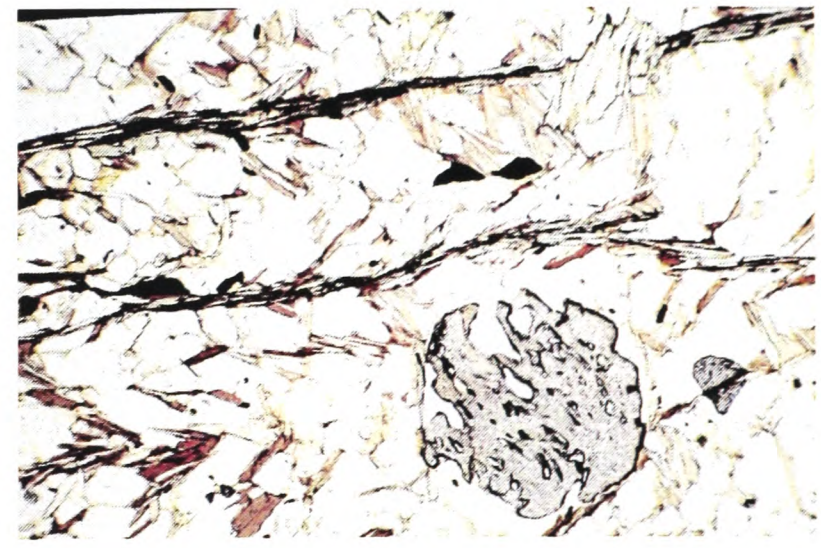
B

(a) S0/S1 defined by a fine grained alignment of green-coloured phengitic muscovite and chlorite. Biotite and chlorite porphyroblasts statically overgrow this fabric. (Sample JDW 6, collected in the overturned limb of Tandi Syncline, south of Goshal village).

(b) S0/S1 defined by a fine grained alignment of green-coloured phengitic muscovite and chlorite. Biotite and garnet porphyroblasts statically overgrow this fabric. (Sample JDW 129, collected in the lower limb of Tandi Syncline, ~5km north of Dhundi).



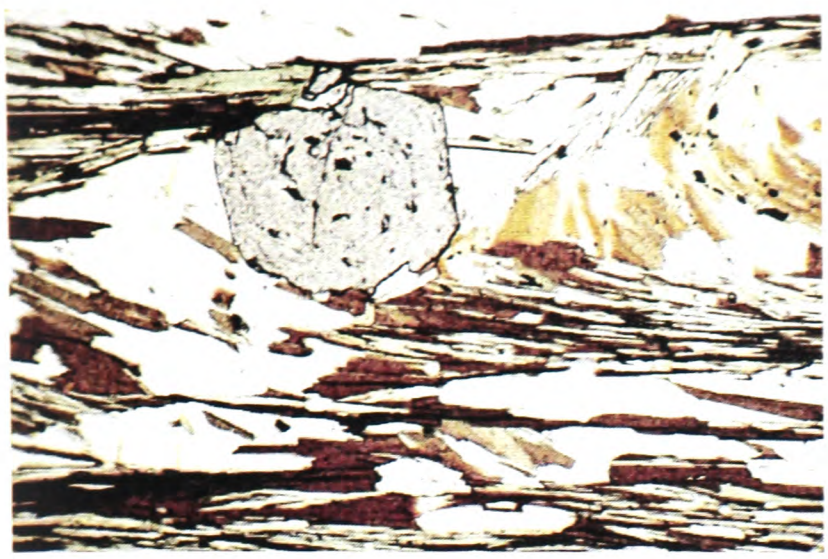
C



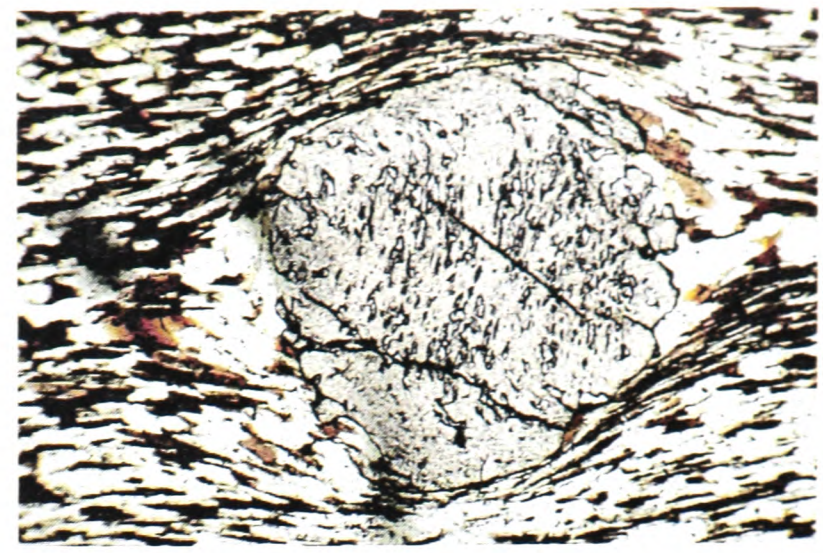
D

(c) S2 crenulation cleavage of S0/S1 in a graphitic pelite. (Sample JDW 33, collected adjacent to the Kulti nala granite, NW of Khoksar).

(d) S2 crenulation cleavage of S0/S1 in a graphitic pelite. A garent porphyroblast overgrows the crenulation fabric . Note the late-stage chlorite overgrowing S2 in the upper part of the picture (Sample JDW 77, collected at Kothi village).



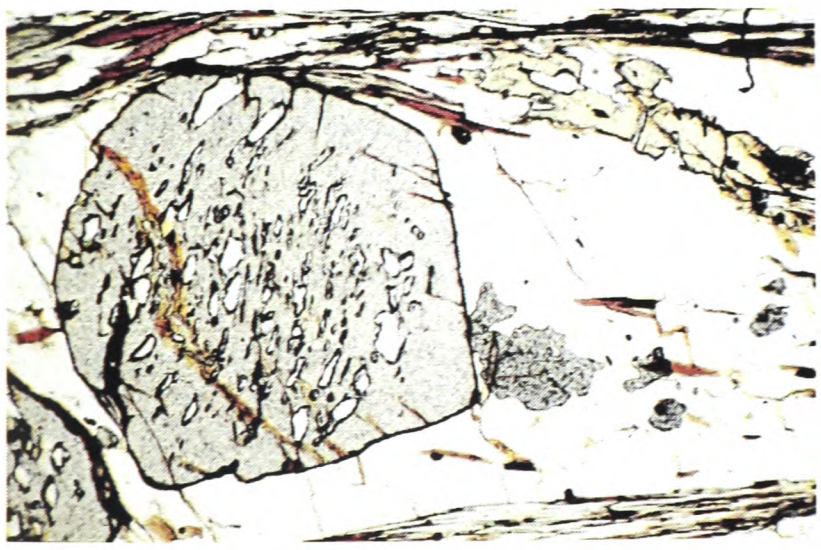
E



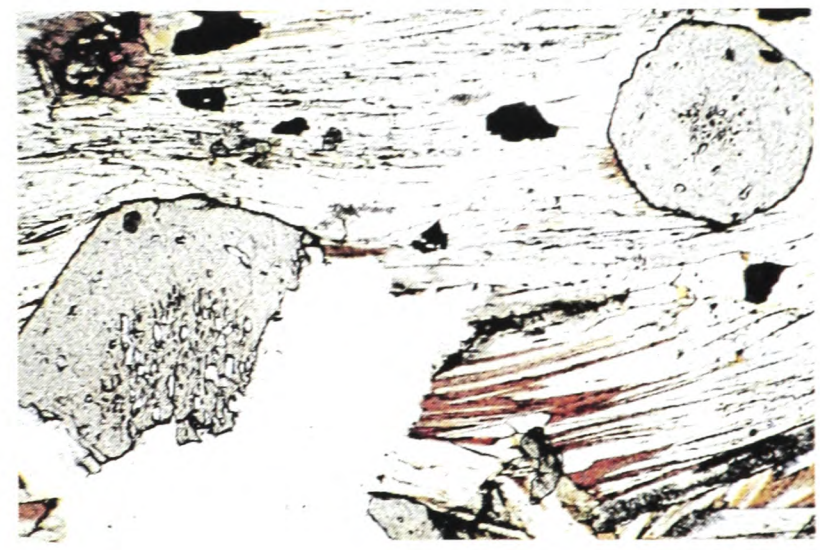
F

(e) S2 crenulation cleavage of S0/S1. A small garnet porphyroblast has overgrown the crenulated S0/S1 fabric and has been slightly resorbed along the S2 cleavage domain. Note the late-stage chlorite overgrowing S2 in the upper part of the picture. (Sample JDW 21, collected at Sissu village).

(f) S0/S1 fabric preserved as an inclusion trail within a garnet porphyroblast. S2 is at a high angle to this inclusion fabric. (Sample JDW 88, collected in the lower limb of the Phojal-Kallath megafold near Bran village).



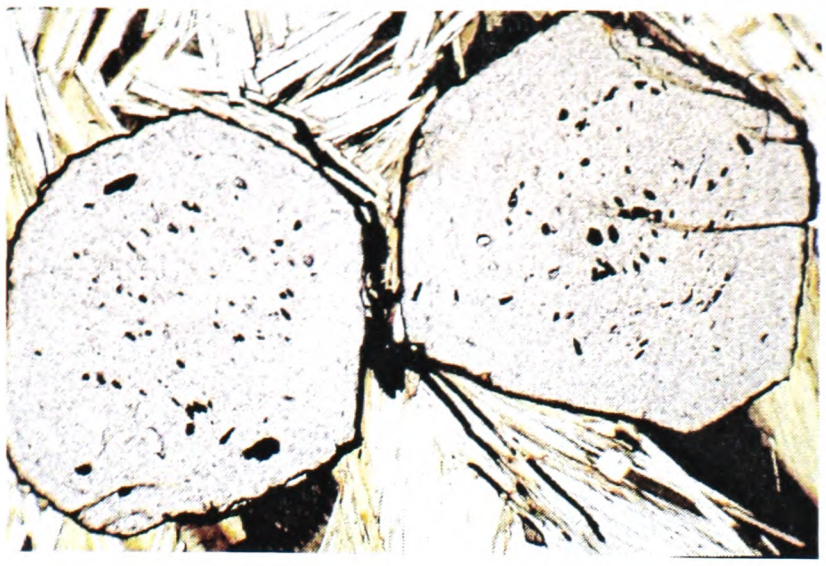
G



H

(g) S0/S1 preserved as an inclusion trail within a garnet porphyroblast. S2 is at a high angle to this inclusion fabric. Note the skeltetal staurolite porphyroblast adjacent to the garnet. (Sample JDW 81, collected in the Beas valley ~5km north of Manali).

(h) Garnet porphyroblasts overgrowing the S2 fabric in the Crystalline Nappe. The garnet cores preserve an inclusion trail (S0/S1?) at a high angle to the S2 fabric. The garnet rims are inclusion free and therefore indicative of multi-stage garnet growth. (Sample JDW 218, collected from core of the Phojal-Kallath megafold, ~500m vertically above Bran village).



I



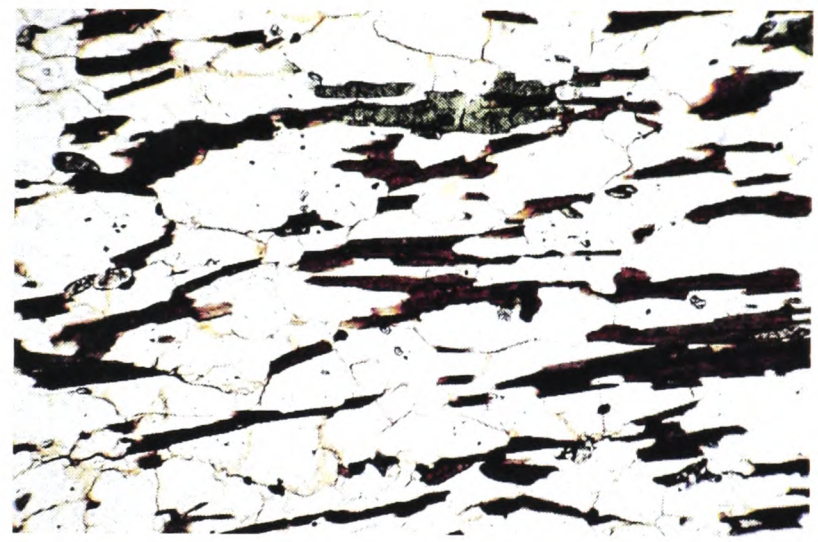
J

(i) Idioblastic garnet porphyroblasts statically overgrowing the S2 fabric. (Sample JDW 72, collected near the summit of the Rhotang Pass immediately above the Rhotang Gneissic Complex).

(j) Sericitised kyanite porphyroblasts enclosed within a coarse-grained matrix of biotite. (Sample JDW 211, collected from within the Rhotang Gneissic Complex, Khoksar village).



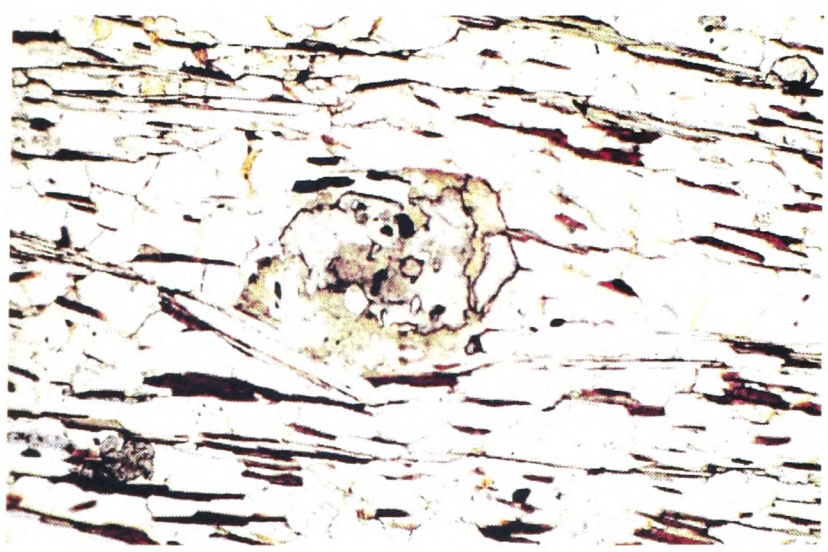
K



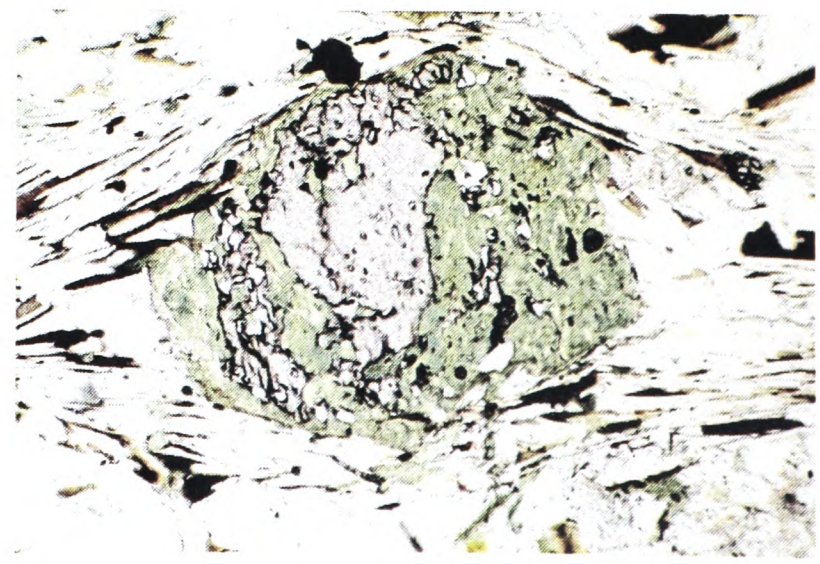
L

(k) Small, skeletal kyanite porphyroblast sub-parallel to the S2 fabric and partly wrapping a large garnet porphyroblast. (Sample JDW 92, collected ~1km north of Manali village).

(l) Small laths of hornblende forming part of the continuous S2 schistosity in the Crystalline Nappe (sample JDW 82, collected in the Beas valley, ~3km north of Manali).



M



N

(m) Chlorite replacing garnet in a semi-pelitic schist. (Sample JDW 18, collected from Sissu village).

(n) Chlorite replacing garnet in a semi-pelitic schist. (Sample JDW 87, collected in the lower limb of the Phojal-Kallath megafold, ~3km north of Katrain).

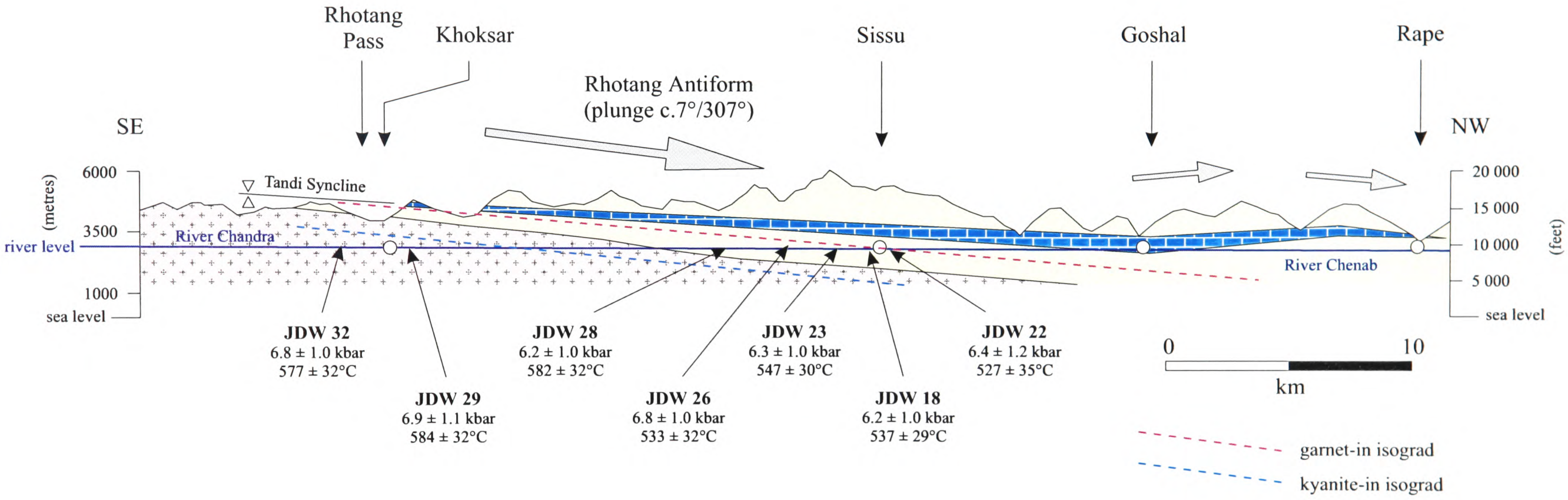
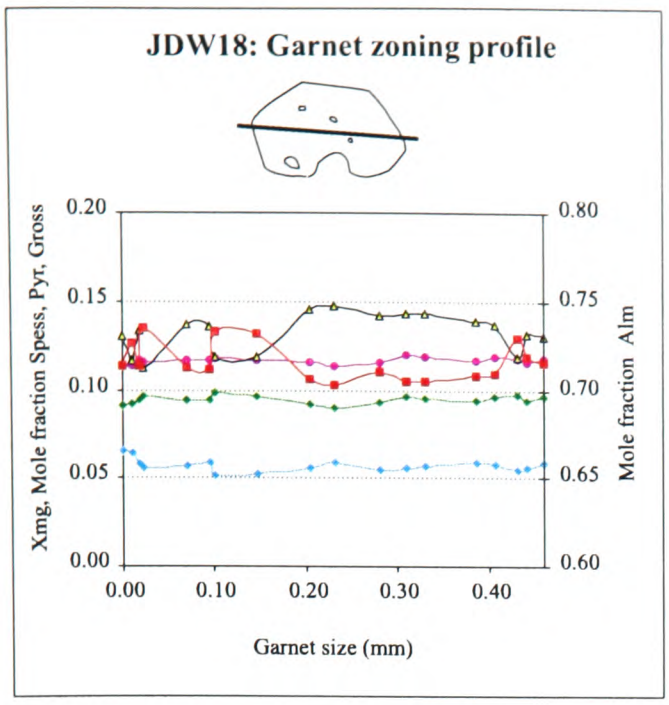
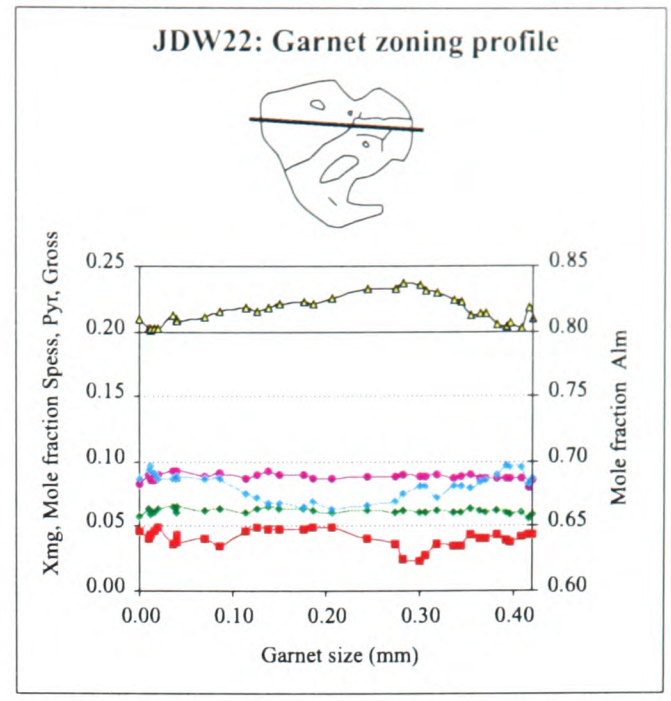
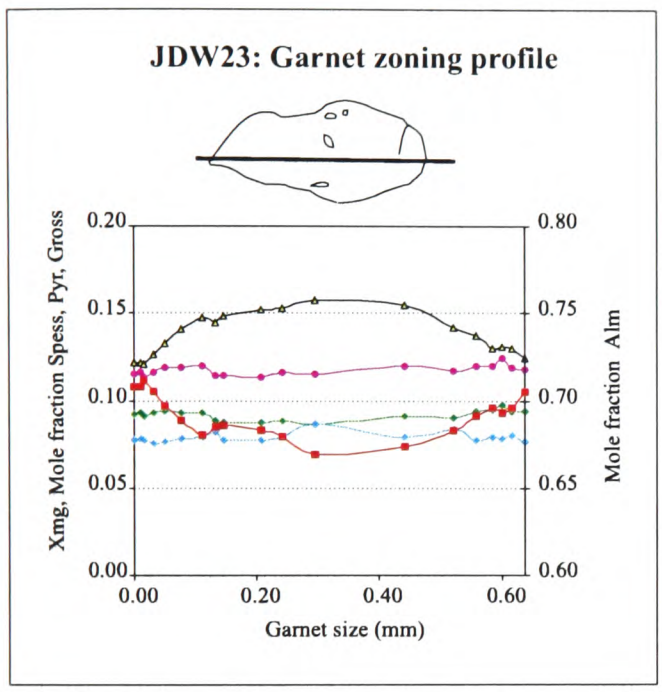
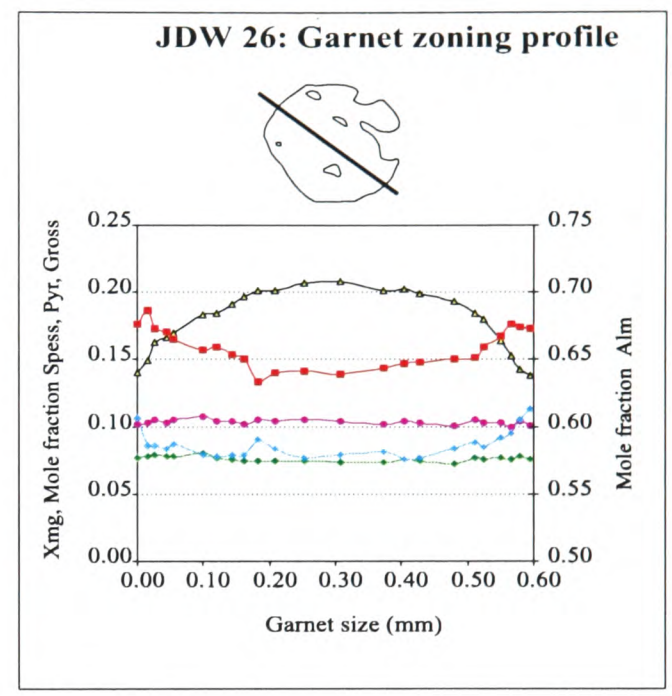


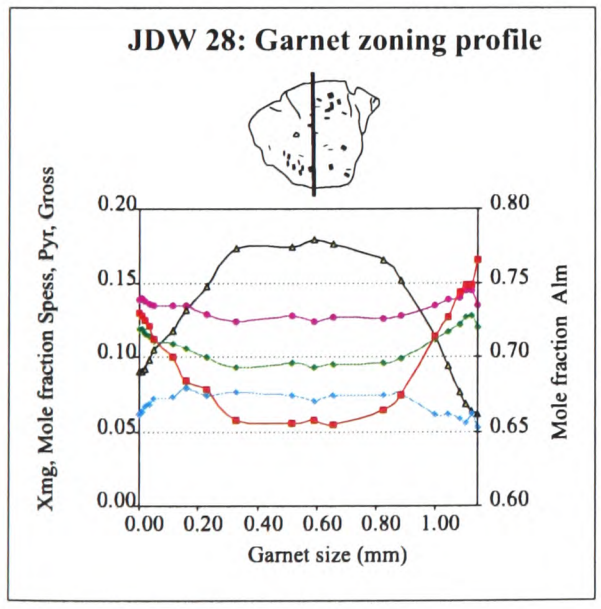
Figure 4.10a: Location of samples collected for mineral chemistry and thermobarometric analysis in the Chandra valley. Preferred P-T result is shown beneath each sample. Full P-T results are shown in Table 4.2. Annotation as for Figure 4.1.

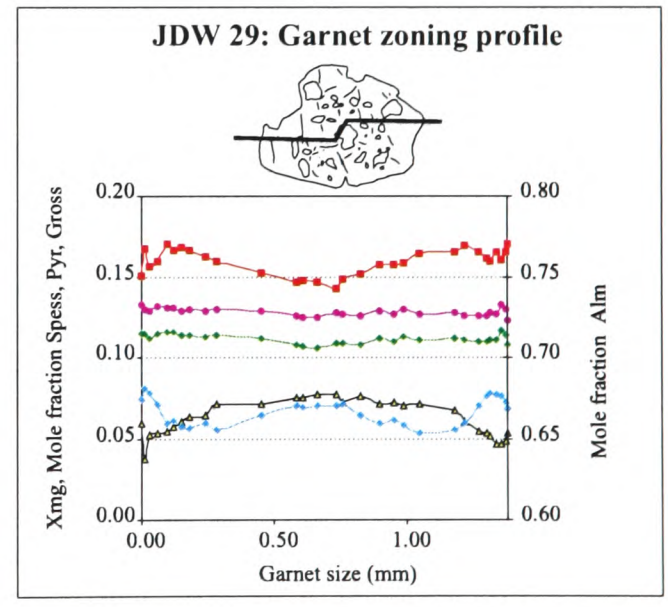


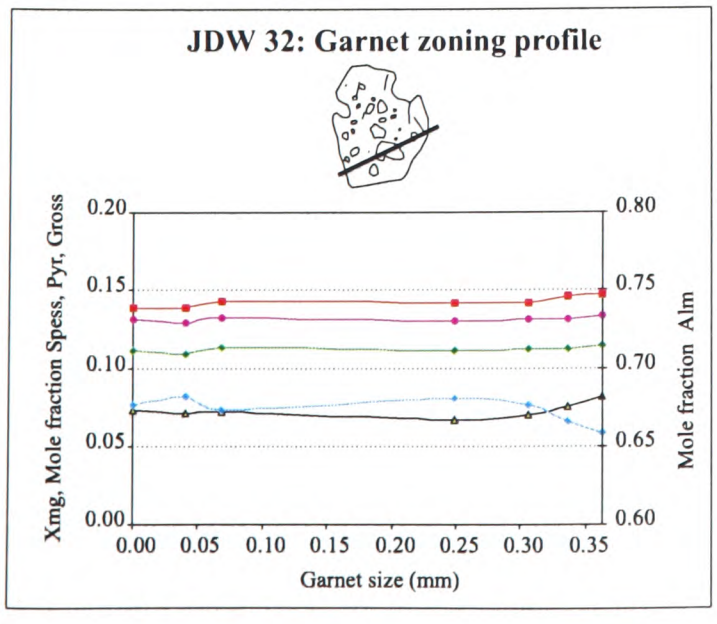












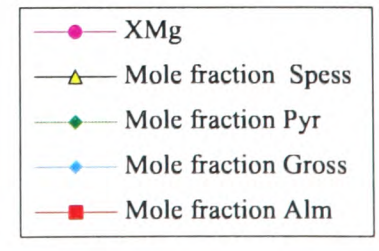


Figure 4.10b: Garnet zoning profiles of samples collected in the Chandra valley

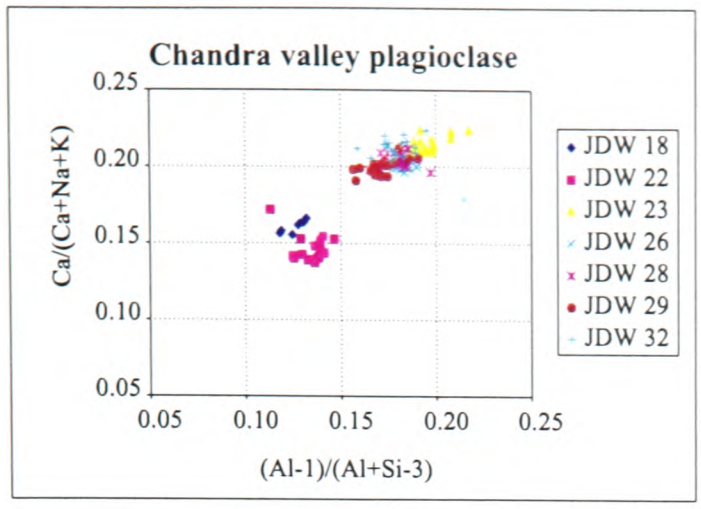


Figure 4.10c: Plagioclase compositions of Chandra valley samples.

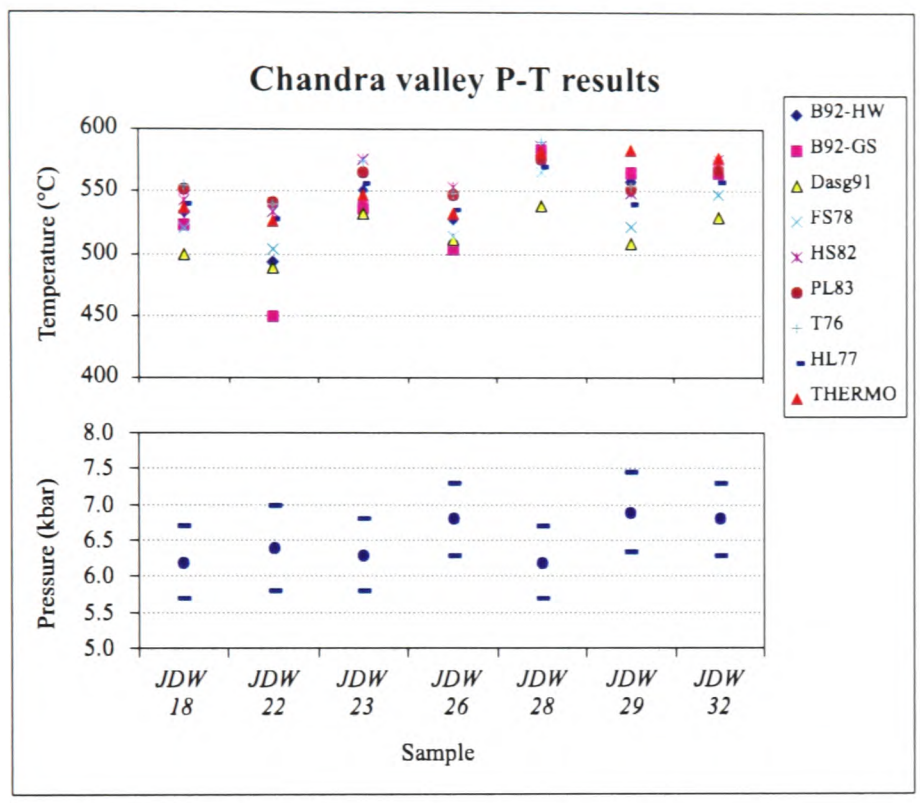


Figure 4.10d: Chandra valley P-T results. (See Table 4.2 for abbreviations)

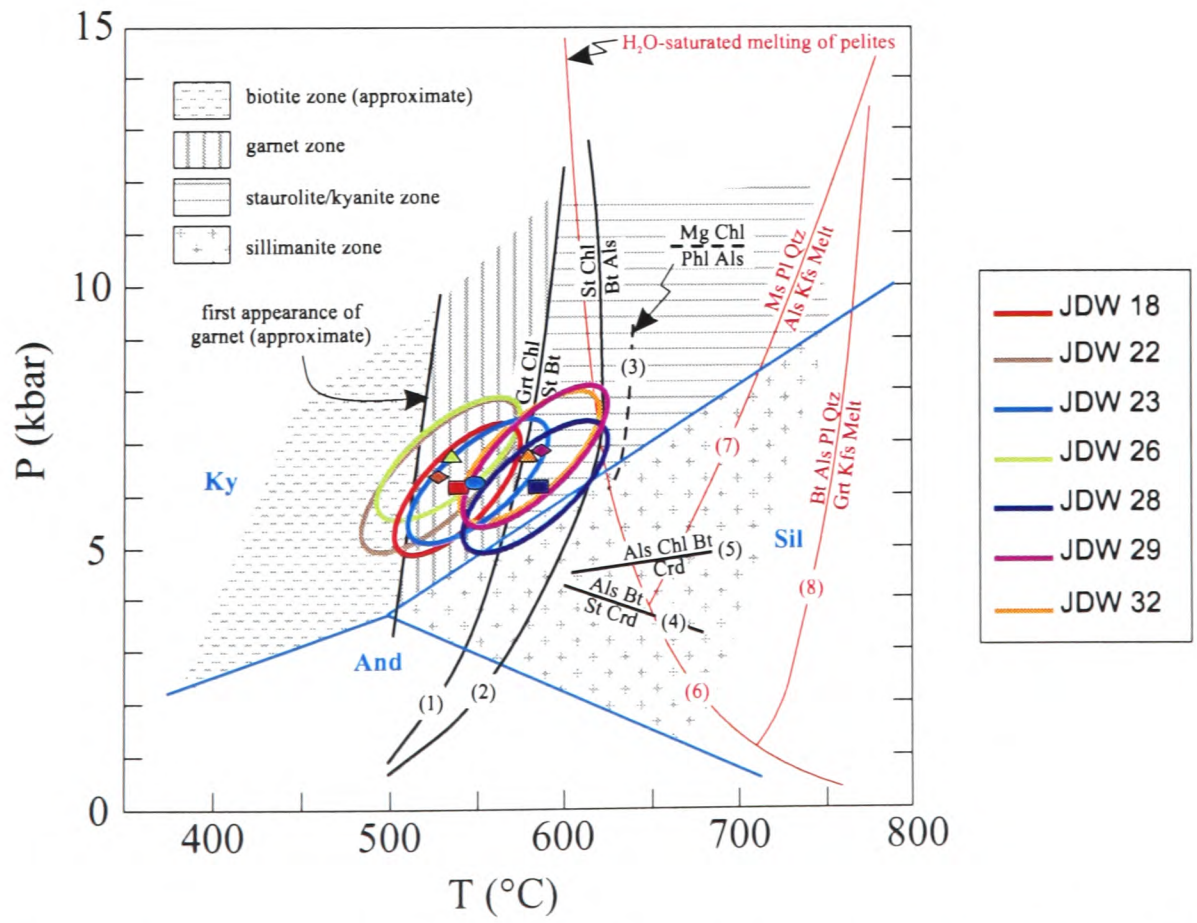


Figure 4.10e: P-T error ellipses for samples in the Chandra valley calculated using THERMOCALC (errors shown at the $1<\sigma<2$ level). The results reflect final equilibration at near-peak conditions and closely match the predicted P-T estimates based on field and petrographic observations. Solid and dashed black lines refer to reactions in the KFMASH and KMASH systems respectively. Reactions (1) to (3) taken from Spear (1993), reactions (4) and (5) taken from Harte (1975). Solid blue lines denote the Al-silicate phase diagram of Holdaway and Mukhopadhyay (1993). Red lines show the important vapour present and vapour absent melting reactions in metapelites. Reaction (6) taken from Thompson (1982), reaction (7) from Peto (1976) and reaction (8) from Le Bretton and Thompson (1988).

SAMPLE	T (°C)	P (kbar)
JDW 129	480 ± 37	5.0 ± 1.2
JDW 54	541 ± 30	6.4 ± 1.0
JDW 57	576 ± 32	6.1 ± 1.0
JDW 92	635 ± 33	7.9 ± 1.2
JDW 93	574 ± 36	7.8 ± 1.1
JDW 50	565 ± 31	7.2 ± 1.0
JDW 32	577 ± 32	6.8 ± 1.0

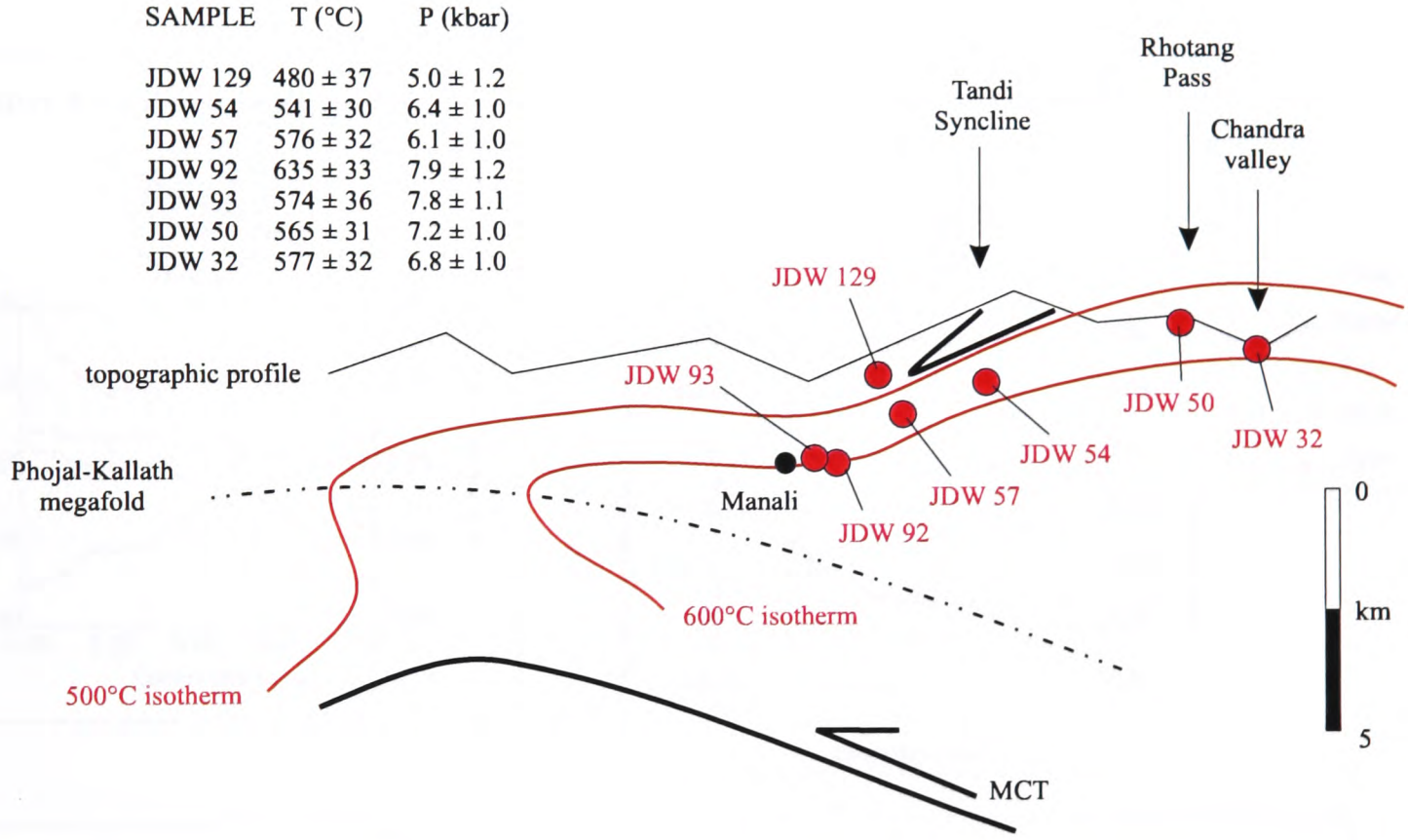
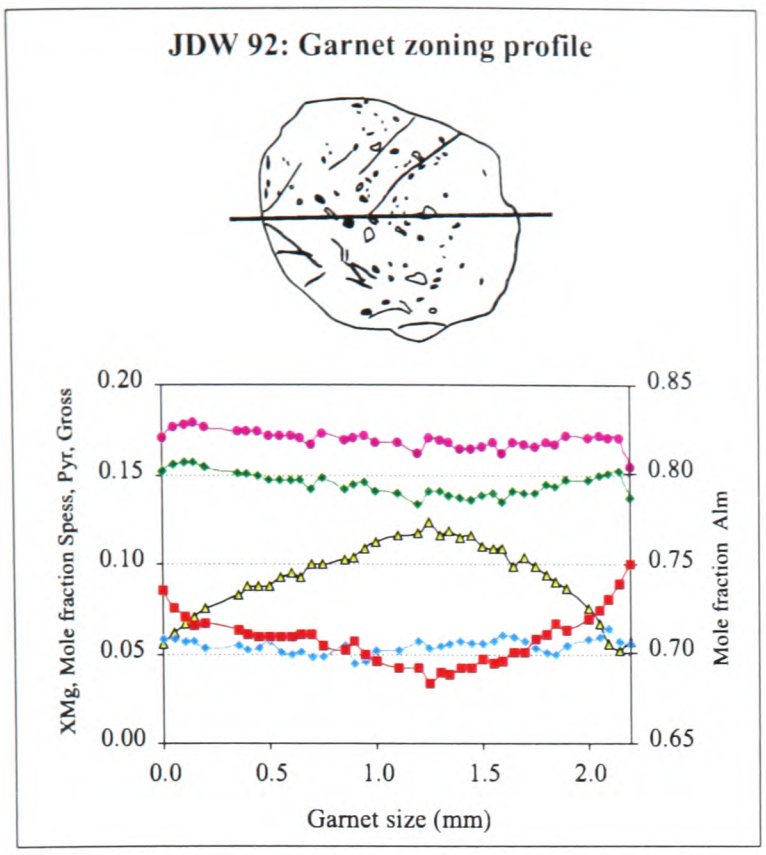
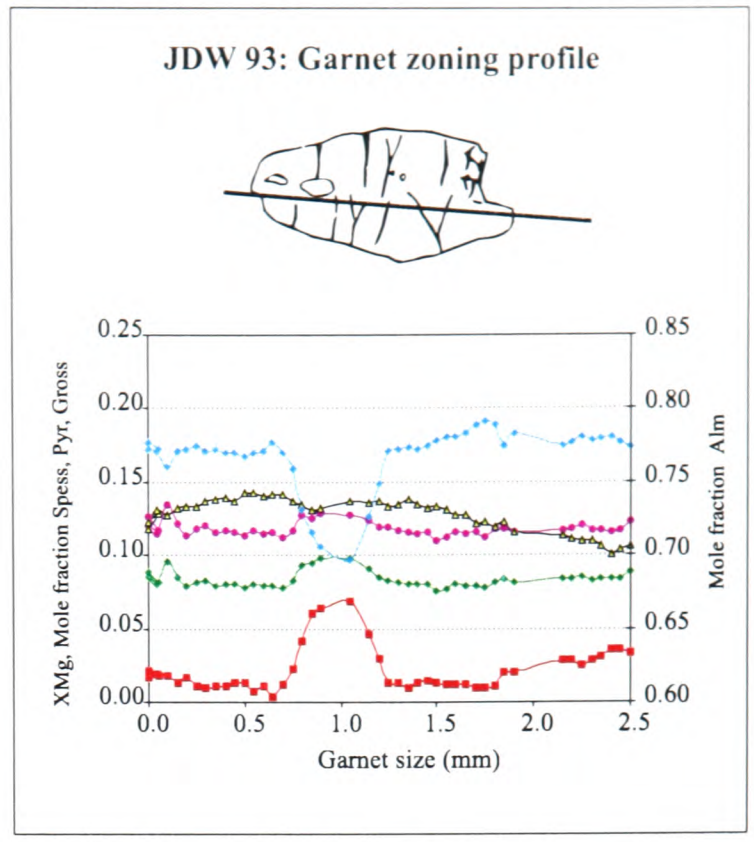
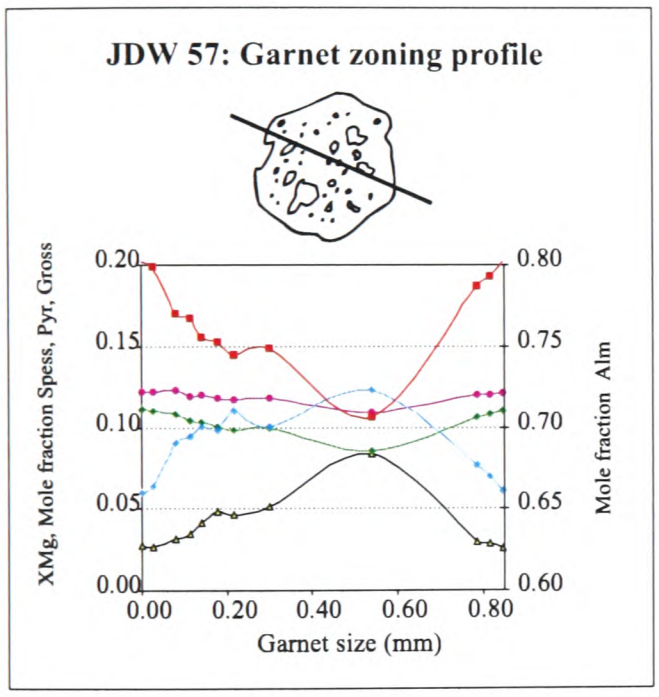
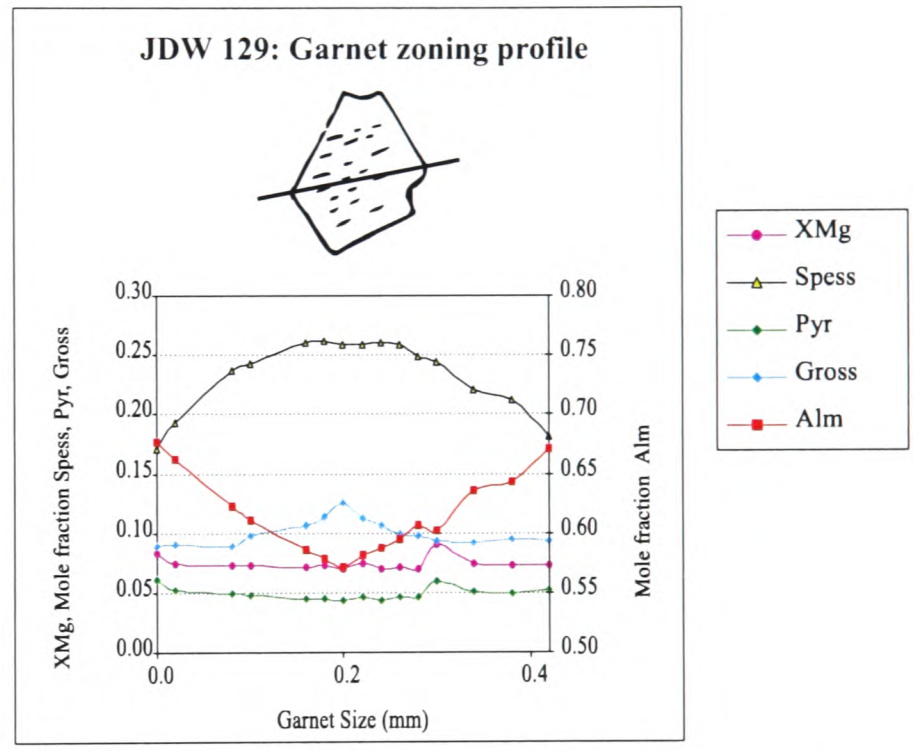


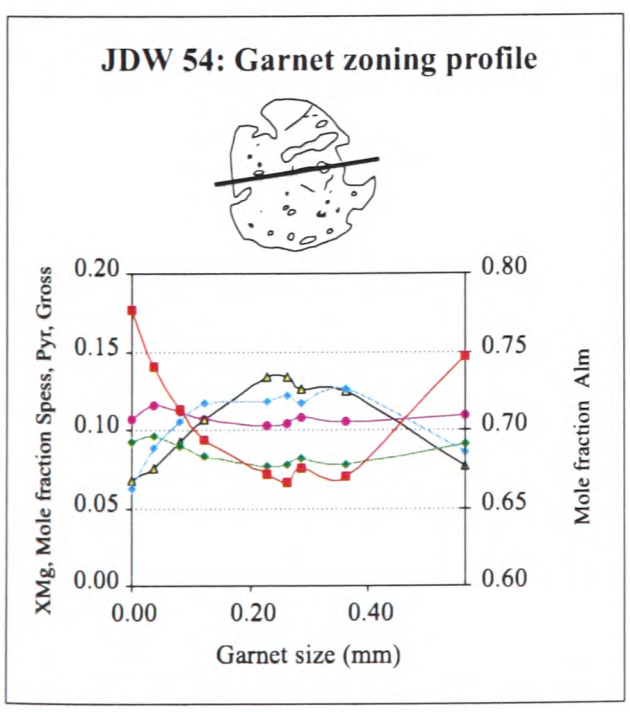
Figure 4.11a: Isotherm pattern in the Crystalline Nappe as determined from garnet-biotite thermometry (modified after Epard et al, 1995). The isotherms appear to be folded around the Phojal-Kallath megafold near the base of the slab. The projected location of samples collected for thermobarometric analysis in this study are shown as red circles. The preferred P-T result for each sample is also shown (see Table 4.3 for full P-T results). Also shown are some of the results from the Chandra valley traverse which project onto this line of section.











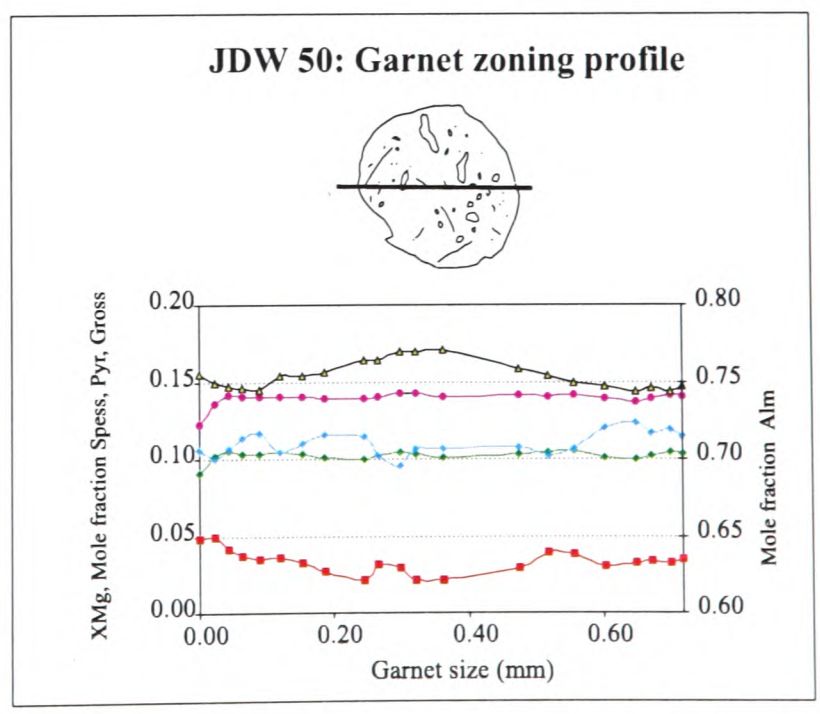


Figure 4.11b: Garnet zoning profiles of samples collected in the Beas valley

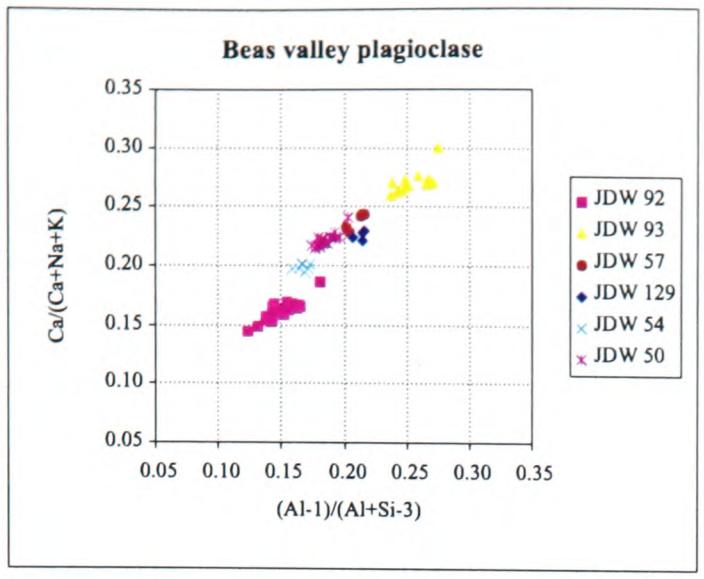


Figure 4.11c: Plagioclase compositions of Beas valley samples.

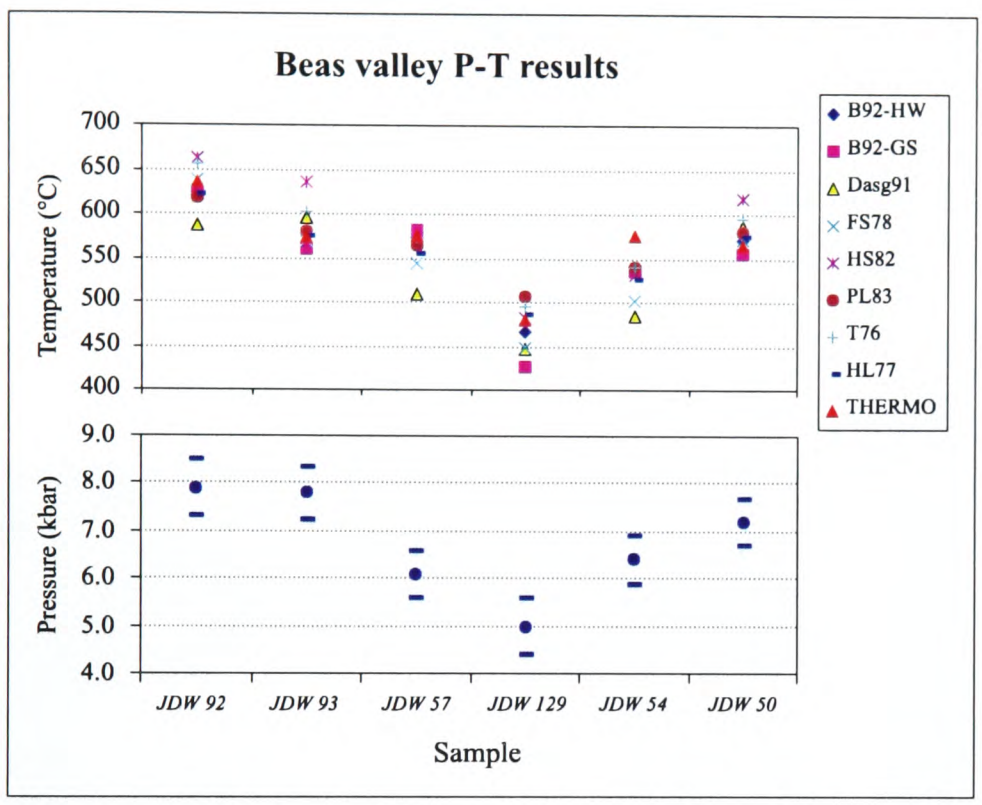


Figure 4.11d: Beas valley P-T results (see Table 4.3 for abbreviations)

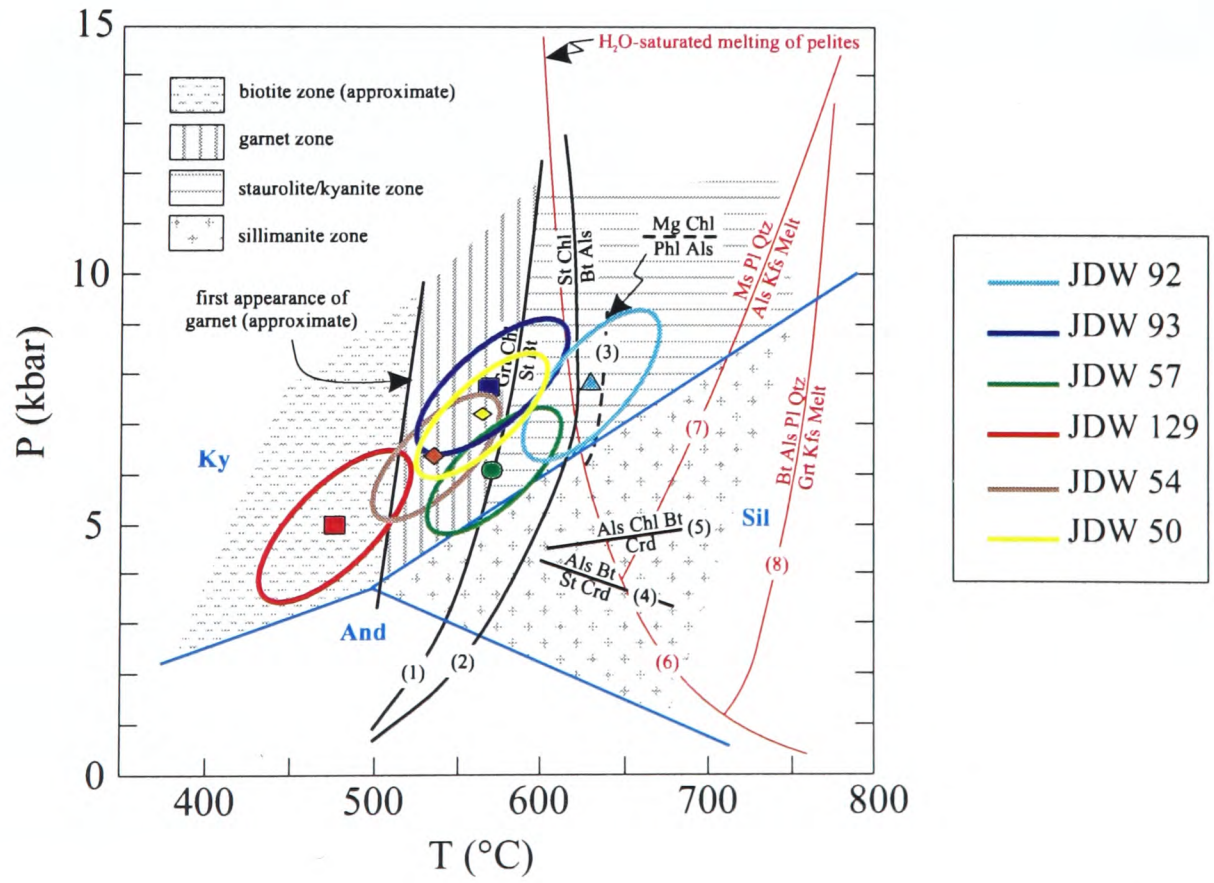
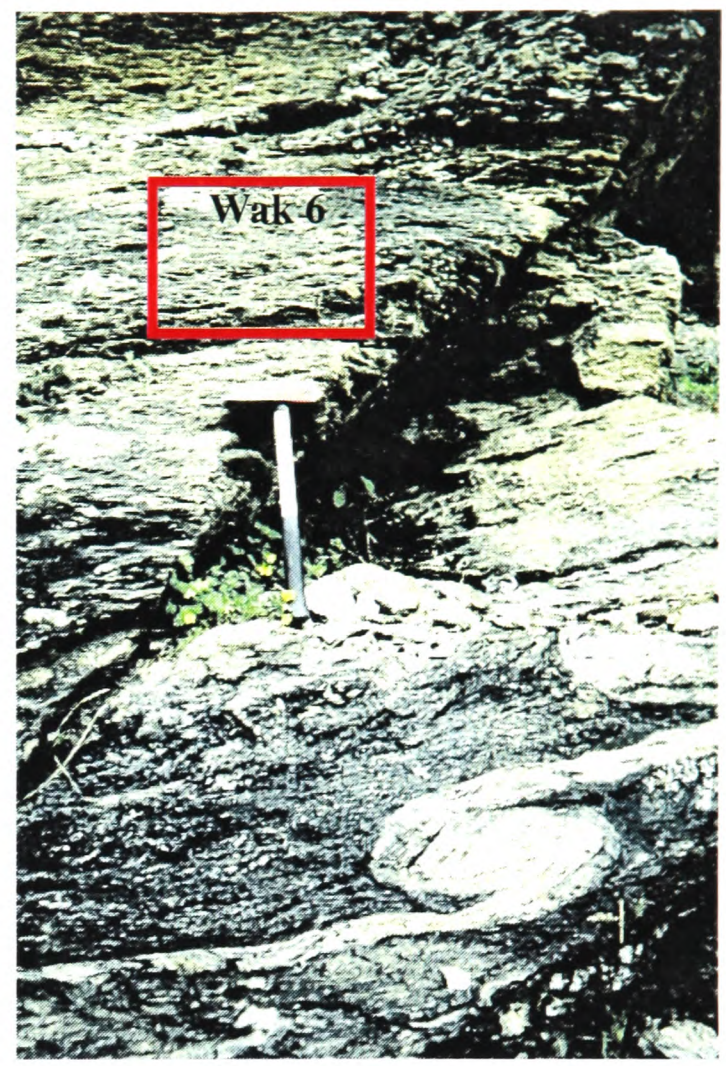


Figure 4.11e: P-T error ellipses for samples in the Beas valley calculated using THERMOCALC (errors shown at the $1<\sigma<2$ level). The results are interpreted to reflect final equilibration at near-peak conditions. Solid and dashed black lines refer to reactions in the KFMASH and KMASH systems respectively. Reactions (1) to (3) taken from Spear (1993), reactions (4) and (5) taken from Harte (1975). Solid blue lines denote the Al-silicate phase diagram of Holdaway and Mukhopadhyay (1993). Red lines show the important vapour present and vapour absent melting reactions in metapelites. Reaction (6) taken from Thompson (1982), reaction (7) from Peto (1976) and reaction (8) from Le Bretton and Thompson (1988).

A



B



C

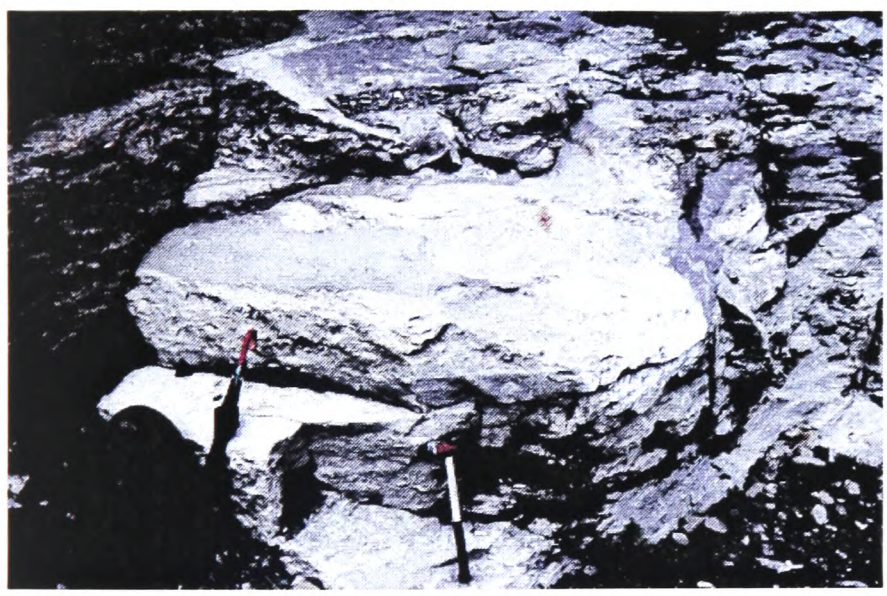


Figure 4.12:
(a) Alternating sequence of layer-parallel leucocratic pegmatites (Qtz + Ms + Pl + Kfs ± Grt ± Tur) and mafic paragneisses (Qtz Bt + Pl + Kfs ± Grt) within the Rhotang Gneissic Complex. The pegmatites contain a strong internal foliation which is parallel to the regional S2 schistosity. (Chandra valley, ~3km west of Khoksar).

(b) Intensely deformed leucocratic pegmatite within a sequence of kyanite-grade metapelites. The pegmatite contains a strong internal foliation which is folded by a SW verging F2 fold, thus suggesting syn-kinematic emplacement during the D2 deformation phase. Boxed area shows location of sample WAK 6 (collected for geochronological analysis, see Chapter 7). (Chandra valley, ~ 3km west of Khoksar).

(c) Disharmonically folded leucocratic pegmatite surrounded by mafic paragneisses. (Chandra valley, ~ 4km west of Khoksar).

Figure 4.13: Leucocratic pegmatites in the Crystalline Nappe (south of the Rhotang Pass).



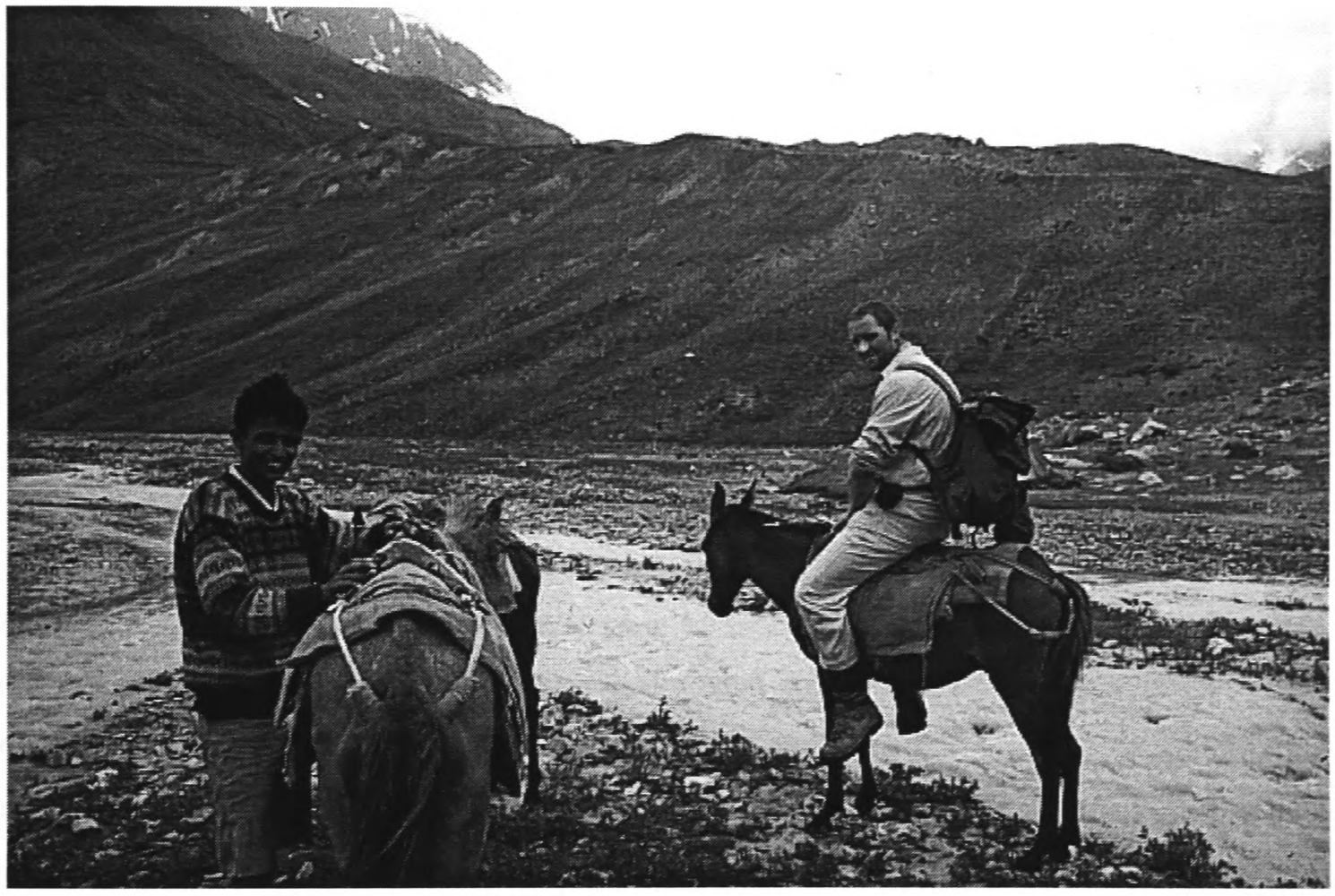
(a) Leucocratic pegmatite folded by a SW verging F2 fold in the kyanite-grade schists and gneisses of the Crystalline Nappe (~1km north of Manali village).



(b) Intensely deformed sequence of psammitic gneisses, quartz veins and leucocratic pegmatites in the core of the Phojal-Kallath megafold (~500m vertically above Bran village). The early generation of pegmaties and quartz veins are folded by SW verging F2 folds. A later generation of undeformed pegmatites intrude along the S2 surfaces (thick white band in lower part of picture).



(c) Disharmonically folded sequence of leucocratic pegmatites and psammitic gneisses in the core of the Phojal-Kallath megafold (Beragram nala, ~5km west of Bran village). The pegmatites cut across the S2 fabric in the Crystalline Nappe and are therefore the product of Himalayan metamorphism.



'Big' Steve riding a tiny horse across a braided river channel at the base of Mt. Gumburanjon. Pieray Lal (left) prepares the saddle for me to mount up.

Chapter 5

Geology of the western-central slab (Chamba Syncline and Miyar nala)

5.1 Introduction

This chapter presents structural and metamorphic observations made during a reconnaissance–style traverse through the Chamba Syncline and Kang La Dome in the western part of the study area (Figure 3.20). The traverse extends as far south as the Kalicha Pass and as far north as the Miyar Fault Zone, which is located on the southern flank of the Kang La Dome (Figure 5.1). Lithologically, the Chamba Syncline consists of a 3-5km-thick succession of unfossiliferous flyschoid sediments which are remarkably similar in appearance to the Precambrian-Cambrian Haimantas exposed in other parts of the study area. This is interpreted to suggest that the Chamba Syncline represents a low-grade, integral part of the High Himalayan Slab as opposed to a tectonic cover-sequence, as has been suggested by some previous authors (see Chapter 3). The northern limit of the Chamba Syncline is taken to be coincident with the first appearance of biotite-grade lithologies near Karpat village (Enclosure 2), and may be coincident with a zone of extensional deformation (see section 5.2.1). North of the Chamba Syncline, the biotite- and garnet-grade sediments of the Haimantas are discordantly intruded by the Precambrian-Cambrian(?) Kade granite (Figure 5.1). This granite becomes more intensely deformed towards the north and eventually gives way to an intercalated sequence of kyanite- and sillimanite-grade metapelites, banded orthogneisses, mafic gneisses, leucocratic pegmatites and crustal melt leucogranites, which collectively constitute the High Himalayan Crystallines (HHC) of the Kang La Dome. The fact that metamorphic grade progressively increases from south to north in Chamba Syncline and Miyar nala makes this an extremely important traverse since it allows the structure of the High Himalayan Slab to be investigated at progressively deeper structural levels.

5.2 Structure of the Chamba Syncline and Miyar nala

5.2.1 Deformation to the south of the Kade granite

Two distinct phases of deformation are recognised within the Haimantas to the south of the Kade granite (D_1 and D_2). In addition, there is tentative structural evidence to support a phase of late-stage extensional deformation (D_3) in this part of the slab.

D_1 deformation

The earliest recognisable phase of deformation in the Haimantas to the south of the Kade granite is characterised by kilometre-scale rounded folds of bedding (F_1) which are associated with a well-developed axial planar cleavage (S_1). These folds are best observed looking towards the NW from high above the southern side of the Chenab valley near the village of Hinsa. This style of deformation is extremely similar to the D_1 deformation phase seen in the Crystalline Nappe, which was responsible for the generation of the NE facing Tandi Syncline (see Chapter 4 for discussion). Indeed, the sub-parallel S_0/S_1 fabric can be traced in the Tandi Group as far west as Rape village, where it maintains a NW-SE strike and dips ~30-40° towards the SW (Enclosure 1). This fabric progressively steepens towards the west, becoming sub-vertical on the northern limb of a major antiform near the village of Udaipur at the confluence of the River Chenab and Miyar nala (Figures 5.1; 5.2a & b). Calcareous sands, silts and shales similar to those observed directly beneath the Tandi Group are exposed in the lower Miyar nala ~8km north of Udaipur (Enclosure 1), thus providing tentative evidence that the Tandi Syncline continues along strike towards the NW (Figure 5.1). The location of antiformal closures either side of the Tandi Syncline remains conjectural, however, owing to a lack of prominent marker horizons within the Haimantas. Black shales provide an indication of where these antiformal closures may be located (Figure 5.1), although it remains entirely speculative as to whether these form part of the same stratigraphic unit. Isoclinal F_1 folds are occasionally observed in regions of particularly high strain (Figure 5.2a), which may be coincident with the closures of major F_1 folds.

Between Udaipur and the Kalicha Pass, F_1 folds have an upright attitude and show no obvious asymmetry (Figure 5.2a). This style of deformation is exemplified by the Manjir Conglomerate, which is folded into the core of a major upright F_1 antiform to the north of the Kalicha Pass (Figure 5.1). North of Udaipur, the S_0/S_1 fabric becomes progressively more inclined towards the SW, thus implying that F_1 folds have a NE sense of vergence (Figure 5.1). This is consistent with the NE facing direction of the Tandi Syncline in the Chandra valley and suggests that D_1 deformation in the Chamba Syncline was also NE directed. Large-scale folds of inferred F_1 origin are overturned towards the NE in the mountainside to the east of Karpat village (Figure 5.2c), although only the lower limbs of these structures are preserved, making it difficult to accurately determine their sense of vergence. The tectonic significance of early NE-facing structures in the High Himalayan Slab was discussed in Chapter 4 with reference to the Tandi Syncline, which is located some 50 km along strike of the Chamba Syncline in the Chandra valley (Enclosure 1). The most likely tectonic explanation of this structure is that it developed in a major backfold during the D_1 deformation phase. The continuity of NE-facing structures along the Chandra valley into the Chamba Syncline implies that this backfolding event was developed on a regional scale. A model to account for this is presented in the summary section at the end of this chapter.

The S_1 cleavage is defined by a strong layering of detrital and metamorphic chlorite, muscovite and ilmenite (Figures 5.2d-f) at low metamorphic grades, with increasing amounts of biotite observed along the S_1 fabric at higher metamorphic grades. D_1 deformation in the Chamba Syncline is

therefore interpreted to be syn-metamorphic. Owing to the relatively low-grade of these sediments, very few mineral stretching lineations were observed on any planar surfaces. Biotite lineations were observed on some S_1 surfaces at higher metamorphic grades and ubiquitously plunged steeply towards the SW in a down-dip direction (Figure 5.1), thus implying that strike-slip deformation was not important in this part of the slab. The Chandra Dextral Shear Zone described in Chapter 4 cannot be traced along strike into the Chamba Syncline, suggesting that this is a localised zone of transpression.

D_2 deformation

D_2 deformation is recognised in the Chamba Syncline by the development of localised F_2 folds in pelitic schists which occasionally display a penetrative S_2 cleavage. F_2 folds are co-axial with F_1 folds and have a similar orientation and plunge to F_2 folds observed in the Chandra valley (Figure 5.1). This implies that there was no significant change in the direction of maximum compressive stress during D_1 and D_2 deformation phases along the entire length of the Chandra and Chenab valleys. Immediately north of Udaipur, S_2 forms a shallowly dipping penetrative cleavage which is axial planar to asymmetrical F_2 folds with sub-horizontal axes (Figures 5.3a & b). These folds are not developed in the adjacent sandstone units, which implies that rheology exerted a strong control on the style of folding in the Chamba Syncline. The asymmetry of these folds is consistent with a top-to-the-north-east kinematic transport direction during the D_2 deformation phase. At some localities in the lower Miyar nala, the intersection of the S_0/S_1 and S_2 fabrics is suggestive of a top-to-the-north-east shear sense (Figure 5.3c), which is confirmed in thin section (Figure 5.3d). These observations suggest that D_2 deformation in the lower Miyar nala was associated with a top-to-the-north-east kinematic transport direction, although It is equally possible that the top-to-the-north-east shear-sense was produced during co-axial flattening of the sub-vertical S_0/S_1 fabric (Figure 5.3e). No evidence was found to support the existence of any major SW-verging folds in the Chamba Syncline.

Extensional deformation in the Chamba Syncline (D_3) ?

The intensity of deformation progressively increases towards the north in the Miyar nala, which is concomitant with a progressive increase in metamorphic grade in the same direction (Enclosure 2). True biotite-grade lithologies are first exposed immediately north of Karpat village, ~16 km north of Udaipur. The transition between the chlorite-zone and the biotite-zone appears to be transitional, with no evidence to suggest that they are separated by any *major* structural or metamorphic discontinuities (Enclosure 2). However, it is important to note that the intensity of deformation is markedly more intense in the biotite-grade lithologies immediately north of Karpat than it is in the chlorite-grade lithologies to the south of Karpat. This suggests the possibility that the transition between these two metamorphic zones may be coincident with a broad zone of distributed deformation. Immediately along strike and to the NW of Karpat village, Frank *et al.* (1995) and Stephenson (1997) observed a similar zone of distributed deformation, which Stephenson (1997) refers to as the Kilar Shear Zone (Enclosure 1). Frank *et al.* (1995) claim that this zone displays extensional fabrics which are

indicative of a top-to-the-south-west shear-sense. This is consistent with the observation that lower-grade lithologies are exposed in the hangingwall to the south and the observed increase in metamorphic grade towards the north. Stephenson (1997) claims that fabrics in this zone display both top-to-the-north-east and top-to-the-south-west shear-sense indicators and that this zone marks the transition between the Chamba Syncline and the crystalline units of the High Himalayan Slab. During personal field investigations, fabrics which displayed both top-to-the-south-west and top-to-the-north-east shear-sense indicators were observed in a zone of intense deformation, ~2 km north of Karpat village (Figure 5.4). These fabrics were observed in an intensely deformed sequence of biotite-grade schists which are cross-cut by several 50-100cm-wide leucocratic pegmatites (Figure 5.4). The tectonic significance of these fabrics remains uncertain. They may imply that the transition between the chlorite zone and the biotite zone is a diffuse extensional shear zone (hereafter referred to as the Karpat Shear Zone), which could well represent a lateral equivalent of the Kilar Shear Zone. More detailed mapping is needed to verify this. It should be stressed that lithologies in the chlorite zone and biotite zone are extremely similar in appearance (i.e. they comprise unfossiliferous, magnesium-rich sands, silts and shales), and that they are all interpreted to form part of the Lower Palaeozoic Haimantas (see Chapter 3). The Karpat Shear Zone is therefore interpreted to be relatively minor, late-stage (syn/post-metamorphic) structure which does not significantly offset the stratigraphic and metamorphic succession in the Miyar nala. The extent to which the Karpat Shear Zone offsets the metamorphic isograds remains uncertain.

5.2.2 Deformation in the Kade granite

North of Karpat, the Haimantas are intruded by the Precambrian-Ordovician Kade granite (Enclosure 1; Figure 5.1). This megacrystic K-feldspar granite is relatively undeformed on its southern margin and displays a weakly-developed SW-dipping foliation which is defined by a slight flattening of quartz and feldspar. This fabric is parallel to the S_0/S_1 fabric in the Chamba Syncline, suggesting that it probably developed during the D_1 deformation phase. The intensity of this fabric increases northwards, such that the Kade granite is best described as a banded augen gneiss/orthogneiss near the village of Patam. None of the observed outcrops displayed any shear-sense indicators, suggesting that this fabric may have developed at depth by co-axial flattening. The Kade granite eventually becomes an intensely foliated orthogneiss to the north of Patam, where it is observed to be intercalated with the kyanite- and sillimanite-grade metapelites of the HHC. The transition between the Kade granite and the HHC is gradational and corresponds to a region of very high strain, hereafter referred to as the Miyar Fault Zone (MFZ).

5.2.3 Deformation in the Miyar Fault Zone and Kang La Dome

The Kang La Dome

The Kang La Dome represents a region of sillimanite-grade migmatitic gneisses and crustal melt leucogranites (i.e. the HHC) which is located in the immediate footwall of the ZSZ in the upper part of

the slab (Enclosures 1 & 2; Figure 5.1). The metamorphic protoliths of lithologies within the Kang La Dome cannot be accurately determined, but are believed to be the high-grade equivalents of the overlying Haimantas and Precambrian-Ordovician granites exposed in the lower grade parts of the High Himalayan Slab in SE Zanskar and NW Lahaul (see Chapter 3). Several lines of evidence support this interpretation: (1) metamorphic grade progressively increases towards the north in the Miyar nala from the chlorite zone through to the sillimanite zone, with no evidence to support the existence of any *major* structural or metamorphic discontinuities in this part of the slab (Figure 5.1); (2) the metapelitic schists and banded orthogneisses and augen gneisses within the Kang La Dome are remarkably similar in appearance to the sediments which comprise the Lower Palaeozoic Haimantas and the Precambrian-Ordovician granites exposed in the lower Miyar nala; and (3) geochronological work by Pognante *et al.* (1990), Noble and Searle (1995) and Chapter 7 of this thesis demonstrates that the protoliths of the HHC are at least Lower Palaeozoic in age. However, the possibility that parts of the HHC within the Kang La Dome represent the pre-Himalayan crystalline basement upon which the Haimantas were deposited cannot be entirely ruled out (see Chapter 3).

Metamorphic grade decreases away from the core of the Kang La Dome in all directions (Enclosure 2). At the top of the slab, this is interpreted to be the result of extensional normal faulting along the ZSZ (Figure 5.1). Fabrics in the ZSZ dip ~15-25° towards the NE (Figure 5.1) and display numerous top-to-the-north-east shear-sense indicators (see Chapter 6). To the south, the decrease in metamorphic grade in the Kang La Dome may be related to a similar process of extensional deformation along the Miyar Fault Zone (see below). The decrease in metamorphic grade towards Darcha is interpreted to be the result of the regional plunge of structures towards the south-east (Enclosure 2).

The Miyar Fault Zone (MFZ)

The Miyar Fault Zone (MFZ) is located in the upper Miyar nala to the north of the Kade granite, on the southern flank of the Kang La Dome (Figures 5.1 & 5.5). The MFZ was originally mapped as the Miyar Thrust by Pognante *et al.* (1990), who described this structure as:

"a shear zone very well exposed in the Miyar Valley, where it dips 30-45° south-westward. Here it is up to a few tens of metres thick and separates the Kade Unit from the HHC. Kyanite-staurolite- and garnet-biotite-bearing mylonites occur along this boundary in the HHC and the Kade Unit, respectively."

No evidence was found to support the existence of well-exposed shear zone in this part of the slab, as suggested by Pognante *et al.* (1990). Personal field observations suggest that the so-called Miyar Thrust actually represents a several-kilometre-wide zone of intense deformation which is recognised in the field by the appearance of an intercalated succession of kyanite- and sillimanite-grade pelitic schists, paragneisses, augen gneisses and orthogneisses which are concordantly (and

occasionally discordantly) intruded by a number of leucocratic pegmatites and crustal melt leucogranites (Figures 5.1 & 5.5).

Deformation is extremely intense throughout the MFZ and most lithologies (with the exception of several discordant, undeformed leucogranites) possess a well-developed tectonic foliation which dips 30-50° towards the SW (Figures 5.1 & 5.5). Biotite and muscovite (and more rarely staurolite, kyanite and sillimanite) define a strong mineral stretching lineation on this foliation which consistently plunges towards the SW in a down-dip direction (Enclosure 3; Figure 5.5). The foliation itself is axial planar to an early generation of isoclinal folds and is folded by a second generation of isoclinal folds (Figures 5.6a & b). The dominant tectonic foliation in the MFZ is, therefore, at the very least, an S_2 fabric and is unrelated to S_0/S_1 fabric seen in the Chamba Syncline further south. Inclusion trails in porphyroblastic staurolites within the MFZ preserve the remains of an earlier tectonic fabric (Figure 5.8b), which may be analogous to the S_0/S_1 fabric seen in the Chamba Syncline. None of the folds in the MFZ showed any systematic sense of vergence and could not be used to ascertain anything about the kinematics associated with isoclinal folding. Nevertheless, the intensity of fabric development in the MFZ provides strong evidence for a major phase of crustal shortening and thickening in this part of the slab, which is almost certainly Himalayan in age. Given the observation that structures in the Chamba Syncline further south are overturned towards the NE, it is possible that the MFZ marks the site of an early SW-dipping thrust.

The latest phase of movement along the MFZ is almost certainly extensional, as indicated by the localised development of extensional shear band fabrics which cross-cut the dominant tectonic fabric in the MFZ (Figures 5.5b & 5.6c). These fabrics are not especially common, suggesting that the MFZ forms part of a several-kilometre-wide zone of extensional deformation. This is consistent with the observation that the MFZ is located directly along strike of the Dharlang Lineament (Enclosure 1), which Stephenson (1997) interpreted to be a major syn-metamorphic detachment located on the southern flank of the Kang La Dome. Indeed, Pognante *et al.*'s (1990) description of the Miyar Thrust actually defines an extensional normal fault which juxtaposes biotite- and garnet-grade assemblages in the hangingwall against staurolite- and kyanite-grade assemblages in the footwall. However, personal field observations do not support this simple metamorphic succession. Figure 5.5b shows a transect through the MFZ which demonstrates that garnet-, staurolite-, kyanite-. sillimanite- and cordierite-bearing assemblages are intercalated throughout this entire zone, with no clear juxtaposition of different metamorphic units above one another. The distinction made by Pognante *et al.* (1990) is therefore considered to reflect a bulk-composition or fluid control, rather than a true metamorphic discontinuity.

5.3 Metamorphism in the Chamba Syncline and Miyar nala

Metamorphic grade is observed to increase progressively from south to north in the Chamba Syncline and Miyar nala (Enclosure 2; Figure 5.1). The increase in metamorphic grade towards the north is consistent with the south-westerly dip of the regional tectonic foliation and the NE vergence

of D_1 and D_2 structures (see section 5.2). Metamorphic isograds are therefore interpreted to be the right way-up and to dip shallowly towards the SW to the south of the Kang La Dome, and towards the NE in the ZSZ at the top of the slab (Figure 5.1). Owing to the mountainous nature of the terrane, the reconnaissance style of mapping and the problems of accurately defining the position of isograds in the field, the dip of the isograds shown on Figure 5.1 should be treated with some scepticism – a more detailed three-dimensional investigation is needed to verify their orientation. The extent to which the Karpat Shear Zone and MFZ disrupt the metamorphic succession is uncertain. Field and petrographic observations suggest that slight increases in metamorphic grade are observed across these structures, although neither appear to be responsible for major disruptions to the metamorphic sequence.

Chlorite zone

The sediments within the Chamba Syncline are located within the chlorite zone (Enclosure 2). Chlorite is observed forming the fine grained matrix between the detrital quartz and feldspar clasts in the more psammitic lithologies and is also observed growing along S_1 cleavage domains in the more pelitic lithologies (Figures 5.2d & e). In some samples, large chlorite stacks are observed growing between the S_1 cleavage lamellae (Figures 5.2e & f).

Ductile deformation fabrics at the outcrop scale are not as well developed in the chlorite zone as they are higher-grade parts of the slab. At the thin section scale, sub-grain development, sutured grain boundaries, undulose extinction and core-and-mantle structures in detrital quartz grains suggest that recovery and dynamic recrystallisation processes were operating in the chlorite zone. Feldspars rarely show evidence of dynamic recrystallisation, although some feldspars occasionally preserve bent twins. Together, these microstructural observations suggest that deformation occurred at temperatures in the range of *c.*300-400°C in the chlorite zone (Tullis & Yund, 1977). Dynamic recrystallisation fabrics are better preserved in the chlorite zone than they are in higher-grade parts of the slab, where they are strongly annealed. This implies that high-temperature re-setting of microstructures has occurred in deeper structural levels, the effects of which have not been felt at shallower structural levels.

Biotite zone

With increasing metamorphic grade, chlorite and phengitic green muscovite become increasingly scarce and are replaced by biotite. This implies that the main biotite-forming reaction in this part of the slab probably involved a continuous KFMASH reaction similar to:

phengite + chlorite → biotite + phengite-poor muscovite + quartz + H_2O

Garnet zone

The first occurrence of garnet in metapelites is taken to mark the position of the garnet-in isograd in the Miyar nala, and is located ~3 km north of Karpat, to the south of the Kade granite (Enclosure 2, Figure 5.1). The position of this isograd is somewhat tenuous since only one garnet-bearing sample

was observed in the field (sample JDW 182). This sample was collected for microstructural examination and thermobarometric analysis (location shown on Figure 5.1). The garnets in this sample are euhedral and appear to be syn/post-kinematic with respect to the matrix foliation (Figure 5.7a), suggesting them to be Himalayan in age. They show no obvious textural evidence of zoning but preserve conventional prograde chemical growth zoning profiles with minor evidence of retrograde re-equilibration at their rims, as defined by a slight increase in X_{Sps} and a decrease in X_{Mg} (Figure 5.7b). Using the techniques outlined in Appendix A, this sample recorded a P-T estimate of 5.9 ± 0.8 kbar and 527 ± 12°C (Table 5.1), which is interpreted to be a near-peak estimate. A pressure of *c.*6 kbar corresponds to an overburden of ~22 km (assuming a lithostatic gradient of 3.71km/kbar), which may have been provided by the overthrusting of units towards the NE during the D_1 deformation phase in the Chamba Syncline (see section 5.2.1). Removal of this overburden could be attributed to uplift and erosion, although it could equally be attributed to rotational deformation in the Chamba Syncline (i.e. it is possible that the S_0/S_1 fabric in the Chamba Syncline once occupied a much flatter-lying attitude than its current upright orientation suggests).

Approximately 3 km to the north of JDW 182, the sediments of the Chamba Syncline and lower Miyar nala are discordantly intruded by the Kade granite (Figure 5.1). This disrupts the metamorphic succession and Barrovian metamorphic assemblages are not observed again until the metapelites in the MFZ are encountered to the north of Patam. Metamorphism in the MFZ and Kang La Dome is discussed in the next section.

5.3.1 Metamorphic mineral growth in the Miyar Fault Zone and Kang La Dome

The MFZ is defined in section 5.2.3 as 'a several-kilometre-wide zone of intense deformation which is recognised in the field by the appearance of an intercalated succession of kyanite- and sillimanite-grade pelitic schists, paragneisses, augen gneisses and orthogneisses which are concordantly (and occasionally discordantly) intruded by a number of leucocratic pegmatites and crustal melt leucogranites'. The following sub-sections describe the appearance of various Barrovian metamorphic minerals seen in the metapelites of the MFZ and attempt to relate the growth of these to the metamorphic evolution experienced by this part of the slab. The location of sample numbers referred to in this section is shown on Figure 5.5b.

Muscovite and biotite

Biotite forms a ubiquitous phase in the metapelites of the MFZ. Most biotites form coarse-grained aggregates which are observed growing parallel to the regional tectonic foliation. Many of the biotites exhibit extensive radiation damage, which is attributed to the decay of radiogenic phases such as monazite and zircon which are particularly abundant in the MFZ. Muscovite is a relatively scarce phase in the metapelites in the MFZ and is only occasionally observed in equilibrium with biotite in some pelites.

Garnet

Garnet is observed forming large rounded porphyroblasts in some of the Al-rich metapelites in the MFZ (samples JDW 186 and JDW 194). Smaller, anhedral garnets are observed in some of the more Al-poor metapelites in the MFZ (e.g. JDW 184). A more detailed description of garnet morphologies in these samples is given in section 5.3.2.

Staurolite

Staurolite is observed in some of the metapelites in the MFZ (e.g. JDW 186, JDW 197). Many of these staurolites contain graphitic inclusions (Figure 5.8a), some of which preserve isoclinal fold closures (Figure 5.8b), suggesting that the staurolite overgrew a pre-existing tectonic fabric. The possibility that this inclusion fabric is pre-Himalayan in age cannot be ruled out entirely, but seems extremely unlikely. This fabric is therefore interpreted to be related to the crustal shortening and thickening history of the High Himalayan Slab during the Tertiary. There is no textural evidence in any of the studied samples to say how staurolite growth occurred, but is believed to have been by a prograde KFMASH reaction similar to:

garnet + chlorite + muscovite → staurolite + biotite + quartz + H_2O

at temperatures of *c.*560-620°C (Figure 5.9). It is also possible that some staurolite growth occurred by the continuous KFMASH reaction:

chlorite + muscovite → staurolite + biotite + quartz + H_2O

Kyanite

Kyanite is observed forming large (*c.*1-5cm) randomly orientated laths in some of the metapelites in the MFZ. It is occasionally observed to be sub-parallel to the dominant tectonic foliation, suggesting it to be pre/syn-kinematic with respect to deformation in the MFZ. Kyanite growth is attributed to the prograde KFMASH reaction:

staurolite + chlorite + muscovite → kyanite + biotite + quartz + H_2O

at temperatures in excess of *c.*580°C (Figure 5.9). Evidence for this reaction is preserved in sample JDW 197, where staurolite is observed being replaced by coarse-grained muscovite (Figures 5.8a & b). Although muscovite is a reactant in the above reaction, the breakdown of staurolite produces more muscovite than is consumed during the growth of kyanite and biotite (Guidotti, 1973). In samples which contain kyanite but no staurolite (e.g. JDW 185 & JDW 195), it is possible that the above reaction went to completion (i.e. the reaction stopped when all the available staurolite was

consumed). It is equally possible that kyanite in these magnesian samples grew at slightly higher temperatures by the prograde KMASH reaction:

$$\text{Mg-chlorite} + \text{muscovite} \rightarrow \text{phlogopite} + \text{kyanite} + H_2O$$

Similar reactions were proposed for the origin of kyanite in the metapelitic schists of the Crystalline Nappe near Khoksar village (see Chapter 4).

Sillimanite

Prismatic and fibrolitic sillimanite are observed growing parallel to and across the dominant tectonic foliation in the MFZ (Figure 5.8c-g). Growth of sillimanite in metapelites is generally attributed to the replacement of kyanite by sillimanite as a result of increasing temperature and/or decreasing pressure (Figure 5.9). However, no textural evidence was observed in any of the studied samples to support this direct transformation. Instead, fibrolite is nearly always observed growing within enclaves of quartz and muscovite (Figure 5.8c-f) and occasionally as fibrous bundles within sheaves of biotite (Figure 5.8g). In some samples, kyanite is occasionally observed to be surrounded by a mantle of coarse grained quartz and muscovite (Figure 5.8h-j). These textures support the work Carmichael (1969), who suggested that the transformation of kyanite to fibrolitic sillimanite occurred by ionic transfer of material in an aqueous fluid involving the reactions:

$$3 \text{ kyanite} + 3 \text{ quartz} + 2\ K^+ + 3\ H_2O \rightarrow 2 \text{ muscovite} + 2\ H^+$$

$$2 \text{ muscovite} + 2\ H^+ \rightarrow 3 \text{ sillimanite} + 3 \text{ quartz} + 2\ K^+ + 3\ H_2O$$

To the north of the MFZ, previous workers have observed a second sillimanite isograd in the Kang La Dome (the sillimanite + K-feldspar isograd), which is closely associated with zones of *in situ* migmatisation and crustal melting (Pognante *et al.*, 1990; Noble & Searle, 1995; Stephenson, 1997; Ayres, 1997). Although not observed personally, the position of this isograd is shown on Enclosure 2 and Figure 5.1. The location of this sillimanite + K-feldspar zone in the core of the Kang La Dome represents a south-eastern continuation of the high-temperature sillimanite-grade migmatitic dome exposed in central Zanskar (Herren, 1987; Stäubli, 1989; Kundig, 1989; Searle & Rex, 1989). In more westerly parts of the slab, this sillimanite-grade metamorphism has been shown to be Miocene in age based on U-Pb crystallisation ages of migmatitic leucosomes and crustal melt leucogranites (Noble & Searle, 1995).

Cordierite

Cordierite is observed in some of the metapelites collected form the MFZ and appears to have grown by a reaction involving the replacement of kyanite and/or sillimanite (Figure 5.8j-l). This

implies that cordierite is a late-stage phase which probably grew at high temperatures during decompression. In sample JDW 186, cordierite is observed overgrowing biotite and graphite-free staurolite porphyroblasts (Figure 5.8m). Textural relationships between the staurolite and cordierite are ambiguous and it remains uncertain whether the staurolite is a product or a reactant in the cordierite-forming reaction. Assuming staurolite to be a product, one possible KFMASH reaction would be:

sillimanite + biotite + $H_2O \rightarrow$ cordierite + staurolite + muscovite (Figure 5.9)

However, the absence of muscovite in sample JDW 186 makes this reaction seem somewhat unlikely.

5.3.2 Garnet zoning profiles

All those samples collected in MFZ which contain garnet were analysed by electron microprobe to establish whether they exhibited any chemical zoning profiles. The techniques used are outlined in Appendix A. The following sections describe the zoning profiles in each sample.

JDW 186

This sample was collected from the southernmost unit of metapelites in the MFZ to the north of the Kade granite (Figure 5.5b) and represents a high-Al pelite which has an assemblage of Qtz + Pl + + Bt + Chl + Grt + Crd. Garnets in this sample form large (up to 5mm in diameter), rounded porphyroblasts which show no textural evidence of zoning (Figure 5.10a). They are extensively resorbed and are mantled by a coarse-grained array of chlorite and biotite. Microprobe analysis of one of these garnets revealed a conventional prograde growth zoning profile with minor retrograde rims, as indicated by a slight increase in X_{Sps} (Figure 5.10b).

JDW 184

This sample was collected ~10m structurally below sample JDW 186 (Figure 5.5b) and represents a low-Al pelite which has an assemblage of Qtz + Pl + Ms + Bt + Grt. Garnets are invariably small and anhedral and show no obvious growth relationships with the matrix foliation (Figure 5.11a). These garnets show no evidence of textural growth zoning and are chemically homogeneous (Figure 5.11b).

JDW 194

This sample was collected from a deeper structural level in the MFZ than samples JDW 186 and JDW184 (Figure 5.5b) and represents a low-Al pelite which has an assemblage of Qtz + Pl + Ms + Bt + Grt. Garnets in this sample preserve textural evidence for more than one phase of growth. Figures 5.12a and b shows an example of one such garnet. The garnet core is sub-rounded and contains randomly orientated ilmenite inclusions (Figures 5.12a). The core is overgrown by a subhedral rim

which contains both ilmenite and apatite inclusions (Figure 5.12b). Figure 5.12c shows similar textural relationships in another garnet from this sample. Here, the sub-rounded garnet core is surrounded by a skeletal rim which appears to overgrow the matrix foliation. A traverse across the garnet shown in Figures 5.12a and b shows that the garnet core preserves a somewhat flattened prograde growth zoning profile, whilst the rim shows evidence of extensive retrograde re-equilibration, as indicated by a marked increase in X_{Sps} and a decrease in X_{Mg} (Figure 5.12d). This profile is characteristic of a garnet which grew during prograde metamorphism and subsequently experienced partial resorbtion (probably at temperatures in excess of *c.*600°C), followed by a renewed phase of growth along its rims (e.g. Tracy, 1982).

5.3.3 Mineral chemistry and thermobarometry

Using the techniques outlined in Appendix A, those samples which contained suitable mineral assemblages were selected for quantitative thermobarometric analysis in an attempt to constrain the conditions of final re-equilibration (compositions of the minerals used are given in Appendix B). Despite the fact that most samples contain biotite ± muscovite ± plagioclase ± garnet ± staurolite ± kyanite ± sillimanite, only samples JDW 186, JDW 185 and JDW 194 contained the necessary metamorphic assemblages needed for P-T calculation (i.e. Grt + Bt + Pl + Ms). Even then, sample JDW 186 contains only minor amounts of plagioclase and no observable muscovite (with the exception of pinitised cordierite), and can therefore only be used to quantify the final temperature of equilibration. Owing to a lack of suitable inclusions in any of the samples, it was not possible to constrain prograde P-T conditions. The results of this work are presented in Table 5.1 and Figure 5.9.

Discussion of P-T results

All of the analysed samples give temperature estimates which are within error of one another at *c.*600°C (Table 5.1). Given the observation that garnets in sample JDW 186 preserve evidence of extensive retrograde resorbtion along their rims, these are unlikely to reflect near-peak estimates. Rocks in the MFZ have therefore experienced temperatures in excess of *c.*600°C. This is consistent with the observation that zones of *in situ* migmatisation are located in the Kang La Dome immediately to the north of the MFZ (Enclosure 2; Figure 5.1). This is also consistent with the interpretation that garnet in sample JDW 194 preserves evidence of partial core homogenisation at temperatures in excess of *c.*600°C. Comparison of the conventional garnet-biotite temperature results with the THERMOCALC results suggests that water activities were probably between 0.5-1.0 during metamorphism (Table 5.1). This is consistent with the observation that many samples are graphite-rich (e.g. Figures 5.8a & b).

The pressure data are more difficult to interpret. Both samples JDW 184 and JDW 194 plot within the kyanite field (Figure 5.9), which is somewhat surprising considering that sillimanite is observed in the majority of samples collected from the MFZ (Figure 5.5b). It would therefore appear

Table 5.1: Miyar nala P-T results

			Conventionall geothermobarometry results												THERMOCALC results														
			Barometry				Garnet-Biotite thermometry																								
Sample	assemblage	comments	P* (kbar)	P** (kbar)	P*** (kbar)	Ave	B 92 (HW)	B 92 (GS)	Das 91	FS 78	HS 82	PL 83	T 76	HL 77	P (kbar)	sd	T (°C)	sd	corr	fit	number of reactions	XH20	end-members excluded	preferred result	estimated overburden (3.71km/kbar)	sd	geotherm (°C/km)	sd
JDW 182	Grt + Bt + Ms + Pl + Chl + Qtz + H2O	average garnet rim and matrix (post-peak)	-	6.9	5.6	6.2	**520**	498	517	514	541	548	553	536	6.3	0.8	570	13	0.378	0.48	10	1.0	fame		21.9	3.0	24.1	3.3
															5.9	**0.8**	**527**	**12**	**0.400**	**0.54**	**10**	**0.5**	**fame**	**X**				
															5.7	0.8	497	11	0.413	0.62	10	0.3	fame					
															5.1	0.7	428	12	0.384	0.96	10	0.1	fame					
JDW 184	Grt + Bt + Ms + Pl + Qtz + H2O	average garnet rim and matrix (post-peak)	-	7.2	5.6	6.4	**578**	565	535	595	618	593	617	591	6.6	1.2	629	38	0.682	1.06	7	1.0			23.4	4.5	25.0	4.8
															6.3	**1.2**	**585**	**36**	**0.680**	**1.10**	**7**	**0.5**	**none**	**X**				
															6.1	1.2	555	35	0.678	1.16	7	0.3						
															5.6	1.3	485	38	0.659	1.42	7	0.1						
JDW 186		average garnet rim and matrix (post-peak)	-				**568**	579	534	551	562	568	578	561																
JDW 194	Grt + Bt + Ms + Pl + Qtz + H2O	average garnet rim and matrix (post-peak)	-	10.4	8.4	9.4	**594**	576	554	617	654	605	634	606	8.8	1.6	646	49	0.684	1.31	7	1.0			31.2	5.2	19.3	3.2
															8.4	**1.4**	**601**	**40**	**0.680**	**1.21**	**7**	**0.5**	**none**	**X**				
															8.1	1.3	570	36	0.677	1.18	7	0.3						
															7.4	1.2	496	33	0.660	1.22	7	0.1						

Garnet-Biotite thermometer abbreviations

B 92 (HW): Bhattacharya et al (1992), using garnet mixing model of Hackler & Wood (1989)
B 92 (GS): Bhattacharya et al (1992) using garnet mixing model of Ganguly & Saxena (1984)
Das 91: Dasgupta et al (1991)
FS 78: Ferry & Spear (1978)
HS 82: Hodges & Spear (1982)
PL 83: Perchuk & Lavrent'eva (1983)
T 76: Thompson (1976)
HL 77: Holdaway & Lee (1977)

Barometer reactions

* GASP (Grt + Als = Pl)
** GPMB-Mg (Grs + Prp + Ms = 3An + Phl)
*** GPMB-Fe (Grs + Alm + Ms = 3An + Ann)

that these samples record pressures which pre-date the growth of sillimanite in the MFZ. Sample JDW 184 records a THERMOCALC pressure of 6.3 ± 1.2 kbar, whilst sample JDW 194 records an estimate of 8.4 ± 1.4 kbar (Table 5.1). Although within error of each other, the tectonic significance of these data remains uncertain. The difference in pressure between these two samples is consistent with the notion that the MFZ represents an extensional shear zone which is responsible for the exhumation of higher-grade lithologies in the Kang La Dome (i.e. JDW 194 was collected from a deeper structural level than JDW 184). However, it is equally possible that both samples were buried to similar depths of *c.*8 kbar and that for some reason, sample JDW 184 records a lower pressure estimate. This could be interpreted to be the result of heterogeneous re-equilibration of samples brought about by fluid fluxing through the MFZ during isothermal decompression (Figure 5.9). A third possibility is that one of the pressure estimates is in error because the analysed minerals were not in equilibrium. However, this is not evident from the average THERMOCALC P-T results (Table 5.1), where disequilibrium mineral compositions might reveal themselves in a poor 'fit' parameter.

5.3.4 Melting in the Miyar Fault Zone and Kang La Dome

Undeformed leucogranites

Several small bodies of undeformed leucogranite were observed cross-cutting the regional tectonic fabric in the MFZ (Figure 5.5). These are clearly late-stage granites which were generated following the attainment of peak-metamorphic conditions in the MFZ. The granites were not studied in detail, but appeared to be similar to other High Himalayan leucogranites exposed in the HHC at the top of the slab (i.e. they are characterised by a mineralogical assemblage of Qtz + Ms + Bt + Pl ± Grt ± Tur). These granites do not represent *in situ* melts since there is no evidence of migmatisation within the MFZ itself. However, previous authors have observed extensive migmatisation in the core of the Kang La Dome to the north of the MFZ (e.g. Herren, 1987; Stäubli, 1989; Kundig, 1989; Searle & Rex, 1989; Pognante *et al.*, 1990; Noble & Searle, 1995; Stephenson, 1997; Ayres, 1997), thus suggesting that the granites are not far travelled. Indeed, the P-T estimates obtained from samples within the MFZ demonstrates that these rocks experienced temperatures of at least *c.*600°C and were therefore close to the water-saturated melting temperature of metapelites (Figure 5.9).

Various models have been proposed to account for the origin of crustal melt leucogranites in the uppermost part of the High Himalayan Slab (see Chapter 2 for discussion). Based on the location of these granites in the footwall of the MFZ, it would appear that the most geologically reasonable mechanism by which they were generated and emplaced was by isothermal decompression of the Kang La Dome. Several lines of evidence suggest that lithologies within the MFZ and Kang La Dome experienced a high temperature decompression: (1) phase relationships in the metapelites of the MFZ preserve evidence for late-stage sillimanite and cordierite growth which is interpreted to have occurred at high temperatures and low pressures; (2) the thermobarometric data presented in section 5.3.3 provide tentative evidence for isothermal decompression in the MFZ; and (3) the

thermobarometric data presented by Pognante *et al.* (1990) provide good evidence for an early phase of metamorphism in the Kang La Dome (M_1) followed by a period of isothermal decompression (M_2). The location of samples collected by Pognante *et al.* (1990) and the results of their P-T work are shown on Enclosure 2.

Leucocratic pegmatites

In addition to the cross-cutting, undeformed crustal melt leucogranites, there are numerous examples of intensely deformed and mylonitised leucocratic pegmatites within the MFZ (Figures 5.5 & 5.6b). They are wholly leucocratic and have a characteristic mineralogy comprising of Qtz + Ms + Pl + ± Grt ± Tur. They are extremely similar in appearance to the pegmatites seen in the Crystalline Nappe at the base of the slab (see Chapter 4). The age of the pegmatites in the MFZ is uncertain. They clearly pre-date intrusion of the undeformed leucogranites and could even be pre-Himalayan in age. However, it seems more likely that they were generated and emplaced during high temperature deformation and metamorphism in the MFZ during the Tertiary. Geochronological analysis of monazite and zircon from these pegmatites may help elucidate this problem.

5.3.5 P-T-t evolution in the MFZ and Kang La Dome

Phase relationships demonstrate that lithologies in the MFZ experienced a Barrovian-type metamorphism which resulted in the prograde growth of garnet-, staurolite- and kyanite-bearing assemblages (Figure 5.9). This is interpreted to have been in response to crustal shortening and thickening following the India-Asia collision, although there are no age data to confirm this. Owing to the intensity of deformation within the MFZ it is difficult, if not impossible, to accurately constrain the kinematics associated with this shortening and thickening history. Phase relationships and quantitative P-T estimates are in good agreement and demonstrate that conditions exceeded *c.*600°C and 6-8 kbar in the MFZ. This is consistent with the P-T work of Pognante *et al.* (1990) and is characteristic of the M_1 metamorphism seen throughout the entire High Himalayan Slab (see Chapter 2). Many of the lithologies in the MFZ contain sillimanite and some also contain cordierite. The exact cordierite-forming reaction is difficult to constrain from the available textural evidence, but almost certainly involves the breakdown of kyanite and sillimanite. Both sillimanite and cordierite are interpreted to have grown in response to decreases in pressure under more-or-less isothermal conditions (Figure 5.9). This is also consistent with the P-T work of Pognante *et al.* (1990) and corresponds to the M_2 metamorphism seen throughout the entire High Himalayan Slab (see Chapter 2). Injection of discordant leucogranites within the MFZ is interpreted to be synchronous with this M_2 metamorphic stage (Figure 5.9).

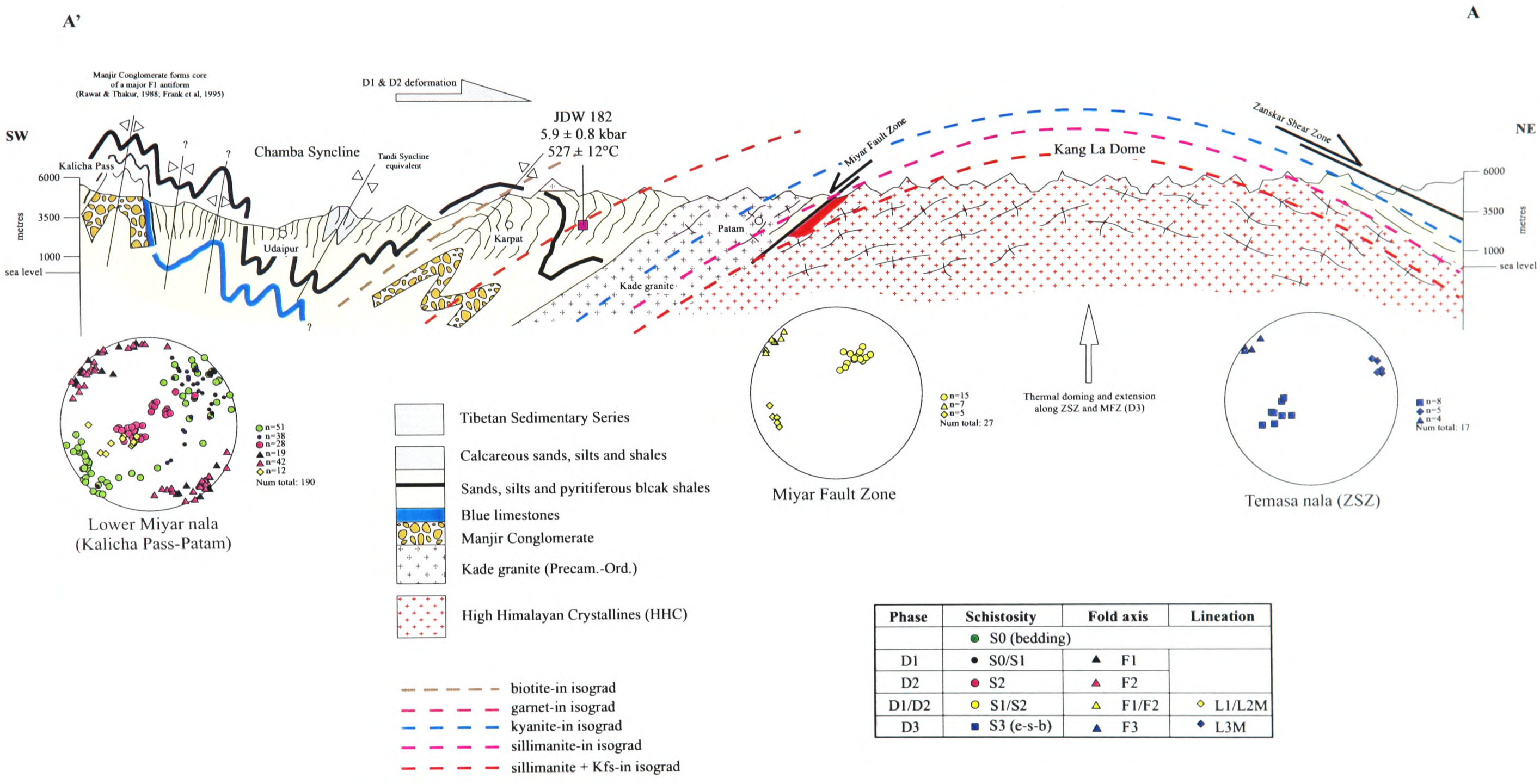
5.4 Summary

Over 25 km of crustal section is exposed along a traverse through the Chamba Syncline and Kang La Dome in the western part of the study area. The southern part of this traverse consists of a sequence of intensely folded sands, silts and shales which form the chlorite- and biotite-grade sediments of the Chamba Syncline and lower Miyar nala. Lithological observations presented in Chapter 3 suggest that these form part of the Lower Palaeozoic Haimantas and are therefore an integral part of the High Himalayan Slab and are not a tectonic cover-sequence, as suggested by some previous authors. Structural observations suggest that these sediments experienced two phases of ductile deformation (D_1 and D_2), both of which appear to have been associated with a top-to-the-north-east kinematic transport direction. This is consistent with the NE facing direction of the Tandi Syncline in the Crystalline Nappe. The development of the Tandi Syncline is attributed to a major phase of NE-backfolding during the early stages of crustal shortening and thickening (see Chapter 4). The mechanism responsible for this remains uncertain, but may have had something to do with the distribution of rigid crustal blocks within the High Himalayan Slab. It is interesting to note that large Precambrian-Ordovician K-feldspar granites are located to the north of the Tandi Syncline and Chamba Syncline (Enclosure 1), and that these may have acted as rigid backstops to deformation, thus promoting the development of NE-facing folds. It is also interesting to note that the oldest stratigraphic unit in the Chamba Syncline (i.e. the Manjir Conglomerate) is exposed in the core of an upright F_1 antiform to the north of the Kalicha Pass (Figure 5.1). To the north of the Kalicha Pass, F_1 folds are progressively overturned towards the NE. To the south, F_1 folds are reported to be overturned towards the SW (Rawat & Thakur, 1988; Frank *et al.*, 1995). Taken together with the fact that the Chamba Syncline has never been buried to any significant depth following the India-Asia collision (i.e. it is located within the chlorite zone), it is suggested that this part of the High Himalayan Slab is located within a major pop-up zone (Figure 5.13).

Metamorphic grade progressively increases from south to north in the Chamba Syncline, reaching sillimanite-grade conditions in Kang La Dome in the upper part of the slab. Metamorphism is interpreted to be dominantly Himalayan in age, although the possibility that some metamorphic assemblages and leucocratic pegmatites are pre-Himalayan in age cannot be unequivocally ruled out from field and petrographic observations alone. The precise orientation of the metamorphic isograds could not be accurately determined in the field, but are interpreted to dip shallowly towards the SW, at a shallower angle than the dip of the regional tectonic foliation.

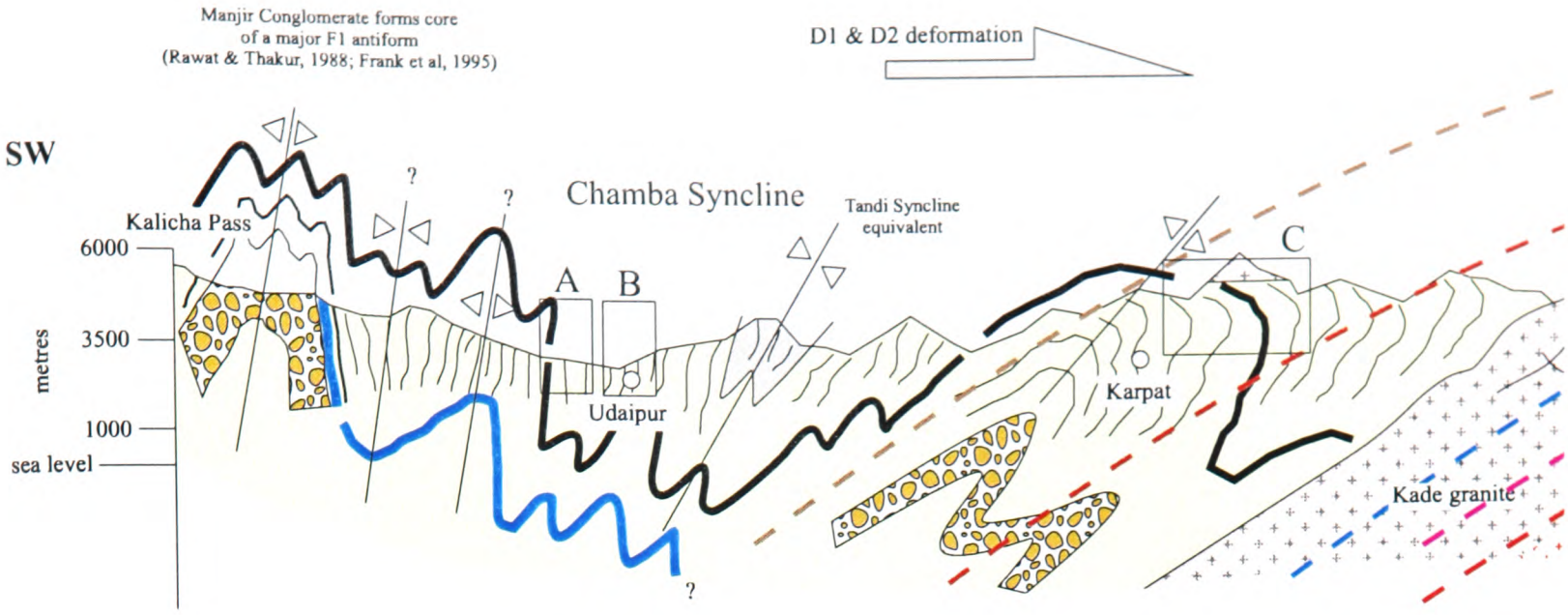
With the possible exception of the Karpat Shear Zone and Miyar Fault Zone (MFZ), no major structural or metamorphic discontinuities were observed in the field between the chlorite-grade lithologies of the Chamba Syncline and the sillimanite-grade lithologies of the Kang La Dome. The Karpat Shear Zone may be a lateral equivalent of the Kilar Shear Zone mapped by Frank *et al.* (1995) and Stephenson (1997), although more detailed mapping is needed to verify this. The Miyar Fault Zone appears to represent a several-kilometre-wide zone of high-temperature extensional deformation located on the southern flank of the Kang La Dome.

Textural evidence suggests that the growth of sillimanite and cordierite in the MFZ was associated with a phase of near-isothermal decompression and was probably contemporaneous with the generation and emplacement of undeformed crustal melt leucogranites. Exhumation of high-grade lithologies in the Kang La Dome is therefore interpreted to be the result of extensive erosion during thermal doming, combined with extensional unroofing in the footwall of the ZSZ (and possibly the MFZ). Similar domal structures have been observed in western and central Zanskar and are always flanked by extensional shear zones (e.g. Stäubli, 1989, Kundig, 1989; Searle *et al.*, 1992). It seems likely that doming in the upper part of the slab was compensated for by downwarping of lower-grade lithologies towards the south, which may explain why chlorite-grade lithologies are preserved in the Chamba Syncline.



Phase	Schistosity	Fold axis	Lineation
	S0 (bedding)		
D1	S0/S1	F1	
D2	S2	F2	
D1/D2	S1/S2	F1/F2	L1/L2M
D3	S3 (e-s-b)	F3	L3M

Figure 5.1: Cross-section through the Chamba Syncline and Kang La Dome in the western part of the study area showing the orientation of major structural fabrics (line of section shown on Enclosure 1).



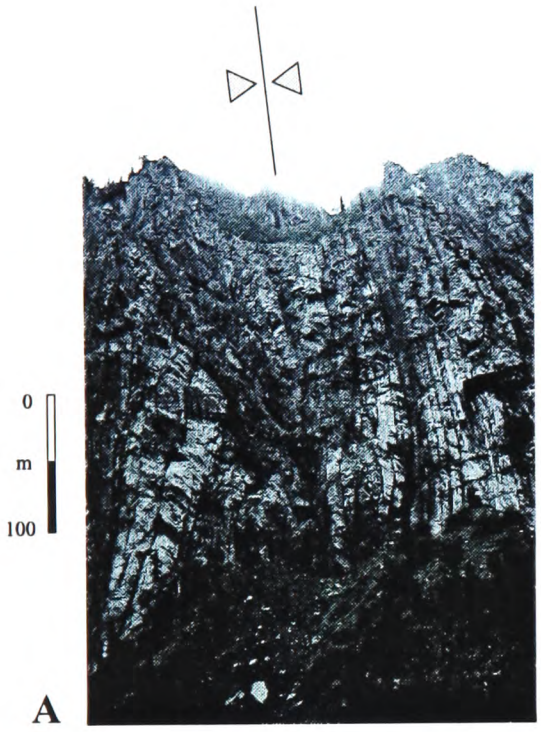




Figure 5.2a: Upright isoclinal F1 synform in a well-bedded sequence of sands, silts and shales belonging to the Lower Palaeozoic Haimantas System in the Chamba Syncline (photograph taken on the northern side of Chenab valley, near Hinsa village).

Figure 5.2b: Sub-vertically bedded sequence of sands, silts and shales exposed on the northern limb of a major antiform in the Chamba Syncline (photograph taken looking NW at the confluence of the Miyar nala and river Chenab, near the village of Udaipur).



Figure 5.2c: Large-scale folds overturned towards the NE in the Miyar nala (photograph taken looking ~east into the mountainside at Karpat village).

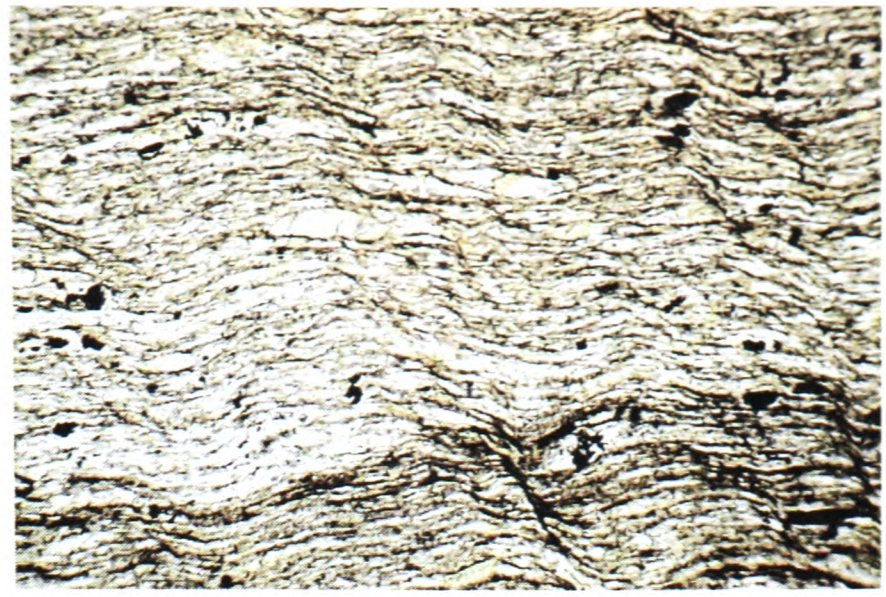


Figure 5.2d: Chlorite and phengitic green-coloured muscovite aligned along the S1 cleavage in a graphitic phyllite collected from the Chamba Syncline. S1 is parallel to compositional layering (S0), which is defined as the contact between graphite-rich and graphite-poor horizons in the lower part of the photograph. Both S0 and S1 are weakly crenulated by an S2 fabric. (Sample JDW 223c, collected in the limb of an isoclinal F1 fold ~6km north of Udaipur). Field of view is c.3mm.



Figure 5.2e: Large chlorite stacks growing between S1 cleavage lamellae in a graphitic siltstone collected from the Chamba Syncline. The detrital nature of the quartz and feldspar grains is evident in this picture. (Sample JDW 222, collected in the limb of an isoclinal F1 fold ~3km north of Udaipur). Field of view is c.3mm.

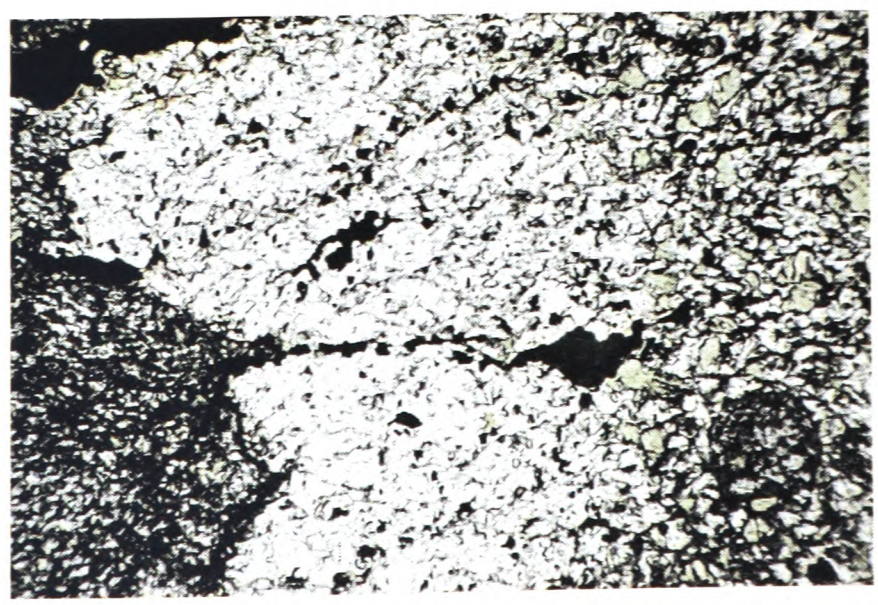


Figure 5.2f: Growth of metamorphic chlorite in a finely laminated calcareous silt belonging to the Lower Palaeozoic Haimantas. Compositional layering (S0) is sub-vertical in the photograph and is defined by the contact between graphite-rich and graphite-poor horizons. F1 microfolds are evident along this contact. S1 is sub-horizontal and is defined by a flattening of detrital quartz and the streaking-out of a detrital(?) ilmenite grain. (Sample JDW 223b, collected from the hinge of an isoclinal F1 fold ~6km north of Udaipur). Field of view is c.3mm.

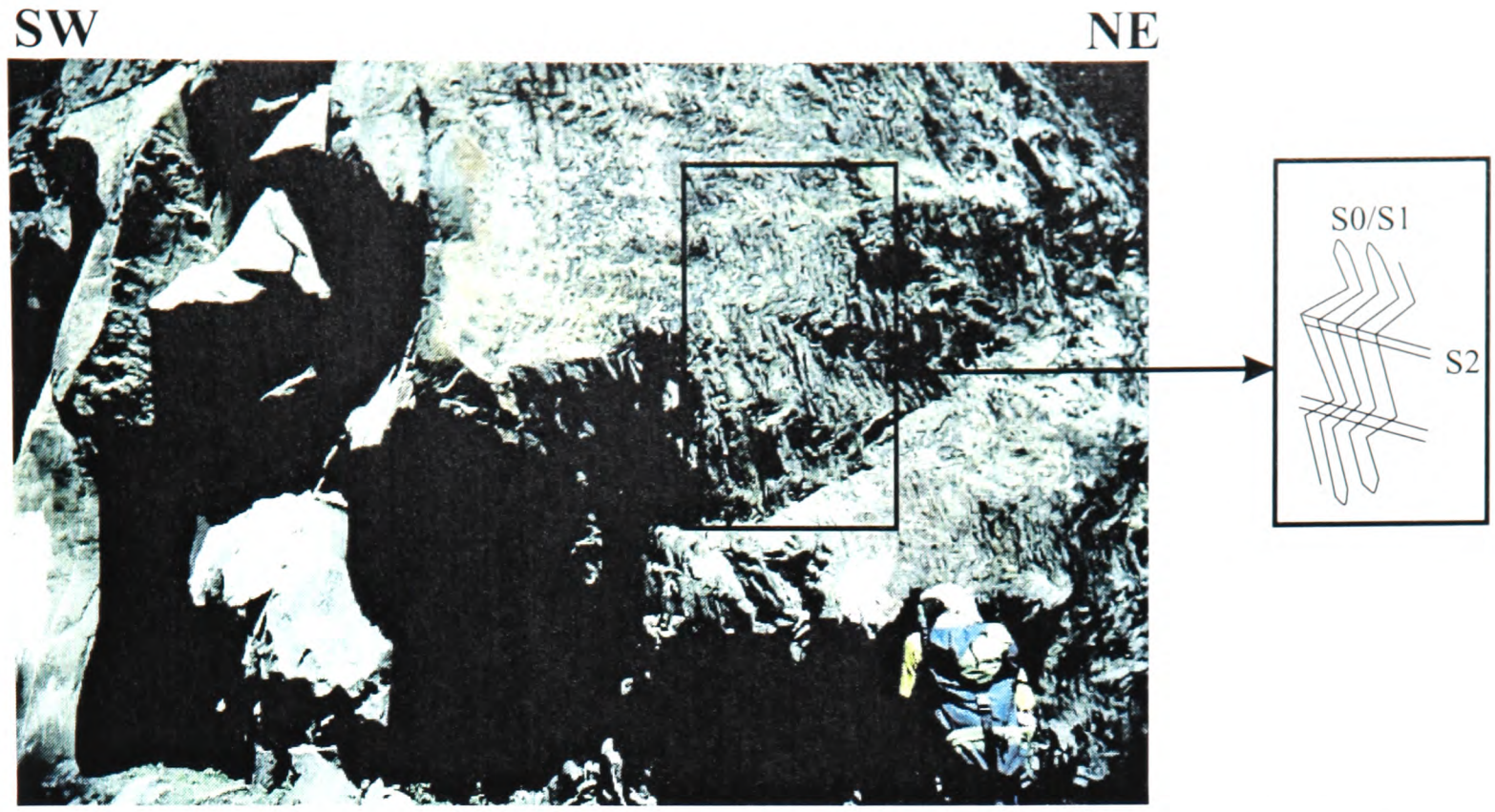


Figure 5.3a: Sub-vertical bedding in an interlayered sequence of sandstones, silts and shales in the Chamba Syncline. S0 and S1 are sub-parallel. The sandstones are relatively unaffected by D2 deformation, whereas the shales are deformed by asymmetrical folds which are suggestive of a top-to-the-north shear sense. S2 is sub-horizontal and is almost perpendicular to S0/S1. (lower Miyar nala, ~500m north of Udaipur).

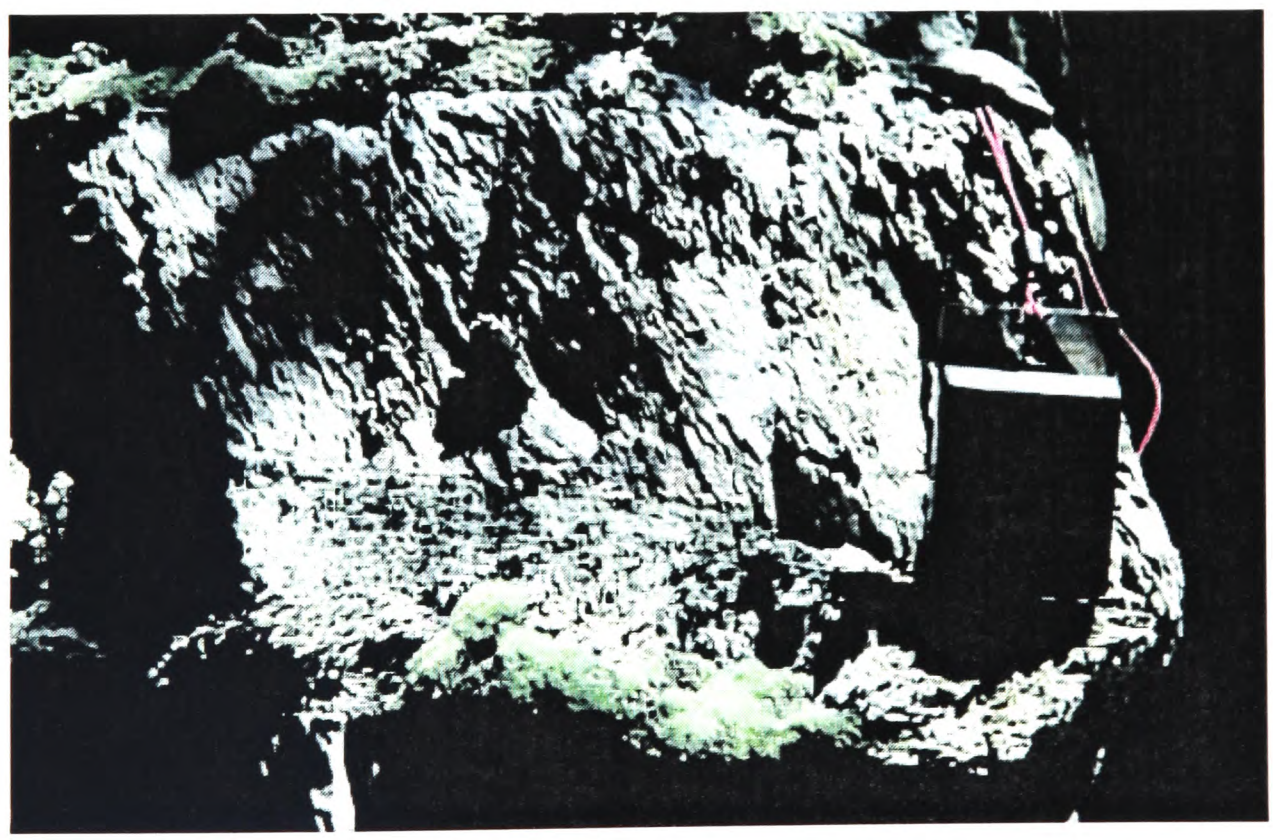


Figure 5.3b: Close-up of the relationship between S0/S1 and the S2 cleavage in the lower Miyar nala. S0/S1 is sub-vertical and is cross-cut by a locally developed S2 fabric.

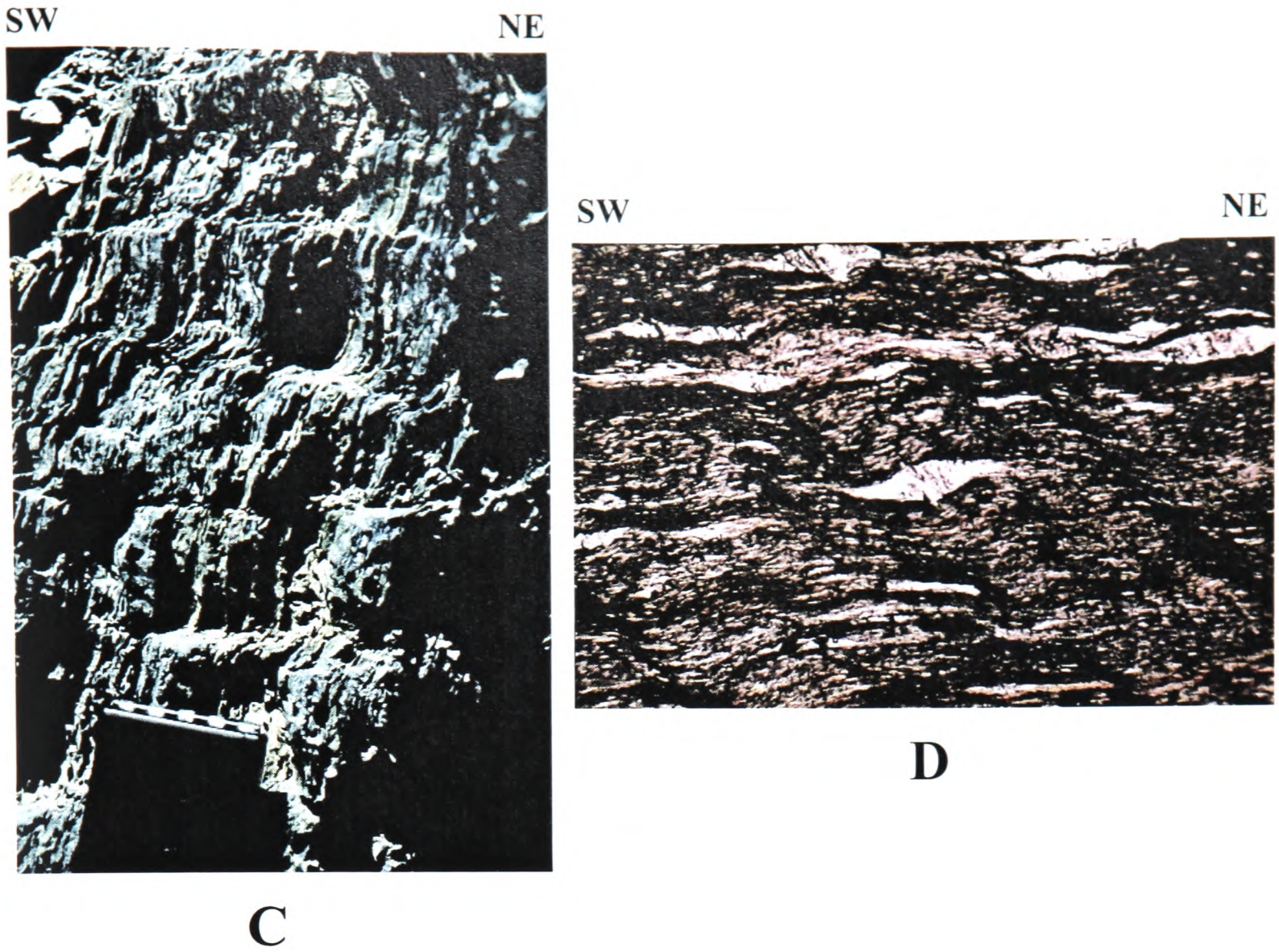


Figure 5.3c: Intersection of the S0/S1 and S2 fabrics giving a top-to-the-north-east shear-sense in a graphitic phyllite in the Chamba Syncline (photograph taken in the lower Miyar nala, ~4km north of Udaipur).

Figure 5.3d: Photomicrograph of an asymmetrical quartz clast showing a top-to-the-north-east shear sense in a graphitic shale (sample JDW 221, collected in the lower Miyar nala, ~1km north of Udaipur). Field of view is c.3mm.

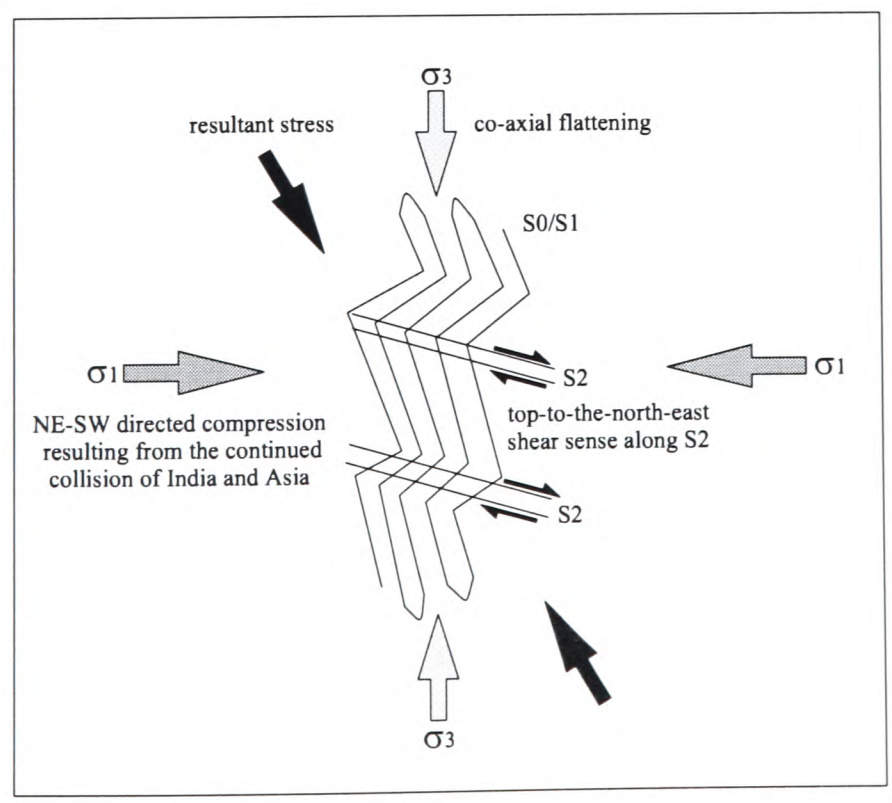


Figure 5.3e: Possible explanation for the origin of the sub-horizontal S2 fabric and top-to-the-north-east shear sense indicators observed in the low-grade sediments in the Chamba Syncline. Co-axial flattening of the sub-vertical S0/S1 fabric combined with an element of horizontal shortening could create these structures.

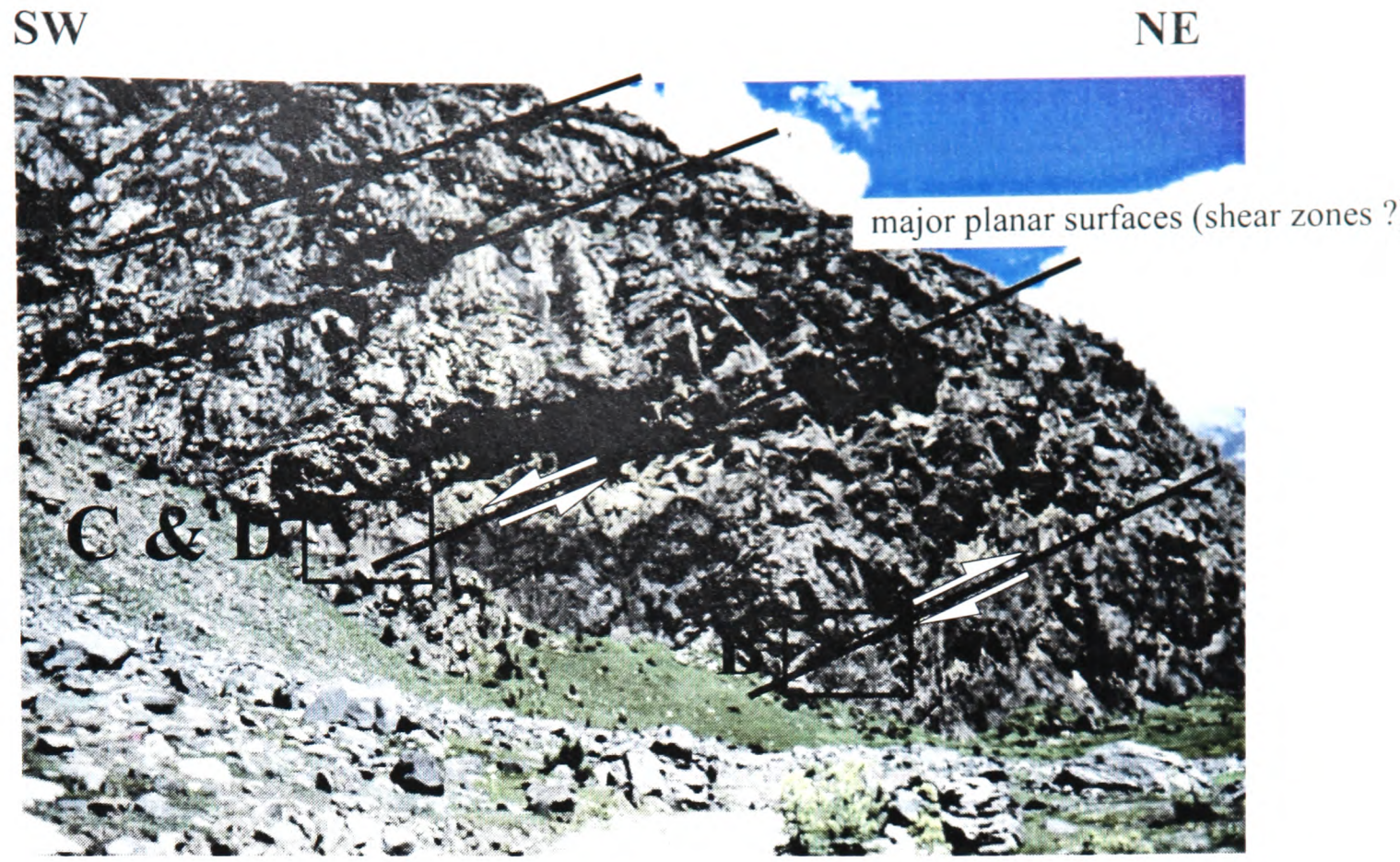


Figure 5.4a: The 'Karpat Shear Zone', located ~2 km north of Karpat village in the Miyar nala. The Karpat Shear Zone is defined as a zone of intense deformation in a sequence of biotite-grade pelites and psammites. Fabrics which show both a top-to-the-north-east and top-to-the-south-west shear sense were observed at this locality (see Figures 5.4a and 5.4b respectively). Weakly deformed leucocratic pegmatites are also observed cross-cutting the regional tectonic foliation (see Figure 5.4c).

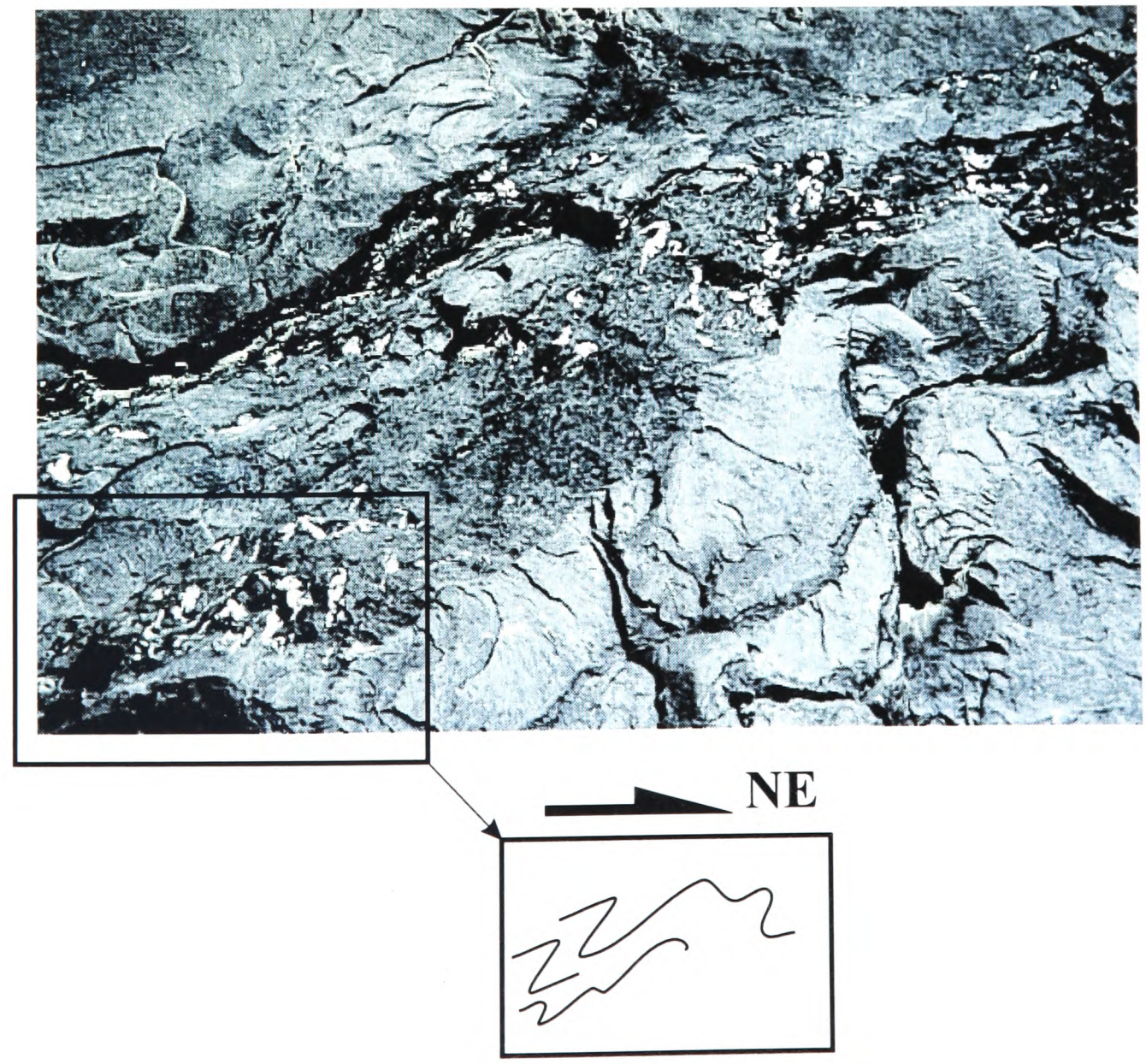


Figure 5.4b: Folded quartz veins within a biotite-grade pelitic schist are overturned towards the NE, and are indicative of a top-to-the-north-east shear sense.

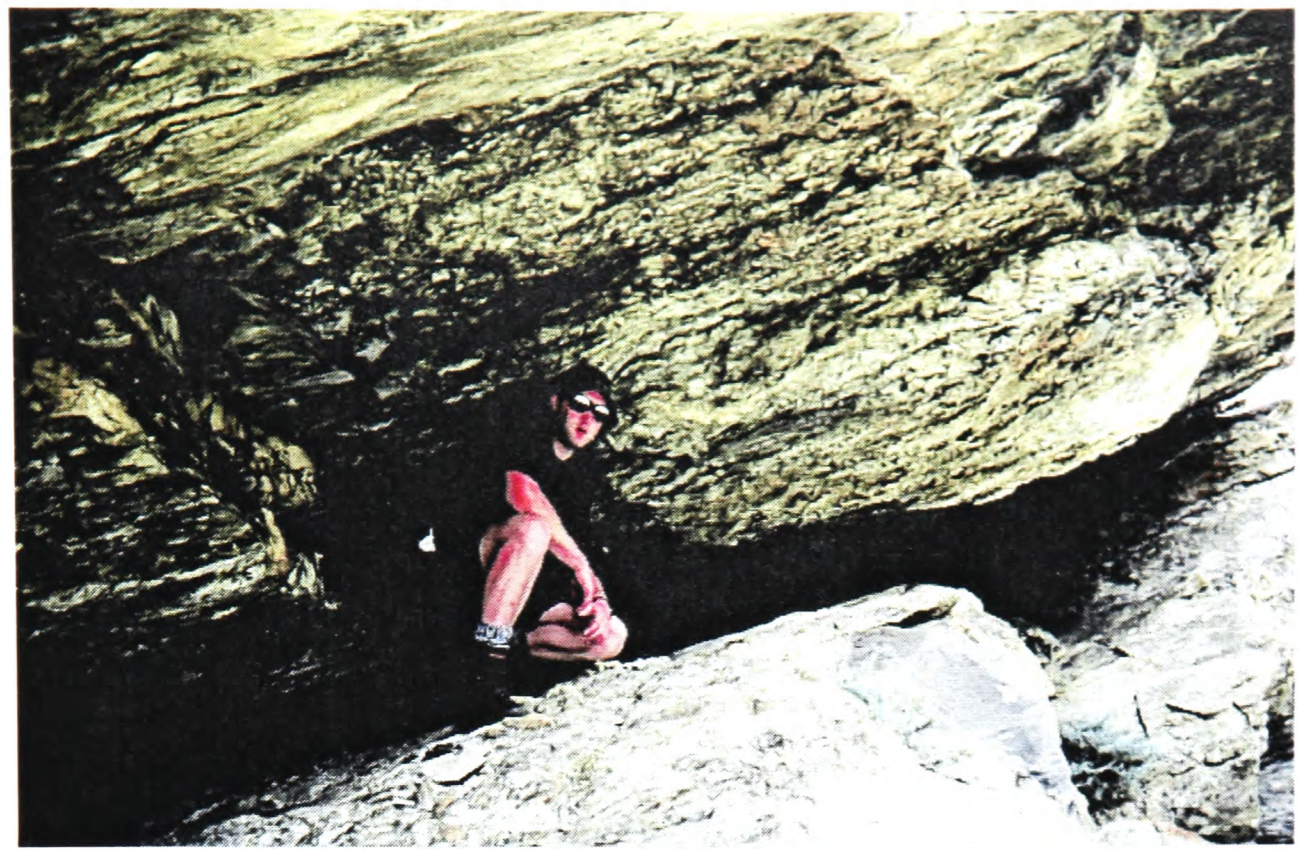


Figure 5.4c: Intense deformation along a major planar surface shown in Figure 5.4a. Extensional shear band fabrics displaying a top-to-the-south-west shear sense were observed along this surface. The significance of these are uncertain: they may suggest that the Karpat Shear Zone is an extensional detachment which separates the chlorite-grade sediments of the Chamba Syncline from the higher-grade lithologies further north.



Figure 5.4d: Leucocratic pegmatite within the shear zone shown above. The pegmatite does not possess a particularly strong tectonic fabric, suggesting that it was emplaced syn/post-kinematically with respect to movement along the shear zone.

SW NE



0 500

m

SW NE

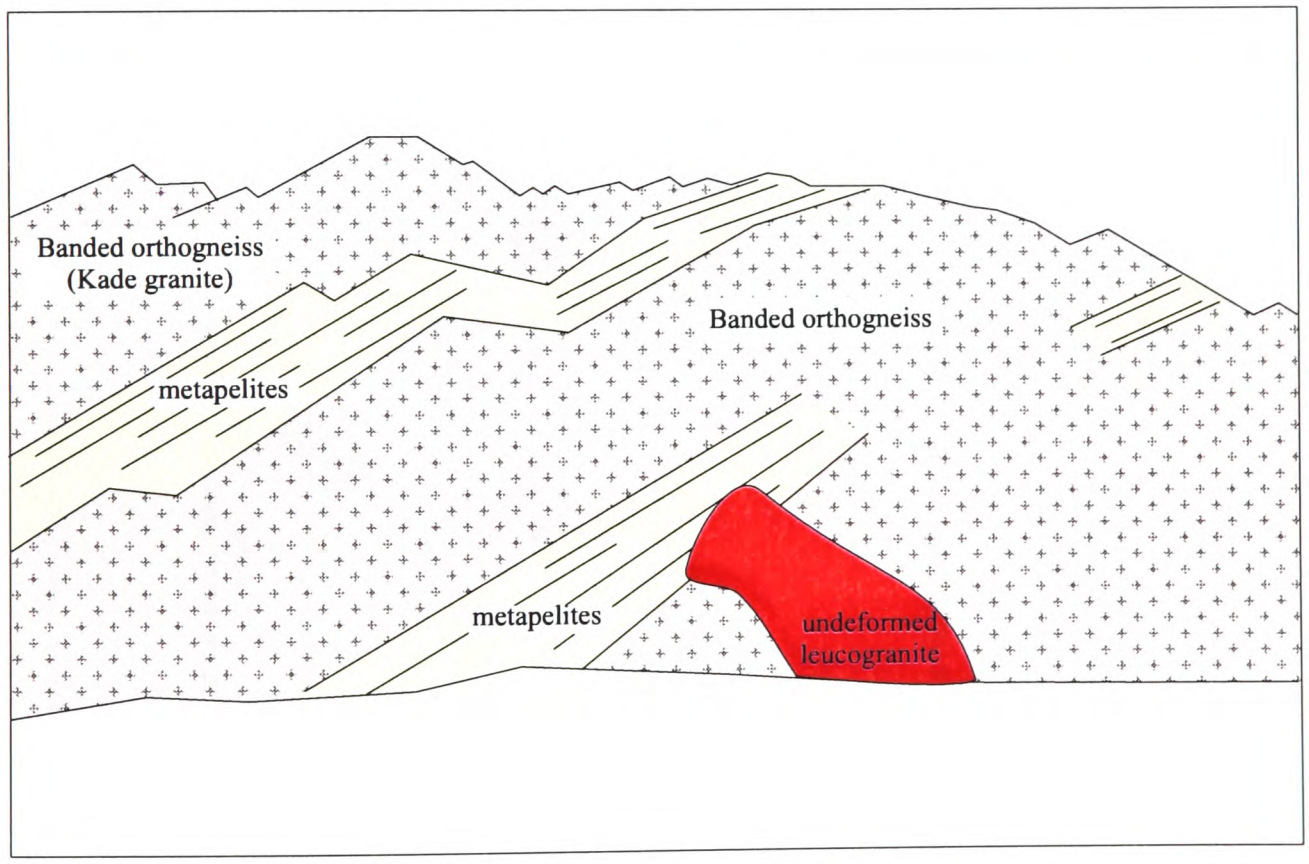
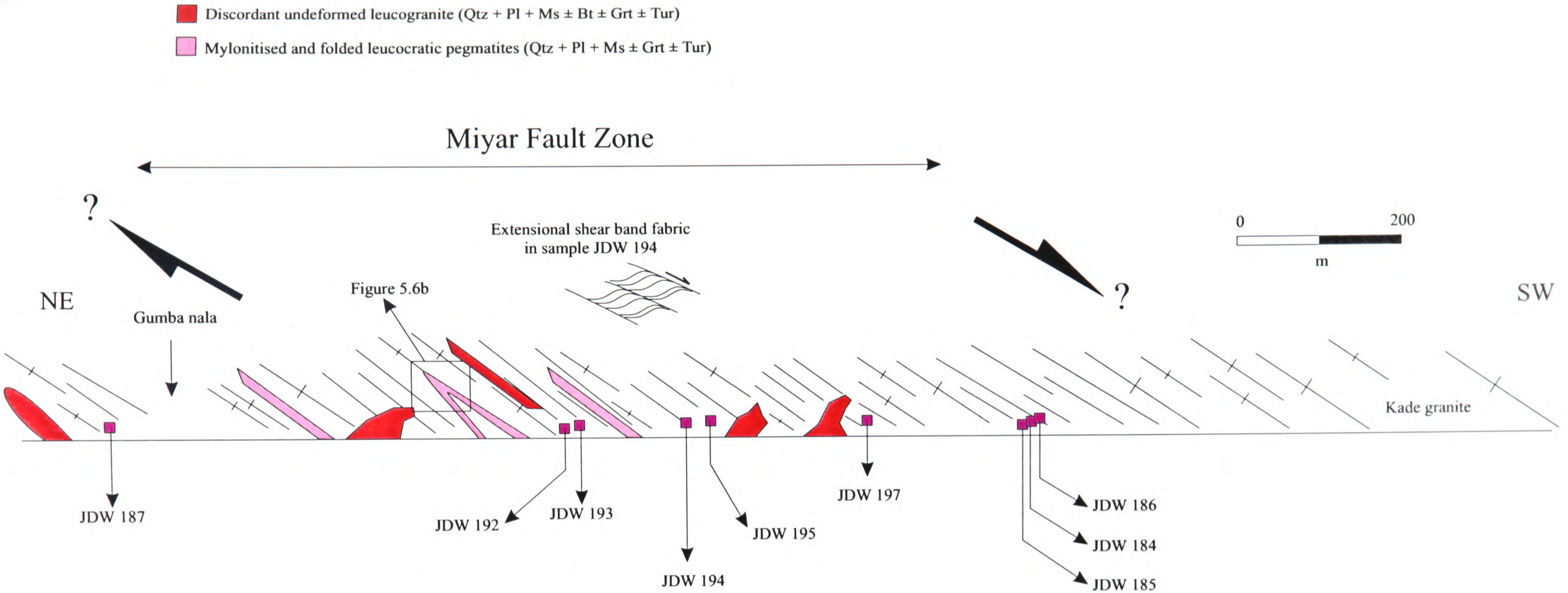


Figure 5.5a: Photograph and interpretative field sketch of the Miyar Fault Zone exposed in the western bank of the Miyar nala to the north of the Kade granite. The fault zone is defined as an intercalated succession of kyanite- and sillimanite-grade pelitic schists, paragneisses, augen gneisses and orthogneisses which are concordantly (and occasionally discordantly) intruded by a number of leucocratic pegmatites and crustal melt leucogranites.



Metamorphic assemblages in shown samples	*Key metamorphic reactions*	*P-T estimates*
JDW 186 Qtz + Pl + Bt + Chl + Grt + St + Crd	Grt = Chl + Bt	568°C
JDW 184 Qtz + Pl + Ms + Bt + Grt		585 ± 36°C, 6.3 ± 1.2 kbar
JDW 185 Qtz + Pl + Bt + Crd + Sil	Ky = Sil; Sil = Crd	
JDW 197 Qtz + Pl + Ms + Bt + St + Ky	St = Ky	
JDW 195 Qtz + Pl + Ms + Bt + Ky	Ky = Ms + Qtz	
JDW 194 Qtz + Pl + Ms + Bt + Grt		601 ± 40°C, 8.4 ± 1.4 kbar
JDW 193 Qtz + Pl + Ms + Bt + Ky + Sil	Ky = Sil	
JDW 192 Qtz + Pl + Ms + Bt + Ky + Sil + Crd	Ky = Sil; Ky = Crd	
JDW 187 Qtz + Pl + Ms + Bt + Sil		

Figure 5.5b: Transect through the Miyar Fault Zone on the eastern side of the Miyar nala. Crossed lines denote banded orthogneiss/augen gneisses, straight lines denote metapelites and psammites/biotite gneisses. Purple boxes show the location of samples referred to in the text.



Figure 5.6a: Isoclinally folded quartz vein in a sequence of biotite gneisses in the MFZ.

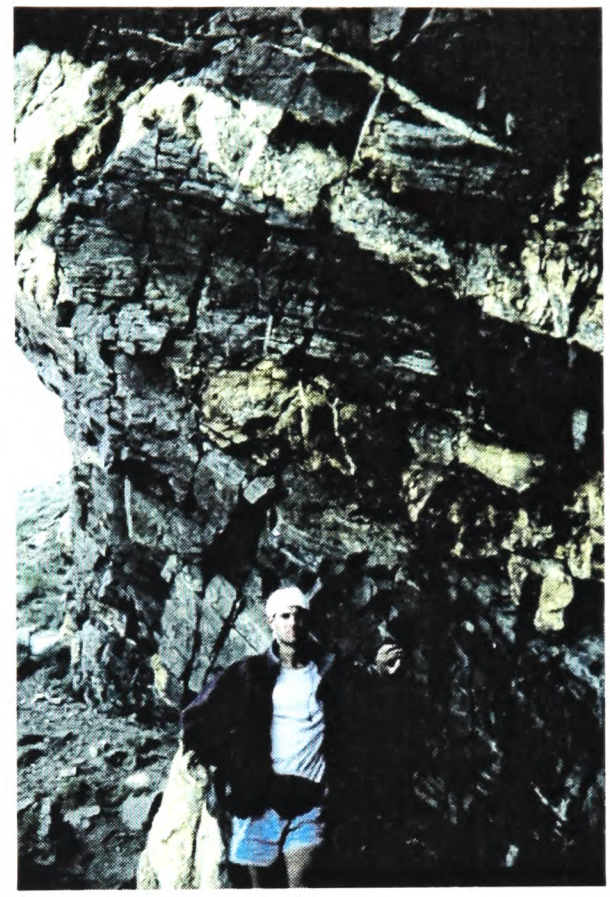


Figure 5.6b: Isoclinally folded leucocratic pegmatite within a sequence of biotite gneisses in the MFZ. The pegmatite was injected prior to the latest phase of deformation in the MFZ and may even be pre-Himalayan in age.

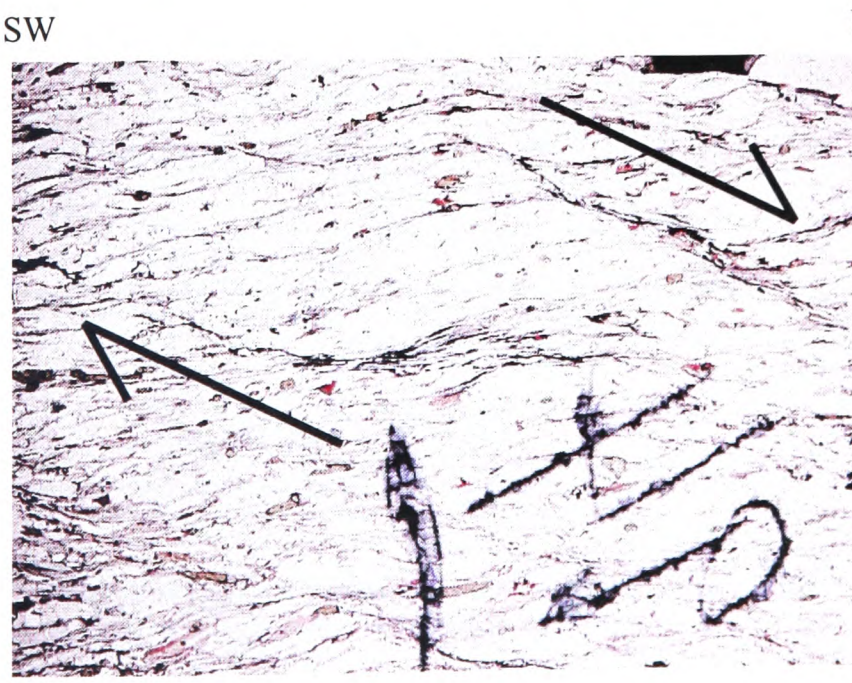


Figure 5.6c: Extensional shear band fabric in sample JDW 194 showing a top-to-the-south-west shear sense. Field of view is c.5mm.

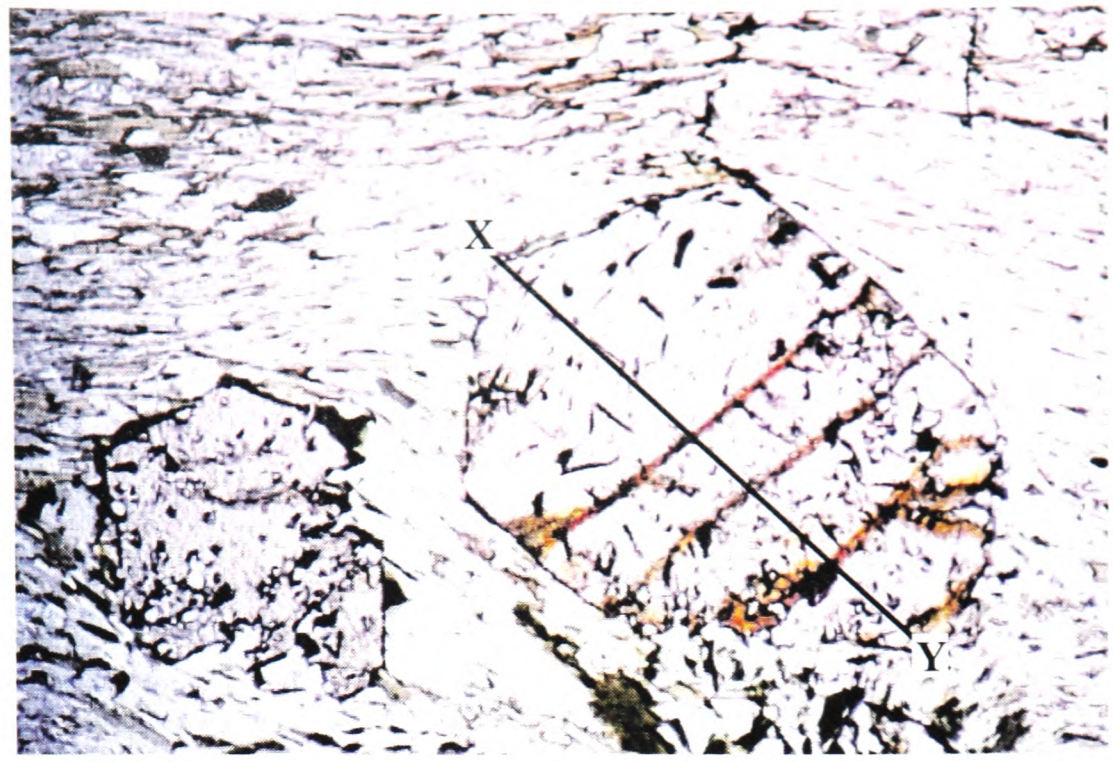


Figure 5.7a: Photomicrograph of garnet in sample JDW 182, collected near the garnet-in isograd in the Miyar nala, ~3 km north of Karpat. The garnet is euhedral and displays no obvious textural evidence of growth zoning. Garnet growth is interpreted to be Himalayan in age and was probably syn/post-kinematic with respect to the D1 deformation phase in the Chamba Syncline. Field of view c.3mm.

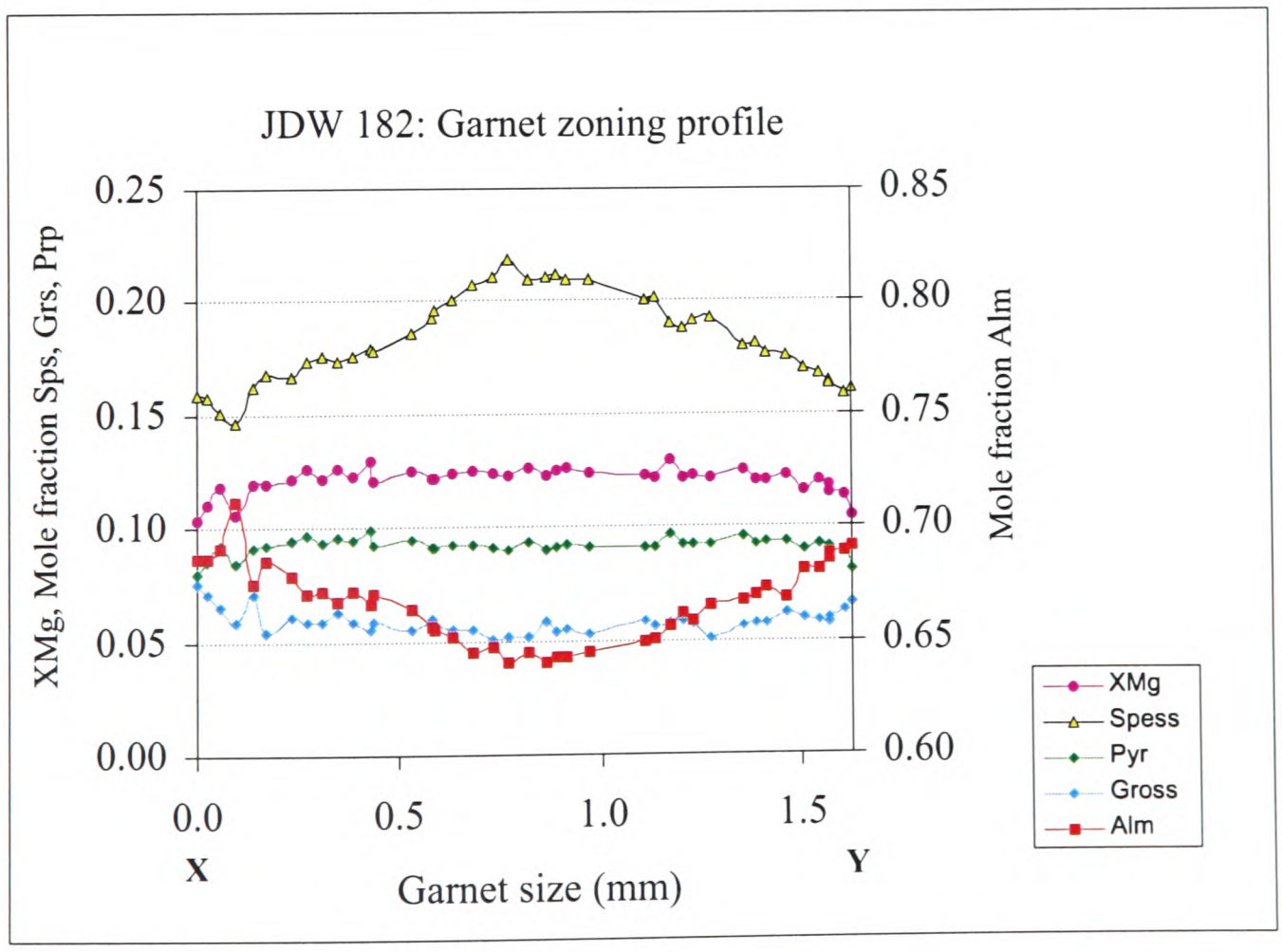


Figure 5.7b: Garnet zoning profile along traverse shown in Figure 5.7a. This is interpreted to be a conventional prograde growth zoning profile with slight evidence for minor retrograde alteration at the garnet rim.

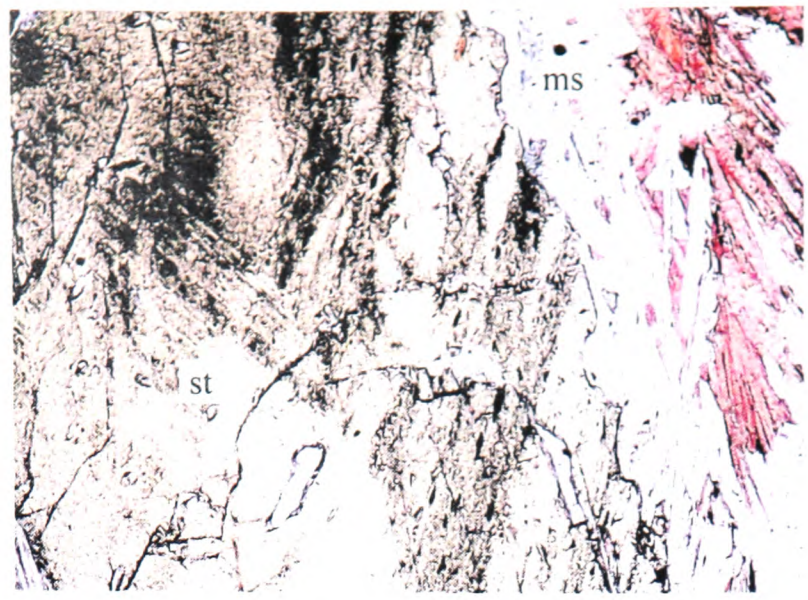


Figure 5.8a: Staurolite porphyroblast containing graphite inclusion trails. The staurolite is mantled by a coarse-grained array of muscovite. Graphite inclusion trails can be traced into the muscovite from the staurolite, suggesting that the muscovite is a product of staurolite breakdown. This is interpreted to be related to the growth of kyanite in this sample during prograde Barrovian metamorphism. growth was related to staurolite breakdown during kyanite growth. Field of view c.4mm. (Sample JDW 197; see Figure 5.5b for location).



Figure 5.8b: Staurolite porphyroblast containing a graphitic inclusion trail which preserves an isoclinal fold closure. Parts of the staurolite are mantled by a coarse-grained array of muscovite, which is interpreted to be related to kyanite growth during prograde metamorphism. A small kyanite porphyroblast can be seen in the upper part of the photograph. Field of view c.4mm. (Sample JDW 197; see Figure 5.5b for location).

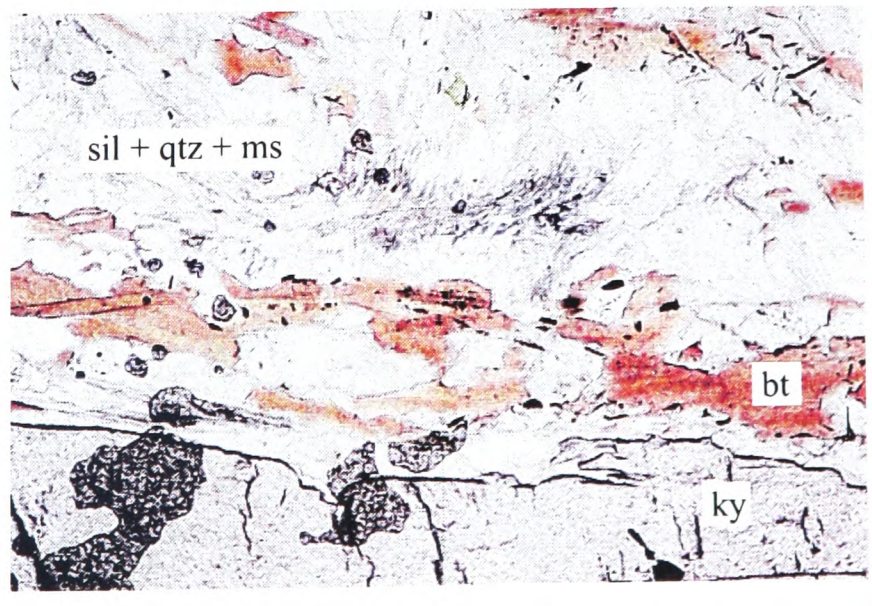


Figure 5.8c: Bundles of randomly orientated fibrolitic sillimanite enclosed within quartz. Part of a large kyanite porphyroblast is visible in the lower part of the photograph. Field of view c.2mm. (Sample JDW 193; see Figure 5.5b for location).

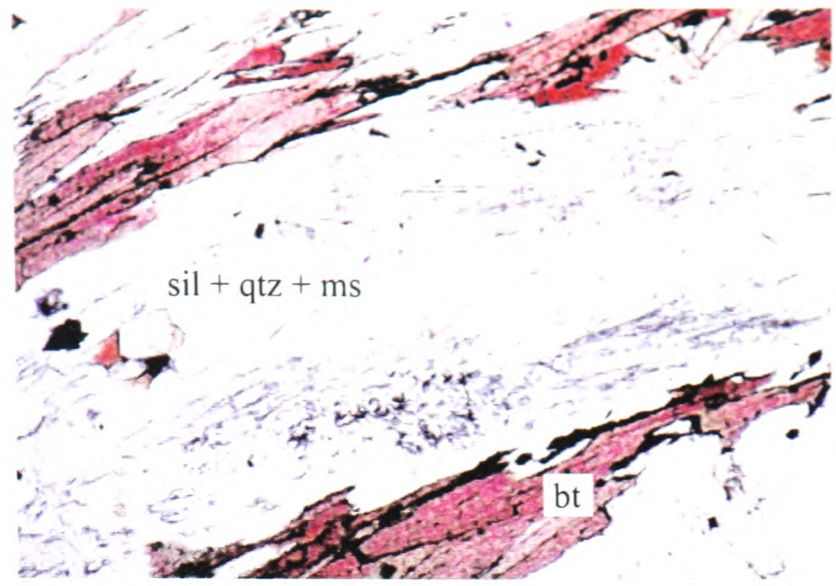


Figure 5.8d: Fibrolitic sillimanite orientated sub-parallel to the regional tectonic foliation in the MFZ. The sillimanite is enclosed within a coarse-grained aggregate of quartz and muscovite. Field of view c.2mm. (Sample JDW 187; see Figure 5.5b for location).

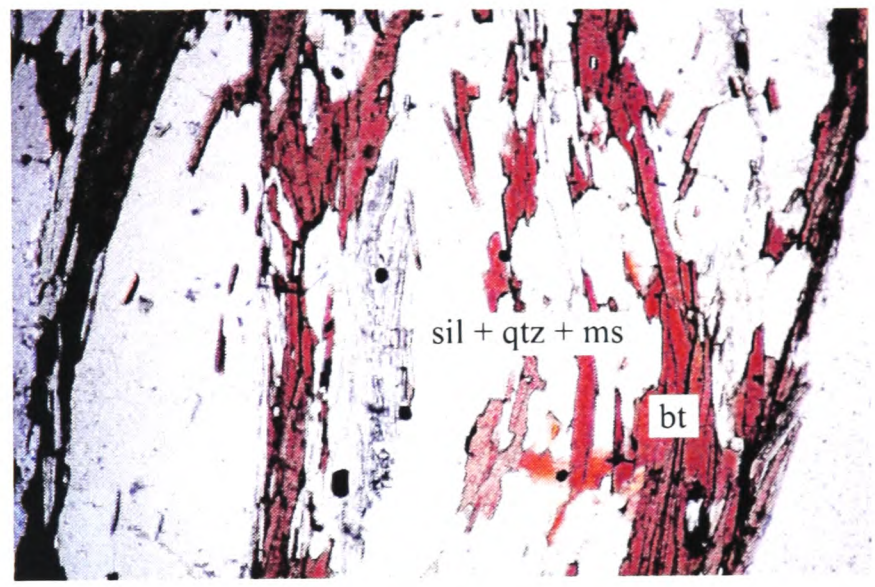


Figure 5.8e: Prismatic sillimanite enclosed within coarse-grained muscovite and quartz Field of view c.2mm. (Sample JDW 187; see Figure 5.5b for location).

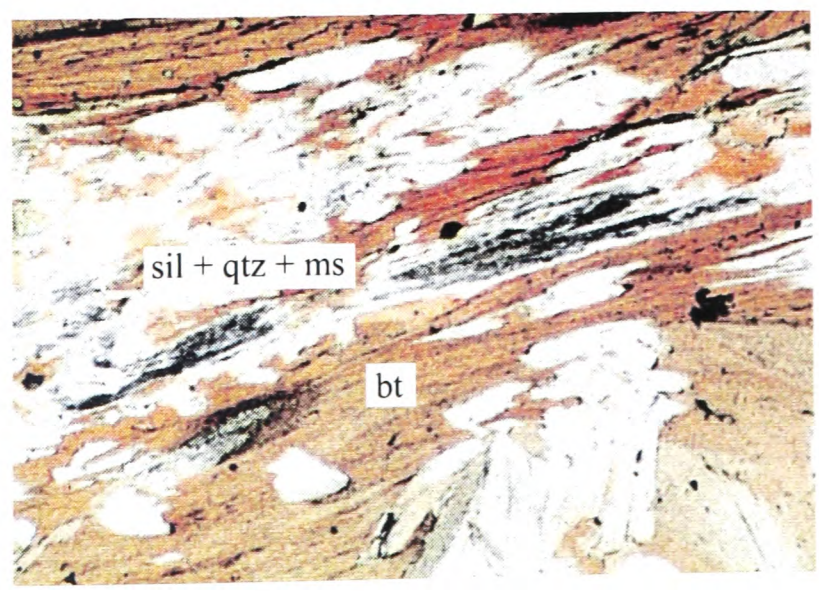


Figure 5.8f: Fibrolitic sillimanite enclosed within quartz. The sillimanite is parallel to the regional tectonic foliation in the MFZ. Field of view c.3mm. (Sample JDW 185; see Figure 5.5b for location).

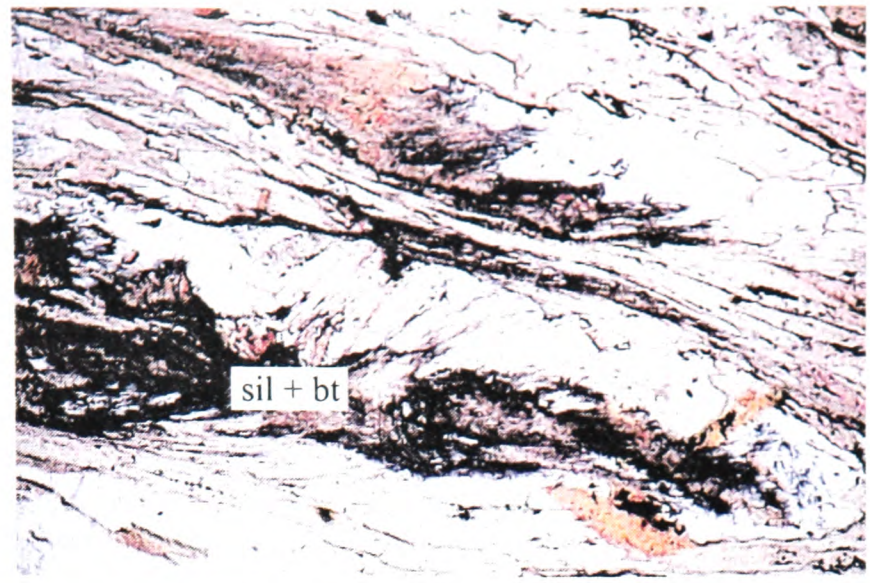


Figure 5.8g: Randomly orientated bundles of fibrolitic sillimanite overgrowing biotite. Field of view c.3mm. (Sample JDW 193; see Figure 5.5b for location).

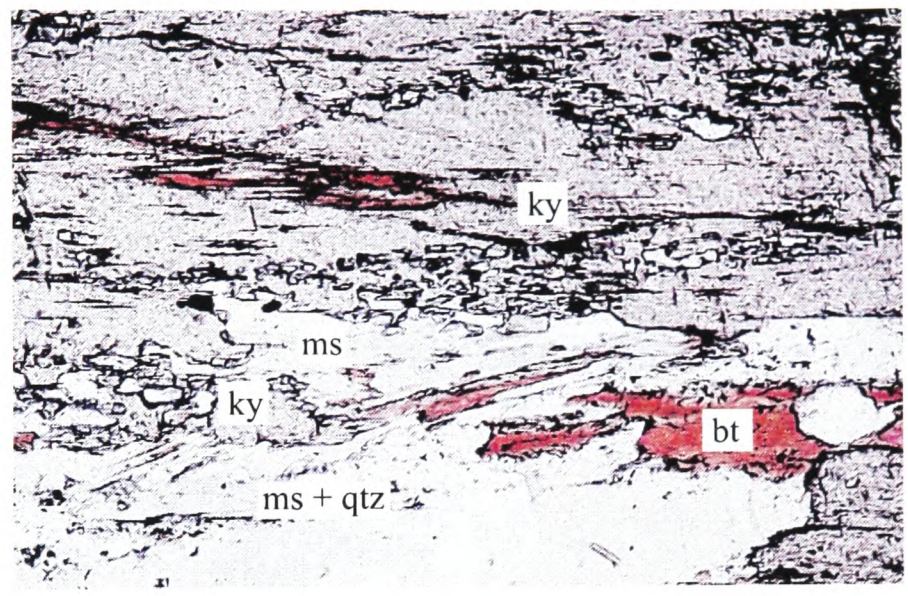


Figure 5.8h: Kyanite replaced by muscovite and quartz. Field of view c.2mm. (Sample JDW 193; see Figure 5.5b for location).

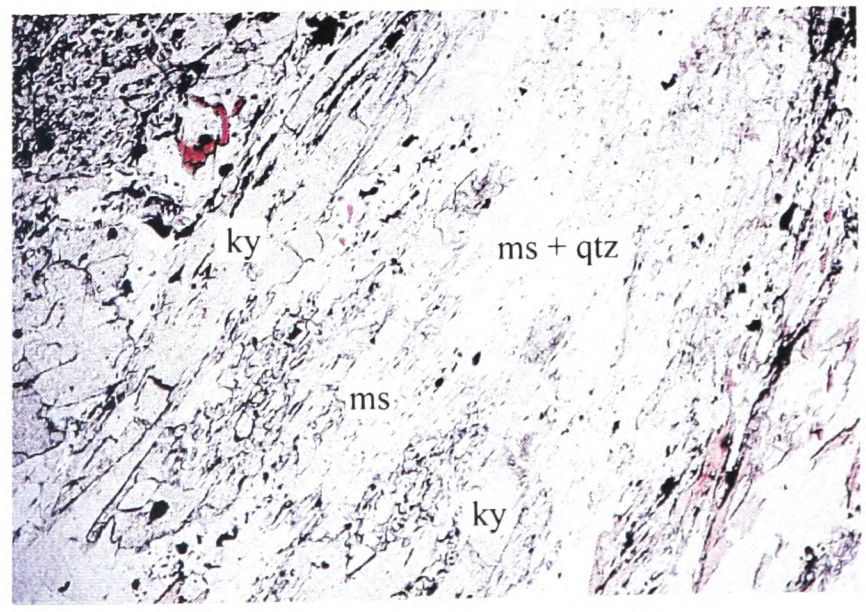


Figure 5.8i: Skeletal kyanite porphroblasts replaced by a coarse-grained aggregate of muscovite and quartz. Field of view c.2mm. (Sample JDW 195; see Figure 5.5b for location).

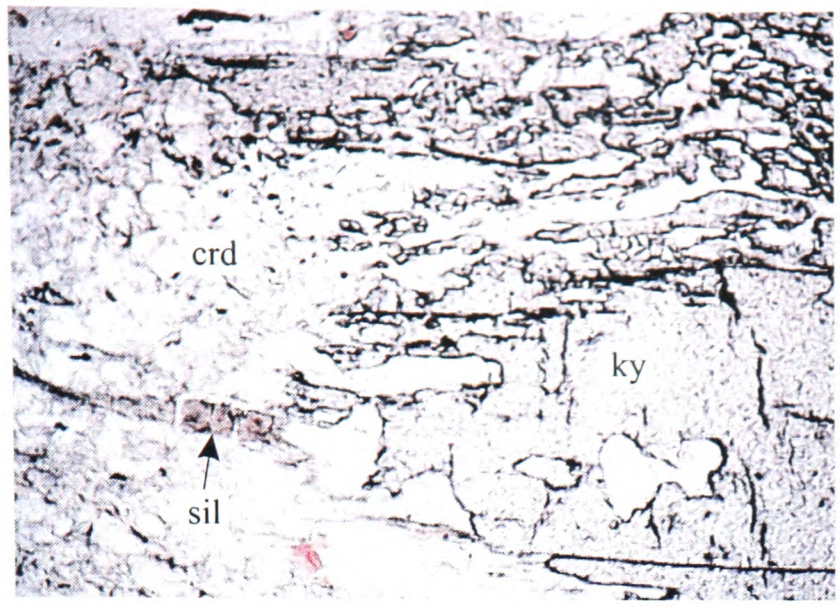


Figure 5.8j: Kyanite and sillimanite replaced by late-stage cordierite. Field of view c.2mm. (Sample JDW 193; see Figure 5.5b for location).

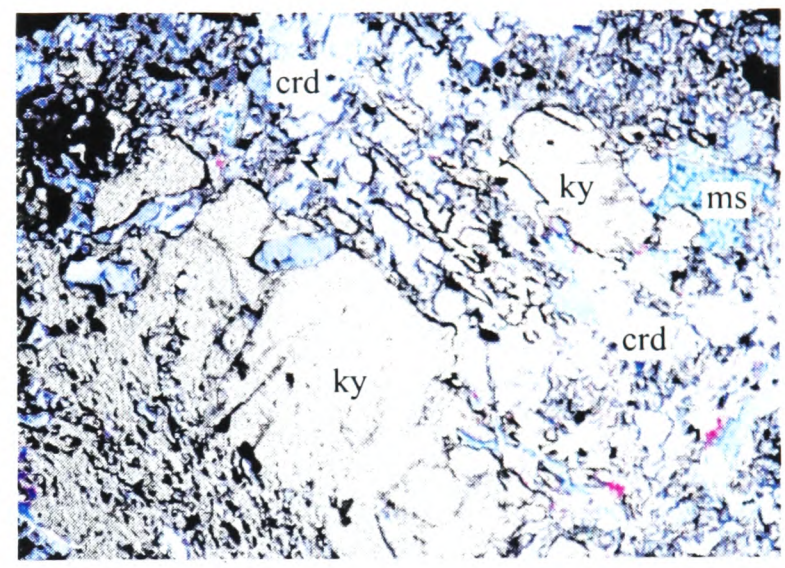


Figure 5.8k: Kyanite replaced by late-stage cordierite. Field of view c.2mm. (Sample JDW 192; see Figure 5.5b for location).

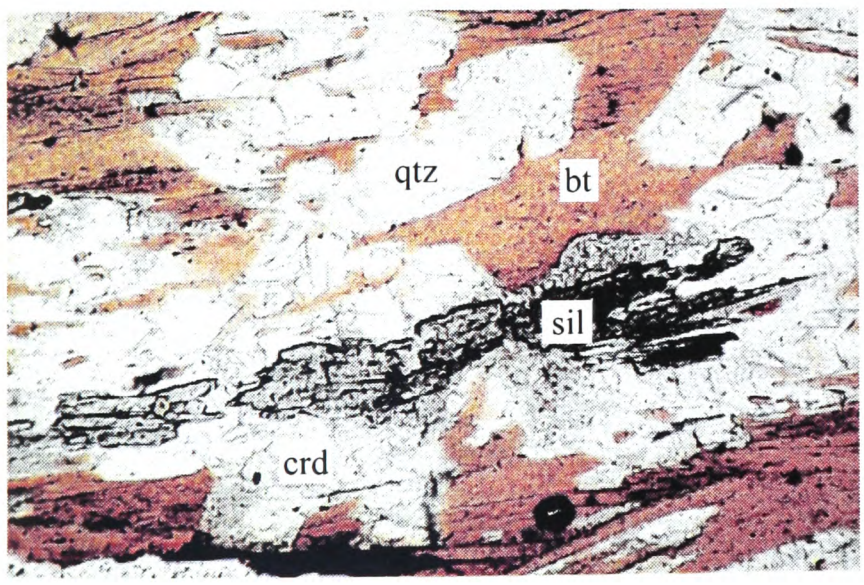


Figure 5.8l: Prismatic sillimanite surrounded by a mantle of late-stage cordierite. Field of view c.2mm. (Sample JDW 185; see Figure 5.5b for location).



Figure 5.8m: Late-stage cordierite overgrowing sub-hedral graphite-free staurolite porphyroblasts and sheaves of biotite. It is uncertain whether the staurolite is a product or a reactant in the cordierite-forming reaction. Field of view c.4mm. (Sample JDW 186; see Figure 5.5b for location).

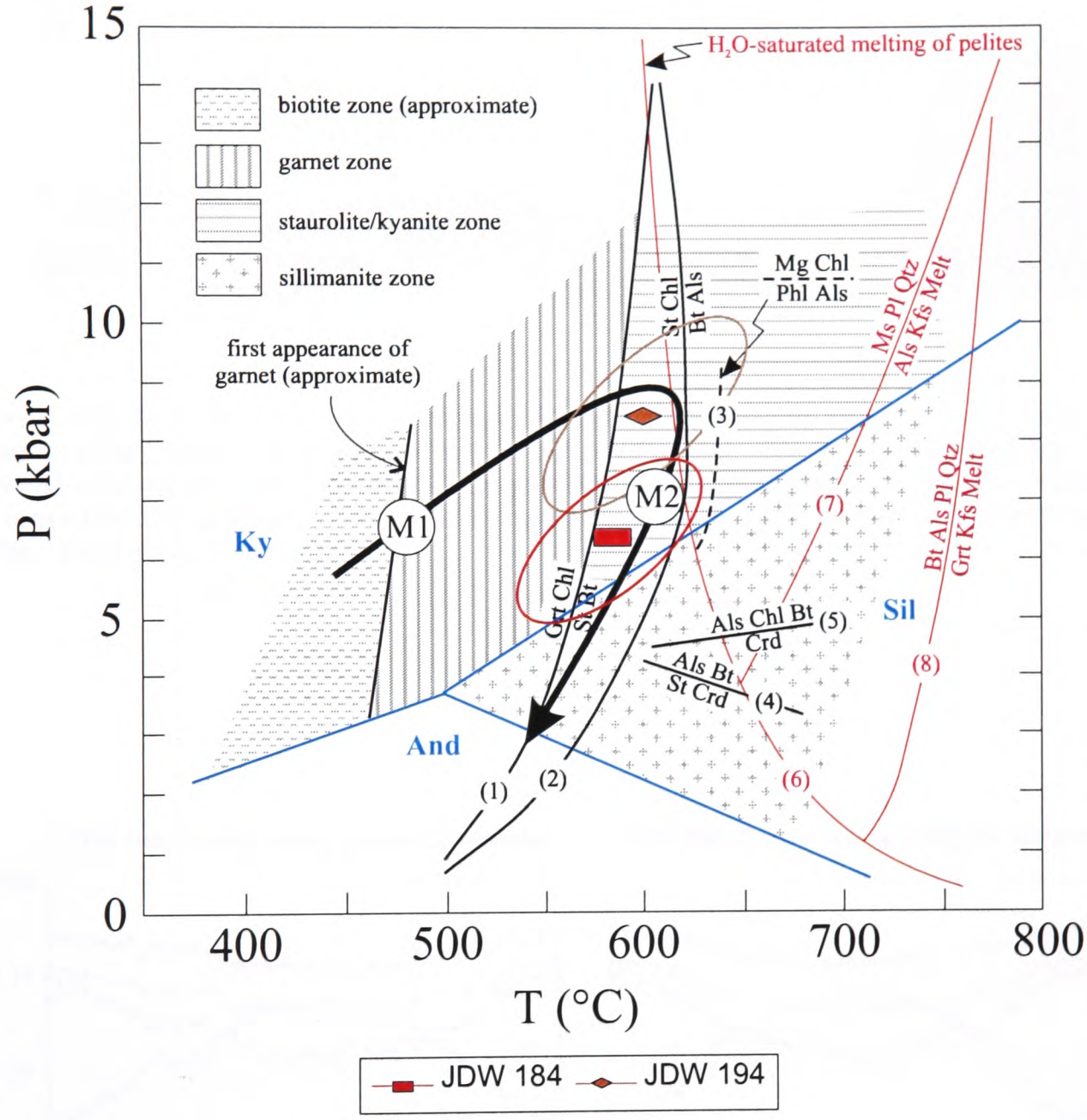


Figure 5.9: Composite petrogenetic grid for metapelites showing the location of important reactions during a Barrovian-type metamorphism. Solid and dashed black lines refer to reactions in the KFMASH and KMASH systems respectively. Reactions (1) to (3) taken from Spear (1993), reactions (4) and (5) taken from Harte (1975). Solid blue lines denote the Al-silicate phase diagram of Holdaway and Mukhopadhyay (1993). Red lines show the important vapour present and vapour absent melting reactions in metapelites. Reaction (6) taken from Thompson (1982), reaction (7) from Peto (1976) and reaction (8) from Le Bretton and Thompson (1988). The position of curves (1) to (5) is dependent upon metamorphic fluid compositions: the curves shift to the left when XH20<1. Ellipses correspond to quantitative P-T estimates of samples JDW 184 and 194 as determined using the computer programme THERMOCALC (Powell & Holland, 1988). Errors are shown at the $1<\sigma<2$ level. Arrows denote the possible P-T pathway of rocks in the MFZ as inferred from phase relationships (M1 = prograde growth associated with crustal shortening and thickening. M2 = near-isothermal decompression associated with uplift and exhumation). Note that textural evidence for the cordierite-forming reaction is poorly constrained. Although it involves the breakdown of sillimanite and kyanite, it may not correspond to reactions (4) and (5) shown above.

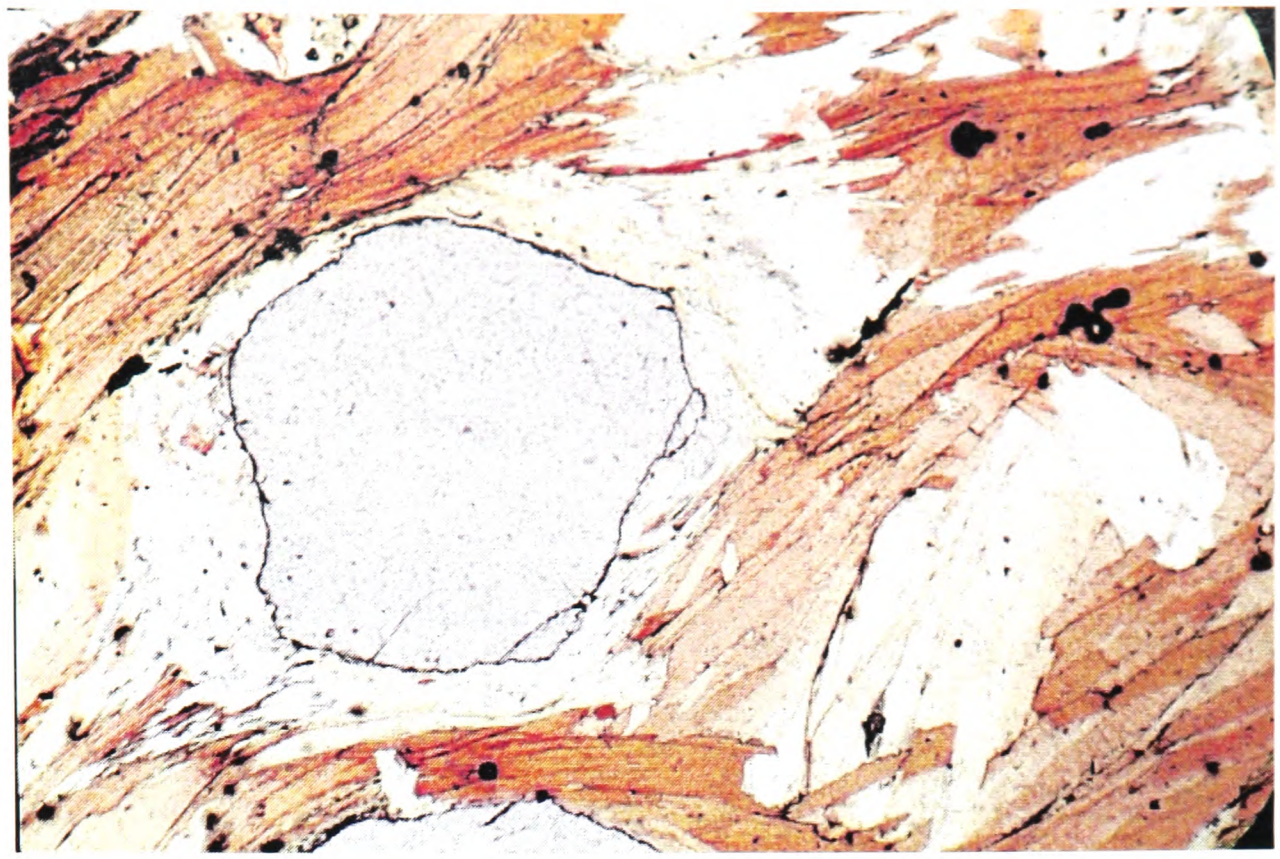


Figure 5.10a: Resorbed garnet porphyroblast in sample JDW 186 (see Figure 5.5b for location). The garnet is inclusion-free and shows no textural evidence of zoning. It is impossible to tell when the garnet grew and what reactions were involved. It is possible (albeit unlikely) that this garnet is restitic in origin and is pre-Himalayan in age. The garnet is mantled by a coarse-grained array of late-stage chlorite and biotite. Field of view c.4mm.

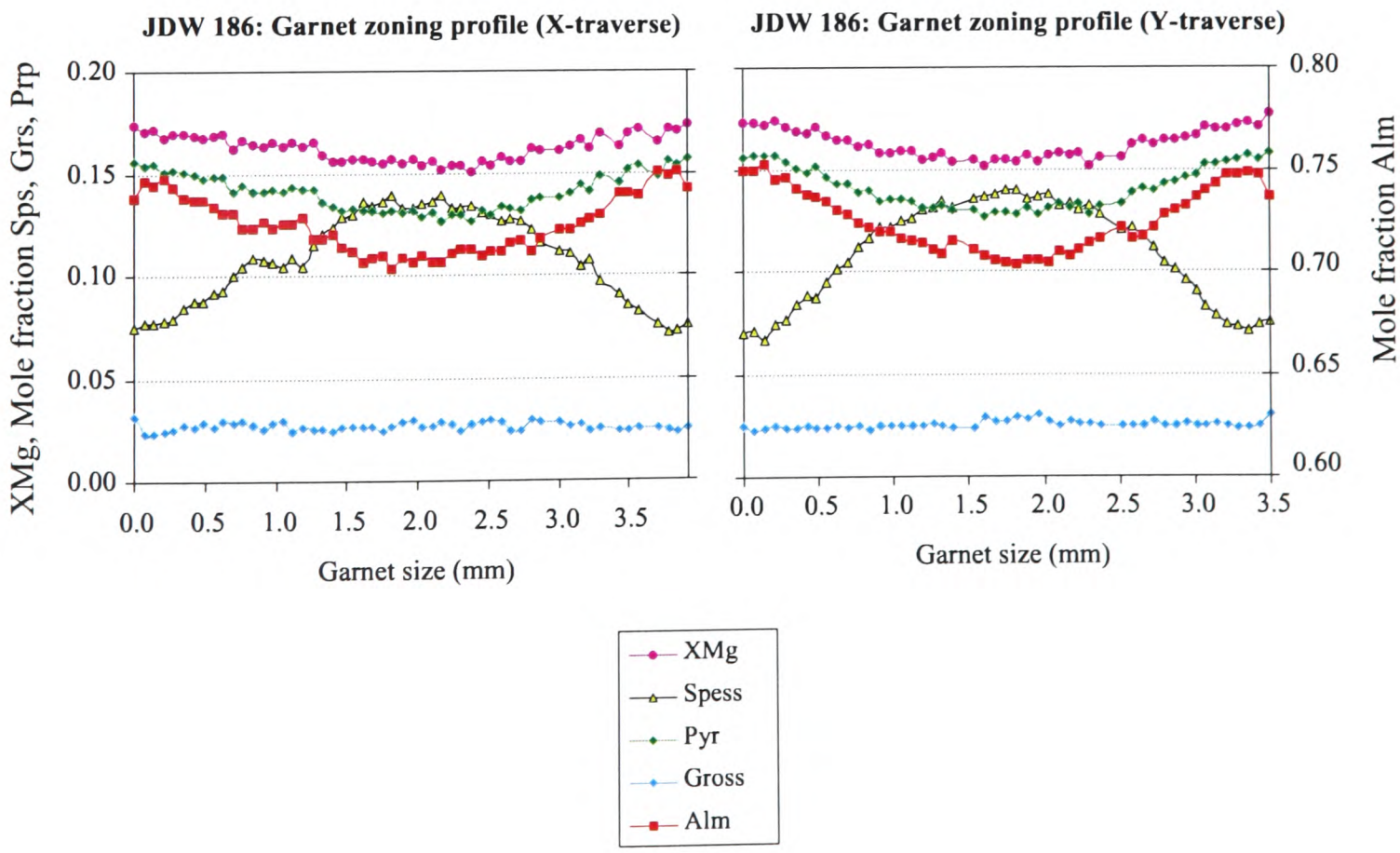


Figure 5.10b: Mutually perpendicular garnet zoning profiles through a similar, but slightly larger resorbed garnet porphyroblast similar to that shown in Fig. 5.10a. The profiles are indicative of prograde garnet growth with retrograde rim re-equilibration, as evidenced by the slight increase in Mn..

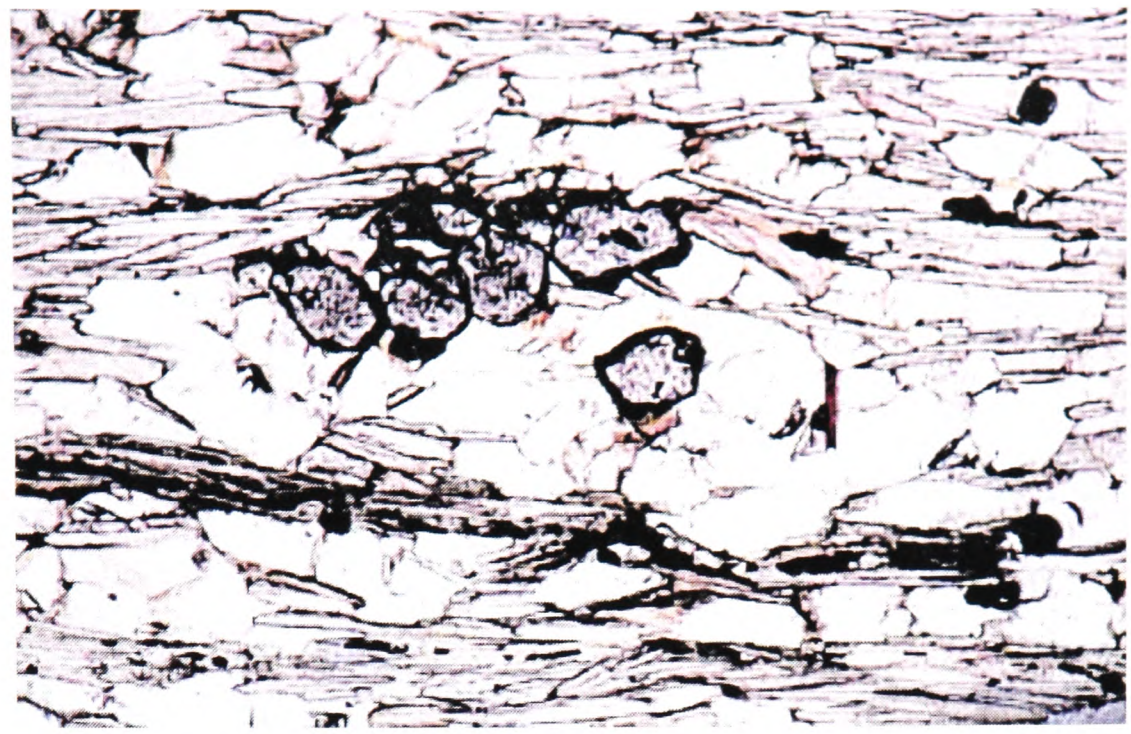


Figure 5.11a: Small garnets in sample JDW 184 (see Figure 5.5b for location). The garnets show no obvious relationship with the matrix foliation and it remains uncertain when they grew. Field of view c.2mm.

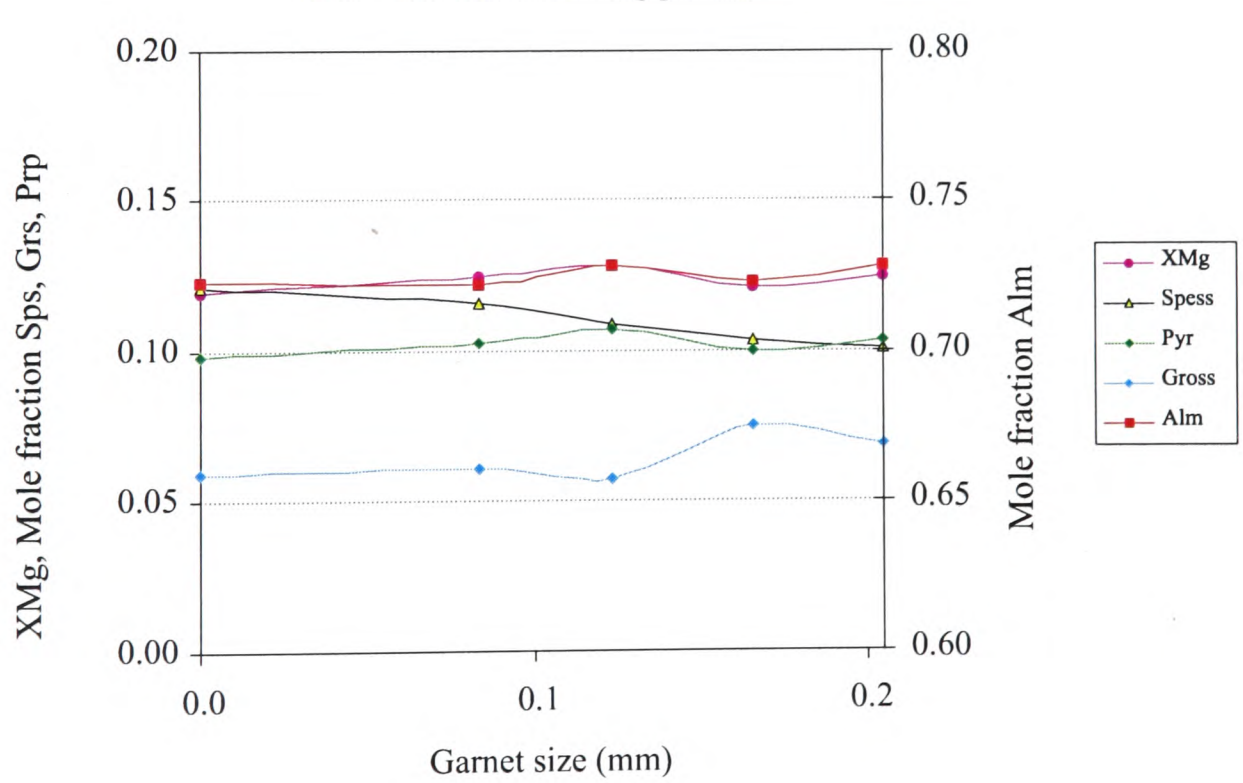


Figure 5.11b: Garnet zoning profile across one of the garnets shown in 5.11a. The garnets are chemically homogeneous, which could reflect diffusional homogenisation at temperatures in excess of c.600°C, or it could reflect the fact that these garnets are too small to display zoning.



Figure 5.12a: Garnet porphyroblasts in sample JDW 194 (see Figure 5.5b for location). The garnets display textural evidence for two phases of growth. Stage 1 corresponds to the growth of the garnet core which contains ilmenite inclusions. Stage 2 corresponds to the growth of garnet the rims, which in addition to the ilmenite, also contain abundant inclusions of apatite and tourmaline. X-Y refers to garnet zoning profile shown in Fig 5.12d. Field of view c.2.5mm.

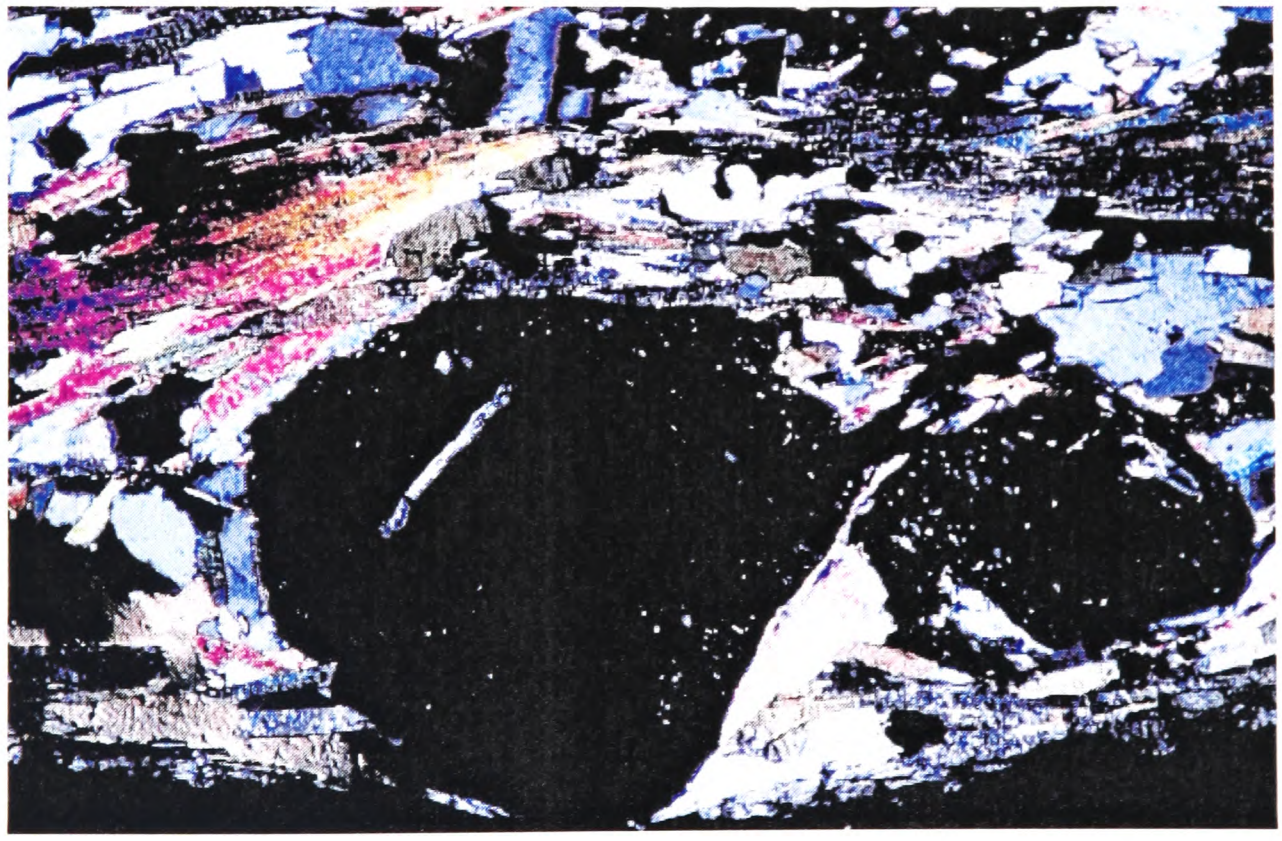


Figure 5.12b: As for 5.12a except in crossed-polars. The core and rim regions are readily distinguished in this photograph (the core is isotropic, whilst the rim contains abundant inclusions of birefringent apatite and tourmaline).

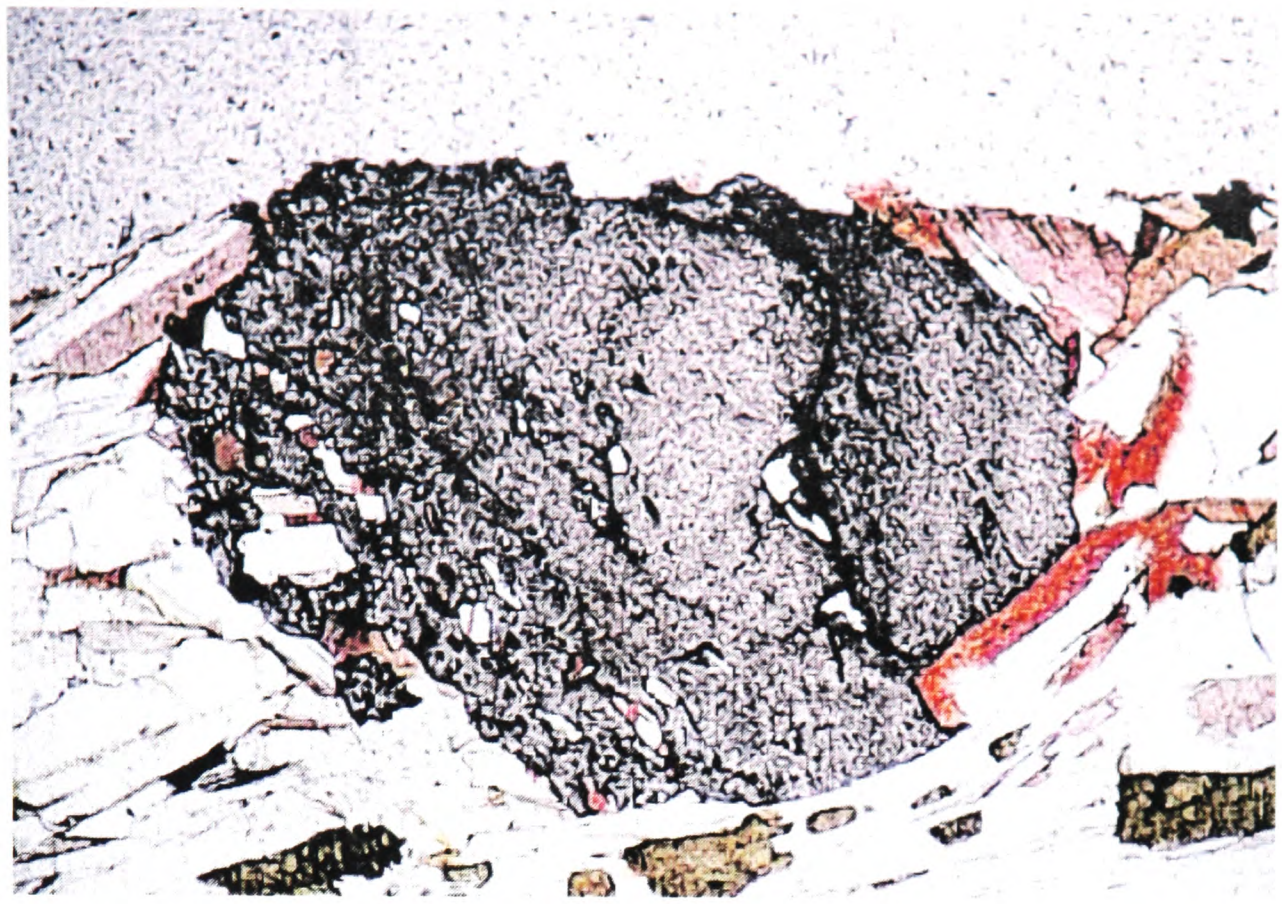


Figure 5.12c: Garnet porphyroblasts in sample JDW 194 (see Figure 5.5b for location). The large garnet in this picture contains ilmenite inclusions which trend at a high angle to the matrix foliation. The rim of the garnet on the right of the picture is ilmenite-free and is more spongy-looking than the core. The rim appears to overgrow the matrix foliation. Field of view c.2.5mm.

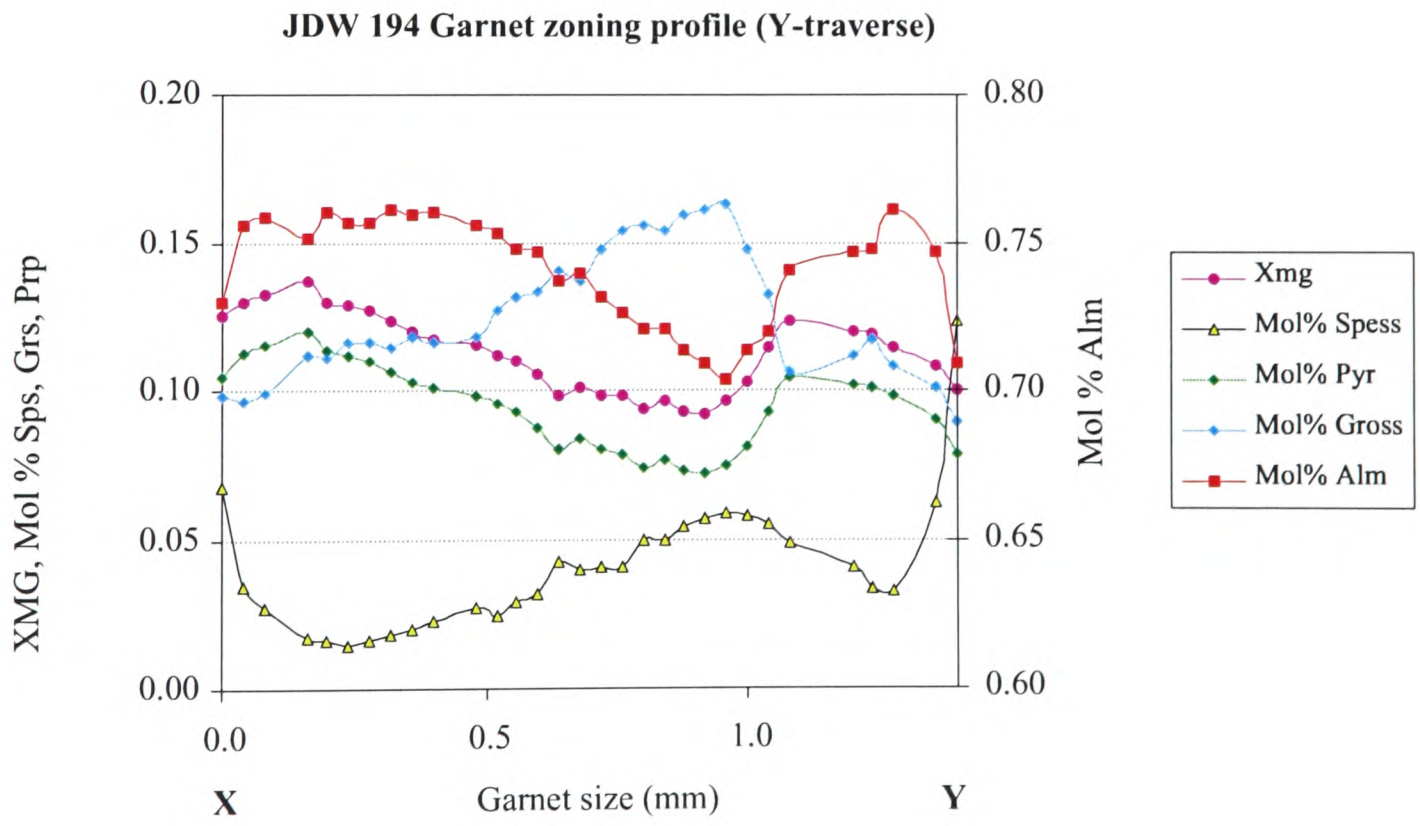


Figure 5.12d: Garnet zoning profile along transect shown in Fig 5.12a. The core defines a slightly flattened prograde growth zoning profile, whilst the rim displays chemical characteristics of retrograde growth.

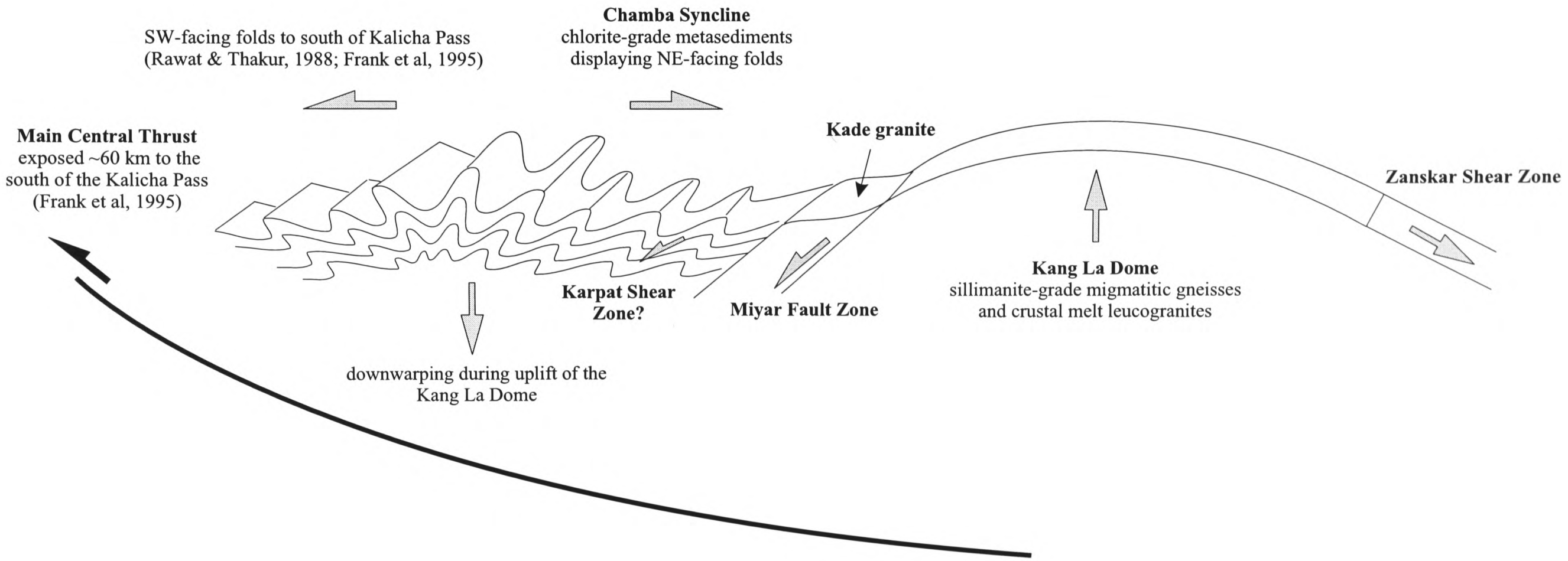


Figure 5.13: Schematic representation of the structure between the MCT and ZSZ in the western part of the study area. The Chamba Syncline represents a region of chlorite-grade Lower Palaeozoic sediments which are deformed by early NE facing folds. These folds can be traced along strike into the Tandi Syncline. The NE-facing folds become progressively more upright towards the south and eventually become SW-facing structures according to the mapping of Rawat & Thakur (1988) and Frank et al (1995). Preservation of the Chamba Syncline is interpreted to be related to structural downwarping as a result of thermal doming of the Kang La Dome at the top of the slab.



The imposing 5700m pinnacle of Mt. Gumburanjon in SE Zanskar (viewed looking towards the south-east along the Kargyak Chu).

Chapter 6

Geology of the upper slab (Darcha-Kargyak)

6.1 Introduction

This chapter discusses the structure and metamorphism in the upper part of the High Himalayan Slab in SE Zanskar and NW Lahaul along a north-south traverse across the Shingo La from Darcha to Kargyak (Figures 3.20 & 6.1; cross-section B-B' on Enclosure 1). Lithologically, this part of the study area is comprised of a thick succession of unfossiliferous calcareous sands, silts and shales which are interpreted to form part of the Precambrian-Cambrian Haimantas. These are underlain to the south of the Shingo La by the Precambrian-Ordovician(?) Kade granite (Chapter 3). The majority of these lithologies are located within the chlorite/biotite zone and have never experienced amphibolite-facies metamorphic conditions (Enclosure 2). Metamorphic grade increases sharply at the very top of the slab into kyanite-grade conditions, where the metasediments and orthogneisses in the footwall of the ZSZ are discordantly intruded by the weakly deformed Gumburanjon leucogranite.

6.2 Structural observations

The structure in the upper part of the slab is extremely complex and is best discussed with reference to the cross-section shown in Figure 6.1. The style of deformation progressively changes from south to north along this traverse, making it difficult to separate structures into discrete deformation phases, as has been done for other parts of the study area.

6.2.1 Contact of the Haimantas with the Kade granite

The Haimantas form an s-parallel contact above the Kade granite to the south of the Shingo La (Figure 6.2a). An intense tectonic foliation is developed within the Kade granite which trends at a high angle to bedding in the overlying sediments (Figure 6.2b). The fact that this fabric cannot be traced into the overlying Haimantas suggests the possibility that the contact is tectonic in origin. However, the sediments immediately above the granite preserve detrital sedimentary textures and do not show any evidence of high strain fabrics which would be expected if this were a tectonic contact. Indeed, the sediments immediately above the granite have a very hard, baked appearance, suggesting the contact to be magmatic in origin (no hornfels textures were observed in any of the samples collected adjacent to the granite to support this interpretation). The exact nature of the contact between the Haimantas and the Kade granite to the south of the Shingo La therefore remains

somewhat ambiguous. It is possible, albeit unlikely, that the fabric within the Kade granite was developed prior to the deposition of the overlying sediments. Such a scenario seems unlikely given the observation that the Kade granite discordantly intrudes the Haimantas near Darcha (Figure 3.8). A second possibility is that this fabric developed during granite emplacement and is unrelated to Himalayan tectonics, although this also seems somewhat unlikely. A third possibility is that deformation partitioning brought about by strong rheological contrasts resulted in this fabric developing in localised shear zones within the Kade granite but not in the overlying sediments during the Himalayan orogeny. This is supported by field observations which demonstrate that fabric development within the Kade granite (and other Lower Palaeozoic granites exposed throughout the study area for that matter) is extremely heterogeneous. Near Darcha, the Kade granite is observed to be a coarse-grained and preserves both equigranular and more locally, porphyritic textures. Tectonic fabrics similar to that shown in Figure 6.2b are only locally developed and become increasingly prevalent towards the west, suggesting that the intensity of deformation within the Kade granite may increase in this direction. This is consistent with the observation that the Kade granite becomes an intensely foliated orthogneiss in the upper Miyar nala to the north of Patam (cross-section A-A' on Enclosure 1), which is located immediately along strike and to the west of the Barai nala (Enclosure 1).

6.2.2 Structure to the south of the Shingo La

The Haimantas immediately above the Kade granite dip 30-40° towards the NE and are deformed by symmetrical MW-style folds with NW-SE trending fold axes (Figures 6.1 & 6.3). These folds are best developed in pelitic lithologies and are only weakly developed in the more competent psammites (Figure 6.3). They show no sense of vergence and cannot be used to discern anything about the kinematics associated with this deformation phase. A weak (non-penetrative) crenulation cleavage is developed along the axial surfaces of these folds and dips shallowly towards the SW (Figures 6.1 & 6.3). They are probably F_1 folds since there is no evidence to support the existence of a preceding phase of folding in these sediments. Despite the absence of evidence for an earlier phase of folding, microstructural observations show that bedding is parallel to a strong planar fabric which is defined by metamorphic muscovite and biotite. This is interpreted to be a flattening fabric which developed in response to flattening of the Haimantas against the Kade granite. However, it could equally be interpreted to represent an axial planar fabric related to an early phase of isoclinal folding. Although isoclinal fold closures were occasionally observed within the Haimantas to the south of the Shingo La, their general absence in this part of the slab suggests the latter possibility to be unlikely.

Deformation in the Haimantas becomes progressively more intense towards the north away from the Kade granite. Deformation is particularly intense near Ramjak campground, to the south of the Shingo La (Figure 6.1). Bedding cannot be traced laterally for any significant distance in this part of the slab and is intensely deformed by flat lying isoclinal folds (Figures 6.4a & b). Individual beds also appear to be truncated by semi-brittle thrusts which show a top-to-the-south-west sense of shear

(Figure 6.4c). These observations suggest that this part of the slab is located within a major crush zone, hereafter referred to as the Shingo Thrust Zone (Enclosure 1; Figure 6.1). North of the Shingo Thrust Zone, bedding progressively steepens and is sub-vertical near the summit of the Shingo La (Figure 6.5a). These sediments are also folded by symmetrical MW-style folds of inferred F_1 origin (Figure 6.5b).

6.2.3 Structure to the north of the Shingo La

The structure to the north of the Shingo La is extremely complex and is dominated by a strong planar fabric which dips ~10-30° towards the S/SE (Figures 6.6 & 6.7a). This represents a change in orientation of almost 180° from the north-easterly-dipping fabrics seen to the south of the pass and implies that the Shingo La is coincident with a major synformal axis (Figure 6.1). This is supported by the observation that lithologies either side of the Shingo La are extremely calcareous and probably form part of the uppermost Haimantas, directly beneath the Middle Cambrian Karsha Formation (see Chapter 3 for lithological discussion).

The dominant south-dipping fabric to the north of the Shingo La is sub-parallel to bedding and appears to be axial planar to isoclinal folds of inferred F_1 origin (Figure 6.7b), suggesting it to be a composite S_0/S_1 fabric. With increasing metamorphic grade, this fabric is progressively replaced by an S_2 crenulation foliation (Figure 6.7c), which remains sub-parallel to S_0/S_1. In the immediate footwall of the ZSZ, the S_2 fabric changes orientation and dips ~20-30° towards the NE (Figure 6.7a), a feature which is attributed to drag folding in the uppermost part of the ZSZ. The S_0/S_1 and S_2 fabrics are overprinted by later fabrics which developed during extension along the ZSZ (Figure 6.7a). These are referred to as S_3 extensional shear band fabrics and are discussed more fully in section 6.2.4. Three readily identifiable fabrics are therefore distinguished on the northern side of the Shingo La, which correspond to three discrete deformation phases (Table 6.1). This contrasts sharply with the structure seen on the southern side of the pass, where fabrics are dominated by bedding (S_0) and are folded by MW-style F_1 folds (see section 6.2.2).

Table 6.1: Fabric elements relating to different deformation phases to the north of the Shingo La

Deformation phase	Fold generation	Planar Fabric	Mineral lineation	Structural features
Deposition	None	S_0	None	Bedding
D_1	F_1	S_1	L_1	Axial planar cleavage (sub-parallel to isoclinal folds)
D_2	F_2	S_2	L_2	Crenulation cleavage
D_3	F_3	e-s-c	L_3	Extensional shear band fabrics (related to movement on the ZSZ)

No major structural or metamorphic discontinuities were observed on crossing the Shingo La. The change in structural style across the Shingo La is therefore interpreted to be related to the fact that deeper structural levels have been exhumed in the footwall of the ZSZ (Figure 6.7a). This is consistent with the observation that metamorphic grade increases sharply towards the top of the slab

from biotite- to kyanite-grade conditions (Figures 6.1 & 6.7a). Beneath the kyanite-grade metapelitic schists in the footwall of the ZSZ, the Haimantas are underlain by an intensely deformed sequence of banded orthogneisses, augen gneisses, biotite gneisses and leucocratic pegmatites (Figures 6.6-6.9). The contact between the schists and granitic/biotite gneisses is s-parallel, which led Pognante *et al.* (1990) to suggest that it represents a late-stage thrust (the Miyar Thrust) which separates the underlying orthogneisses (HHC) from the overlying kyanite-grade Haimantas (or Kade Unit, to use the terminology of Pognante *et al.*). Personal field observations demonstrate that the so-called Miyar Thrust is not a late-stage structure because: (1) the contact is cross-cut by the Gumburanjon leucogranite (Figure 6.8); and (2) ZSZ-related extensional fabrics are observed in lithologies either side of this contact (see section 6.2.4). The possibility that the contact marks the site of an old thrust which developed during D_1/D_2 cannot be discounted from the available field evidence, but seems unlikely given that thermobarometric estimates from garnet-bearing schists either side of this contact record similar P-T results (see section 6.3.3).

The origins of the S_0/S_1 and S_2 fabrics on the northern side of the Shingo La remains uncertain. They testify to intense crustal shortening and thickening in the upper part of the slab, which is probably, although not necessarily Himalayan in age. The kinematics associated with this deformation could not be ascertained in the field, owing to strong overprinting and re-orientation of early-formed structures by ZSZ-related deformation. As demonstrated by the stereonet data presented in Figure 6.7a, the orientation of early-formed fold axes is extremely variable, ranging from NW-SE to NE-SW. In the immediate footwall of the ZSZ, most early fold axes plunge shallowly towards the NE (Figure 6.7a), a feature which is attributed to rotation during intense D_3 deformation.

L_1 and L_2 mineral lineations are defined on S_1 and S_2 surfaces as streaked-out sheaves of muscovite and biotite. Immediately north of the Shingo La these plunge shallowly towards the WSW/SW in a down-dip direction (Figure 6.7a & Enclosure 3). Whilst this may be related to the kinematics associated with D_1 and D_2 deformation phases, it is more likely to be related to the sliding of units towards the WSW/SW during ZSZ-related D_3 deformation (see section 6.2.4). In the immediate footwall of the ZSZ, all mineral lineation (L_1-L_3) plunge towards the NE in a down-dip direction, a feature which is attributed to deformation in the ZSZ (see section 6.2.4).

6.2.4 The Zanskar Shear Zone

The ZSZ represents a major syn/post-metamorphic extensional detachment which can be traced almost continuously along the top of the High Himalayan Slab in western, central and SE Zanskar (Searle, 1986; Herren, 1987; Jain & Manickavasagam, 1993; Dransfield, 1994; Ayres, 1997; this study). It represents a local equivalent of the South Tibetan Detachment system which extends along almost the entire length of the Himalaya and separates the weakly metamorphosed rocks of the Tibetan Sedimentary Series from high-grade rocks of the High Himalayan Slab (see Chapter 2).

The ZSZ in central and western Zanskar is identified as the region at the top of the slab which is dominated by an intense NE-dipping tectonic fabric which displays abundant top-to-the-north-east

shear-sense indicators (Herren, 1987; Dransfield, 1994). In western Zanskar, the ZSZ is reported to comprise several discrete shear zones which have an overall width of between ~2-7km and a structural thickness of ~2-3km (Herren, 1987). In central Zanskar, the ZSZ has a structural thickness of ~3-5km (Dransfield, 1994), although it is also reported to form a single, well-exposed normal fault in places (Ayres, 1997). Further east, the ZSZ is less-well defined. Mapping by Spring and Crespo-Blanc (1992) and Vannay and Steck (1995) failed to identify a major extensional shear zone in the uppermost part of the High Himalayan Slab in NW Lahaul (i.e. north of the Baralacha La). Instead, these authors identified a relatively high angle (*c.*40-45°) semi-brittle normal fault which separates the amphibolite-grade sediments of the High Himalayan Slab from the weakly metamorphosed sediments of the Tibetan Sedimentary Series (Enclosure 2). This structure is referred to as the Sarchu Normal Fault (SNF) and probably represents a lateral equivalent of the ZSZ. Why the ZSZ thins into a narrow zone of semi-brittle deformation in this part of the slab remains uncertain. It may reflect deformation partitioning across a much wider area, rather than into a condensed zone of intense deformation. Alternatively, it could equally be the result of late-stage brittle normal faulting which has exhumed the ductile portion of the ZSZ in the footwall and downthrown it in the hangingwall.

A detailed study of the ZSZ was made in the vicinity of Mt. Gumburanjon at the eastern end of the Kargyak Chu in SE Zanskar (Figure 6.6). The structural top of the ZSZ is readily identified since it separates the intensely deformed and metamorphosed rocks of the High Himalayan Slab from the less intensely deformed and metamorphosed sediments of the Tibetan Sedimentary Series (Figure 6.10). Beneath this, the ZSZ represents a zone of intense and extremely complicated deformation which displays both top-to-the-E/NE and top-to-the-WSW/SW shear sense indicators (Figure 6.7a). The overall width and thickness of the ZSZ to the north of the Shingo La is difficult to define since it represents a zone of distributed deformation. Unlike central and western Zanskar, only the uppermost 300-400m of the ZSZ displays a NE-dipping tectonic foliation (Figure 6.7a). The dominant tectonic foliation to the north of the Shingo La dips ~10-30° towards the S/SE (Figures 6.6 & 6.7a), and is overprinted by ZSZ-related C'-type extensional shear bands which show both top-to-the-E/NE and top-to-the-WSW/SW shear-sense indicators (Figures 6.7a). The first appearance of extensional fabrics which give a top-to-the-north-east shear sense was used to define the lower bounding limit of the ZSZ, giving the structure an outcrop width of *c.*5km and a structural thickness of *c.*1-2km to the north of the Shingo La (Figure 6.7a).

NE-directed ductile fabrics in the ZSZ

Planar fabrics in the immediate footwall of the ZSZ dip ~20-30° towards the NE and show a well-developed mineral stretching lineation which plunges ~20-25° in a down-dip direction (Figure 6.7a). Shear sense indicators in this zone include well-developed C'-type extensional shear bands (Figures 6.11a-e), asymmetrical feldspar augen (Figure 6.11f) and asymmetrical pegmatite pods (Figure 6.11g),

all of which show a top-to-the-north-east shear sense and are indicative of NE-directed extension along the ZSZ.

Shear bands dip ~20-40° towards the NE (Figure 6.7a), suggesting that the actual dip of the ZSZ to be slightly shallower than this (see discussion in Passchier & Trouw, 1996). The shear bands cross-cut the earlier S_0/S_1 and S_2 fabrics and wrap porphyroblastic mineral phases such as garnet and staurolite (Figures 6.11b & d), thus implying that the ZSZ represents a late-stage structure which post-dates the growth of amphibolite-facies Barrovian assemblages. The shear bands are defined by the growth of metamorphic muscovite, biotite and chlorite along discrete S-surfaces (Figure 6.11a-e), suggesting that extension occurred under at least greenschist facies conditions. Since C'-type shear bands are believed to develop during the later stages of extensional deformation in shear zones (e.g. Platt & Vissiers, 1980), then the earliest phase of extension along the ZSZ probably occurred at high temperatures at mid-crustal levels. This is supported by the 1-2km structural thickness of the ZSZ and plastic deformation textures seen in K-feldspar augen (Figure 6.11f), which imply that temperatures must have been in excess of ~400-450°C (Tullis & Yund, 1977) during extension.

With increasing distance away from the footwall (towards the south), the intensity of ZSZ-related deformation progressively decreases. This is concomitant with a change in the dip of the dominant tectonic foliation ~10-30° towards the S/SE (Figure 6.7a) and a decrease in metamorphic grade from kyanite- to biotite-grade conditions (Enclosure 2). C'-type extensional shear bands are occasionally observed cross-cutting the southerly-dipping tectonic fabric in the region between the Shingo La and the Gumburanjon leucogranite (Figure 6.7a). These shear bands wrap previously formed biotite porphyroblasts and are therefore syn/post-metamorphic in origin (Figure 6.11h-j). They generally dip 20-40° towards the E/NE and show a top-to-the-E/NE shear sense, suggesting that they are temporally related to extension along the ZSZ.

No evidence was found to support any major strike-slip movement along the ZSZ to the north of the Shingo La. However, ductile fabrics in the ZSZ to the south of Padum (Temasa nala) provide strong evidence that extension in this part of the slab was associated with a minor component of dextral strike slip (Figure 6.12).

Brittle fabrics in the ZSZ

The Tibetan Sedimentary Series in the immediate hangingwall of the ZSZ forms a 50-75m-thick cataclastic mélange (Figure 6.13a). Large, randomly orientated blocks of brown dolomite (from the Cambrian Karsha Formation) and red conglomerate (from the Devonian Thaple Formation) are incorporated into this zone. Late-stage brittle normal-faults dipping *c.*40-50° to the north-east are also observed cutting across the ductile fabrics in the footwall of the ZSZ (Figure 6.13b), suggesting that extension must have continued at depth whilst higher structural levels were exhumed through the brittle-ductile transition. Many of the garnets in the immediate footwall of the ZSZ are extensively

cracked and have been partly replaced by chlorite (Figure 6.13c). Such textures are interpreted to have formed as amphibolite-facies lithologies were exhumed through the brittle-ductile transition.

WSW/SW verging ductile structures in the ZSZ

Many structures to the north of the Shingo La show a top-to-the-WSW/SW shear sense. Some of these structures are compressional (Figure 6.14a-c), suggesting that NE directed extension along the ZSZ was preceded by, and/or was broadly contemporaneous with periods of WSW/SW directed folding and thrusting(?). This is hardly surprising given the fact that the Himalaya have been under a state of constant compression since the India-Asia collision some 54-50 Ma (see Chapter 1). In addition to these compressional structures, extensional shear-band fabrics which show a top-to-the-WSW/SW shear-sense were occasionally observed cross-cutting the south-dipping $S_0/S_1/S_2$ fabric on the northern side of the Shingo La (Figures 6.7a & 6.14d & e). Development of these shear bands is interpreted to be related to doming in the immediate footwall of the ZSZ as deeper structural levels were progressively exhumed. Doming would cause southerly-dipping lithological units to extend towards the WSW/SW, thus creating a combination of WSW/SW verging compressional folds, aswell as WSW/SW-dipping extensional shear band fabrics.

6.3 Metamorphism in the ZSZ

The majority of lithologies exposed in the upper part of the study area are located within the chlorite/biotite zone (Enclosure 2) and have never been buried to any significant depth following the India-Asia collision. Metamorphic grade increases sharply at the very top of the slab in the immediate footwall of the ZSZ (Figure 6.7a), suggesting that this structure was responsible for the exhumation of high-grade lithologies. Given the decrease in metamorphic grade away from the ZSZ towards the south, it seems likely that burial of the upper part of the slab was accomplished by the overthrusting of units towards the SW along a major structure which may well have been an early pre-cursor to the ZSZ.

6.3.1 Metamorphic mineral growth in relation to deformation in metapelites

This section discusses the growth of Barrovian index minerals in metapelites and their temporal relationship to the development of fabrics on the northern side of the Shingo La. The results of this work are summarised as a time-event sequence in Figure 6.15.

Chlorite

Chlorite is rarely observed in the metapelites exposed on the northern side of the Shingo La. It is generally observed growing as a late-stage phase along extensional shear bands (Figure 6.11e) and as a retrograde phase replacing garnet (Figure 6.13c).

Muscovite and biotite

Plates of muscovite and biotite are observed forming the dominant southerly-dipping S_0/S_1 fabric in the metapelites exposed on the northern side of the Shingo La. In the biotite-grade lithologies exposed immediately north of the Shingo La, muscovite has a distinct green hue, indicative of an Fe^{2+}-rich phengitic composition. Pure white muscovite is observed in the higher-grade lithologies exposed in the footwall of the ZSZ. Muscovite and biotite are also observed forming the S_2 crenulation cleavage, and occasionally define the extensional shear bands in the ZSZ. Muscovite and biotite growth therefore appears to have occurred continually in the upper part of the slab where temperatures were sufficiently high (*c.*350°C).

Large biotite porphyroblasts are observed statically overgrowing the S_0/S_1 fabric in the magnesium-rich pelites of the Haimantas immediately north of the Shingo La and frequently contain graphitic and quartz inclusion trails which preserve the remains of the S_0/S_1 fabric (Figure 6.16a). Some biotites preserve graphitic inclusion trails which trend at a high angle to one another (e.g. sample JDW 240 shown in Figure 6.11i). Two possible scenarios can be envisaged to explain this relationship: (1) it represents mechanical re-orientation of a pre-existing grain; or (2) it represents multiple phases of biotite growth. The latter interpretation is preferred since the graphitic inclusion trail in lower part of the porphyroblast shown in Figure 6.11i is observed to bend into the matrix foliation. Many of the biotites in sample JDW 240 show a top-to-the-north-east shear sense, which is interpreted to be related to movement along the ZSZ. If correct, then this implies that porphyroblastic biotite growth may have been syn-kinematic with respect to D_3 deformation along the ZSZ (Figure 6.15). It is possible, albeit unlikely, that the tectonic significance of these shear sense indicators has been mis-interpreted and that they actually attest to a major phase of NE directed deformation in the upper part of the slab prior to the initiation of significant extension along the ZSZ.

Garnet

Garnet is a ubiquitous phase in the amphibolite-facies metapelites exposed in the footwall of the ZSZ. They are frequently wrapped by C'-type extensional shear band fabrics (e.g. Figure 6.11d), thus implying that garnet growth pre-dated movement along the ZSZ. Many garnets contain straight, curved, or crenulated inclusion trails which probably represent the remains of the S_0/S_1 fabric (e.g. Figures 6.16b-d). Field evidence demonstrates that some garnets grow across the S_2 crenulation fabric (Figure 6.11b), suggesting that garnet growth continued at high temperatures during D_2 and ceased growing following the initiation of extension along the ZSZ (Figure 6.15).

Staurolite

Staurolite is also a common metamorphic phase in the amphibolite-facies metapelitic schists in the footwall of the ZSZ. It is observed in some samples overgrowing the S_2 crenulation fabric at the expense of garnet (Figure 6.16e), thus implying that staurolite growth was syn/post-kinematic with respect to the development of the S_2 fabric and post-dated the growth of porphyroblastic garnet (Figure

6.15). Staurolite growth is interpreted to pre-date extension along the ZSZ, although no textural evidence was found to support this.

Kyanite

Kyanite was observed in some float samples collected from the scree slopes at the base of the Gumburanjon leucogranite. It forms centimetric porphyroblasts which are sub-parallel to the S_2 fabric, suggesting that kyanite growth was pre/syn-kinematic with respect to the D_2 deformation phase and was broadly contemporaneous with staurolite growth (Figure 6.15).

Sillimanite

Sillimanite is not observed in any of the metapelites in the footwall of the ZSZ. However, small bundles of fibrolitic sillimanite was observed in one sample of biotite gneiss collected from a xenolith within the Gumburanjon leucogranite.

6.3.2 Garnet zoning profiles

Four samples of garnet bearing metapelitic schist (JDW 154, JDW 155, JDW 156 & Wak 9) and two samples of garnet-bearing biotite gneiss (JDW 159A & JDW 159B) were collected from the deepest structural levels of the ZSZ for microprobe analysis. The location of samples is shown on Figure 6.17. The samples were analysed using an electron microprobe to determine whether they exhibit any chemical zoning. The results are discussed individually for each sample in the following sub-sections.

JDW 154

Two types of garnet are identified in this sample: (1) rounded garnets with ilmenite inclusion trails at a high angle to the matrix foliation (Figure 6.16b); and (2) elongate garnets with ilmenite inclusion trails parallel to the matrix foliation (Figure 6.11d). The difference in orientation of the inclusion trail patterns is interpreted to reflect deformation partitioning on a microscopic scale, rather than two discrete phases of garnet growth. This is supported by the observation that both types of garnet have similar compositions (Figures 6.18a & b), suggesting that both grew at approximately the same time. Neither types of garnet show any textural evidence of zoning, although chemical profiles show them to preserve prograde growth zoning profiles with slightly retrograde rims (Figures 6.18a & b). The cores of the garnets have reasonably flat element profiles, which may reflect diffusional homogenisation at high temperatures (*c.*600-650°C).

JDW 155

This garnet shows good textural evidence of zoning, with an inclusion-rich core (defined by aligned grains of quartz and ilmenite) and an inclusion-free rim (Figure 6.16d). This is reflected in the garnet zoning profile which shows a marked compositional unconformity at this boundary (Figure

6.18c). This is good evidence for two-stage garnet growth. The early stage is interpreted to be post S_0/S_1, whilst the latter stage is probably syn-S_2 (Figure 6.15). Both stages of growth are associated with prograde conditions, as indicated by the progressive decrease in X_{Sps} and the increase in X_{Mg} from core to rim (Figure 6.18c).

JDW 156

Only rim analyses were taken from this sample for the purpose of P-T estimation (see section 6.3.3).

Wak 9

This garnet is relatively small (<1mm) and shows evidence for slight resorbtion along its rims. It displays no textural evidence of zoning, but preserves a prograde growth zoning profile with slightly retrograde rims (Figure 6.18d).

JDW 159A

This represents a sample of Bt + Ms + Pl + Grt paragneiss collected from the banded orthogneisses structurally beneath the kyanite-grade metapelitic schists (Figure 6.17). Garnets in this sample are extremely small (<0.3mm) and show no obvious textural relationship with the matrix foliation. These garnets are chemically homogeneous and show no evidence of zoning (Figure 6.18e).

JDW 159B

This sample was collected in close proximity to JDW 159A and is also a biotite gneiss. Garnets in this sample form large poikiloblasts with abundant inclusions of quartz, apatite and ilmenite. Owing to the number of inclusions in this garnet, the profile shown in Figure 6.18f is incomplete. The decreasing iron content and increasing manganese content at the garnet rim may be suggestive of retrograde growth over a homogenised core.

6.3.3 Mineral chemistry and thermobarometry

In all of the above samples, mineral analyses of muscovite, biotite and plagioclase were made both adjacent to and away from the garnet of interest in an attempt to determine whether there was any variation in composition at the thin section scale. Using the techniques outlined in Appendix A, minerals believed to be in textural equilibrium were chosen for use in quantitative P-T analysis (compositions of the minerals used are given in Appendix B). The results of this work are presented in Table 6.2 and Figure 6.19.

Temperature data

Several conventional garnet-biotite geothermometers were used for comparative purposes (Figure 6.19a). The spread of results is quite large (*c.*±70°C), with the thermometer of Dasgupta (1991)

Table 6.2: Zanskar Shear Zone P-T results

			Conventionall geothermobarometry results												THERMOCALC results										
			Barometry				Garnet-Biotite thermometry																		
Sample	assemblage	comments	P* (kbar)	P** (kbar)	P*** (kbar)	Ave	B 92 (HW)	B 92 (GS)	Darg 91	FS 78	HS 82	PL 83	T 76	HL 77	P (kbar)	sd	T (°C)	sd	corr	fit	number of reactions	XH20	end-members excluded	preferred result	estimated overburden (3.71km/kbar)	sd
WAK 9	Grt + Bt + Ms + Pl + St + Qtz + H2O	average garnet and staurolite rim with averaged matrix (post-peak)	-	7.9	6.3	7.1	**600**	604	556	598	626	595	620	594	7.8	1.2	676	35	0.602	1.17	9	1.0			28.9	4.5
															7.8	1.3	640	36	0.606	1.29	9	0.5				
															PT result outside fit parameters							0.3				
															PT result outside fit parameters							0.1				
WAK 9	Grt + Bt + Ms + Pl + Qtz + H2O	average garnet rim and matrix (post-peak)													**6.9**	**1.1**	**632**	**36**	**0.696**	**0.98**	**7**	**1.0**	**mst, fst**	**X**	25.6	4.1
															6.6	1.0	589	33	0.693	0.93	7	0.5	mst, fst			
															6.4	1.0	559	30	0.690	0.95	7	0.3	mst, fst			
															5.9	1.0	489	31	0.670	1.14	7	0.1	mst, fst			
JDW 154	Grt + Bt + Ms + Pl + Qtz + H2O	average garnet rim and matrix (post-peak)	-	7.8	6.3	7.0	**551**	549	494	512	554	546	551	534	7.4	1.2	624	43	0.722	1.18	7	1.0				
															7.1	**1.1**	**582**	**38**	**0.716**	**1.16**	**7**	**0.5**	**none**	**X**	26.3	4.1
															6.8	1.1	552	36	0.713	1.18	7	0.3				
															6.1	1.2	482	37	0.695	1.36	7	0.1				
JDW 155	Grt + Bt + Ms + Pl + St + Qtz + H2O	average garnet and staurolite rim with averaged matrix (post-peak)	-	7.4	6.0	6.7	**579**	586	535	562	588	575	591	569	7.6	1.1	671	33	0.597	1.12	9	1.0				
															7.7	1.2	637	34	0.602	1.22	9	0.5				
															7.6	1.3	612	35	0.604	1.34	9	0.3				
															PT result outside fit parameters							0.1				
JDW 155	Grt + Bt + Ms + Pl + Qtz + H2O	average garnet rim and matrix (post-peak)													6.9	1.1	634	38	0.699	1.04	7	1.0	mst, fst			
															6.6	**1.0**	**591**	**33**	**0.696**	**1.00**	**7**	**0.5**	**mst, fst**	**X**	24.5	3.7
															6.4	1.0	561	31	0.693	1.01	7	0.3	mst, fst			
															5.9	1.1	491	32	0.673	1.19	7	0.1	mst, fst			
JDW 156	Grt + Bt + Ms + Pl + St + Qtz + H2O	average garnet and staurolite rim with averaged matrix (post-peak)	-	8.4	6.8	7.6	**606**	616	542	596	625	594	618	592	7.8	1.1	669	31	0.606	1.04	9	1.0				
															7.7	1.1	634	31	0.609	1.11	9	0.5				
															7.7	1.2	609	32	0.610	1.21	9	0.3				
															PT result outside fit parameters							0.1				
JDW 156	Grt + Bt + Ms + Pl + Qtz + H2O	average garnet rim and matrix (post-peak)													7.2	1.2	641	38	0.702	1.04	7	1.0	mst, fst			
															6.9	**1.1**	**597**	**33**	**0.698**	**0.97**	**7**	**0.5**	**mst, fst**	**X**	25.6	4.1
															6.6	1.0	566	31	0.695	0.96	7	0.3	mst, fst			
															6.1	1.0	495	30	0.675	1.12	7	0.1	mst, fst			
JDW 159A	Grt + Bt + Ms + Pl + Qtz + H2O	average garnet rim and matrix (post-peak)	-	7.2	5.6	6.4	**606**	605	574	625	650	610	641	612	**6.6**	**1.1**	**637**	**36**	**0.691**	**0.90**	**7**	**1.0**	**none**	**X**	24.5	4.1
															6.3	1.0	594	33	0.689	1.00	7	0.5				
															6.1	1.1	563	34	0.686	1.12	7	0.3				
															5.6	1.3	494	40	0.667	1.48	7	0.1				
JDW 159B	Grt + Bt + Ms + Pl + Qtz + H2O	average garnet rim and matrix (post-peak)	-	8.2	6.7	7.5	**597**	599	565	592	628	592	615	589	7.6	1.1	647	38	0.717	1.01	7	1.0				
															7.3	**1.0**	**603**	**34**	**0.712**	**1.00**	**7**	**0.5**	**none**	**X**	27.1	3.7
															7.0	1.0	572	32	0.709	1.03	7	0.3				
															6.4	1.2	500	35	0.690	1.27	7	0.1				

Garnet-Biotite thermometer abbreviations

B 92 (HW): Bhattacharya et al (1992), using garnet mixing model of Hackler & Wood (1989)
B 92 (GS): Bhattacharya et al (1992) using garnet mixing model of Ganguly & Saxena (1984)
Das 91: Dasgupta et al (1991)
FS 78: Ferry & Spear (1978)
HS 82: Hodges & Spear (1982)
PL 83: Perchuk & Lavrent'eva (1983)
T 76: Thompson (1976)
HL 77: Holdaway & Lee (1977)

Barometer reactions

* GASP (Grt + Als = Pl)
** GPMB-Mg (Grs + Prp + Ms = 3An + Phl)
*** GPMB-Fe (Grs + Alm + Ms = 3An + Ann)

consistently giving the lowest estimates. The spread of results is reduced to *c.*±50°C if the Dasgupta temperature is ignored. No observable trends are evident in Figure 6.19a, with most results showing that the temperature of final re-equilibration in all of the analysed samples was ~600°C. JDW 154 is an exception to this, which is attributed to the lower X_{Mg} value of this garnet compared to the other analysed samples (Figure 6.18). THERMOCALC records consistently higher temperatures than any of the independent thermometers (Table 6.2), which is interpreted to reflect variations in X_{H2O}. Reducing X_{H2O} when using THERMOCALC has the effect of progressively lowering the temperature estimates (Table 6.2). By matching the THERMOCALC temperature with the garnet-biotite thermometer of B92(HW), it is possible to estimate the composition of the metamorphic fluid, which appears to be between 0.5-1.0 for all of the analysed samples (Table 6.2). This is not unreasonable given the observation that many of the samples contain significant amounts of graphite in the matrix. Averaging all the preferred THERMOCALC temperature data shown in Table 6.2 suggests that rocks in this part of the footwall of the ZSZ equilibrated at ~607 ± 35°C (Figure 6.19b). Based on the observation that many of the garnets preserve prograde growth zoning profiles with evidence for slightly retrograde rims in some samples, it is reasonable to assume that these represent slightly post-peak temperatures.

Staurolite was observed to form part of the equilibrium assemblage in some of the analysed samples (Table 6.2). None of the analysed staurolites showed any evidence of chemical zoning. When incorporated into the THERMOCALC thermodynamic dataset, staurolite has the effect of increasing temperatures by as much as 50°C for any given X_{H2O} in some samples (e.g. Wak 9). Although staurolite forms part of the equilibrium assemblage, the thermodynamic properties of staurolite are poorly constrained (Holland & Powell, 1990), hence it has been excluded from the dataset for the purpose of quantitative P-T work.

Pressure data

In the absence of kyanite in any of the analysed samples, pressures were calculated using Grt-Ms-Bt-Pl barometry. This technique relies upon the exchange of Ca between garnet and plagioclase (e.g. Spear *et al.*, 1991). Analysis of several plagioclase grains in each sample showed that X_{An} varies relatively little in most samples (Figure 6.20) and that the cores of some plagioclases are slightly enriched in Ca. Some samples (e.g. JDW 159B) show more considerable variations in plagioclase composition which is represented by decreasing X_{An} from core to rim. In an attempt to calculate pressure, it is assumed that each sample has equilibrated at the thin section scale and that the average rim composition of the matrix plagioclases is representative of final equilibration with the garnet rims. Rim compositions of matrix plagioclase ubiquitously have the lowest anorthite content and should, therefore, record the highest pressure estimate (Spear *et al.*, 1991). The preferred THERMOCALC pressure estimates for each of the samples are shown in Table 6.2 and Figure 6.19. The data are

consistent with final re-equilibration at pressures of 6-8kbar (average of all the analysed samples is 6.9 ± 1.1kbar).

6.3.4 P-T evolution

There is limited evidence for a P-T-time path preserved in the metapelites in the footwall of the ZSZ. Very few prograde or retrograde metamorphic reactions were identified in thin section and the absence of suitable inclusions in porphyroblastic garnets precluded the use of inclusion thermobarometry (cf. St. Onge, 1987) as a means of estimating prograde P-T conditions. However, the sequence of metamorphic mineral growth shown in Figure 6.15 is characteristic of a typical Barrovian-type prograde evolution associated with increasing temperatures at moderate pressures (Figure 6.19b) and is characteristic of the M_1 metamorphism seen throughout the High Himalayan Slab along the entire ~2500km length of this metamorphic terrane. All of the analysed samples were collected in close proximity to one another (Figure 6.17) and record near-peak P-T estimates of 6-8kbar and 607 ± 35°C (Figure 6.19b). The absence of sillimanite in any of the studied samples implies that rocks exposed in the immediate footwall of the ZSZ have not experienced sillimanite-grade conditions. This may help constrain the retrograde P-T path above the kyanite=sillimanite transition (Figure 6.19b).

6.3.5 Estimated throw across the ZSZ

A simple comparison of metamorphic grade either side of the ZSZ provides a crude means of estimating the total throw across this fault. Rocks in the hangingwall of the ZSZ are only weakly metamorphosed and have clearly never been buried to any significant depth following the India-Asia collision. The Tibetan Sedimentary Series in SE Zanskar is believed to have an original sedimentary thickness of *c.*2.5-4 km (Garzanti *et al*, 1987; McElroy *et al*, 1990; Spring & Crespo-Blanc, 1992). Allowing for doubling, or even trebling of this original thickness by folding and thrusting, then the maximum overburden in the hangingwall of the ZSZ could not have exceeded *c.*10-12km. This is supported by the results of illite crystallinity measurements of rocks exposed in the hangingwall of the Sarchu Normal Fault (SNF), which show that the Tibetan Sedimentary Series have not exceeded middle/upper anchizonal conditions (Spring and Crespo-Blanc, 1992). These observations imply that no more than *c.*5-10km of overburden has been removed from the Tibetan Sedimentary Series by uplift and erosion. Conversely, average near-peak conditions in the deepest exposed part of the footwall record P-T estimates of *c.*6.9 ± 1.1 kbar and 607 ± 35°C (see section 6.3.3), thus implying that *c.*25-30km of overburden has been removed from the uppermost part of the High Himalayan Slab (assuming a lithostatic gradient of 3.71km/kbar). Assuming that *c.*5-10km of exhumation in the footwall of the ZSZ was accomplished through wholesale uplift and erosion (thus accounting for the removal of overburden in the hangingwall), then it is reasonable to propose that the remaining *c.*20km was removed by extensional unroofing and erosion associated with movement along the ZSZ. This is

comparable to the estimated throw across the ZSZ in western Zanskar, which Herren (1987) calculated to be *c.*19km, based on the telescoping of metamorphic isograds in the footwall. Assuming that the present day dip of the ZSZ (*c.*20-30°) has remained constant through time, then the total amount of slip along the ZSZ is estimated to be *c.*40-60km (Figure 6.21). Simple angular relationships therefore suggest that rocks currently exposed in the footwall of the ZSZ were located between 35-55 km horizontally away from their present location prior to initiation of extension along the ZSZ.

6.4 Crustal melting: the Gumburanjon leucogranite

6.4.1 Field relationships

The Gumburanjon leucogranite is a typical Qtz + Ms + Kfs + Pl ± Grt ± Bt ± Tur-bearing High Himalayan leucogranite which intrudes into the immediate footwall of the ZSZ at the eastern end of the Kargyak Chu (Figure 6.22). It is located at the south-eastern nose of the Kang La Dome and appears to be centred on a small domal structure which is defined by the progressive change in orientation of the pre-shear-band fabric around the granite (Figure 6.6). This doming effect is probably related to the emplacement of the granite, although it could equally represent relatively late-stage doming associated with the exhumation of high-grade assemblages in the footwall of the ZSZ.

Like other High Himalayan leucogranites, the Gumburanjon leucogranite consists of an anastomosing network of s-parallel sills (Figures 6.23a & b) and discordant leucogranite dykes (Figures 6.23c & d) which coalesce towards the centre of the intrusion to form an impressive granite face over 1000m high (Figure 6.23e-g). The percentage volume of granite relative to other lithologies decreases away from the centre of the intrusion (Figure 6.6). The pelitic schists at the margin of the intrusion are cross-cut by thick quartz veins (Figure 6.23h), which are presumably related to late-stage crystallisation of hydrothermal fluids. Within the granite, large blocks of biotite gneiss (Qtz + Pl + Bt ± Grt) form xenolith-like bodies which remain sub-parallel to the regional tectonic fabric (Figures 6.23a-g). This fabric cannot be traced into the adjacent granite, which is only weakly deformed. This implies that the Gumburanjon leucogranite was intruded as a series of layer-parallel sheets and post-dated the development of the S_2 fabric in the footwall of the ZSZ (Figure 6.15).

The Gumburanjon leucogranite does not intrude the Tibetan Sedimentary Series which is interpreted to suggest that the youngest phase of extension along the ZSZ post-dated emplacement of this granite (Figure 6.15). However, the Gumburanjon leucogranite is largely undeformed, which suggests the alternative interpretation that emplacement of the granite post-dated movement along the ZSZ. This is partly supported by field observations which show that some of the undeformed granite dykes cross-cut the mylonitic fabrics in the ZSZ (Figure 6.23i). These seemingly contradictory field observations can be explained by deformation partitioning within the ZSZ: extensional deformation could have been partitioned into mylonitic horizons located in the uppermost 100m of the ZSZ, thus explaining why the majority of this granite is only weakly deformed. Loose boulders of intensely deformed leucogranite were observed in the scree slopes at the base of Mt. Gumburanjon, but were

never observed *in situ*. These boulders provide evidence that the Gumburanjon leucogranite was probably emplaced syn-kinematically with respect to movement along the ZSZ.

No contact metamorphic aureole was observed in the country rocks immediately adjacent to the Gumburanjon leucogranite. The absence of a thermal aureole could be interpreted to suggest that the Gumburanjon leucogranite was intruded into rocks which were still at reasonably high temperatures. However, the absence of a thermal aureole could also be related to the fact that: (1) the majority of the Gumburanjon leucogranite is centred on an intensely deformed sequence of banded orthogneisses, augen gneisses and biotite gneisses (Figure 6.6), which are unlikely to show any textural or mineralogical evidence of a thermal aureole; and (2) the metapelitic schists immediately adjacent to the Gumburanjon leucogranite have experienced upper amphibolite conditions (*c.*7kbar and 600°C) and are therefore unlikely to show the effects of contact metamorphism.

Leucocratic pegmatites

A number of intensely deformed leucocratic pegmatites with a typical mineralogy of Qtz + Kfs + Pl + Ms ± Grt ± Tur form several-metre-wide s-parallel sills in the footwall of the ZSZ (Figures 6.22 & 6.24). These pegmatites are observed both in the kyanite-grade metapelitic schists of the Haimantas and in the underlying banded orthogneisses, augen gneisses and biotite gneisses. The pegmatites possess a strong internal foliation which is parallel to the pre-shear band fabric in the ZSZ (Figure 6.24c) and are frequently folded by pre-ZSZ structures (Figure 6.24d). They are cross-cut by a number of undeformed dykes and sills which form part of the Gumburanjon leucogranite (Figures 6.23c & d; 6.24c), thus suggesting that they are probably unrelated to the generation and emplacement of the Gumburanjon leucogranite itself.

The origin of these pegmatites remains uncertain. They show a close spatial relationship with biotite gneisses which have a typical mineralogy of Qtz + Pl + Bt ± Grt (Figure 6.24a), suggesting that they may represent locally derived migmatitic leucosomes. However, it is equally possible that the pegmatites were not locally derived and that they were sourced from much deeper crustal levels. The age of these pegmatites is also uncertain. Whilst they may be related to metamorphism of the High Himalayan Slab during the Tertiary, there remains the possibility that they are pre-Himalayan in age and that they were emplaced during an earlier metamorphic/magmatic event (see Chapter 7 for a geochronological discussion pertaining to the age of these pegmatites).

6.4.2 Phase relationships and geochemistry

It was not the purpose of this thesis to study in detail the phase relationships and geochemistry of the Gumburanjon leucogranite. This has already been done by various workers (e.g. Ferrara *et al.*, 1991; Ayres, 1997) and it was felt unnecessary to repeat this work. This section therefore presents a brief description of textures and mineralogical compositions observed in the Gumburanjon leucogranite. In addition, it presents XRF and CIPW normative analyses of four samples of

undeformed leucogranite (Wak 22, Wak 23, Wak 24 & Wak 27) and two samples of mylonitised leucocratic pegmatites (Wak 21 & Wak 26) collected from the immediate vicinity of Mt. Gumburanjon. These samples were collected primarily for geochronological analyses (see Chapter 7) and were not specifically collected for geochemical analysis. The location and field relationships of these samples are shown in Figures 6.22-6.24. The XRF results and CIPW-norms are presented in Table 6.3.

Textures and whole-rock geochemistry

The Gumburanjon leucogranite represents a composite intrusion which is comprised of a number of layer-parallel granite sheets which enclose blocks of biotite gneiss (Figure 6.23). Owing to the inaccessibility of the majority of the Gumburanjon leucogranite and the constant danger of rockfall, very few of these granites were observed *in situ*. Examination of abundant float samples collected from the scree slopes at the base of Mt. Gumburanjon revealed that the majority of material has a mineralogical composition of Qtz + Ms + Pl + Kfs with variable amounts of Bt ± Grt ± Tur. No temporal distinction could be made between biotite leucogranites and tourmaline leucogranites, as suggested by Ayres (1997). The majority of the granites are equigranular and medium/coarse grained. K-feldspar phenocrysts occasionally give some of the samples a porphyritic appearance. Some of the smaller leucogranite dykes are much finer grained and are best described as aplites. The leucocratic pegmatites which are cross-cut by the Gumburanjon leucogranite (Figure 6.24) are characterised by a mineralogy comprising of Qtz + Ms + Pl + Kfs + Grt ± Tur and are conspicuous in that they possess no biotite. These pegmatites clearly pre-date intrusion of the main Gumburanjon leucogranite. Accessory phases in both the granites and the leucocratic pegmatites include zircon, uraninite and apatite.

Typical bulk-rock compositions of samples collected from the Gumburanjon leucogranite are shown in Table 6.3 (analytical procedures for whole-rock geochemistry are outlined in Appendix C). These data show that the majority of granites have high SiO_2 (~70-75 wt%) and aluminium (~15 wt%) contents and show typical peraluminous affinities (i.e. molar A/CNK<1). The data are consistent with those presented by Ayres (1997) and Ferrara *et al.* (1991). Ayres (1997) demonstrated that many of the granites which comprise the Gumburanjon leucogranite plot close to a minimum eutectic composition in the Qtz-Ab–Or system (pp 64) and are indicative of crystallisation pressures of *c.*1-4kbar and water activities of 0.7-1.0. Samples Wak 21 and Wak 26 (intensely deformed leucocratic pegmatites) show similar bulk-rock compositions to the undeformed leucogranite samples (Wak 22, Wak 23, Wak 24 & Wak 27).

Table 6.3: Whole-rock geochemistry of samples collected from the Gumburanjon leucogranite

	WAK 21 leucocratic pegmatite Qtz + Pl + Ms + Grt + Tur	WAK 22 undeformed leucogranite Qtz + Pl + Ms + Bt + Grt + Tur	WAK 23 undeformed leucogranite Qtz + Pl + Ms + Bt + Grt + Tur	WAK 24 undeformed leucogranite Ms + Bt + Tur + Grt	WAK26 leucocratic pegmatite Qtz +Pl + Ms ± Grt ± Tur	WAK27 undeformed leucogranite Qtz + Pl + Ms + Bt + Grt + Tur
SiO2	74.60	74.06	75.28	74.30	75.76	73.96
TiO2	0.03	0.01	0.04	0.03	0.03	0.04
Al2O3	14.91	15.94	14.82	14.51	14.94	14.63
Fe2O3	0.76	0.48	0.66	0.55	1.09	0.77
MnO	0.15	0.16	0.02	0.02	0.32	0.06
MgO	0.02	b.l.d.	0.05	0.01	b.l.d	b.l.d
CaO	0.42	0.20	0.55	0.45	0.47	0.56
Na2O	3.19	5.58	4.94	4.88	5.39	4.70
K2O	5.71	3.71	3.68	3.91	2.23	4.04
P2O5	0.27	0.22	0.14	0.11	0.14	0.16
Dry Total	100.06	100.37	100.17	98.78	100.37	98.92
A/CNK	1.26	1.19	1.17	1.14	1.27	1.16
CIPW Norms						
q	33.63	27.34	31.39	30.11	34.62	30.12
c	3.35	2.90	2.03	1.68	3.13	1.88
or	33.77	21.94	21.77	23.13	13.19	23.90
ab	26.96	47.16	41.75	41.24	45.55	39.72
an	0.32	-0.44	1.82	1.52	1.42	1.74
lc	0.00	0.00	0.00	0.00	0.00	0.00
ne	0.00	0.00	0.00	0.00	0.00	0.00
ac	0.00	0.00	0.00	0.00	0.00	0.00
di	0.00	0.00	0.00	0.00	0.00	0.00
wo	0.00	0.00	0.00	0.00	0.00	0.00
hy	0.95	0.68	0.68	0.50	1.51	0.72
ol	0.00	0.00	0.00	0.00	0.00	0.00
mt	0.34	0.22	0.30	0.25	0.49	0.35
il	0.06	0.02	0.08	0.06	0.06	0.08
ap	0.59	0.48	0.31	0.24	0.31	0.35
Total	99.97	99.97	100.29	98.72	100.28	98.85

b.l.d. below limit of detection

Isotope geochemistry

Table 6.4 presents Rb-Sr and Sm-Nd analyses of a number of samples collected from different parts of the Gumburanjon leucogranite (analytical procedures for Rb/Sr isotopic analysis are outlined in Appendix D). These include the samples collected and analysed during personal investigation, together with samples collected and analysed by Ferrara *et al.* (1991) and Ayres (1997). The data show that the Gumburanjon leucogranite has high $^{87}Sr/^{86}Sr_{initial}$ ratios of 0.749-0.782 (assuming an age of 21 Ma: see Chapter 7), and low $^{143}Nd/^{144}Nd$ ratios of 0.51189-0.51204 (Ferrara *et al*, 1991). These isotopic compositions are consistent with derivation from a crustal source, which is believed to be the high-grade metapelites and Precambrian-Ordovician orthogneisses of the underlying HHC. The extreme heterogeneity of the Sr isotopic data is interpreted to reflect both derivation from an inhomogeneous source and poor magma mixing. The variation in these data precludes the use of the Rb-Sr technique as a means of dating the age of the Gumburanjon leucogranite. Rb-Sr mica cooling ages of *c.*20-18 Ma have been obtained from the Gumburanjon leucogranite by Ferrara *et al.* (1987, 1991). These data are discussed more fully in Chapter 7.

A curious feature of the data presented in Table 6.4 is the extremely high $^{87}Sr/^{86}Sr_{initial}$ ratio of pegmatite samples Wak 21 and Wak 26 (2.394 & 3.038 respectively). The high $^{87}Sr/^{86}Sr$ ratios are

indicative of extreme ^{87}Sr enrichment. Pegmatites, by definition, are enriched in volatiles and it remains possible that these high $^{87}Sr/^{86}Sr_{initial}$ values are related to isotopic fractionation during pegmatite formation. However, they may also be interpreted to suggest that these pegmatites have experienced a long crustal residence time and may, therefore, be significantly older than Tertiary in age. Assuming an initial $^{87}Sr/^{86}Sr$ ratio of *c.*0.700 in these pegmatites, then the calculated age for Wak 21 and Wak 26 is *c.*790 Ma and 1450 Ma respectively. U-Pb data presented in Chapter 7 suggests that these pegmatites may actually be *c.*500 Ma.

Table 6.4: Rb/Sr and Sm/Nd from the Gumburanjon leucogranite

Sample	Rb (ppm)	Sr (ppm)	Rb/Sr calculated	$^{87}Rb/^{86}Sr$ calculated	$^{87}Sr/^{86}Sr$ measured	Error 2σ %	$^{87}Sr/^{86}Sr_{initial}$ (21Ma)	$^{143}Nd/^{144}Nd$	(2σ error)
Undeformed leucogranite (this study)									
Wak 22	434	12.9	33.74	98.62	0.811493	0.00004	0.78208		
Wak 23	230	103.4	2.22	6.46	0.752762	0.00002	0.75084		
Wak 24	255	66.1	3.86	11.21	0.754839	0.00002	0.75149		
Wak 27	274	53.6	5.12	14.87	0.754267	0.00002	0.74983		
Mylonitised leucocratic pegmatites (this study)									
Wak 21	454	9.9	45.61	154.31	2.439744	0.00010	2.39372		
Wak 26	255	7.9	32.24	114.85	3.072033	0.00009	3.03778		
Undeformed leucogranite (Ferrara *et al.*, 1991)									
G1	233	97.8	2.38	6.95	0.77512	0.00006	0.77305	0.511963	0.000041
G2	221	67.4	3.28	9.53	0.75597	0.00010	0.75313		
G3	249	72.1	3.45	10.05	0.75445	0.00011	0.75145		
G4	272	100.0	2.72	7.91	0.75561	0.00019	0.75325		
G5	296	66.9	4.42	12.86	0.75682	0.00014	0.75298		
G6	252	81.2	3.10	9.02	0.75531	0.00030	0.75262		
G7	285	47.8	5.96	17.34	0.75681	0.00022	0.75164		
G8	242	72.5	3.34	9.73	0.75416	0.00017	0.75126		
G9	232	84.2	2.76	8.02	0.75145	0.00009	0.74906	0.512015	0.000024
G10	248	77.1	3.22	9.36	0.75612	0.00005	0.75333	0.511886	0.000023
G11	284	97.3	2.92	8.49	0.75637	0.00008	0.75384		
G12	217	73.0	2.97	8.62	0.75356	0.00007	0.75099	0.511931	0.000025
G13	200	94.7	2.11	6.14	0.75637	0.00005	0.75454		
G14	278	99.9	2.78	8.10	0.75637	0.00005	0.75395	0.51204	0.000023
G15	223	104.0	2.14	6.24	0.7528	0.00008	0.75094		
G16	229	102.0	2.25	6.53	0.75511	0.00007	0.75316		
Z597	231	84.0	2.75	7.98	0.75428	0.00008	0.75190		
Undeformed leucogranite (Ayres, 1997)						(1σ error)			
G2	253	110.0	2.30	6.69	0.76243	0.00002	0.76043		
G8	257	140.0	1.84	5.29	0.75118	0.00002	0.74960		
G18	290	68.0	4.26	12.38	0.75775	0.00002	0.75406		
G19	293	72.0	4.07	11.80	0.75724	0.00002	0.75372		

6.4.3 Generation of the Gumburanjon leucogranite

The Gumburanjon leucogranite is typical of many of the High Himalayan leucogranites exposed in the upper part of the High Himalayan Slab. The processes responsible for the generation of these granites remain poorly understood (see Chapter 2). They are clearly the product of high temperature conditions and are generally considered to have formed during sillimanite-grade metamorphism in the upper part of the slab. This is supported by field observations in the HHC of SE Zanskar which show that the High Himalayan leucogranites are consistently located above zones of sillimanite-grade migmatitic gneisses. This relationship is superbly demonstrated in the Temasa nala, to the north-west

of the Gumburanjon leucogranite (Figure 3.18a; Enclosure 1) and was also observed in the footwall of the Miyar Fault Zone in the Miyar nala (see Chapter 5). Although no sillimanite-grade migmatites were observed in the immediate vicinity of the Gumburanjon leucogranite, structural projection and downward extrapolation of metamorphic gradient from regions along strike suggests that the Gumburanjon leucogranite is underlain by a zone of sillimanite-grade migmatitic gneisses similar to those observed in western and central Zanskar (Figure 6.22). Whether these are the source of the Gumburanjon leucogranite remains uncertain. In central Zanskar, Ayres (1997) observed ambiguous field relationships between the underlying migmatites and the overlying leucogranite sheets. In places, the migmatites are cut by leucogranites, whilst in others, the migmatites appear to feed the granite sheets. Both migmatites and leucogranites in central Zanskar have similar $^{87}Sr/^{86}Sr$ ratios (0.724-0.786 and 0.751-0.773 respectively: Ayres, 1997), suggesting a possible link between migmatisation and leucogranite emplacement. Based on their geochronological studies, Noble and Searle (1995) concluded that the migmatitic leucosomes were the source for the higher level plutons in central Zanskar. However, in central Nepal, Inger and Harris (1993) concluded that migmatites in the Langtang Valley had a different $^{87}Sr/^{86}Sr$ ratio to the overlying leucogranite sheets and could not act as a source horizon for the granites even during disequilibrium melting. Massey (1994) further suggests that the leucogranites in central Nepal have migrated >10 km from their source.

The absence of any sillimanite-grade migmatitic assemblages in the immediate vicinity of the pluton suggests that the Gumburanjon leucogranite is unlikely to be an *in situ* melt. The granite must, therefore, have been generated from a source located at depth and subsequently migrated to higher structural levels. Exactly how far the granite has migrated from its source remains uncertain. The distance any granite can travel from its source is governed by a number of factors, including the melt temperature and the thermal capacity of the granite to travel through the crust before it crystallises. The fact that the Gumburanjon leucogranite is comprised of an anastomosing network of narrow dykes and sills (Figure 6.23a) suggests that it was unlikely to have had the thermal potential to travel far from its source. The fact that the Gumburanjon leucogranite is located in the immediate footwall of the ZSZ further suggests that it probably crystallised relatively quickly owing to the chilling effects of the overlying hangingwall (this assumes that the Gumburanjon leucogranite was emplaced syn-kinematically with respect to extension along the ZSZ, which is supported by field evidence presented in section 6.4.1 and geochronological evidence presented in Chapter 7).

Melting temperature: dehydration melt reactions vs. water-saturated melt reactions

The kyanite-grade metapelitic schists adjacent to the Gumburanjon leucogranite record near-peak temperatures of 607 ± 35°C (Figure 6.19b). Since these rocks show no evidence of partial melting, it is reasonable to assume that melting must have occurred in excess of these temperatures. The exact temperature at which crustal melting occurs is dependent upon a number of factors, most importantly the mineralogical composition of the source rock, pressure and the availability of water. Water-saturated melting of metapelites occurs at temperatures of ~600-650°C at pressures above

~3kbar (reaction 6 in Figure 6.19b). Dehydration melting of muscovite in pelites occurs at progressively higher temperatures with increasing pressures (reaction 7 in Figure 6.19b), although the exact position of this curve is strongly dependent upon the bulk-rock composition of the source rock (Patiño Douce & Harris, 1998). Most High Himalayan leucogranites are believed to have formed by dehydration melting of muscovite at temperatures in excess of *c.*700°C (e.g. Inger & Harris, 1993).

Ayres (1997) demonstrated that the Gumburanjon leucogranite displays similar Rb, Sr and Ba trends to the Langtang granites of central Nepal (Inger & Harris, 1993) and therefore concluded that melting probably occurred by dehydration of muscovite, rather than water-saturated reactions. Recent experimental work by Patiño Douce and Harris (1998), demonstrates that water-saturated melts are chemically distinct from those produced by dehydration melting in that they are more trondhjemitic in composition (Figure 6.25a). This is due to the fact that H_2O-fluxed melting consumes a greater amount of plagioclase in the source rock than does fluid-absent melting (Patiño Douce & Harris, 1998). This effect is less pronounced at lower pressures, resulting in a degree of overlap between the water-saturated and dehydration melting fields (Figure 6.25a). Data from the Gumburanjon leucogranite (including data from Ayres, 1997) plot to the right of the trondhjemite field within this field of overlap (Figure 6.25b) and are therefore difficult to interpret. If melting occurred at low pressures (*c.*6kbar), then it may have been by either water-saturated and/or dehydration melt reactions. Conversely, if melting occurred at higher pressures (*c.*10kbar), then it was more likely to have been by dehydration melt reactions. Unfortunately, there are no independent constraints on the pressure at which melting took place because the source rocks are not exposed.

Using the Zr concentration in leucogranite melts, Watson and Harrison (1983) suggested that it is possible to calculate the temperature at which peraluminous melts were formed using the equation:

$$\ln D_{Zr} = \{-3.80-[0.85\ (M-1)]\} + 12900/T$$

where D_{Zr} is the ratio of Zr concentration in the zircon to that in the melt, T is the temperature (K) and M is the cation ratio (Na+K+2Ca)/(Al*Si) of the melt. Application of this thermometer to the four samples of undeformed leucogranite collected from the Gumburanjon pluton gives melt temperatures which vary between 644-688°C (Table 6.5). These temperatures are similar to those obtained from the Gumburanjon leucogranite by Ayres (1997) and are slightly lower than the temperatures recorded by other High Himalayan leucogranites (e.g. Inger & Harris, 1993). They are consistent with either water-saturated melting at high pressures (>7kbar), or dehydration/water-saturated melting at low pressures (<7kbar). They are too low to permit dehydration melting at higher pressures and suggest that the Gumburanjon leucogranite was generated at pressures of <7kbar (Figure 6.26). However, the reliability of these temperatures is highly uncertain owing to the fact that this thermometer assumes that zircon is saturated within the melt. If the melt is oversaturated with respect to zircon (i.e. the melt contains entrained/inherited zircons), this will result in a temperature overestimate. Conversely, if the melt is undersaturated in zircon this will lead to a temperature underestimate. Geochronological

data presented in Chapter 7 show that the Gumburanjon leucogranite contains a significant amount of inherited monazite and is therefore also likely to contain large amounts of inherited zircon. This is consistent with the work of Noble and Searle (1995), who demonstrated that the High Himalayan leucogranites in central Zanskar do contain inherited zircon.

Table 6.5: Melt temperature of the Gumburanjon leucogranite based on XRF data and the geothermometer of Watson and Harrison (1983)

Sample	Zr concentration in melt (ppm)	T°C
Wak 22	22	645
Wak 23	31	666
Wak 24	23	644
Wak 27	42	688
Average	29	661

6.4.4 Emplacement of the Gumburanjon leucogranite

The maximum pressure at which the Gumburanjon leucogranite could have been emplaced cannot have exceeded *c.*7kbar, the maximum pressure recorded by the country rocks into which the granite intrudes (Figure 6.26). This is supported by the geochemical work of Ayres (1997) who demonstrated that the Gumburanjon leucogranite was most probably generated by dehydration melt reactions at temperatures of *c.*600-700°C and pressures of <7kbar (see section 6.4.3). The country rock temperature at the time of intrusion is uncertain, although the absence of any metamorphic aureole associated with the Gumburanjon leucogranite suggests that the granite was emplaced into country rock which was still at reasonably high temperatures. Establishing the depth of emplacement of the Gumburanjon leucogranite would help constrain the pressure-temperature-time (P-T-t) history, and place a lower limit on the distance the granite has travelled from its source. Unfortunately, despite having an assemblage suitable for pressure calibration (garnet + biotite + muscovite + plagioclase), the high spessartine content of the magmatic garnets (X_{Sps} 0.33) and the low anorthite component of the plagioclase (X_{An} <0.05) precluded the use of conventional geobarometers (Table 6.6). Geochemical data presented by Ayres (1997) demonstrate that the Gumburanjon leucogranite is a eutectic melt which crystallised at pressures of *c.*1-4kbar. This is slightly shallower than the ~4-7kbar crystallisation pressure of migmatitic leucosomes in the HHC of central and western Zanskar (D. Waters, pers. com.).

Table 6.6: Average garnet and feldspar electron microprobe analyses from sample Wak 23

Feldspar				Garnet			
Oxide wt%		Cation totals (8 oxygens)		Oxide wt%		Cation totals (12 oxygens)	
SiO2	67.24	Si	2.97	SiO2	36.50	Si	3.00
TiO2	-	Ti	-	TiO2	0.05	Ti	0.00
Al2O3	19.79	Al	1.03	Al2O3	20.66	Al	2.00
FeO	0.05	Fe2+	0.00	FeO	27.30	Fe2+	1.88
MnO	-	Mn	-	MnO	14.80	Mn	1.03
MgO	-	Mg	-	MgO	0.41	Mg	0.05
CaO	0.93	Ca	0.04	CaO	0.44	Ca	0.04
Na2O	9.98	Na	0.85	Na2O	-	Na	-
K2O	1.63	K	0.10	K2O	-	K	-
BaO	-	Ba	-	BaO	-	Ba	-
Total	99.62	Sum	4.99	Total	100.15	Sum	8.00
		An	4%			Alm	63%
		Ab	86%			Sps	34%
		Or	10%			Pyr	2%
						Gr	1%

6.5 Summary and discussion

Field and petrographic observations of structures and metamorphic textures in the rocks in the upper part of the High Himalayan Slab in SE Zanskar and NW Lahaul show evidence of polyphase deformation and metamorphism. The Precambrian/Cambrian age of the Haimantas suggests the possibility that some of these fabrics are pre-Himalayan in age, although this is impossible to confirm from field observations alone. Deformation is therefore interpreted to be dominantly Himalayan in age. The majority of lithologies are located within the chlorite/biotite zone and have never been buried to any significant depth following the India-Asia collision. Metamorphic grade rapidly increases at the very top of the slab, which is attributed to extensional unroofing of lithologies in the immediate footwall of the Zanskar Shear Zone (ZSZ). Growth of garnet-, staurolite- and kyanite-grade lithologies is interpreted to be related to prograde Barrovian metamorphism (M_1), associated with crustal shortening and thickening in the upper part of the slab. The kinematics of this burial history could not be elucidated owing to strong overprinting of fabrics by structures which are associated with extension along the ZSZ. However, the decrease in metamorphic grade towards the south-west of the ZSZ strongly suggests that burial of the upper part of the slab was accomplished by thrusting of units towards the SW along a major thrust, which may have been a precursor to the ZSZ.

The ZSZ is *c.*1-2km thick and represents a zone of intense deformation which shows abundant top-to-the-north-east shear-sense indicators. Field and petrographic observations demonstrate that the initiation of this movement post-dated the growth of porphyroblastic mineral growth at the top of the slab. P-T estimates obtained from M_1 metamorphic assemblages suggest that near-peak conditions of *c.*6.9 ± 1.1 kbar and 607 ± 35°C were attained in the deepest exposed structural levels in the footwall of the ZSZ. Lithologies in the Tibetan Sedimentary Series are only weakly metamorphosed, suggesting that exhumation of M_1 assemblages in the High Himalayan Slab was largely controlled by extensional unroofing along the ZSZ. Based on comparisons of relative structural depth either side of

the ZSZ, the throw and heave across this structure is estimated to be *c.*20 km and *c.*35-55km respectively.

Movement along the ZSZ is believed to have initiated shortly after peak-metamorphic conditions were attained at the top of the slab. This is broadly contemporaneous with the generation and emplacement of the Gumburanjon leucogranite in the immediate footwall of the ZSZ. The absence of a thermal aureole around the Gumburanjon leucogranite suggests that it was emplaced into rocks which were still reasonably hot. The small size of the Gumburanjon leucogranite and its location in the immediate footwall of the ZSZ suggests that it is not a far travelled granite and that it was probably generated in a zone of sillimanite-grade migmatitic gneisses located at deeper structural levels beneath the Gumburanjon leucogranite. Geochemical data presented by Ayres (1997) suggest that the Gumburanjon leucogranite was generated by dehydration melt reactions at temperatures of *c.*650-700°C, which constrains the depth of melting at <7 kbar (Figure 6.26). Generation of the granite by this mechanism provides strong evidence for a temporal link between extensional normal faulting and crustal melting and questions the validity of models which seek to invoke melting by shear heating along the MCT. Indeed, structural projection of the MCT towards the NE in SE Zanskar and NW Lahaul suggests that the Gumburanjon leucogranite was generated *c.*10km above the MCT zone (Figure 6.27).

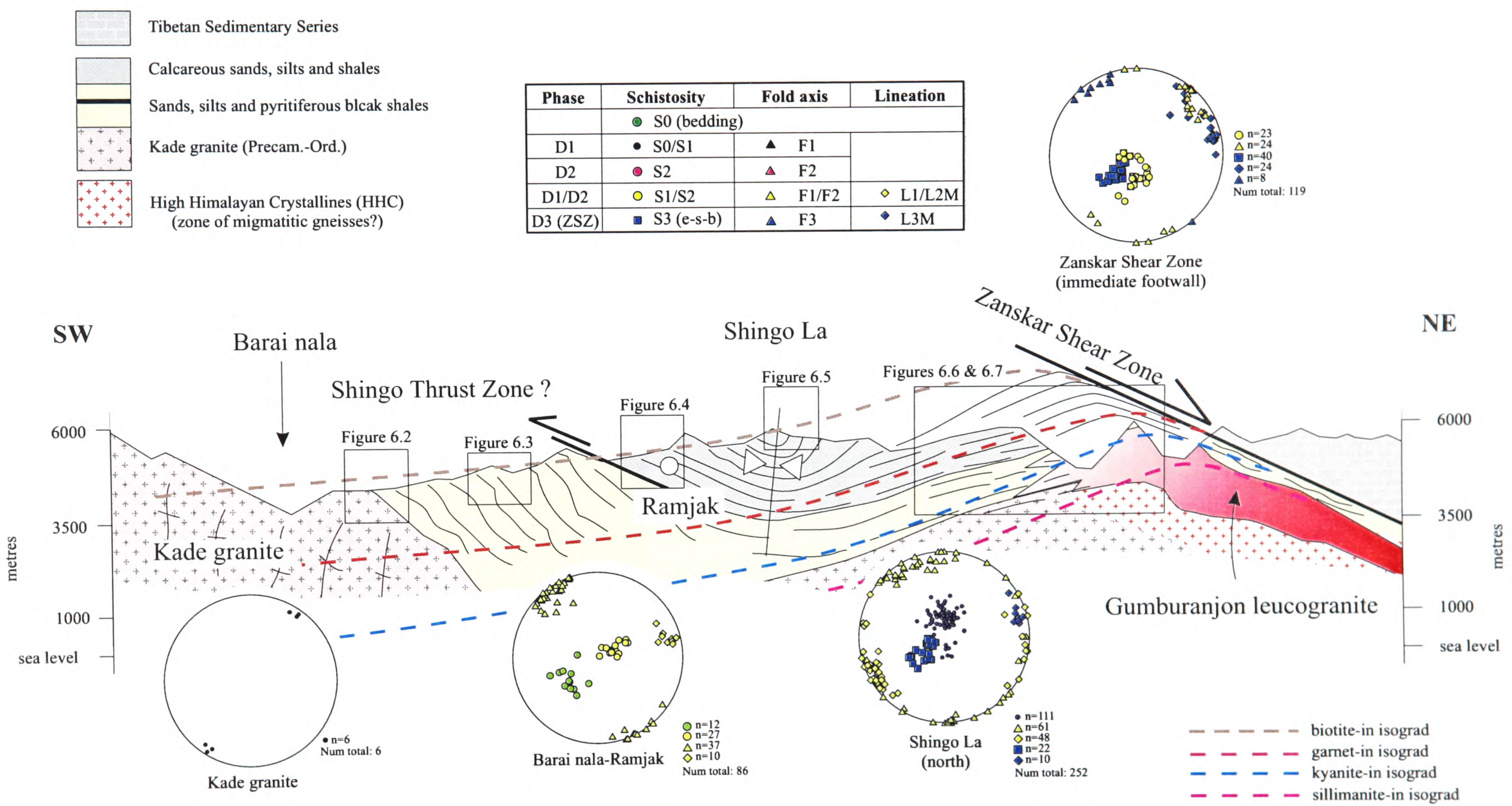


Figure 6.1: Cross-section through the upper part of the High Himalayan Slab in SE Zanskar and NW Lahaul (cross-section B-B' shown on Enclosure 1). Equal-area stereonets show the orientation of major structural fabrics. Boxed regions show the location of subsequent figures.

NE SW



Figure 6.2a: Contact of the Kade granite with the overlying sands, silts and shales of the Haimantas. A strong tectonic fabric is developed in the granite (see Figure 6.2b), which is not observed in the overlying sediments and trends at a high angle to bedding.

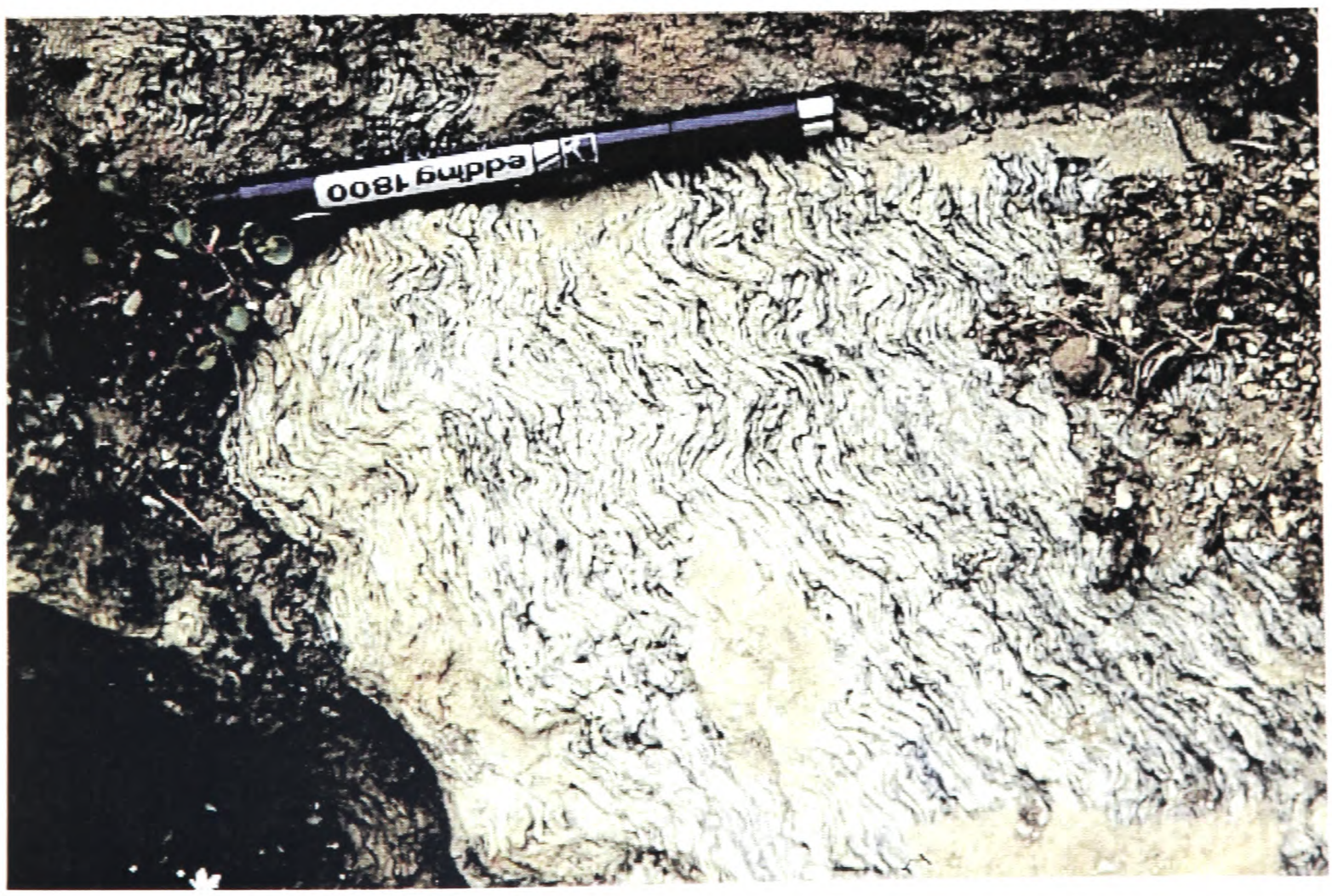


Figure 6.2b: Planar tectonic fabric in the Kade granite defined by flattened grains of quartz and feldspar.



Figure 6.3a: NE-dipping beds of sand and silt deformed by symmetrical MW-style folde (~2km south of Ramjak campground).



Figure 6.3b: Close-up of MW-style folds in sands and silts (~2km south of Ramjak campground)

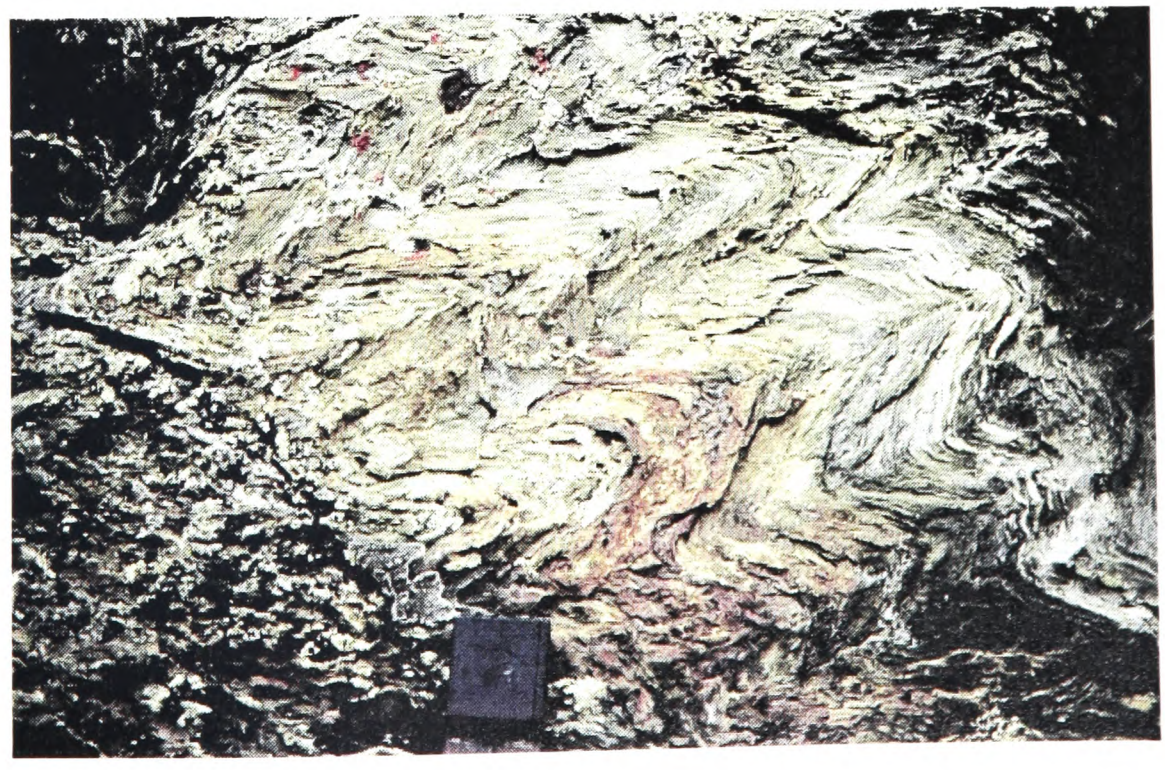


Figure 6.3c: Close-up of well-developed MW-style folds in calcareous-rich pelites (~2km south of Ramjak campground).

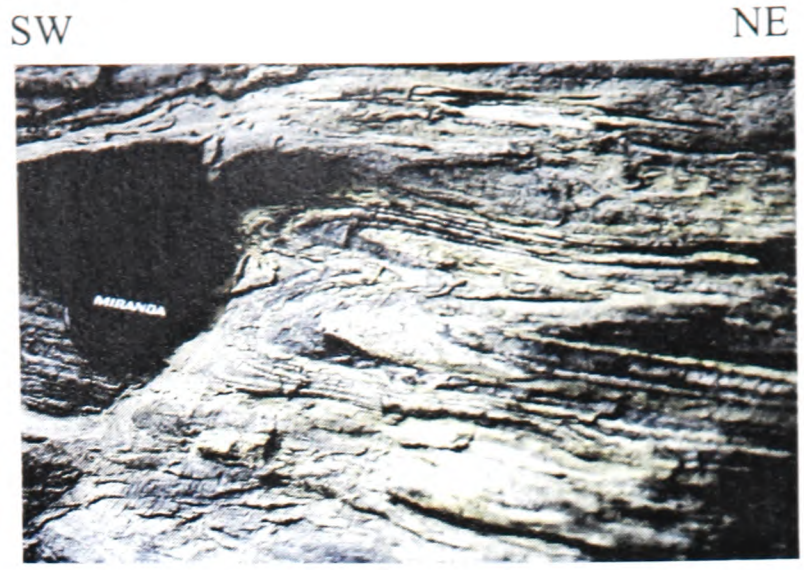


Figure 6.4a: Flat-lying isoclinal folds of bedding (Ramjak campground).



Figure 6.4b: Intensely deformed sequence of sands, silts and shales dipslaying isoclinal fold closures and NE-dipping semi-brittle dislocations which are interpreted to form part of a major crush zone (Ramjak campground).

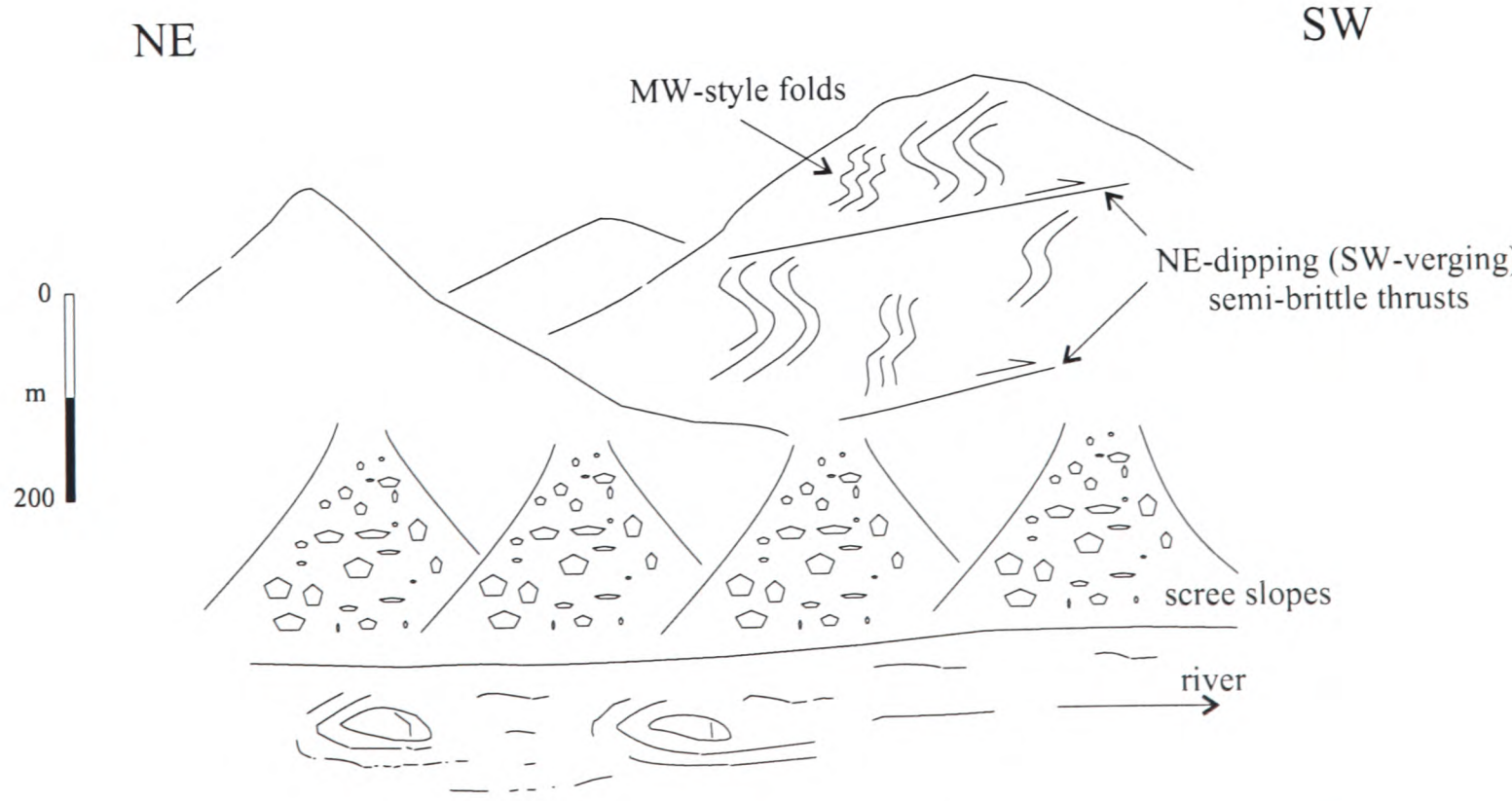


Figure 6.4c: View looking ~SE across the river from Ramjak campground showing prominent NE-dipping semi-brittle thrusts with a top-to-the-SW sense of motion.

SW NE



Figure 6.5a: Vertically bedded sands silts and shales near the summit of the Shingo La.

SW NE

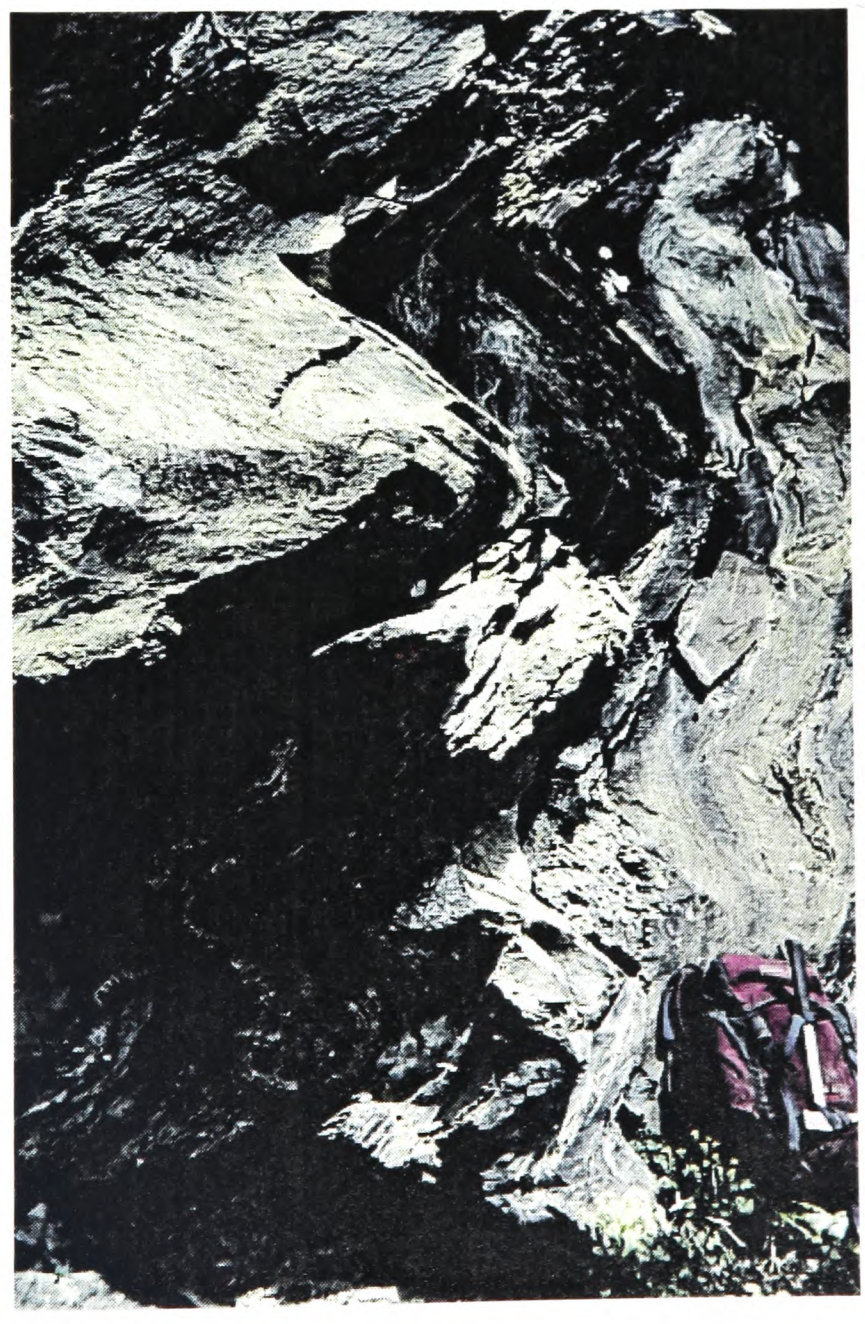


Figure 6.5b: Close-up of MW-style folds seen in the sediments near the summit of the Shingo La. These may represent F2 folds, based on the observation that bedding is parallel to a strong flattening fabric, which may be related to an earlier phase of isoclinal folding.

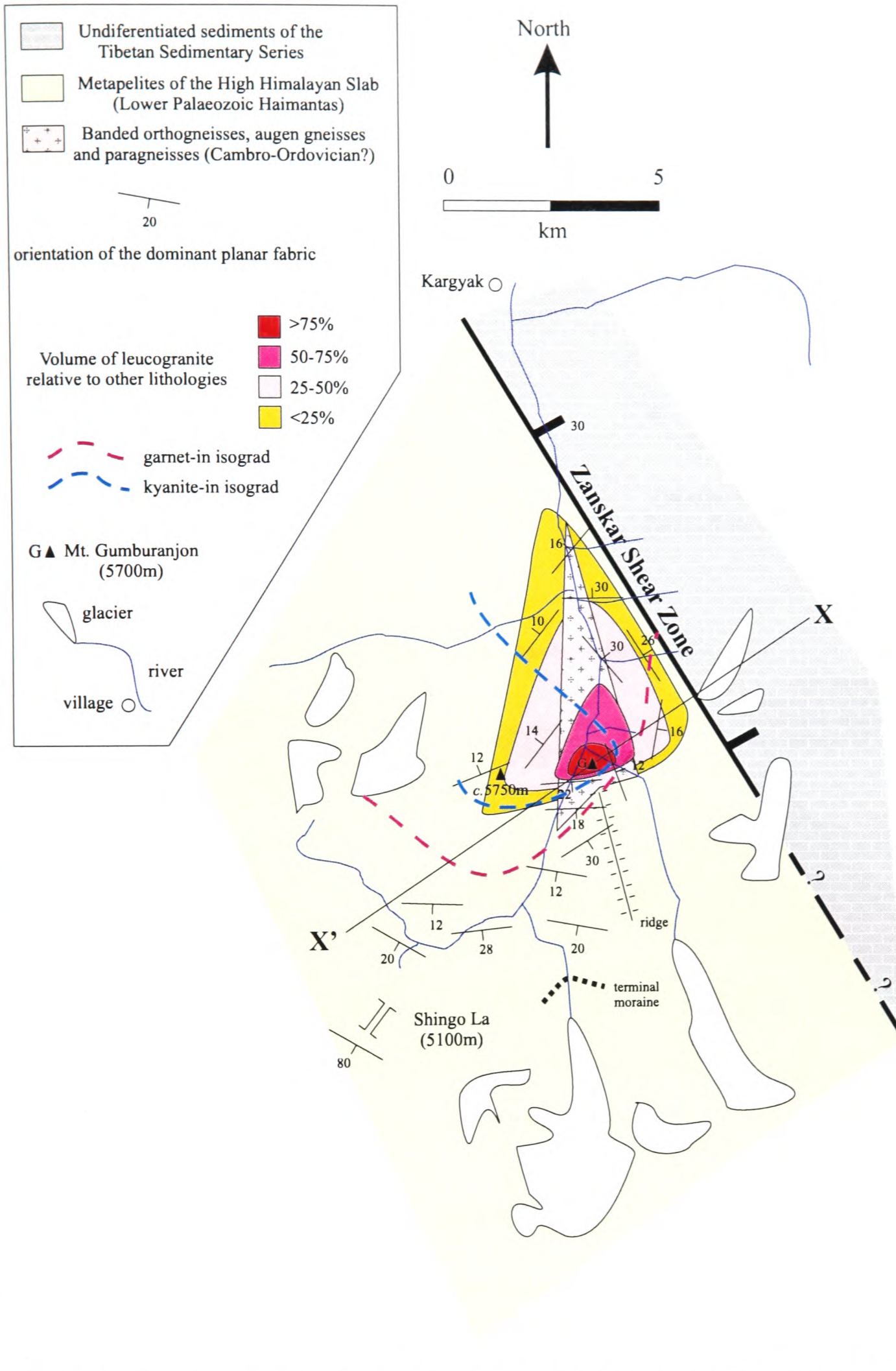
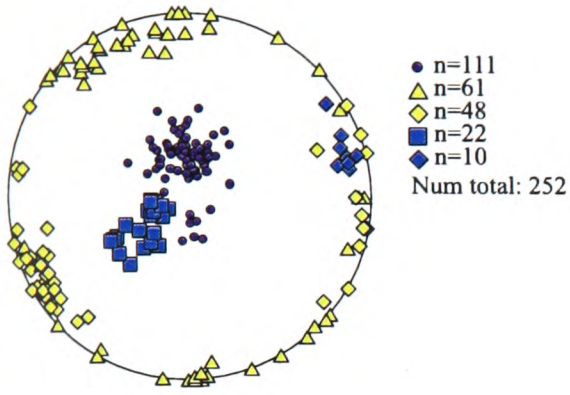
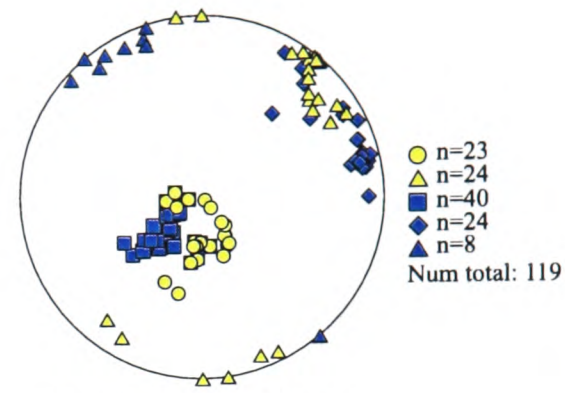


Figure 6.6: Lithological and structural map of the area to the north of the Shingo La. The dominant tectonic foliation generally dips ~10-30° towards the south, but is also observed to be domed around the Gumburanjon leucogranite and is dragged into parallelism with the NE-dipping fabric in the immediate footwall of the Zanskar Shear Zone. X-X' marks the line of section shown on Figure 6.7a.

Phase	Schistosity	Fold axis	Lineation
	S0 (bedding)		
D1	S0/S1	F1	
D2	S2	F2	
D1/D2	S1/S2	F1/F2	L1/L2M
D3 (ZSZ)	S3 (e-s-b)	F3	L3M



Shingo La
(north)



Zanskar Shear Zone
(immediate footwall)

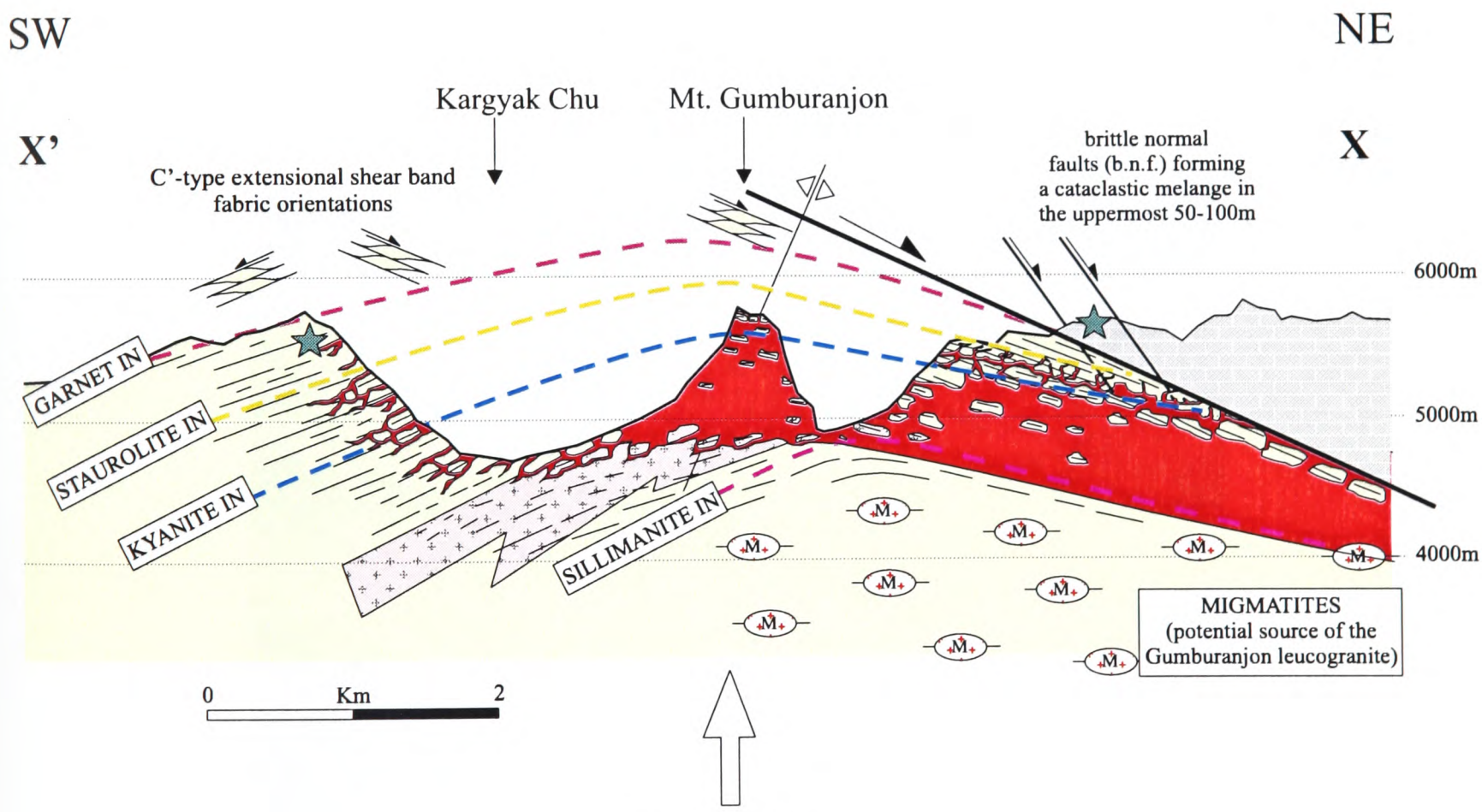


Figure 6.7a: Cross-section through the uppermost part of the High Himalayan Slab in SE Zanskar immediately north of the Shingo La. See Figure 6.6 for location of section.

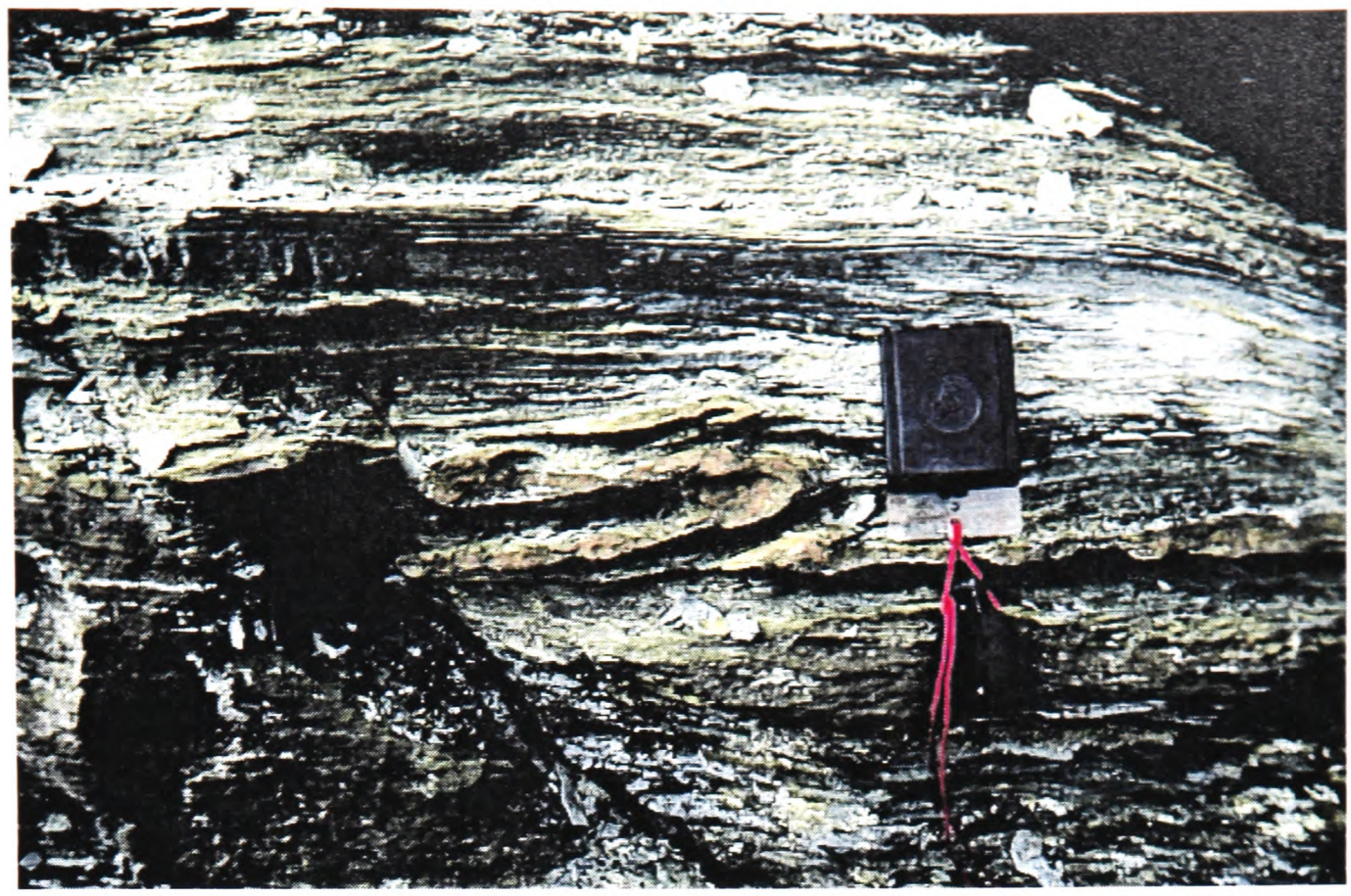


Figure 6.7b: Isoclinally folded quartz vein in the biotite-grade sediments to the north of the Shingo La. Bedding (S0) is sub-parallel to a well-developed axial planar cleavage (S1).

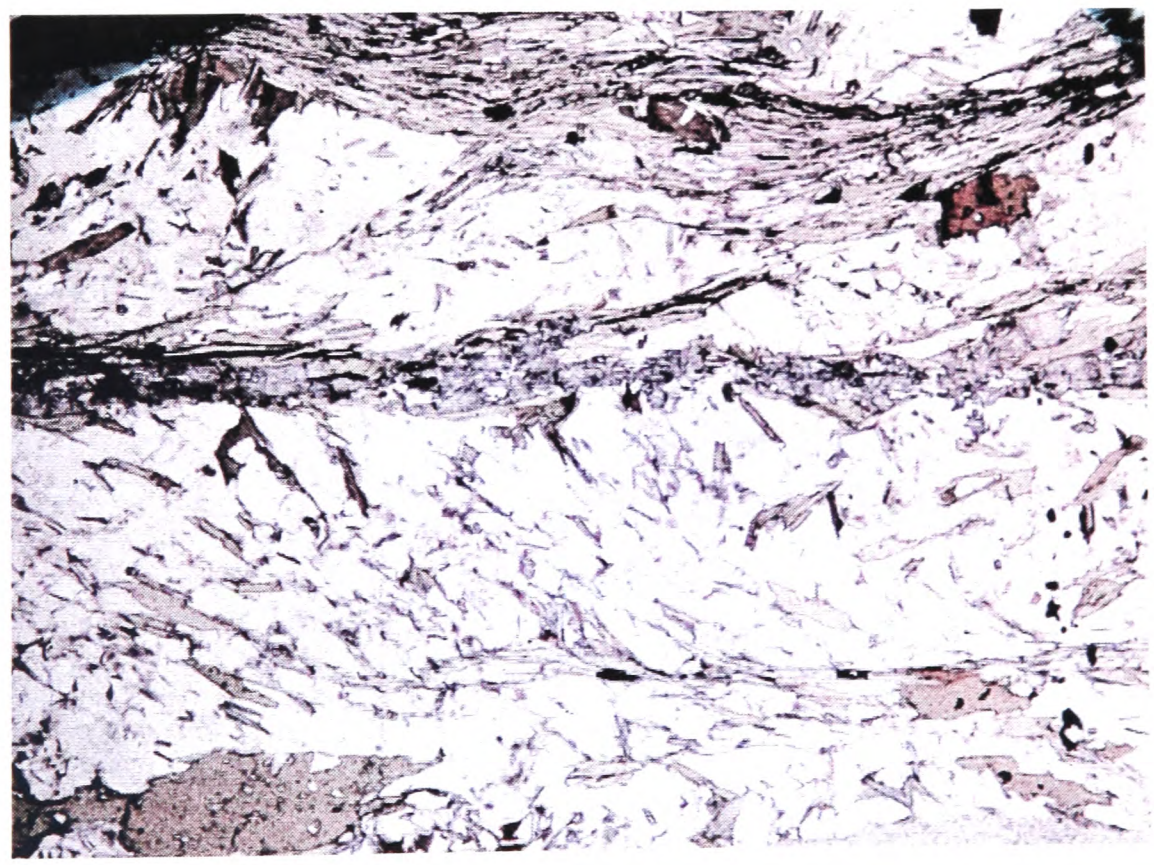


Figure 6.7c: S2 crenulation cleavage of the S0/S1 fabric in a garnet-staurolite schist collected from the northern side of the Shingo La in the footwall of the ZSZ (Sample JDW 150A). Field of view c. 4mm.



Figure 6.8: View looking ~NE at the Gumburanjon leucogranite on the northern side of the Shingo La. The dominant tectonic foliation dips ~10-30° towards the south/south-east and is cross-cut by the weakly deformed leucogranite. The Haimantas are metamorphosed to kyanite-grade conditions and are underlain by an intensely deformed sequence of banded orthogneisses, augen gneisses and mafic paragneisses.



Figure 6.9a: Intensely deformed sequence of banded orthogneisses, augen gneises, biotite gneisses and leucocratic pegmatites beneath the kyanite-grade metapeltic schists of the Haimantas.

SW NE



Figure 6.9b: Intensely deformed augen gneiss beneath the metapelitic schists of the Haimantas showing top-to-the -north-east shear sense indicators.

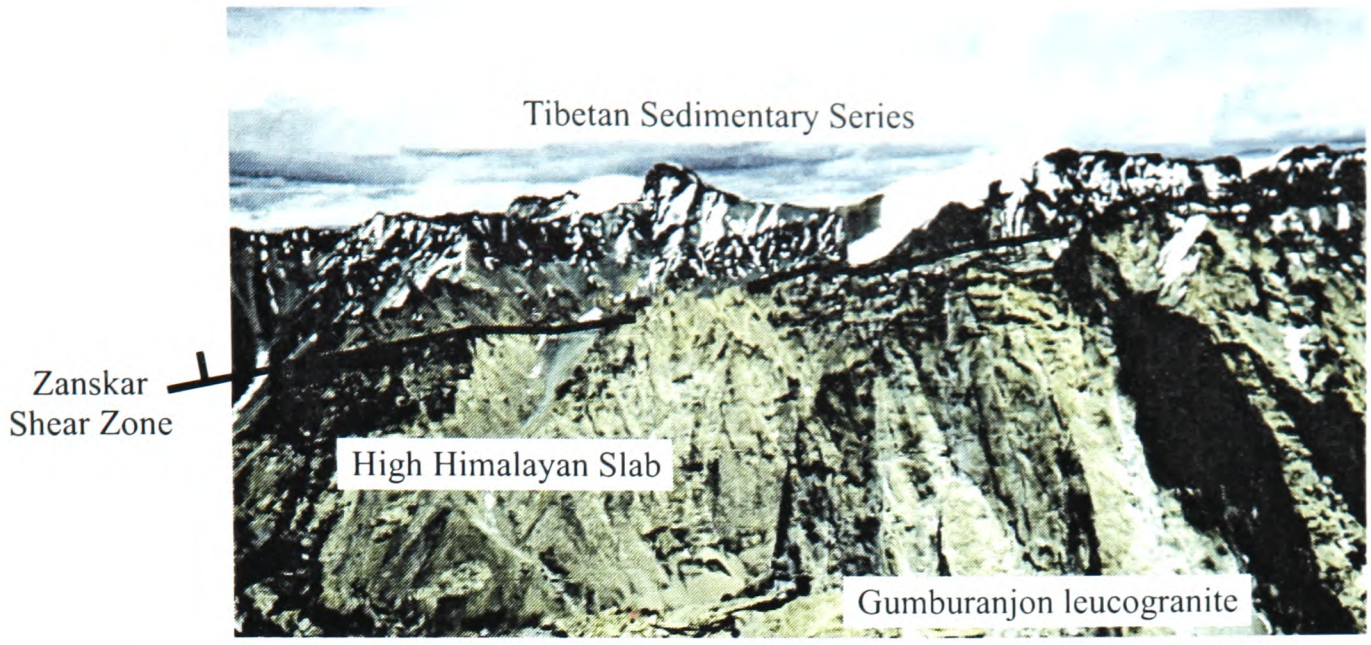


Figure 6.10a: Looking ~NE across the Gumburanjon leucogranite at the contact between the High Himalayan Slab and the Tibetan Sedimentary Series. The visible face of the Gumburanjon leucogranite is c.800m high.

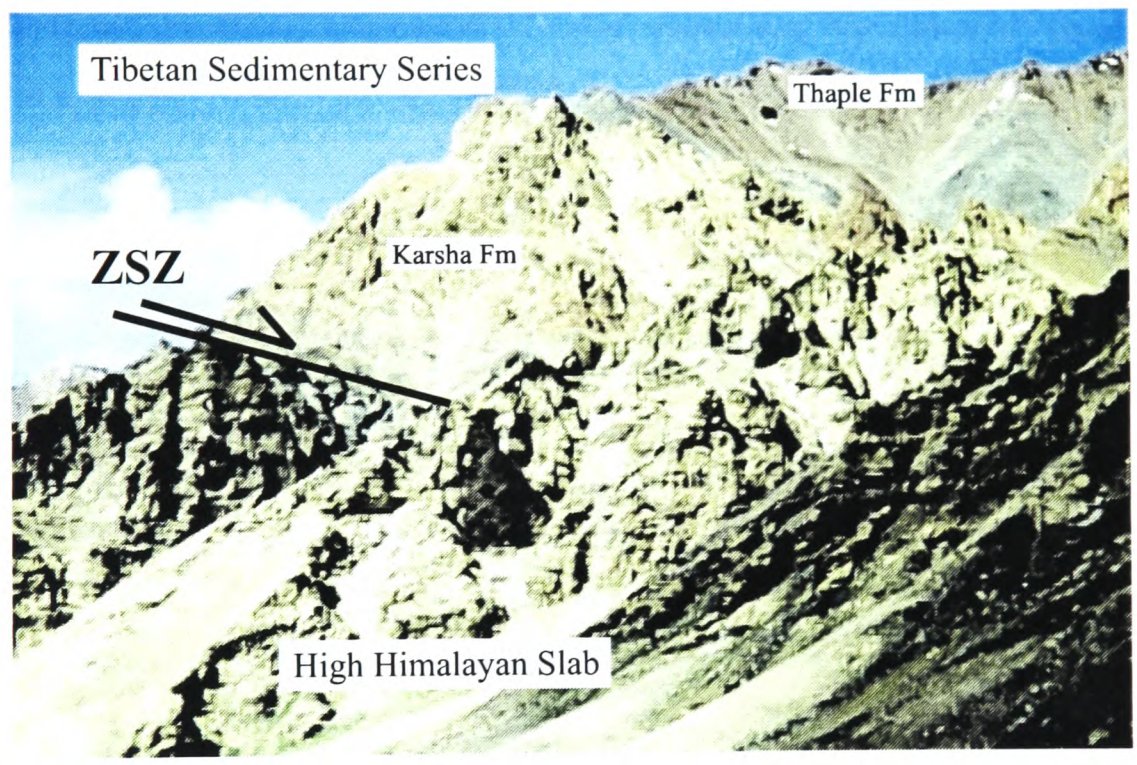


Figure 6.10b: Looking ~NW along the Kargyak Chu at the contact between the High Himalayan Slab and the Tibetan Sedimentary Series.

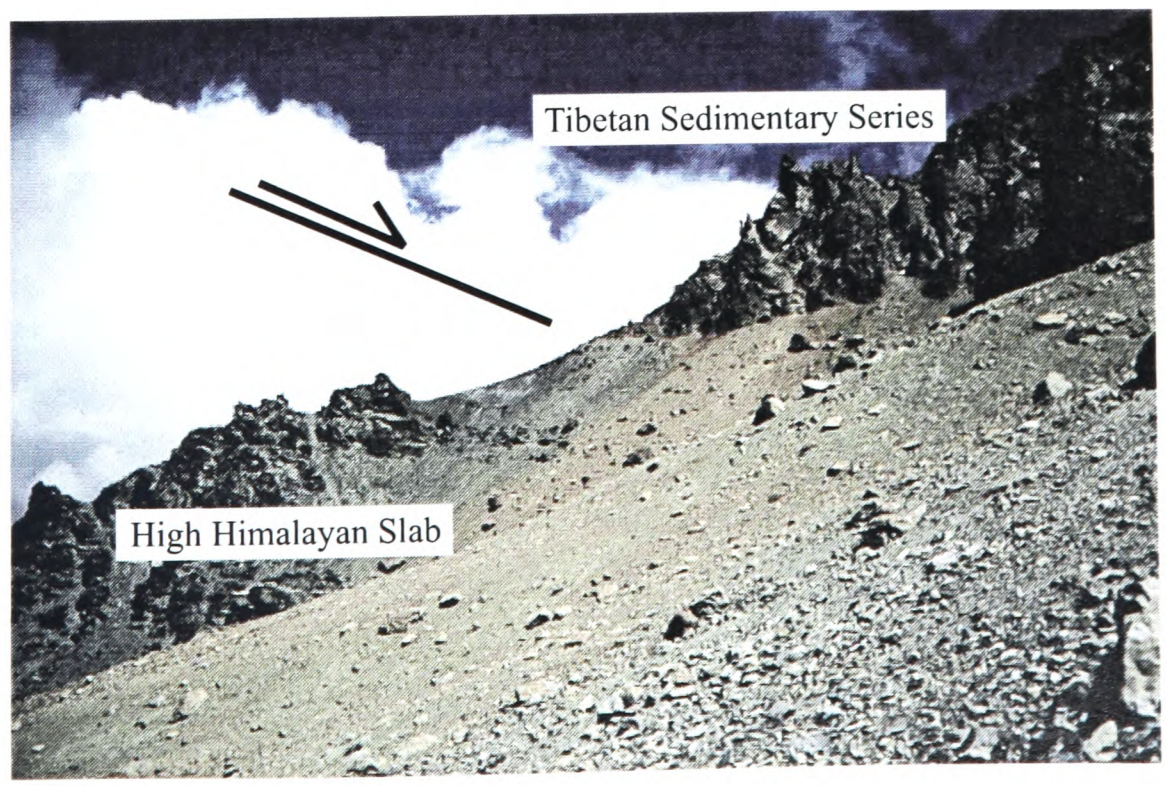


Figure 6.10c: Weathered gully marking the contact between the High Himalayan Slab and the Tibetan Sedimentary Series.

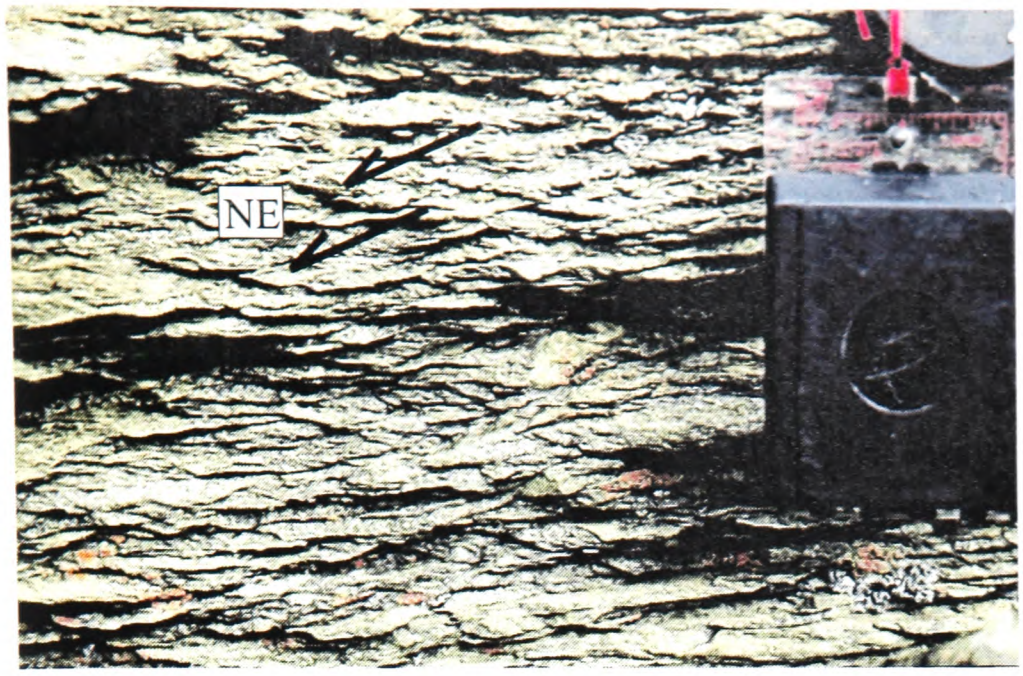


Figure 6.11a: C'-type extensional shear band fabric in a staurolite-grade metapelitic schist, giving a top-to-the-north-east shear-sense (footwall of Zanskar Shear Zone).

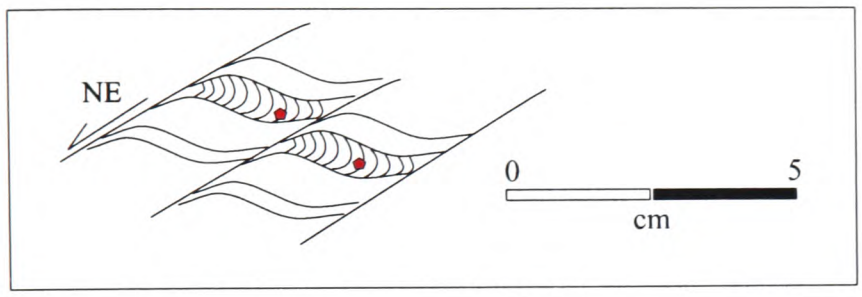


Figure 6.11b: Field sketch of the extensional shear band fabric shown above. The shear bands cross-cut an S2 crenulation fabric which is partly overgrown by euhedral garnet porphyroblasts. Movement on the ZSZ therefore post-dated the porphyroblastic growth stage of Barrovian metamorphic assemblages at the top of the slab.

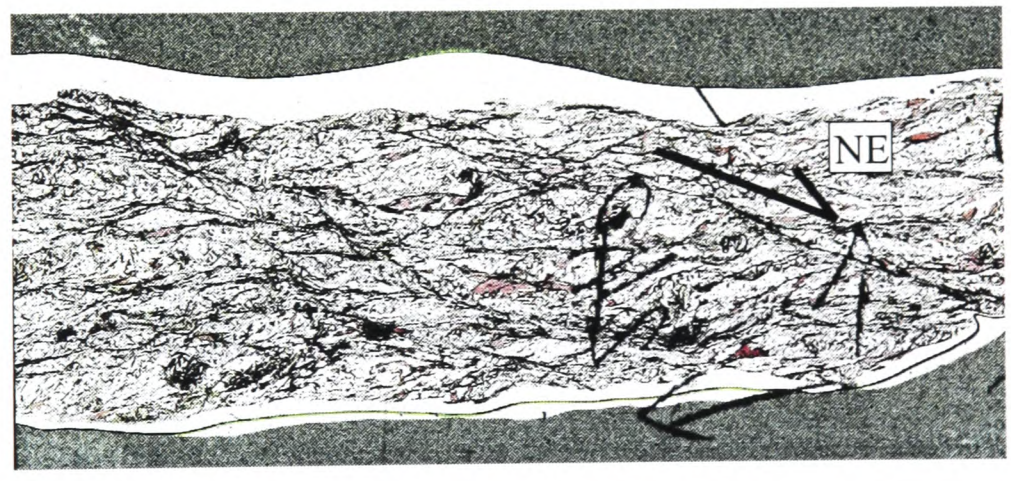


Figure 6.11c: Photomicrograph of the extensional shear band fabric in the ZSZ at the thin section scale (sample JDW 150B, collected near the summit of the 5700m peak to the west of Mt. Gumburanjon (see Figure 6.6 for location)). Field of view c. 3cm.

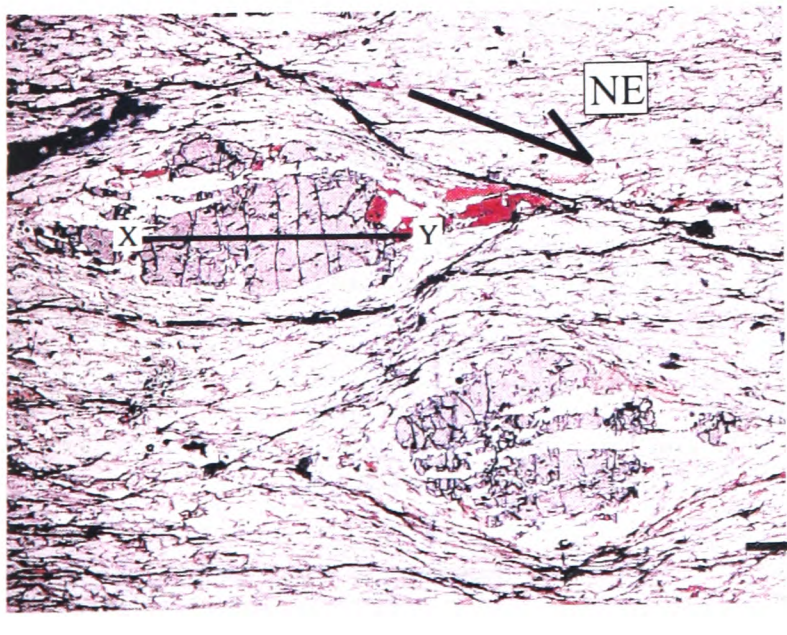


Figure 6.11d: Photomicrograph of the extensional shear band fabric in the ZSZ at the thin section scale (sample JDW 154; location shown on Figure 6.17). The shear bands wrap the elongate garnet porphyroblasts and cross-cut the sub-horizontal S2 fabric. Ilmenite inclusion trails in the garnets are sub-parallel to the S2 fabric, suggesting garnet growth to be syn/post S2. Pressure shadows are symmetrical either side of the garnets, which is indicative of co-axial flattening of the foliation around a rigid body.. Line of section X-Y denotes the location of the garnet zoning profile shown in Figure 6.18b.. Field of view c.1cm.

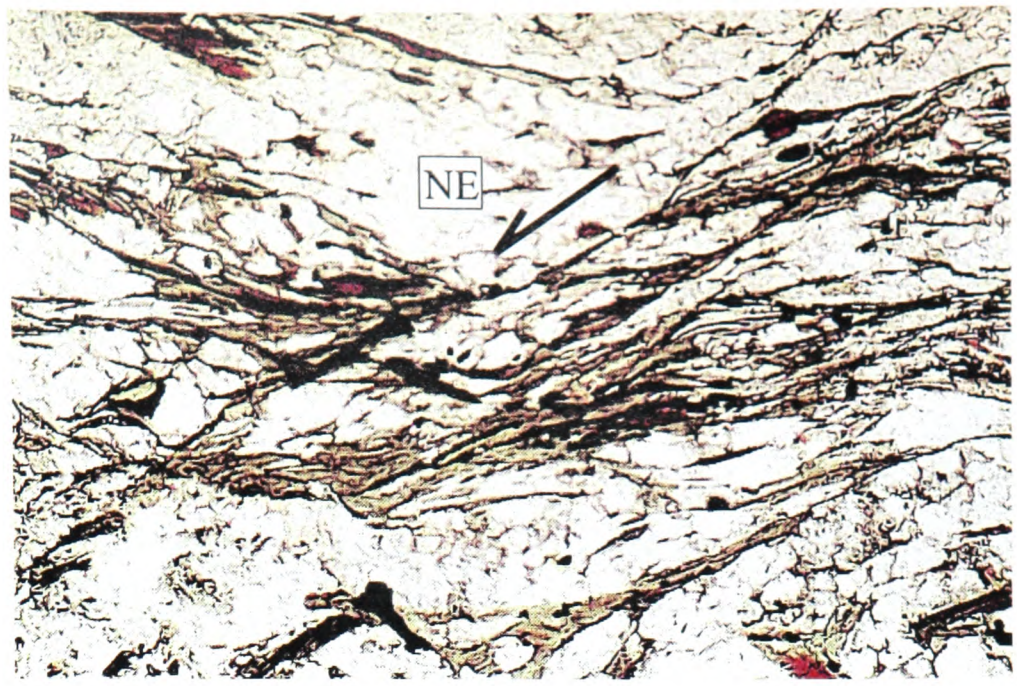


Figure 6.11e: Chlorite growth along an extensional shear band in a staurolite-grade metapelitic schist (sample JDW 150B, location as for 6.11c). Field of view c.3mm.

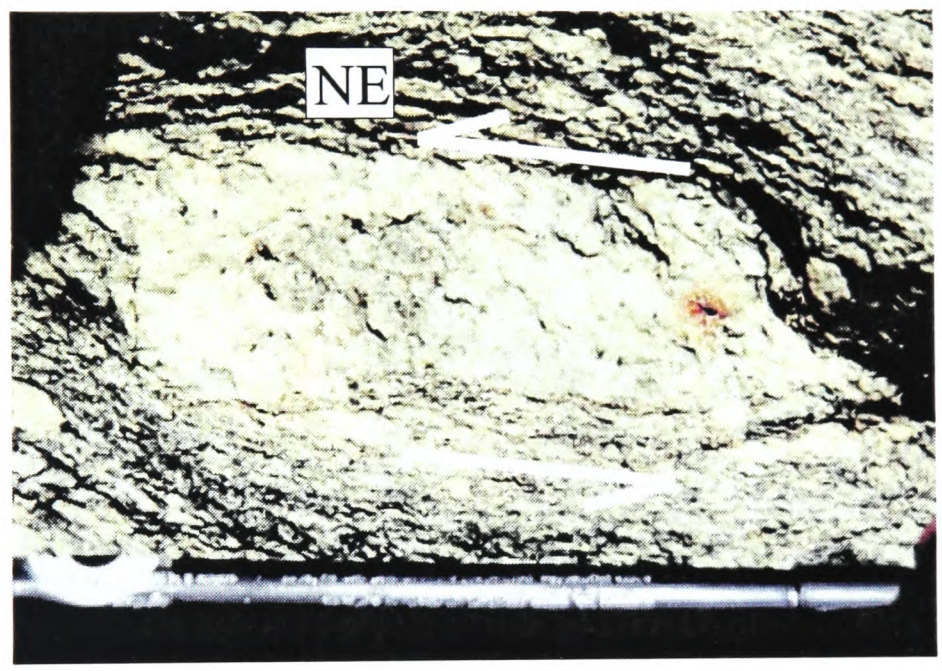


Figure 6.11f: K-feldspar phenocryst displaying a prominent top-to-the-north-east shear sense (granitic gneisses, ~500m south of the main face of the Gumburanjon leucogranite)

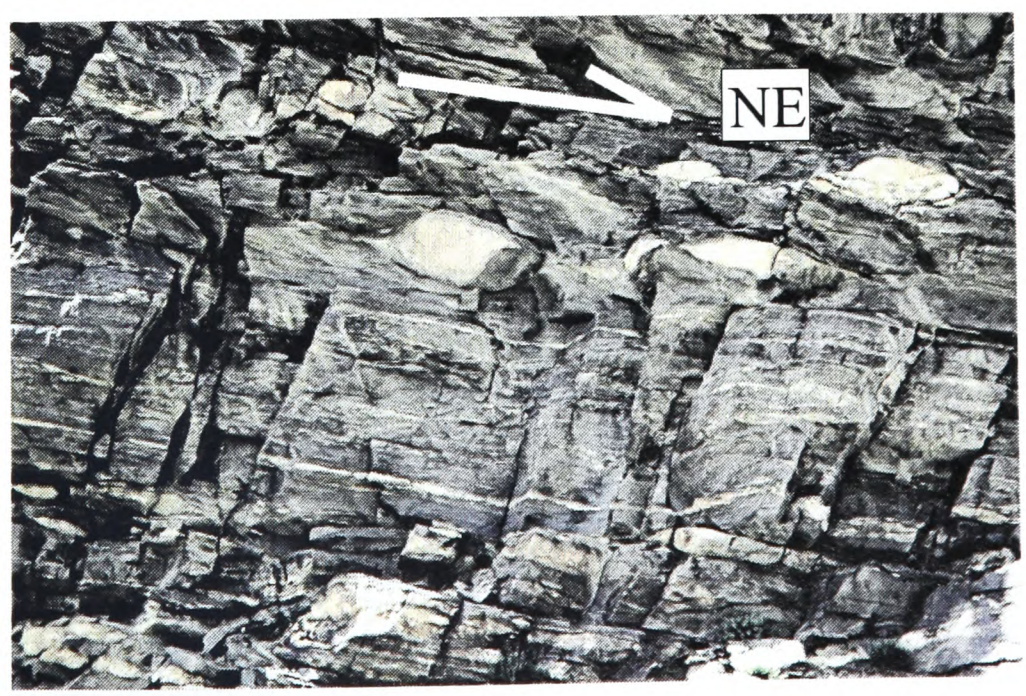


Figure 6.11g: Asymetrical pegmatite pod showing a distinct top-to-the-north-east sense of shear (immediate footwall of the ZSZ, ~2km NW of the main face of the Gumburanjon leucogranite).

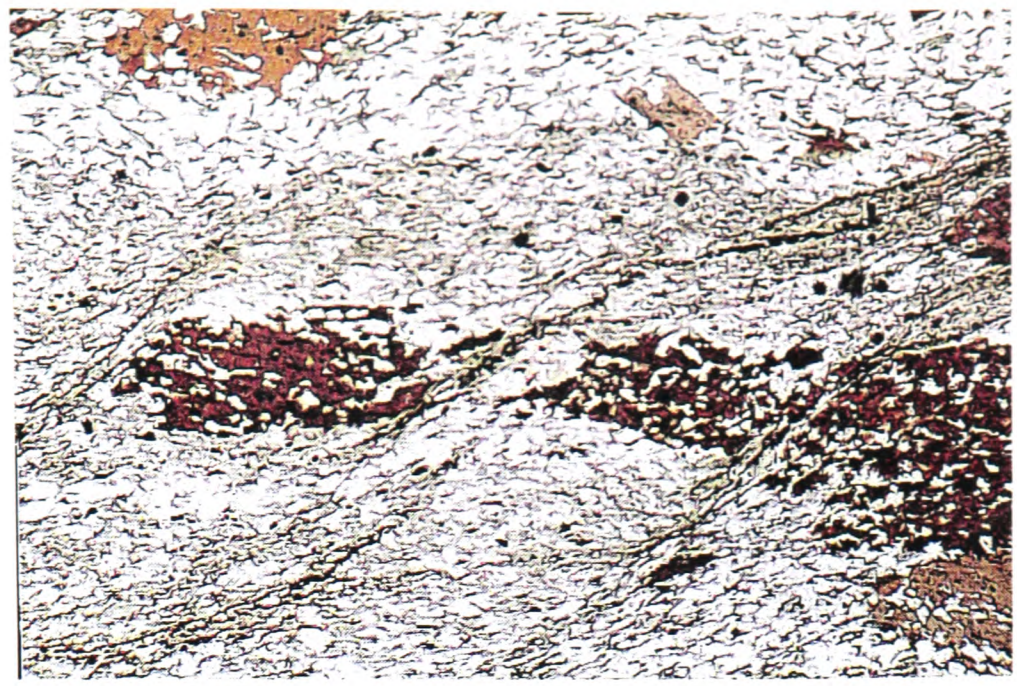


Figure 6.11h: Top-to-the-north-east extensional shear band fabric in the biotite-grade pelitic schists of the Haimantas (sample JDW 238, ~3km north of the summit of the Shingo La). Field of view c.3mm.



Figure 6.11i: Biotite fish showing a top-to-the-north-east shear sense (sample JDW 240, ~3km north of the summit of the Shingo La). Note that the graphitic inclusion trail in the main part of the porphyroblast is at a high angle to the matrix foliation and appears to bend into the foliation in the lower part of the photograph. A smaller biotite preserves an inclusion trail which is parallel to the matrix foliation in the upper part of the photo. This is good evidence for at least two stages of biotiet growth, the latest of which was syn-kinematic with respect to extension along the ZSZ. Field of view c.3mm.



Figure 6.11j: Biotite fish showing a top-to-the-north-east shear sense (sample JDW 240, ~3km north of the summit of the Shingo La). Field of view c.3mm.

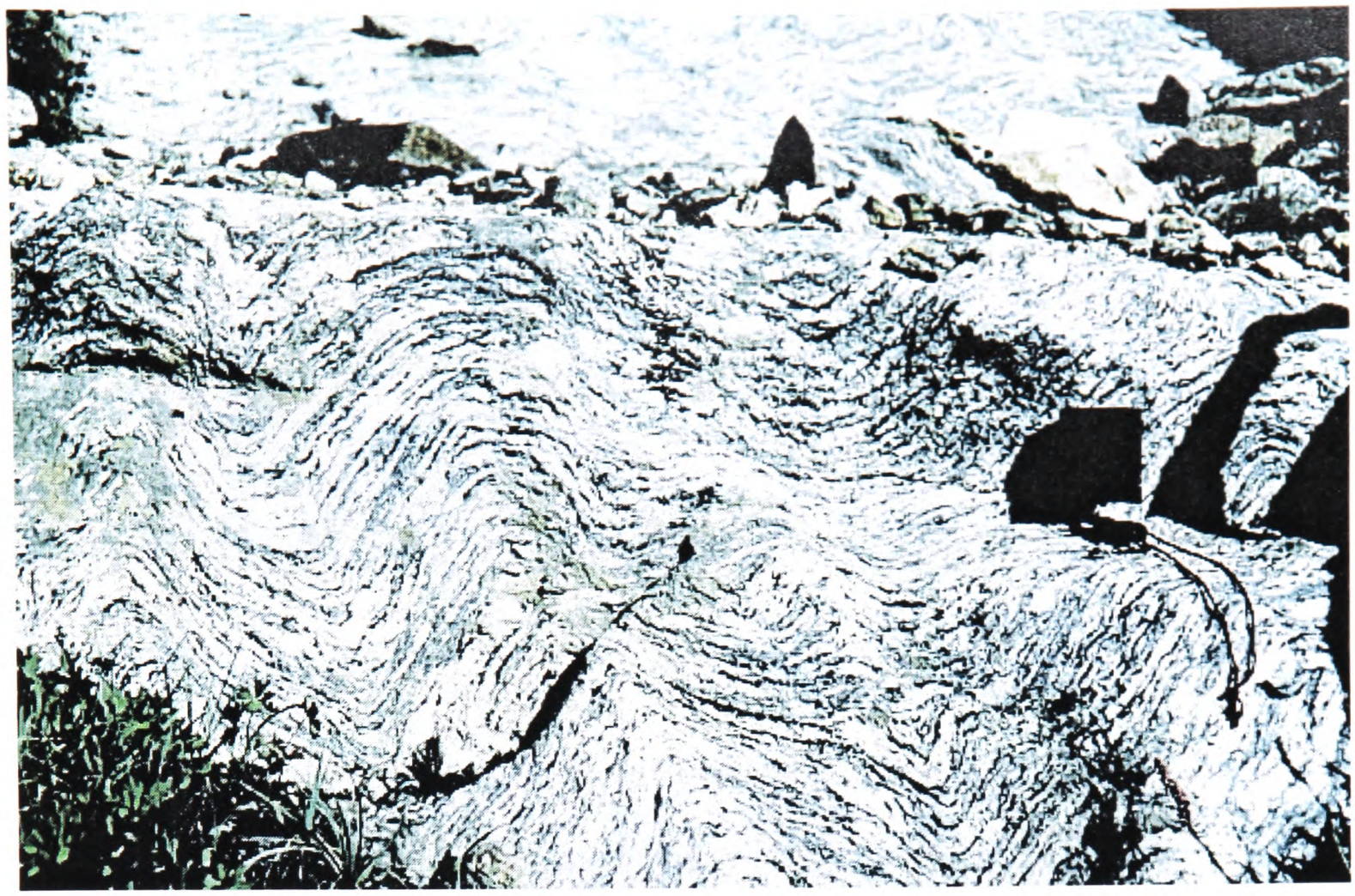


Figure 6.12a: Late-stage ductile folds developed in sillimanite-grade migmatitic gneisses in the immediate footwall of the ZSZ (Temasa nala, south-east of Padum).

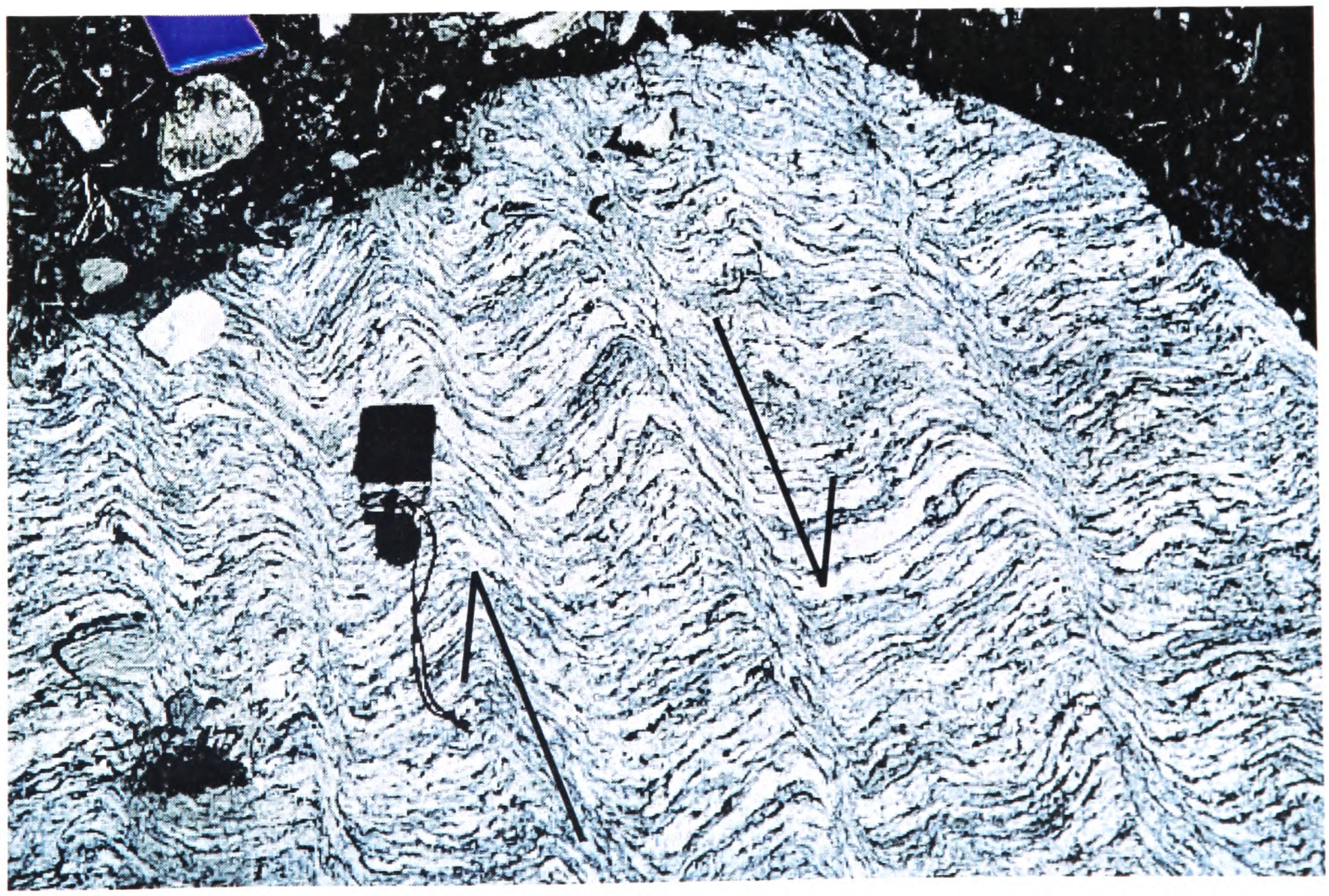


Figure 6.12b: Looking down on the Y-Z plane of the above folds. The axial surfaces of these folds form minor shear zones which give a dextral (top-to-the-west) shear sense. These folds are interpreted to be related to movement along the ZSZ and are indicative of a component of dextral strike-slipmotion during extension.



Figure 6.13a: Looking ~NW at the cataclastic melange within the immediate hangingwall of the ZSZ. Large blocks of sediments from the Tibetan Sedimentary Series are randomly orientated within this zone (note the conspicuous block of brown dolomite in the centre of the picture). Photograph taken ~3km NW of the main face of the Gumburanjon leucogranite.



Figure 6.13b: NE-plunging slickenlines on a 40-50° dipping fault surface in the biotite-grade sediments in the footwall of the ZSZ.

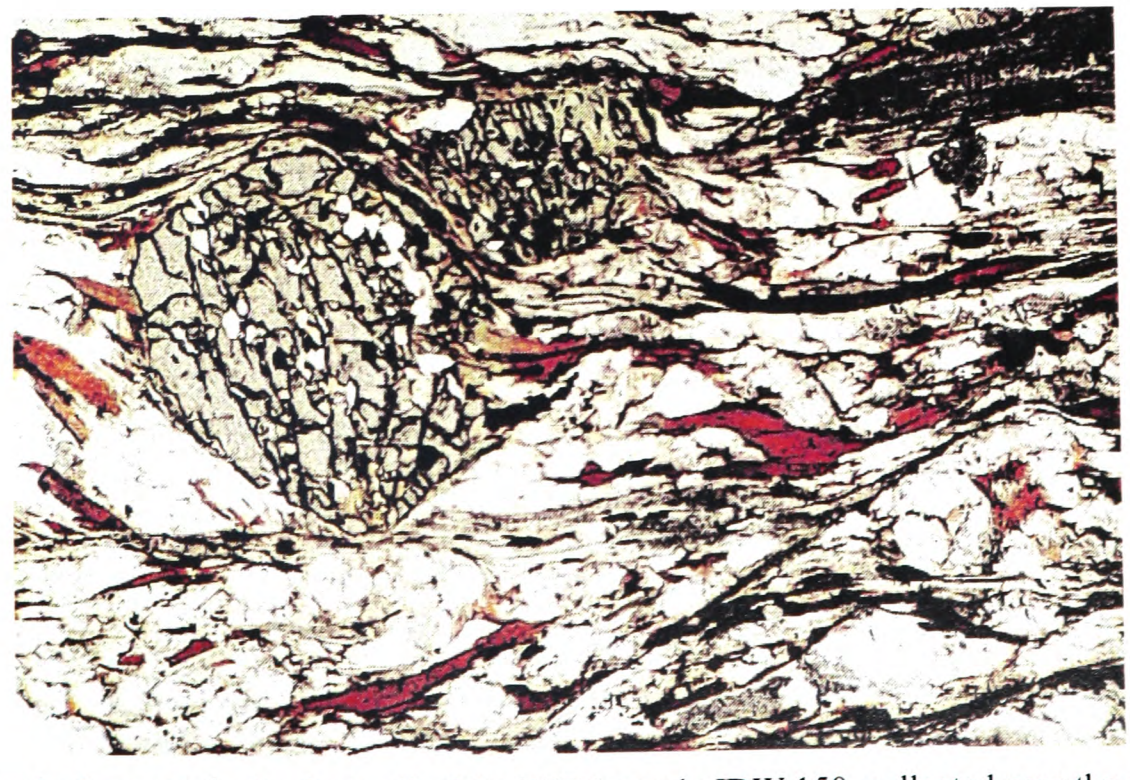


Figure 6.13c: Cracked garnets in the footwall of the ZSZ (sample JDW 150, collected near the summit of the 5700m peak to the west of Mt. Gumburanjon). Note the NE-dipping C'-type extensional shear bands in the right of the picture. Field of view c.1mm.

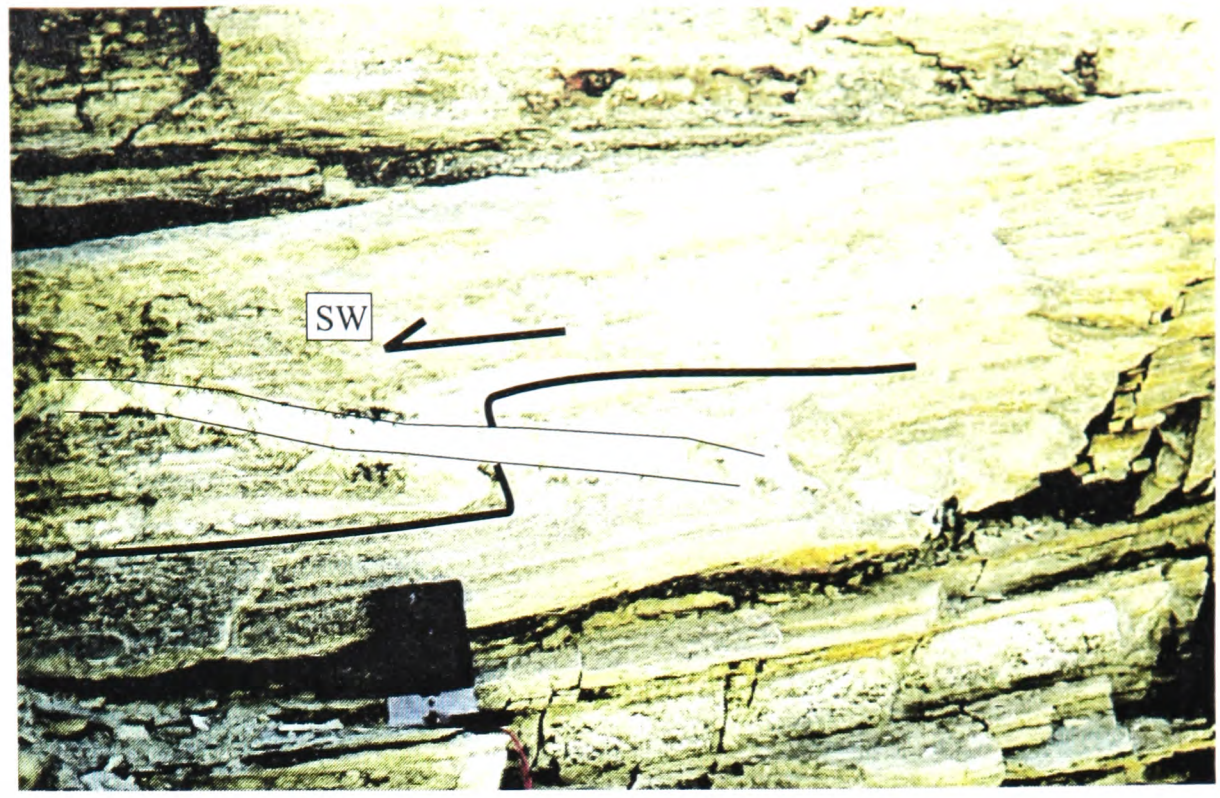


Figure 6.14a: SW-verging fold in the ZSZ. The fold is intruded along its axial surface by an undeformed leucogranite vein. Emplacement of leucogranites at the top of the slab is interpreted to be syn-kinematic with respect to extension along the ZSZ (see text for details), suggesting that SW-directed compression was continuing in the High Himalayan Slab whilst the ZSZ was active.

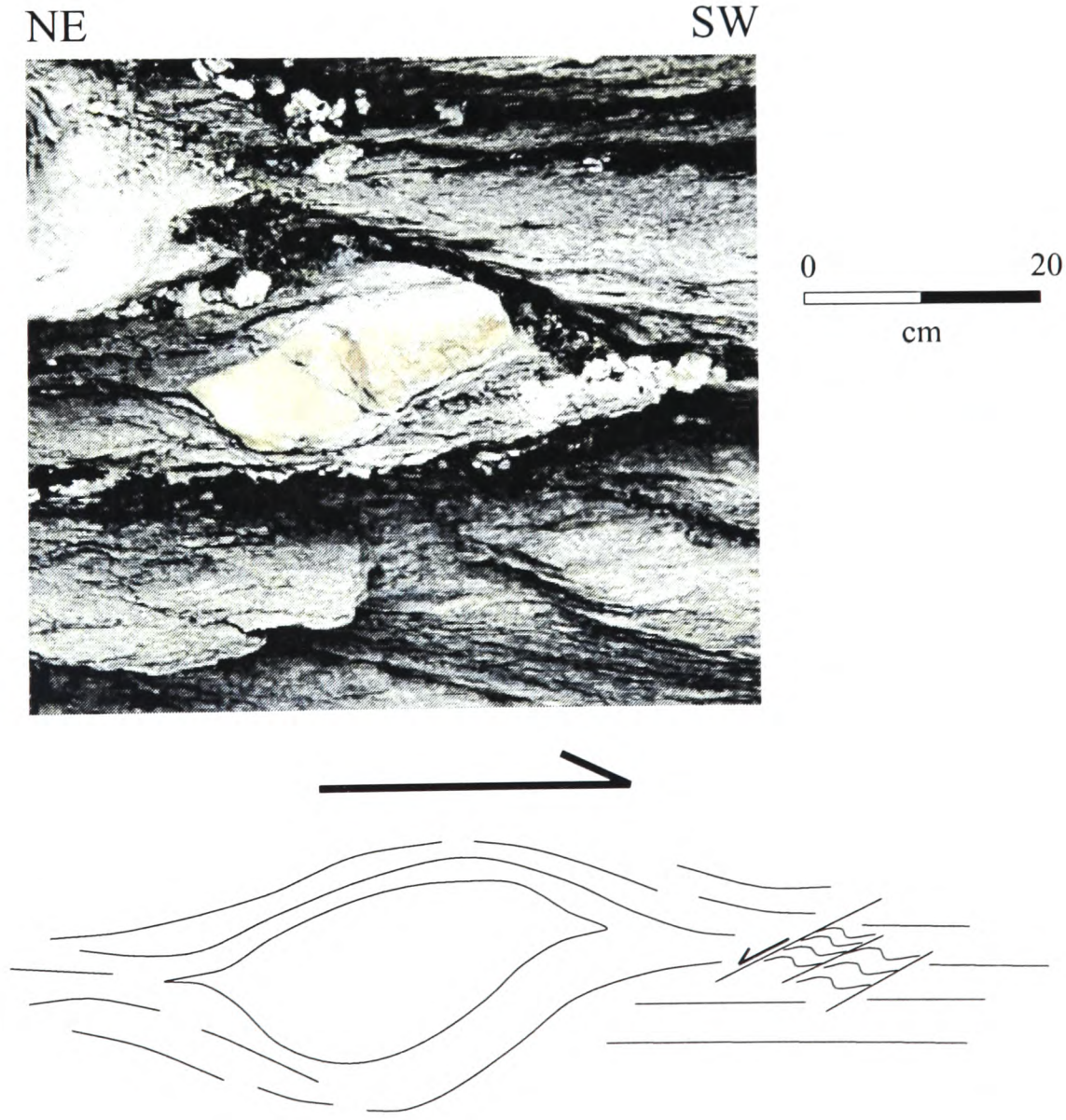


Figure 6.14b: Asymmetrical quartz augen showing a top-to-the-SW shear sense. Top-to-the-north-east extensional shear band fabrics are observed in the metapelitic schists immediately adjacent to the augen and are clearly the younger structures.



Figure 6.14c: SW verging microfolds in a biotite-grade graphitic phyllite (sample JDW 242, collected ~5km south of the main face of the Gumburanjon leucogranite). Field of view c.3mm.

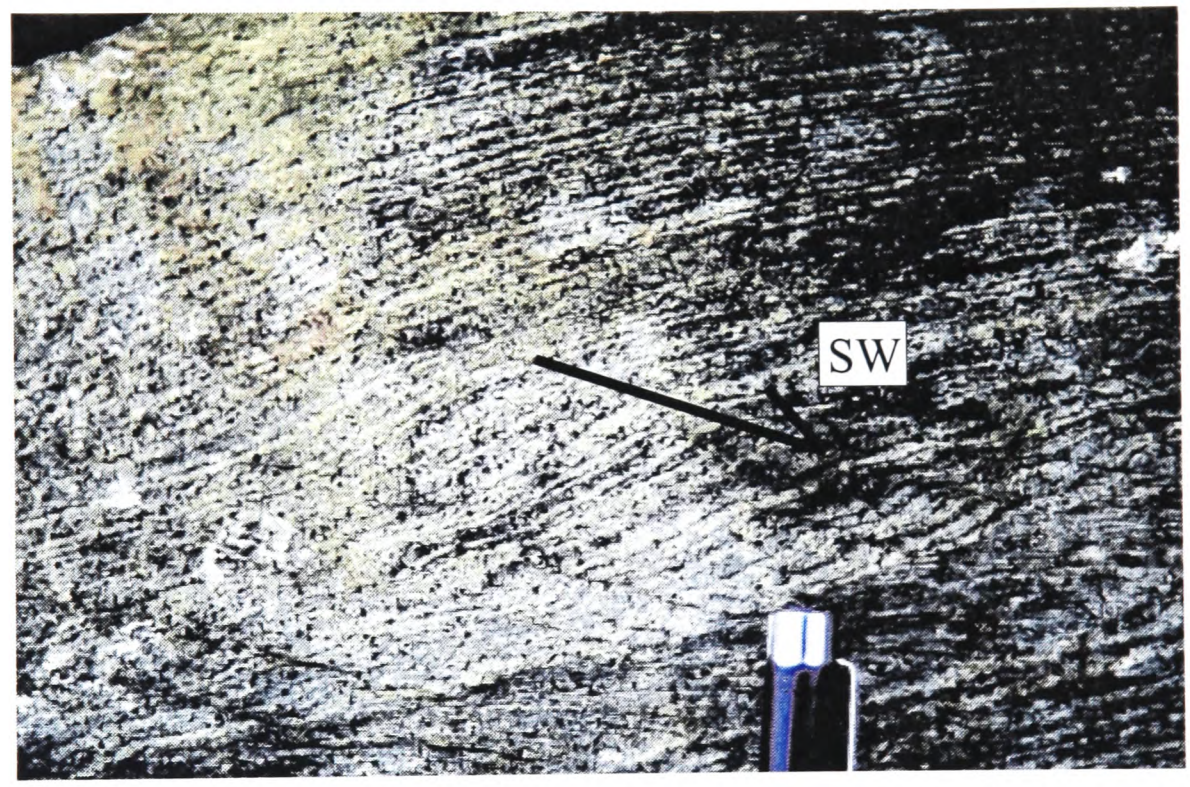


Figure 6.14d: Extensional shear band fabric showing a top-to-the-SW shear-sense in the biotite-grade phyllitic schists of the Haimantas to the north of the Shingo La .

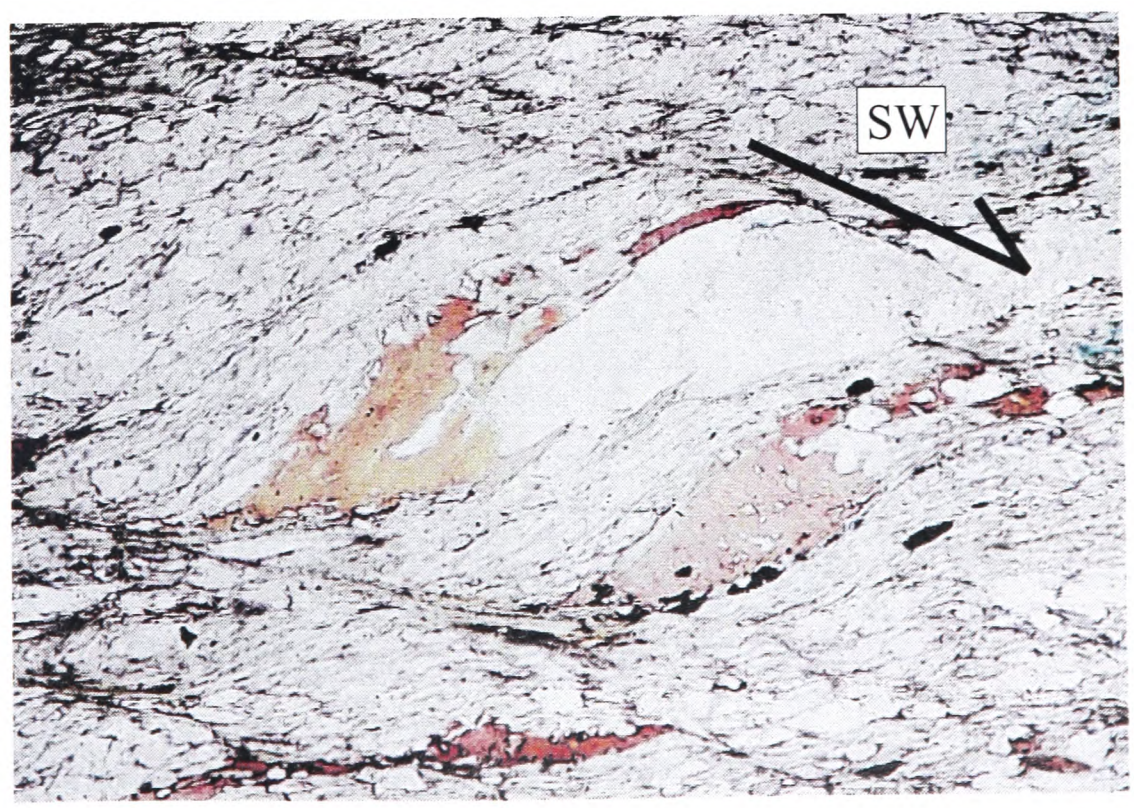


Figure 6.14e: Close-up of the top-to-the-SW shear bands shown above (sample JDW 244). Field of view c.3mm.

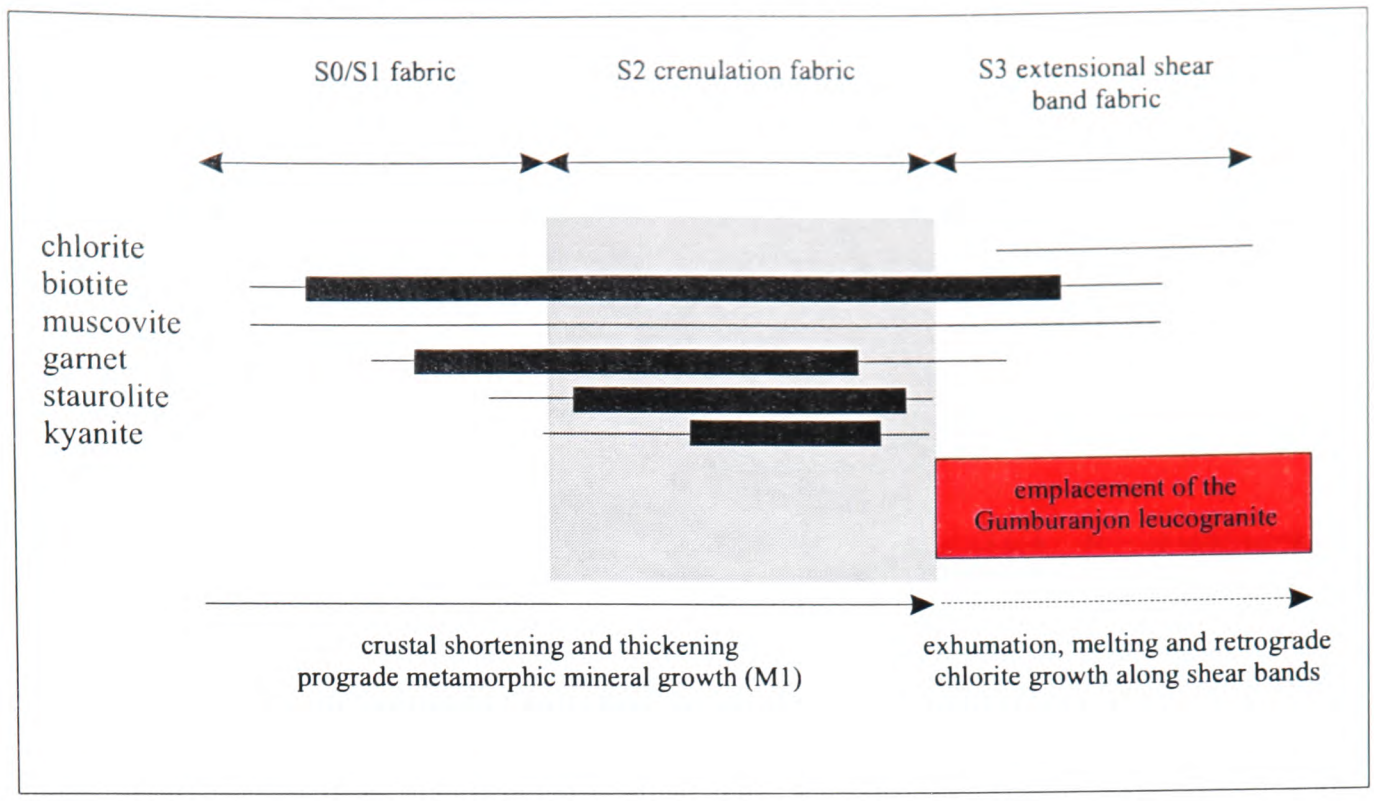


Figure 6.15: Summary diagram showing the relative timing of Barrovian metamorphic mineral growth in relation to the development of structural fabrics to the north of the Shingo La. Black boxes denote porphyroblastic growth stages.

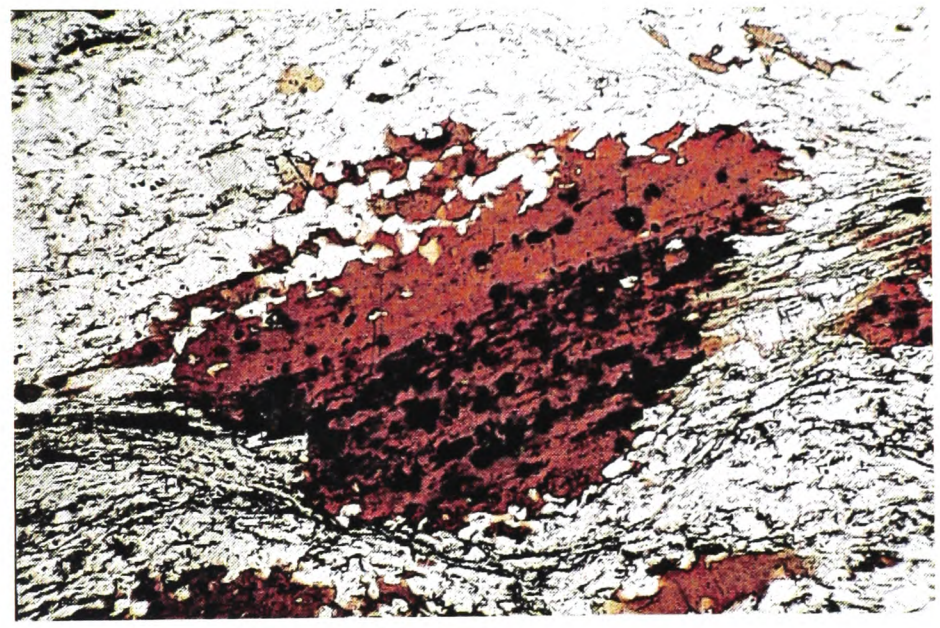


Figure 6.16a: Porphyroblastic biotite statically overgrowing the S0/S1 fabric (sample JDW 239, collected ~5km south of the main face of the Gumburanjon leucogranite). Field of view c.3mm.

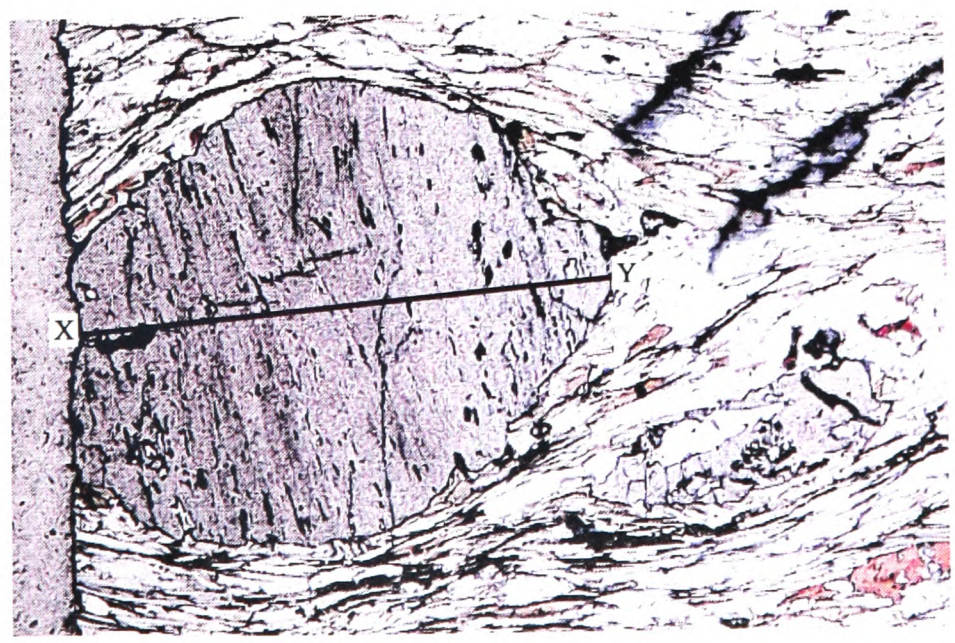


Figure 6.16b: Rounded garnet porphyroblast preserving a straight ilmenite inclusion trail (S0/S1?), which trends at a high angle to the external S2 fabric (sample JDW 154; see Figure 6.17 for location). Line of section X-Y denotes the orientation of the zoning profile traverse shown in Figure 6.18a. Field of view c.5mm.

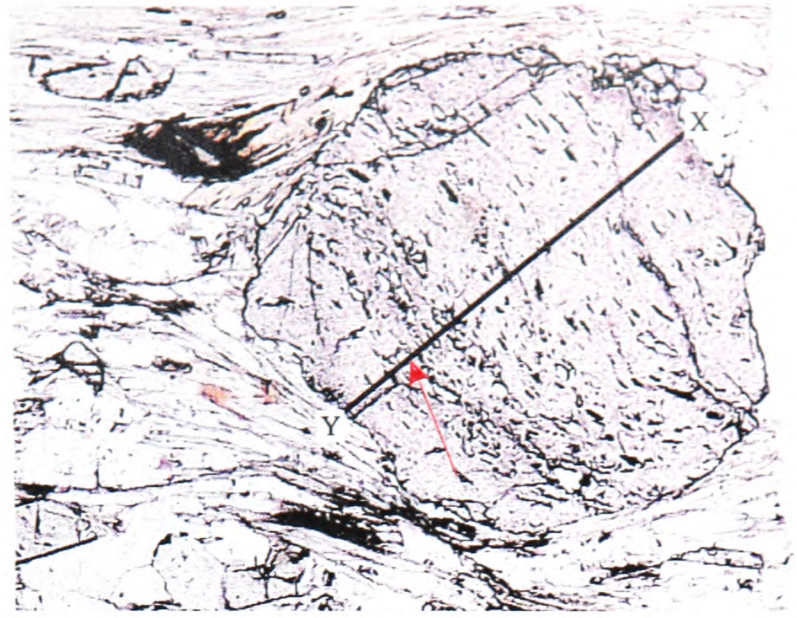


Figure 6.16c: Curved inclusion trail (S0/S1?) preserved in the core of a rounded garnet porphyroblast. The garnet rim is inclusion free, suggesting that garnet growth occurred in two stages. Line of section X-Y denotes the orientation of the zoning profile traverse shown in Figure 6.18c. Red arrow denotes the position of the chemical unconformity revealed in Figure 6.18c. Field of view c.5mm. (Sample JDW 155; see Figure 6.17 for location)



Figure 6.16d: Elongate garnet porphyroblast displaying a crenulated inclusion pattern (S0/S1?). Small staurolites are evident in the upper part of the photograph. (Sample JDW 156; see Figure 6.17 for location). Field of view c.3mm.

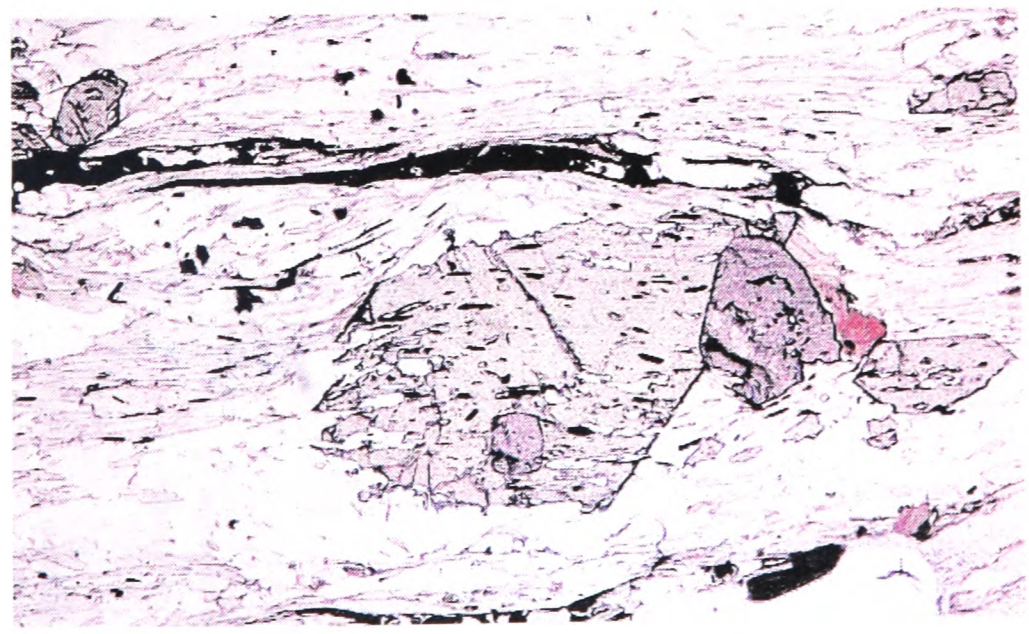
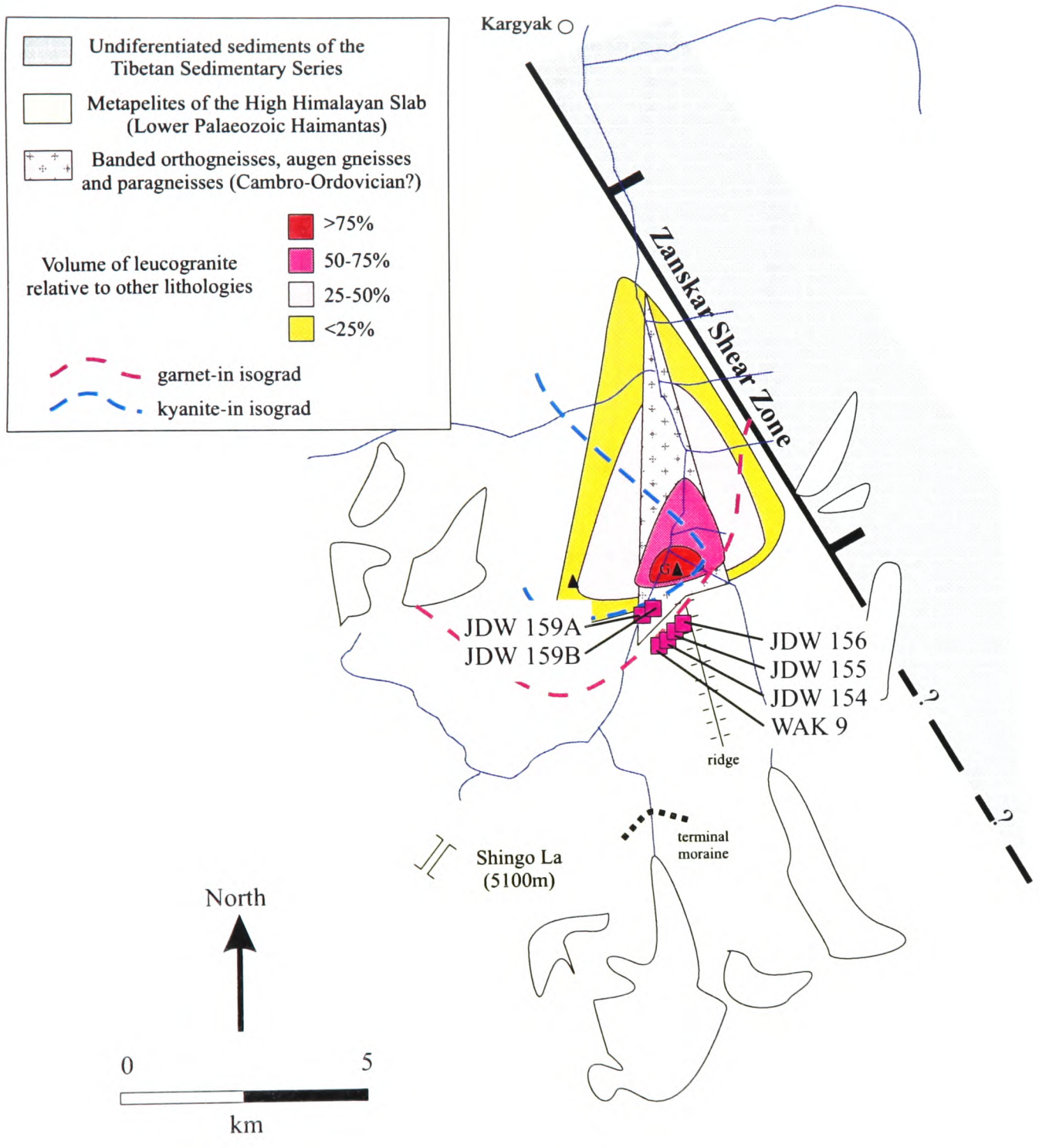


Figure 6.16e: Euhedral staurolite porphyroblast overgrowing the S2 fabric in the ZSZ. The staurolite appears to be growing at the expense of garnet, providing evidence for the prograde KFMASH reaction Grt + Chl = St + Bt (sample JDW 151B; collected near the summit of the 5700m peak to the SW of Mt. Gumburanjon; see Figure 6.6 for location). Field of view c.1cm.





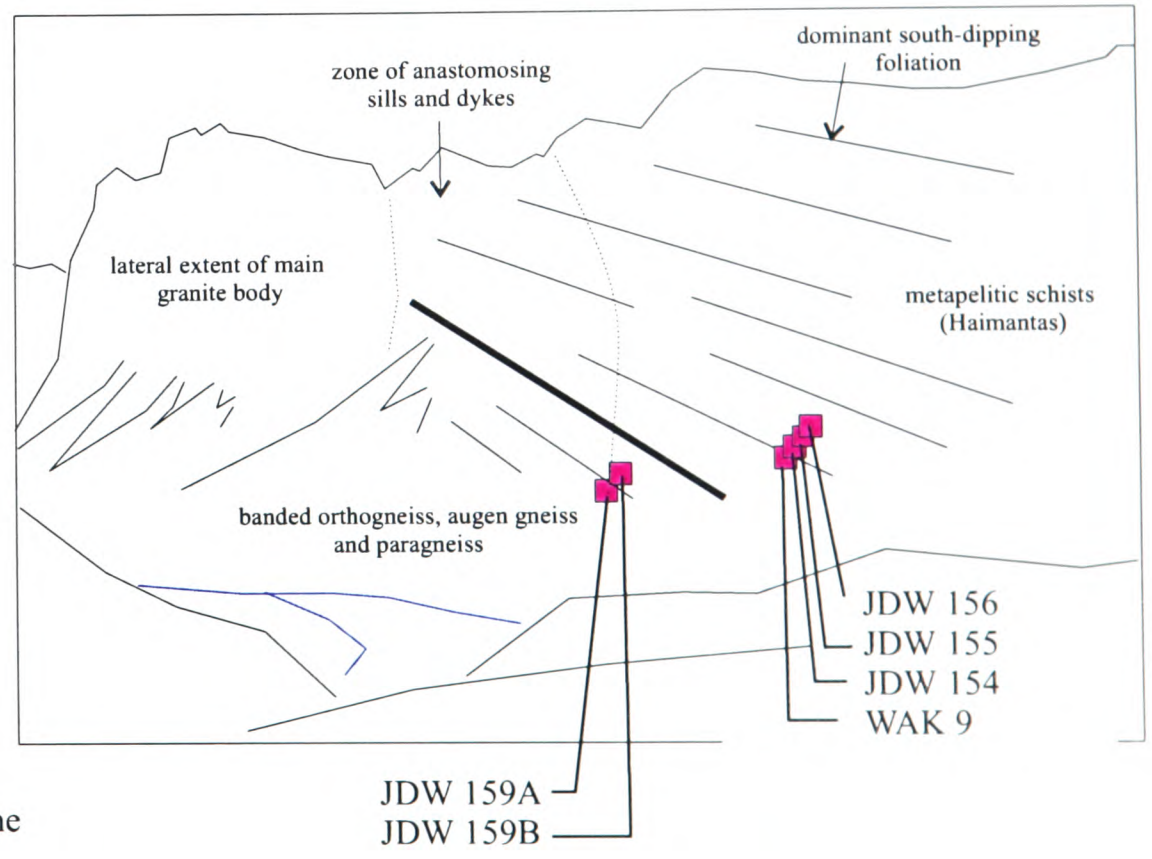
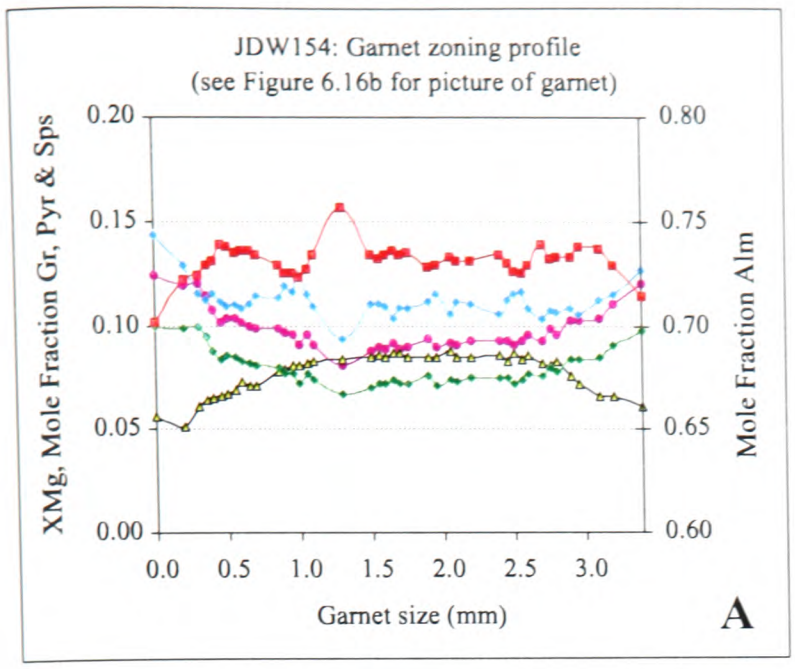
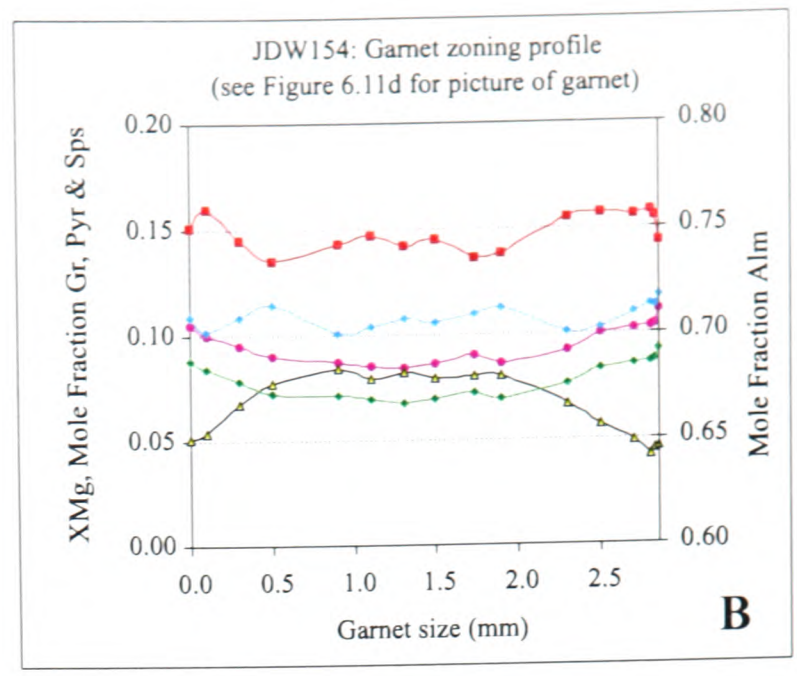
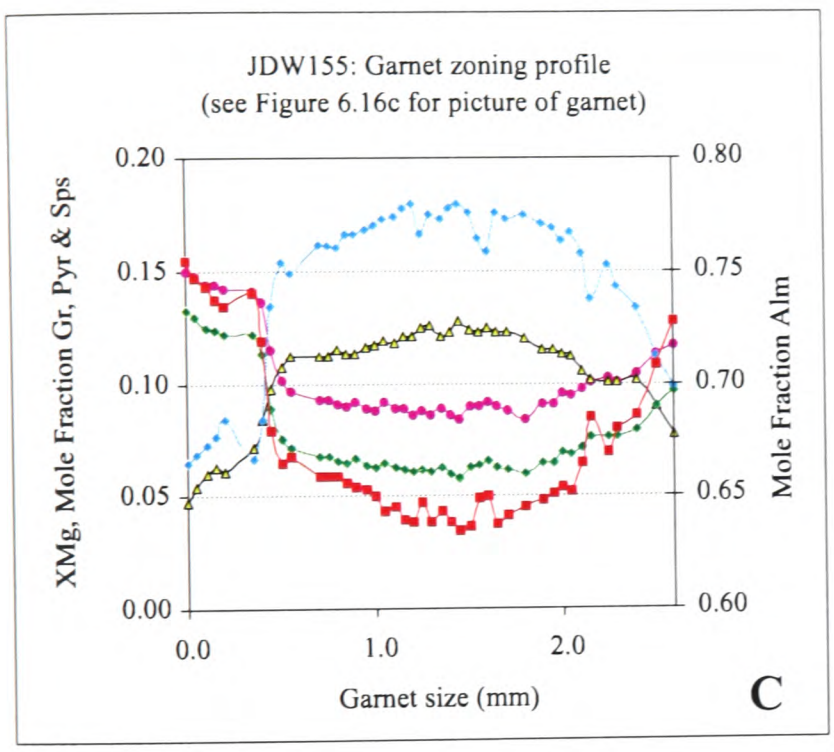
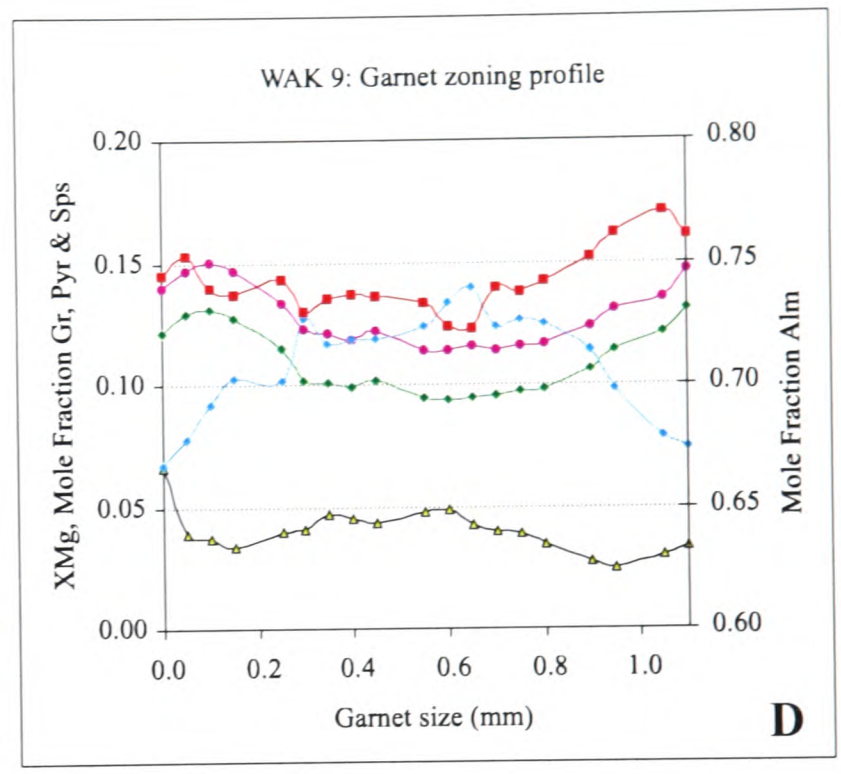


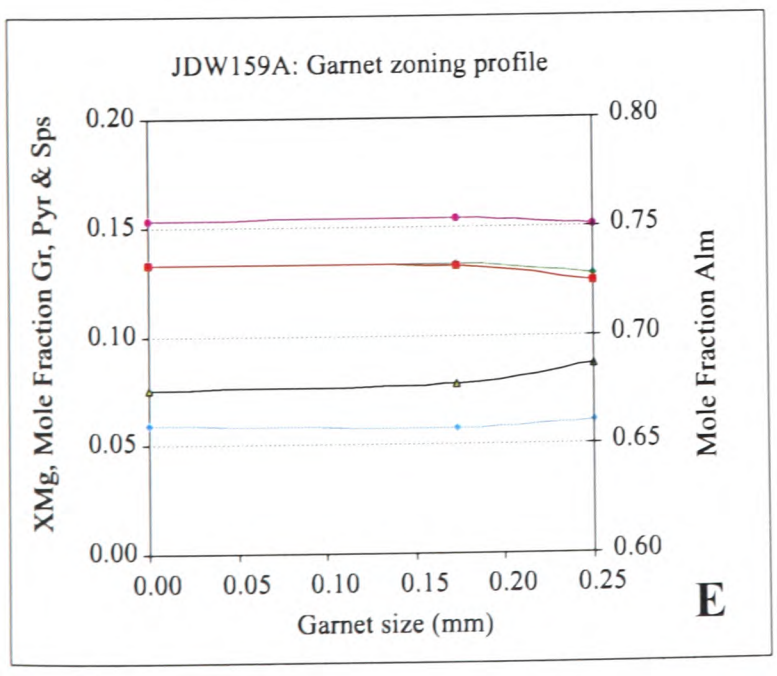
Figure 6.17: Location of samples collected for thermobarometric analysis in the footwall of the Zanskar Shear Zone.

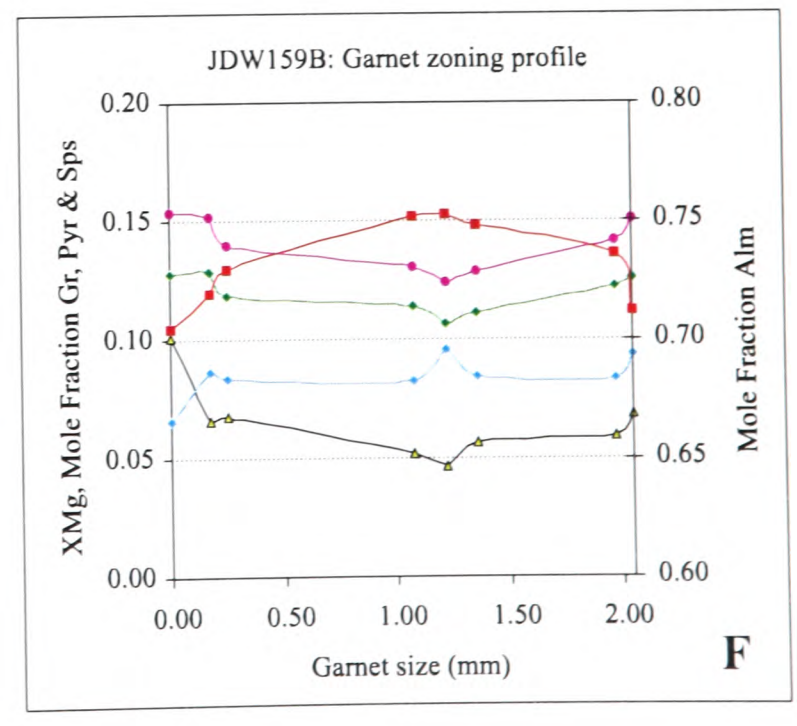












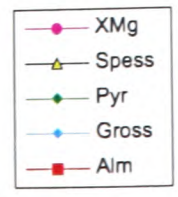
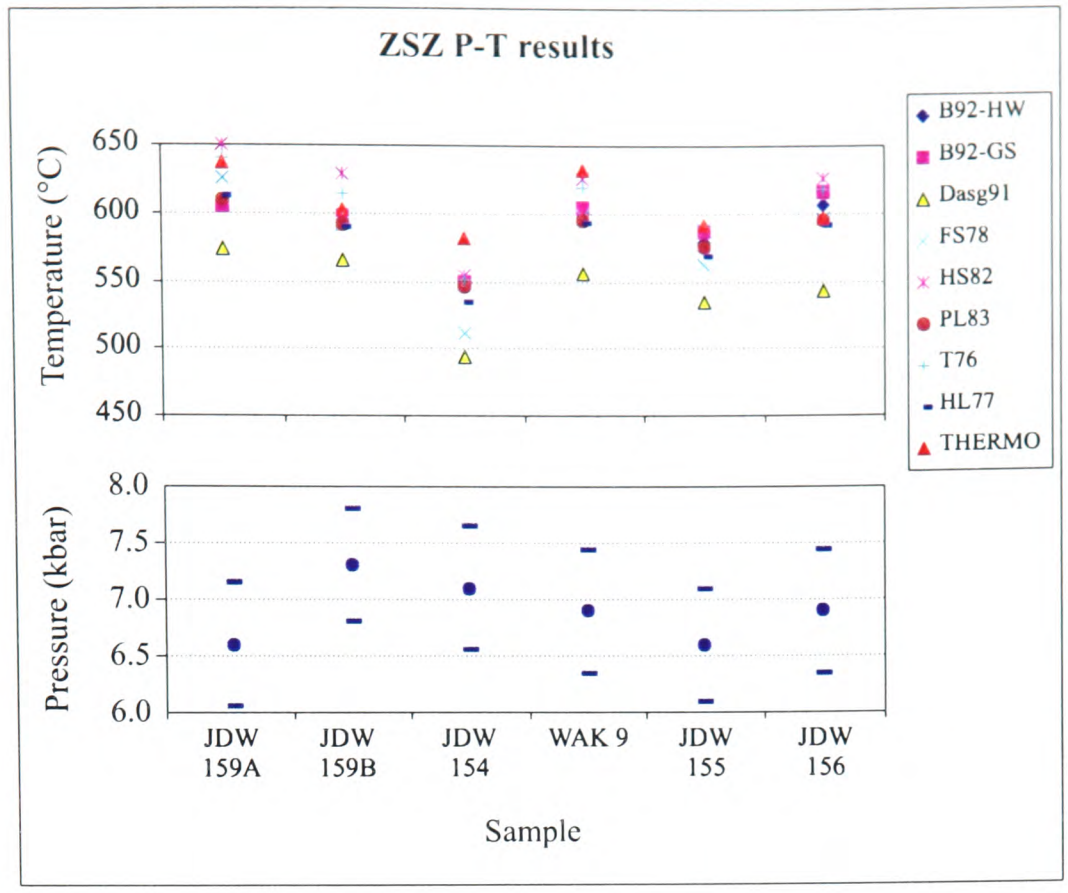


Figure 6.18: Selected garnet zoning profiles from samples collected in the footwall of the ZSZ (see Figure 6.17 for location).

(a)



(b)

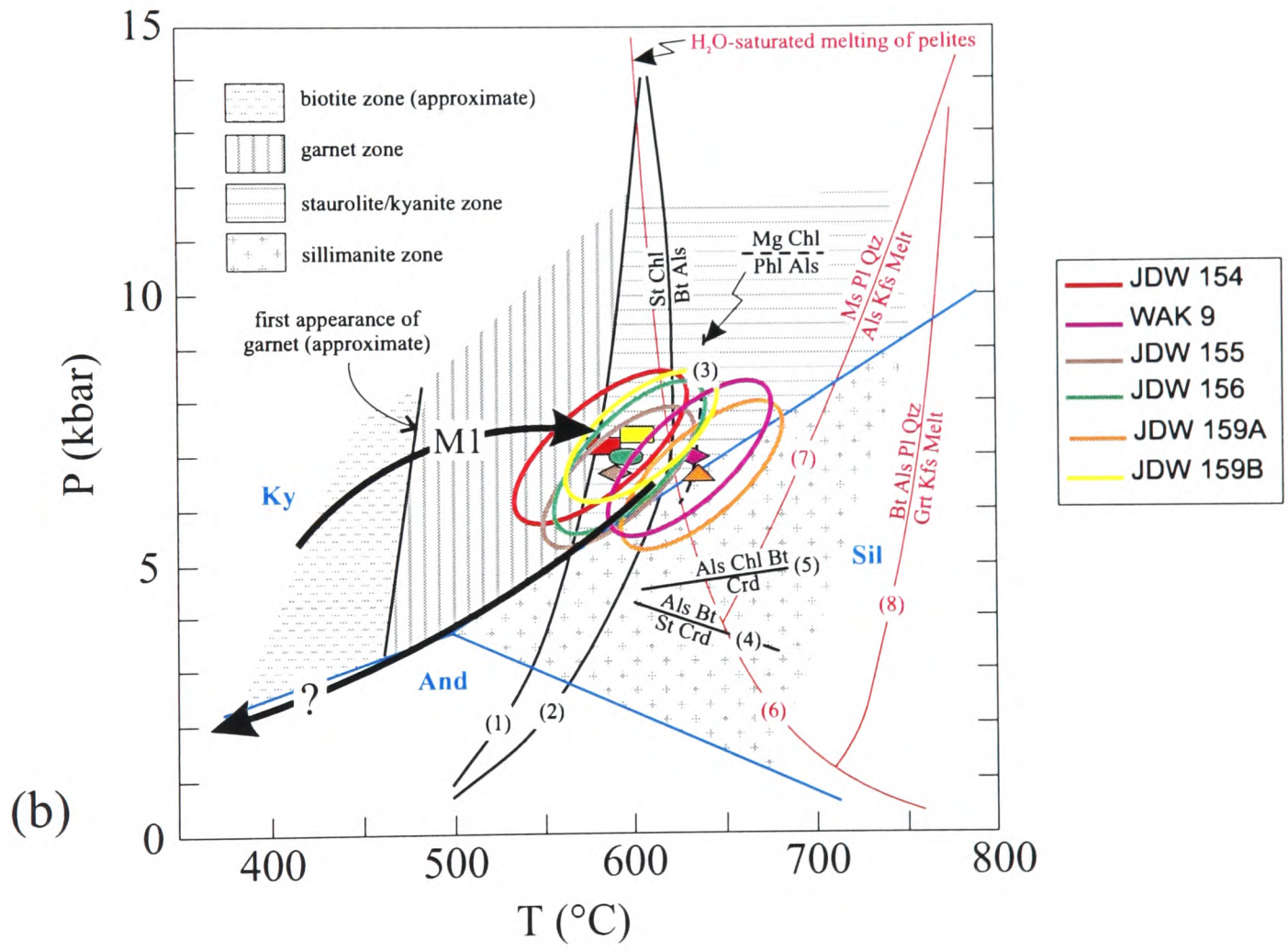
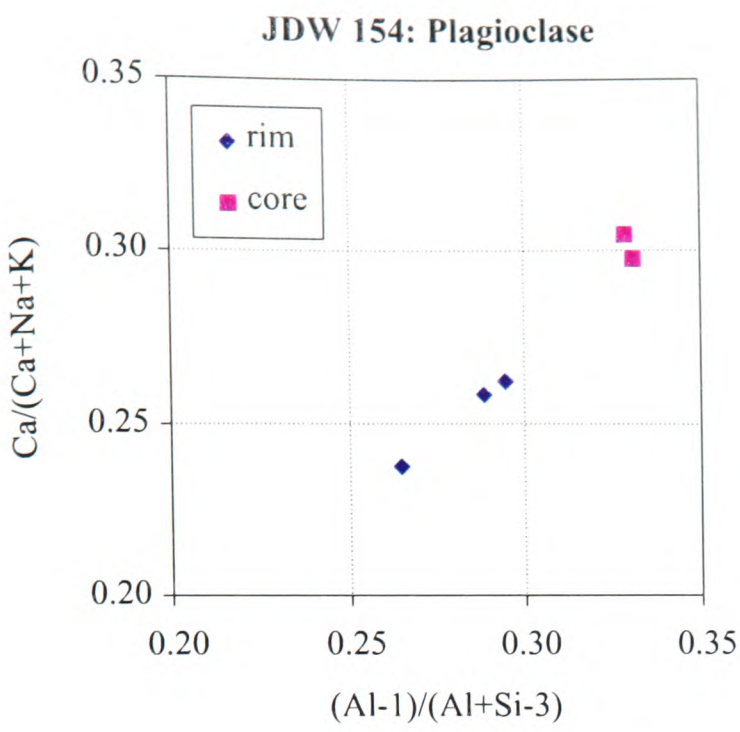
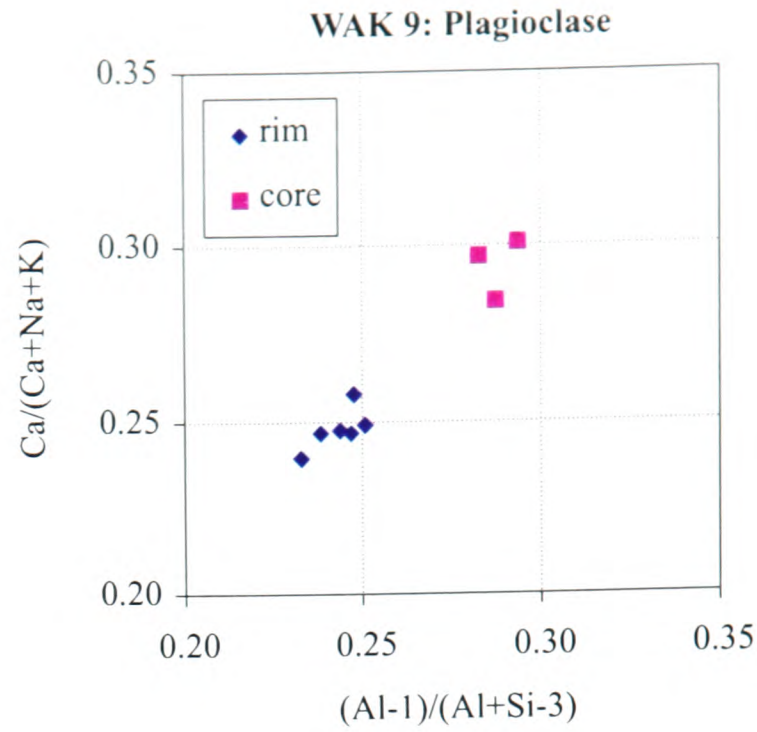


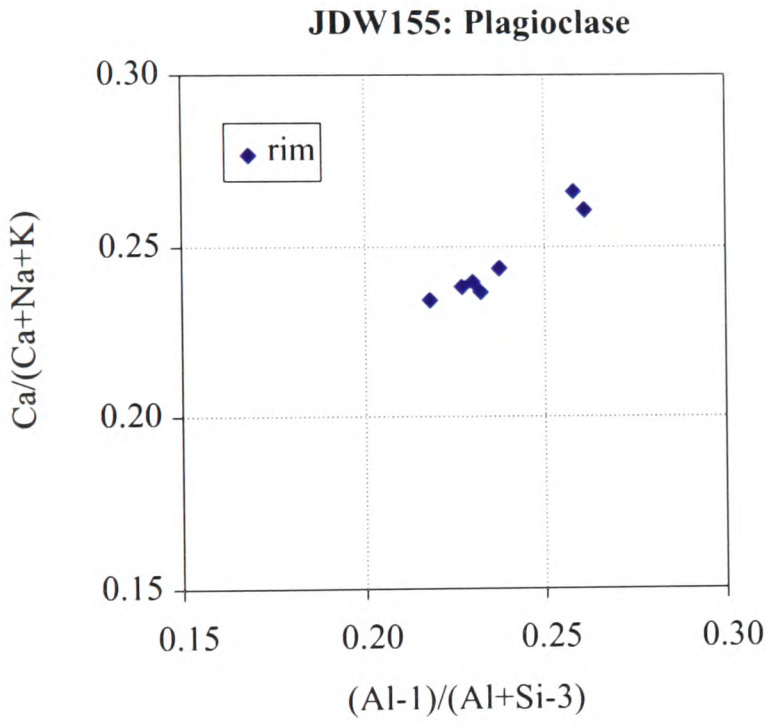
Figure 6.19: P-T results of samples collected from the footwall of the Zanskar Shear Zone (see Figure 6.17 for location).

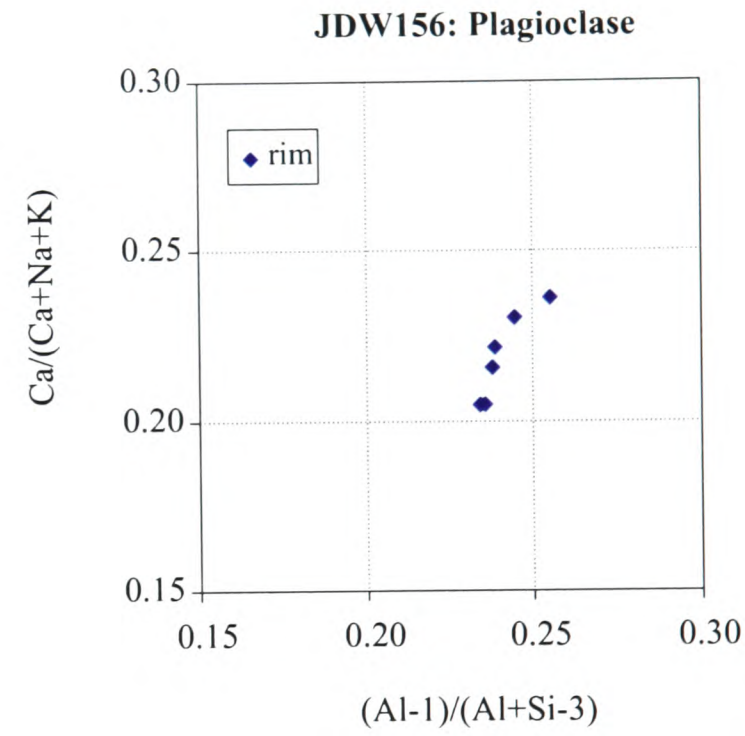
(a) Comparison of different garnet-biotite thermometers (see Table 6.2 for abbreviations) and preferred pressure results using THERMOCALC (see Table 6.2)

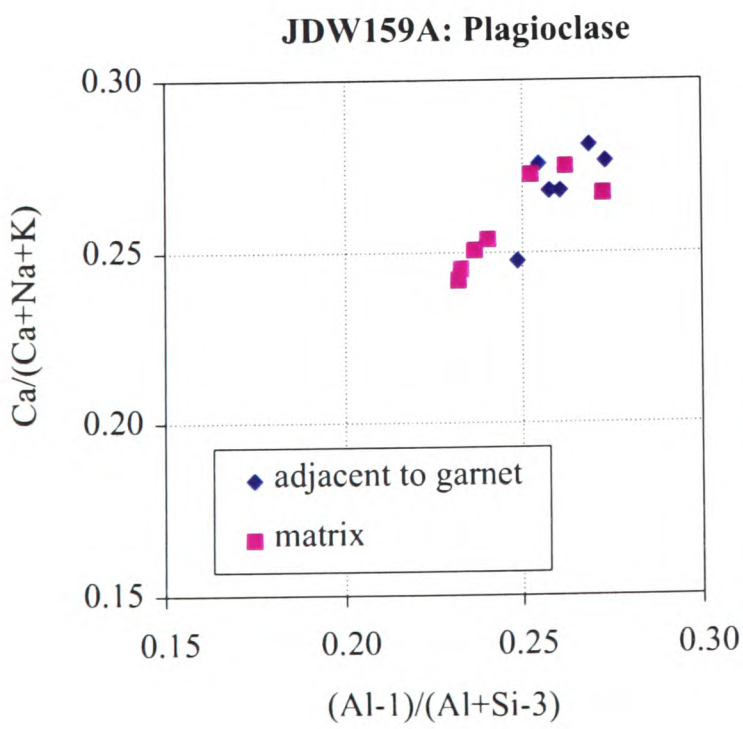
(b) Plot of the preferred THERMOCALC P-T results on a composite petrogenetic grid. Ellipses are shown at the $1<\sigma<2$ level and fit well with the observed phase relationships seen in thin section. These are interpreted to reflect near-peak conditions based on the garnet zoning profiles shown in Figure 6.18. The similarity of results suggests that these rocks may have experienced similar P-T histories. This is not unreasonable given that all of these samples were collected in close proximity to one another (see Figure 6.17). The prograde P-T path is impossible to accurately define, but is probably similar to the M1 metamorphism seen throughout the entire High Himalayan Slab. The retrograde P-T path is equally difficult to define, although the absence of sillimanite in any of the samples suggests that these rocks may have been exhumed close to the kyanite=sillimanite tie line. Solid and dashed black lines refer to reactions in the KFMASH and KMASH systems respectively. Reactions (1) to (3) taken from Spear (1993), reactions (4) and (5) taken from Harte (1975). Solid blue lines denote the Al-silicate phase diagram of Holdaway and Mukhopadhyay (1993). Red lines show the important vapour present and vapour absent melting reactions in metapelites. Reaction (6) taken from Thompson (1982), reaction (7) from Peto (1976) and reaction (8) from Le Breton and Thompson (1988).











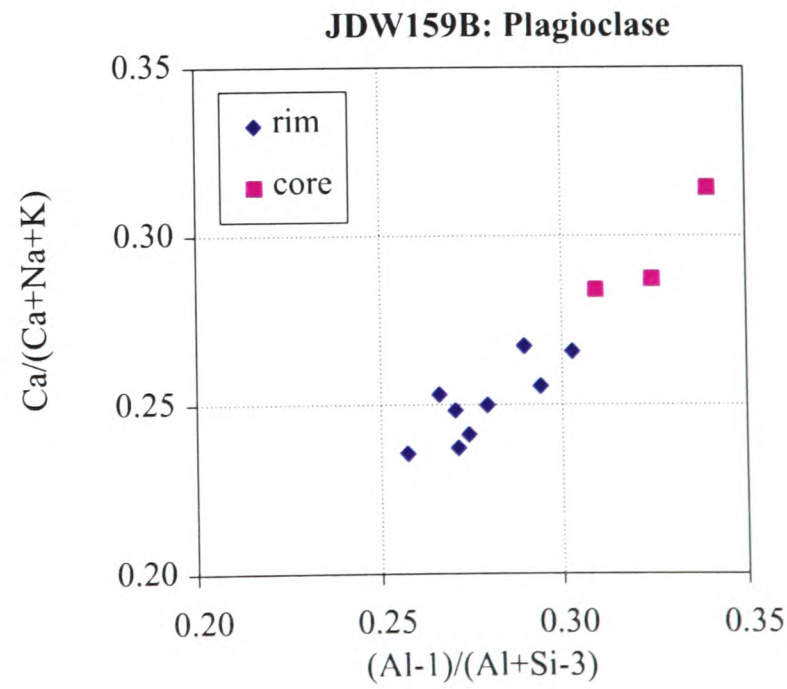


Figure 6.20: Plagioclase analyses of samples collected in the footwall of the Zanskar Shear Zone.

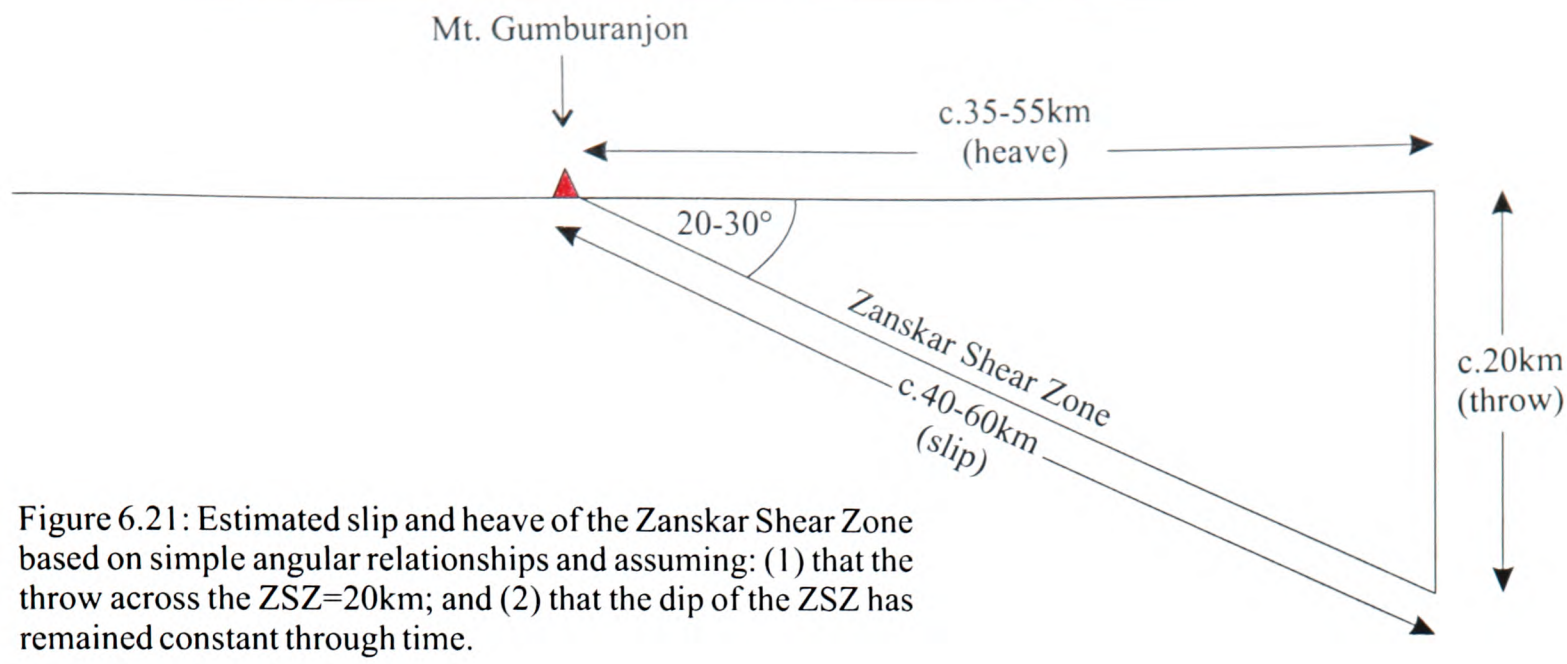


Figure 6.21: Estimated slip and heave of the Zanskar Shear Zone based on simple angular relationships and assuming: (1) that the throw across the ZSZ=20km; and (2) that the dip of the ZSZ has remained constant through time.

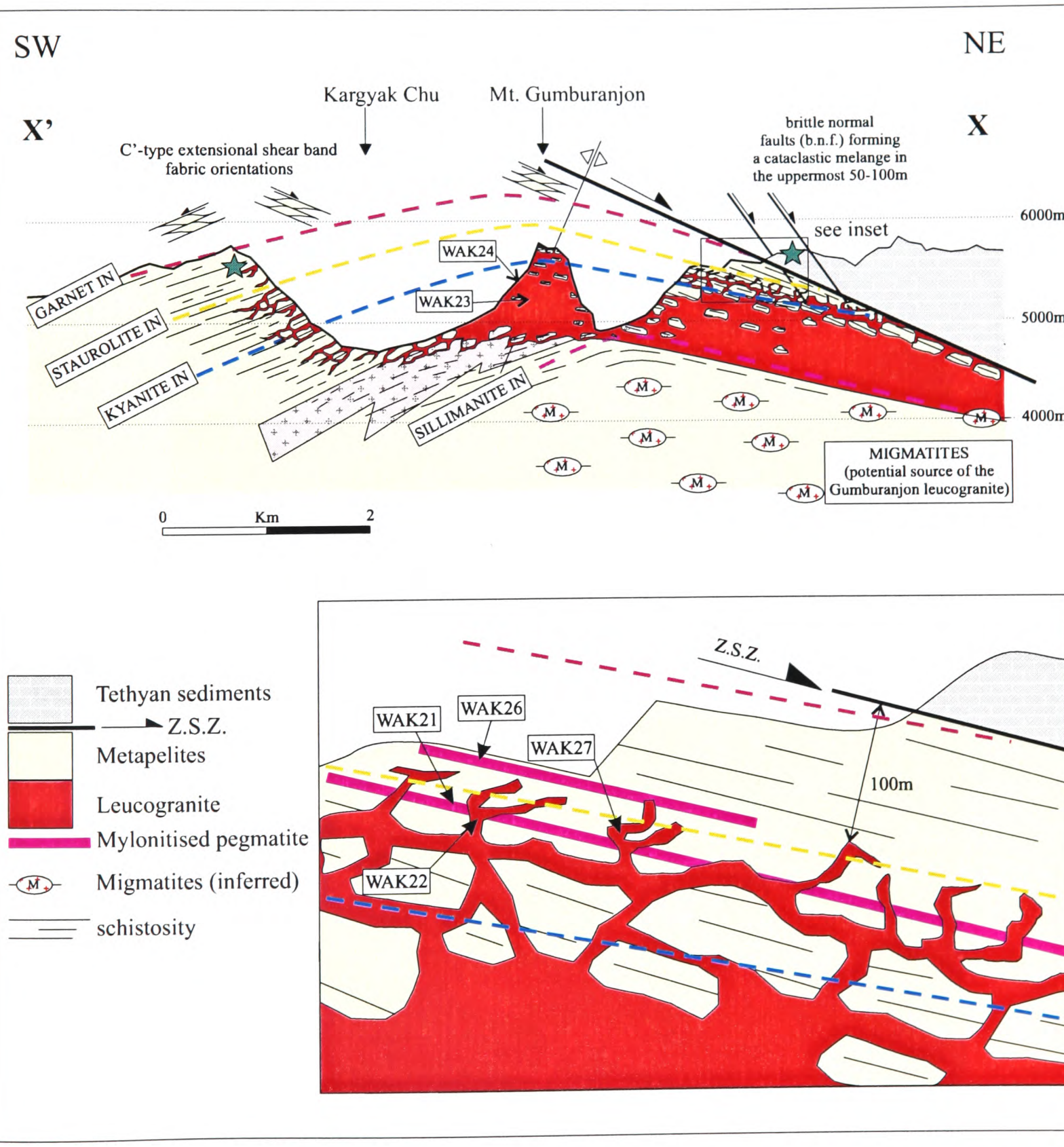


Figure 6.22: Schematic diagram showing the field relationships of the Gumburanjon leucogranite with the Zanskar Shear Zone. Note the cross-cutting relationships between the leucogranite dykes and the mylonitised pegmatite veins. Also not the absence of any leucogranite in the uppermost 100m of the shear zone. The relative positions of samples collected for geochemical and geochronological analysis are shown schematically. Field photographs of the above relationships are shown in Figures 6.23 and 6.24.

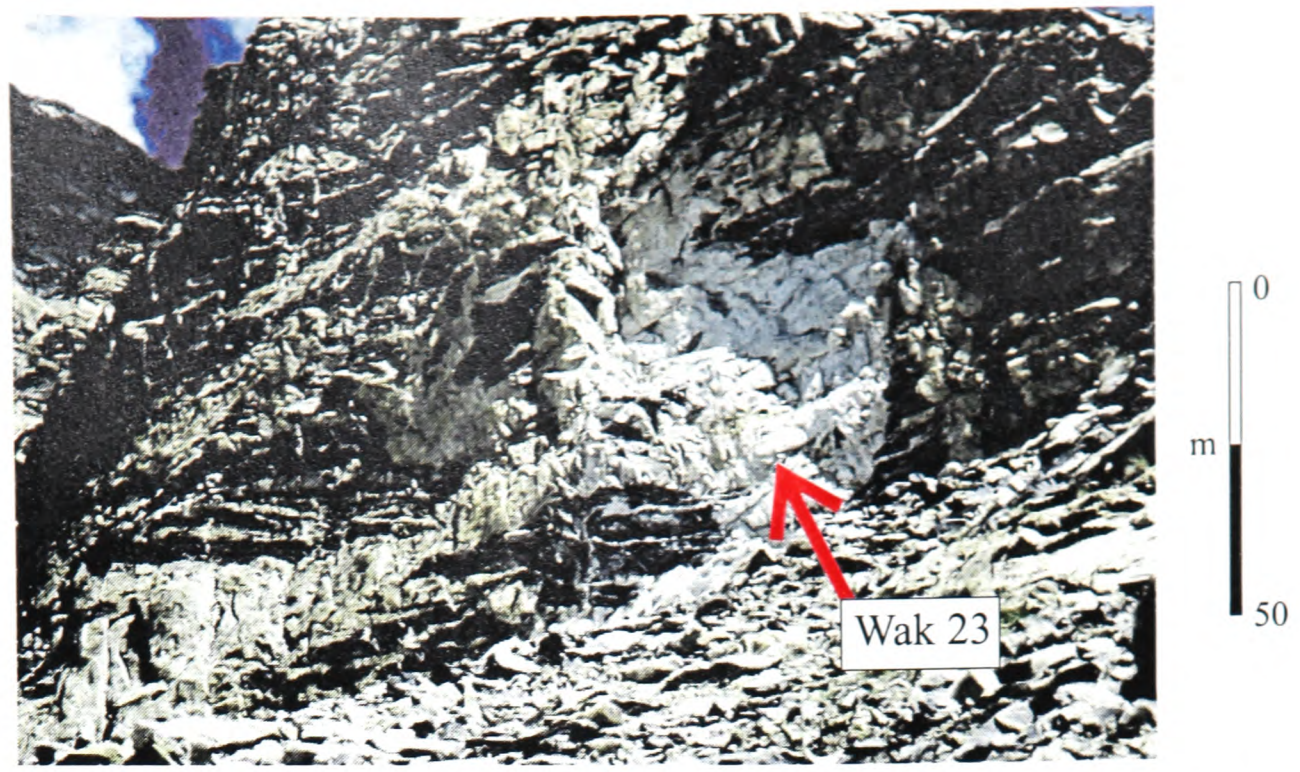


Figure 6.23a: Anastomosing network of weakly deformed s-parallel sills and undeformed discordant dykes at the margin of the Gumburanjon leucogranite. Blocks of biotite gneiss form layer-parallel xenolith-like bodies between the granite sheaves. Also shown is the location of sample Wak 23, collected for geochemical and geochronological analysis.

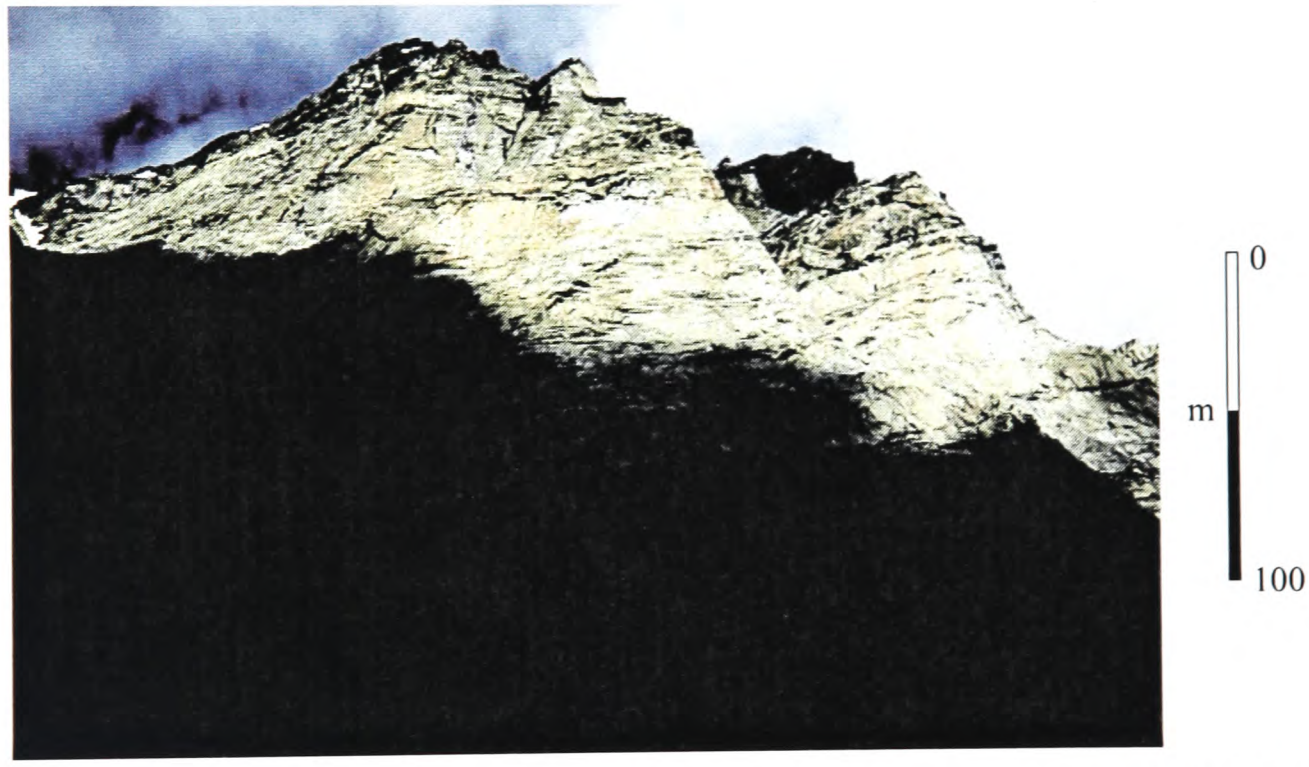


Figure 6.23b: S-parallel leucogranite sheaves enclosing blocks of biotite gneiss on the northern side of the Kargyak Chu, south of the main granite face.

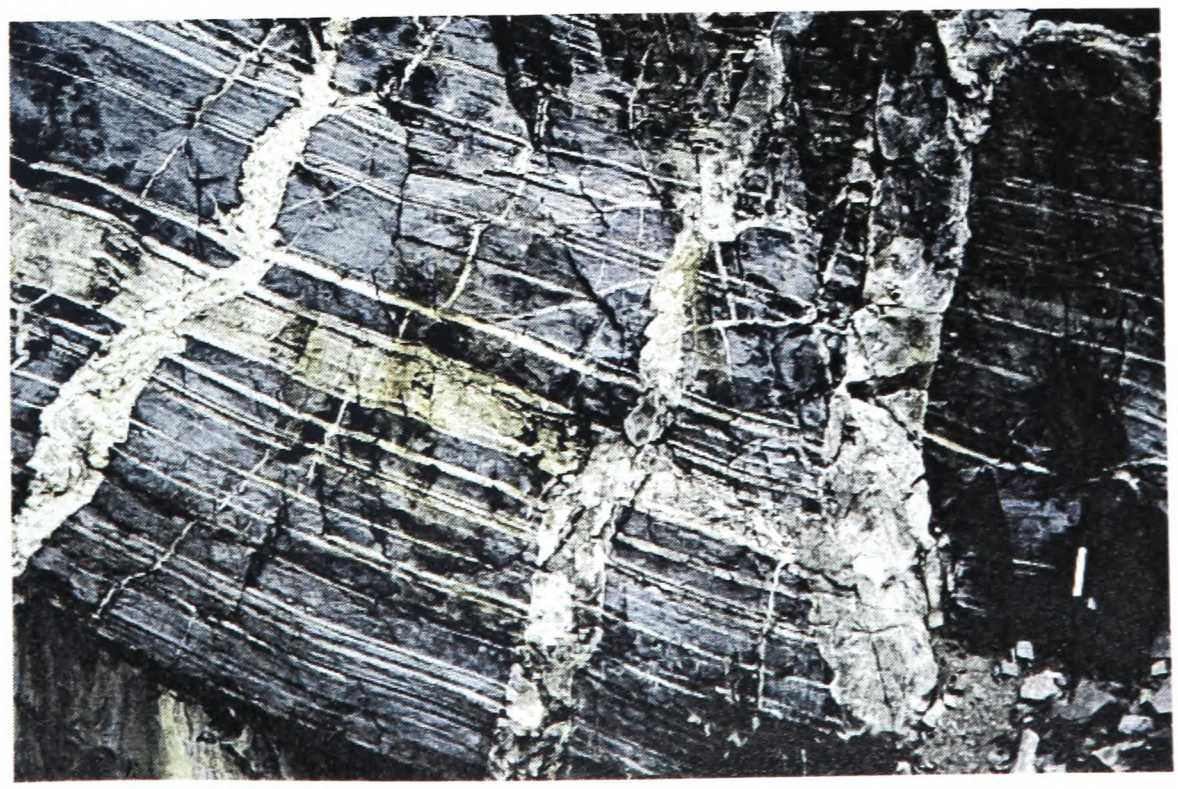


Figure 6.23c: Discordant aplite veins cross-cutting an intensely deformed sequence of banded orthogneisses, biotite gneisses and leucocratic pegmatites to the south-east of the Gumburanjon leucogranite. Rucksack in right of picture gives scale.

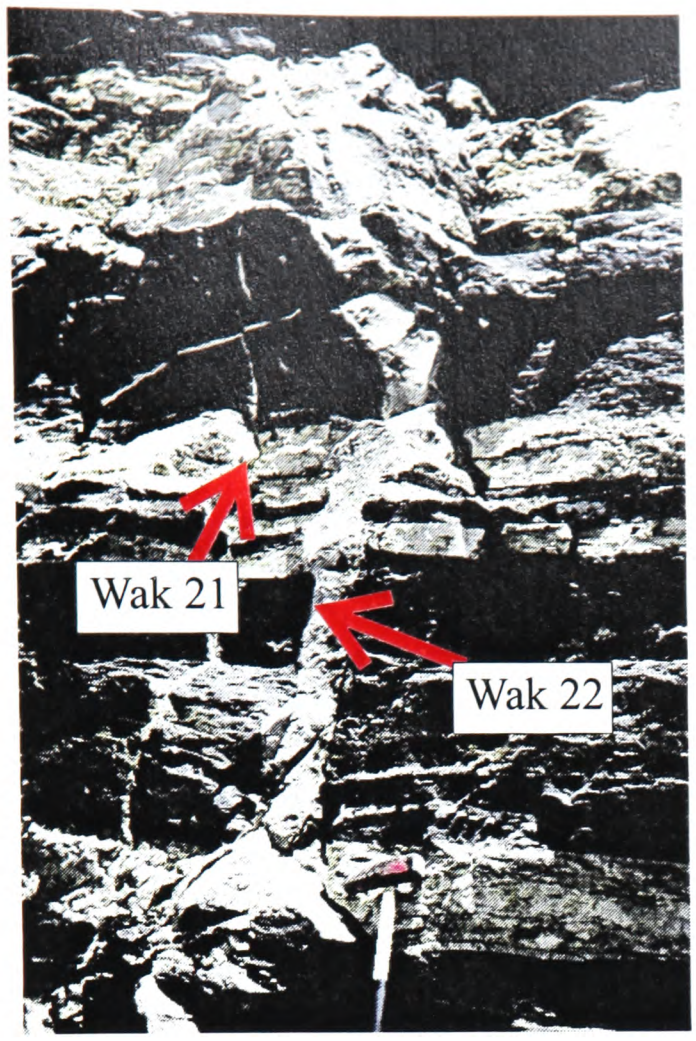


Figure 6.23d: Undeformed leucogranite dyke (Wak 22) cross-cutting an intensely deformed succession of biotite gneisses and leucocratic pegmatites (Wak 21), ~500m south-east of the main granite face.

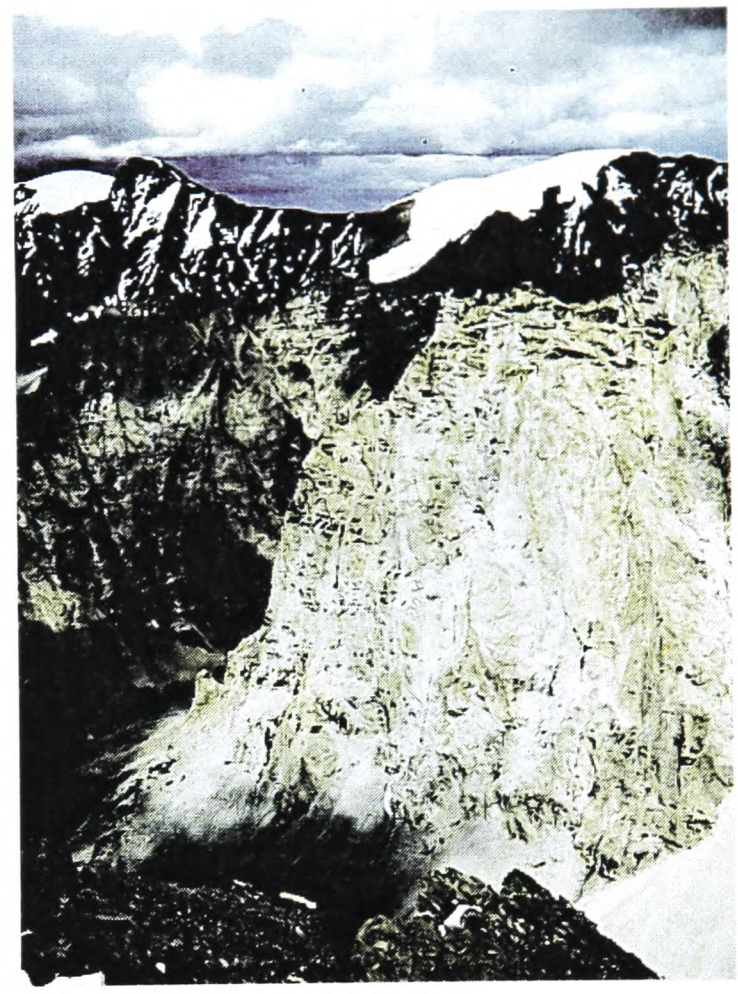


Figure 6.23e: Looking down at the main face of the Gumburanjon leucogranite from the c.5750m peak to the west of Mt. Gumburanjon (see Figure 6.6 for location). Note that the main face of Mt. Gumburanjon comprises 90-100% leucogranite, and enclsoses large blocks of biotite gneiss which remain parallel to the regional tectonic foliation.

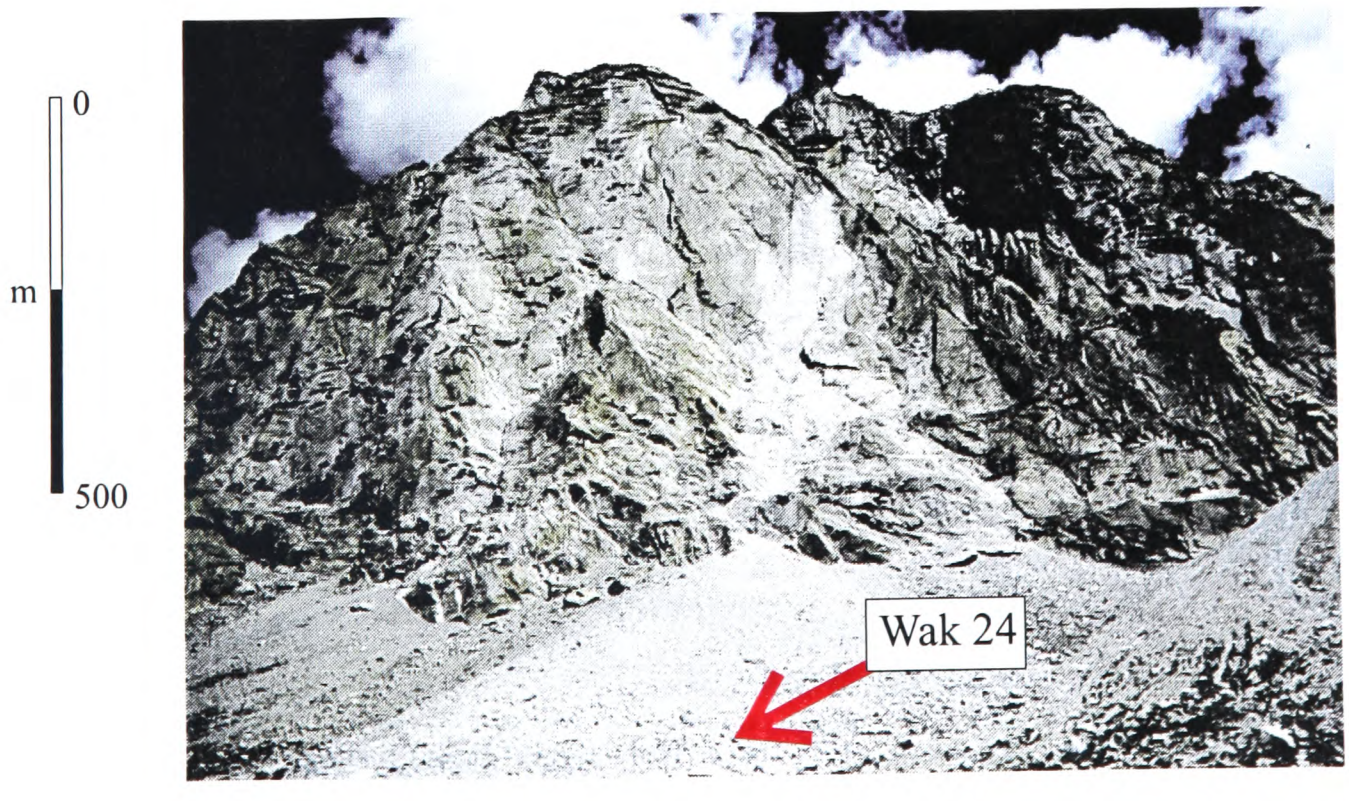


Figure 6.23f: Looking up at the main face of the Gumburanjon leucogranite. The white scar marks the site of a recent rockfall. Sample Wak 24 was collected from the fresh scree slopes at the base of this rockfall.

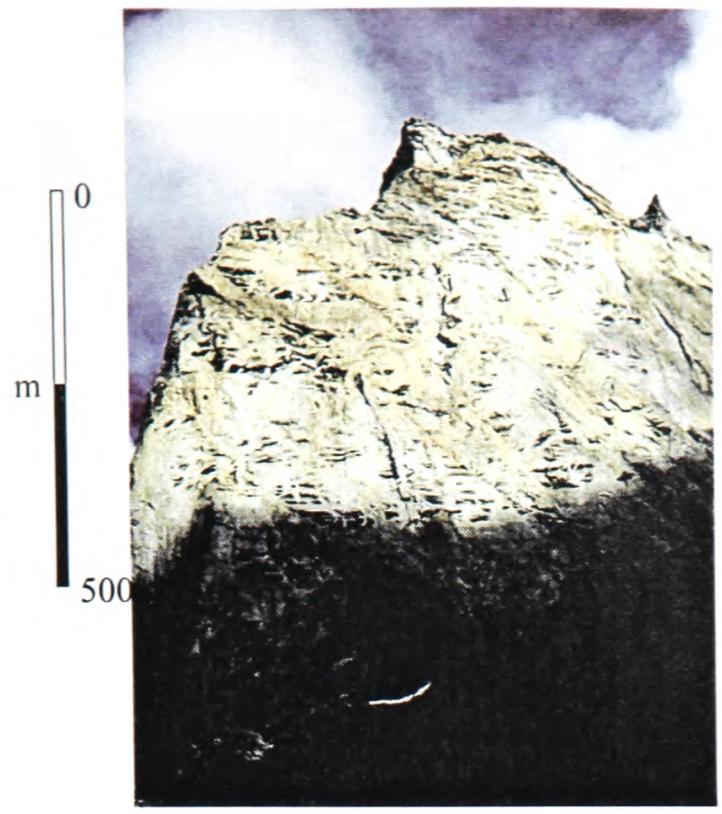


Figure 6.23g: Looking up at the main face of the Gumburanjon leucogranite. The s-parallel nature of the blocks of biotite gneiss enclosed within the granite is clearly visible.

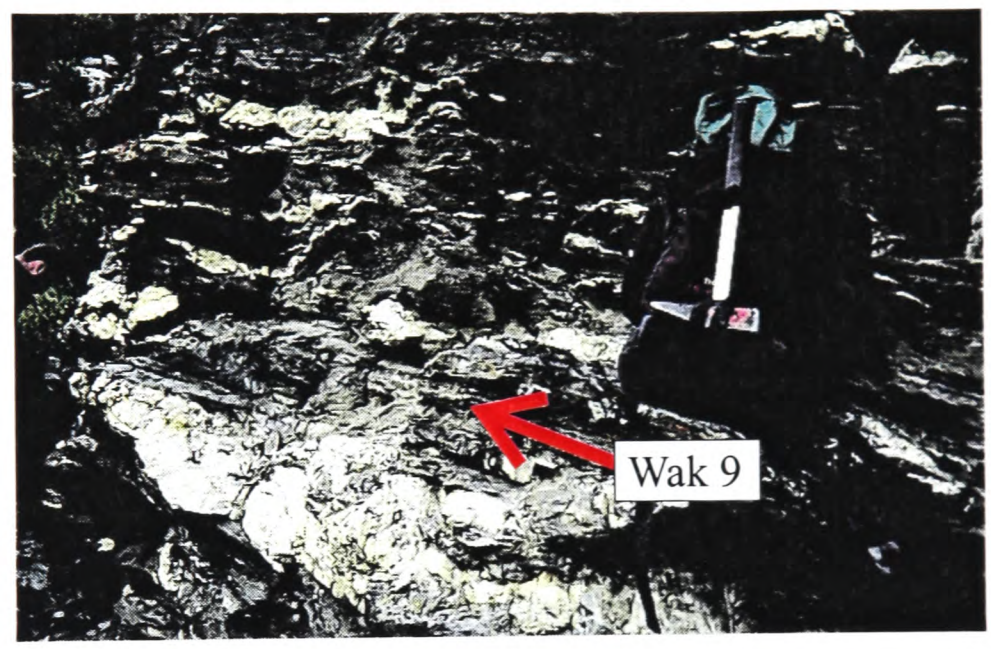


Figure 6.23h: Abundant quartz veining in the staurolite-grade metapelitic schists adjacent to the Gumburanjon leucogranite. These are interpreted to have crystallised from hydrothermal fluids associated with emplacement of the granite. Wak 9 (metapelitic schist) was collected from this locality for the purpose of geochronological analysis (see Chapter 7).

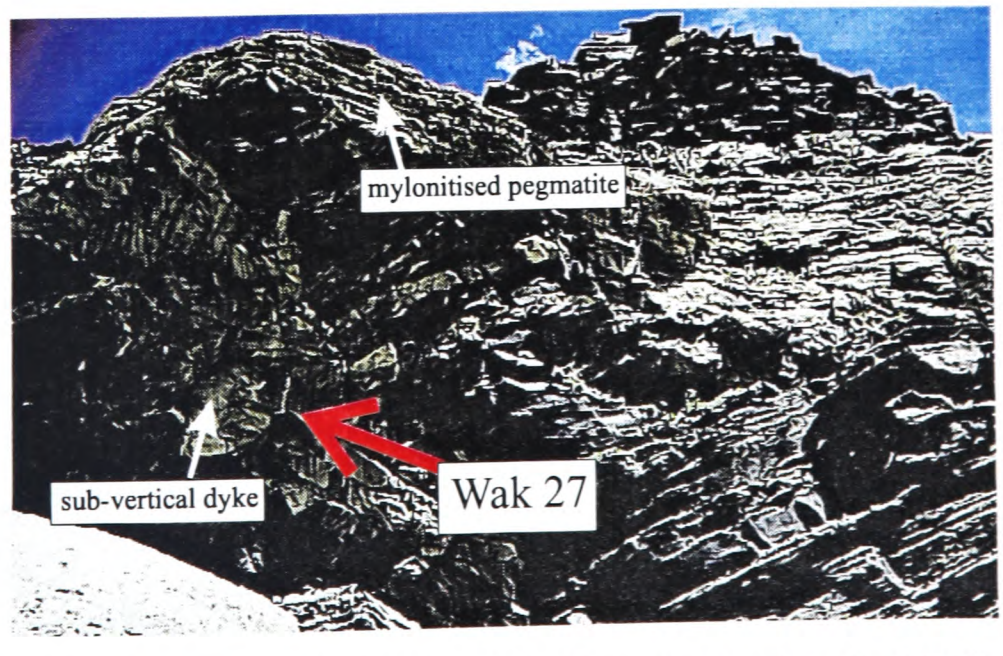


Figure 6.23i: 10m-wide discordant aplitic dyke (Wak 27) cross-scutting the NE-dipping fabric in the immediate footwall of the ZSZ. An intensely mylonitised leucocratic pegmatite is visible immediately above the dyke, and represents an along strike equivalent of the pegmatite from which sample Wak 26 was collected (see Figure 6.24b).



Figure 6.24a: Intensely deformed sequence of leucocratic pegmatites (Qtz + Pl + Kfs + Ms + Grt) and biotite gneisses (Qtz + Pl + Bt ± Grt) in the immediate footwall of the ZSZ. The pegmatites have been extensively boudinaged during extension. Compasss clinometer gives scale.



Figure 6.24b: Intensely deformed sequence of NE-dipping leucocratic pegmatites, biotite gneisses and metapelitic schists in the immediate footwall of the ZSZ. Location of sample Wak 26 is shown.

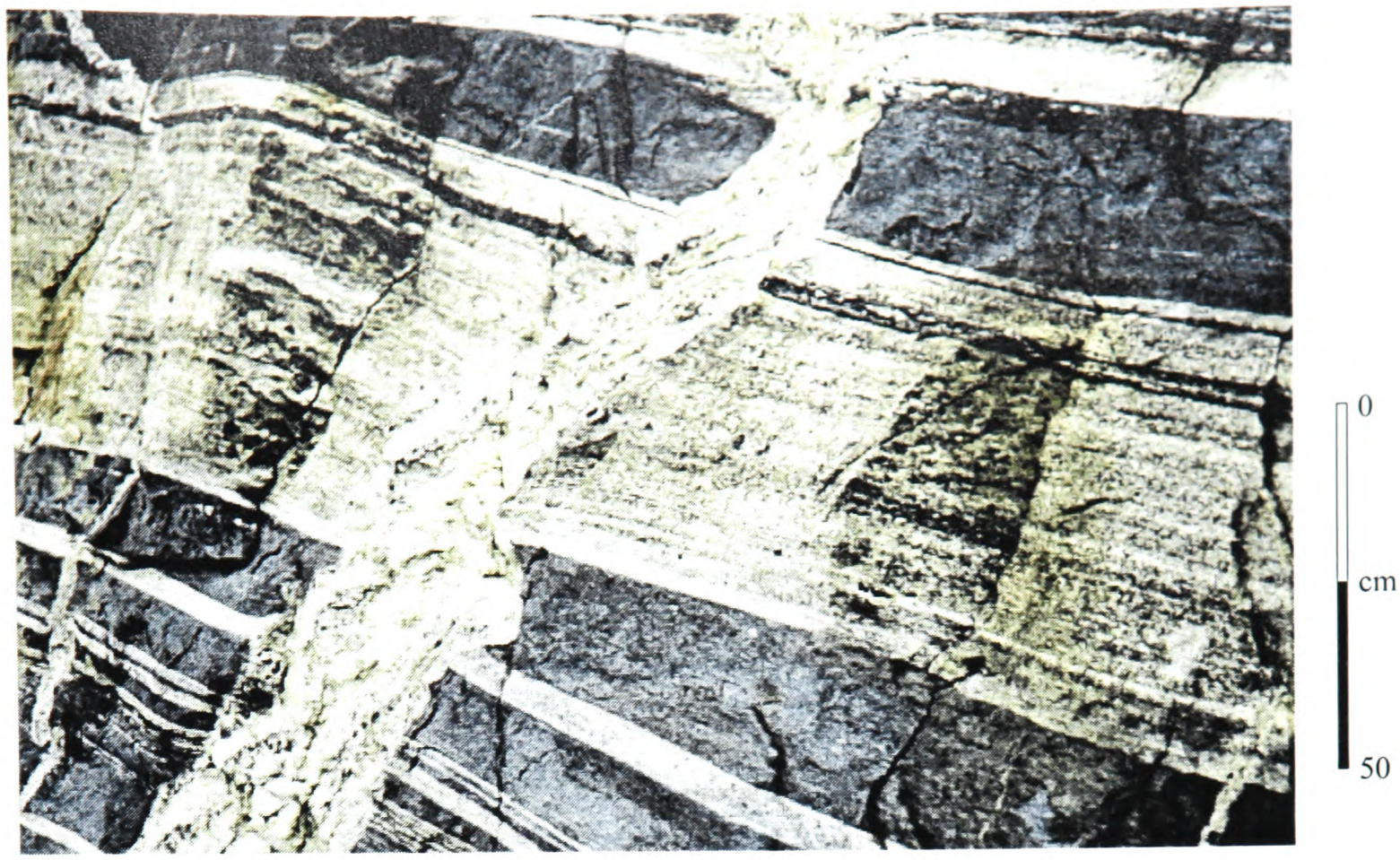


Figure 6.24c: Close-up of the relationship between the intensely deformed leucocratic pegmatites and the undeformed leucogranites in the footwall of the ZSZ. Note the intense fabric development in the pegmatite and their close association with the pale grey biotite gneisses.

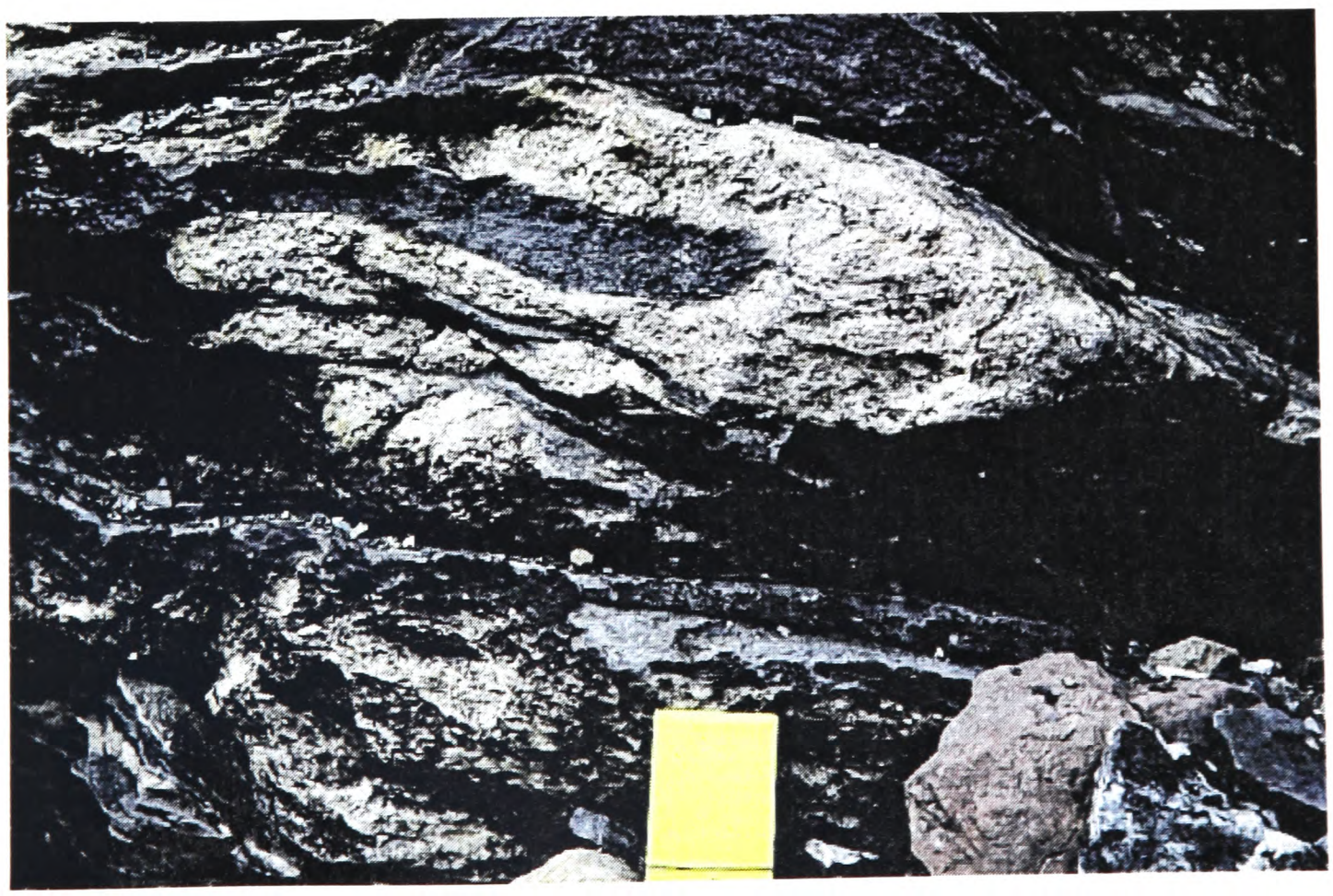


Figure 6.24d: Isoclinally folded leucocratic pegmatite in the footwall of the ZSZ. The fold is interpreted to be a pre-ZSZ compressional structure. Notebook in lower-middle of photo gives scale.

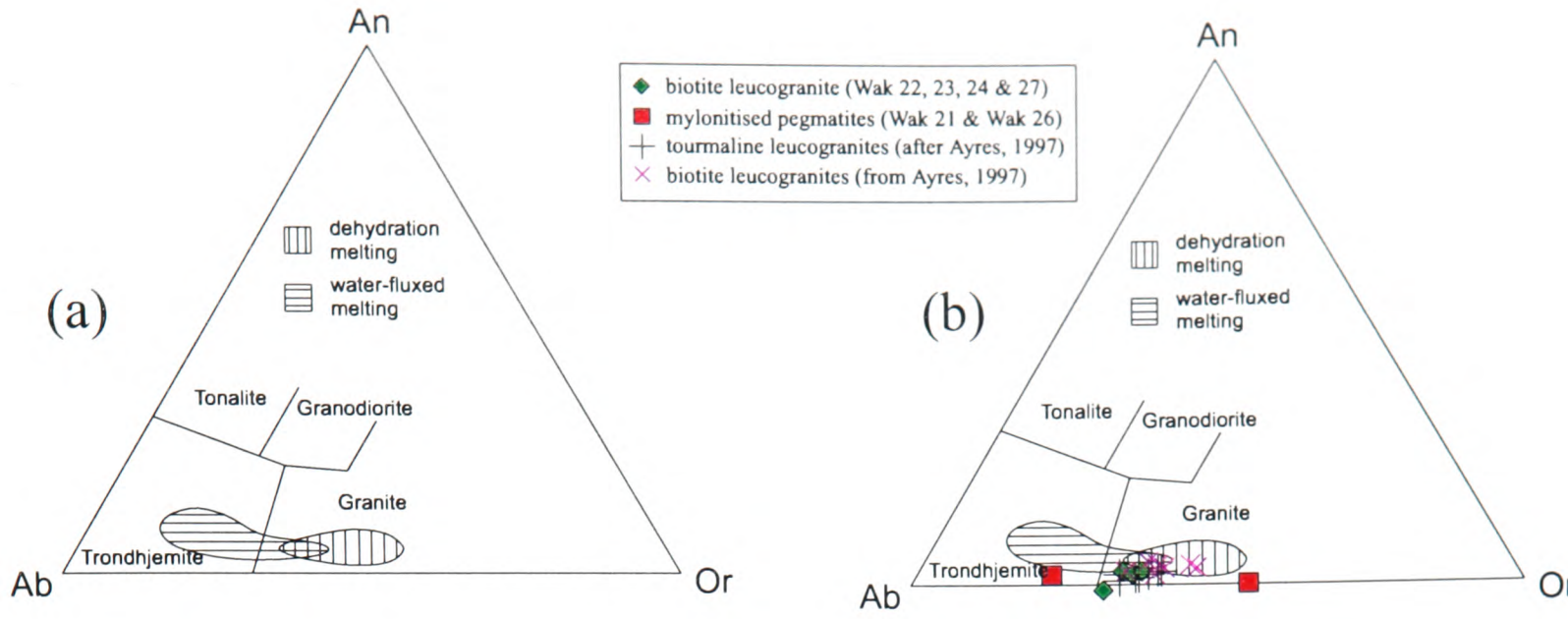


Figure 6.25:
(a) Compositional ranges of experimentally generated melts (patterned areas) in the An-Ab-Or system (after Patino Douce & Harris, 1998). Water-saturated melts are more trondhjemitic in composition owing to the fact that water-fluxed melting consumes a greater proportion of plagioclase in the source rock than does dehydration melting. This effect is less pronounced at lower pressures, resulting in a degree of overlap between the two fields.
(b) Plots of samples collected from the Gumburanjon leucogranite (including data from Ayres, 1997). Most of the data plot in the field of overlap and are therefore difficult to interpret. Nevertheless, the data appear to be more consistent with dehydration melting than water-saturated melting.

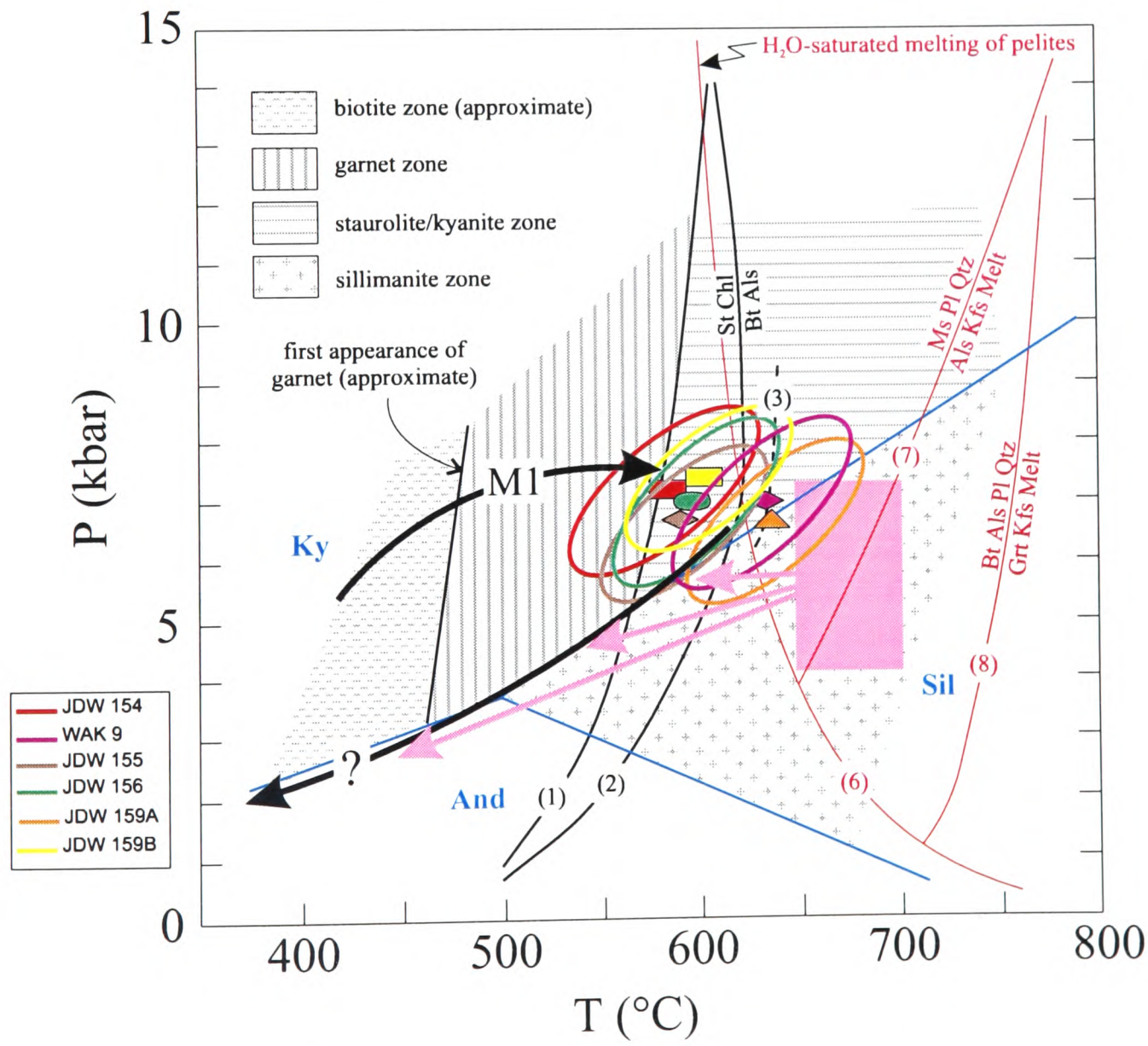


Figure 6.26: Generation and emplacement of the Gumburanjon leucogranite (annotation as for Figure 6.19b). Trace element modelling by Ayres (1997) suggests that melting occurred by dehydration of muscovite at temperatures of c.650-700°C. If correct, this constrains the maximum depth of melting at <c.7kbar (pink box). The depth of emplacement and the distance the granite has travelled from its source is more difficult to constrain. The granite could have been emplaced at any point in time on the retrograde P-T pathway (pink arrows). The absence of any thermal aureole associated with the Gumburanjon leucogranite, however, suggests that the country rocks were still at reasonably high temperatures at the time of emplacement. Geochemical data presented by Ayres (1997) suggests that the granite crystallised at pressures of c.1-4kbar. P-T estiamtes on migmatitic leucosomes in central Zanskar suggest crystallisation occurred at c.4-7kbar (D. Waters, pers. com.)

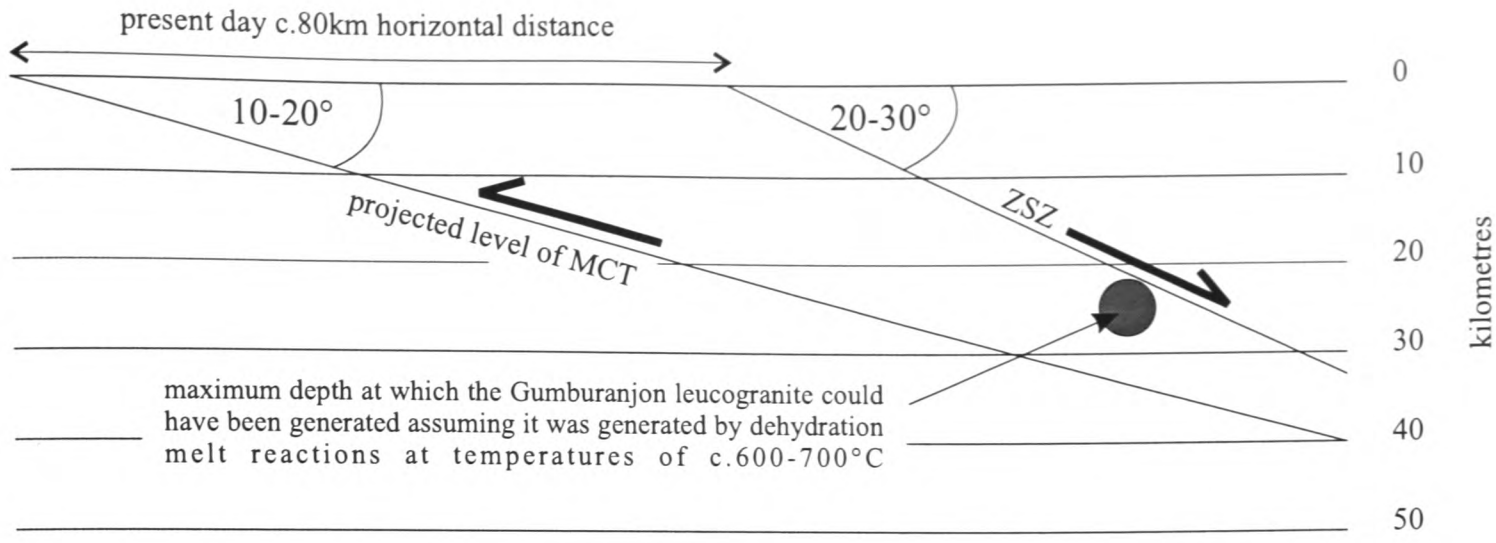
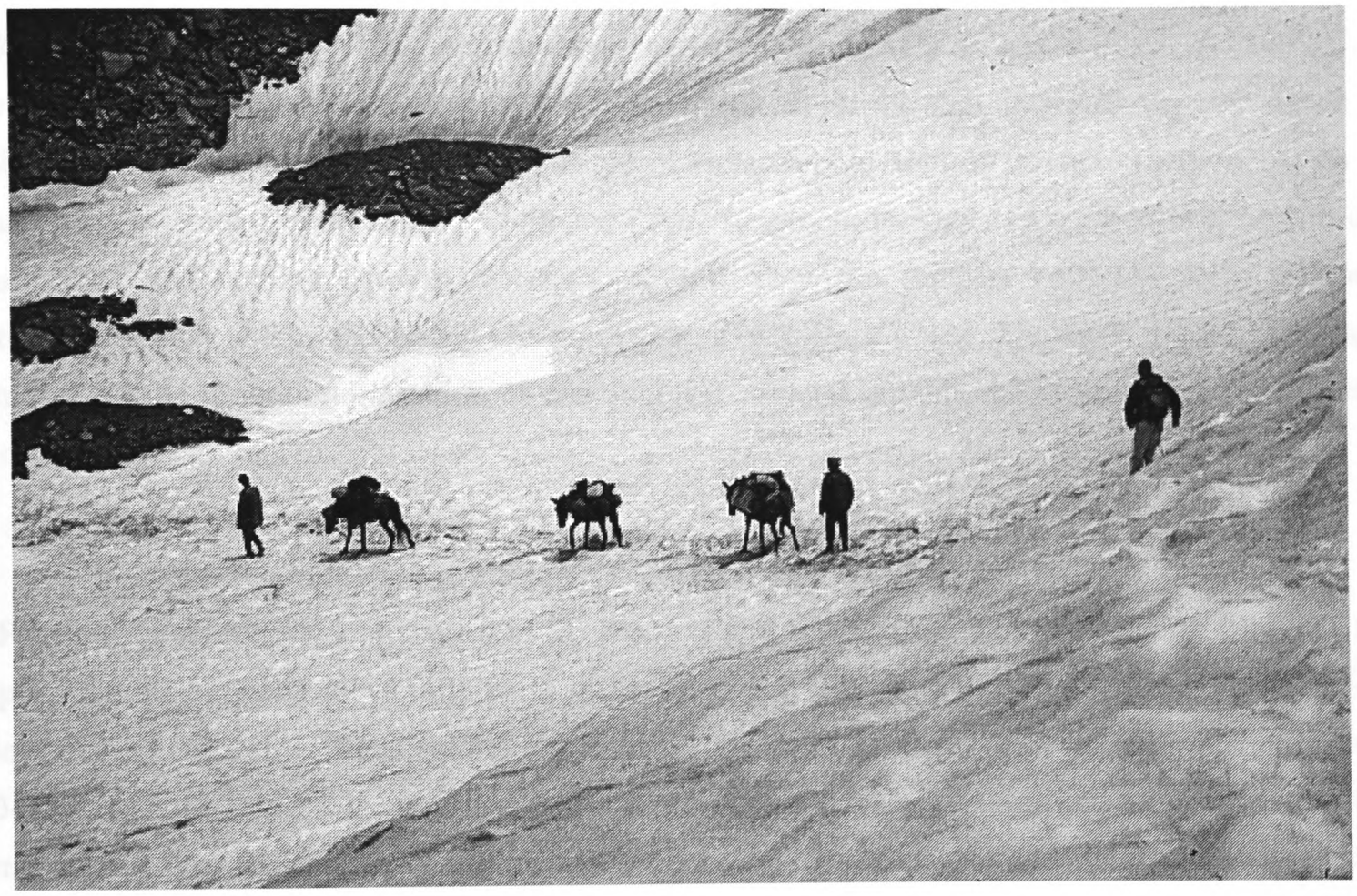


Figure 6.27: Diagram showing the relationship between the MCT, ZSZ and the maximum depth at which the Gumburanjon leucogranite could have been generated. If the above relationships are correct, it suggests that decompression, rather than shear-heating along the MCT was the mechanism by which the granite was generated.



Crossing a snowfield at 5000m altitude on the northern side of the Shingo La.

Chapter 7

U-Pb and $^{40}Ar/^{39}Ar$ geochronology

7.1 Introduction

Lithological and structural mapping, combined with quantitative thermobarometric constraints, provide an insight into the structural and metamorphic evolution of the High Himalayan Slab in SE Zanskar and NW Lahaul. This structural and metamorphic history is summarised in Figure 7.1. Since the style of deformation is extremely heterogeneous across the slab, it is virtually impossible to correlate different deformation phases and stages of metamorphic mineral growth from one region to another using textural criteria alone. U-Pb and $^{40}Ar/^{39}Ar$ geochronology can be used to constrain the crystallisation and cooling ages of metamorphic and magmatic samples collected from different structural positions within the slab. In particular, it was hoped that this work would place age constraints on the timing and duration of metamorphic mineral growth and its temporal relationship with crustal melting.

7.2 Previous geochronological studies in SE Zanskar and NW Lahaul

Previous geochronological studies in SE Zanskar and NW Lahaul have focused on the large K-feldspar granites exposed in various parts of the slab and have relied almost entirely upon Rb-Sr whole-rock techniques. These studies consistently yielded Precambrian-Ordovician ages between *c.*450-600 Ma (see Table 3.1). Although the reliability of these ages is questionable owing to the extreme mobility of Rb and Sr during metamorphism, Lower Palaeozoic ages of 472 +9/-6 Ma and ~460 Ma have been obtained from granitic samples collected within the HHC using U-Pb techniques by Pognante *et al.* (1990) and Noble and Searle (1995) respectively. These ages are consistent with the Rb-Sr data and support a Precambrian-Ordovician age for the megacrystic granites.

Relatively few studies have attempted to constrain the age of Tertiary metamorphism and magmatism in the High Himalayan Slab of SE Zanskar and NW Lahaul. The majority of these are based on Rb-Sr and $^{40}Ar/^{39}Ar$ cooling ages of metamorphic and magmatic muscovite and biotite in different parts of the slab (see Figure 7.2). At the top of the slab, Ferrara *et al.* (1987 & 1991) obtained muscovite and biotite Rb-Sr cooling ages from the Gumburanjon leucogranite of 20.7 ± 0.3 Ma and ~18 Ma respectively (Figure 7.2). Villa and Oddone (1988) obtained $^{40}Ar/^{39}Ar$ muscovite cooling ages of ~19 Ma from the same samples. These ages obey the traditional age sequence of t(Ms, Rb-Sr) > t(Ms, $^{40}Ar/^{39}Ar$) > t(Bt, Rb-Sr) and suggest a cooling rate of ~100°C/my (Ferrara *et al.*, 1991). None of these cooling ages accurately constrain the emplacement age of the granite, but suggest it to be around 21 Ma, similar to the U-Pb ages of the High Himalayan leucogranites in

western and central Zanskar (Noble & Searle, 1995). Further towards the south-east, Spring and Crespo-Blanc obtained similar early Miocene K-Ar cooling ages of 22.8 ± 0.5 Ma and 20.5 ± 0.4 Ma from muscovite and biotite separates extracted from a granitic dyke in the footwall of the Sarchu Shear Zone at the top of the slab (Figure 7.2).

At the base of the slab, Frank *et al.* (1977) suggested that rocks within the Crystalline Nappe in the area between Manali and Khoksar had cooled below the muscovite blocking temperature for diffusive loss of Sr by 29 ± 4 Ma, whilst biotites cooled considerably later at ~16 Ma (Figure 7.2). Mehta (1977) obtained similar muscovite and biotite cooling ages for rocks in the same region (Figure 7.2), although the method used by Mehta to calculate these ages is somewhat questionable (it takes the Rb/Sr data from the mineral separates (muscovite and biotite) and combines it with the initial $^{87}Sr/^{86}Sr$ ratio of the whole rock to establish a two point isochron). Frank *et al.'s.* Rb-Sr cooling ages are interpreted by Epard *et al.* (1995) to suggest that peak-metamorphism in the Crystalline Nappe occurred prior to *c.*32 Ma. However, although the closure temperature for diffusive loss of Sr in muscovite is generally thought to be ~500°C (Wagner *et al.*, 1977), recent studies show that it may be as high as 600-650°C (Villa, 1998), in which case these may represent near-peak ages.

Frank *et al.* (1977) obtained biotite Rb-Sr cooling ages of 21 ± 1 Ma for rocks collected within the MCT zone, which are older than the 16 Ma ages recorded from the internal parts of the slab (Figure 7.2). These authors interpret this to suggest that thrusting along the MCT in NW Lahaul occurred between *c.*16-21 Ma, which is similar to the interpreted age of thrusting along the MCT in western Zanskar between 17-23 Ma (Stephenson, 1997).

7.3 Sample choice and location

Metamorphic samples

1-2-kg-sized samples of staurolite- and kyanite-grade metapelitic schist were collected from positions believed to be representative of the upper (Wak 9), middle (Wak 6) and lower (Wak 3) parts of the High Himalayan Slab in SE Zanskar and NW Lahaul (Figure 7.2). Wak 9 was collected from the top of the slab in the immediate footwall of the ZSZ and is intruded by the Gumburanjon leucogranite (see Figure 6.17). Wak 6 was collected from within the Rhotang Gneissic Complex near the village of Khoksar (see Figure 4.12b). Wak 3 was collected in the lower part of the slab near Manali. It is important to note, however, that this sample was collected approximately 5 km structurally above the projected level of the MCT and does not, therefore, represent the base of the slab *sensu stricto*.

Petrographic observations demonstrate that the mineral assemblages in each of these samples grew during a regional Barrovian-type metamorphism which developed in response to crustal shortening and thickening of the Indian plate following the India-Asia collision (Figure 7.1). U-Pb dating of metamorphic monazite from these samples should, therefore, help place age constraints on the timing and duration of metamorphism across the slab.

Magmatic samples

The Gumburanjon leucogranite represents a typical High Himalayan leucogranite which was generated and emplaced in the immediate footwall of the ZSZ following the growth of Barrovian metamorphic assemblages in the surrounding country rocks (see Chapter 6). Three 1-2-kg sized samples of undeformed leucogranite (Wak 23, Wak 24 and Wak 27) were collected for geochronological analysis in an attempt to constrain the crystallisation and cooling age of this pluton. The location of these samples relative to one another is shown schematically in Figure 6.22. Field photographs of these samples are shown in Figures 6.23a (Wak 23), 6.23f (Wak 24) and 6.23i (Wak 27).

The Gumburanjon leucogranite cross-cuts a number of intensely deformed leucocratic pegmatites which are clearly older than the granite itself. In an attempt to establish the age difference between the Gumburanjon leucogranite and the pegmatites, two samples of mylonitised pegmatite (Wak 21 and Wak 26) were collected for geochronological analysis. The location of these samples is shown schematically in Figure 6.22. Field photographs of these samples are shown in Figures 6.23d (Wak 21) and 6.24b (Wak 26).

7.4 U-Pb geochronology

Standard crushing and heavy-liquid separation techniques were used to extract heavy mineral separates from all of the samples collected for geochronological analysis. Single-grain analysis of monazite, xenotime and uraninite collected from these samples was performed using isotope dilution thermal ionisation mass spectrometric (IDTIMS) techniques similar to those reported by Hawkins and Bowring (1997) at the Massachusetts Institute of Technology, Boston, U.S.A. (a brief description of this technique is given in Appendix E). No zircon geochronology was attempted owing to reports of widespread inheritance in metamorphic and magmatic rocks within the High Himalayan Slab (e.g. Copeland *et al.*, 1988; Parrish & Tirrul, 1989; Noble & Searle, 1995).

7.4.1 U-Pb systematics of monazite, xenotime and uraninite

Monazite is a light rare earth element phosphate [$(LREE)PO_4$] that occurs in a wide variety of rock types, but preferentially grows in low Ca-bearing metapelitic schists and peraluminous granites (Overstreet, 1967). Xenotime is a heavy rare earth element phosphate [$(HREE)PO_4$] that essentially forms a solid solution series with YPO_4 (Franz *et al.*, 1996). Monazite shows increasing solid solution with xenotime with increasing temperature (Heinrich *et al.*, 1997). Uraninite (UO_2) also commonly occurs with monazite and xenotime in magmatic rocks.

Monazite abundance tends to increase with increasing metamorphic grade (Overstreet, 1967), which has led to suggestions that its growth is favoured at conditions in excess of ~500°C (Smith & Barreiro, 1990; Kingsbury *et al.*, 1993; Harrison *et al.*, 1997a). The metamorphic reactions involved in growing monazite, however, remain poorly understood. Detrital and authigenic monazite are believed to be metastable at low-metamorphic grades (Sawka *et al.*, 1986; Smith & Barreiro, 1990) and tend to form distinct crystal morphologies which are markedly different from those formed during

metamorphic or magmatic growth (Parrish, 1990; Franz *et al.*, 1996). Monazite inheritance has been reported in a number of geochronological studies (e.g. Copeland *et al.*, 1988; Parrish, 1990), which raises questions pertaining to the closure temperature of this mineral system. Parrish (1990) estimates this temperature to be *c.*725 ± 25°C, suggesting that Pb-loss in metamorphic monazite is likely to be insignificant (Zhu *et al.*, 1997).

A common feature of many magmatic monazite analyses is that they plot above the concordia (reverse discordance), owing to an excess of ^{206}Pb in the sample. Schärer (1984) attributed this to disequilibrium incorporation of ^{230}Th into the monazite lattice during crystallisation. Since ^{230}Th decays to ^{206}Pb with a half-life of 75, 400yrs, an excess of ^{206}Pb is generated which is unsupported by ^{238}U. Magmatic monazite analyses which are concordant, or plot below concordia should be treated with extreme caution and do not necessarily reflect the crystallisation age of the sample, especially where there is evidence of inheritance (e.g. Copeland *et al.*, 1988). Xenotime and uraninite, however, have low Th contents and preferentially exclude ^{230}Th in equilibrium amounts during crystallisation. Xenotime and uraninite therefore show an apparent ^{206}Pb deficiency and tend to plot slightly below concordia. Excess, or deficiency of ^{206}Pb in magmatic monazite, xenotime and uraninite creates problems when interpreting $^{206}Pb/^{238}U$ ages. For these reasons, the $^{207}Pb/^{235}U$ age is generally considered to be the most meaningful. The $^{207}Pb/^{206}Pb$ ages are unreliable owing to the problems associated with common lead corrections for very young samples. ^{206}Pb excess in monazite can give samples a 'futuristic', or negative $^{207}Pb/^{206}Pb$ age (Schärer, 1984; Parrish, 1990).

The steep slope of the concordia line for ages younger than 50 Ma makes interpretation of young U-Pb data extremely difficult, since it is virtually impossible to distinguish between grains which have experienced substantial Pb-loss and those which have not. The reason for this is that grains which were originally concordant, or nearly so, at the time of crystallisation are unlikely to move any significant distance away from the concordia as a result of diffusional Pb-loss.

7.4.2 Metamorphic age constraints (results and interpretation)

Between four and six single grains of metamorphic monazite were analysed from each sample of metamorphic schist (Wak 3, Wak 6 and Wak 9), the results of which are shown in Table 7.1a and in Figures 7.3a-c. Owing to the choice of method used (i.e. crushing of whole-rock samples), it remains uncertain whether the analysed monazite from each sample was located within porhyroblastic phases such as garnet and kyanite, or whether it formed part of the matrix assemblage. Brief petrographic descriptions of each sample, together with morphological descriptions of monazite and the geological significance and interpretation of the results are discussed individually for each of these samples in the following sub-sections.

7.4.2.1 Wak 3 (kyanite-bearing metapelite, Manali)

Wak 3 has an equilibrium metamorphic assemblage of Qtz + Pl + Ms + Bt + Grt + Ky. Accessory monazite, zircon, rutile, ilmenite, apatite, pyrite and tourmaline were also identified in this sample. Wak 3 was collected immediately adjacent to sample JDW 92, which records a near-peak

Table 7.1a: U-Pb data of metamorphic samples Wak 3, Wak 6 and Wak 9.

Sample Fraction	Weight (µg)	Concentrations U (ppm)	Pb (ppm)	206 Pb / 204 Pb	208 Pb*† / 206 Pb	206 Pb¥ / 238 U	% err	Errors 2-sigma (%) 207 Pb¥ / 235 U	% err	207 Pb¥ / 206 Pb	% err	Age(Ma) 206 Pb / 238 U	207 Pb / 235 U	207 Pb / 206 Pb	Corr. coef.	Pb§ (pg)
Wak 3																
M1; t, oi, sa	6.0	2172	125	819	3.157	0.01555	(0.17)	0.11628	(0.34)	0.05424	(0.29)	**99.5**	**111.7**	**381.2**	0.55	15.9
M2; t, oi, sa	1.0	1818	66	178	2.165	0.01179	(0.82)	0.08899	(2.21)	0.05474	(1.93)	**75.6**	**86.6**	**401.4**	0.51	12.1
M3; cl, if, rd, fl	2.0	4094	50	441	1.732	0.00497	(0.53)	0.03187	(0.77)	0.04653	(0.54)	**31.9**	**31.9**	**25.2**	0.72	7.4
M4; t, oi, sa	2.0	9849	142	757	1.371	0.00674	(0.27)	0.04650	(0.39)	0.05006	(0.27)	**43.3**	**46.2**	**197.7**	0.72	8.6
Wak 6																
M1; y, t, oi, sr, fl	4.0	3166	925	1095	5.064	0.05459	(0.16)	0.42477	(0.25)	0.05643	(0.19)	**342.7**	**359.5**	**469.3**	0.67	37.3
M2: y, t, oi, sr, fl	5.0	3824	1527	1082	7.406	0.05405	(1.01)	0.42500	(1.10)	0.05703	(0.44)	**339.4**	**359.6**	**492.5**	0.92	62.2
M3: y, t, oi, sr, fl	6.0	3382	1077	5825	5.332	0.05749	(0.10)	0.44601	(0.17)	0.05627	(0.14)	**360.3**	**374.5**	**463.0**	0.58	12.3
M4: y, t, oi, sr, fl	8.0	2014	1342	3544	11.785	0.05976	(0.12)	0.46617	(0.17)	0.05658	(0.12)	**374.2**	**388.5**	**475.0**	0.71	17.0
M5: cl, if, rd, fl	2.0	2156	374	757	5.618	0.02980	(0.28)	0.22504	(0.62)	0.05478	(0.52)	**189.3**	**206.1**	**403.2**	0.54	8.3
Wak 9																
M1; y, if, rb	11.0	4824	81	699	3.027	0.00466	(0.15)	0.03002	(0.27)	0.04669	(0.22)	**30.0**	**30.0**	**33.4**	0.59	23.5
M2: y, if, rb	8.0	7317	141	606	3.526	0.00474	(0.14)	0.03064	(0.31)	0.04690	(0.27)	**30.5**	**30.6**	**43.9**	0.51	31.3
M3: y, if, rb	20.0	1941	32	392	2.895	0.00464	(0.17)	0.02989	(0.46)	0.04671	(0.41)	**29.8**	**29.9**	**34.6**	0.46	30.2
M4; y, t, oi, rb,	14.0	2162	42	108	3.035	0.00460	(0.23)	0.03089	(1.95)	0.04868	(1.84)	**29.6**	**30.9**	**132.3**	0.52	97.5
M5: y, t, oi, rb	16.0	2518	44	452	3.236	0.00457	(0.20)	0.02944	(0.57)	0.04675	(0.52)	**29.4**	**29.5**	**36.5**	0.45	26.8
M6; y, t, oi, rb	9.0	968	17	170	2.993	0.00449	(0.61)	0.02831	(2.20)	0.04571	(2.00)	**28.9**	**28.3**	**-17.5**	0.44	16.9

Note: All analyses represent single grains. m = monazite, u = uraninite, x = xenotime.

g=green, y=yellow, cl=clear, t=turbid; oi=opaque inclusions; if=inclusion-free; an=angular, sa=sub-angular, rd=rounded, sr=sub-rounded, rh=rhombahedral, fl=flat

Sample weights are estimated by using a video monitor and are known to within 40%.

* Radiogenic Pb. † Measured ratio corrected for spike and fractionation only.

¥ Corrected for fractionation, spike, blank, and initial common Pb.

Mass fractionation correction of 0.15%/amu ± 0.04%/amu (atomic mass unit) was applied to single-collector Daly analyses and 0.12%/amu ± 0.04% for dynamic Faraday-Daly analyses.

§ Total common-Pb in analyses.

Total procedural blank for Pb ranged from 0.65 to 3.7 pg and < 1.0 pg for U.

Blank isotopic composition: 206Pb/204Pb = 19.10 ± 0.1, 207Pb/204Pb =15.71 ± 0.1, 208Pb/204Pb = 38.65 ± 0.1.

Corr. coef. = correlation coefficient.

Age calculations are based on the decay constants of Steiger and Jäger (1977).

Common-Pb corrections were calculated by using the model of Stacey and Kramers (1975) and the interpreted age of the sample.

Table 7.1b: U-Pb data of samples of undeformed leucogranite collected from the Gumburanjon leucogranite

Sample Fraction	Weight (µg)	Concentrations U (ppm)	Pb (ppm)	206 Pb / 204 Pb	208 Pb*† / 206 Pb	206 Pb¥ / 238 U	% err	Errors 2-sigma (%) 207 Pb¥ / 235 U	% err	207 Pb¥ / 206 Pb	% err	Age(Ma) 206 Pb / 238 U	207 Pb / 235 U	207 Pb / 206 Pb	Corr. coef.	Pb§ (pg)
WAK-23																
M1; y, t, oi, sr	3.0	8779	836	7017	1.480	0.04332	(0.69)	0.33453	(0.71)	0.05600	(0.18)	**273.4**	**293.0**	**452.5**	0.97	10.1
M2; y, t, oi, sr	5.0	2751	32	262	2.345	0.00374	(0.48)	0.02401	(1.05)	0.04657	(0.89)	**24.1**	**24.1**	**27.4**	0.54	13.8
M3; y, t, oi, sr	6.0	2417	19	153	1.112	0.00343	(0.48)	0.02172	(0.73)	0.04590	(0.53)	**22.1**	**21.8**	**-7.4**	0.69	23.4
M4; y, t, oi, sr	5.0	3323	75	331	1.308	0.01022	(0.17)	0.07479	(0.37)	0.05308	(0.31)	**65.5**	**73.2**	**332.3**	0.55	32.6
M5; y, t, oi, sr	10.0	3488	21	404	0.838	0.00341	(0.23)	0.02140	(0.55)	0.04550	(0.48)	**21.9**	**21.5**	**-28.7**	0.51	18.9
U1	15.1	257978	769	6157	0.003	0.00326	(0.36)	0.02106	(0.36)	0.04679	(0.06)	**21.0**	**21.2**	**38.4**	0.99	132.3
U2	15.8	201431	603	13315	0.003	0.00330	(0.13)	0.02133	(0.14)	0.04685	(0.04)	**21.3**	**21.4**	**41.6**	0.95	50.5
U3	18.6	53397	160	8296	0.004	0.00329	(0.21)	0.02130	(0.25)	0.04692	(0.13)	**21.2**	**21.4**	**45.2**	0.86	25.2
U4	22.5	62428	190	3271	0.003	0.00330	(0.09)	0.02131	(0.11)	0.04683	(0.05)	**21.2**	**21.4**	**40.7**	0.88	91.0
WAK-24																
M1; y, t, oi, sa	11.0	10042	116	56	0.915	0.00342	(0.31)	0.02211	(1.63)	0.04688	(1.52)	**22.0**	**22.2**	**43.3**	0.43	639.8
M2; y, t, oi, sa	12.0	16022	114	198	0.865	0.00357	(0.15)	0.02137	(0.53)	0.04346	(0.50)	**23.0**	**21.5**	**-141.2**	0.38	250.9
M3; y, t, oi, sa	8.0	1490	34	371	2.644	0.00682	(0.33)	0.04826	(0.70)	0.05129	(0.58)	**43.8**	**47.9**	**253.8**	0.55	14.2
M4; y, t, oi, sa	4.0	31073	152	589	0.527	0.00336	(0.24)	0.02106	(0.46)	0.04554	(0.37)	**21.6**	**21.2**	**-26.9**	0.59	52.2
U1	95.0	215963	658	2267	0.004	0.00327	(0.19)	0.02113	(0.20)	0.04682	(0.06)	**21.1**	**21.2**	**40.1**	0.95	190.8
U2	96.7	136371	465	500	0.015	0.00326	(0.23)	0.02118	(0.27)	0.04714	(0.12)	**21.0**	**21.3**	**56.2**	0.88	5700.9
X1	13.0	1930	6	587	0.026	0.00331	(0.34)	0.02134	(1.08)	0.04677	(0.97)	**21.3**	**21.4**	**37.2**	0.45	9.4
WAK-27																
M1; y, t, oi, sa	5.0	7492	116	286	2.158	0.00518	(0.26)	0.03473	(0.53)	0.04863	(0.44)	**33.3**	**34.7**	**130.3**	0.57	46.6
M2; y, t, oi, sa	4.0	7829	87	190	2.150	0.00357	(0.40)	0.02177	(1.41)	0.04418	(1.29)	**23.0**	**21.9**	**-100.5**	0.42	45.8
M3; y, t, oi, sa	4.0	7331	65	436	1.622	0.00363	(0.25)	0.02205	(0.67)	0.04407	(0.59)	**23.4**	**22.1**	**-106.8**	0.48	17.1
M4; y, t, oi, sa	4.0	3251	39	334	2.651	0.00360	(0.57)	0.02206	(1.12)	0.04440	(0.92)	**23.2**	**22.2**	**-88.3**	0.58	9.1
U1	2.8	166304	521	8971	0.005	0.00345	(0.10)	0.02225	(0.12)	0.04682	(0.07)	**22.2**	**22.3**	**40.1**	0.83	11.6
U2	2.8	179953	567	2291	0.006	0.00338	(0.14)	0.02185	(0.17)	0.04685	(0.10)	**21.8**	**22.0**	**41.4**	0.81	47.9

Note: All analyses represent single grains. m = monazite, u = uraninite, x = xenotime.

g=green, y=yellow, cl=clear, t=turbid; oi=opaque inclusions; if=inclusion-free; an=angular, sa=sub-angular, rd=rounded, sr=sub-rounded, rh=rhombahedral, fl=flat

Sample weights are estimated by using a video monitor and are known to within 40%.

* Radiogenic Pb. † Measured ratio corrected for spike and fractionation only.

¥ Corrected for fractionation, spike, blank, and initial common Pb.

Mass fractionation correction of 0.15%/amu ± 0.04%/amu (atomic mass unit) was applied to single-collector Daly analyses and 0.12%/amu ± 0.04% for dynamic Faraday-Daly analyses.

§ Total common-Pb in analyses.

Total procedural blank for Pb ranged from 0.65 to 3.7 pg and < 1.0 pg for U.

Blank isotopic composition: 206Pb/204Pb = 19.10 ± 0.1, 207Pb/204Pb =15.71 ± 0.1, 208Pb/204Pb = 38.65 ± 0.1.

Corr. coef. = correlation coefficient.

Age calculations are based on the decay constants of Steiger and Jäger (1977).

Common-Pb corrections were calculated by using the model of Stacey and Kramers (1975) and the interpreted age of the sample.

Table 7.1c: U-Pb data of samples of mylonitised leucocratic pegmatites collected from the ZSZ

		Concentrations						Errors 2-sigma (%)				Age(Ma)				
Sample	Weight	U	Pb	206 Pb	208 Pb*†	206 Pb¥		207 Pb¥		207 Pb¥		206 Pb	207 Pb	207 Pb	Corr.	Pb§
Fraction	(µg)	(ppm)	(ppm)	204 Pb	206 Pb	238 U	% err	235 U	% err	206 Pb	% err	238 U	235 U	206 Pb	coef.	(pg)
WAK-21																
M1; y, t, oi, sr	6.0	25580	618	899	0.783	0.01461	(0.20)	0.10323	(0.25)	0.05125	(0.15)	**93.5**	**99.8**	**251.9**	0.81	149.1
M2; g, t, oi, sa	1.0	53535	6461	2330	0.910	0.06999	(0.22)	0.54315	(0.26)	0.05629	(0.13)	**436.1**	**440.5**	**463.7**	0.86	124.2
U1	96.7	327121	14709	231525	0.007	0.04627	(4.24)	0.35750	(4.24)	0.05604	(0.04)	**291.6**	**310.3**	**453.9**	0.99	242.4
U2	120.7	157350	6654	245309	0.008	0.04916	(3.69)	0.38069	(3.69)	0.05616	(0.04)	**309.4**	**327.5**	**458.9**	0.99	404.9
U3	216.3	183658	6266	204581	0.007	0.03737	(1.63)	0.28522	(1.63)	0.05535	(0.04)	**236.5**	**254.8**	**426.6**	0.99	459.4
WAK-26																
M1; y, t, oi, an	2.0	79848	1008	967	1.536	0.00550	(0.18)	0.03546	(0.29)	0.04679	(0.22)	**35.3**	**35.4**	**38.5**	0.65	70.9
M2; g, t, oi, an	7.0	140761	1115	3561	0.496	0.00589	(0.10)	0.03680	(0.11)	0.04533	(0.05)	**37.8**	**36.7**	**-38.0**	0.88	103.8
M3; g, t, oi, an	20.0	55235	733	497	1.360	0.00600	(0.41)	0.03698	(0.53)	0.04469	(0.31)	**38.6**	**36.9**	**-72.5**	0.81	873.2
M4; y, t, oi, an	165.0	31139	194	1839	0.480	0.00461	(1.80)	0.02923	(1.81)	0.04596	(0.13)	**29.7**	**29.3**	**-4.5**	0.99	831.1
M5; g, t, oi, an	9.0	33130	255	6421	0.462	0.00588	(0.08)	0.03685	(0.10)	0.04543	(0.05)	**37.8**	**36.7**	**-32.5**	0.84	17.9
M6; g, t, oi, an	7.0	14154	189	539	1.612	0.00553	(0.09)	0.03588	(0.30)	0.04705	(0.28)	**35.6**	**35.8**	**51.5**	0.40	64.4
U1	15.1	206752	5838	26723	0.013	0.03072	(0.27)	0.22721	(0.27)	0.05364	(0.04)	**195.1**	**207.9**	**355.8**	0.99	229.3
U2	17.8	118514	3610	25606	0.013	0.03311	(0.23)	0.24771	(0.24)	0.05426	(0.05)	**210.0**	**224.7**	**381.7**	0.98	174.3

Note: All analyses represent single grains. m = monazite, u = uraninite, x = xenotime.

g=green, y=yellow, cl=clear, t=turbid; oi=opaque inclusions; if=inclusion-free; an=angular, sa=sub-angular, rd=rounded, sr=sub-rounded, rh=rhombahedral, fl=flat

Sample weights are estimated by using a video monitor and are known to within 40%.

* Radiogenic Pb. † Measured ratio corrected for spike and fractionation only.

¥ Corrected for fractionation, spike, blank, and initial common Pb.

Mass fractionation correction of 0.15%/amu ± 0.04%/amu (atomic mass unit) was applied to single-collector Daly analyses and 0.12%/amu ± 0.04% for dynamic Faraday-Daly analyses.

§ Total common-Pb in analyses.

Total procedural blank for Pb ranged from 0.65 to 3.7 pg and < 1.0 pg for U.

Blank isotopic composition: 206Pb/204Pb = 19.10 ± 0.1, 207Pb/204Pb =15.71 ± 0.1, 208Pb/204Pb = 38.65 ± 0.1.

Corr. coef. = correlation coefficient.

Age calculations are based on the decay constants of Steiger and Jäger (1977).

Common-Pb corrections were calculated by using the model of Stacey and Kramers (1975) and the interpreted age of the sample.

P-T estimate of 635 ± 33°C and ~7.9 ± 1.2 kbar (see Table 4.3). Monazite from Wak 3 was recovered in the magnetic fraction at 17°/0.6A. Two populations of monazite were identified on the basis of petrographic observations. Population 1 have a rounded, plate-like morphology and are generally colourless, translucent grains which are free of opaque inclusions; they typically range in size from 30-70 μm, although their smallest dimension (thickness) is ubiquitously <20μm. Population 2 are slightly larger in size (50-70 μm), are more sub-angular in shape and have a cloudy appearance containing numerous opaque inclusions of an unknown mineralogy. Petrographic observations did not reveal the presence of any growth zoning in either monazite population.

Results and interpretation

Monazite grains M1, M2 and M4 (all belonging to population 2) plot below concordia and are older than the age of the India-Asia collision (Figure 7.3a). These are therefore interpreted to be pre-Himalayan monazites and are unrelated to Tertiary metamorphism of the High Himalayan Slab. A crude linear regression through all of the grains (including M3) yields an upper intercept of 498 ± 84 Ma and a lower intercept of 31 ± 4.9 Ma (MSWD = 17). Although this regression has no statistical significance, it suggests that Wak 3 contains a generation of Palaeozoic monazite that could either be detrital in origin, or could have grown during an early metamorphic event. Given the probable Precambrian-Cambrian age of the Haimantas (see Chapter 3 for discussion), it seems unlikely that these grains are detrital in origin and therefore implies that the Haimantas preserve evidence for a Lower Palaeozoic metamorphic event (see section 7.4.4).

Monazite grain M3 (the only analysed grain from population 1) is more-or-less concordant at ~32 Ma. The significance of this age is uncertain and can be interpreted in a number of ways. One possibility is that it represents significant Pb-loss at ≤32 Ma from an older grain. This seems unlikely given the high blocking temperature of monazite (*c.*725 ± 25°C) and its propensity to retain chemical zoning profiles even after experiencing granulate-grade conditions (Zhu *et al.*, 1997). P-T estimates from samples adjacent to Wak 3 (i.e. JDW 92) demonstrate that maximum temperatures attained in this part of the slab did not exceed 635 ± 35°C (Table 4.3). A more reasonable interpretation is that it reflects metamorphic monazite growth at ~32 Ma, which is undoubtedly related to crustal shortening and thickening during the D_1 and D_2 deformation phases in the Crystalline Nappe (Figure 7.1). Whether this is a near-peak, or prograde age is uncertain. Given the protracted nature of Barrovian-type metamorphic events, it seems likely that it reflects an average of multiple phases of monazite growth.

7.4.2.2 Wak 6 (kyanite-bearing metapelite, Khoksar)

Wak 6 has a metamorphic assemblage similar to that of Wak 3, with the exception that it does not contain garnet and is, therefore, unsuitable for thermobarometric analysis. P-T constraints from adjacent samples, however, are indicative of near-peak conditions of ~584 ± 32°C and ~6.9 ±1.1 kbar (sample JDW 29, Table 4.2). Monazite from Wak 6 was recovered in the magnetic fraction at 17°/0.55A. Two populations of monazite were identified on the basis of petrographic observations.

Population 1 have a rounded, plate-like morphology with a colourless, translucent appearance and are free of opaque inclusions; they typically range in size from 30-70 μm, although their smallest dimension (thickness) is ubiquitously <20μm. Population 2 are slightly larger in size (50-70 μm), are more sub-rounded in shape and have a cloudy-yellow appearance containing numerous opaque inclusions of an unknown mineralogy. No zoning was detected petrographically.

Results and interpretation

None of the monazite analyses from Wak 6 reveal any evidence pertaining to Tertiary thermal events in the High Himalayan Slab of SE Zanskar and NW Lahaul. Monazite from both populations 1 and 2 are interpreted to be old grains that plot well below concordia on a crude mixing line which has an upper intercept of 489 ± 30 Ma and a lower intercept of 59 ± 65 Ma (MSWD = 19), (Figure 7.3b). Forcing the lower intercept through 33 ± 3 Ma (based on the ~32 Ma age from Wak 3) gives an upper intercept of 479 ± 16 Ma (MSWD = 29). Both regressions have no statistical significance, but are consistent with the interpretation that the Haimantas contain a component of Lower Palaeozoic monazite, which have subsequently experienced partial Pb-loss and/or neoblastic overgrowth during a younger thermal event.

7.4.2.3 Wak 9 (staurolite-bearing metapelite, Mt. Gunburanjon)

Wak 9 has a metamorphic assemblage of Qtz + Pl + Ms + Bt + Grt + St with accessory monazite, xenotime, zircon, tourmaline, rutile, ilmenite, apatite and pyrite. P-T constraints from Wak 9 and adjacent samples reveal near-peak-conditions of *c.* 607 ± 35°C and 6.9 ± 1.1 kbar (see Table 6.2), similar to those recorded from the lower part of the slab (Wak 3). Although no preferred spatial distribution of radiogenic accessory phases could be identified in thin section, several hand-picked grains of monazite were observed partly overgrowing flakes of biotite, suggesting that monazite growth was syn/post-metamorphic. Whether this biotite grew during prograde metamorphism, or whether it was associated with post-peak recrystallisation could not be resolved petrographically.

Owing to the abundance of staurolite and garnet in this sample, a more rigorous magnetic technique was used: monazite and xenotime were eventually collected from the non-magnetic fraction at 17°/0.36A. Monazites in sample Wak 9 are considerably larger than those in either Wak 3 or Wak 6, varying in size from 50-150μm, with the smallest dimension (thickness) ranging from 20-50μm, depending on crystal shape. Two populations of monazite were recognised petrographically. Population 1 form rounded, slightly flattened rhombohedral grains that are a translucent yellow colour and contain no visible inclusions. Population 2 are slightly larger and form elongate, subhedral to euhedral rhombs which are also translucent yellow in colour and contain numerous opaque inclusions of an uncertain mineralogy. Microprobe analysis of a number of grains from population 2 revealed them to be rich in YPO_4 (xenotime). However, despite analysis of several grains suspected to be xenotime, the $^{208}Pb/^{206}Pb$ ratio of these grains suggests that they are probably monazite (Table 7.1a).

Results and interpretation

None of the grains from Wak 9 show any evidence of inheritance; all of them reveal extremely similar $^{207}Pb/^{235}U$ and $^{206}Pb/^{238}U$ ages of ~29-31 Ma (Table 7.1a). Several lines of evidence suggest that these ages record the growth of metamorphic monazite during Barrovian metamorphism in the upper part of the slab at this time: (1) the grains are quite large (50-150μm), and are therefore unlikely to have experienced any significant diffusional Pb-loss; and (2) some of the monazites contain biotite inclusions, suggesting that monazite growth was syn/post-metamorphic. The fact that the majority of grains plot below concordia (Figure 7.3c), may reflect partial Pb-loss from slightly older grains.

7.4.3 Magmatic age constraints (results and interpretation)

Numerous grains of magmatic monazite, xenotime and uraninite were analysed from three samples of undeformed leucogranite (Wak 23, Wak 24 and Wak 27) and two samples of mylonitised pegmatite (Wak 21 and Wak 26), the results of which are shown in Tables 7.1b & c and in Figures 7.4 & 7.5. Morphological descriptions of monazite, xenotime and uraninite and the geological significance and interpretation of the results are discussed individually for each of these samples in the following sub-sections.

7.4.3.1 Wak 23 (undeformed leucogranite, Mt. Gumburanjon)

Wak 23 represents an undeformed sample of leucogranite which was collected from an anastomosing network of dykes and sills near the margin of the Gumburanjon leucogranite (Figures 6.22 & 6.23a). Monazite and uraninite were recovered from the magnetic fraction at 17°/1.0A using standard magnetic techniques. Monazite typically forms relatively small (50-70μm), rounded, plate-like grains which have a translucent pale honey-coloured appearance containing minor opaque inclusions of an unknown mineralogy. These grains are similar in morphology to those of typical magmatic monazite (Parrish, 1990). Uraninite grains are typically 50-70μm in size and have subhedral to euhedral crystal shapes (rhombdodecahedral), with well-defined crystal faces.

Results and interpretation

Wak 23 contains both primary magmatic and inherited monazite. Monazite grains M3 and M5 are reversely discordant (Figure 7.4a) and have negative $^{207}Pb/^{206}Pb$ ages (Table 7.1b), which suggests that they contain excess ^{206}Pb from decay of ^{230}Th (Schärer, 1984) and have not experienced any significant Pb-loss since crystallisation. The $^{207}Pb/^{235}U$ age of these grains is 21.8 ± 0.2 Ma and 21.5 ± 0.1 Ma respectively and is similar to the weighted-average age of 21.4 ± 0.2 Ma recorded by the three most clustered uraninite grains (U2, U3, U4). It would appear, therefore, that the crystallisation age of Wak 23 is close to 21.5 ± 0.5 Ma. It is important to note that the U concentrations in all of the uraninite grains is quite low (Table 7.1b). Whilst this may be the result of erroneous weight and/or density estimations, it could equally imply that these grains represent intergrowths/overgrowths of uraninite with/on other mineral phases.

Monazite grain M2 is concordant at 24.1 Ma (Figure 7.4a). Given the fact that magmatic monazite generally plot above concordia, together with the fact that Wak 23 contains inherited monazite (grains M1 and M4) suggests that the *c.*24 Ma age of grain M2 probably reflects either partial Pb-loss from an older grain and/or new monazite growth on a xenocrystic core.

Monazite grains M1 and M4 plot well below the concordia and are interpreted to be xenocrystic in origin (Figure 7.4a). These grains were probably incorporated into the melt during partial melting of the surrounding country rock. A forced York Fit through M1, M4 and 21.5 ± 0.5 Ma reveals an upper intercept age of 462 ± 38 Ma (MSWD = 21), which suggests that these grains are similar in age to the *c.*500 Ma inherited monazite grains identified in metamorphic samples Wak 3 and Wak 6. This implies that the Gumburanjon leucogranite was probably sourced from deeper-level equivalents of the metamorphic schists currently exposed in the footwall of the ZSZ.

7.4.3.2 Wak 24 (undeformed leucogranite, Mt. Gumburanjon)

Wak 24 was collected from a newly-formed talus slope at the base of the central part of the Gumburanjon leucogranite (Figures 6.22 & 6.23f). This sample has an almost identical mineralogy and bulk-rock composition to Wak 23 (see Table 6.3). Monazite, xenotime and uraninite from Wak 24 were recovered from the non-magnetic fraction at 17°/0.35A. Wak 24 contains considerably less monazite than does Wak 23 and a much larger proportion of uraninite. Xenotime was also identified in Wak 24, although this could not be petrographically distinguished from monazite. Monazite and uraninite morphologies are identical to those described from Wak 23.

Results and interpretation

The results of Wak 24 are extremely similar to those of Wak 23, with reversely discordant grains M2 and M4 giving $^{207}Pb/^{235}U$ ages of 21.5 ± 0.1 Ma and 21.2 ± 0.1 Ma respectively (Table 7.1b, Figure 7.4b). Normally discordant uraninite (U1 and U2) and xenotime (X1) grains give $^{207}Pb/^{235}U$ ages of 21.2 ± 0.1 Ma, 21.3 ± 0.1 Ma and 21.4 ± 0.3 Ma respectively. The best interpretation of the crystallisation age of Wak 24 is therefore 21.3 ± 0.1 Ma (MSWD = 2.3), the weighted-average $^{207}Pb/^{235}U$ age of uraninite grains U1, U2 and monazite grain M4. This is virtually indistinguishable from the crystallisation age of Wak 23 at ~21.5 Ma. Monazite grain M1 plots on concordia and gives a slightly older $^{207}Pb/^{235}U$ age of 22.2 ± 0.4 Ma. This probably reflects either partial re-setting and/or new monazite growth on xenocrystic cores. An inherited component is also evident in Wak 24, as indicated by monazite grain M3. A forced York fit without statistical significance through M3 and 21.3 ± 0.2 Ma gives an upper intercept of 431 ± 23 Ma. As with Wak 23, the concentration of U in the uraninite grains is low (Table 7.1b), suggesting that they may not be pure uraninite.

7.4.3.3 Wak 27 (undeformed leucogranite, ZSZ)

Wak 27 represents a discordant leucogranite dyke which cross-cuts a mylonitic horizon within the ZSZ (Figure 6.23i) and was collected approximately 500m away from the main face of the Gumburanjon leucogranite. It is slightly finer grained than either Wak 23 or Wak 24, but has

essentially the same mineralogy and bulk composition (Table 6.3). No xenotime was identified in Wak 27, although abundant monazite and uraninite were collected in the magnetic fraction at 17°/0.6A. Monazite and uraninite morphologies are identical to those described from Wak 23.

Results and interpretation

Monazite grains M2, M3 and M4 are reversely discordant and give a weighted-average $^{207}Pb/^{235}U$ age of 22.1 ± 0.4 Ma (MSWD = 1.3), which is perhaps the best estimate of the crystallisation age of this sample (Table 7.1b, Figure 7.4c). The normally discordant uraninite grains U1 and U2 are in good agreement with this and give $^{207}Pb/^{235}U$ ages of 22 Ma and 22.3 Ma respectively (Table 7.1b). The crystallisation age of Wak 27 at ~22 Ma appears to be slightly, although significantly older than that of Wak 23 or Wak 24. This is somewhat surprising given the observed field relationships which suggest Wak 27 to be a late-stage discordant granite dyke which cross-cuts the mylonitic fabric in the ZSZ (Figure 6.23i). These data suggest that either the ZSZ had ceased moving at ~22 Ma, or that movement along the ZSZ was accommodated at a higher structural level following emplacement of Wak 27. Given the fact that no leucogranite dykes or sills are observed in the uppermost 100-150m of the ZSZ (Figure 6.22), it seems more likely that extension was indeed accommodated at a higher structural level in the ZSZ following the emplacement of this granite dyke.

As with Wak 23 and Wak 24, an inherited monazite component is present in Wak 27 (grain M1), which is interpreted to be the result of incorporation of xenocrystic monazite grains into the melt from the surrounding country rock at the time of melt formation.

7.4.3.4 Wak 21 (mylonitised pegmatite, Mt. Gumburanjon)

Wak 21 represents a mylonitised pegmatite vein which intrudes the garnet-staurolite-grade metapelites in the ZSZ and is cross-cut by a number of undeformed leucogranite dykes close to the main face of the Gumburanjon leucogranite (Figure 6.23d). Although Wak 21 has a similar bulk composition to samples Wak 23, Wak 24 and Wak 27 (see Table 6.3), it is mineralogically distinct from these samples owing to the absence of biotite and a greater abundance of garnet and tourmaline (see Chapter 6).

Approximately twelve monazites were extracted from Wak 21. Morphologically, these were divided into two distinct populations. Population 1 were collected in the non-magnetic fraction at 17°/0.5A and are extremely similar to the monazite described in Wak 23 (i.e. pale honey-coloured grains with a rounded, plate-like appearance). Population 2 were collected in the magnetic fraction at 17°/0.5A, are a much deeper yellow/green colour and contain more numerous opaque inclusions of an uncertain mineralogy.

Results and interpretation

All of the uraninite and monazite grains analysed from this sample plot below the concordia and appear to be much older than Tertiary in age (Figure 7.5a; Table 7.1c). The geological significance of these data are difficult to interpret. If Wak 21 was generated and emplaced during the Tertiary, then

the monazite and uraninite grains must have been scavenged from the melt protolith at the time of pegmatite formation and are therefore inherited. If correct, this is one of the few examples of uraninite inheritance in the geological literature. An unforced York fit through the three uraninite analyses gives an upper and lower intercept of 499 ± 26 Ma and 73 ± 21 Ma respectively (MSWD = 0.22), (Figure 7.5a). The upper intercept age is consistent with the *c.*500 Ma ages recorded in many of the other metamorphic and magmatic samples analysed in this study and suggests that Wak 21 may be Lower Palaeozoic in age. It is possible, however, that the uraninites have experienced significant U-loss, in which case this age is anomalously old; if correct, then the real age of Wak 21 may be closer to the lower intercept age of 73 ± 21 Ma. An unforced York fit through the two monazite analyses gives upper and lower intercepts of 471 ± 13 Ma and 57.3 ± 3.8 Ma respectively (MSWD = 0), (Figure 7.5a). The upper age intercept is similar to that revealed by the uraninites and appears to confirm that Wak 21 crystallised *c.*500 Ma, or that this sample contains a large component of *c.*500 Ma inherited grains.

7.4.3.5 Wak 26 (mylonitised pegmatite, ZSZ)

Wak 26 represents a mylonitised pegmatite vein which intrudes the garnet-staurolite-grade metapelites in the ZSZ (Figure 6.24b) and was collected approximately 500m away from the main face of the Gumburanjon leucogranite, ~50m vertically above sample Wak 27 (Figure 6.23i). Wak 26 has a similar mineralogical and bulk rock composition to Wak 21 (Table 6.3). No xenotime was found in Wak 26 and only limited occurrences of monazite were observed. Uraninite forms the most abundant radiogenic accessory phase in this sample. Both monazite and uraninite were collected in the magnetic fraction at 17°/0.6A. Monazite grains in sample Wak 26 are rather turbid looking and form relatively large (70-100μm), amorphous grains which have a deep-green/yellow colour and contain numerous opaque inclusions of an uncertain mineralogy. Back-scattered electron imaging of a polished section through one of these monazite grains revealed an overgrowth texture, with a rounded core overgrown by an anhedral rim. It would appear, therefore, that some of these grains might record multiple stages of monazite growth, which, given the choice of analytical technique (whole grain dissolution), cannot be resolved into their constituent parts.

Results and interpretation

Table 7.1c presents the results of six monazite and two uraninite analyses from Wak 26. These are plotted on a conventional concordia diagram in Figure 7.5b. As with Wak 21, Wak 26 contains a pre-Himalayan uraninite component which could be inherited (if Wak 26 is Himalayan in age), or it could reflect the original crystallisation age of the pegmatite (if it is pre-Himalayan in origin). An unforced York fit through the two uraninite grains reveals upper and lower intercepts of 583 ± 17 Ma and 122 ± 4 Ma respectively, the geological significance of which is uncertain. As in other samples, U concentrations in the uraninites are low and variable (Table 7.1c), suggesting that the uraninite grains may represent partial overgrowths on existing mineral phases such as magnetite.

In addition to the uraninite data, Wak 26 also reveals an interesting and complex array of monazite U-Pb ages which scatter between 30-37 Ma (Table 7.1c & Figure 7.5b). Grains M1 and M6 plot on and slightly below concordia between *c.*35-36 Ma. If these are metamorphic monazites which grew in the solid state following the crystallisation of Wak 26, then it is possible that they record the age of Barrovian metamorphism in the upper part of the slab at this time. This is a feasible interpretation given that Wak 9 records similar, but slightly younger monazite ages of c29 Ma (Figure 7.3c). Grains M2, M3, M4 and M5 all plot above concordia (Figure 7.5b), suggesting that these grains contain excess ^{206}Pb and could be magmatic in origin. The $^{207}Pb/^{235}U$ age of these grains is *c.* 36-37 Ma and is similar, albeit slightly older than the age of grains M1 and M6.

The youngest grain (M4) is also reversely discordant and gives a $^{207}Pb/^{235}U$ age of 29.3 Ma. The possibility that this grain crystallised at *c.*35-36 Ma and has subsequently experienced partial Pb-loss during protracted high temperature metamorphism is a possibility, but seems unlikely given that rocks in the footwall of the ZSZ have not been metamorphosed beyond *c.*650°C (see Table 6.2). The *c.*29 Ma age of grain M4 is therefore interpreted to reflect new monazite growth at this time and is in keeping the age of metamorphic monazite in sample Wak 9.

To summarise, given that sectioned and polished grains of monazite preserve evidence of growth zoning and the problems of inheritance in Wak 26, the age data presented in Table 7.1c and Figure 7.5b should be treated with extreme caution. The best interpretation is that these data provide evidence for a major thermal perturbation in the High Himalayan Slab between *c.*29-37 Ma, which may reflect the age of pegmatite formation, or could equally reflect metamorphism of a pre-Himalayan pegmatite at this time.

7.4.4 Summary of the U-Pb data

The U-Pb results which have implications for Tertiary thermal events in the High Himalayan Slab of SE Zanskar and NW Lahaul are summarised in Table 7.2. In addition to these Tertiary ages, many of the samples contain an inherited/old monazite component which has implications for the pre-Himalayan thermal history of the metamorphic protoliths in the High Himalayan Slab.

Table 7.2: Summarised U-Pb ages relating to Tertiary thermal events in the High Himalayan Slab of SE Zanskar and NW Lahaul

Sample	Description	Location	$^{207}Pb/^{235}U$ age	interpretation
Wak 3	metamorphic schist	lower slab	31.9 ± 0.4 (grain M3)	Major thermal perturbation Near-peak Barrovian metamorphism?
Wak 6	metamorphic schist	middle slab	#	#
Wak 9	metamorphic schist	upper slab	~30 Ma*	Major thermal perturbation Near-peak Barrovian metamorphism?
Wak 23	undeformed leucogranite	central part of Gumburanjon leucogranite	21.5 ± 0.5*	Magmatic crystallisation (M_2 metamorphism)
Wak 24	undeformed leucogranite	central part of Gumburanjon leucogranite	21.3 ± 0.1*	Magmatic crystallisation (M_2 metamorphism)
Wak 27	undeformed leucogranite	discordant dyke cross-cutting the ZSZ	22.1 ± 0.4*	Magmatic crystallisation (M_2 metamorphism)
Wak 21	leucocratic pegmatite	intensely deformed s-parallel sill in the ZSZ	#	#
Wak 26	leucocratic pegmatite	intensely deformed s-parallel sill in the ZSZ	~29-37 Ma	Major thermal perturbation prograde Barrovian metamorphism?

# denotes no Tertiary ages recorded
* average age of analyses

Metamorphic protoliths and evidence for a pre-Himalayan metamorphism

Most of the analysed samples contain an inherited monazite component which are highly discordant and generally give upper intercept ages of *c.*450-500 Ma. This implies that the protoliths of the High Himalayan Slab are at least Lower Palaeozoic in age, which is consistent with the stratigraphic observations presented in Chapter 3. Given the probable Precambrian-Cambrian age of the Haimantas, it seems extremely unlikely that these inherited grains are detrital in origin. Indeed, none of the analysed grains showed any textural evidence of abrasion or pitting, as might be expected if the grains had been reworked. The 450-500 Ma ages therefore provide evidence for a major thermal event during the Cambro-Ordovician. Whether this was a regional Barrovian-type event, or whether it was a localised thermal event related to the intrusion of the large Precambrian-Ordovician granites remains uncertain. Geochronological analysis of samples located at progressively increasing distances away from these granites may help resolve this problem (ie. if monazite growth was related to contact metamorphism during granite emplacement, then those samples located away from the granite contacts should not contain the 450-500 Ma monazite component). Intrusion of these granites must have been associated with some sort of tectonic activity, although whether this was extensional (as suggested by Le Fort, 1986), or compressional (as suggested by Frank *et al.*, 1995) remains entirely speculative. Structural and textural observations in the low-grade parts of the High Himalayan Slab in SE Zanskar and NW Lahaul failed to reveal any convincing evidence to support the existence of a major pre-Himalayan deformation and Barrovian metamorphism, which favours emplacement in a rift-type setting. However, it remains possible that these granites were emplaced at higher structural levels and that evidence for the pre-Himalayan deformation and metamorphism is preserved in deeper structural levels. Strong overprinting by Tertiary deformation and metamorphism makes it virtually impossible to verify this possibility. Pognante and Lombardo (1989) provided tentative evidence that some metabasites in the HHC which are cross-cut by the Precambrian-Ordovician granites preserve evidence of a high pressure pre-Himalayan metamorphism.

Timing of regional Barrovian metamorphism: M_1

Inherent problems associated with dating rocks that record multiple stages of accessory mineral growth during protracted high-grade metamorphic events makes interpretation of metamorphic monazite ages extremely difficult. Of the three samples analysed (Wak 3, Wak 6 and Wak 9), only Wak 3 and Wak 9 preserve any evidence of Tertiary thermal events (Table 7.2). Both samples suggest that there was a major thermal perturbation in the High Himalayan Slab at *c.*29-32 Ma, which is interpreted to reflect monazite growth during regional Barrovian metamorphism at this time. Owing to the prolonged and diachronous nature of regional Barrovian metamorphism, it remains uncertain as to whether these ages are associated with prograde metamorphism, near-peak conditions, or age-averaging of multiple phases of monazite growth. Monazite ages from pegmatite sample Wak 26 provide tentative evidence that temperatures may have been in excess of ~500°C as early as 37 Ma in the upper part of the slab (Table 7.2).

The metamorphic monazite ages presented in this work are similar to the Sm-Nd ages of metamorphic garnets in central and western Zanskar (Vance and Harris, 1996). These authors obtained Sm-Nd core-rim ages of 33.3 ± 0.5 - 31.2 ± 0.5 Ma and 30.9 ± 1.8 Ma - 26.3 ± 0.8 Ma from two garnets collected from the kyanite- and sillimanite-grade zone of the slab. These results demonstrate that Barrovian metamorphism was a protracted event and are consistent with the 29-37 Ma ages recorded by samples Wak 3, Wak 9 and Wak 26. These ages are also consistent with simple thermal models which predict that peak-metamorphic conditions in a thrust-thickened regime should be attained ~20-30 Ma after the timing of initial collision (e.g. Oxburgh & Turcotte, 1974; England & Richardson, 1977; England & Thompson, 1984), if we accept the timing of the India-Asia collision to be 50-54 Ma (Searle *et al.*, 1987; Garzanti & van Haver, 1987).

Age of crustal melting: M_2

U-Pb data from the Gumburanjon leucogranite define a very narrow range of crystallisation ages between 21-22 Ma (Table 7.2) These are consistent with the ages of many of the other High Himalayan leucogranites in the High Himalayan Slab (see Table 2.2) and are quite distinct from the *c.*29-37 Ma ages observed in the metamorphic schists. This suggests a temporal separation between monazite growth in pelitic schists (M_1) and crustal melting (M_2). Structural and geochemical data presented in Chapter 6 suggest that the Gumburanjon leucogranite is a relatively localised melt which has not migrated far from its source. This suggests that M_1 and M_2 form part of a single, continuously evolving metamorphic event and raises questions as to why no ages between *c.*22-29 Ma are recorded in any of the samples collected from the top of the slab. One possible explanation is that the lack of overlap between the metamorphic ages and the leucogranite ages reflects the paucity of the current dataset. Further analyses of monazite from sample Wak 9 might well reveal the existence of ages between 22-29 Ma.. A second possibility is that the metamorphic ages are recording prograde growth of monazite when temperatures reach *c.*500°C (Smith & Barreiro, 1990), in which case peak metamorphic conditions could be significantly younger than *c.*30 Ma.

Leucogranite source rock provenance and melt temperature

All of the analysed samples of undeformed leucogranite (Wak 23, Wak 24 and Wak 27) and leucocratic pegmatites (Wak 21 and Wak 26) were observed to contain an inherited component of monazite. Wak 21 and Wak 26 may also contain inherited uraninite, which if correct, suggests that uraninite has a blocking temperature which is similar, if not higher than that of monazite. Crude linear regressions through the inherited monazite and uraninite data consistently yield upper age intercepts of 450-500 Ma, which suggests that the source of the Gumburanjon leucogranite is at least Lower Palaeozoic in age. This is consistent with the work of Noble and Searle (1995), who made similar observations in the High Himalayan leucogranites of central Zanskar. The most probable source of the Gumburanjon leucogranite is therefore interpreted to be the deeper level equivalents of the Precambrian-Cambrian Haimantas and Precambrian-Ordovician granites which are exposed throughout the High Himalayan Slab of SE Zanskar and NW Lahaul.

The presence of inherited monazite in the Gumburanjon leucogranite suggests that the temperature of melt formation was below the blocking temperature for diffusional Pb-loss in monazite (~725 ± 25°C; Parrish, 1990). This is consistent with the geochemical data presented in Chapter 6 which suggest that the Gumburanjon leucogranite formed at temperatures between *c.*650-700°C. It is important to note, however, that the melt residence times of the High Himalayan leucogranites is interpreted to be less than 50 ka (Ayres *et al.*, 1997), which implies that even at higher melting temperatures, some inherited monazite is likely to survive.

7.5 $^{40}Ar/^{39}Ar$ geochronology

Aliquots of muscovite and biotite were hand-picked from metamorphic samples Wak 3, Wak 6 and Wak 9 and magmatic samples Wak 21, Wak 23, Wak 26 and Wak 27 for the purpose of $^{40}Ar/^{39}Ar$ analysis. After washing in distilled water, acetone, and ethanol, the samples were wrapped in Sn foil and irradiated at the McMaster University research reactor. The samples were packaged along with synthetic salts (to facilitate corrections for interfering reactions) and the neutron fluence monitor Fish Canyon sanidine (28.03 Ma; Renne et al., 1994). $^{40}Ar/^{39}Ar$ analyses were performed at the Massachusetts Institute of Technology (M.I.T.), using stepwise heating resistance-furnace techniques similar to those reported by Hodges *et al.* (1994). Calculation of the *J* parameter and corrections for interfering reactions were performed by K.V. Hodges at M.I.T. Further details of analytical procedures and a complete set of stepwise-heating results for each sample are given in Appendix F.

The results are interpreted to represent the time at which the samples cooled through ~400-350°C and 350-300°C, the nominal closure temperature for Ar diffusion in muscovite and biotite respectively (McDougall & Harrison, 1988; Hames & Cheney, 1997). Some samples yielded release spectra with well-defined plateaus according to the criteria of Snee *et al.* (1980), whilst others defined linear arrays on isochron diagrams (Podosek *et al.*, 1973; Roddick *et al.*, 1980); in these cases, the array met the criteria for an isochron when its calculated mean squared weight deviation (MSWD) was compared with the expected value of 1.0 at the 2σ confidence level (Wendt & Carl, 1991). In order to achieve the necessary MSWD at the 2σ confidence level, it was necessary in some samples to exclude certain heating steps from the dataset used to calculate the isochron age (the steps omitted are shown in Figures 7.6a-g and correspond to the heating steps tabulated in Appendix F). Linear regressions were performed using the methods outlined by York (1969) using the computer programme ISOPLOT ver. 2.92 (Ludwig, 1990). Plateau and isotope correlation diagrams for each of the analysed samples are shown in Figure 7.6 and the results summarised in Table 7.3.

Table 7.3: Summarised $^{40}Ar/^{39}Ar$ results from different parts of the High Himalayan Slab in SE Zanskar and NW Lahaul

Sample	Mineral	Plateau age* (Ma)	$^{39}Ar_p(\%)^{\dagger}$	Isochron Age **	$^{39}Ar_i(\%)^{\dagger\dagger}$	$^{40}Ar/^{36}Ar_0$	MSWD#
Wak 3	Muscovite	-	-	22.0 ± 0.8	84.1	318.5 ± 11.5	1.65
Wak 3	Biotite	-	-	-	-	-	-
Wak 6	Muscovite	22.11 ± 0.32	98.2	21.7 ± 0.6	99.2	331.1 ± 25.2	1.46
Wak 6	Biotite	-	-	-	-	-	-
Wak 9	Muscovite	20.49 ± 0.30	100.0	20.4 ± 0.6	100.0	302.1 ± 15.2	1.06
Wak 9	Biotite	25.53 ± 0.41	46.7	25.9 ± 0.2	51.9	317.27 ± 7.7	0.88
Wak 21	Muscovite	20.90 ± 0.29	98.9	20.8 ± 0.7	100.0	299.4 ± 10.6	1.78
Wak 23	Muscovite	20.41 ± 0.34	90.6	20.2 ± 0.5	98.1	303.3 ± 5.8	1.48
Wak 23	Biotite	20.82 ± 0.27	99.0	20.9 ± 0.5	100.0	289.9 ± 7.9	1.02
Wak 26	Muscovite	21.09 ± 0.29	90.8	20.8 ± 0.6	94.9	305.8 ± 11.9	0.74
Wak 27	Muscovite	20.40 ± 0.28	98.9	20.6 ± 0.6	99.4	292.3 ± 6.5	1.75
Wak 27	Biotite	20.02 ± 0.27	100.0	20.0 ± 0.3	100.0	299 ± 18	0.85

All uncertainties are quoted at the 2σ confidence level.

*Calculated following the method of Snee *et al.* (1988).

†Percentage of total K-derived ^{39}Ar evolved from heating steps on the plateau.

**Isochron ages were calculated using the fitting algorithm of York (1969).

††Percentage of total ^{39}Ar evolved from heating steps used for regression.

#MSWD reflects the quality of the linear fit to the data for each sample. Following the approach of Wendt and Carl (1991), the range of MSWD values for all samples is within 2σ uncertainty of the expected value of 1.0.

7.5.1 Metamorphic $^{40}Ar/^{39}Ar$ results and interpretation (Wak 3, Wak 6, Wak 9)

$^{40}Ar/^{39}Ar$ release spectra and isotope correlation diagrams for samples Wak 3, Wak 6 and Wak 9 are shown in Figures 7.6a-c. Owing to a lower closure temperature for argon diffusion in biotite compared to that in muscovite (McDougall & Harrison, 1988), the former should record the younger cooling age (unless the sample cooled extremely rapidly, in which case it is possible that both ages will be within error of each other). Figures 7.6a & b show that biotite ages in Wak 3 and Wak 6 are consistently older than the muscovite ages, which suggests that excess Ar is present in these samples. Indeed, the biotite ages in these samples are actually older than the interpreted age of Barrovian metamorphism as determined from U-Pb analysis of metamorphic monazite (see Table 7.2). Excess Ar is a common problem in biotite and has been reported from adjacent parts of the High Himalayan Slab in western and central Zanskar (e.g. Searle *et al.*, 1992; Stephenson, 1997; T.M. Harrison, pers. com.). Where identified, excess Ar gives an unreliable and geologically meaningless biotite cooling age. Excess Ar is not always easy to identify, as sample Wak 9 testifies (Figure 7.6c). In this sample, the biotite plateau and isotope correlation ages are within error of each other at ~25.5 Ma, with neither showing any real evidence for the presence of excess Ar. However, the fact that this is still >5 Ma older than the muscovite age suggests that excess Ar probably does exist in this sample.

The presence of excess Ar in Wak 3, Wak 6 and Wak 9 biotites questions the reliability of the muscovite ages, since these too may contain excess Ar. The release spectrum of Wak 3 muscovite has a characteristic saddle-shape and does not define a plateau age according to the criteria of Snee *et al.* (1988), (Figure 7.6a). Previous work suggests that this kind of release spectrum is indicative of the presence of excess Ar in a sample (Lanphere & Dalrymple, 1976). However, when plotted on an

isotope correlation diagram, a linear regression through the Wak 3 muscovite data reveals a $^{36}Ar/^{40}Ar$ ratio that is statistically indistinguishable from that of modern air (Figure 7.6a). This suggests that excess Ar is unlikely to have a significant effect on the age of this sample, which is interpreted to be 22.0 ± 0.8 Ma.

Wak 6 has a mild saddle-shaped release spectrum (Figure 7.6b), which may suggest contamination by excess Ar. This appears to be supported by a very low $^{36}Ar/^{40}Ar$ intercept on the isotope correlation diagram, although this intercept is within error (albeit quite a large error) of modern air. The isochron age of Wak 6 is 21.7 ± 0.6 Ma, and is statistically indistinguishable from the plateau age of 22.1 ± 0.3 Ma (Figure 7.6b). It would appear, therefore, that the muscovite cooling age of Wak 6 is similar to that of Wak 3. This fits well with the Rb-Sr mica cooling ages of samples in the Crystalline Nappe determined by Frank *et al.* (1977) and Mehta (1977), (Figure 7.2) and obeys the traditional age sequence of t(Ms, Rb-Sr) > t(Ms, $^{40}Ar/^{39}Ar$) > t(Bt, Rb-Sr).

Despite having quite large errors, the release spectrum of Wak 9 muscovite defines a plateau age of 20.5 ± 0.3 Ma, which is virtually identical to its isochron age of 20.4 ± 0.6 Ma (Figure 7.6c). Both these ages incorporate 100% of the total $^{39}Ar_{(K)}$ released (Table 7.3) and are therefore interpreted to be reliable cooling ages. It is interesting to note that this age is slightly younger than the muscovite cooling ages of Wak 3 (22 ± 0.8 Ma) and Wak 6 (21.7 ± 0.6 Ma). These data therefore suggest that rocks at the top of the slab cooled slightly later than those at the base. The opposite appears to be true in western Zanskar, where Searle *et al.* (1992) suggest that muscovite cooling ages become progressively younger away from the top of the slab. Searle *et al.* (1992) interpret this to reflect diachronous cooling through 300-350°C in a direction which is consistent with the foreland propagating piggy-back style of thrusting. Although only three samples were analysed in SE Zanskar and NW Lahaul, the northward younging direction of the muscovite cooling ages could imply that underthrusting along the MCT initiated at the base of the slab before extension developed along the ZSZ at the top of the slab. This is pure speculation, however, and it is equally likely that the difference in the muscovite $^{40}Ar/^{39}Ar$ ages across the slab merely reflects a complex history of hydrothermal episodes with new overgrowths of chemically resolvable micas on pre-existing xenocrystic cores (e.g. Hodges & Bowring, 1995; Hames & Cheney, 1997).

7.5.2 Magmatic $^{40}Ar/^{39}Ar$ results and interpretation (Wak 21, Wak 23, Wak 26 and Wak 27)

$^{40}Ar/^{39}Ar$ release spectra and isotope correlation diagrams for pegmatite samples Wak 21 and Wak 26 are shown in Figures 7.6d & e. Only muscovite could be analysed from these samples since they are wholly leucocratic and do not contain biotite. $^{40}Ar/^{39}Ar$ release spectra and isotope correlation diagrams for undeformed leucogranite samples Wak 23 and Wak 27 are shown in Figures 7.6f & g. All of the data display well-behaved $^{40}Ar/^{39}Ar$ systematics and define good plateau and isochron ages, with no indication of excess Ar in any of the samples. The data are in good agreement with the *c.*21-19 Ma Rb-Sr and $^{40}Ar/^{39}Ar$ ages reported from the Gumburanjon leucogranite by previous works (Figure 7.2). Muscovite separates from all of the samples analysed in this work yielded $^{40}Ar/^{39}Ar$ isochron ages between 20.2 ± 0.5 Ma and 20.8 ± 0.7 Ma (Table 7.3). Biotites from Wak 23 and Wak 27 gave isochron ages of 20.9 ± 0.5 Ma and 20.0 ± 0.3 Ma, respectively. Both of

these ages are within uncertainty of the isochron ages of coexistent muscovite (Table 7.3), suggesting rapid cooling of the upper part of the slab at 20-21 Ma. This interpretation is supported by the observation that the muscovite ages for Gumburanjon leucogranite samples are only slightly younger than the intrusion ages as interpreted from U-Pb data: 20.2 Ma *vs.* 21.5 Ma for Wak 23, and 20.6 Ma *vs.* 22.1 Ma for Wak 27 (compare Tables 7.2 & 7.3). Given the probable magmatic temperatures of the Gumburanjon leucogranite (*c.*650-700°C), cooling to $^{40}Ar/^{39}Ar$ mica closure temperatures of about 400-300°C may have occurred at rates approaching ~200°C/my, twice as fast as those envisioned by Ferrara *et al.* (1991).

Several possible scenarios can be envisaged to explain the extremely rapid rate of cooling in the Gumburanjon leucogranite. One possibility is that the Gumburanjon leucogranite was emplaced into rocks which were already cold (<300°C) at ~21-22 Ma. If this were the case, however, one might expect to see evidence of a thermal aureole in the surrounding country rock: this is not supported by field or petrographic evidence (see Chapter 6). Furthermore, given the relatively small size of the Gumburanjon leucogranite, this granite is unlikely to have had the thermal capacity to travel any significant distance in rocks which were already cold. In addition to these field observations, the $^{40}Ar/^{39}Ar$ muscovite age of Wak 9 (20.4 ± 0.6 Ma), suggests that the surrounding country rocks cooled at exactly the same time as the granite (however, note that Wak 9 biotite records an older cooling age of *c.*25 Ma, with no conclusive evidence to support the existence of excess Ar in this sample Figure 7.6c). Whilst it is possible that emplacement of the Gumburanjon leucogranite resulted in the partial re-setting of Wak 9 muscovite at *c.* 20 Ma, there is no evidence in the $^{40}Ar/^{39}Ar$ release spectra to suggest that this sample experienced more than one phase of cooling below 400-350°C (Figure 7.6c). Rapid cooling at the top of the slab at *c.*20-21 Ma is therefore interpreted to be the result of extensional unroofing along the ZSZ combined with extensive surface erosion. Simple thermal models presented in section 7.6 help constrain the timing and extent of this movement.

7.5.3 Summary of the $^{40}Ar/^{39}Ar$ data

All of the reliable and meaningful $^{40}Ar/^{39}Ar$ data presented in this thesis plot within a very narrow age bracket between ~20-22 Ma (Table 7.3), suggesting that the entire High Himalayan Slab cooled through *c.*400-300°C at approximately the same time. This is consistent with muscovite and biotite $^{40}Ar/^{39}Ar$ and K-Ar cooling ages from western and central Zanskar, where samples collected from different structural positions show evidence of rapid cooling between 17-20 Ma (Searle *et al.*, 1992; Vance & Kelley, 1994; Stephenson, 1997; Searle *et al.*, 1998). The similarity in the cooling ages of samples Wak 9, Wak 21, Wak 23, Wak 26 and Wak 27 at the top of the slab is interpreted to be the result of rapid tectonic denudation by displacement on the ZSZ. These ages also coincide with the interpreted age of thrusting along the MCT in NW Lahaul at *c.*16-21 Ma (Frank *et al.*, 1977). The contemporaneity of movement along the ZSZ and MCT suggests a model whereby the entire High Himalayan Slab was exhumed as a more-or-less coherent tectonic unit between these bounding structures.

7.6 Thermal modelling

Two of the biggest problems associated with the evolution of the uppermost part of the High Himalayan Slab in SE Zanskar and NW Lahaul concern the timing of movement along the ZSZ and the depth at which the Gumburanjon leucogranite was emplaced. P-T-t constraints from the immediate footwall of the ZSZ in the vicinity of Mt. Gumburanjon allow broad constraints to be placed on the exhumation history at the top of the slab (Figure 7.7), but fail to answer the above questions. Thermal modelling provides a means of testing the links between the pressure-temperature (P-T) path, the temperature-time (T-t) history derived from geochronological data, and the changes of tectonic regime that accompany exhumation. Waters *et al* (paper in preparation), have recently completed a study in which a one-dimensional finite-difference conductive thermal model is used to simulate the retrograde P-T-t evolution of the upper part of the High Himalayan slab in central and western Zanskar. In that study, the metamorphic and geochronological data are fitted by a three-stage exhumation history involving a period of rapid extensional movement along the ZSZ between periods of slower unroofing by erosion. Using the same model as Waters *et al*, it is possible to: (1) simulate the P-T path for rocks in the footwall of the ZSZ in SE Zanskar (Figure 7.8a); and (2) match the observed temperature-time history determined from the U-Pb and $^{40}Ar/^{39}Ar$ results (Figure 7.8b). Models which successfully match both these criteria can be used to predict the temperature and depth at which the Gumburanjon leucogranite was emplaced, bracket the age of extensional normal faulting along the ZSZ and provide constraints on the relative importance of erosion versus extension during unroofing of the footwall.

For the models to be successful, a number of geological criteria must also be fulfilled to maintain the observed field relationships: (1) The model must account for the absence of a metamorphic aureole, which is attributed to intrusion of the Gumburanjon leucogranite into country rock which was still reasonably hot: a minimum estimate of this temperature is 450°C, assuming that the granite was emplaced into the ZSZ whilst it was still below the brittle-ductile transition. This is a reasonable assumption given the fact that the Gumburanjon leucogranite is not observed cutting across cataclastic melanges in the uppermost part of the ZSZ (Figure 6.22); and (2) The model must account for the observed structural depths exposed in the footwall and hanging wall of the ZSZ (i.e. the model must be capable of stripping off a considerable thickness from the footwall whilst removing no more than *c.*5-10 km from the hanging wall, as discussed in Chapter 6).

7.6.1 Description of the model

The one-dimensional finite-difference conductive thermal model used here is essentially the same as that used by England *et al.* (1992). The model assumes a vertical array of nodes (spaced at 1km intervals) with uniform thermal properties. Initial conditions for the model represent an equilibrium thermal profile which is fixed at *c.*630°C and 8 kbar, the assumed near-peak P-T estimate of lithologies exposed in the deepest structural levels in the footwall of the ZSZ (see Chapter 6). Based on the metamorphic monazite age data from sample Wak 9, these conditions are interpreted to have

been attained at *c.*30 Ma. The starting conditions are generated assuming that the conductivity and diffusivity of the crust are 2.25 (W/m/K), and 31.56 (sq. km/Ma) respectively, that there is no internal heat production and that the lower boundary is a constant basal heat flux (Table 7.4). All these variables can be altered if required, which basically allows the model to be tailored to fit any P-T-t path.

Three models were tested using the same initial starting conditions (Table 7.4), in an attempt to demonstrate the different effects of extensional *vs.* erosional unroofing at the top of the slab. Exhumation is simulated by truncating the thermal profile at regular time intervals by the required amount. The unroofing effect of an extensional detachment is simulated by excising part of the hangingwall at each time interval, at a rate specified by the exhumation-rate parameter. This slightly over-estimates the cooling effect on the footwall, because it does not take into account the fact that each new section of hangingwall will have been heated slightly by virtue of being in contact with hot footwall at higher structural levels. However, this may be partly cancelled out by the fact that the one-dimensional model does not take into account lateral heat conduction. One of the most important factors in this modelling is the structural distance between the extensional detachment and the piece of crust being exhumed. The Gumburanjon leucogranite is located in the immediate footwall of the ZSZ and essentially forms part of the shear zone itself. The effects of modelling exhumation of a piece of crust located within a shear zone may lead to unrealistic results, hence it was assumed in models 2 and 3 that the ZSZ was located 1km structural above the point of interest.

Table 7.4: Thermal modelling parameters

	Unroofing mechanism	*Start time*	*Duration*	*Rate*	*Amount*	*Cumulative amount*
Model 1	Erosion	30	30	1.0	30	30
Model 2	Extension along ZSZ	30	10	2.25	25	25
	Erosion	20	20	0.25	5	30
Model 3	Erosion	30	7	0.05	0.35	0.35
	Extension along ZSZ	23	3	8.55	25.65	26.0
	Erosion	20	20	0.2	4.0	30.0

Starting conditions for all models are based on the interpreted peak-metamorphic P-T estimates recorded by metapelitic schists in the footwall of the ZSZ of *c.*630°C and 8 kbar. In order to start exhumation under these conditions, the following parameters were used in all of the above models: *Thermal properties of crust*: Conductivity = 2.25 (W/m/K); Diffusivity = 31.56 (sq. km/Ma); Internal heat production = 0. *Lower boundary conditions*: Constant heat flux = 40.0 (mW/m2); Depth to lower boundary = 125 km. *Lithostatic gradient* = 3.71 km/kbar

Model 1: uniform erosion with no extensional unroofing

The inadequacy of simplistic models is illustrated by Model 1, in which unroofing of the footwall is accomplished purely by erosion at a uniform rate of 1mm/year over a duration of 30 Ma. The results show that the predicted P-T path would pass along the sillimanite = kyanite reaction curve and close to the Al_2SiO_5 triple point (Figure 7.8a). Whilst this is not dissimilar to the interpreted P-T

trajectory shown in Figure 7.7, the temperature-time path predicted by this model does not fit the observed cooling data shown in Figure 7.8b. This model is clearly unrealistic and more rapid exhumation in the earlier stages is needed to cool the footwall more quickly.

Model 2: Unroofing via extensional normal faulting along the ZSZ between 30-20 Ma

This model investigates a two-stage exhumation history, whereby extensional exhumation along the ZSZ is followed by a period of erosional exhumation (Table 7.4). Extension along the ZSZ is initiated immediately after peak-metamorphic conditions were attained in the country rocks at 30 Ma. Extension is assumed to be a continuous process that lasted for 10 Ma and stopped shortly after emplacement of the Gumburanjon leucogranite. Since ~30 km of rock has been exhumed in the footwall of the ZSZ, it is impossible for the rate of extensional exhumation to exceed 3mm/yr in this model. Similarly, if it is less than 2mm/yr, then more than 10 km of overburden is stripped off the hangingwall during the remaining 20 Ma of erosional unroofing, which violates the model parameters outlined above. A value of 2.5mm/yr was therefore chosen to represent the rate of exhumation along the ZSZ between 30-20 Ma. The remaining 5 km of overburden is removed by erosional exhumation between 20-0 Ma (Table 7.4).

The P-T trajectory predicted by this model (Figure 7.8a) closely matches that shown in Figure 7.7. In addition, the predicted temperature-time curve shown in Figure 7.8b shows a good fit to the observed $^{40}Ar/^{39}Ar$ cooling ages. If we accept the parameters of this model, it suggests that emplacement of the Gumburanjon leucogranite between 21-22 Ma took place at pressures of 2-3 kbar (Figure 7.8a), similar to those reported in central Nepal (Inger and Harris, 1993). Since the country rock temperature at this depth is ~350-400°C, it implies that the Gumburanjon leucogranite must have travelled a considerable distance from its source horizon, in which case, the inferred zone of sillimanite-grade migmatitic gneisses beneath the Gumburanjon leucogranite (Figure 6.22) is unlikely to have acted as a source for the granite.

This model is considered to be unrealistic for two reasons: (1) the Gumburanjon leucogranite is a relatively small pluton that intrudes the immediate footwall of the ZSZ and is unlikely to have had the thermal potential to have travelled a significant distance from its source; and (2) slow unroofing along the ZSZ at rates of 2.5mm/yr are likely to produce retrograde metamorphic textures in the pelitic schists located in the footwall. This is not borne out by textural observations and garnet zoning profiles of samples collected from the footwall of the ZSZ in the immediate vicinity of the Gumburanjon leucogranite (see Chapter 6).

Model 3: Unroofing via extensional normal faulting along the ZSZ between 23-20 Ma

This model invokes a three-stage exhumation history involving two periods of erosional exhumation either side of a very brief period of extensional exhumation along the ZSZ. Extensional unroofing along the ZSZ is invoked during between 23-20 Ma (Table 7.4), which is contemporaneous with emplacement of the Gumburanjon leucogranite. As illustrated in Figure 7.8a, the P-T trajectory

predicted by this model closely matches that predicted by Model 2. In order to satisfy the observed $^{40}Ar/^{39}Ar$ cooling data, an exhumation rate of 8.55mm/yr is necessary to cool the footwall through 300-350°C by 20-21 Ma from a starting temperature of 630°C at 23 Ma (Figure 7.8b). Whilst this may seem unreasonably high, exhumation rates of *c.*8–9 mm/yr are observed ~60 km along strike in western and central Zanskar (Waters *et al.*, paper in preparation). Recently obtained geochronological data from the Mount Everest region in southern Tibet constrain another strand of the South Tibetan detachment system (the Qomolangma detachment) to have accommodated unroofing at a rate of ~8.2 mm/yr (Hodges *et al.*., in press).

This model predicts that emplacement of the Gumburanjon leucogranite took place at pressures of ~3-6 kbar (Figure 7.8a), similar to the crystallisation depth of migmatitic leucosomes in western and central Zanskar (Waters *et al.*, paper in preparation). The corresponding temperature of the surrounding country rock during emplacement is predicted to be between ~450-550°C, still well below the estimated emplacement temperature of the granite itself (~650-700°C), but high enough for the Gumburanjon leucogranite to be considered a relatively localised melt which was generated from the inferred zone of sillimanite-grade migmatites beneath the granite (Figure 6.22).

7.7 Discussion: crustal melting and extension

Although the above models are extremely simplistic and are based on the assumption that peak-metamorphic conditions of *c.*630°C and 8 kbar were attained at 30 Ma, they demonstrate a close temporal relationship between crustal melting and extension. Based on field and geochemical observations which suggest the Gumburanjon leucogranite to be a locally sourced granite (Chapter 6), it seems unlikely that any significant extension could have occurred along the ZSZ prior to *c.*23 Ma, since this would have the effect of chilling the footwall well below the temperature necessary for melting to occur (i.e. Model 2). However, initiation of slip along the ZSZ prior to 23 Ma cannot be entirely ruled out. The models do not predict the time at which cessation of slip along the ZSZ occurred. Instead, both models 2 and 3 assume that extension ceased at 20 Ma, based on the mica $^{40}Ar/^{39}Ar$ cooling ages of metamorphic and magmatic samples in the footwall of the ZSZ. This may be somewhat unrealistic given that Rb-Sr cooling ages from a more westerly strand of the ZSZ suggest that extension may have continued to 16 Ma (Inger, 1998).

Given the fact that the Gumburanjon leucogranite is interpreted to have been sourced ~10 km structurally above the projected level of the MCT (Figure 6.27), then it seems probable that extension was the dominant mechanism involved in granite generation and emplacement at the top of the slab. This supports the earlier work of Harris and Massey (1994), who suggested that the High Himalayan leucogranites in central Nepal were generated by decompression during exhumation, and refutes the work of those authors who suggest that the High Himalayan leucogranites were generated by shear-heating along the MCT (e.g. Le Fort, 1981; Harrison *et al.*, 1997b).

Whether melting was triggered by extensional unroofing along the ZSZ, or whether melting was the cause of extensional at the top of the slab remains unclear. It is possible that the earliest phases of crustal melting occurred in direct response to temperature increases brought about primarily as a result of crustal shortening and thickening. Temperatures may have been enhanced somewhat in the upper part of the slab owing to conductivity differences between the overlying Tibetan Sedimentary Series (low conductivity) and the underlying High Himalayan Slab (high conductivity and enriched in radiogenic elements), as suggested by Jaupart and Provost (1985). Rheological changes brought about by crustal melting would weaken the High Himalayan Slab and precipitate normal faulting as the slab attempted to regain dynamic stability (e.g. Davis *et al.*; 1983 Platt, 1986; Hollister, 1993; Hodges *et al.*, 1996; Figure 2.9). The earliest stages of extension along the ZSZ may, therefore, have developed in direct response to crustal melting in deeper structural levels. Once initiated, movement along the ZSZ would result in decompression of the footwall, thus precipitating further melting, probably by dehydration melt reactions owing to the positive slope of this curve (Figure 7.7).

Despite the close temporal and spatial relationship between crustal melting and extension, it seems extremely unlikely that melting alone could trigger extension. Some other mechanism must be involved in order to force the High Himalayan Slab out of dynamic stability. Uplift along the base of the slab by thrusting along the MCT is the obvious mechanism by which to do this, and is supported by the similarity of cooling ages in the MCT zone with those in the ZSZ (Figure 7.2). The fact that Wak 3 records a slightly older $^{40}Ar/^{39}Ar$ muscovite age (22.0 ± 0.8 Ma) than Wak 9 (20.4 ± 0.6 Ma), is tentative evidence that uplift and cooling at the base of the slab preceded melting and extension at the top of the slab.

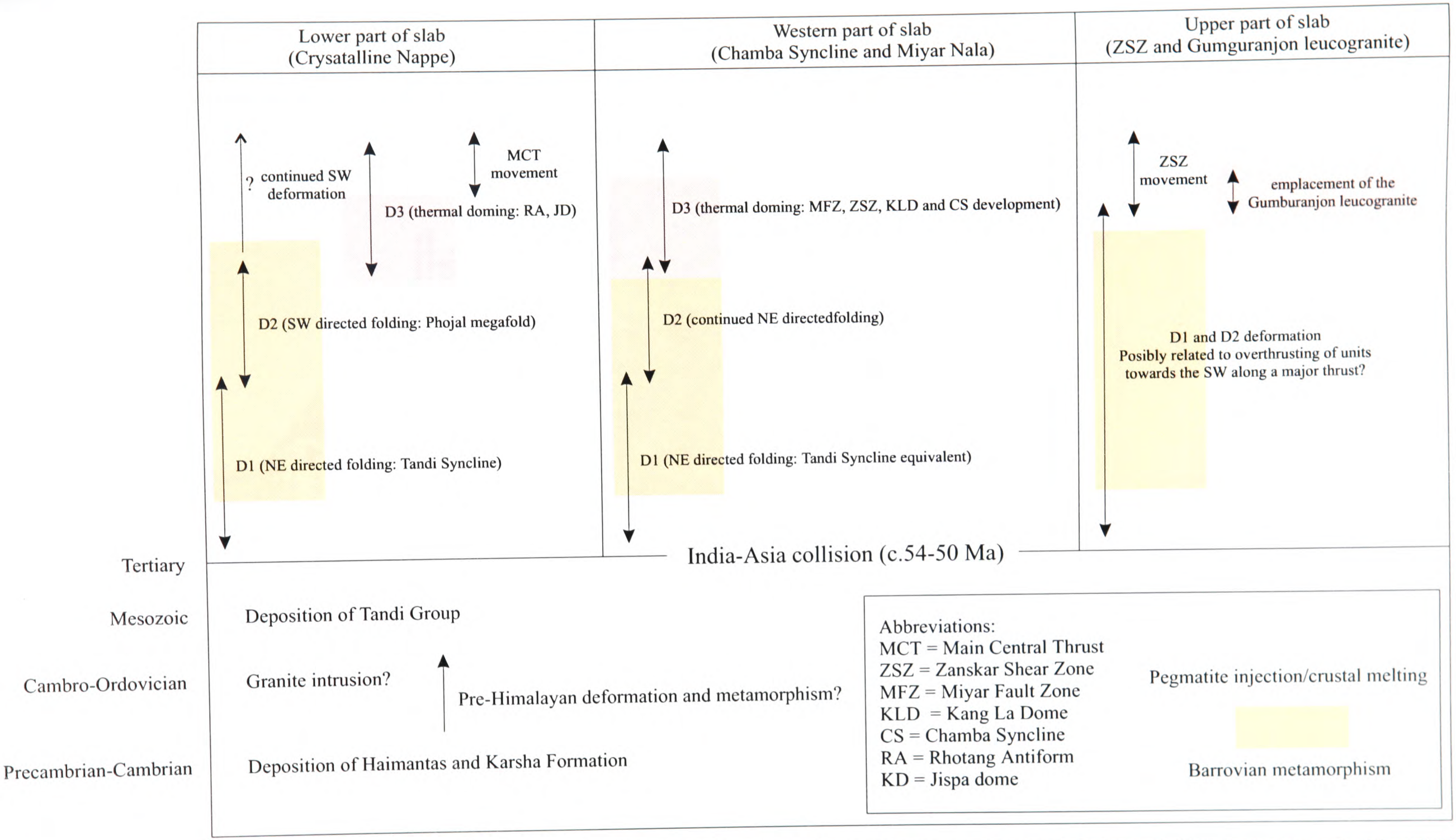


Figure 7.1 Summarised structural and metamorphic history of different parts of the High Himalayan Slab in SE Zanskar and NW Lahaul as determined from field and microstructural observations presented in Chapters 3-6. Owing to the heterogeneity of deformation across the study area, it is virtually impossible to accurately correlate different deformation phases from one region to another. Consequently, the timing of metamorphic mineral growth cannot be constrained from region to region. Geochronology provides the only means of correlating metamorphic mineral growth/cooling across such large areas.

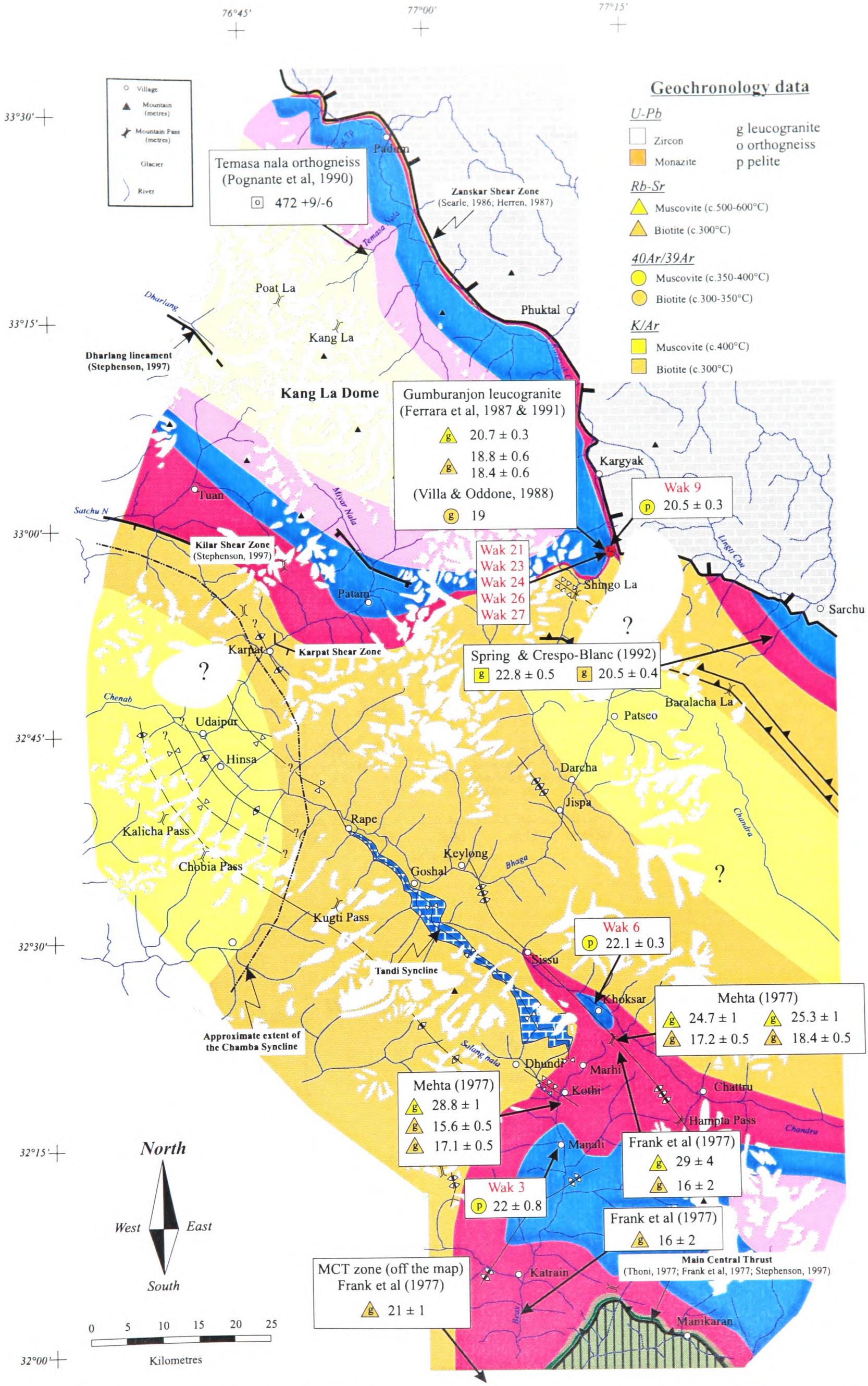
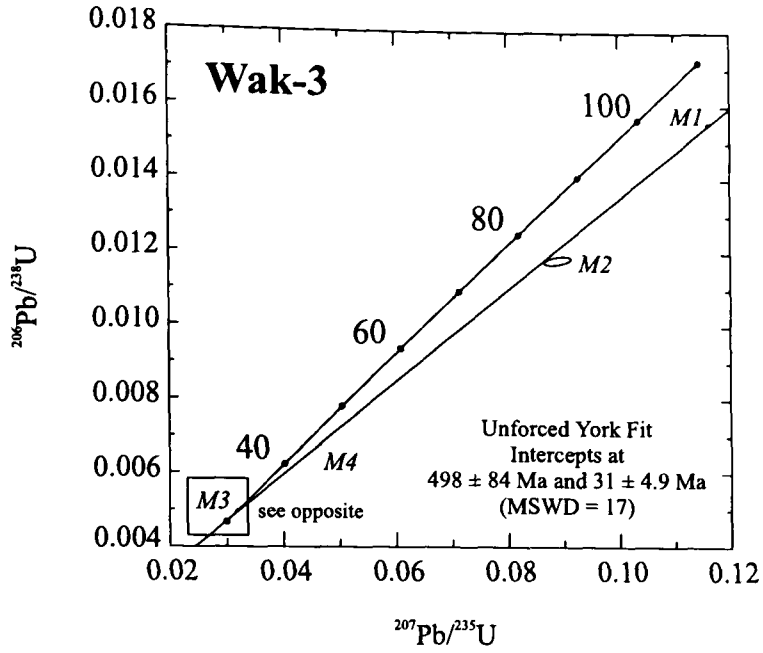
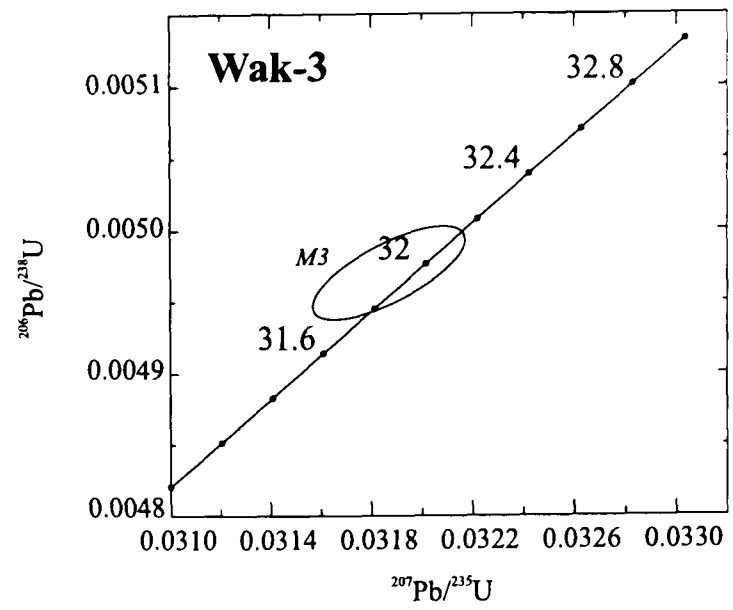
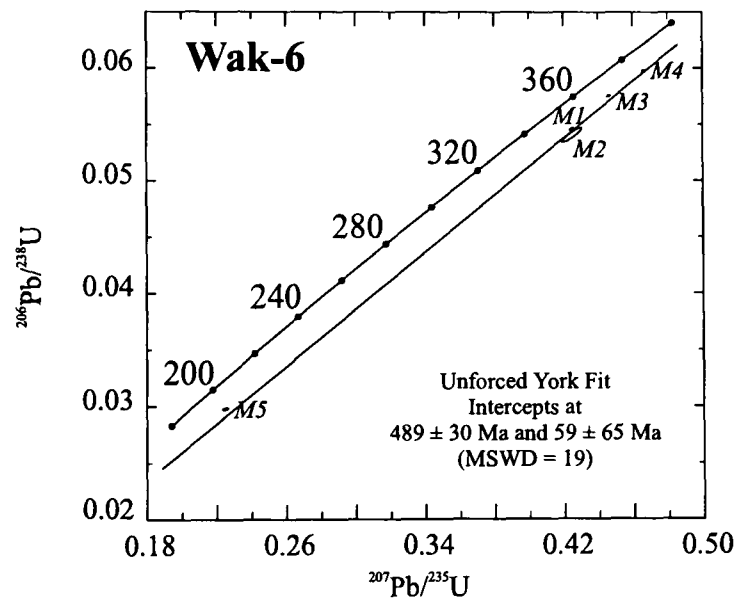


Figure 7.2: Map showing the location of samples collected for geochronological analysis (red text) and the results of previous geochronological work within the study area. For comparative purposes, the results of the muscovite cooling ages from samples Wak 3, Wak 6 and Wak 9 are shown. See text and subsequent figures and tables for other results.

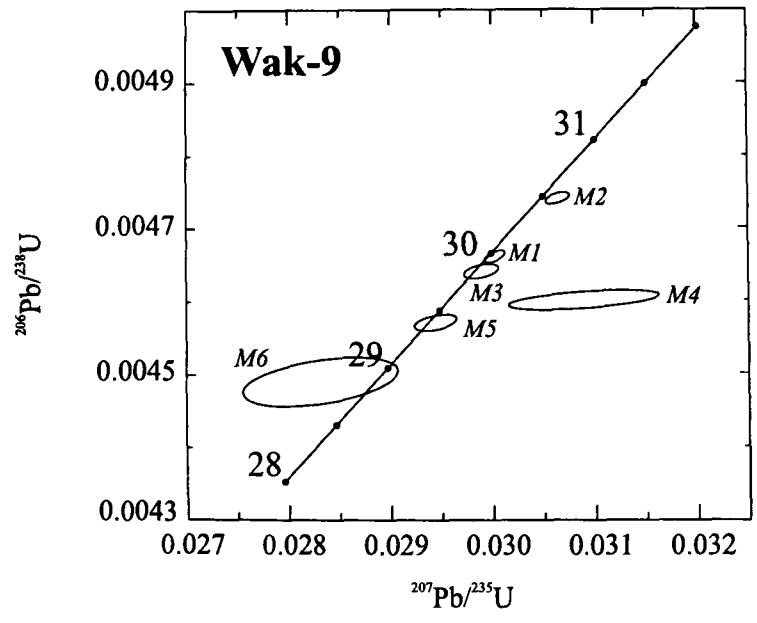




(a)

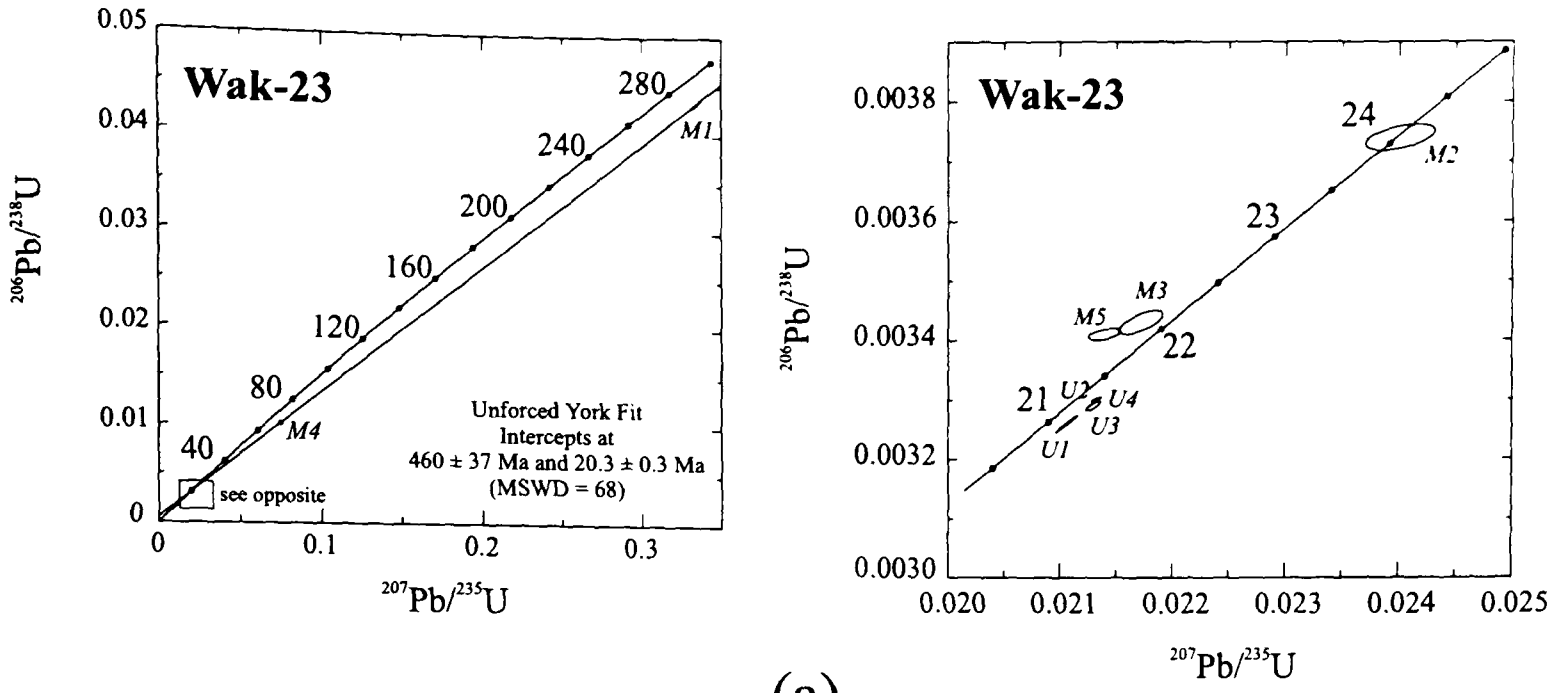


(b)

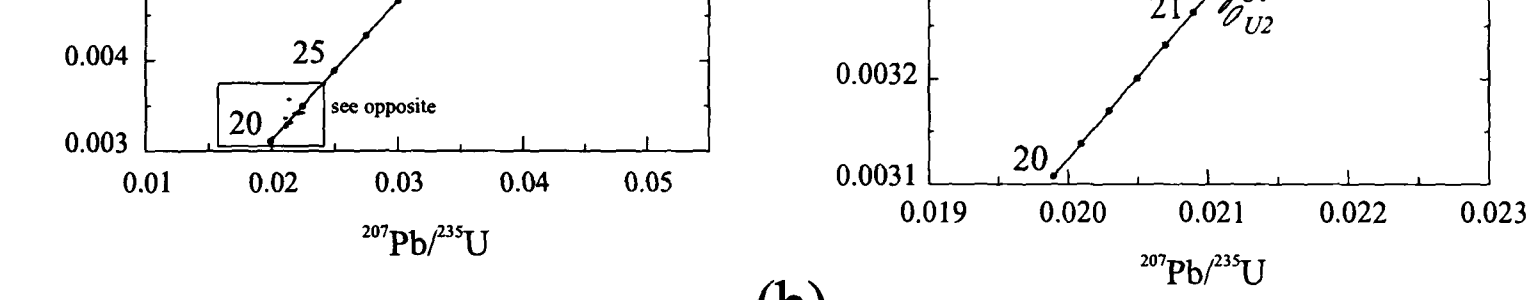


(c)

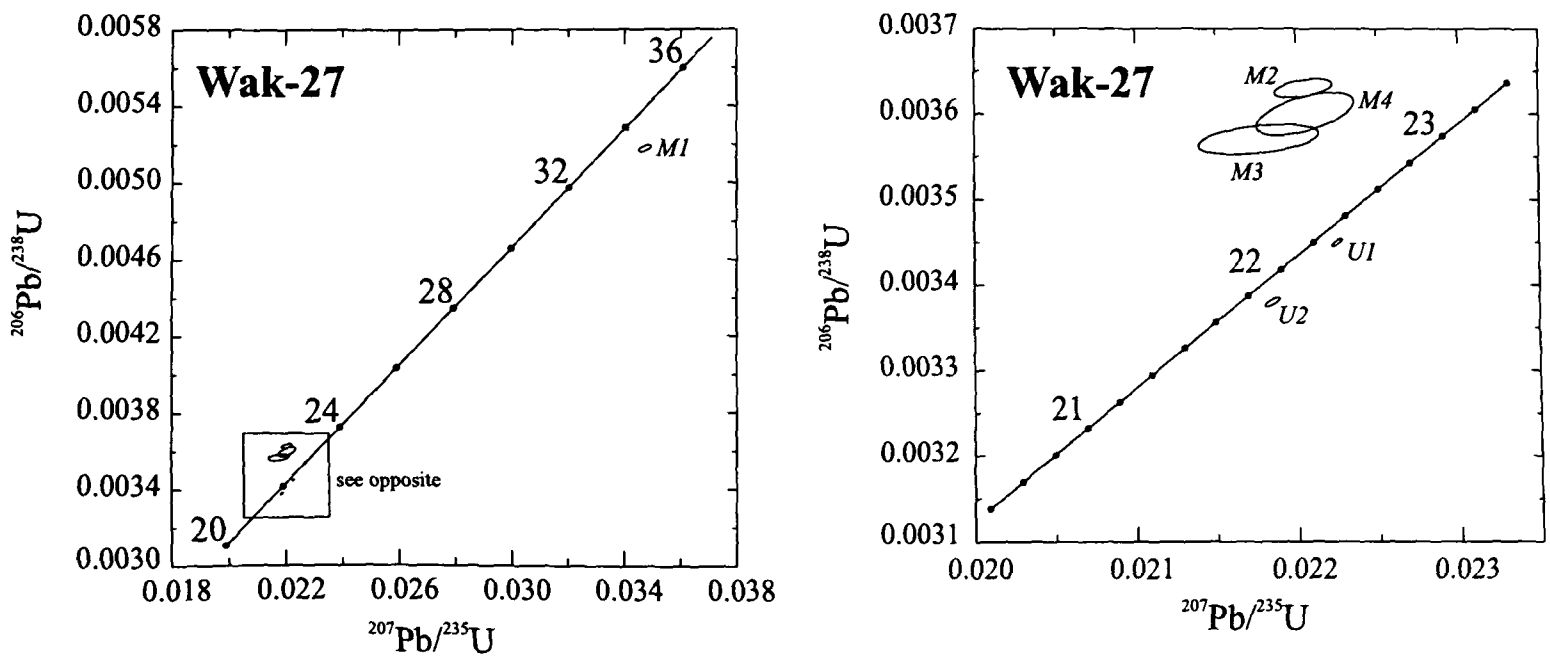
Figure 7.3: U-Pb concordia diagrams for metamorphic samples Wak 3, Wak 6 and Wak 9 (see Table 7.1a for data).



(a)

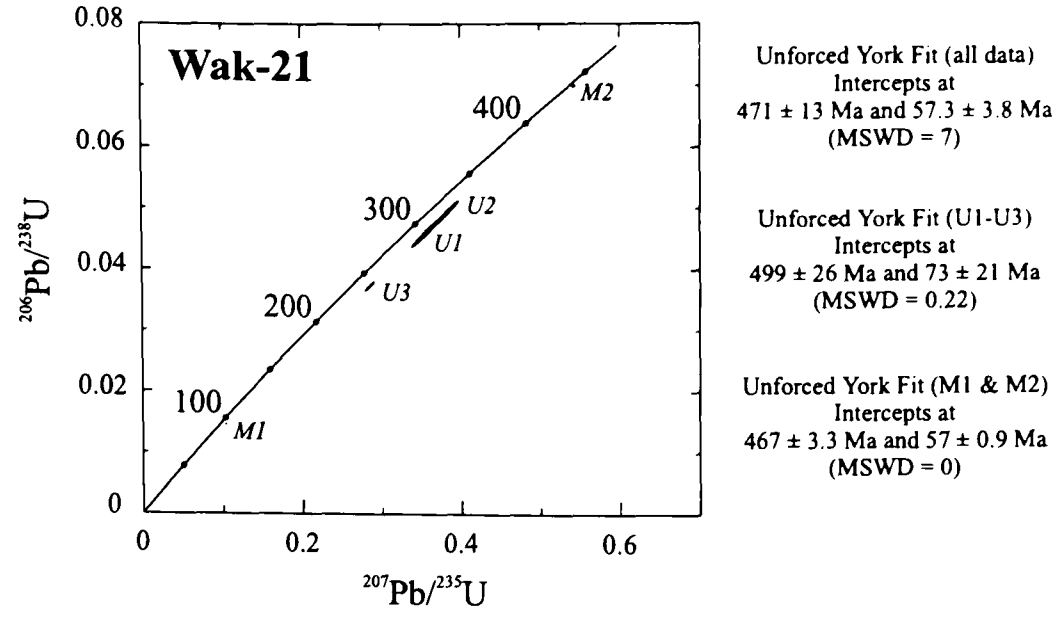


(b)

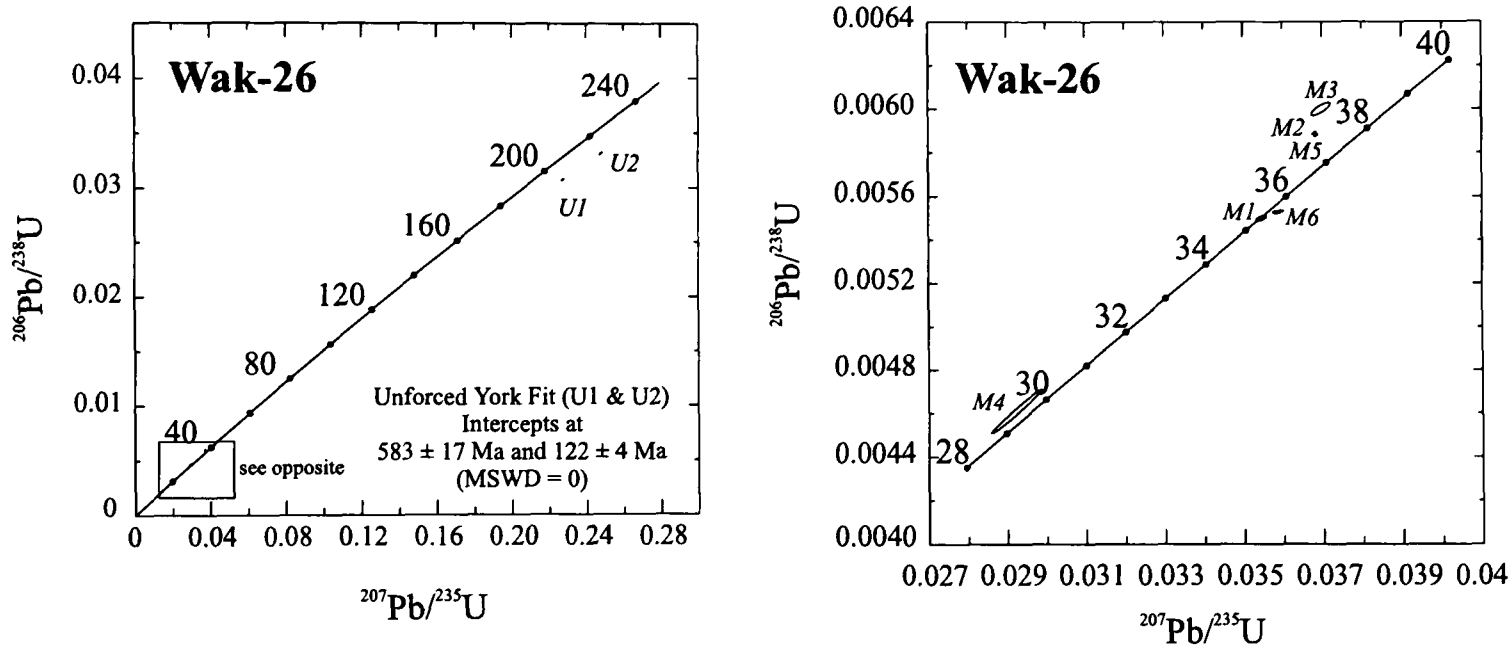


(c)

Figure 7.4: U-Pb concordia diagrams for magmatic samples Wak 23, Wak 24 and Wak 27 (see Table 7.1b for data)

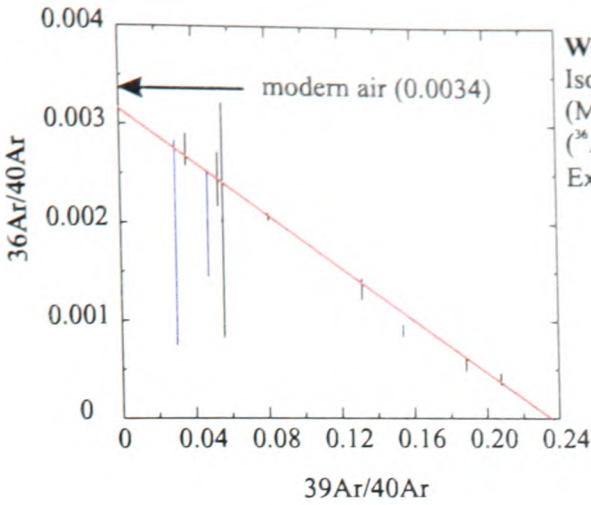


(a)

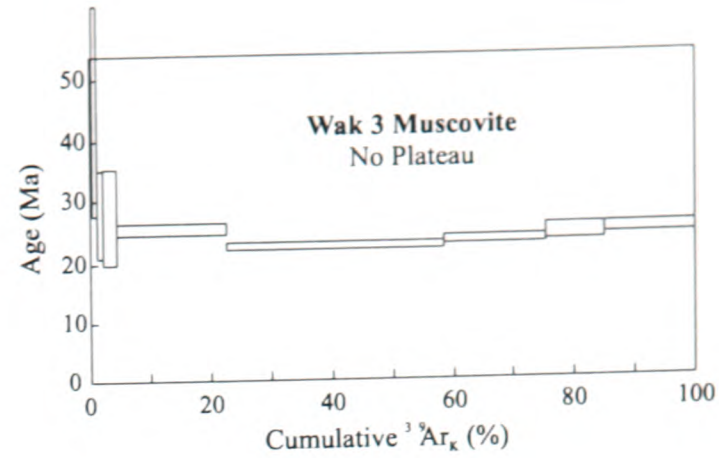


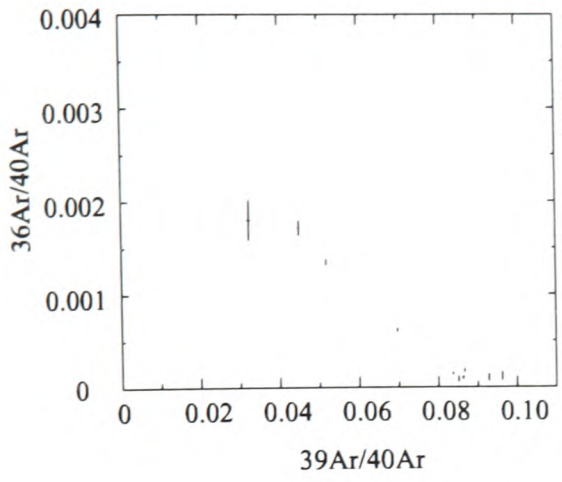
(b)

Figure 7.5: U-Pb concordia diagrams for pegmatite samples Wak 21 and Wak 26 (see Table 7.1c for data).



Wak 3 Muscovite
Isochron age: 22.0 ± 0.8 Ma
(MSWD = 1.65)
$(^{36}Ar/^{40}Ar)_o$: 0.00314 ± 4%
Excluding steps 1, 3 & 10 (blue)





Wak 3 Biotite
No statistically significant isochron possible

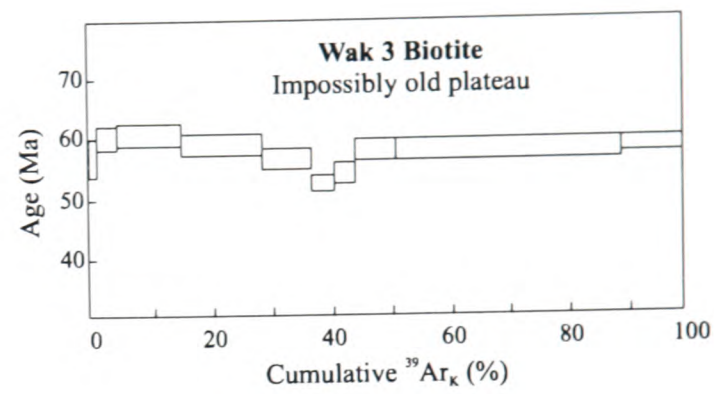
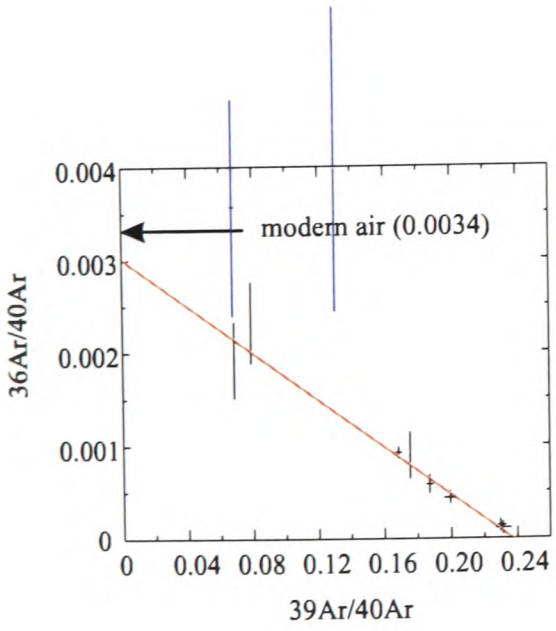
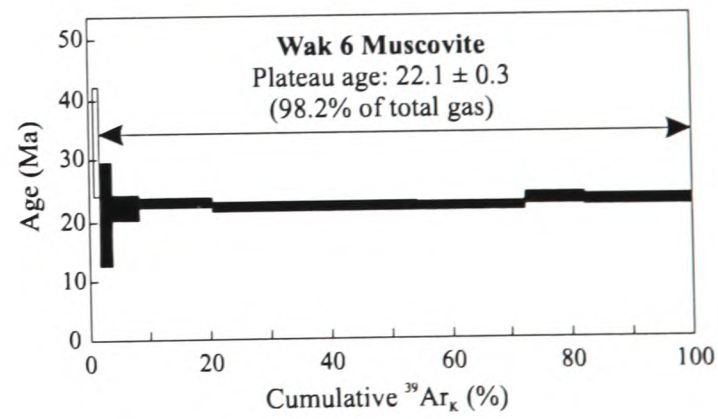
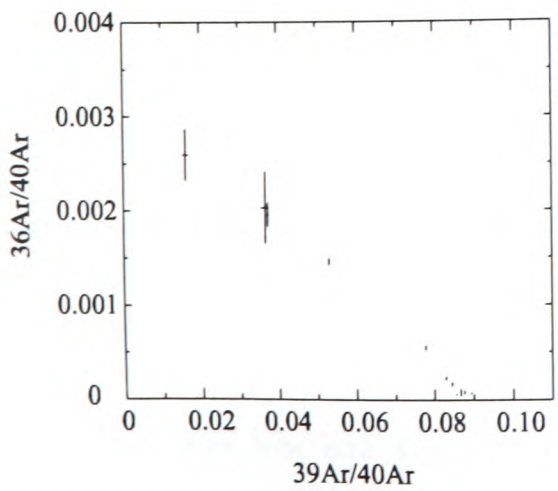


Figure 7.6a: Wak 3 muscovite and biotite cooling data (lower part of slab).



Wak 6 Muscovite
Isochron age: 21.7 ± 0.6 Ma
(MSWD = 1.46)
$(^{36}Ar/^{40}Ar)_o$: 0.00302 ± 8%
Excluding steps 1, 2 (blue)





Wak 6 Biotite
No statistically significant isochron possible

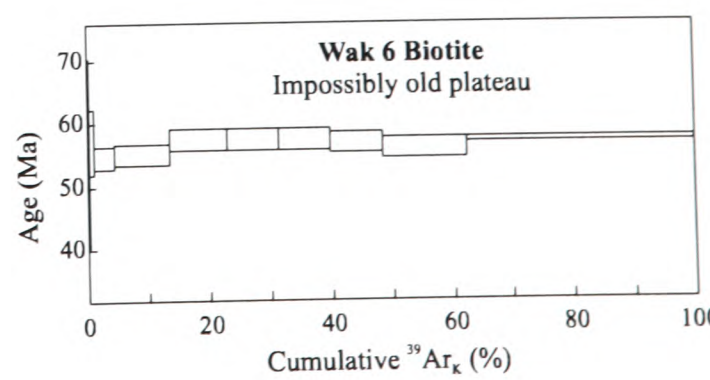
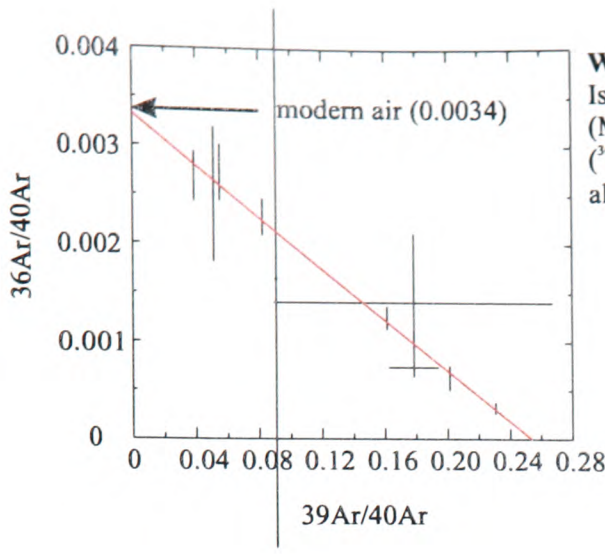
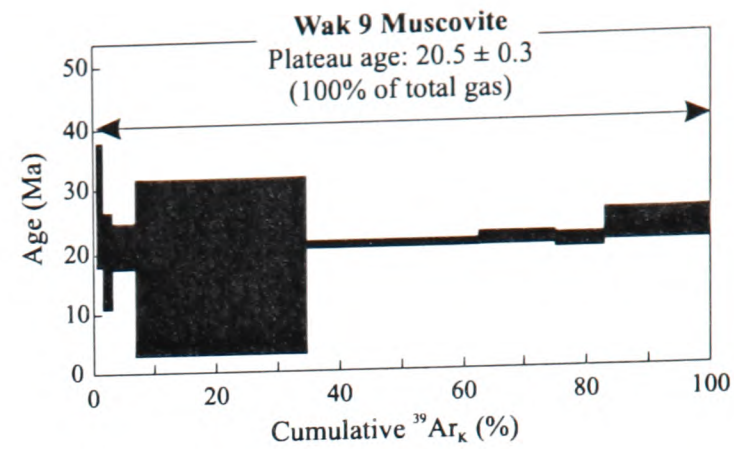
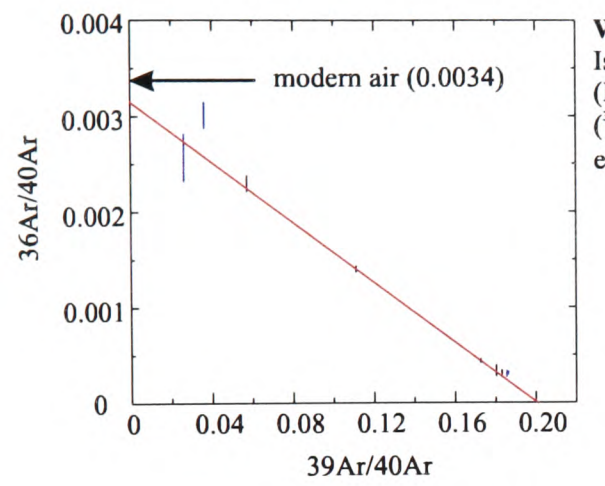


Figure 7.6b: Wak 6 muscovite and biotite cooling data (middle part of slab).



Wak 9 Muscovite
Isochron age: 20.4 ± 0.6 Ma
(MSWD = 1.06)
$(^{36}Ar/^{40}Ar)_o$: 0.00331 ± 5%
all steps included





Wak 9 Biotite
Isochron age: 25.9 ± 0.2 Ma
(MSWD = 0.88)
$(^{36}Ar/^{40}Ar)_o$: 0.00315 ± 2%
excluding steps 1,2 & 9-11 (blue)

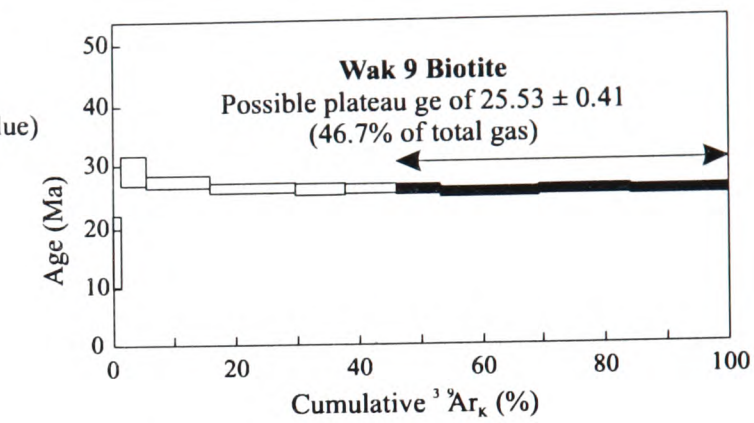
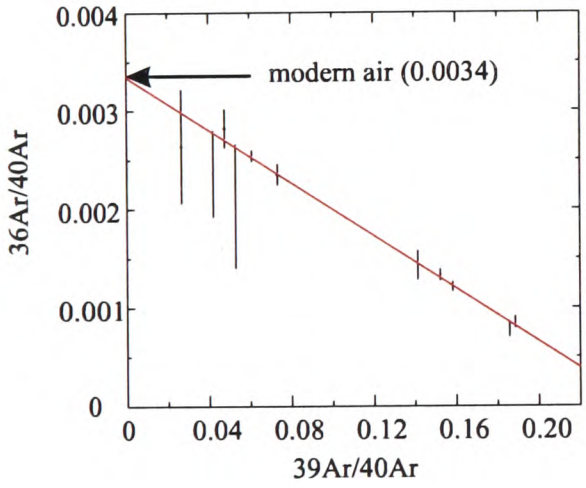


Figure 7.6c: Wak 9 muscovite and biotite cooling data (upper part of slab).



Wak 21 Muscovite
Isochron age: 20.8 ± 0.7 Ma
(MSWD = 1.78)
$(^{36}Ar/^{40}Ar)_o$: 0.00334 ± 4%
all steps included

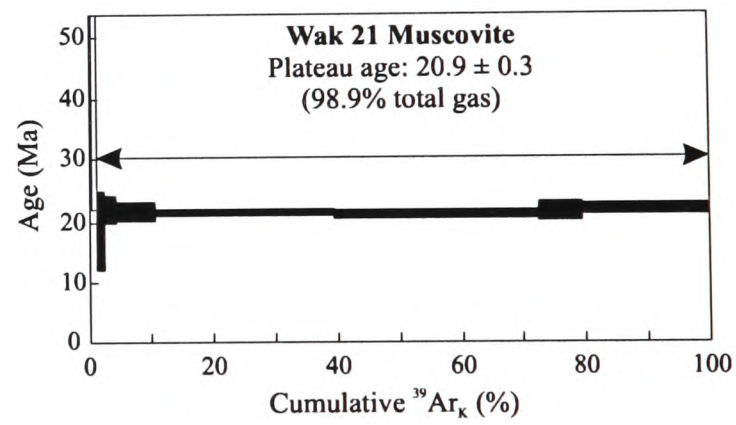
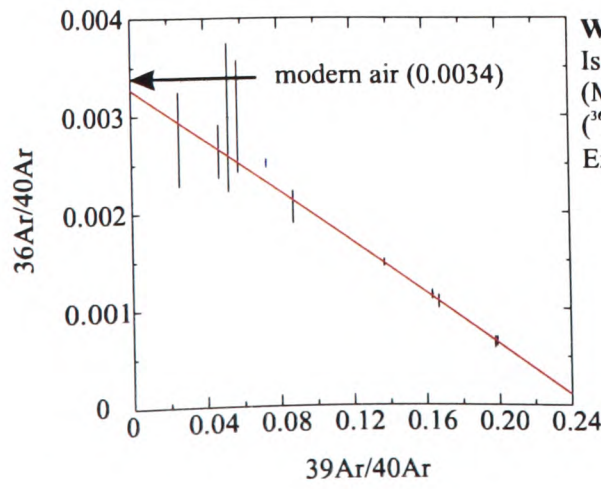


Figure 7.6d: Wak 21 muscovite cooling data (leucocratic pegmatite).



Wak 26 Muscovite
Isochron age: 20.8 ± 0.6 Ma
(MSWD = 0.74)
$(^{36}Ar/^{40}Ar)_o$: 0.00327 ± 4%
Excluding step 6 (blue)

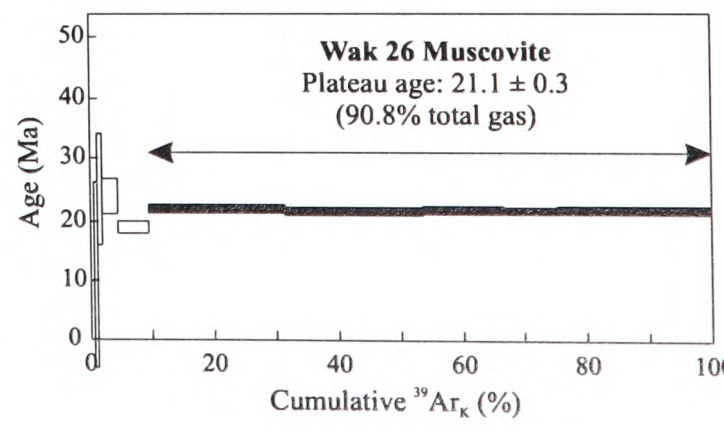
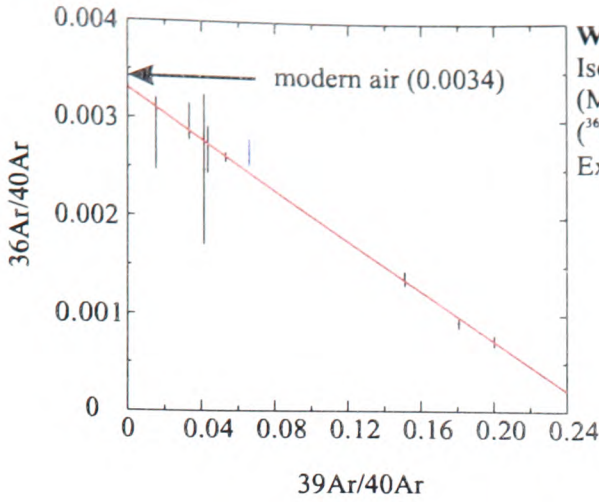
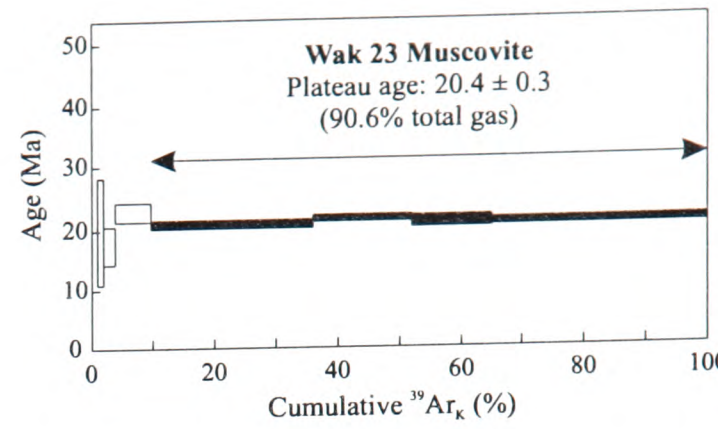
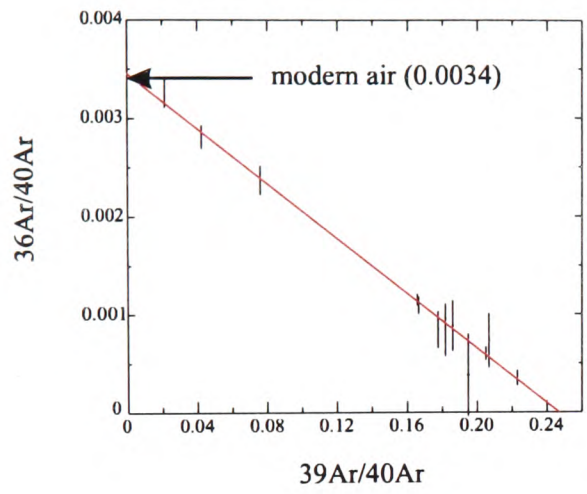


Figure 7.6e: Wak 26 muscovite cooling data (leucocratic pegmatite).



Wak 23 Muscovite
Isochron age: 20.2 ± 0.5 Ma
(MSWD = 1.48)
$(^{36}Ar/^{40}Ar)_o$: 0.00330 ± 2%
Excluding step 5 (blue)





Wak 23 Biotite
Isochron age: 20.9 ± 0.5 Ma
(MSWD = 1.02)
$(^{36}Ar/^{40}Ar)_o$: 0.00345 ± 3%
all steps included

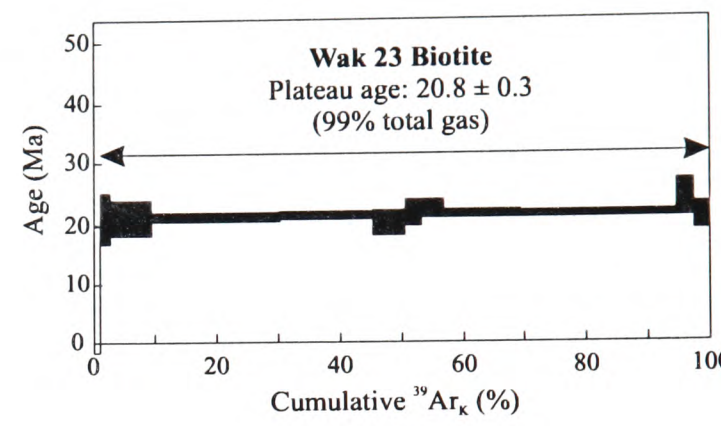
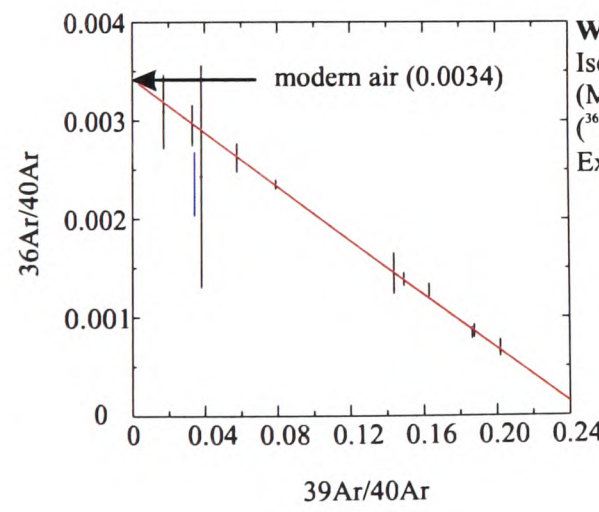
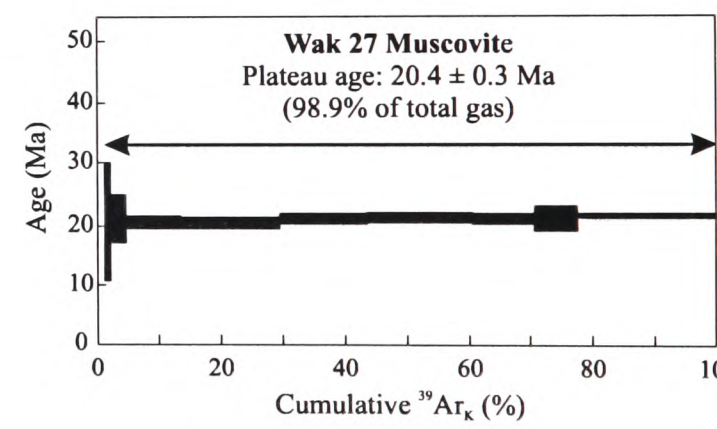
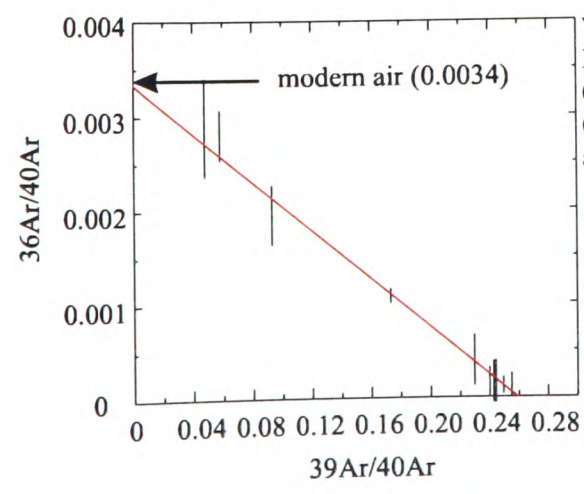


Figure 7.6f: Wak 23 muscovite and biotite cooling data (undeformed leucogranite, close to the central part of the Gumburanjon pluton).



Wak 27 Muscovite
Isochron age: 20.6 ± 0.6 Ma
(MSWD = 1.75)
$(^{36}Ar/^{40}Ar)_o$: 0.00342 ± 2%
Excluding step 3 (blue)





Wak 27 Biotite
Isochron age: 20.0 ± 0.3 Ma
(MSWD = 0.85)
$(^{36}Ar/^{40}Ar)_o$: 0.00334 ± 5%
all steps included

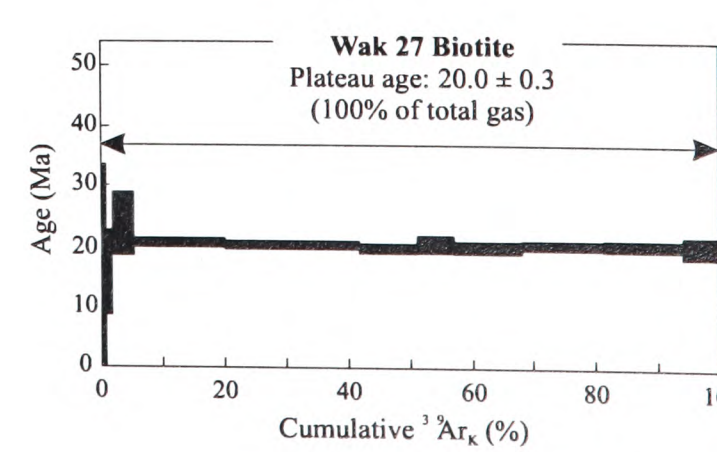


Figure 7.6g: Wak 27 muscovite and biotite cooling data (undeformed leucogranite dyke, discordantly intruding the zanskar shear Zone ~50m below Wak 26).

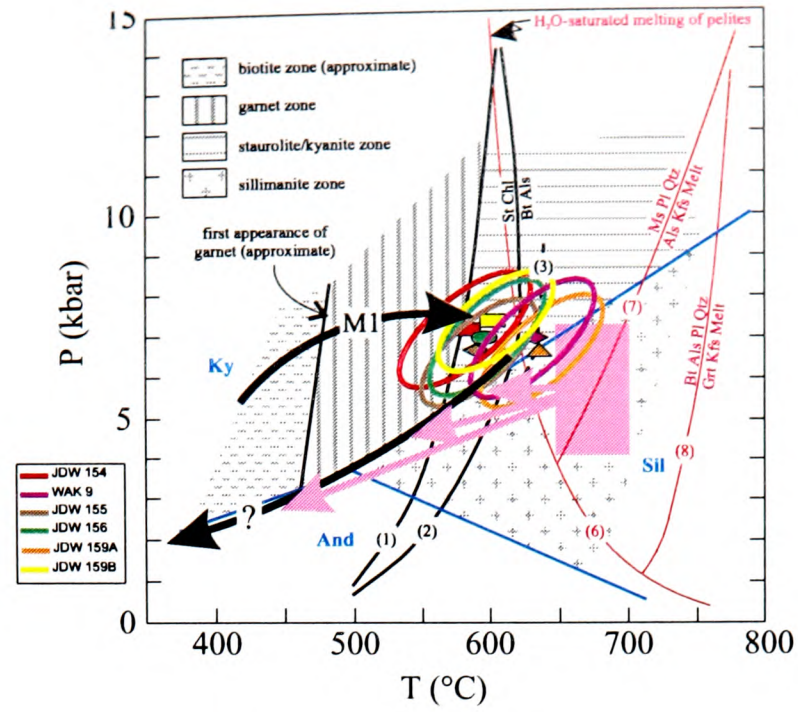


Figure 7.7: Interpreted retrograde P-T trajectory of rocks in the footwall of the ZSZ from near-peak conditions of c.630°C and 7-8 kbar. The Gumburanjon leucogranite is believed to have been generated by dehydration of muscovite at temperatures of c.650-700°C and pressures of <7kbar (pink box). The distance the granite has travelled from its source and the depth of emplacement are more difficult to constrain (pink arrows). The absence of a thermal aureole suggests that the country rocks were at temperatures above c.450°C during emplacement.

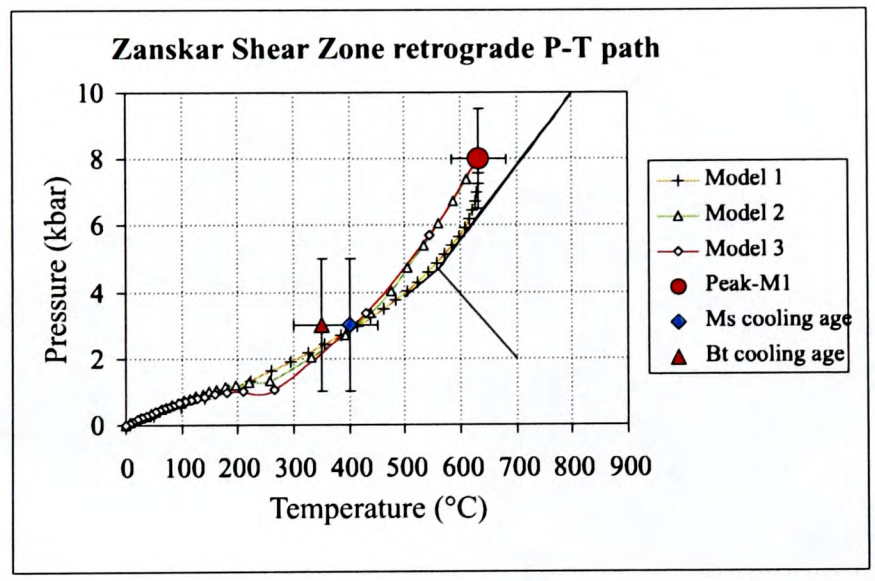


Figure 7.8a: Modelled P-T pathway of rocks in the immediate footwall of the ZSZ adjacent to the Gumburanjon leucogranite. All three models have similar P-T trajectories which are close to that shown in Figure 7.7. Symbols on curves denote 1 Ma intervals from the timing of monazite growth at 30 Ma.

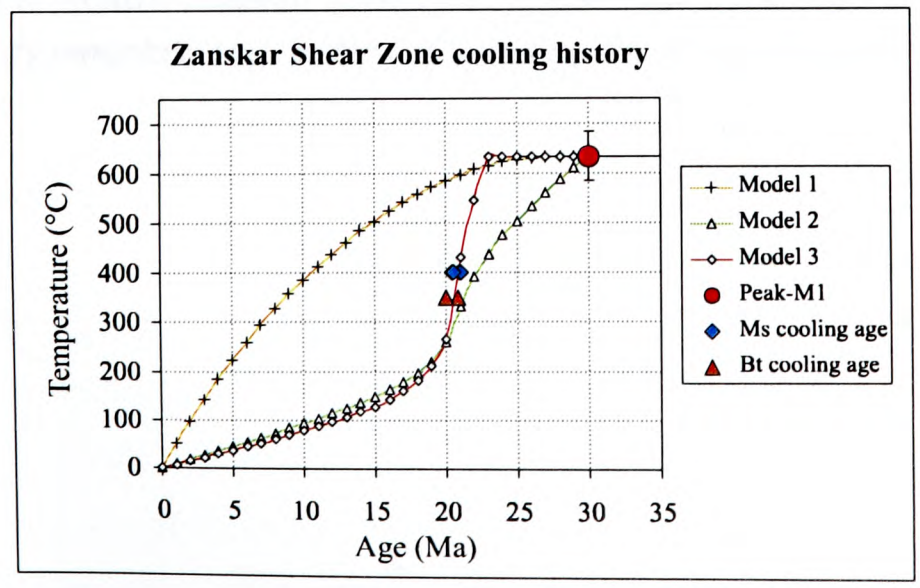


Figure 7.8b: Modelled T-t pathway of rocks in the immediate footwall of the ZSZ adjacent to the Gumburanjon leucogranite. Both models 2 and 3 offer good fits to the temperature data, whilst model 1 does not cool the footwall quickly enough to match the 40Ar/39Ar ages. Symbols on curves denote 1 Ma intervals from the timing of monzite growth in the country rocks at 30 Ma. Note that in model 2 the country rocks are below 450°C at 21-22 Ma, whilst in model 3 they are at c.450-550°C.

Chapter 8

Summary and conclusions

8.1 Introduction

This chapter summarises the work presented in Chapters 3-7 of this thesis. Figure 8.1 presents a time-event chart which summarises the depositional and tectono-metamorphic evolution of the High Himalayan Slab in SE Zanskar and NW Lahaul. Figure 8.2 presents a tectonic model which charts the syn/post-collisional history of the High Himalayan Slab following the India-Asia collision some 54-50 Ma ago. The pre- and syn/post-collisional history is synthesised in the following sections.

8.2 Pre-collision history

Field mapping across a large part (*c.*10,000 km^2) of the High Himalayan Slab in SE Zanskar and NW Lahaul demonstrates that the metasedimentary protoliths of this metamorphic terrane show remarkable lithological similarity across the entire study area and are interpreted to comprise a 3-5km-thick succession of unfossiliferous sands, silts and shales which were deposited in an extensive sedimentary basin during the Precambrian/Cambrian (Chapter 3). These sediments are collectively referred to as the Haimantas and are tentatively correlated with the Phe Formation in the Tibetan Sedimentary Series. They are extremely immature deposits and were derived from a magmatic source rock provenance, the location of which cannot be readily determined.

The Haimantas become increasingly calcareous towards the top of the succession, suggestive of an overall shallowing-up of the sedimentary sequence. They are overlain by the dolomitic Middle Cambrian(?) Karsha Formation in the upper part of the slab and are discordantly intruded by a number of large K-feldspar granites of Precambrian-Ordovician age. The available field evidence suggests that these granites are unlikely to represent the crystalline basement upon which the Haimantas were deposited (discordant contacts were observed along many of these granites). Indeed, the shallowing-up sequence seen in the Haimantas, together with the S-type geochemical signature of the granites (Thöni, 1977) suggests they may have been generated and emplaced in a major collisional tectonic setting at the end of the Cambrian. This is supported by geochronological data presented in Chapter 7 which demonstrates that the Haimantas preserve evidence for a phase of monazite growth at *c.*500 Ma. This may be related to a regional Barrovian-type metamorphism which preceded granite emplacement. However, field and microstructural analysis of the chlorite- and biotite-grade sediments within the Haimantas failed to find any convincing evidence to support the existence of a major pre-Himalayan deformation and metamorphism. This suggests the possibility that the granites were emplaced in a rift-type setting, in which case growth of monazite at *c.*500 Ma may be related to contact metamorphism in a major thermal aureole.

In the Chandra valley, the Haimantas are overlain by the Permian-Jurassic Tandi Group, which an interbedded sequence of marine limestones, dolomites, graphite-rich marls, sandstones, quartzites and calcarenites. The fact that the Tandi Group form an outlier within the High Himalayan Slab suggests it was deposited in a small rift basin located to the south of Neo-Tethys (Figure 8.2a). The Tandi Group is folded into the core of an isoclinal, NE-facing syncline (the Tandi Syncline). This deformation is undoubtedly Himalayan in age and attests to intense crustal shortening and thickening of the Indian plate margin following the India-Asia collision some 50-54 Ma ago (Searle *et al.*, 1987; Garzanti & van Haver, 1988).

8.3 Syn/post-collisional history

Following the India-Asia collision, the High Himalayan Slab in SE Zanskar and NW Lahaul experienced a polyphase deformation history associated with the progressive burial and subsequent exhumation of this metamorphic terrane. The net result of this was to create a ~70-100-km-wide zone of chlorite- to sillimanite-grade lithologies which are structurally bounded along the base by the Main Central Thrust (MCT) and along the top by the Zanskar Shear Zone (ZSZ), a local equivalent of the South Tibetan Detachment system.

The High Himalayan Slab in SE Zanskar and NW Lahaul is unique in that it does not display the uniform NE-dipping tectonic foliation seen in other parts of the High Himalaya. Deformation was extremely heterogeneous across the slab and it is virtually impossible to correlate structural fabrics and stages of metamorphic mineral growth from one region to another from field and microstructural observations alone (see Chapters 4-6). Metamorphism is interpreted to be dominantly Himalayan in age, although geochronological evidence supports the existence of a *c.*500 Ma thermal event of some kind. Field mapping of metamorphic isograds reveals a pattern of high-grade metamorphic domes (e.g. the Kang La Dome) and low-grade metamorphic depressions (e.g. the Chamba Syncline). The low-grade regions show both lithological and structural continuity with the underlying higher-grade regions, suggesting them to be an integral part of the High Himalayan Slab, rather than a tectonic cover-sequence. These regions have clearly never been buried to any significant depth following the India-Asia collision and preserve useful information pertaining to the early stages of collision.

8.3.1 Burial history

Burial of the upper part of the slab

The kinematics associated with crustal shortening and thickening in the upper part of the High Himalayan Slab in SE Zanskar and NW Lahaul are poorly constrained. Metamorphic grade is observed to increase towards the north, suggesting the possibility that the protoliths of the High Himalayan slab were progressively buried by overthrusting of the Tibetan Sedimentary Series towards the SW along a major thrust, which may have been a precursor to the ZSZ (Figure 8.2b).

Burial of the lower part of the slab

In the lower part of the slab, thickening initially occurred by NE directed isoclinal folding, leading to the development of the NE-facing Tandi Syncline (Figure 8.2b). The kinematics of this deformation are difficult to reconcile with classic Himalayan models which show the majority of structures in the High Himalayan Slab to be SW-facing. The Tandi Syncline is therefore interpreted to form part of a major backfold which developed on the southern side of a large Precambrian-Ordovician granite (the Kade granite). NE-facing structures are not seen on the northern side of this granite in the upper part of the slab, thus implying that the granite may have acted as a rigid backstop to deformation, promoting the development of NE-facing structures. NE-facing folds can be traced along strike of the Tandi Syncline into the chlorite-grade sediments of the Chamba Syncline, suggesting that early NE-directed deformation was developed on a regional scale in this part of the Himalaya. The fact that lithologies within the Chamba Syncline are located within the chlorite-zone, together with the NE-facing direction of early fold structures suggests that the Chamba Syncline forms part of a major pop-up zone which developed to the south of the Kade granite (Figure 5.13).

In the higher-grade lithologies beneath the Tandi Syncline, fold structures are consistently overturned towards the SW. The best example of this is the Phojal-Kallath megafold which represents a kilometre-scale nappe located immediately above the projected level of the MCT at the base of the slab. Metamorphic isograds appear to be folded around this structure, producing the characteristic inverted metamorphic sequence at the base of the slab. Microstructural observations demonstrate that this deformation was syn-metamorphic and probably pre-dated the most intense phase of movement along the MCT (Figures 8.1 & 8.2c & d).

Metamorphism in response to crustal shortening and thickening

A protracted metamorphic episode developed in response to the continuously changing thermal structure of the High Himalaya, brought about by crustal shortening and thickening following the India-Asia collision some 50-54 Ma (Figures 8.2b & c). Growth of typical Barrovian-type metamorphic assemblages is related to the prograde thermal history (M_1) of the slab which reached conditions of 6-8 kbar and 550-650°C in the deepest exposed levels. $^{40}Ar/^{39}Ar$ cooling ages of metamorphic muscovite from these regions demonstrates that peak-metamorphic conditions were attained prior to *c.*22 Ma. Metamorphic monazite from the upper and lower parts of the slab record $^{207}Pb/^{235}U$ ages of *c.*30 Ma and *c.*32 Ma respectively. Given the fact that monazite is not especially prone to Pb-loss (Zhu *et al.*, 1997), these ages are interpreted to reflect monazite growth at temperatures in excess of *c.*500°C. However, whether this growth occurred during the prograde P-T pathway, or whether it reflects near-peak conditions remains uncertain. The possibility that these results reflect an age-averaging of growth zoned monazite cannot be ruled out.

Crustal melting

In deeper structural levels, temperatures were sufficiently high to promote *in situ* migmatisation of sillimanite-grade pelitic schists, leading to the generation of crustal melt leucogranites. Crustal melting is closely associated with the growth of sillimanite- and cordierite-bearing assemblages and is attributed to an M_2 metamorphic stage which post-dated the growth of garnet-, staurolite- and kyanite-bearing assemblages during the M_1 metamorphic stage. It should be stressed, however, that both M_1 and M_2 form part of a continuously evolving metamorphic event, with no evidence to support a period of cooling between them. M_2 metamorphism is related to decompression of the High Himalayan Slab under high temperature conditions and is associated with the development of large-scale metamorphic domes which are flanked by extensional detachments, namely the ZSZ and Miyar Fault Zone (MFZ).

The Gumburanjon leucogranite represents a higher-level pluton which has been detached from its source and is located in the immediate footwall of the ZSZ at the eastern end of the Kargyak Chu. Geochemical data suggest that it was generated by dehydration melting of muscovite at temperatures of *c.*650-700°C and pressures of <7 kbar (Chapter 6). Field relationships, thermobarometric and geochronological data demonstrate that the Gumburanjon leucogranite was intruded into the immediate footwall of the ZSZ at 21-22 Ma at pressures of *c.*3-6 kbar, corresponding to depths of *c.*11-22 km. Muscovite and biotite $^{40}Ar/^{39}Ar$ cooling ages are indicative of this granite cooling rapidly to 300-350°C by 20-21 Ma, a process which is attributed to rapid exhumation in the immediate footwall of the ZSZ (Chapter 7). Field and thermobarometric data imply that it was intruded into rocks which were still hot (below the brittle-ductile transition), and that it was probably sourced from an underlying zone of sillimanite-grade migmatites. Whether crustal melting was triggered by normal faulting, or whether crustal melting de-stabilised the High Himalayan Slab and triggered normal faulting remains uncertain. Irrespective of this 'chicken and egg' problem, the available evidence suggests that normal faulting and crustal melting are inextricably linked and that shear heating along the MCT was not the major mechanism involved in melt generation. This is largely based on the observation that the Gumburanjon leucogranite was generated at depths of *c.*11-21 km, which is still *c.*5-10 km structurally above the projected level of the MCT (Figure 6.27). The similarity of mica cooling ages in the MCT and ZSZ does suggest, however, that thrusting along the MCT may have forced the High Himalayan Slab out of dynamic equilibrium, thus facilitating extensional collapse and crustal melting in the upper part of the slab (Figure 8.2d).

8.3.2 Exhumation history

Rocks of different metamorphic grade are exposed within the High Himalayan Slab of SE Zanskar and NW Lahaul. Chlorite- and biotite-grade lithologies are exposed in metamorphic depressions, whilst kyanite- and sillimanite-grade lithologies are exposed in the cores of metamorphic domes, which are flanked by major extensional detachments (namely the ZSZ and possibly the MFZ). The distribution of metamorphic facies suggests that thermal doming and extensional unroofing were important mechanisms in the exhumation of the slab. Thermal doming of high-grade regions appears

to have been compensated for by structural downwarping of lower-grade regions, the best example of this being the Chamba Syncline (Figure 5.13).

The highest-grade parts of the slab are consistently located in the footwall of the ZSZ, suggesting that normal faulting was of fundamental importance in the exhumation history of the slab. Deformation along the ZSZ was accommodated in a 1-2km-thick zone of biotite- to kyanite-grade mylonites which display abundant top-to-the-north-east shear-sense indicators. Comparisons of metamorphic grade either side of the ZSZ suggest that the throw across this fault is in the order of *c.*20 km. Simple angular relationships combined with quantitative P-T data imply that rocks exposed in the footwall were once located ~35-55km to the north of their current position (Figure 6.21). The absence of major molasse basins in the Tibetan Sedimentary Series implies that the hangingwall remained stationary relative to the footwall during exhumation. The majority of this movement is believed to have occurred during a very brief period of activity between *c.*20-23 Ma (Figure 8.2d). This is based on the fact that: (1) movement along the ZSZ in SE Zanskar and NW Lahaul appears to have been broadly contemporaneous with thrusting along the MCT at *c.*21-16 Ma (Frank *et al.*, 1977); and (2) Rb-Sr and $^{40}Ar/^{39}Ar$ cooling ages from across the entire High Himalayan Slab in SE Zanskar and NW Lahaul obey the traditional age sequence of t(Ms, Rb-Sr) > t(Ms, $^{40}Ar/^{39}Ar$) > t(Bt, Rb-Sr) and indicate that cooling below *c.*350-400°C in currently exposed levels was accomplished by *c.*21-22 Ma (Figure 7.2). This strongly suggests that the entire slab was extruded as an orogenic wedge between the MCT and ZSZ during the early Miocene, supporting the model of Searle and Rex (1989). If these age data are correct, then it is conceivable that the High Himalayan Slab in SE Zanskar and NW Lahaul reached its maximum elevation at *c.*21 Ma and that those lithologies currently exposed were located to within a few kilometres of the earth's surface by this time. For the past *c.*20 million years, unroofing in the High Himalayan Slab is believed to have been accommodated by limited brittle normal faulting and erosional exhumation (Figures 8.2e & f).

8.4 Regional tectonic implications

The work presented in this thesis demonstrates that the most intense period of tectonic activity in the High Himalayan Slab of SE Zanskar and NW Lahaul occurred between *c.*20-23 Ma. This corresponds to the timing of crustal melt generation and emplacement, extensional normal faulting along the ZSZ and thrusting along the MCT. Similar age relationships are observed along the entire ~2500 km length of the High Himalayan Slab from Bhutan to western Zanskar (see Chapter 2). The contemporaneity of this deformation is quite remarkable and suggests that some underlying driving mechanism triggered this period of intense tectonic activity. If this entire process is self-governing, then it would appear that it takes ~30 Ma from the timing of initial collision for the crust to become overthickened in continent-continent orogenic belts such as the Himalaya.

8.5 Future work

This work presents new structural, metamorphic and geochronological data pertaining to the evolution of an area covering *c.*10 000 km^2 in the High Himalayan Slab in SE Zanskar and NW Lahaul. More detailed field mapping in areas of specific structural and metamorphic interest will undoubtedly shed further light on the pre- and syn/post-collisional history in this part of the Himalaya. However, the usefulness of field mapping in its own right is somewhat limited. One of the most important features of this work is that it demonstrates that some of the key issues concerning our understanding of the Himalaya are related to the timing and duration of important thermal and tectonic events. Given the structural and metamorphic framework this thesis provides, the challenge for future workers will be to perform a thorough geochronological study across the entire slab. In particular, if we are to place more emphasis on metamorphic monazite age data, then a better understanding of the metamorphic reactions involved in monazite growth during Barrovian-type events is essential. It is also important to identify whereabouts in the metamorphic assemblage individual grains of monazite are located. Ideally, grains should be chosen which are preferentially located in different porphyroblastic phases such as garnet, staurolite and kyanite so that the prograde metamorphic evolution of the sample can be accurately determined. Sm-Nd and Lu-Hf dating of garnets themselves may shed further light on the timing of Barrovian metamorphic mineral growth in the Himalaya, and may help determine whether any of the garnets are pre-Himalayan in age.

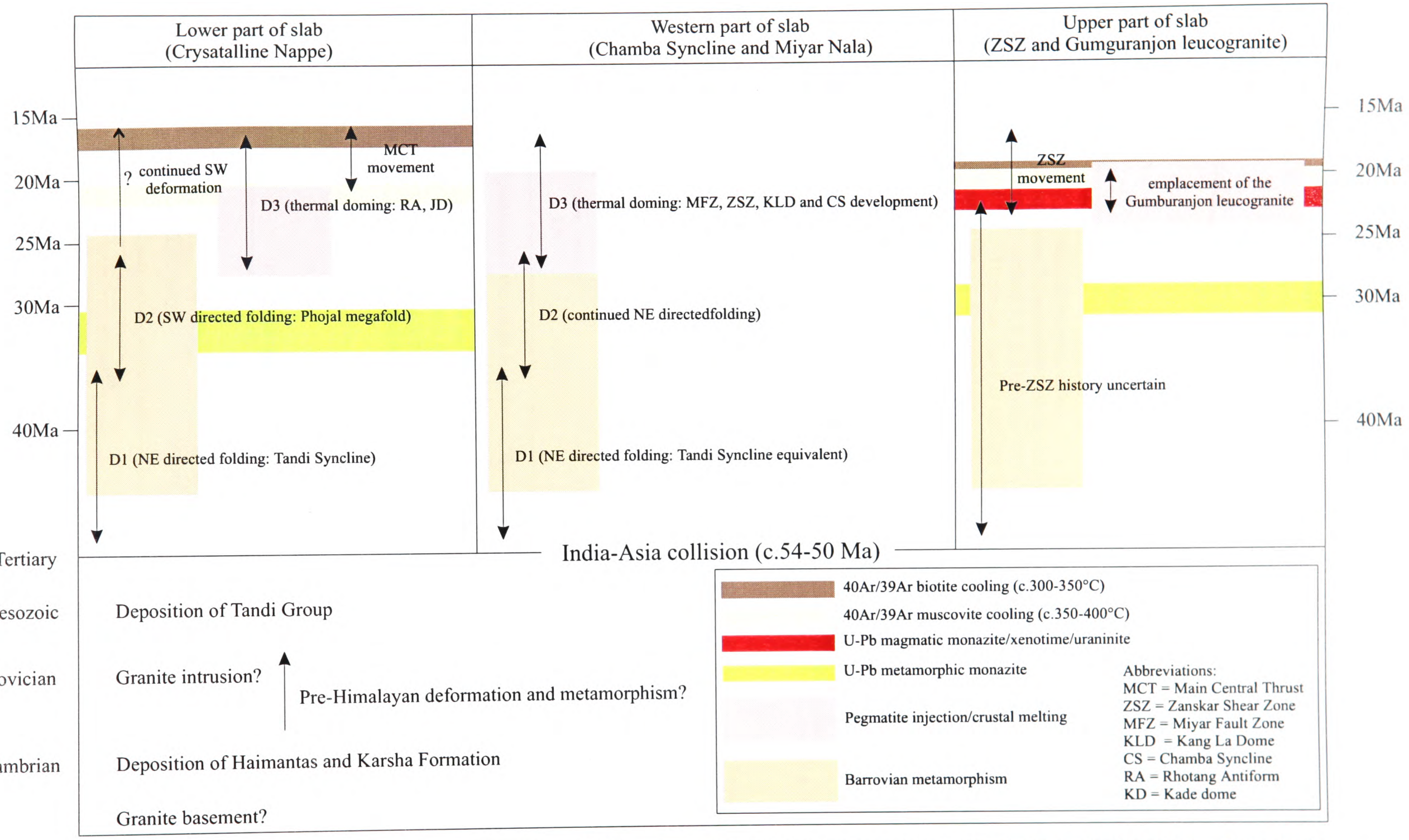


Figure 8.1 Summarised structural and metamorphic history of different parts of the High Himalayan Slab in SE Zanskar and NW Lahaul. Owing to the heterogeneity of deformation across the study area, it is virtually impossible to accurately correlate different deformation phases from one region to another. Consequently, the timing of metamorphic mineral growth cannot be constrained from region to region. U-Pb and 40Ar/39Ar studies provide a means of correlating important thermal and cooling events in different parts of the study area.

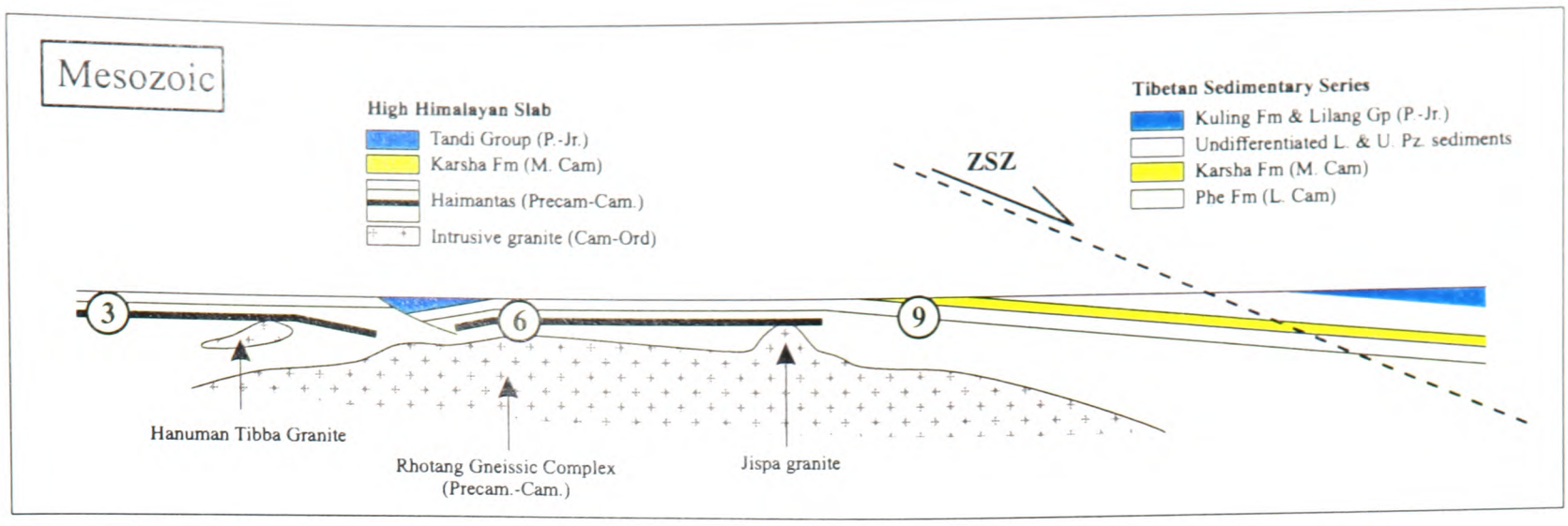


Figure 8.2a: Mesozoic palinspastic reconstruction of the High Himalayan Slab in SE Zanskar and NW Lahaul. The protoliths of the slab represent the equivalents of the sediments now exposed in the Tibetan Sedimentary Series to the north of the ZSZ. Circled numbers 3, 6 & 9 refer to the samples of metamorphic schist collected for geochronological analysis (see Chapter 7). These are used as marker horizons in the subsequent figures to chart the burial and exhumation of the slab following the India-Asia collision some 54-50 Ma ago (Searle et al, 1987; Garzanti & Van Haver, 1988).

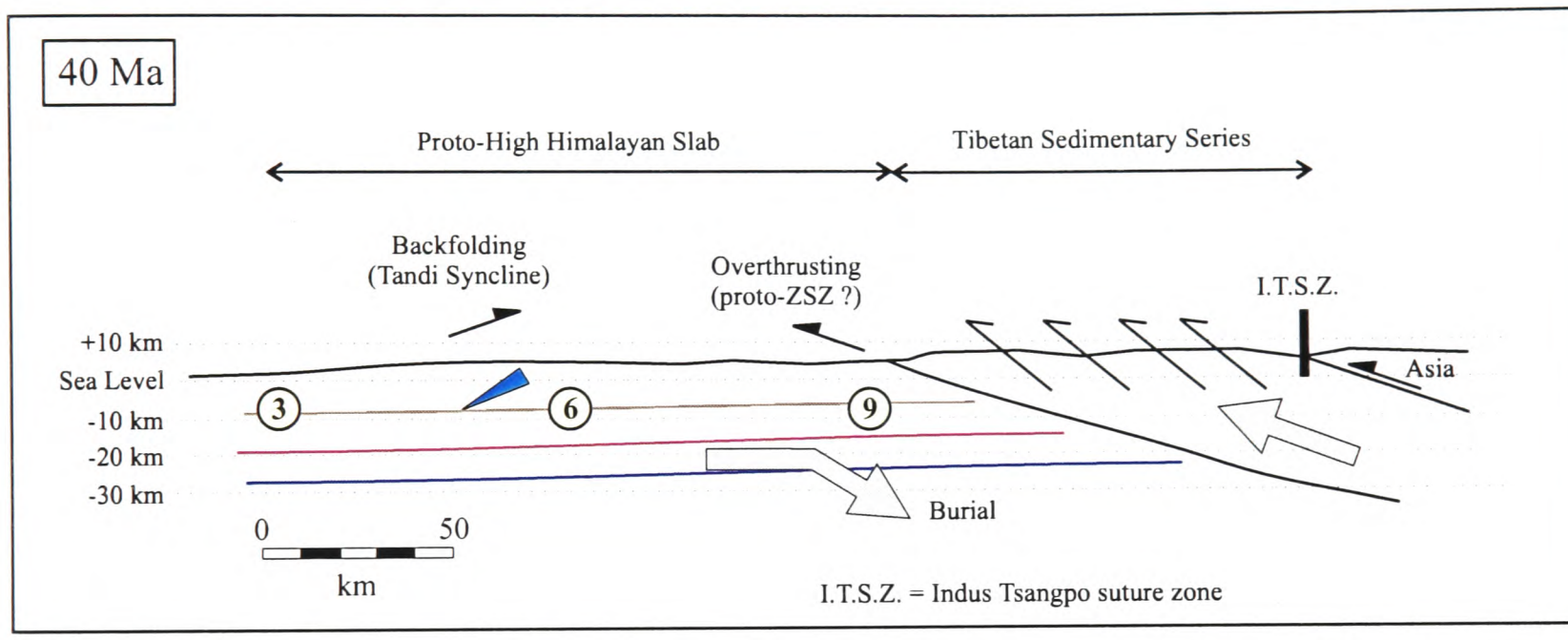


Figure 8.2b: Configuration of the High Himalayan Slab at ~45 Ma, shortly after collision. The early stages of deformation at the base of the slab are associated with NE-directed folding, leading to the development of the NE facing Tandi Syncline. In the upper part of the slab, thickening is interpreted to occur by thrusting of units towards the SW along a major thrust, which may have been a precursor to the ZSZ. The geometry of the isograds is difficult to constrain at this stage and is assumed to represent a layer-cake geometry. Solid lines denote active structures, dashed lines denote incipient structurres, dotted lines denote inactive structures.

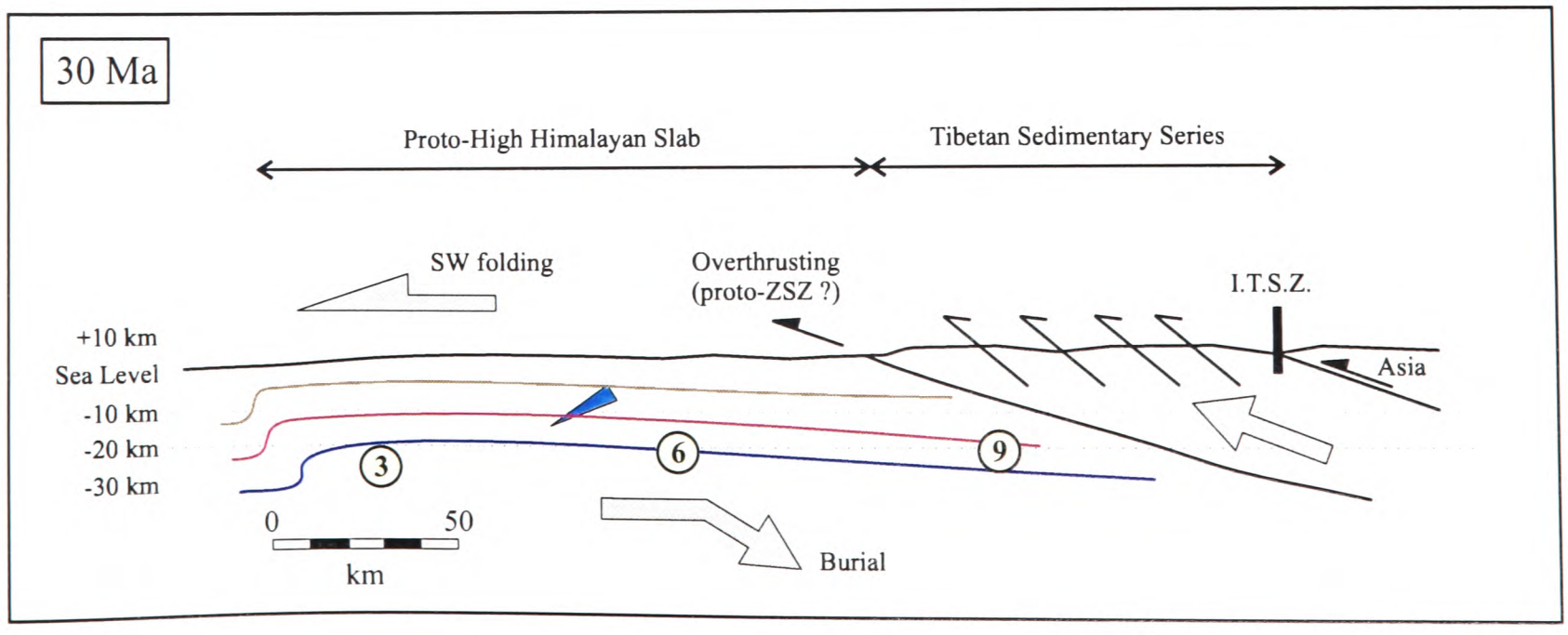


Figure 8.2c: Configuration of the High Himalayan Slab at ~30 Ma. The protoliths of the slab are experiencing kyanite-grade metamorphism (M1) as a direct result of intense crustal shortening and thickening. The early phase of NE-directed folding at the base of the slab is now overprinted by SW-vergent folds, leading to the development of the Phojal-Kallath megafold.

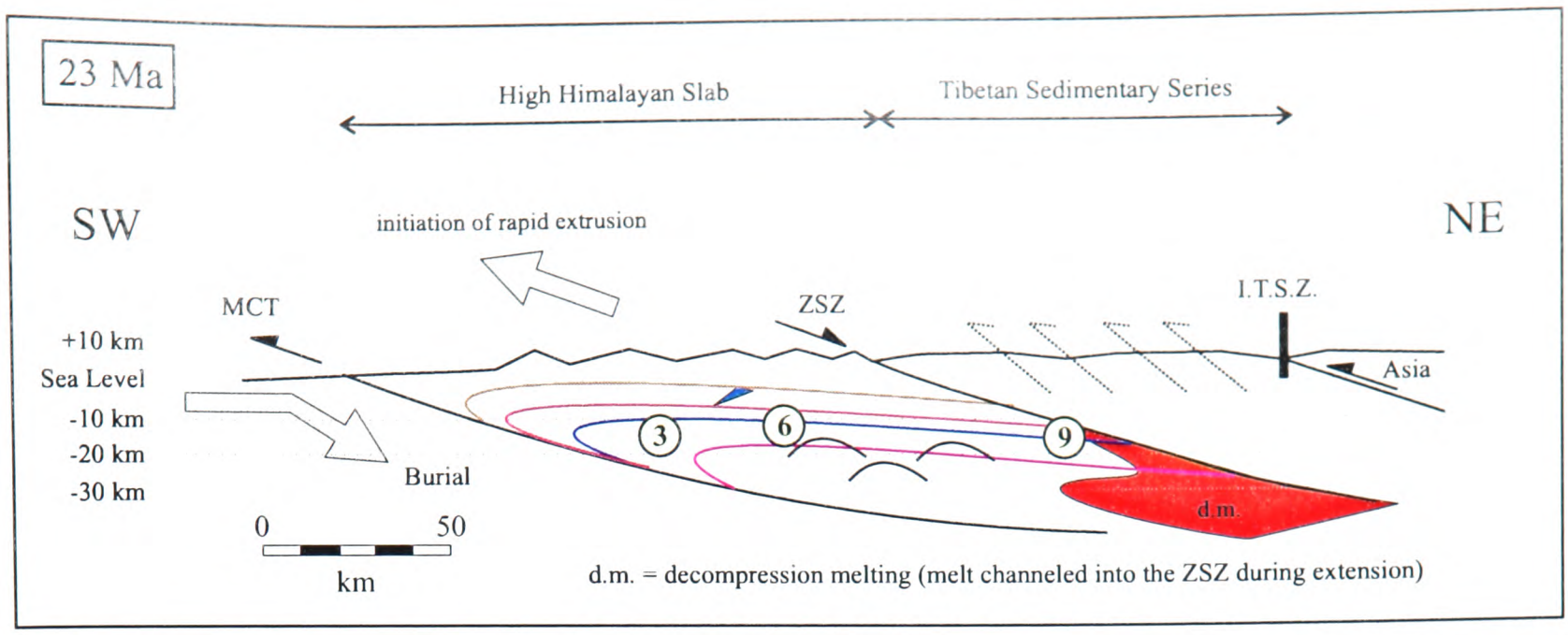


Figure 8.2d: Configuration of the High Himalayan Slab at c.23 Ma, immediately prior to the main phase of movement along the ZSZ and MCT. SW folding results in the initiation of the Phojal-Kallath megafold above the MCT, whilst thermal domes develop in hotter parts of the slab. Exhumation of the slab between the MCT and ZSZ results in decompression melting of deeper structural levels and the growth of M2 metamorphic assemblages. Crustal melts are channeled into the ZSZ and are rapidly chilled.

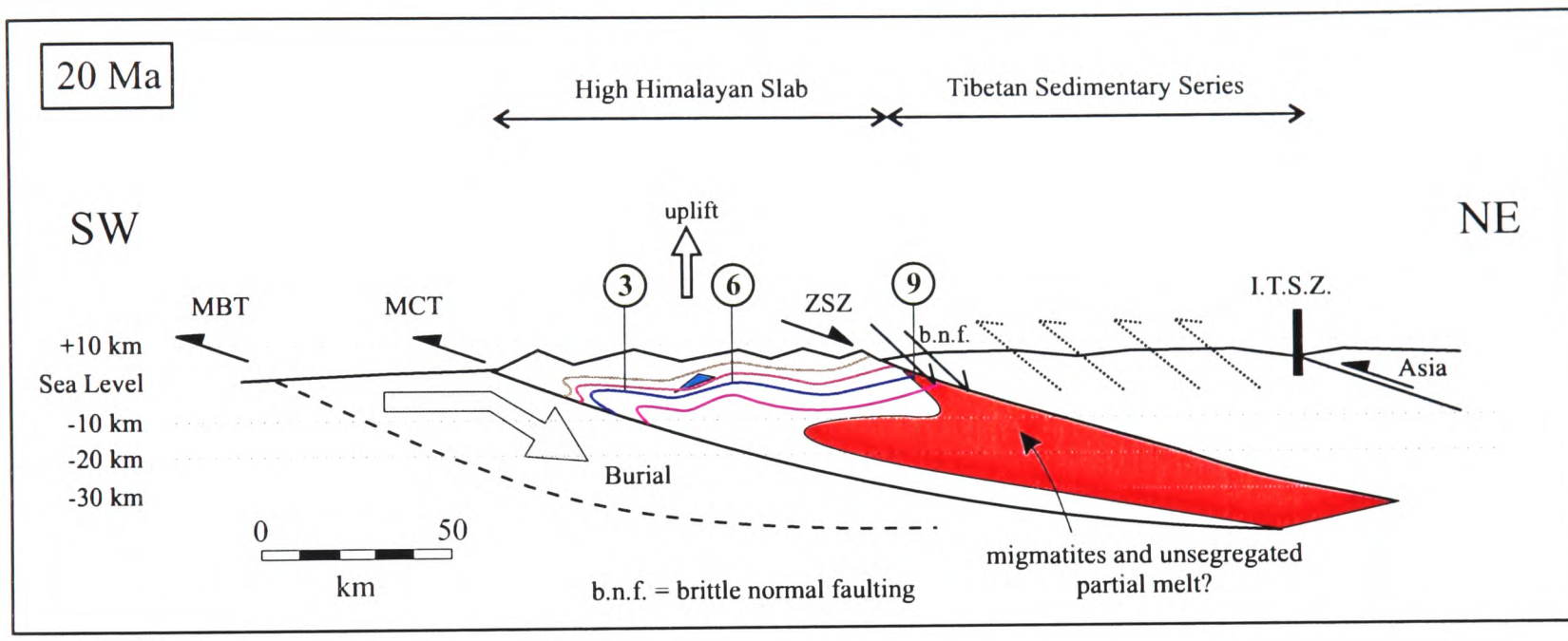


Figure 8.2e: Configuration of the High Himalayan Slab at c.20 Ma. 40Ar/39Ar cooling data suggest that rocks in the MCT, ZSZ and internal parts of the slab had cooled below c.350-400°C (the nominal closure temperature for diffusive loss of Ar in muscovite) by this time. Movement along the ZSZ and MCT is believed to have slowed considerably at this time. For the past ~20 Ma, unroofing is interpreted to have occurred by uplift, surface erosion and perhaps minor amounts of brittle normal faulting along the ZSZ, together with rejuvenated movement on the MCT.

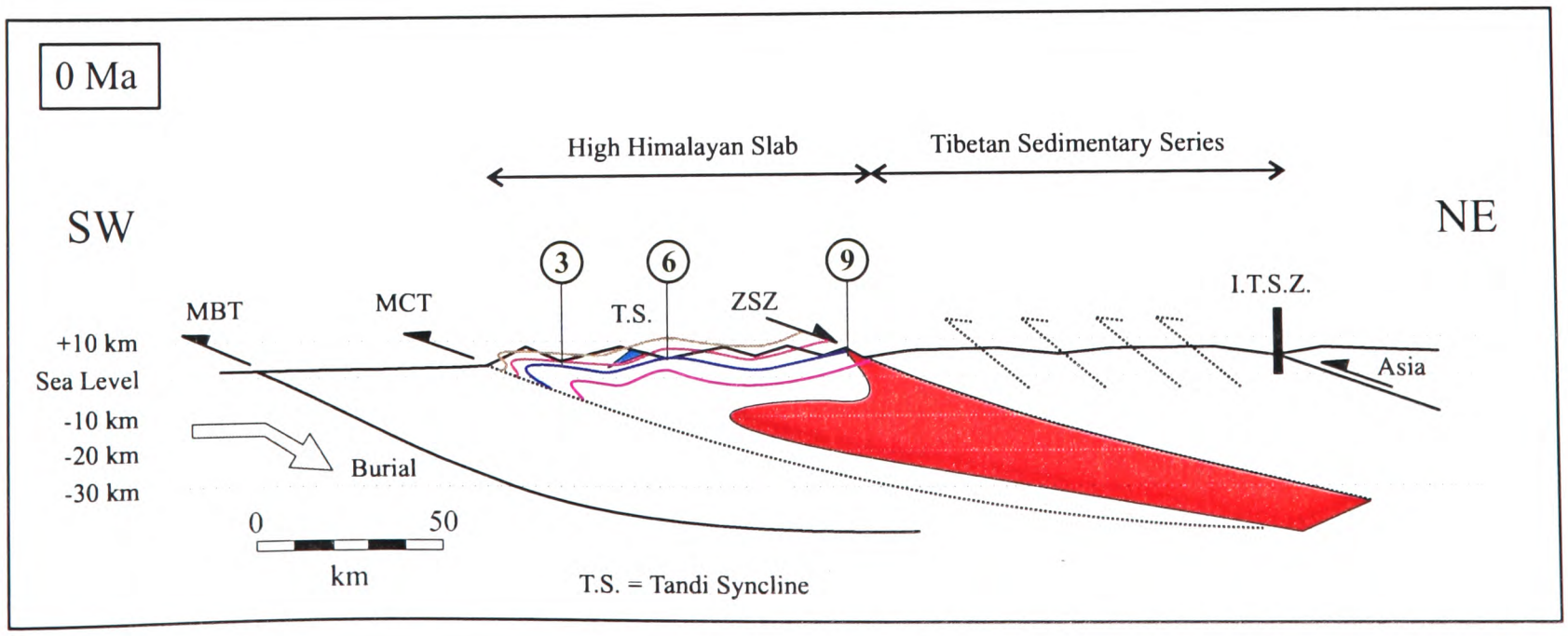


Figure 8.2f: Present day configuration of the High Himalayan Slab in SE Zanskar and NW Lahaul. The metamorphic isograds are folded around the Phojal-Kallath megafold at the base of the slab and the Gumburanjon leucogranite is located in the immediate footwall of the ZSZ. The Tandi Syncline is preserved at shallow structural levels and represents a relic of the earliest phase of deformation (see Figure 8.2b).

REFERENCES

Allegre, C.J. *et al*, 1984. Structure and evolution of the Himalaya-Tibet orogenic belt. *Nature*, **307**, 17-25.

Argand, E. 1924. La tectonique de l'Asie. C.R. 13 Cong. Géol. Int., 1922, 171-372.

Arita, K. 1983. Origin of the inverted metamorphism of the Lower Himalayas, central Nepal. *Tectonophysics*, **95**, 43-60.

Arita, K., Hayashü, D. & Yoshida, M. 1982. Geology and structure of the Pokhara-Piuthan area, central Nepal. *Journal of the Nepal Geological Society*, **2**, 5-29.

Avouac, J.-P. & Tapponnier, P. 1993. Kinematic model of active deformation in Central Asia. *Geophysical Research Letters*, **20**, 895-898.

Ayres, M.W. 1997. Trace-element behaviour during high-grade metamorphism and anatexis of the Himalayas. *Unpublished PhD thesis*, Open University.

Ayres, M.W., Harris, N. & Vance, D. 1997. Possible constraints on anatectic melt residence times from accessory mineral dissolution rates: an example form Himalayan leucogranites. *Mineralogical Magazine*, **61**, 29-36.

Baud, A., Gaetani, M., Garzanti, E. Fois, E., Nicora, A. & Tintori, A. 1984. Geological observations in southeastern Zanskar and adjacent Lahul area (northwestern Himalaya). *Eclogae Geologicae Helvetica*, **77**, 171-197.

Beck, A. *et al.* 1995. Stratigraphic evidence for an early collision between north-west India and Asia. *Nature*, **373**, 55-58.

Bell, T.H. 1985. Deformation partitioning and porphyroblast rotation in metamorphic rocks: a radical reinterpretation. *Journal of Metamorphic Geology*, **3**, 109-118.

Besse, J. & Courtillot, V., Pozi, J.P., Westphal, M. & Zhou, Y.X. 1984. Palaeomagnetic estimates of crustal shortening in the Himalayan thrusts and Zangbo suture. *Nature*, **311**, 621-626.

Besse, J. & Courtillot, V. 1988. Palaeogeographic maps of the continents bordering the Indian Ocean since the early Jurassic. *Journal of Geophysical Research*, **93**, B10, 11,791-11,808.

Bhattacharya, A., Mohanty, L., Maji, A., Sen, S. K. & Raith, M. 1992. Non-ideal mixing in the phlogopite-annite binary: constraints from experimental data on Mg-Fe partitioning and a reformulation of the biotite-garnet geothermometer. *Contributions to Mineralogy and Petrology*, **111**, 87-93.

Bletcher, J.D., 1997. The Shamsan Series of the Aden Volcano, Yemen: eruption and inversion of a zoned magma chamber? *Unpublished Ph.D. thesis*, Oxford University, England.

Bird, P. 1978. Initiation of intracontinental subduction in the Himalaya. *Journal of Geophysical Research*, **83**, B10, 4975-4986.

Brown, R.L. & Nazarchuk, J.H. 1993. Annapurna detachment fault in the Greater Himalaya of central Nepal: *In*: Treloar, P. J. & Searle, M. P. (eds), *Himalayan Tectonics*, Geological Society, London, Special Publication **74**, 461-473.

Brunel, M. & Kienast, J.R. 1986. Étude pétro-structurale des chevauchements ductiles himalayenes sur la transversale de l'Everest-Makalu (Népal oriental). Canadian Journal of Earth Sciences., **23**, 1117-1137.

Burchfiel, B.C. & Royden, L.H. 1985. North-south extension within the convergent Himalayan region. *Geology*, **13**, 679-682.

Burchfiel, B.C., Zhiliang, C., Hodges, K.V., Yuping, L., Royden, L.H., Changrong, D. & Jiene, X. 1992. The South Tibetan Detachment, Himalayan Orogen: Extension contemporaneous with and parallel to shortening in a collisional mountain belt. *Geological Society of America Bulletin*, Special Paper, **269**.

Burg, J.P., Brunel, M., Gapais, D., Chen, G.M. & Liu, G.H. 1984. Deformation of leucogranites of the crystalline Main Central Sheet in southern Tibet (China). *Journal of Structural Geology*, **6**, 535-542.

Burg, J.-P., Davy, P. & Martinod, J. 1994. Shortening of analogue models of the continental lithosphere: new hypothesis for the formation of the Tibetan Plateau. *Tectonics*, **13**, 475-483.

Butler, R.W.H., Prior, D.J. & Knipe, R.J. 1989. Neotectonics of the Nanga Parbat Syntaxis, Pakistan, and crustal stacking in the NW Himalaya. *Earth and Planetary Science Letters*, **94**, 329-343.

Carmichael, D.M. 1969. On the mechanism of prograde metamorphic reactions in quartz-bearing pelitic rocks. *Contributions to Mineralogy and Petrology*, **20**, 244-267.

Chang, C. *et al.*, 1986. Preliminary conclusions of the Royal Society and Academia Sinicia 1985 geotraveerse of Tibet. *Nature*, **323**, 501-507.

Chatterjee, N. D., and Flux, S., 1986. Thermodynamic mixing properties of muscovite-paragonite crystalline solutions at high temperatures and pressures and their geological applications: *Journal of Petrology*, **27**, 677-693.

Chen, Y., Courtillot, V. Cogne, J.-P., Besse, J., Yang, Z. & Enkin, R. 1993. The configuration of Asia prior to the collision of India: Cretaceous palaeomagnetic constraints. *Journal of Geophysical Research*, **98**, B12, 21,927-21,941.

Chernoff, C.B., and Carlson, W.D., 1997. Disequilibrium for Ca during growth of pelitic garnet: *Journal of Metamorphic Geology*, **15**, 421-438.

Coleman, M. & Hodges, K. 1995. Evidence for Tibetan plateau uplift before 14 Myr ago from a new minimum age for east-west extension. *Nature*, **374**, 49-52.

Coleman, M.E. 1996. Orogen-parallel and orogen-perpendicular extension in the central Nepalese Himalayas. *GSA Bulletin*, **108**, 1594-1607.

Coleman, M.E. & Parrish, R.R. 1995. Constraints on Miocene high-temperature deformation and anatexis within the Greater Himalaya from U-Pb geochronology. *EOS (Transactions, American Geophysical union)*, **76**, F708.

Copeland, P., Harrison, T.M., Kidd, W.S., Ronghau, X. & Yuquan, Z. 1987. Rapid early Miocene acceleration of uplift in the Gangdese Belt, Xizang (southern Tibet), and its bearing on accommodation mechanisms of the India-Asia collision. *Earth and Planetary Science Letters*, **86**, 240-252.

Copeland, P., Parrish, R.R. & Harrison, T.M. 1988. Identification of inherited radiogenic Pb in monazite and its implications for U-Pb systematics. *Nature*, **333**, 760-763.

Copeland, P. & Harrison, T.M. 1990. Episodic rapid uplift in the Himalaya revealed by $^{40}Ar/^{39}Ar$ analysis of detrital K-feldspar and muscovite, Bengal fan. *Geology*, **18**, 354-357.

Copeland, P., Harrison, T.M. & Le Fort, P. 1990. Age and cooling of the Manaslu granite: implications for Himalayan tectonics. *Journal of Volcanology and Geothermal Research*, **44**, 33-50.

Coward, M. *et al.*, 1986. Collision tectonics in the NW Himalayas. *In*: Coward, M.P. & Ries, A.C. (eds), *Collision Tectonics*, Geological Society, London, Special Publication **19**, 203-219.

Dalmayrac & Molnar, 1981. Parallel thrust and normal faulting in Peru and constraints on the state of stress. *Earth and Planetary Science Letters*, **55**, 473-481.

Dasgupta, S., Sengupta, P., Guha, D. & Fukuoka, M. 1991. A refined garnet-biotite Fe-Mg exchange geothermometer and its application in amphibolites and granulites. *Contributions to Mineralogy and Petrology*. **109**; 130-137.

Davis, D. Suppe, J. & Dahlen, F.A. 1983. Mechanics of fold-and-thrust belts and accretionary wedges. *Journal of Geophysical Research*, **88**, 1153-1172.

Debon, F., Le Fort, P. Sheppard, S. M. F. & Sonet, J. 1986. The four plutonic belts of the Transhimalaya-Himalaya; a chemical, mineralogical, isotopic and chronological synthesis along a Tibet-Nepal section. *Journal of Petrology*, **27**, 219-250.

Deer, W.A., Howie, R.A. & Zussman, J. 1989. An introduction to the rock-forming minerals. Longman, Wiley and Sons, 528pp.

Deniel, C., Vidal, P., Fernandez, A., Le Fort, P. & Peucat, J. 1987. Isotopic study of the Manaslu granite (Himalaya, Nepal): inferences on the age and source of the Himalayan leucogranites. *Contributions to Mineralogy and Petrology*, **96**, 78-92.

Dewey, J. F. 1988. Extensional collapse of orogens. *Tectonics*, **7**, 1123-1139.

Dewey, J.F. & Bird, J.M. 1970. Mountain belts and the new global tectonics. *Journal of Geophysical Research*, **75**, 2625-2647.

Dewey, J.F. & Burke, K.C.A. 1973. Tibetan, Variscan and Precambrian basement reactivation: products of a continental collision. *Journal of Geology*, **81**, 683-692.

Dewey, J.F., Shackleton, R.M., Chang, C. & Sun, Y. 1988. The tectonic evolution of the Tibetan Plateau. *Philosophical Transactions of the Royal Society of London*, **A326**, 379-413.

Dewey, J.F., Cande, S.& Pitman, W.C. 1989. Tectonic evolution of the India/Eurasia collision zone. *Eclogae Geologicae Helvetia*, **82**, 717-734.

Dietrich, V. & Gansser, A. 1981. The leucogranites of the Bhutan Himalaya (crustal anatexis versus mantle melting). *Bull. Suisse Minéral. Pétrogr.*, **61**, 177-202.

Draganits, E. Grasseman, B., Frank, W. Miller, C. & Wiesmayr, G. 1998. The sedimentary protoliths of the HHC in the Chamba-Lahaul area NW-Himalayas, India. *(Abstract) 13th Himalayan-Karakoram-Tibet Workshop, Peshawar.*

Dransfield, M.W. 1994. Extensional exhumation of high-grade metamorphic rocks in western Norway and the Zanskar Himalaya. *Unpublished Ph.D. thesis*, Oxford University.

Droop, G.T.R. 1987. A general equation for estimating Fe3+ concentrations in ferromagnesian silicate and oxides from microscope analyses using stoichiometric criteria. *Mineralogical Magazine*, **51**, 431-435.

Edmond, J.M. 1992. Himalayan tectonics, weathering processes, and the strontium isotope record in marine limestones, *Science*, **258**, 1594-1597.

Edwards, M.A. & Harrison, T.M. 1997. When did the roof collapse? Late Miocene north-south extension in the High Himalaya revealed by Th-Pb monazite dating of the Khula Kangri granite. *Geology*, **25**, 543-546.

Engel, A.E.G. & Engel, C.G. 1960. Progressive metamorphism and granitisation of the major paragneiss, NW Adirondack Mountains, New York, II. *Bulletin of the geological Society of America*, **71**, 1-58.

England, P., Le Fort, P., Molnar, P. & Pêcher, A. 1992. Heat sources for Tertiary metamorphism and anatexis in the Annapurna-Manaslu region of central Nepal. Journal of Geophysical Research, **97**, B2, 2107-2128.

England, P.C. & Richardson, S.W. 1977. The influence of erosion upon the mineral facies of rocks from different metamorphic environments. *Journal of the Geological Society, London*, **134**, 201-213.

England, P.C. & Thompson, A.B. 1984a. Pressure-temperature-time paths of regional metamorphism, Part I: Heat transfer during the evolution of regions of thickened continental crust. *Journal of Petrology* **25**, 894-928.

England, P.C. & Houseman, G.A. 1988. The mechanics of the Tibetan Plateau. *Philosophical Transactions of the Royal Society of London*, **A326**, 301-319.

England, P.C. & Molnar, P. 1993a. The interpretation of inverted metamorphic isograds using simple physical calculations. *Tectonics* **12**, 145-157.

England, P.C. & Molnar, P. 1993b. Cause and effect among thrust and normal faulting, anatectic melting and exhumation in the Himalaya. *In*: Treloar, P. J. & Searle, M. P. (eds), *Himalayan Tectonics*, Geological Society, London, Special Publication **74**, 401-411.

Enkin, R. Yang, Z.Y., Chen, Y. & Courtillot, V. 1992. Palaeomagnetic constraints on the geodynamic history of China from the Permian to the Present. *Journal of Geophysical Research*, **97**, 13,953-13,989.

Epard, J.L., Steck, A., Vannay, J.C. & Hunziker, J. 1995. Tertiary Himalayan structures and metamorphism in the Kulu Valley (Mandi-Khoksar transect of the Western Himalaya)-Shikar Beh Nappe and Crystalline Nappe. *Schweiz. Mineral. Petrogr. Mitt.* **75**, 59-84.

Etheridge, M.A., Wall, V.J., Cox, S.F. & Vernon, R.H. 1984. High fluid pressures during regional metamorphism: implications for mass transfer and deformation mechanisms. *Journal of Geophysical Research*, **89**, 4344-4458.

Ferrara, G., Lombardo, F., Tonarini, S. & Turi, B. 1987. New Rb/Sr data on granitoids from Gumburanjon and Kade Chu (High Himalaya). *Himalayan-Karakoram-Tibet Workshop* (abstract volume), Nancy, 33.

Ferrara, G., Lombardo, F., Tonarini, S. & Turi, B. 1991. Sr, Nd and O isotopic characterisation of the Gophu La and Gumburanjon leucogranites (High Himalaya). *Schweiz. Mineral. Petrogr. Mitt.* **71**, 35-51.

Ferry, J.M. & Spear, F.S. 1978. Experimental calibration of the partitioning of Fe and Mg between garnet and biotite. *Contributions to Mineralogy and Petrology*, **66**, 113-117.

Frank, M. & O'Nions, R.K. 1998. Sources of Pb for the Indian Ocean ferromanganese crusts: a record of Himalayan erosion? *Earth and Planetary Science Letters*, **158**, 121-130..

Frank, W., Thoni, M. & Purtscheller, F. 1977. Geology and petrography of Kulu - South Lahul area. *Colloques internationaux du C.N.R.S.*, **286**, 147-172.

Frank, W., Baud, A., Honegger, K. & Trommsdorff, V. 1987. Comparative studies on profiles across the NW Himalayas. *In*: The Anatomy of Mountain Belts, Schaer, J.P. & Rodgers, J. (eds.), pp. 261-275, Princeton University Press, Princeton, N.J.

Frank, W., Grasseman, B., Guntli, P. & Miller, C. 1995. Geological map of the Kishtwar-Chamba-Kulu region (NW Himalayas, India). *Jahbruch der Geologischen Bundesantalt Wien,* **138**, 299-308.

Franz, G., Andrehs, G. & Rhede, D. 1996. Crystal chemistry of monazite and xenotime from Saxothuringian-Moldanubian metapelites, NE Bavaria, Germany. *European Journal of Mineralogy*, **8**, 1097-1118.

Fuchs, G. 1967. Zum Bau des Himalaya. *Denkschr. Osterr. Akad. Wiss., math.-naturw. Kl.* **113**, 1-211.

Fuchs, G. 1975. Contribution to the geology of the north-western Himalaya. *Abh. Geol. B.A.*, **32**, 59 S.

Fuchs, G. 1979. On the geology of western Zanskar. *Jahrbuch der Geologischen Bundesanstalt Wien*, **125**, 1-50.

Fuchs, G. & Linner, M. 1995. Geological traverse across the western Himalaya- a contribution to the geology of eastern Ladakh, Lahul and Chamba. *Jahbruch der Geologischen Bundesantalt Wien* **138**, 655-688.

Gaetani, M., Casnedi, R., Fois, E., Garzanti, E., Jadoul, F., Nicora, A. & Tintori, A. 1986. Riv. Ital. Paleont. Stratigr., **91**, 443-448.

Gaetani, M. & Garzanti, E. 1991. Multicycle history of the Northern India continental margin (Northwestern Himalaya). *American Association of Petroleum geologists Bulletin*, **75**, 1427-1446.

Ganguly, J. & Saxena, S.R. 1984. Mixing properties of aluminosilicate garnets: constraints from natural and experimental data, and applications to geothermo-barometry. *American Mineralogist*, **69**, 88-97.

Gansser, A. 1964. Geology of the Himalayas. Chichester: J. Wiley & Sons, 289pp.

Gansser, A. 1977. Sci. Terre Himalaya: C.N.R.S. 268, 147-166

Gansser, A. 1983. Geology of the Bhutan Himalaya. Denkschr. Schweiz. Naturforsch. Ges., Vol. **96**, Birkhäuser Verlag, Basel, 181pp.

Garzanti, E. 1993. Sedimentary evolution and drowning of a passive margin shelf (Giumal Group; Zanskar Tethys Himalaya, India): Palaeoenvironmental changes during final breakup of Gondwanaland. *In*: Treloar, P.J. & Searle, M.P. (eds), *Himalayan Tectonics*, Geological Society, London, Special Publication **74**, 277-298.

Garzanti, E., Baud, A. & Mascle, G. 1987. Sedimentary record of the northward flight of India and its collision with Eurasia (Ladakh Himalaya, India). *Geodynamica Acta*, **1**, 87-102.

Garzanti, E. & van-Haver, T. 1988. The Indus clastics: forearc basin sedimentation in the Ladakh Himalaya (India). *Sedimentary Geology*, **59**, 237-249.

Ghent, E.D. & Stout, M.Z. 1981. Geobarometry and geothermometry of plagioclase-biotite-garnet-muscovite assemblages. *Contributions to Mineralogy and Petrology*, **76**, 92-97.

Geisbach, C.L. 1891. Geology of the Central Himalaya. *Mem. Geol. Surv. India*, **23**, 1-232.

Grujic, D., Casey, M., Davidson, C., Hollister, L.S., Kündig, R., Pavliis, T. & Schmid, S. 1996. Ductile extrusion of the Higher Himalayan Crystalline in Bhutan: evidence from quartz microfabrics. *Tectonophysics*, **260**, 21-43.

Guidotti, C.V. 1973. Compositional variation of muscovite as a function of metamorphic grade ad assemblage in metapelites from NW Maine. *Contributions to Mineralogy and Petrology*, **42**, 33-42.

Guidotti, C.V. 1974. Transition from Staurolite to Sillimanite Zone, Rangeley Quadrangle, Maine. *Geological Society of America Bulletin*. **85**; 475-490.

Guillot, S., Le Fort, P. & Pêcher, A. 1994a. Comparison of the emplacement of some High Himalayan leucogranites. Mustang, Manaslu and Kula-Kangri. *Journal of the Nepal Geological Society*, **10**, 101-102.

Guillot, S., Hodges, K., Le Fort, P. & Pêcher, A. 1994b. New constraints on the age of the Manaslu leucogranite: Evidence for episodic tectonic denudation in the central Himalayas. Geology, **22**, 559-562.

Guillot, S., Le Fort, P., Pêcher, A., Barman, M.R. & Aprahamian, J. 1995. Contact metamorphism and depth of emplacement of the Manaslu granite (central Nepal). Implications for Himalayan orogenesis. *Tectonophysics*, 241, 99-119.

Hackler, R. T. & Wood., B. J., 1989. Experimental determination of Fe and Mg exchange between garnet and olivine and estimation of Fe-Mg mixing properties in garnet: *American Mineralogist*, **74**, 994-999.

Hames, W.E. & Cheney, J.T. 1997. On the loss of ^{40}Ar from muscovite during polymetamorphism . *Geochimica et Cosmochimica Acta*, 61, 3863-3872.

Harris, N., Inger, S. & Massey, J. 1993. The role of fluids in the formation of High Himalayan leucogranites. *In* : Treloar, P. J. & Searle, M. P. (eds), *Himalayan Tectonics*, Geological Society, London, Special Publication **74**, 391-400.

Harris, N. & Massey, J. 1994. Decompression and anatexis of Himalayan metapelites. *Tectonics*, **13**, 1537-1546.

Harris, N. Ayres, M. & Massey, J. 1995. The incongruent melting of muscovite: implications for the geochemistry and extraction of granite magmas. *Journal of Geophysical Research*, **100**, 15,777-15787.

Harrison, T.M., Copeland, P. Kidd, W.S. & Yin, A. 1992. Raising Tibet. *Science*, **255**, 1663-1670.

Harrison, T.M. *et al.* 1993. Isotopic preservation of Himalayan-Tibetan uplift, denudation and climate histories of two molasse deposits. *Journal of Geology*, **101**, 157-175.

Harrison, T.M. McKeegan, K.D. & Le Fort, P. 1995. Identification of inherited monazite in the Manaslu leucogranite by 208Pb/232Th ion microprobe dating: crystallisation age and tectonic significance. *Earth and Planetary Science Letters*, **133**, 271-282.

Harrison, T.M., Ryerson, F.J. , Le Fort, P., Yin, A., Lovera, O.M. & Catlos, E.J. 1997a. A late Miocene-Pliocene origin for the Central Himalayan inverted metamorphism. Earth and Planetary Science Letters, **146**, E1-E7.

Harrison, T.M., Lovera, O.M. & Grove, M. 1997b. New insights into the origin of two contrasting Himalayan granite belts. *Geology*, **25**, 899-902.

Harte, B. 1975. Determination of a pelite petrogenetic grid for the Eastern Scottish Dalradian. *Carnegie Institution Geophysical Laboratory*, Washington, Yearbook 74, 438-446.

Hawkins, D.P. & Bowring, S.A. 1997. U-Pb systematics of monazite and xenotime: case studies from the Palaeo-Proterozoic of the Grand Canyon, Arizona. *Contributions to Mineralogy and Petrology*, **127**, 87-103.

Hawkins, D.P., Bowring, S.A., Ilg, B.R., Karlstrom, K.E. & Williams, M.L. U-Pb geochronologic constraints on the Palaeoproterozoic crustal evolution of the Upper Granite Gorge, Grand Canyon, Arizona. *Geological Society of America Bulletin*, **108**, 1167-1181.

Heim, A. & Gansser, A. 1939. Central Himalaya – Geological observations of Swiss expedition, 1936. *Societe Helvetique Science Naturelle Memoires*, **73**, 245.

Heinrich, W., Andrehs, G. & Franz, G. 1997. Monazite-xenotime miscibility gap thermometry. 1: An empirical calibration. *Journal of Metamorphic Geology*, **15**, 3-16.

Herren, E. 1987. Zanskar shear zone: northeast-southwest extension within the Higher Himalaya. *Geology*, **15**, 409-413.

Hildebrand, P.J. 1998. The Hindu Kush of Pakistan: mountain range evolution from active margin to continent-continent collision. *Unpublished Ph.D. thesis*, Oxford University, England .

Hirn, A.1988. Features of the crust-mantle structure of the Himalayas-Tibet: a comparison with seismic traverses of Alpine, Pyrenean and Variscan orogenic belts. *Philosophical Transactions of the Royal Society of London*, **A326**, 17-32.

Hirn, A., Lepine, J.-L., Jobert, G., Sapin, M., Wittlinger, G., Xin, X.-Z., Yuan, G.-E., Jing, W.-X., Wen, T.-J., Bai, X.-S., Pandey, M.R. & Tater, J.M. 1984a. Crustal structure and variability of the Himalayan border of Tibet. *Nature*, **307**, 23-25.

Hirn, A., Nercessian, A. Sapin, M., Jobert, G., Zhong Xin, X., En Yuan, E., De Yuan, L. & Ji Wen, T. 1984b. Lhasa block and bordering sutures -a continuation of a 500km Moho traverse through Tibet. *Nature*, **307**, 25-27.

Hodges, K., Bowring, S., Davidek, K., Hawkins, D. & Krol, M., in press. Evidence for rapid displacement on Himalayan normal faults and the importance of tectonic denudation in the evolution of mountain ranges. *Geology*.

Hodges, K.V. & Spear, F.S. 1982. Geothermometry, geobarometry and the Al2SiO5 triple point at Mt. Moosilauke, New Hampshire. *American Mineralogist* **67**, 1118-1134.

Hodges, K.V. & Crowley, P.D. 1985. Error estimation and empirical geothermobarometry for pelitic systems. *American Mineralogist*, **70**, 702-709.

Hodges, K.V. & Silverberg, D.S. 1988. Thermal evolution of the Greater Himalaya, Garhwal, India. *Tectonics* **7**, 583-600.

Hodges, K.V., Le Fort, P. & Pêcher, A. 1988a. Possible thermal buffering by crustal anatexis in collisional orogens: Thermobarometric evidence from the Nepalese Himalaya. *Geology*, **16**, 707-710.

Hodges, K.V., Parrish, R.R., Housh, T.B., Lux, D.R., Burchfiel, B.C., Royden, L.H. & Chen, Z. 1992. Simultaneous Miocene extension and shortening in the Himalayan orogen. *Science,* **258**, 1466-1470.

Hodges, K. V., Hames, W. E., Olszewski, W. J., Burchfiel, B. C., Royden, L. H. & Chen, Z., 1994. Thermobarometric and $^{40}Ar/^{39}Ar$ geochronologic constraints on Eohimalayan metamorphism in the Dinggyê area, southern Tibet. *Contributions To Mineralogy and Petrology*, **117**, 151-163.

Hodges, K.V. & Bowring, S.A. 1995. 40Ar/39Ar thermochronology of isotopically zoned micas: Insights from the southwestern USA Proterozoic orogen. *Geochimica et Cosmochimica Acta*, **59**, 3205-3220.

Hodges, K.V., Parrish, R.R. & Searle, M.P. 1996. Tectonic evolution of the central Annapurna Range, Nepalese Himalayas. *Tectonics*,**15**, 1264-1291.

Holdaway, M.J. & Lee, S.M. 1977. Fe-Mg cordierite stability in high-grade pelitic rocks based on experimental, theoretical, and natural observations. *Contributions to Mineralogy and Petrology*. **63**; 175-198.

Holdaway, M.J., & Mukhopadhyay, B., 1993. A re-evaluation of the stability relations of andalusite: Thermochemical data and phase diagram for the aluminium silicates: *American Mineralogist*, **78**, 298-315.

Holland, T.J.B. & Powell, R. 1990. An enlarged and updated internally consistent thermodynamic dataset with uncertainties and correlations: the system K2O-Na2O-CaO-MgO-MnO-FeO-Fe2O3-Al2O3-TiO2-SiO2-C-H2-O2. *Journal of Metamorphic Geology* **8**, 89-124.

Holland, T.J.B. and Powell, R., 1992. Plagioclase feldspars: Activity composition relations based upon Darken's quadratic formalism and Landau theory: *American Mineralogist*, **77**, 53-61.

Hollister, L.S. 1993. The role of melt in the uplift and exhumation of orogenic belts: *Chemical Geology*, **108**, 31-48.

Honegger, K., Dietrich, V., Frank, W., Gansser, A., Thoni, M. & Trommsdorff, V. 1982. Magmatism and metamorphism in the Ladakh Himalayas (the Indus-Tsangpo suture zone). *Earth and Planetary Science Letters* **60**, 253-292.

Honegger, K., Le Fort, P., Mascle, G.& Zimmerman, J.-L. 1989. The blueschists along the Indus Suture Zone in Ladakh, NW Himalayas. *Journal of Metamorphic Geology*, **7**, 57-72.

Hubbard, M.S. 1989. Thermobarometric constraints on the thermal history of the Main Central Thrust zone and Tibetan Slab, eastern Nepal Himalaya. *Journal of Metamorphic Geology*, **7**, 19-30.

Hubbard, M.S. & Harrison, T.M. 1989. $^{40}Ar/^{39}Ar$ age constraints on deformation and metamorphism in the Main Central Thrust zone and Tibetan Slab, eastern Nepal Himalaya. *Tectonics* **8**, 865-880.

Hubbard, M.S. 1996. Ductile shear as a cause of inverted metamorphism: an example from the Nepal Himalaya. *Journal of Geology*, **104**, 493-499.

Hughes, N.C. & Droser, M.L. 1992. Trace fossils from the Phe Formation (Lower Cambrian), Zanskar valley, northwestern India. *Memoirs Queensland Museum,* **32**, 139-144.

Inger, S. 1998. Timing of an extensional detachment during convergent orogeny: New Rb-Sr geochronological data from the Zanskar Shear Zone, northwestern Himalaya. *Geology*, **26**, 223-226.

Inger, S. & Harris, N.B.W. 1992. Tectonothermal evolution of the High Himalayan Crystalline Sequence, Langtang Valley, northern Nepal. *Journal of Metamorphic Geology*, **10**, 439-452.

Inger, S. & Harris, N. 1993. Geochemical constraints on leucogranite magmatism in the Langtang valley, Nepal Himalaya. *Journal of Petrology*, **34**, 345-368.

Jain, A.K. & Manickavasagam, R.M. 1993. Inverted metamorphism in the intracontinental ductile shear zone during Himalayan collision tectonics. *Geology*, **21**, 407-410.

Jaupart, C. & Provost, A. 1985. Heat focusing, granite genesis and inverted metamorphic gradients in continental collision zones. *Earth and Planetary Science Letters*, **73**, 385-397.

Johannes, W., and Holtz, F., 1990. Formation and composition of H2O undersaturated granitic melts: *in* Ashworth, J. R., and Brown, M. (eds), *High temperature metamorphism and anatexis*: London, Unwin Hyman, 87-104.

Johnson, M.R.W. 1994. Volume balance of erosional loss and sediment deposition related to Himalayan uplifts. *Journal of the Geological Society of London*, **151**, 217-220.

Khan, M.A., Jan, M.Q. & Weaver, B.L. 1993. Evolution of the lower arc crust in Kohistan, N Pakistan: temporal arc magmatism through early, mature and intra-arc rift stages. *In*: Treloar, P.J. & Searle, M.P. (eds). *Himalayan Tectonics*, Geological Society, London, Special Publication **74**, 123-138.

Kingsbury, J.A., Miller, C.F., Wooden, J.L. & Harrison, T.M. 1993. Monazite paragenesis and U-Pb systematics in rocks of the eastern Mojave Desert, California, U.S.A.; implications for thermochronometry. *Chemical Geology*. **110**, 147-167.

Klootwijk, C.T. 1984. A review of the Indian Phanerozoic palaeomagnetism: implications for the India-Asia collision. *Tectonophysics*, **105**, 331-353.

Klootwijk, C.T., Conaghan, P.J. & Powell, C.M. 1985. The Himalayan arc, oroclinal bending and back-arc spreading. *Earth and Planetary Science Letters*, **75**, 167-183.

Klootwijk, C.T., Gee, J.S., Peirce, J.W., Smith, G.M. & McFadden, P.L. 1992. An early India-Asia contact: palaeomagnetic constraints from Ninetyeast Ridge, ODP leg 121. *Geology*, **20**, 395-398.

Kretz, R., 1983. Symbols for rock-forming minerals: *American Mineralogist*, **68**, 277-279.

Krogh, T. E., 1973. A low contamination method for the hydrothermal decomposition of zircon and extraction of U and Pb for isotopic age determinations: *Geochemica et Cosmochemica Acta*, **37**, 485-494.

Kündig, R. 1989. Domal structures and high-grade metamorphism in the Higher Himalayan Crystalline, Zanskar region, northwest Himalaya, India. *Journal of Metamorphic Geology*, **7**, 43-55.

Lanphere, M.A. & Dalrymple, G.B. 1976. Identification of excess ^{40}Ar by the $^{40}Ar/^{39}Ar$ age spectrum technique. *Earth and Planetary Science Letters*, **32**, 141-148.

Le Breton, N. & Thompson, A.B. 1988. Fluid-absent (dehydration) melting of biotite in metapelites in the early stages of crustal anatexis. Contributions to mineralogy and Petrology, **99**, 226-237.

Le Fort, P. 1975. Himalayas: The collided range. Present knowledge of the continental arc. *American Journal of Science*. **275**, 1-44.

Le Fort, P. 1981. Manaslu leucogranite: a collision signature of the Himalaya. A model for its genesis and emplacement. *Journal of Geophysical Research*, **86**, B11, 10545-10568.

Le Fort, P. 1986. Metamorphism and magmatism during the Himalayan collision. *In*: Coward, M. P. & Ries, A. C. (eds), *Collision Tectonics*, Geological Society, London, Special Publication **19**, 159-172.

Le Fort, P., Debon, F., Pêcher, A., Sonet, J., Vidal, P. 1986. The 500 Ma magmatic event in Alpine southern Asia, a thermal episode at Gondwana scale. *Sciences de la Terre* **47**, 191-209.

Le Fort, P., Cuney, M., Deniel, C., France-Lanord, C., Sheppard, S.M.F., Upreti, B.N. & Vidal, P. 1987. Crustal generation of the Himalayan leucogranites. *Tectonophysics* **134**, 39-57.

Lin, J. & Watts, D.R. 1988. Palaeomagnetic constraints on Himalayan-Tibetan tectonic evolution. *Philosophical Transactions of the Royal Society of London*, **A326**, 177-188.

Ludwig, K.R. 1989. Pb.Dat: a computer program for processing raw Pb-U-Th isotope data. *U.S. Geological Survey Open-File report,* 88-557.

Ludwig, K.R. 1990. ISOPLOT 2.11 for MS-DOS: A plotting and regression program for radiogenic-isotope data, for IBM-PC compatible computers: *U.S. Geological Survey Open-File report.*

Lydekker, R. 1883. The geology of the Kashmir and Chamba territories, and the British district of Khagan. *Mem. Geol. Surv. India*, **22**, 1-344.

Lyon-Caen, H. & Molnar, P. 1983. Constraints on the structure of the Himalaya from an analysis of gravity anomalies and a flexural model of the lithosphere. *Journal of Geophysical Research*, **88**, 8171-8192.

Lyon-Caen, H. & Molnar, P. 1985. Gravity anomalies, flexure of the Indian plate, and the structure, support and evolution of the Himalaya and Ganga Basin. *Tectonics*, **4**, 513-538.

MacFarlane, A.M. 1995. An Evaluation of the inverted metamorphic gradient at Langtang National Park, Central Nepal Himalaya. *Journal of Metamorphic Geology*, **13**, 595-612.

MacFarlane, A.M., Hodges, K.V. & Lux, D. 1992. A structural analysis of the Main Central Thrust zone, Langtang National Park, central Nepal Himalaya. *Geological Society of America Bulletin*, **104**, 1389-1402.

McDougall, I. & Harrison, T.M. 1988. *Geochronology and thermochronology by the $^{40}Ar/^{39}Ar$ method.* Oxford monograph on Geology and Geophysics, **9**.

McElroy, R., Cater, J., Roberts, I., Peckham, A. & Bond, M. 1990. The structure and stratigraphy of SE Zanskar, Ladakh Himalaya. *Journal of the Geological Society, London* **147**, 989-997.

Mahar, E.M., Baker, J.M., Powell, R., Holland, T.J.B. & Howell, N. 1997. The effect of Mn on mineral stability in metapelites. *Journal of Metamorphic Geology* **15**, 223-238.

Maluski, H. & Matte, P. 1984. Ages of Alpine tectonometamorphic events in the northwestern Himalaya (northern Pakistan) by ^{39}Ar-^{40}Ar method. *Tectonics*, **3**, 1-18.

Massey, J.A. 1994. Metamorphism, melting and fluids during Himalayan orogenesis. *Unpublished Ph.D. thesis*, Open University, U.K.

Mehta, P.K. 1977. Rb-Sr geochronology of the Kulu-Mandi belt: its implications for the Himalayan tectonogenesis. *Geol. Rdsch.*, **66**, 156-174.

Ménard, G. & Molnar, P. 1988. Collapse of a Hercynian Tibetan Plateau into a late Palaeozoic European Basin and Range province, *Nature,* **334**, 235-237.

Metcalfe, R.P. 1993. Pressure, temperature and time constraints on metamorphism across the Main Central Thrust zone and High Himalayan slab in the Garhwal Himalaya. *In*: Treloar, P.J. & Searle, M.P. (eds.), *Himalayan Tectonics*, Geological Society Special Publication, **74**, 485-509.

Molnar, P. 1984. Structure and tectonics of the Himalaya: constraints and implications of geophysical data. *Annual Review Earth and Planetary Science Letters*, **12**, 489-518.

Molnar, P. 1988. A review of the geophysical constraints on the deep structure of the Tibetan Plateau, the Himalaya and the Karakoram, and their tectonic implications. *Philosophical Transactions of the Royal Society of London*, **A326**, 33-88.

Molnar, P. & Tapponnier, P. 1975 Cenozoic Tectonics of Asia: effects of a continental collision. *Science*, **189**, 419-426.

Molnar, P. & Tapponnier, P. 1978. Active tectonics of Tibet. *Journal of Geophysical Research*, **83**, 5361-5375

Molnar, P., England, P. & Martinod, J. 1983. Mantle dynamics, uplift of the Tibetan Plateau, and the Indian monsoon. *American Geophysical Union, Reviews in Geophysics*, **31**, 357-396.

Montel, J-M. 1993. A model for monazite/melt equilibrium and application to the generation of granitic magmas. *Chemical Geology*, **110**, 127-146.

Najman, Y., Pringle, M.S., Johnson, M.R.W., Robertson, A.H.F., Wijbrans, J. & Oliver, G.J.H. 1997. $^{40}Ar/^{39}Ar$ dating of detrital micas in early Himalayan foredeep sediments, northern India: implications for early Himalayan tectonics and exhumation history. *(Abstract) 12th Himalayan-Karakoram-Tibet Workshop, Rome.*

Nanda, N.M. & Singh, M.P. 1976. Stratigraphy and sedimentation of the Zanskar area, Ladakh and adjoining parts of Lahaul region of Himachal Pradesh. *Himalayan Geology*, **6**, 365-388.

Nazarchuk, J.H. 1993. Structure and geochronology of the Greater Himalaya, Kali Gandaki region, west-central Nepal. Unpublished Ph.D. thesis, Carleton University, Ottawa, Canada.

Nelson, K.D., Zhao, W., Brown, L.D., Kuo, J., Che, J., Liu, X., Klemperer, S.L., Makovsky, Y., Meissner, R., Mechie, J., Kind, R., Wenzel, F., Ni, J., Nabelek, J., Leshou, C., Tan, H., Wei, W., Jones, A.G., Booker, J., Unsworth, M., Kidd, W.S.F., Hauck, M., Alsdorf, D., Ross, A., Cogan, M., Wu, C., Sandvol, E., Edwards. M. 1996. Partially molten middle crust beneath southern Tibet: Synthesis of project INDEPTH results. *Science* **274**, 1684-1688.

Newton, R.C. and Hasselton, H.T. 1981. Thermodynamics of the garnet-plagioclase- Al_2SiO_5-quartz geobarometer: *Thermodynamics of minerals and melts, advances in physical geochemistry*, **1**, 131-148, Springer-Verlag, New York.

Noble, S.R. & Searle, M.P. 1995. Age of crustal melting and leucogranite formation from U-Pb zircon and monazite dating in the western Himalaya, Zanskar, India. *Geology* **12**, 1135-1138.

Noble, S.R. & Searle, M.P. 1998. Permian granitoids of the High Himalayan Slab, Zanskar Himalaya. *(Abstract) 13th Himalayan-Karakoram-Tibet Workshop, Peshawar.*

Overstreet, W.C. 1967. The geologic occurrence of monazite. *Geological Survey Professional Paper*, 327pp.

Oxburgh, E.R. & Turcotte, D.L. 1974. Thermal gradients and regional metamorphism in overthrust terrains with special reference to the Eastern Alps. *Schweiz. Mineral. Petrogr. Mitt.*, **54**, 641-662.

Parrish, R.R. 1990. U-Pb dating of monazite and its application to geological problems. *Canadian Journal of Earth Sciences*, **27**, 1431-1450.

Parrish, R.R. & Tirrul, R. 1989. U-Pb age of the Baltoro granite, northwest Himalaya, and implications for monazite U-Pb systematics. *Geology*, **17**, 1076-1079.

Parrish, R.R. & Hodges, K.V. 1992. U-Pb geochronology of igneous and metamorphic rocks near the Main Central Thrust in the Langtang area, central Nepal Himalaya (abstract). *7th Himalayan-Karakoram-Tibet Workshop, Oxford.*

Parrish, R.R. & Hodges, K.V. 1996. Isotopic constraints on the age and provenance of the Lesser and Greater Himalayan sequences, Nepalese Himalaya. *GSA Bulletin*, **108**, 904-911.

Parrish, R.R., Grujic, D., Hollister, L., Klepeis, K., Kündig, R. & Dorji, T. 1997. Reconnaissance observations in the Bhutan Himalaya (abstract). *12th Himalaya-Karakoram-Tibet Workshop, Rome.*

Passchier, C.W. and Trouw, R.A.J. 1996. *Micro-tectonics*, Springer-Verlag Berlin Heidelberg.

Patiño Douce, A.E., and Harris, N.B.W., 1998. Experimental constraints on Himalayan anatexis: *Journal of Petrology*, **39**, 689-710.

Patrait, P. & Achache, J. 1984. India-Eurasia collision chronology has implications for crustal shortening and driving mechanisms of plates. *Nature*, **311**, 615-621.

Pêcher, A. 1978. Déformations et métamorphisme associés à une zone de cisaillement, exemple du Grand Chevauchement Central himalayen (MCT), transversale des Annapurnas et du Manaslu, Népal. Unpublished Ph.D. thesis, Grenoble.

Pêcher, A. 1989. The metamorphism in the central Himalaya. *Journal of Metamorphic Geology*, **7**, 31-41.

Perchuk., L.L. & Lavrent'eva, I.V. 1983. Experimental investigation of exchange equilibria in the system cordierite-garnet-biotite. *In*: Saxena, S.K. (ed.), Kinetics and equilibrium in mineral reactions (pp. 199-239), Springer-Verlag. New York, NY, United States.

Pëto, P. 1976. An experimental investigation of melting reactions involving muscovite and paragonite in the silica-saturated portion of the system K_2O-Na_2O-Al_2O_3-SiO_2-H_2O to 15kbar total pressure. *Programmes in experimental Petrology*, NERC 3rd report, London, 41-45.

Petterson, M.G. & Windley, B.F.1985. Rb-Sr dating of the Kohistan batholith in the Trans-Himalaya of North Pakistan, and tectonic implications. *Earth and Planetary Science Letters*, **74**, 45-57.

Pickett, J., Jell, J. Conaghan, P. & Powell, C.M.A. 1975. Jurassic invertebrates from the Himalayan Central Gneiss. *Alcheringa*, **1**, 71-85.

Pinet, C. & Jaupart, C. 1987. A thermal model for the distribution in space and time of the Himalayan granites. *Earth and Planetary Science Letters*, **84**, 87-99.

Platt, J.P. 1986. Dynamics of orogenic wedges and the uplift of high-pressure metamorphic rocks. *Geological Society of America Bulletin*, **97**, 1037-1053.

Platt, J.P. & Vissiers, R.L.M. 1980. Extensional structures in anisotropic rocks. *Journal of Structural Geology*, **2**, 397-410.

Podosek, F.A, Huneke, J.C., Gancarz, A.J. & Wasserburg, G.J. 1973. A Study of Samples from the Lunar Highlands Returned by the Unmanned Luna 20 Spacecraft. *Geochimica et Cosmochimica Acta*, **37**, 887-904.

Pognante, U., Genovese, G., Lombardo, B. & Rossetti, P. 1987. Preliminary data on the High Himalayan Crystallines along the Padum-Darcha traverse (south-eastern Zanskar, India). *Rendiconti della Societa Italiana di Mineralogia e Petrologia* **42**, 95-102.

Pognante, U & Lombardo, B. 1989. Metamorphic evolution of the High Himalayan Crystallines in SE Zanskar, India. *Journal of Metamorphic Geology*, **7**, 9-17.

Pognante, U., Castelli, D., Benna, P., Genovese, G., Oberli, F., Meier, M., Tonarini, S. 1990. The crystalline units of the High Himalayas in the Lahul-Zanskar region (northwest India): metamorphic-tectonic history and geochronology of the collided and imbricated Indian plate. *Geological Magazine* **127**, 101-116.

Pognante, U. & Benna, P. 1993. Metamorphic zonation, migmatisation and leucogranites along the Everest transect of Eastern Nepal and Tibet: record of an exhumation history. *In*: Treloar, P. J. & Searle, M. P. (eds), *Himalayan Tectonics*, Geological Society, London, Special Publication **74**, 401-411.

Potts. P. J., 1987. *A handbook of silicate rock analysis*: Blackie and Son Ltd, Glasgow.

Potts., P. J., Tyndale, A.G., Issacs, M.C., 1983. On the precision of electron microprobe data: new test for the homogeneity of mineral standards: *American Mineralogist*, **68**, 1237-1242.

Powell, C. & Conaghan, P.J. 1973. Polyphase deformation in Phanerozoic rocks of the central Himalayan gneiss, northwest India. *Journal of Geology*, **81**, 127-143.

Powell, C.M. 1986. Continental underplating model for the rise of the Tibetan Plateau. *Earth and Planetary Science Letters*, **81**, 79-94.

Powell, R. & Holland, T.J.B. 1985. An internally consistent thermodynamic dataset with uncertainties and correlations: 1. Methods and a worked example. *Journal of Metamorphic Geology*, **3**, 327-342.

Powell, R. & Holland, T.J.B. 1988. An internally consistent dataset with uncertainties and correlations: 3. Applications to geobarometry, worked examples and a computer program. Journal of Metamorphic Geology, **6**, 173-204.

Pudsey, . C.J. 1986. The Northern Suture, Pakistan: margin of a Cretaceous island-arc. *Geological Magazine*, **123**, 405-423.

Rattan, S.S. 1973. Stratigraphy and sedimentation of the Chamba area Western Himachal Pradesh. *Himalayan Geology*, **3**, 231-248.

Rawat, B.S. & Thakur, V.C. 1988. Lithostratigraphy and structure of the Central Crystallines and the Phanerozoic metasedimentaries of the Lahaul and Bharmour regions of Himachal in north-western Himalaya. *Publ. Cent. Adv. stud. Geol, Panjab Univ., Chandigarh*, **3**, 97-111.

Reddy, S.M., Searle, M.P. & Massey, A.M. 1993. Structural evolution of the High Himalayan Gneiss sequence, Langtang Valley, Nepal. *In*: Treloar, P.J. & Searle, M.P. (eds.), *Himalayan Tectonics*, Geological Society Special Publication, **74**, 375-389.

Renne, P. R., Deino, A. L., Walter, R. C., Turrin, B. D., Swisher, C. C., Becker, T. A., Curtis, G. H., Sharp, W. D. & Jaouni, A.-R., 1994. Intercalibration of astronomical and radioisotopic time. *Geology*, **22**, 783-786.

Reuber, I. 1986. Geometry of accretion and oceanic thrusting of the Spontang ophiolite, Ladakh-Himalaya. *Nature*, **321**, 592-596.

Reuber, I. 1989. The Dras arc: two successive volcanic events on eroded oceanic crust. *Tectonophysics*, **161**, 93-106.

Roddick, J. C., Cliff, R. A. & Rex, D. C., 1980. The evolution of excess argon in Alpine biotites – A ^{40}Ar-^{39}Ar analysis. *Earth and Planetary Science Letters*, **48**, 185-208.

Sawka, W.N., Banfield, J.F. & Chappell, B.W. 1986. A weathering-related origin of widespread monazite in S-type granites. *Geochimica et Cosmochimica Acta*, **50**, 171-175.

Scaillet, B., France-Lanord, C., & Le Fort, P. 1990. Badrinath-Gangotri plutons (Garhwal, India): petrological and geochemical evidence for fractionation processes in a High Himalayan leucogranite. *Journal of Volcanology and Geothermal Research*, **44**, 163-188.

Scaillet, B., Pichavant, M. & Roux, J. 1995. Experimental crystallisation of leucogranite magmas. *Journal of Petrology*, **36**, 663-705.

Schärer, U. 1984. The effect of initial ^{230}Th disequilibrium on young U-Pb ages: the Makalu case, Himalaya. *Earth and Planetary Science Letters*, **67**, 191-204.

Schärer, U., Hamet, J. & Allègre, C.J. 1984a. The Transhimalayan (Gangdese) plutonism in the Ladakh region: a U-Pb and Rb-Sr study. *Earth and Planetary Science Letters*, **67**, 327-339.

Schärer, U., Xu, R. & Allègre, C.J. 1986. U-(Th)-Pb systematics and ages of Himalayan leucogranites, south Tibet. *Earth and Planetary Science Letters*, **77**, 35-48.

Schärer, U., Xu, R.-H. & Allègre, C.J. 1984b. U-Pb geochronology of Gangdese (Transhimalaya) plutonism in the Lhasa-Xigaze region, Tibet. *Earth and Planetary Science Letters*, **69**, 311-320.

Schelling, D. & Arita, K. 1991. Thrust tectonics, crustal shortening and the structure of the far-eastern Nepal Himalaya. *Tectonics*, **10**, 851-862.

Searle, M.P. 1986. Structural evolution and sequence of thrusting in the High Himalayan, Tibetan-Tethys and Indus suture zones of Zanskar and Ladakh, Western Himalaya. *Journal of the Geological Society*, **8**, 923-936.

Searle, M.P. & Fryer, B.J. 1986. Garnet, tourmaline and muscovite-bearing leucogranites, gneisses and migmatites of the Higher Himalayas from Zanskar, Kulu, Lahoul and Kashmir. *In*: Coward, M. P. & Ries, A.C. (eds), *Collision Tectonics*, Geological Society, London, Special Publication **19**, 83-94.

Searle, M.P., Windley, B.F., Coward, M.P., Cooper, D.J.W., Rex, A.J., Rex, D., Tingdong, L., Xuchang, X., Jan, M.Q., Thakur, V. & Kumar, S. 1987. The closing of Tethys and the tectonics of the Himalayas. *Bulletin of the Geological Society of America*, **98**, 678-701.

Searle, M.P., Cooper, D.J.W. & Rex, A.J. 1988. Collision tectonics of the Ladakh-Zanskar Himalaya. *Philosophical Transactions of the Royal Society of London*, **A326**, 117-150.

Searle, M.P. & Rex, A.J. 1989. Thermal model for the Zanskar Himalaya. *Journal of Metamorphic Geology*, **7**, 127-134.

Searle, M.P. 1991. Geology and Tectonics of the Karakoram Mountains. Chichester: Wiley.

Searle, M.P., Waters, D.J., Rex, D.C. & Wilson, R.N. 1992. Pressure, temperature and time constraints on Himalayan metamorphism from eastern Kashmir and western Zanskar. *Journal of the Geological Society, London*, ***149***, 753-773.

Searle, M.P. & Khan, M.A. 1996. Geological map of North Pakistan.

Searle, M.P. 1996a. Geological evidence against large-scale pre-Holocene offsets along the Karakoram Fault: Implications for limited extrusion of the Tibetan plateau. *Tectonics*, **15**, 171-186.

Searle, M.P. 1996b. Cooling history, erosion, exhumation and kinematics of the Himalaya-Karakoram-Tibet orogenic belt. *In*: Yin, A. & Harrison, T.M. (eds), *The Tectonic Evolution of Asia*, 110-137, Cambridge University Press.

Searle, M.P., Parrish, R.R., Hodges, K.V., Hurford, A., Ayres, M.W. & Whitehouse, M.J. 1997a. Shisha Pangma leucogranite, south Tibetan Himalaya: Field relations, geochemistry, age, origin and emplacement. *Journal of Geology* , **105**, 295-317.

Searle, M.P., Corfield, R.I, Stephenson, B.J. & McCarron, J. 1997b. Structure of the north Indian continental margin in the Ladakh-Zanskar Himalayas: implications for the timing of obduction of the Spontang ophiolite, India-Asia collision and deformation events in the Himalaya. *Geological Magazine,* **134**, 297-316.

Searle, M.P., Waters, D.J., Dransfield, M.W., Stephenson, B.J., Walker, C.B., Walker, J.D. & Rex, D.C. 1998. Thermal and mechanical models for the structural evolution of the Zanskar High Himalaya. *Submitted.*

Sengör, A.M.C. 1985. The story of Tethys: how many wives did Okeanos have? *Episodes*, **8**, 3-12.

Shanker, R., Kumar, G. & Saxena, S.P. 1989 Stratigraphy and sedimentation in Himalaya. A re-appraisal. *Geological Survey of India Special Publication*, **26**, 1-60.

Shi, Y. & Wang, C-Y. 1987. Two-dimensional modelling of the P-T-t paths of regional metamorphism in simple overthrust terrains. *Geology*, **15**, 1048-1051.

Smith, A.B. 1988. Late Palaeozoic biogeography of East Asia and palaeontological constraints on plate tectonic reconstructions. *Philosophical Transactions of the Royal Society of London*, **A326**, 180-227.

Smith, H.A. & Barreiro, B. 1990. Monazite U-Pb dating of staurolite grade metamorphism in pelitic schists. *Contributions to Mineralogy and Petrology*, **105**, 602-615.

Snee, L. W., Sutter, J. F. & Kelley, W. C., 1988. Thermochronology of economic mineral deposits: Dating the stages of mineralization at Panasqueira, Portugal, by high-precision $^{40}Ar/^{39}Ar$ age spectrum techniques on muscovite. *Economic Geology*, **83**, 335-354.

Spear, F. S., 1991. On the interpretation of peak metamorphic temperatures in the light of garnet diffusion during cooling: *Journal of Metamorphic Geology*, *9*, 379-388.

Spear, F.S. 1993. Metamorphic phase equilibria and pressure-temperature-time paths. Mineralogical Society of America.

Spring, L. & Crespo-Blanc, A. 1992. Nappe tectonics, extension and metamorphic evolution in the Indian Tethys Himalaya (Higher Himalaya, SE Zanskar and NW Lahul). *Tectonics*, **11**, 978-989.

Srikantia, S.V., Ganesan, T.M., Rao, R.N. Sinha, P.K. & Tirkey, B. 1980. Geology of Zanskar area, Ladakh Himalaya. *Himalayan Geology*, **8**/2, 1009-1033.

Srikantia, S.V. & Bhargava, O.N. 1982. An outline of the structure of the area between the Rhotang Pass in Lahaul and the Indus Valley in Ladakh. *Geological Survey of India*, 193-203.

Stacey, J.S. & Kramers, J.D. 1975. Approximation of terrestrial lead isotope evolution by a two-stage model. *Earth and Planetary Science Letters*, **26**, 207-221.

Stäubli, A. 1989. Polyphase metamorphism and the development of the Main Central Thrust. *Journal of Metamorphic Geology*, **7**, 73-93.

Steck, A., Spring, L., Vannay, J.C., Masson, H., Stutz, E., Bucher, H., Marchant, R. & Tieche, J.C. 1993a. Geological transect across the northwestern Himalaya in eastern Ladakh and Lahul (A model for the continental collision of India and Asia). *Eclogae Geologicae Helvetiae*, **86**, 219-263.

Steiger, R. H., and Jäger, E., 1977. Subcommision on geochronology: convention on the use of decay constants in geo- and cosmochronology: *Earth and Planetary Science Letters*, **36**, 359-362.

Stephenson, B.J. 1997. The tectonic and metamorphic evolution of the Main Central Thrust zone and High Himalaya around the Kishtwar and Kulu windows, northwest India. *Unpublished Ph.D. thesis*, Oxford University.

Stolickza, F. 1865. Geological sections across the Himalaya mountains from Wangtu Bridge on the river Sutlej to Sungdo on the indus, with an account of the formation in Spiti, accompanied by a revision of all known fossils from that district. *Mem. Geol. Surv. India*, **5**, 1-154.

St-Onge, M.R. 1987. Zoned poikiloblastic garnets: P-T paths and syn-metamorphic uplift through 30Km of structural depth, Wompay Orogen, Canada. *Journal of Petrology*, **28**, 1-21.

Sullivan, M.A., Windley, B.F., Saunders, A.D., Haynes, J.R. & Rex, D.C. 1993. A palaeogeographic reconstruction of the Dir group: evidence for magmatic arc migration within Kohistan, N. Pakistan. *In*: Treloar, P.J. & Searle, M.P. (eds), *Himalayan Tectonics*, Geological Society, London, Special Publication **74**, 139-160.

Swapp, S.M. & Hollister, L.S. 1991. Inverted metamorphism within the Tibetan Slab of Bhutan: evidence for a tectonically transported source. *Canadian Mineralogist*, **29**, 1019-1041.

Tapponnier, P. *et al*, 1981a. The Tibetan side of the India-Eurasia collision. *Nature*, **294**, 405-410.

Tapponnier, P., Mercier, J.L., Armijo, R., Tonglin, H. & Ji, Z. 1981b. Field evidence for normal faulting in Tibet. *Nature*, **294**, 410-414.

Tapponnier, P., Peltzer, G. & Armijo, 1986. On the mechanics of the collision between India and Asia. *In*: Coward, M. P. & Ries, A. C. (eds), *Collision Tectonics*, Geological Society, London, Special Publication **19**, 115-157.

Thakur, V.C. 1994. Deformation in the Chamba Nappe and Main Central Thrust in Kashmir Himalaya. (Abstract) 11th Himalayan-Karakoram-Tibet Workshop, Ascona.

Thakur V.C. & Pande, I.C. 1971. The stratigraphy and deformation in the areas around Chamba, Himachal Pradesh. Bull. Ind. Geol. Assoc., **4**, 68-75.

Thakur, V.C. & Tandon, S.K. 1976. Significance of pebble and mineral lineation in the Chamba syncline of Punjab Himalaya, Himachal Pradesh, India. *Geological Magazine*, **113**, 141-149.

Thompson, A.B. 1976. Mineral reactions in pelitic rocks; II, Calculation of some P-T-X(Fe-Mg) phase relations. *American Journal of Science*, **276**, 425-454.

Thompson, A.B. 1982. Dehydration melting of pelitic rocks and the generation of H2O-undersaturated granitic liquids. *American Journal of Science*, **276**, 1567-1595.

Thompson, A.B. & England, P.C. 1984. Pressure-temperature-time paths of regional metamorphism, Part II: Some petrological constraints from mineral assemblages in metamorphic rocks. *Journal of Petrology*, **25**, 929-55.

Thoni, M. 1977. Geology, structural evolution and metamorphic zoning in the Kulu valley (Himachal Himalaya, India). *Mitt. Ges. Geol. Bergbaustud. Osterr.*, **24**, 125-187.

Tracy, R.J. 1982. Compositional zoning and inclusions in metamorphic minerals. *Mineralogical Society of America Reviews in Mineralogy*, **10**, 355-397.

Tracy, R.J., Robinson, P. and Thompson, A.B., 1976. Garnet composition and zoning in the determination of temperature and pressure of metamorphism, central Massachusetts: *American Mineralogist*, **61**, 762-775.

Trommsdorff, V., Dietrich, V. & Honegger, K. 1983. The Indus Suture Zone: Palaeotectonic and igneosu evolution in the Ladakh Himalaya. In: Hsü, K.J. (ed.) Mountain Building (213-220), Academic Press, London.

Tullis & Yund. 1977. Experimental deformation of dry Westerly Granite. *Journal of Geophysical Research*, **82**, 5705-5718.

Valdiya, K.S. 1980b. The two intracrustal boundary thrusts of the Himalaya. *Tectonophysics*, **66**, 323-348.

Valdiya, K.S. 1988. Tectonics and evolution of the central sector of the Himalaya. *Philosophical Transactions of the Royal Society of London*, **A326**, 151-175.

Vance, D.R. & Kelley, S. 1994. Ar-Ar constraints on erosional versus extensional unroofing in orogenic belts: the Zanskar Himalaya, NW India. *Mineralogical Magazine*, **58A**, 930-932.

Vance, D. & Harris, N. 1996. Precise Sm-Nd ages from Himalayan garnets: temporal controls on metamorphism. Abstract, *Metamorphic Studies Group*, Kingston University, UK.

Vannay, J.C. 1993. Géologie des chaines du Haut Himalaya et du Pir Panjal au Haut-Lahaul (NW Himalaya, Inde): Palaéogeographie et tectonique. *Mem. Geol. Laussane*, **16**, 1-148.

Vannay, J.C. & Steck, A. 1995. Tectonic evolution of the High Himalaya in Upper Lahul (NW Himalaya, India). *Tectonics*, **14**, 253-263.

Vannay, J.C. & Hodges, K.V. 1996. Tectonometamorphic evolution of the Himalayan metamorphic core between the Annapurna and Dhaulagiri, central Nepal. *Journal of Metamorphic Geology*,. **14**, 635-656.

Vannay, J.C. & Grasseman, B. 1998. Inverted metamorphism in the High Himalaya of Himachal Pradesh (NW India): phase equilibria versus thermobarometry. *Schweiz. Mineral. Petrogr. Mitt.* **78**, 107-132.

Vidal, P., Cocherie, A. & Le Fort, P. 1982. Geochemical investigations of the origin of the Manaslu leucogranite (Himalaya, Nepal). *Geochimica et Cosmochimica Acta*, **46**, 2279-2292.

Villa, I.M. 1998. Isotopic closure. *Terra Nova*, **10**, 42-47.

Villa, I.M. & Oddone, M. 1988. $^{39}Ar/^{40}Ar$ ages of Himalayan leucogranites decrease eastwards. *Himalayan-Karakoram-Tibet Workshop* (abstract volume), Lausanne, 16.

Wadia, D.N. 1931. The syntaxis of the Northwest Himalaya: its rocks, tectonics and orogeny. *Rec. Geol. Surv. Ind*, **65**, 189-220.

Wagner, G.A., Reimer, G.M. & Jäger, E. 1977. Cooling ages derived by apatite fission track, mica Rb-Sr, and K-Ar dating: the uplift and cooling history of the Central Alps. *Mem. Inst. Geol. Mineral. Univ. Padova*, **30**, 1-27.

Waters *et al.*, in prep. Metamorphic profiles across the High Himalaya in western Zanskar, India.

Waters, D.J., Searle, M.P., Dransfield, M.W., Rex, D.C. & Stephenson, B.J.1996. Metamorphic profiles across the High Himalaya in western Zanskar, India. (Poster) 12th Himalayan-Karakoram-Tibet Workshop, Flagstaff

Watson, E.B. and Harrison, T.M., 1983. Zircon saturation revisited: temperature and composition effects in a variety of crustal magma types: *Earth and Planetary Science Letters*, **64**, 295-304.

Wang, Y.G. & Sun, D.L. 1985. The Triassic and Jurassic palaeogeography and evolution of the Qinghai-Xizang (Tibet) Plateau. *Canadian Journal of Earth Sciences*, **22**, 195-204.

Wendt, I. & Carl, C., 1991. The statistical distribution of the mean squared weighted deviation. *Chemical Geology*, **86**, 275-285.

Wernicke, B.P., Christiansen, R.L., England, P.C. & Sonder, L.J. 1987. Tectonomagmatic evolution of Cenozoic extension in the North America Cordillera. In: Coward, M.P., Dewey, J.F. & Hancock, P.L. (eds), *Continental extensional tectonics*, Geological Society Special Publication, **28**, 203-221,

Wilson, M. 1989. Igneous Petrogenesis: a global tectonic approach. Chapman & Hall, 466pp.

York, D., 1969. Least-squares fitting of a straight line with correlated errors. *Earth and Planetary Science Letters*, **5**, 320-324.

Zeitler, P.K., Sutter, J.F., Williams, I.S., Zartman, R. & Tahirkheli, R.A.K., 1989. Geochronology and Temperature History of the Nanga Parbat-Haramosh Massif, Pakistan. *Geological Society of America Special Publication*, 232.

Zhao, W., Nelson, K.D. & Project INDEPTH team. 1993. Deep seismic reflection evidence for continental underthrusting beneath southern Tibet. *Nature*, **366**, 557-559.

Zhu, X.K., O'Nions, R.K., Belshaw,N.S. & Gibb, A.J. 1997. Significance of in situ SIMS chronometry of zoned monazite from the Lewisian granulites, northwest Scotland. *Chemical-Geology*, **135**, 35-53.

Appendix A

Mineral chemistry and thermobarometry: methods and techniques

A.1 Mineral chemistry

Samples were selected for mineral chemistry analysis on the basis of their petrography. Polished thin sections (30μm thick) were prepared for each sample and coated with a 200 μm thick layer of carbon to prevent the build up of charge. Minerals were analysed using a Cambridge Instruments Microscan 9 electron microprobe, which has two wavelength dispersive spectrometers. The microprobe was calibrated by running known standards at regular intervals. An Opus personal computer automatically converted the measured element concentrations to element percentages using ZAF corrections. The operation conditions during analysis were as follows: beam size ~0.5-1.0 μm, beam current = $4x10^{-8}$ A, accelerating potential = 20 kv. Under this set-up the excitation volume of the target area has a maximum diameter of 3μm.

Cations were calculated using the M9Lotus2 computer programme (Norman Charnley, pers. comm.). Fe^{3+} was calculated for some minerals using the charge balance method of Droop (1987), although this was nearly always zero for garnets and impossible to calculate for biotite. Mineral analyses were plotted on various compositional diagrams to assess their stoichiometry, identify patterns of zoning and to determine whether multiple generations of mineral groups are present in a single thin section. The procedure for different mineral groups is outlined below.

Garnet

Garnet zoning profiles were plotted using compositional data obtained from microprobe traverses across porphyroblasts in directions parallel to and perpendicular to the matrix foliation. Ca, Mg, Fe Mn and X_{Mg} were plotted in relation to the distance from the edge of the garnet. Compositional zoning is attributed to slow diffusion in the garnet lattice during growth at temperatures <650°C and implies that garnet grew by fractional crystallisation from the matrix (e.g. Tracy *et al.*, 1976; Tracy, 1982). The absence of compositional zoning has been attributed to both rapid crystal growth, or homogenisation of a previously formed zoning profile by diffusion at temperatures in excess of *c.*600-650°C (e.g. Tracy, 1982).

Muscovite

The mineral chemistry of muscovite was studied by plotting Si cations against Fe, Mg, Na and Ti to assess the extent of phengite (Fe, Mg) and paragonite (Na) substitution. The paragonite content is expected to increase with temperature as the muscovite-paragonite miscibility gap narrows (Guidotti, 1973; Chatterjee & Flux, 1986). Conversely, increased Fe and Mg content is favoured by decreasing temperature and increased pressure. The phengite content is monitored by the Si content, which is 6 in pure muscovite (for 22 oxygens), but can be as high as 7.8 for the most Si-rich phengites known. Peak-metamorphic assemblages will therefore have a low celadonite content (Mg end-member) and a high paragonite content (Na end-member).

Biotite

Biotite chemistry was studied by plotting Ti cation abundance against octahedral Al (which, for a formula unit with 22 oxygens is calculated as Al+Si–8). The major substitutions in biotite (Fe/Mg ratio and Al content) tend to reflect bulk composition rather than metamorphic grade. However, if there is a Ti saturating phase in the rock such as sphene, or rutile, the Ti content of the biotite may be used as an indicator of metamorphic grade. Ti content is thought to increase with increasing P-T conditions (Engel & Engel, 1960). X_{Mg} is a good way of investigating the extent of Fe-Mg exchange in biotite, which is useful for comparing matrix biotite compositions with those adjacent to garnets, where extensive Fe-Mg exchange between phases might be expected.

Plagioclase

Plagioclase chemistry was studied by monitoring the An content of the grain (established from a plot of Ca/(Ca + Na + K) against (Al-1)/(Al+Si-3)). This also allowed the stoichiometry of the analyses to be checked, with good results showing a 1:1 correlation. Anorthite content is expected to increase with increasing P-T conditions (Deer *et al.*, 1989), as demonstrated by the appearance of albite in rocks of greenschist-facies metamorphism.

Staurolite and cordierite

Staurolite and cordierite chemistry was studied from zoning profiles of X_{Mg} across individual grains in directions parallel and perpendicular to the matrix foliation grain. The use of staurolite and cordierite during P-T calculations, however, was of limited use owing to the poor reliability of the Fe staurolite and Fe cordierite end member in the thermodynamic dataset (Holland & Powell, 1990). This did not detract from their use in constructing P-T pathways from petrogenetic grids.

A.2 Thermobarometric analysis: conventional techniques *vs.* THERMOCALC

In an attempt to quantitatively constrain the pressure-temperature (P-T) conditions, samples were specifically selected for thermobarometric analysis. In the field, pelites of similar bulk composition containing the mineral assemblage Qtz + Pl + Ms + Bt ± Grt ± St ± Ky ± Sill ± Crd were collected along transects parallel and perpendicular to strike. Petrographic analysis identified assemblages which showed evidence of textural equilibrium. Minerals believed to be in equilibrium were analysed using the electron microprobe. In order to minimise the 'counting error' of the microprobe, replicate analyses of mineral compositions were analysed and averaged for use in thermobarometric calculations. The averages used for P-T work in each sample are listed in Appendix B. 'Rogue' mineral compositions were identified from their anomalous chemistry plots (as outlined in section A1), and were not included into the thermodynamic dataset. Where possible, analyses were made of minerals immediately adjacent to one another, since these are more likely to have equilibrated together. Where this was not possible, replicate analyses were made of matrix minerals to ensure that there were no significant variations in composition at the thin section scale.

Two complementary methods were used to calculate P-T results: (1) conventional thermobarometry, and (2) the computer program THERMOCALC version 2.4 (Powell & Holland, 1988), in conjunction with the internally consistent dataset of Holland & Powell (1990).

Conventional thermobarometry

Conventional thermobarometry relies upon the simultaneous solution of the garnet-biotite (GB) thermometer with the garnet-muscovite-plagioclase-biotite (GMPB) geobarometer (Ghent & Stout, 1981; Hodges & Crowley, 1985). Use of the garnet-aluminosilicate-plagioclase (GASP) geobarometer (Newton & Haselton, 1981) was limited, owing to the rare occurrence of both garnet and aluminosilicate in the same sample. Several GB thermometers were used in this work for compare purposes. The results of this work are presented in Tables 4.2, 4.3, 5.1 and 6.2. In order to be consistent with previous and ongoing P-T work here at Oxford (e.g. Stephenson, 1997; Hilderbrand, 1998), the garnet-biotite thermometer of Bhattacharya *et al.* (1992) using the garnet mixing model of Hackler and Wood (1989) was taken to be the preferred result.

THERMOCALC (Powell & Holland, 1988)

THERMOCALC uses the activities of mineral end-members to calculate P-T results. Activities were calculated using the WAX computer programme (D.J. Waters, pers. comm.), the 'run' temperature for which was determined from solution of the Bhattacharya *et al.* (1992) garnet-biotite geothermometer using the garnet mixing model of Hackler and Wood (1989). The WAX programme uses the following mixing models to calculate end-member activities: biotite and cordierite (ideal ionic mixing on sites); muscovite (K-Na mixing model of Chatterjee & Flux, 1986); plagioclase (Darken's quadratic formalism (model 4 in Holland & Powell, 1992)); garnet (non-ideal mixing model of

Newton & Haselton, 1981); and staurolite (Fe-Mg ideal mixing). THERMOCALC assumes that Al_2SiO_5 and SiO_2 are pure phases and, therefore, have an activity of 1.

THERMOCALC was run in 'average P-T' mode using the activities calculated by Wax. A complete set of independent reactions was calculated in each case. The number of reactions involved in each P-T estimate are shown in Tables 4.2, 4.3, 5.1 and 6.2, together with the correlation (corr.) between the uncertainties on pressure and temperature. The 'fit' parameter describes the averaging of the number of equilibria found. If the 'fit' parameter is larger than the minimum 'fit' specified by the program for a statistically valid result, then the chosen phases have probably not equilibrated at the same time, or the activity models are incorrect. Those samples which plotted outside the 'fit' parameter are shown in Tables 4.2, 4.3, 5.1 and 6.2.

A.3 Errors in P-T estimates

Quantitative thermobarometry is subject to many errors, not least the assumption that the minerals observed in thin section are at equilibrium with one another and formed at the same time under the same P-T conditions. In addition to this initial assumption, other sources of error include: (1) analytical errors; (2) calibration errors; (3) activity calculations. All of these errors are propagated through the P-T calculation process, which results in a quantitative estimate of the standard deviation in pressure and temperature away from the calculated value. THERMOCALC typically gives pressure errors of ± 1 kbar and temperature errors of ± 20-40°C. These errors are quoted at the $1<\sigma<2$ range.

Analytical errors originate from the analytical uncertainty of the microprobe and are sample specific. A numerical estimate of analytical uncertainty can be derived from the variation in X-ray count-rate at the characteristic peak on a specific element. In general, for the data collected in this study, these error estimates have a 2σ variation of <2%.

Calibration errors are reaction specific. The uncertainty on any single reaction is quite large, but is greatly reduced when more than one reaction is taken into consideration. This is one of the main advantages of using THERMOCALC, since it uses a number of independent phase equilibria to calculate P-T results.

Activity calculations account for the largest source of error in any P-T estimate. The activity models used in this work are given in section A.2.

Appendix B

Averaged mineral analyses used in thermobarometric calculations

(see Enclosure 2 for location of samples and Tables 4.2, 4.3, 5.1 and 6.2 for P-T results)

Sample	JDW 18	JDW 18	JDW 18	JDW 18	JDW 22	JDW 22	JDW 22	JDW 22	JDW 23	JDW 23	JDW 23	JDW 23
Min	Grt	Bt	Ms	Pl	Grt	Bt	Ms	Pl	Grt	Bt	Ms	Pl
Average of	18	11	6	7	51	12	16	14	7	12	3	18
SiO2	36.96	36.13	46.60	65.03	36.88	35.54	46.33	64.70	37.49	35.68	45.92	63.29
TiO2	0.03	1.62	0.36	-	0.02	2.13	0.56	-	0.04	1.69	0.51	-
Al2O3	20.69	18.07	34.47	21.65	20.75	18.02	33.86	21.77	21.04	18.39	34.11	22.93
FeO	32.53	18.93	1.07	-	28.25	21.14	1.58	-	31.16	20.18	1.84	-
MnO	5.94	0.12	0.02	-	9.39	0.21	0.02	-	5.50	0.14	0.03	-
MgO	2.41	9.59	0.71	-	1.53	8.29	0.97	-	2.34	9.53	0.88	-
CaO	2.03	0.01	0.00	3.44	2.72	0.00	0.00	3.09	2.71	0.00	0.00	4.58
Na2O	-	0.11	1.45	9.88	-	0.12	0.71	9.99	0.06	0.16	0.75	9.20
K2O	-	9.64	9.17	0.11	-	9.13	9.83	0.11	0.05	9.58	9.63	0.14
BaO	-	-	0.49	-	-	0.00	0.68	-	-	-	0.51	-
Total	100.60	94.24	94.35	100.12	99.55	94.59	94.26	99.65	100.39	95.34	94.19	100.14
Oxygens	12	22	22	8	12	22	22	8	12	22	22	8
Si	2.985	5.552	6.246	2.863	3.005	5.494	6.242	2.860	3.010	5.456	6.202	2.797
Ti	0.002	0.188	0.036	-	0.002	0.248	0.057	-	0.003	0.195	0.052	-
Al	1.970	3.274	5.449	1.124	1.994	3.284	5.378	1.135	1.992	3.315	5.431	1.195
Fe2+	2.198	2.434	0.120	-	1.925	2.733	0.179	-	2.092	2.580	0.208	-
Mn	0.407	0.016	0.003	-	0.649	0.027	0.003	-	0.374	0.018	0.005	-
Mg	0.290	2.196	0.141	-	0.185	1.911	0.195	-	0.280	2.172	0.178	-
Ca	0.176	0.006	0.000	0.162	0.237	0.001	0.001	0.146	0.233	0.002	0.000	0.217
Na	-	0.034	0.378	0.843	-	0.037	0.186	0.856	0.009	0.046	0.197	0.788
K	-	1.891	1.569	0.006	-	1.801	1.690	0.006	0.005	1.869	1.660	0.008
Ba	-	-	0.026	-	-	0.000	0.036	-	-	-	0.027	-
Sum	8.028	15.585	13.967	4.999	7.997	15.535	13.950	5.003	7.999	15.650	13.958	5.004
XMg	0.117	0.474	0.542	-	0.088	0.412	0.521	-	0.118	0.457	0.462	-
Mol% Alm	0.72	-	-	-	0.64	-	-	-	0.70	-	-	-
Mol% Spess	0.13	-	-	-	0.22	-	-	-	0.13	-	-	-
Mol% Pyr	0.09	-	-	-	0.06	-	-	-	0.09	-	-	-
Mol% Gross	0.06	-	-	-	0.08	-	-	-	0.08	-	-	-

Sample	JDW 26	JDW 26	JDW 26	JDW 26	JDW 28	JDW 28	JDW 28	JDW 28	JDW 29	JDW 29	JDW 29	JDW 29
Min	Grt	Bt	Ms	Pl	Grt	Bt	Ms	Pl	Grt	Bt	Ms	Pl
Average of	4	8	5	17	3	5	10	21	3	20	21	17
SiO2	37.80	35.95	47.16	64.04	38.04	36.07	46.89	63.90	37.62	36.08	46.38	63.61
TiO2	0.02	1.94	0.48	-	0.05	1.44	0.36	-	0.02	1.46	0.40	-
Al2O3	21.16	18.34	34.31	22.83	21.10	18.66	35.26	22.66	20.78	18.08	35.21	22.41
FeO	30.63	20.55	1.54	-	34.34	18.96	1.48	-	34.54	18.51	1.01	-
MnO	6.35	0.14	0.02	-	2.90	0.10	0.02	-	2.21	0.08	0.01	-
MgO	1.97	9.20	0.97	-	3.19	10.44	0.55	-	2.86	10.46	0.67	-
CaO	3.63	0.01	0.00	4.31	2.01	0.00	0.00	4.39	2.54	0.01	0.00	4.35
Na2O	-	0.25	1.04	9.38	-	0.38	1.91	9.40	-	0.26	1.83	9.54
K2O	-	9.31	9.89	0.14	-	9.28	8.49	0.13	-	8.97	8.76	0.12
BaO	-	-	0.50	-	-	-	0.26	-	-	-	0.40	
Total	101.55	95.67	95.91	100.70	101.62	95.33	95.21	100.48	100.58	93.90	94.67	100.03
												-
Oxygens	12	22	22	8	12	22	22	8	12	22	22	8
Si	3.007	5.475	6.252	2.811	3.012	5.469	6.211	2.812	3.014	5.533	6.184	2.814
Ti	0.001	0.222	0.048	-	0.003	0.165	0.036	-	0.001	0.168	0.041	-
Al	1.985	3.293	5.362	1.182	1.970	3.336	5.505	1.176	1.963	3.269	5.534	1.169
Fe2+	2.038	2.618	0.171	-	2.274	2.404	0.164	-	2.314	2.375	0.112	-
Mn	0.428	0.018	0.004	-	0.194	0.013	0.003	-	0.150	0.011	0.002	-
Mg	0.233	2.089	0.191	-	0.376	2.360	0.108	-	0.342	2.392	0.134	-
Ca	0.309	0.003	0.000	0.203	0.170	0.000	0.000	0.207	0.218	0.006	0.001	0.206
Na	-	0.075	0.267	0.798	-	0.111	0.490	0.803	-	0.076	0.473	0.818
K	-	1.809	1.672	0.008	-	1.794	1.434	0.007	-	1.754	1.491	0.007
Ba	-	-	0.026	-	-	-	0.013	-	-	-	0.021	-
Sum	8.000	15.599	13.990	5.001	8.000	15.651	13.964	5.005	8.003	15.580	13.990	5.014
XMg	0.103	0.444	0.528	-	0.142	0.495	0.394	-	0.129	0.502	0.545	-
Mol% Alm	0.68	-	-	-	0.75	-	-	-	0.77	-	-	-
Mol% Spess	0.14	-	-	-	0.06	-	-	-	0.05	-	-	-
Mol% Pyr	0.08	-	-	-	0.12	-	-	-	0.11	-	-	-
Mol% Gross	0.10	-	-	-	0.06	-	-	-	0.07	-	-	-

Sample	JDW 32	JDW 32	JDW 32	JDW 32	JDW 50	JDW 50	JDW 50	JDW 50	JDW 54	JDW 54	JDW 54	JDW 54
Min	Grt	Bt	Ms	Pl	Grt	Bt	Ms	Pl	Grt	Bt	Ms	Pl
Average of	52	17	11	18	5	16	8	22	2	4	3	6
SiO2	37.63	35.99	47.14	63.25	37.70	35.61	45.35	62.97	37.04	35.28	45.44	62.69
TiO2	0.06	1.55	0.43	-	0.07	1.73	0.45	0.00	0.02	1.65	0.36	-
Al2O3	20.68	18.17	35.11	22.47	20.44	17.80	33.79	22.59	20.53	17.83	34.24	21.99
FeO	33.14	19.10	1.37	-	28.74	18.80	1.82	0.00	33.70	19.24	1.38	-
MnO	3.43	0.12	0.02	-	6.54	0.15	0.02	0.00	3.15	0.07	0.02	-
MgO	2.76	9.97	0.71	-	2.61	9.91	0.64	0.00	2.29	9.51	0.67	-
CaO	2.59	0.00	0.00	4.63	4.21	0.00	0.01	4.82	2.56	0.00	0.00	4.29
Na2O	-	0.23	1.34	9.38	-	0.25	1.24	9.26	-	0.26	1.49	9.50
K2O	-	9.26	8.86	0.11	-	9.41	9.52	0.12	-	8.96	9.11	0.10
BaO	-	0.14	0.30	-	-	0.20	0.41	0.00	-	0.15	0.35	-
Total	100.30	94.53	95.28	99.83	100.31	93.86	93.24	99.76	99.27	92.93	93.06	98.57
Oxygens	12	22	22	8	12	22	22	8	12	22	22	8
Si	3.022	5.516	6.236	2.806	3.023	5.507	6.194	2.797	3.016	5.508	6.189	2.815
Ti	0.003	0.178	0.043	-	0.004	0.201	0.046	-	0.001	0.193	0.037	-
Al	1.958	3.283	5.476	1.175	1.932	3.247	5.442	1.183	1.971	3.283	5.497	1.164
Fe2+	2.226	2.448	0.151	-	1.928	2.432	0.207	-	2.294	2.512	0.157	-
Mn	0.234	0.016	0.003	-	0.444	0.020	0.002	-	0.217	0.010	0.005	-
Mg	0.331	2.276	0.139	-	0.312	2.284	0.131	-	0.277	2.213	0.136	-
Ca	0.223	0.000	0.002	0.220	0.362	0.000	0.002	0.229	0.224	0.002	0.001	0.206
Na	-	0.069	0.344	0.806	-	0.075	0.328	0.798	-	0.077	0.394	0.827
K	-	1.810	1.495	0.007	-	1.856	1.660	0.007	-	1.784	1.583	0.006
Ba	-	0.008	0.015	-	-	0.012	0.022	-	-	0.009	0.019	-
Sum	7.996	15.604	13.903	5.013	8.006	15.634	14.033	5.014	7.999	15.588	14.014	5.019
XMg	0.129	0.482	0.480	-	0.139	0.484	0.386	-	0.108	0.468	0.472	-
Mol% Alm	0.74	-	-	-	0.63	-	-	-	0.76	-	-	-
Mol% Spess	0.08	-	-	-	0.15	-	-	-	0.07	-	-	-
Mol% Pyr	0.11	-	-	-	0.10	-	-	-	0.09	-	-	-
Mol% Gross	0.07	-	-	-	0.12	-	-	-	0.07	-	-	-

Sample	JDW 57	JDW 57	JDW 57	JDW 57	JDW 129	JDW 129	JDW 129	JDW 129	JDW 92	JDW 92	JDW 92	JDW 92
Min	Grt	Bt	Ms	Pl	Grt	Bt	Ms	Pl	Grt	Bt	Ms	Pl
Average of	2	7	4	5	16	7	3	4	2	9	14	14
SiO2	37.32	35.54	45.15	61.60	36.66	35.26	45.68	62.21	37.59	35.72	45.72	64.00
TiO2	0.02	1.48	0.38	-	0.05	1.69	0.31	-	0.46	2.34	0.90	-
Al2O3	20.59	17.98	34.50	22.71	21.09	18.39	34.15	22.99	21.24	18.28	34.67	21.82
FeO	35.95	19.61	1.13	-	29.20	20.69	1.83	-	33.85	18.38	1.38	-
MnO	1.175	0.03	0.01	-	8.54	0.13	0.03	-	2.54	0.08	0.01	-
MgO	2.785	9.61	0.56	-	1.36	8.61	0.97	-	3.69	9.86	0.78	-
CaO	2.12	0.00	0.00	5.11	3.12	0.01	0.00	4.72	2.02	0.00	0.00	3.33
Na2O	-	0.16	1.66	8.95	-	0.19	0.82	8.89	-	0.22	1.41	9.60
K2O	-	8.70	8.82	0.13	-	9.11	9.84	0.10	-	9.11	9.07	0.09
BaO	-	0.15	0.32	-	-	-	-	-	-	-	-	-
Total	99.96	93.26	92.52	98.49	100.02	94.08	93.63	98.90	101.38	94.00	93.93	98.84
Oxygens	12	22	22	8	12	22	22	8	12	22	22	8
Si	3.015	5.521	6.169	2.775	2.978	5.469	6.193	2.783	2.976	5.478	6.149	2.852
Ti	0.001	0.173	0.039	-	0.003	0.197	0.031	-	0.027	0.270	0.091	-
Al	1.961	3.294	5.557	1.206	2.020	3.363	5.456	1.212	1.983	3.304	5.497	1.146
Fe2+	2.429	2.549	0.129	-	1.984	2.684	0.208	-	2.242	2.357	0.155	-
Mn	0.081	0.004	0.002	-	0.588	0.017	0.003	-	0.170	0.010	0.001	-
Mg	0.336	2.224	0.114	-	0.165	1.992	0.196	-	0.435	2.255	0.156	-
Ca	0.184	0.002	-	0.246	0.271	0.002	0.001	0.226	0.171	0.001	0.000	0.159
Na	-	0.049	0.439	0.782	-	0.058	0.217	0.771	-	0.065	0.367	0.830
K	-	1.724	1.537	0.007	-	1.802	1.703	0.006	-	1.783	1.557	0.005
Ba	-	0.009	0.017	-	-	-	-	-	-	-	-	-
Sum	8.004	15.546	14.002	5.017	8.009	15.583	14.007	4.999	8.005	15.523	13.973	4.992
XMg	0.122	0.466	0.469	-	0.077	0.426	0.484	-	0.163	0.489	0.503	-
Mol% Alm	0.80	-	-	-	0.66	-	-	-	0.74	-	-	-
Mol% Spess	0.03	-	-	-	0.20	-	-	-	0.06	-	-	-
Mol% Pyr	0.11	-	-	-	0.05	-	-	-	0.14	-	-	-
Mol% Gross	0.06	-	-	-	0.09	-	-	-	0.06	-	-	-

Sample	JDW 93	JDW 93	JDW 93	JDW 93	JDW 154	JDW 154	JDW 154	JDW 154	JDW 155	JDW 155	JDW 155	JDW 155	JDW 155
Min	Grt	Bt	Ms	Pl	Grt	Bt	Ms	Pl	Grt	Bt	Ms	Pl	St
Average of	2	18	13		4	13	6	3	4	11	4	7	9
SiO2	37.83	35.53	45.68	61.19	37.70	35.41	47.34	61.53	37.72	35.84	46.17	62.37	27.85
TiO2	0.05	2.18	0.70	-	0.06	1.97	0.65	-	0.04	1.35	0.46	-	0.58
Al2O3	21.64	18.05	34.08	23.70	21.23	19.05	34.83	23.80	21.08	19.94	35.35	23.71	53.88
FeO	28.25	19.72	1.48	-	34.33	19.62	1.26	-	34.23	18.48	0.77	-	13.60
MnO	4.99	0.18	0.02	-	2.17	0.16	0.02	-	2.56	0.13	0.00	-	0.33
MgO	2.26	9.40	0.97	-	2.28	9.27	0.88	-	3.27	10.69	0.69	-	1.54
CaO	6.16	0.00	0.00	5.56	3.99	0.01	0.01	5.87	2.39	0.00	0.01	5.23	0.01
Na2O	-	0.16	0.81	8.22	-	0.27	0.83	8.15	-	0.35	1.28	8.81	-
K2O	-	9.16	9.78	0.12	-	8.80	9.54	0.14	-	8.91	9.50	0.12	-
BaO	-	-	-	-	-	0.14	0.22	-	-	-	-	-	-
Total	101.17	94.39	93.52	98.78	101.75	94.70	95.57	99.49	101.29	95.69	94.22	100.26	97.78
Oxygens	12	22	22	8	12	22	22	8	12	22	22	8	23
Si	2.991	5.470	6.188	2.746	2.991	5.419	6.250	2.744	2.998	5.382	6.174	2.758	3.863
Ti	0.003	0.252	0.071	-	0.003	0.226	0.065	-	0.002	0.152	0.046	-	0.060
Al	2.016	3.275	5.441	1.254	1.986	3.437	5.422	1.251	1.975	3.529	5.573	1.236	8.811
Fe2+	1.868	2.539	0.167	-	2.278	2.512	0.139	-	2.275	2.321	0.086	-	1.578
Mn	0.334	0.024	0.003	-	0.146	0.021	0.002	-	0.172	0.016	0.000	-	0.038
Mg	0.265	2.156	0.196	-	0.269	2.115	0.174	-	0.387	2.393	0.138	-	0.319
Ca	0.522	0.000	0.000	0.267	0.340	0.003	0.001	0.281	0.203	0.001	0.001	0.248	0.001
Na	-	0.048	0.214	0.715	-	0.080	0.211	0.705		0.102	0.331	0.755	-
K	-	1.799	1.690	0.007	-	1.718	1.607	0.008		1.708	1.620	0.007	-
Ba	-	-	-	-	-	0.009	0.011	-		-	-	-	-
Sum	7.998	15.563	13.971	4.988	8.013	15.536	13.883	4.988	8.012	15.605	13.969	5.004	14.671
XMg	0.124	0.459	0.538	-	0.106	0.457	0.557	-	0.145	0.508	0.614	-	0.168
Mol% Alm	0.62	-	-	-	0.75	-	-	-	0.75	-	-	-	-
Mol% Spess	0.11	-	-	-	0.05	-	-	-	0.06	-	-	-	-
Mol% Pyr	0.09	-	-	-	0.09	-	-	-	0.13	-	-	-	-
Mol% Gross	0.17	-	-	-	0.11	-	-	-	0.07	-	-	-	-

Sample	JDW 156	JDW 156	JDW 156	JDW 156	JDW 56	JDW 159A	JDW 159A	JDW 159A	JDW 159A	JDW 159B	JDW 159B	JDW 159B	JDW 159B
Min	Grt	Bt	Ms	Pl	St	Grt	Bt	Ms	Pl	Grt	Bt	Ms	Pl
Average of	2	6	5	6	5	7	12	12	6	1	8	6	9
SiO2	37.82	35.97	46.25	62.73	27.67	37.98	35.62	46.16	61.34	37.73	35.72	47.75	61.19
TiO2	0.04	1.78	0.44	-	0.65	0.02	2.16	0.63	-	0.02	2.15	0.70	-
Al2O3	21.26	19.66	35.96	23.33	53.94	21.00	18.97	34.60	23.94	21.35	18.98	35.40	23.62
FeO	34.64	18.92	0.95	0.17	12.88	33.48	18.90	1.29	-	32.47	18.22	1.16	-
MnO	0.86	0.06	0.02	-	0.25	3.84	0.17	0.02	-	3.07	0.18	0.01	-
MgO	3.26	9.74	0.58	-	1.22	3.35	9.54	0.79	-	3.23	10.05	0.84	-
CaO	2.58	0.00	0.00	4.98	0.04	2.18	0.01	0.00	5.65	3.33	0.02	0.00	5.76
Na2O	-	0.36	1.35	8.58	-	-	0.26	1.02	8.37	-	0.31	0.82	8.15
K2O	-	8.61	9.14	0.12	-	-	9.29	9.89	0.12	-	8.72	9.43	0.16
BaO	-	0.14	0.26	-	-	-	-	-		-	0.20	0.33	-
Total	100.46	95.24	94.95	99.91	96.66	101.85	94.92	94.39	99.43	101.20	94.54	96.43	98.87
Oxygens	12	22	22	8	23	12	22	22	8	12	22	22	8
Si	3.014	5.432	6.142	2.779	3.867	3.005	5.427	6.192	2.738	2.991	5.436	6.242	2.745
Ti	0.002	0.202	0.044	-	0.069	0.001	0.247	0.064	-	0.001	0.246	0.069	-
Al	1.997	3.500	5.630	1.219	8.888	1.958	3.406	5.470	1.259	1.995	3.406	5.455	1.249
Fe2+	2.308	2.390	0.106	0.006	1.505	2.214	2.408	0.144	-	2.153	2.319	0.127	-
Mn	0.059	0.009	0.003	-	0.030	0.257	0.022	0.002	-	0.206	0.023	0.002	-
Mg	0.387	2.192	0.114	-	0.254	0.395	2.167	0.158	-	0.382	2.279	0.163	-
Ca	0.221	0.002	0.000	0.236	0.011	0.185	0.003	0.000	0.270	0.283	0.008	0.000	0.277
Na	-	0.107	0.349	0.737	-	-	0.075	0.265	0.725	-	0.092	0.207	0.709
K	-	1.659	1.548	0.007	-	-	1.807	1.693	0.007	-	1.693	1.572	0.009
Ba	-	0.008	0.013	-	-	-	-	-		-	0.012	0.017	-
Sum	7.986	15.499	13.948	4.984	14.620	8.015	15.563	13.988	4.998	8.010	15.508	13.851	4.989
Xmg	0.144	0.479	0.522	-	0.144	0.151	0.474	0.523	-	0.151	0.496	0.564	-
Mol% Alm	0.78	-	-	-	-	0.73	-	-	-	0.71	-	-	-
Mol% Spess	0.02	-	-	-	-	0.08	-	-	-	0.07	-	-	-
Mol% Pyr	0.13	-	-	-	-	0.13	-	-	-	0.13	-	-	-
Mol% Gross	0.07	-	-	-	-	0.06	-	-	-	0.09	-	-	-

Sample	WAK 9	WAK 9	WAK 9	WAK 9	WAK 9	JDW 182	JDW 182	JDW 182	JDW 182	JDW 182	JDW 184	JDW 184	JDW 184	JDW 184
Min	Grt	Bt	Ms	Pl	St	Grt	Bt	Ms	Pl	Chl	Grt	Bt	Ms	Pl
Average of	2	8	5	6	14	2	13	15	4	15	13	7	1	6
SiO2	37.83	35.10	46.27	62.08	27.59	37.41	35.38	45.24	63.90	23.95	37.54	35.37	46.26	63.41
TiO2	0.02	1.46	0.44	-	0.61	0.03	1.48	0.42	-	0.09	0.02	2.28	0.54	-
Al2O3	21.10	19.59	35.76	23.76	53.77	20.55	17.44	33.21	21.81	20.97	21.14	19.11	34.83	22.53
FeO	34.32	19.12	0.89	-	12.83	30.75	20.39	2.74	-	25.54	32.84	19.83	1.37	0.07
MnO	2.27	0.10	0.01	-	0.25	7.06	0.14	0.05	-	0.29	5.00	0.17	0.04	-
MgO	3.22	9.77	0.60	-	1.49	2.02	9.49	0.69	-	14.05	2.60	8.64	0.87	-
CaO	2.52	0.06	0.00	5.25	0.06	2.47	0.00	0.01	3.37	0.00	2.04	0.03	0.00	4.19
Na2O	-	0.35	1.32	8.72	0.02	-	0.21	1.24	9.76	0.01	-	0.30	1.04	9.15
K2O	-	8.69	9.36	0.13	0.04	-	9.34	9.58	0.50	0.05	-	8.65	9.19	0.15
BaO	-	-	-	-	-	-	0.13	0.29	-	0.02	-	-	-	-
Total	101.27	94.24	94.65	99.94	96.64	100.28	94.00	93.46	99.34	84.98	101.18	94.38	94.14	99.51
Oxygens	12	22	22	8	23	12	22	22	8	14	12	22	22	8
Si	3.004	5.376	6.157	2.754	3.860	3.022	5.506	6.196	2.844	2.626	2.998	5.427	6.196	2.816
Ti	0.001	0.168	0.044	-	0.064	0.002	0.173	0.044	-	0.007	0.001	0.263	0.055	-
Al	1.975	3.536	5.609	1.242	8.866	1.957	3.200	5.362	1.144	2.710	1.990	3.455	5.498	1.179
Fe2+	2.279	2.452	0.099	-	1.500	2.078	2.654	0.314	-	2.341	2.193	2.545	0.153	0.003
Mn	0.152	0.013	0.002	-	0.029	0.483	0.019	0.006	-	0.027	0.339	0.022	0.005	-
Mg	0.382	2.231	0.119	-	0.309	0.244	2.201	0.140	-	2.296	0.310	1.975	0.174	-
Ca	0.214	0.011	0.000	0.249	0.009	0.213		0.004	0.161	0.001	0.175	0.005	0.000	0.199
Na	-	0.103	0.340	0.750	0.005	-	0.064	0.329	0.843	0.005	-	0.089	0.269	0.788
K	-	1.699	1.589	0.007	0.006	-	1.855	1.675	0.029	0.007	-	1.694	1.570	0.008
Ba	-	-	-	-	-	-	0.008	0.015	-	0.001	-	-	-	-
Sum	8.007	15.588	13.959	5.003	14.648	7.998	15.680	14.081	5.020	10.017	8.006	15.474	13.920	4.993
Xmg	0.143	0.477	0.543	-	0.171	0.105	0.454	0.308	-	0.495	0.124	0.437	0.531	-
Mol% Alm	0.75	-	-	-	-	0.69	-	-	-	-	0.73	-	-	-
Mol% Spess	0.05	-	-	-	-	0.16	-	-	-	-	0.11	-	-	-
Mol% Pyr	0.13	-	-	-	-	0.08	-	-	-	-	0.10	-	-	-
Mol% Gross	0.07	-	-	-	-	0.07	-	-	-	-	0.06	-	-	-

Sample	JDW 186	JDW 186	JDW 194	JDW 194	JDW 194	JDW 194
Min	Grt	Bt	Grt	Bt	Ms	Pl
Average of	2	12	2	8	8	14
SiO2	38.03	36.66	37.88	35.40	45.88	64.80
TiO2	0.02	1.46	0.03	2.35	0.70	-
Al2O3	20.97	17.84	20.86	18.63	34.69	21.05
FeO	33.81	16.29	32.38	20.65	1.28	-
MnO	3.26	0.09	4.23	0.29	0.01	-
MgO	4.03	12.00	2.32	7.62	0.68	-
CaO	0.98	0.02	3.30	0.02	0.00	2.79
Na2O	-	0.32	-	0.20	0.84	9.99
K2O	-	8.41	-	8.63	9.57	0.23
BaO	-	0.18	-	0.23	0.34	-
Total	101.08	93.27	100.99	94.02	94.00	98.87
Oxygens	12	22	12	22	22	8
Si	3.018	5.585	3.024	5.486	6.181	2.886
Ti	0.002	0.167	0.002	0.274	0.071	-
Al	1.962	3.204	1.963	3.403	5.510	1.105
Fe2+	2.244	2.076	2.162	2.676	0.145	-
Mn	0.219	0.012	0.286	0.038	0.002	-
Mg	0.476	2.725	0.276	1.761	0.137	-
Ca	0.084	0.006	0.282	0.006	0.001	0.133
Na	-	0.096	-	0.061	0.219	0.863
K	-	1.634	-	1.706	1.645	0.013
Ba	-	0.011	-	0.014	0.018	-
Sum	8.001	15.511	7.994	15.422	13.925	5.000
Xmg	0.175	0.568	0.113	0.397	0.489	-
Mol% Alm	0.74	-	0.72	-	-	-
Mol% Spess	0.07	-	0.10	-	-	-
Mol% Pyr	0.16	-	0.09	-	-	-
Mol% Gross	0.03	-	0.09	-	-	-

Appendix C

Whole-rock geochemistry: XRF analysis

C.1 Specimen preparation

For each sample, 200-1000 grams of fresh, unweathered rock was crushed in a jaw crusher. Approximately 100 grams of the resultant coarse crush was processed in a tungsten carbide swing mill to produce the whole-rock powder for XRF analysis.

Major elements were analysed on fused glass beads which were prepared as follows. Whole-rock powder was dried for ~12 hours at 1000°C to remove all H_2O. This was mixed in a 5:1 ratio with Spectrolux 100B flux ($LiBO_4$), which had been dried at 600°C for ~12 hours. The dried mixture was placed in a zirconia grained Pt-5%Au alloy crucible and heated to 1050°C for seven minutes. During this fusing process, the mixture was stirred at 2½ minute intervals to homogenise the liquid and avoid entrapment of gas bubbles. The melt was poured into a pre-warmed Pt-Au alloy casting mould and quenched over a jet of cool air. The crucible and mould were cleaned before each fusing in boiling 6M HCl.

Trace elements were analysed on pressed-powder pellets which were prepared by mixing 10 grams of whole-rock powder with 1 ml of *moivol* glue. The powder and glue were mixed using an agate pestle and mortar before being pressed in hydraulic piston for thirty seconds at ~7 tonnes pressure. The pellet was dried at 60°C for ~12 hours.

C.2 XRF specification and operating conditions

Major and trace element analyses were performed on a Philips PW1400 X-ray fluorescence wavelength-dispersive spectrometer in the Department of Earth Sciences, Oxford. X-rays were generated using a Rh tube, with LiF(22), LiF(200), PE and PX(1) diffracting crystals. The machine was calibrated using international geostandards. All analyses were performed by K. Parrish.

C.3 Limits of detection and errors in XRF analysis

XRF measurements are based on X-ray count rates at the relevant X-ray lines. In order to detect an element in a sample, the counting peak must be resolvable from the background radiation. Consequently, the time spent counting the X-rays and/or the concentration of the element must be sufficiently high to produce a suitably large peak X-ray/background ratio. The lowest concentration of specific elements that can be quantitatively determined under normal operating conditions ("limit of determination") has been defined by Potts (1987) and are shown in Table C1.

Element	ppm	Wt%
Si	1000	0.032
Ti	240	0.001
Al	600	0.078
Fe	260	0.004
Mn	240	0.001
Mg	1200	0.075
Ca	140	0.012
Na	2400	0.233
K	140	0.021
P	140	0.031
Ga	6	
Zn	9	
Cu	6	
Ni	6	
Co	6	
Cr	10	
V	10	
Ba	24	
Rb	3	
Sr	3	
Y	3	
Zr	6	
Nb	6	
Pb	6	
Th	9	
U	6	

Table C1: Detection limits for wavelength-dispersive XRF analyses. The ppm data is after Potts (1987) and represents the limit of determination for a wide variety of rock types under typical routine operating conditions. For major elements, glass bead values have been used. For trace elements, powder pellet values have been used. Major element oxides are normally quoted as a wt%, hence their limits of determination have also been expressed as such.

Consistent with XRF spectrometry as a whole, the precision of the Oxford XRF spectrometer is high, as illustrated by replicate analyses of single specimens (e.g. Bletcher, 1997). The mean analysis of a single sample that was measured ten times, together with the coefficients of variation (CV%=100xstandard deviation/mean analysis) are shown in Table C2.

Element	Average	CV%
SiO2	64.7	0.07
TiO2	0.65	0.34
Al2O3	16.04	0.1
Fe T	4.03	0.15
MnO	0.06	1.1
MgO	2.21	0.85
CaO	3.84	0.16
Na2O	4.12	0.49
K2O	3.19	0.14
P2O5	0.16	1.15
Total	99.01	
Ga	20.6	1.5
Zn	62.3	1.2
Cu	21.1	3.8
Ni	36.2	1.7
Co	23.3	9.4
Cr	54	3.4
V	72.1	2.4
Ba	11388.3	0.6
Rb	62.7	0.6
Sr	715.7	0.3
Y	12.6	4.5
Zr	174.4	0.3
Nb	8.8	4.1
Pb	21.1	4.5
Th	6.4	4.8
U	b.l.d.	b.l.d.

Table C2: Precision of the Oxford XRF spectrometer (after Bletcher, 1997). b.l.d. = below limit of detection

Appendix D

Whole-rock Rb-Sr analysis

D.1 Sample preparation, dissolution and separation

Depending upon the concentration of Sr in the sample (as determined by XRF analysis), either 100mg (for samples with >100ppm Sr), or 150mg (for samples with <100ppm Sr) of whole-rock powder was placed in FEP beakers. Complete rock dissolution was carried out by using 10ml concentrated HF and 1ml concentrated HNO3 and placing the beaker into PTFE evaporators with a flow of filtered air through them, and evaporated until incipient dryness. The residue was taken up in 4ml 3.0M HCl, sealed and left to dissolve for 2 hours. The solution was then placed in a centrifuge tube and spun at 2000rpm for 10 minutes in order to separate any residue.

Sr was extracted from the dissolved rock-forming elements using cation exchange on AG50W-X12 200-400 mesh resin in 3.0M HCl. The elution for the columns used in Oxford is as follows:

1. Equilibrate columns with 5ml of 3.0M HCl.
2. Load 2ml of the dissolved sample and allow columns to drain.
3. Pass 2 X 0.5ml of 3.0M HCl and allow columns to drain.
4. Pass 1ml of 3.0M HCl and allow columns to drain.
5. Pass 2ml of 3.0M HCl and allow columns to drain.
6. Pass 15ml of 3.0M HCl and allow columns to drain.
7. Pass and collect 8ml of 3.0M HCl containing the Sr fraction.

The columns were cleaned by repeated graded elution with water, 3.0M HCl and 6M HCl.

The Sr fractions were evaporated in PTFE evaporators. A drop of aqua-regia (concentrated HCl and concentrated HNO3 in the proportion 3:1) was added prior to evaporation to 'hard' dryness.

D.2 Mass spectrometer specifications and operating conditions

Analyses were performed on the VG Isomass 54E single collector mass spectrometer using a Faraday collector in the Age and Isotope Laboratory, Department of Earth Sciences, Oxford. Runs were automated by the Analyst computer program (Ludwig, 1992).

D.3 Elemental concentration determination

The whole-rock XRF analyses were used for Rb and Sr concentration determination.

D.4 Isotopic analysis

The samples were re-dissolved in 4µl of de-ionised water. 2µl of each sample plus 1µl of H3PO4 were places on a single Ta filament. The filaments were gently evaporated to dryness, then allowed to glow to a dull cherry-red colour by passing a small current though them.

Data was taken on 2-6v ^{88}Sr beams, usually obtained with filament current of 2.8A. The $^{87}Sr/^{86}Sr$ was normalised to $^{86}Sr/^{88}Sr = 0.1194$ (Steiger & Jeiger, 1977). The value of the NBS987 standard collected during the analytical runs was statistically identical to the published value, so no correction was necessary.

Appendix E

U-Pb analytical techniques

Isotope dilution thermal ionisation mass spetrometric (IDTIMS) techniques were used in an attempt to obtain relaible and precise U-Pb geochronological data from single grains of monazite, xenotime and urananite. All mineral chemistry and mineral analyses were performed at the Massachusetts Institute of Technology (MIT), in Boston, USA. Monazite, xenotime and urananite were separated from samples of metamorphic schists and leucogranites by standard crushing, heavy liquid and magnetic procedures. Individual crystals were measured, photographed and washed in acetone prior to dissolution. Samples were dissolved in 300µl teflon nanocapsules containing 11-12 N HCl and a mixed ^{205}Pb-^{233}U-^{235}U tracer solution. Mineral chemistry for all samples was performed by K. Davideck. To ensure complete dissolution, grains were dissolved for 30 to 48 hours at 180°C inside a Parr bomb and the contents subsequently dried down. An additional 150µl of 11-12 N HCl was added and the contents heated for a further 24 hours at 180°C inside a Parr bomb. Lead and uranium were separated from monazite, xenotime and urananite using HCl based ion exchange chromatography modified after Krogh (1973). The samples were analysed using conventional thermal ionization mass spectrometry on a VG Sector mass spectrometer. All analyses were performed by S. Bowring and M. Martin. Lead was analysed either: (1) in static mode, using Faraday detectors for all isotopes except ^{204}Pb, which was measured simultaneously with the Daly detector in ion counting mode; or (2) by peak-jumping using a Daly detector in ion counting mode. Uranium was analysed as a metal in static mode using Faraday collectors. Statistical analysis of the data uses the algorithms of Ludwig (1989). Additional analytical procedures can be found in Hawkins and Bowring (1997).

Appendix F

$^{40}Ar/^{39}Ar$ analytical techniques

Resistance furnace $^{40}Ar/^{39}Ar$ procedures were used in an attempt to obtain accurate and precise geochronological constraints on the closure ages of muscovites and biotites separated from metamorphic schists and leucogranite samples. Pure mineral separates of muscovites and biotites were prepared using standard crushing, magnetic and paper shaking techniques. In addition, samples were hand picked in ethanol in order to achieve the desired purity (>99%). All micas were washed consecutively in distilled water, methanol and acetone prior to being weighed (all samples weighed between 40-50mg) and wrapped in individual aluminium foil packets for irradiation. Samples were irradiated in position 5C at the McMaster University research reactor for a duration of 12 hours with Cd shielding. Reagent-grade CaF2, K2SO4 and KCl were included in the irradiation package to facilitate interference corrections. The fast neutron flux was monitored using Fish Canyon sanidine (27.95Ma, Renne *et al* 1994). Irradiated samples were analysed in the Cambridge Laboratory for Argon Isotope Research (CLAIR) at the Massachusetts Institute of Technology. All analyses were performed by M. Krol and B. Olszewski.

Resistance furnace extraction of gas from the mica samples was accomplished using a double-vacuum assembly, whilst laser fusion analysis of the Fish Canyon sanidine was achieved using a Coherent 10W Ar-ion laser in multi-line mode. Evolved gases were analysed with a MAP 215-50 mass spectrometer using a Faraday collector for furnace samples and an electron multiplier for laser samples. Analytical blanks for the MIT $^{40}Ar/^{39}Ar$ furnace extraction line vary as a function of temperature during incremental heating experiments. Over the course of this study, blanks at M/e 40 ranged from 1.7 x 10-15 moles at 900K to 6.6 x 10-15 at 1550 K. Calculation of the *J* parameter and corrections for interfering reactions were performed by K.V. Hodges at M.I.T. Additional laboratory procedures, descriptions of facilities and propagation of uncertainties can be found in Hodges *et al* (1994). The results of the stepwise heating analyses for each sample are shown in Table F1.

Table F1: $^{40}Ar/^{39}Ar$ data

Wak 3 Muscovite			J Value:	0.002884	±	0.000058					
step #	*Temperature (K)*	*$^{36}Ar/^{40}Ar$*	*$^{36}Ar/^{40}Ar$ error*	*$^{39}Ar/^{40}Ar$*	*$^{39}Ar/^{40}Ar$ error*	*$^{39}Ar_K$ (moles)*[1]	*Cumulative $^{39}Ar_K$ (%)*[2]	*$^{40}Ar^*$ (%)*[3]	*Age (Ma)*[4]	*Age error (Ma, w/ J)*[5]	*Age error (Ma, w/o J)*[6]
1	900	1.80E-03	1.05E-03	3.02E-02	4.69E-04	6.40E-15	0.18	46.73	78.72	51.04	51.02
2	950	2.02E-03	1.20E-03	5.59E-02	8.79E-04	1.10E-14	0.48	40.22	37.08	32.39	32.38
3	1000	1.99E-03	5.45E-04	4.76E-02	5.08E-04	2.14E-14	1.08	41.15	44.39	17.18	17.16
4	1050	2.74E-03	1.70E-04	3.62E-02	1.15E-04	4.14E-14	2.22	19.13	27.32	7.15	7.13
5	1100	2.44E-03	2.76E-04	5.32E-02	1.11E-04	7.78E-14	4.38	27.82	27.00	7.87	7.86
6	1150	2.06E-03	4.29E-05	8.09E-02	4.15E-05	6.54E-13	22.54	39.00	24.93	0.95	0.81
7	1200	4.07E-04	5.64E-05	2.08E-01	3.13E-04	1.30E-12	58.64	87.89	21.91	0.60	0.41
8	1250	5.54E-04	6.78E-05	1.89E-01	3.81E-04	6.02E-13	75.35	83.55	22.91	0.71	0.55
9	1350	1.33E-03	1.13E-04	1.32E-01	1.46E-04	3.45E-13	84.91	60.81	23.88	1.39	1.31
10	1550	9.14E-04	6.49E-05	1.54E-01	2.00E-04	5.44E-13	100.00	72.95	24.48	0.80	0.64

Wak 3 Biotite			J Value:	0.002904	±	0.000090					
step #	*Temperature (K)*	*$^{36}Ar/^{40}Ar$*	*$^{36}Ar/^{40}Ar$ error*	*$^{39}Ar/^{40}Ar$*	*$^{39}Ar/^{40}Ar$ error*	*$^{39}Ar_K$ (moles)*[1]	*Cumulative $^{39}Ar_K$ (%)*[2]	*$^{40}Ar^*$ (%)*[3]	*Age (Ma)*[4]	*Age error (Ma, w/ J)*[5]	*Age error (Ma, w/o J)*[6]
1	900	1.80E-03	2.17E-04	3.23E-02	4.12E-04	1.09E-14	0.29	46.8	74.37	10.28	10.03
2	950	1.71E-03	8.20E-05	4.50E-02	2.21E-04	4.56E-14	1.52	49.39	56.68	3.25	2.75
3	1000	1.34E-03	3.17E-05	5.17E-02	9.84E-05	1.33E-13	5.08	60.29	60.06	2.04	0.93
4	1050	6.14E-04	2.18E-05	6.96E-02	5.02E-05	4.02E-13	15.88	81.84	60.57	1.9	0.47
5	1100	1.44E-04	1.22E-05	8.37E-02	5.98E-05	5.05E-13	29.46	95.7	58.94	1.8	0.22
6	1150	1.78E-04	2.10E-05	8.66E-02	1.19E-04	3.09E-13	37.77	94.71	56.43	1.75	0.37
7	1175	1.14E-04	4.86E-05	9.63E-02	1.69E-04	1.43E-13	41.6	96.59	51.85	1.75	0.76
8	1200	9.97E-05	4.10E-05	9.28E-02	1.77E-04	1.29E-13	45.06	97.01	53.98	1.77	0.67
9	1250	9.98E-05	1.93E-05	8.63E-02	8.04E-05	2.58E-13	51.99	97.01	57.99	1.79	0.34
10	1350	1.04E-04	4.75E-06	8.61E-02	5.52E-05	1.40E-12	89.68	96.9	58.07	1.77	0.09
11	1550	8.36E-05	3.20E-05	8.51E-02	7.87E-05	3.84E-13	100	97.49	59.06	1.88	0.57

Table F1 (continued): $^{40}Ar/^{39}Ar$ data

Wak 6 Muscovite			J Value:	0.002884	±	0.000058					
step #	*Temperature (K)*	*$^{36}Ar/^{40}Ar$*	*$^{36}Ar/^{40}Ar$ error*	*$^{39}Ar/^{40}Ar$*	*$^{39}Ar/^{40}Ar$ error*	*$^{39}Ar_K$ (moles)[1]*	*Cumulative $^{39}Ar_K$ (%)[2]*	*$^{40}Ar^*$ (%)[3]*	*Age (Ma)[4]*	*Age error (Ma, w/ J)[5]*	*Age error (Ma, w/o J)[6]*
1	900	3.57E-03	1.17E-03	6.80E-02	1.24E-03	7.65E-15	0.25	0.01	< 0.01	26.50	26.50
2	950	4.12E-03	1.66E-03	1.31E-01	1.63E-03	1.56E-14	0.76	0.01	< 0.01	19.61	19.61
3	1000	1.92E-03	4.08E-04	6.88E-02	4.03E-04	3.25E-14	1.82	43.41	32.56	8.98	8.96
4	1050	2.32E-03	4.42E-04	7.90E-02	3.53E-04	6.45E-14	3.93	31.45	**20.59**	8.52	8.51
5	1100	8.87E-04	2.48E-04	1.75E-01	3.95E-04	1.34E-13	8.30	73.71	**21.75**	2.19	2.15
6	1150	9.15E-04	5.73E-05	1.69E-01	1.99E-03	3.69E-13	20.35	72.89	**22.39**	0.73	0.58
7	1200	1.07E-04	7.13E-05	2.31E-01	4.74E-03	1.05E-12	54.58	96.73	**21.64**	0.77	0.64
8	1250	1.37E-04	6.78E-05	2.30E-01	3.61E-03	5.43E-13	72.34	95.84	**21.60**	0.71	0.56
9	1350	5.84E-04	1.01E-04	1.87E-01	2.16E-03	3.01E-13	82.16	82.66	**22.85**	0.98	0.87
10	1550	4.44E-04	7.02E-05	2.00E-01	3.82E-03	5.46E-13	100.00	86.80	**22.51**	0.84	0.71

Wak 6 Biotite			J Value:	0.002865	±	0.000087					
step #	*Temperature (K)*	*$^{36}Ar/^{40}Ar$*	*$^{36}Ar/^{40}Ar$ error*	*$^{39}Ar/^{40}Ar$*	*$^{39}Ar/^{40}Ar$ error*	*$^{39}Ar_K$ (moles)[1]*	*Cumulative $^{39}Ar_K$ (%)[2]*	*$^{40}Ar^*$ (%)[3]*	*Age (Ma)[4]*	*Age error (Ma, w/ J)[5]*	*Age error (Ma, w/o J)[6]*
1	900	2.60E-03	2.72E-04	1.62E-02	6.69E-04	4.31E-15	0.1	23.32	72.73	24.85	24.75
2	950	2.04E-03	3.80E-04	3.68E-02	1.05E-03	8.18E-15	0.28	39.85	55.16	15.46	15.37
3	1000	1.96E-03	1.27E-04	3.75E-02	2.41E-04	3.54E-14	1.08	42.02	57.04	5.32	5.04
4	1050	1.46E-03	3.62E-05	5.32E-02	1.07E-04	1.49E-13	4.46	56.82	54.41	1.91	1.01
5	1100	5.46E-04	2.22E-05	7.78E-02	8.74E-05	4.02E-13	13.57	83.83	54.9	1.69	0.43
6	1150	2.26E-04	1.51E-05	8.29E-02	6.49E-05	4.17E-13	23.01	93.28	57.27	1.73	0.27
7	1200	1.64E-04	1.80E-05	8.44E-02	7.54E-05	3.74E-13	31.48	95.12	57.35	1.74	0.32
8	1250	7.79E-05	3.56E-05	8.66E-02	6.71E-05	3.72E-13	39.91	97.66	57.39	1.82	0.61
9	1300	8.15E-05	1.46E-05	8.76E-02	6.41E-05	3.87E-13	48.66	97.55	56.7	1.71	0.25
10	1350	6.90E-05	6.99E-06	8.93E-02	4.70E-05	6.08E-13	62.42	97.92	55.84	1.67	0.12
11	1550	6.01E-05	1.59E-06	8.55E-02	6.19E-05	1.66E-12	100	98.18	58.41	1.74	0.05

Table F1 (continued): $^{40}Ar/^{39}Ar$ data

Wak 9 Muscovite			J Value:	0.002884	±	0.000058					
step #	*Temperature (K)*	$^{36}Ar/^{40}Ar$	$^{36}Ar/^{40}Ar$ *error*	$^{39}Ar/^{40}Ar$	$^{39}Ar/^{40}Ar$ *error*	$^{39}Ar_K$ *(moles)* [1]	*Cumulative* $^{39}Ar_K$ *(%)* [2]	$^{40}Ar^*$*(%)* [3]	*Age (Ma)* [4]	*Age error (Ma, w/ J)* [5]	*Age error (Ma, w/o J)* [6]
1	900	2.51E-03	6.92E-04	5.12E-02	4.57E-04	1.02E-14	0.31	25.95	**26.18**	20.48	20.47
2	950	1.65E-03	2.77E-03	9.07E-02	7.95E-04	1.55E-14	0.78	51.16	**29.12**	46.20	46.19
3	1000	2.69E-03	2.58E-04	3.88E-02	3.70E-04	2.81E-14	1.64	20.48	**27.24**	10.10	10.08
4	1050	2.73E-03	2.86E-04	5.50E-02	2.27E-04	5.11E-14	3.19	19.33	**18.19**	7.92	7.91
5	1100	2.28E-03	1.94E-04	8.21E-02	2.66E-04	1.18E-13	6.76	32.62	**20.55**	3.61	3.59
6	1150	1.41E-03	7.12E-04	1.78E-01	8.91E-02	9.25E-13	34.85	58.44	**16.98**	14.43	14.42
7	1200	3.21E-04	6.29E-05	2.31E-01	6.47E-04	9.15E-13	62.66	90.42	**20.31**	0.58	0.42
8	1250	6.31E-04	1.27E-04	2.02E-01	3.22E-04	4.04E-13	74.92	81.29	**20.89**	1.05	0.96
9	1350	1.25E-03	1.21E-04	1.61E-01	2.94E-04	2.66E-13	83.00	63.15	**20.26**	1.21	1.14
10	1550	7.43E-04	9.96E-05	1.78E-01	1.59E-02	5.60E-13	100.00	77.96	**22.62**	2.65	2.61

Wak 9 Biotite			J Value	0.002904	±	0.000090					
step #	*Temperature (K)*	$^{36}Ar/^{40}Ar$	$^{36}Ar/^{40}Ar$ *error*	$^{39}Ar/^{40}Ar$	$^{39}Ar/^{40}Ar$ *error*	$^{39}Ar_K$ *(moles)* [1]	*Cumulative* $^{39}Ar_K$ *(%)* [2]	$^{40}Ar^*$*(%)* [3]	*Age (Ma)* [4]	*Age error (Ma, w/ J)* [5]	*Age error (Ma, w/o J)* [6]
1	900	2.57E-03	2.54E-04	2.62E-02	2.96E-04	1.02E-14	0.28	24.07	47.55	14.69	14.62
2	950	3.01E-03	1.42E-04	3.63E-02	1.48E-04	3.91E-14	1.37	11.05	15.87	6.04	6.02
3	1000	2.30E-03	8.73E-05	5.71E-02	7.92E-05	1.45E-13	5.4	32.12	29.25	2.5	2.33
4	1050	1.40E-03	3.70E-05	1.11E-01	1.08E-04	3.78E-13	15.91	58.5	27.42	0.98	0.51
5	1100	4.37E-04	2.25E-05	1.73E-01	3.12E-04	4.96E-13	29.72	87.01	26.23	0.83	0.2
6	1150	3.34E-04	6.43E-05	1.80E-01	3.42E-04	2.91E-13	37.81	90.06	26	0.97	0.55
7	1200	2.82E-04	1.88E-05	1.83E-01	1.83E-04	2.99E-13	46.13	91.6	26.04	0.81	0.16
8	1250	3.06E-04	3.70E-05	1.83E-01	3.14E-04	2.57E-13	53.27	90.88	25.84	0.85	0.31
9	1300	3.11E-04	2.22E-05	1.86E-01	2.12E-04	5.73E-13	69.23	90.71	25.35	0.8	0.18
10	1350	2.98E-04	3.13E-05	1.86E-01	1.82E-04	5.31E-13	84	91.12	25.58	0.83	0.26
11	1550	3.18E-04	1.83E-05	1.86E-01	1.77E-04	5.75E-13	100	90.51	25.41	0.79	0.15

Table F1 (continued): $^{40}Ar/^{39}Ar$ data

Wak 21 Muscovite			J Value:	0.002884	±	0.000058					
step #	*Temperature (K)*	*$^{36}Ar/^{40}Ar$*	*$^{36}Ar/^{40}Ar$ error*	*$^{39}Ar/^{40}Ar$*	*$^{39}Ar/^{40}Ar$ error*	*$^{39}Ar_K$ (moles)*[1]	*Cumulative $^{39}Ar_K$ (%)*[2]	*$^{40}Ar^*$ (%)*[3]	*Age (Ma)*[4]	*Age error (Ma, w/ J)*[5]	*Age error (Ma, w/o J)*[6]
1	900	2.64E-03	5.78E-04	2.67E-02	6.64E-04	9.40E-15	0.22	21.93	42.28	32.55	32.54
2	950	2.03E-03	6.33E-04	5.29E-02	1.53E-04	1.31E-14	0.53	39.90	38.87	18.04	18.03
3	1000	2.36E-03	4.41E-04	4.20E-02	2.74E-04	2.49E-14	1.12	30.42	37.33	15.84	15.83
4	1050	2.82E-03	2.01E-04	4.76E-02	7.90E-04	4.65E-14	2.23	16.70	**18.17**	6.51	6.50
5	1100	2.35E-03	1.13E-04	7.33E-02	6.49E-04	8.91E-14	4.35	30.50	**21.53**	2.39	2.35
6	1150	2.54E-03	5.89E-05	6.09E-02	5.25E-05	2.67E-13	10.68	25.02	**21.27**	1.53	1.47
7	1200	1.21E-03	5.05E-05	1.58E-01	1.54E-04	1.22E-12	39.73	64.15	**20.99**	0.64	0.49
8	1250	8.46E-04	6.45E-05	1.89E-01	1.96E-04	9.59E-13	62.51	74.94	**20.57**	0.66	0.52
9	1300	1.33E-03	5.95E-05	1.52E-01	5.11E-04	4.21E-13	72.51	60.58	**20.61**	0.73	0.60
10	1350	1.43E-03	1.48E-04	1.41E-01	2.25E-04	2.92E-13	79.45	57.73	**21.14**	1.65	1.59
11	1550	7.83E-04	7.92E-05	1.86E-01	1.82E-04	8.65E-13	100.00	76.80	**21.40**	0.78	0.65

Wak 23 Muscovite			J Value:	0.002884	±	0.000058					
step #	*Temperature (K)*	*$^{36}Ar/^{40}Ar$*	*$^{36}Ar/^{40}Ar$ error*	*$^{39}Ar/^{40}Ar$*	*$^{39}Ar/^{40}Ar$ error*	*$^{39}Ar_K$ (moles)*[1]	*Cumulative $^{39}Ar_K$ (%)*[2]	*$^{40}Ar^*$ (%)*[3]	*Age (Ma)*[4]	*Age error (Ma, w/ J)*[5]	*Age error (Ma, w/o J)*[6]
1	900	2.84E-03	3.67E-04	1.53E-02	2.17E-04	8.42E-15	0.19	16.08	53.78	35.73	35.72
2	950	2.48E-03	7.72E-04	4.14E-02	5.18E-04	1.26E-14	0.46	26.79	33.35	28.16	28.16
3	1000	2.97E-03	1.92E-04	3.32E-02	3.16E-04	2.38E-14	0.99	12.26	19.10	8.80	8.79
4	1050	2.68E-03	2.35E-04	4.34E-02	1.01E-04	4.43E-14	1.97	20.74	24.72	8.24	8.22
5	1100	2.66E-03	1.36E-04	6.60E-02	7.41E-04	8.71E-14	3.89	21.33	16.75	3.19	3.18
6	1150	2.61E-03	5.27E-05	5.32E-02	9.19E-05	2.49E-13	9.39	22.82	22.18	1.57	1.51
7	1200	1.40E-03	5.37E-05	1.51E-01	1.39E-04	1.21E-12	36.08	58.70	**20.15**	0.67	0.54
8	1250	9.20E-04	6.07E-05	1.81E-01	5.27E-04	7.29E-13	52.18	72.75	**20.85**	0.66	0.52
9	1350	1.37E-03	7.23E-05	1.51E-01	1.66E-04	6.33E-13	66.17	59.62	**20.43**	0.83	0.73
10	1550	7.32E-04	5.70E-05	2.00E-01	2.58E-04	1.53E-12	100.00	78.28	**20.25**	0.59	0.43

Table F1 (continued): $^{40}Ar/^{39}Ar$ data

Wak 23 Biotite			J Value:	0.002884	±	0.000058					
step #	*Temperature (K)*	*$^{36}Ar/^{40}Ar$*	*$^{36}Ar/^{40}Ar$ error*	*$^{39}Ar/^{40}Ar$*	*$^{39}Ar/^{40}Ar$ error*	*$^{39}Ar_K$ (moles)* [1]	*Cumulative $^{39}Ar_K$ (%)* [2]	*$^{40}Ar^*$ (%)* [3]	*Age (Ma)* [4]	*Age error (Ma, w/ J)* [5]	*Age error (Ma, w/o J)* [6]
1	900	3.26E-03	1.50E-04	2.16E-02	1.30E-04	4.00E-14	1.01	3.64	8.75	10.62	10.62
2	950	2.81E-03	1.21E-04	4.25E-02	1.03E-04	7.27E-14	2.85	16.84	**20.53**	4.35	4.33
3	1000	2.37E-03	1.51E-04	7.61E-02	1.03E-04	2.54E-13	9.28	30.09	**20.47**	3.05	3.02
4	1050	1.15E-03	5.57E-05	1.66E-01	1.68E-04	8.31E-13	30.29	65.90	**20.57**	0.65	0.51
5	1100	3.50E-04	7.57E-05	2.23E-01	3.22E-04	5.97E-13	45.39	89.57	**20.81**	0.66	0.52
6	1150	7.28E-04	2.82E-04	2.07E-01	3.18E-04	2.03E-13	50.52	78.40	**19.64**	2.11	2.07
7	1175	8.42E-04	2.74E-04	1.82E-01	3.17E-04	1.03E-13	53.14	75.05	**21.38**	2.33	2.29
8	1200	8.39E-04	1.88E-04	1.78E-01	3.19E-04	1.54E-13	57.03	75.14	**21.88**	1.67	1.61
9	1250	1.09E-03	8.61E-05	1.67E-01	1.53E-04	4.86E-13	69.32	67.72	**21.04**	0.89	0.79
10	1300	5.96E-04	6.67E-05	2.05E-01	2.49E-04	1.00E-12	94.67	82.29	**20.80**	0.65	0.50
11	1350	3.77E-04	4.25E-04	1.95E-01	7.55E-04	9.90E-14	97.17	88.78	**23.57**	3.34	3.31
12	1550	8.76E-04	2.64E-04	1.86E-01	4.88E-04	1.12E-13	100.00	74.05	**20.63**	2.20	2.16

Wak 26 Muscovite			J Value:	0.002884	±	0.000058					
step #	*Temperature (K)*	*$^{36}Ar/^{40}Ar$*	*$^{36}Ar/^{40}Ar$ error*	*$^{39}Ar/^{40}Ar$*	*$^{39}Ar/^{40}Ar$ error*	*$^{39}Ar_K$ (moles)* [1]	*Cumulative $^{39}Ar_K$ (%)* [2]	*$^{40}Ar^*$ (%)* [3]	*Age (Ma)* [4]	*Age error (Ma, w/ J)* [5]	*Age error (Ma, w/o J)* [6]
1	900	2.76E-03	4.91E-04	2.57E-02	3.02E-04	1.10E-14	0.21	18.48	36.99	28.74	28.73
2	950	2.98E-03	7.67E-04	5.25E-02	6.24E-04	1.53E-14	0.50	11.92	11.78	22.32	22.32
3	1000	2.99E-03	5.78E-04	5.77E-02	3.43E-04	2.95E-14	1.06	11.68	10.52	15.32	15.31
4	1050	2.63E-03	2.82E-04	4.73E-02	1.28E-04	4.99E-14	2.00	22.43	24.53	9.05	9.04
5	1100	2.05E-03	1.70E-04	8.75E-02	2.12E-04	1.14E-13	4.14	39.40	23.28	2.98	2.94
6	1150	2.50E-03	4.85E-05	7.41E-02	2.43E-04	2.67E-13	9.19	26.09	18.24	1.07	1.00
7	1200	1.47E-03	4.35E-05	1.37E-01	1.03E-04	1.17E-12	31.25	56.58	**21.34**	0.64	0.48
8	1250	6.62E-04	5.39E-05	1.99E-01	2.64E-04	1.20E-12	53.92	80.35	**20.89**	0.59	0.41
9	1300	1.07E-03	7.24E-05	1.67E-01	1.77E-04	6.82E-13	66.80	68.27	**21.15**	0.78	0.66
10	1350	1.14E-03	5.17E-05	1.63E-01	8.04E-04	4.46E-13	75.23	66.39	**21.03**	0.65	0.50
11	1550	6.50E-04	6.33E-05	1.98E-01	2.27E-04	1.31E-12	100.00	80.72	**21.11**	0.64	0.49

Table F1 (continued): $^{40}Ar/^{39}Ar$ data

Wak 27 Muscovite			J Value:	0.002884	±	0.000058					
step #	*Temperature (K)*	*$^{36}Ar/^{40}Ar$*	*$^{36}Ar/^{40}Ar$ error*	*$^{39}Ar/^{40}Ar$*	*$^{39}Ar/^{40}Ar$ error*	*$^{39}Ar_K$ (moles)*[1]	*Cumulative $^{39}Ar_K$ (%)*[2]	*$^{40}Ar^*$ (%)*[3]	*Age (Ma)*[4]	*Age error (Ma, w/ J)*[5]	*Age error (Ma, w/o J)*[6]
1	900	3.09E-03	3.78E-04	1.72E-02	5.03E-04	9.01E-15	0.22	8.64	25.93	33.32	33.32
2	950	2.43E-03	1.13E-03	3.79E-02	8.69E-04	1.22E-14	0.52	28.07	38.12	44.82	44.81
3	1000	2.38E-03	3.34E-04	3.57E-02	2.55E-04	2.39E-14	1.10	29.76	42.83	14.05	14.02
4	1050	2.95E-03	2.14E-04	3.31E-02	7.84E-05	4.63E-14	2.23	12.77	**19.95**	9.85	9.85
5	1100	2.62E-03	1.52E-04	5.76E-02	1.76E-04	9.22E-14	4.48	22.66	**20.35**	4.03	4.01
6	1150	2.35E-03	4.61E-05	7.92E-02	8.87E-05	3.70E-13	13.51	30.41	**19.88**	0.97	0.89
7	1175	1.27E-03	8.13E-05	1.63E-01	1.62E-04	6.61E-13	29.63	62.49	**19.83**	0.85	0.76
8	1200	6.87E-04	8.76E-05	2.02E-01	2.49E-04	5.78E-13	43.73	79.63	**20.42**	0.77	0.66
9	1250	8.60E-04	7.24E-05	1.88E-01	2.17E-04	7.03E-13	60.89	74.51	**20.55**	0.72	0.59
10	1300	1.39E-03	7.20E-05	1.49E-01	1.65E-04	3.89E-13	70.38	58.81	**20.38**	0.84	0.73
11	1350	1.45E-03	2.14E-04	1.44E-01	2.97E-04	2.83E-13	77.30	57.09	**20.53**	2.30	2.26
12	1550	8.36E-04	6.50E-05	1.87E-01	2.38E-04	9.31E-13	100.00	75.22	**20.88**	0.67	0.53

Wak 27 Biotite			J Value:	0.002884	±	0.000058					
step #	*Temperature (K)*	*$^{36}Ar/^{40}Ar$*	*$^{36}Ar/^{40}Ar$ error*	*$^{39}Ar/^{40}Ar$*	*$^{39}Ar/^{40}Ar$ error*	*$^{39}Ar_K$ (moles)*[1]	*Cumulative $^{39}Ar_K$ (%)*[2]	*$^{40}Ar^*$ (%)*[3]	*Age (Ma)*[4]	*Age error (Ma, w/ J)*[5]	*Age error (Ma, w/o J)*[6]
1	900	2.88E-03	5.24E-04	4.78E-02	3.37E-04	1.98E-14	0.52	15.03	**16.28**	16.70	16.70
2	950	2.80E-03	2.70E-04	5.82E-02	2.92E-04	3.85E-14	1.52	17.37	**15.47**	7.08	7.08
3	1000	1.95E-03	3.25E-04	9.30E-02	2.64E-04	1.40E-13	5.17	42.47	**23.62**	5.32	5.30
4	1050	1.08E-03	7.59E-05	1.73E-01	2.14E-04	5.67E-13	19.99	67.92	**20.33**	0.78	0.67
5	1100	1.17E-04	9.39E-05	2.49E-01	3.45E-04	8.41E-13	41.97	96.41	**20.03**	0.70	0.57
6	1150	1.31E-04	1.25E-04	2.55E-01	4.55E-04	3.52E-13	51.18	96.02	**19.51**	0.84	0.75
7	1200	1.60E-04	2.19E-04	2.44E-01	5.54E-04	2.35E-13	57.31	95.17	**20.24**	1.42	1.37
8	1250	2.44E-04	1.47E-04	2.44E-01	4.17E-04	4.19E-13	68.26	92.68	**19.65**	1.00	0.92
9	1300	2.18E-04	1.02E-04	2.40E-01	3.97E-04	5.06E-13	81.49	93.43	**20.17**	0.76	0.65
10	1350	1.62E-04	1.32E-04	2.44E-01	4.29E-04	4.84E-13	94.14	95.09	**20.21**	0.91	0.82
11	1550	3.88E-04	2.68E-04	2.30E-01	4.96E-04	2.24E-13	100.00	88.43	**19.94**	1.82	1.77

All uncertainties reported at the 2s level

1: Moles of 39Ar derived from neutron bombardment of 39K.

2: Cumulative percentage of 39K- derived 39Ar.

3: Percentage of 40Ar derived from radioactive decay of 40K.

4: Bold values indicate steps defining a plateau.

5: Includes propagated uncertainty in J.

6: Does not include propagated uncertainty in J.